Modeling ductile damage for complex loading paths

Trong Son Cao

ParisTech
INSTITUT DES SCIENCES ET TECHNOLOGIES
PARIS INSTITUTE OF TECHNOLOGY

MINES ParisTech

Ecole doctorale n° 364 : Sciences fondamentales et appliquées

Doctorat ParisTech

T H È S E

pour obtenir le grade de docteur délivré par

l'École nationale supérieure des mines de Paris

Spécialité "Sciences et génie des matériaux – Materials science and engineering"

présentée et soutenue publiquement par

Trong Son CAO

le 03 Octobre 2013

Modeling ductile damage for complex loading paths

Modélisation de l'endommagement ductile sous trajets de chargement complexes

Directeur de thèse : **Pierre-Olivier BOUCHARD**
Directeur de thèse : **Pierre MONTMITONNET**

Jury

M. José CESAR DE SA, Professeur, Department of Mechanical Engineering, University of Porto	Rapporteur
M. Pierre-Yves MANACH, Professeur, Directeur du LIMATB, Université de Bretagne-Sud	Rapporteur
M. Jacques BESSON, Directeur de recherche CNRS, Directeur du CDM, Mines Paristech	Examinateur
Mme Anne-Marie HABRAKEN, Directrice de recherche FNRS, MS²F-ArCEnCo, Université de Liège	Présidente du jury
M. Eric MAIRE, Directeur de recherche CNRS, MATEIS, INSA Lyon	Examinateur
M. Pierre-Olivier BOUCHARD, Docteur, HDR, CEMEF, Mines Paristech	Examinateur
M. Pierre MONTMITONNET, Directeur de recherche CNRS, CEMEF, Mines Paristech	Examinateur
M. Christian BOBADILLA, Ingénieur, ArcelorMittal Research and Development, Gandrange	Invité
M. Christophe VACHEY, Ingénieur, Ugitech Research and Development, Ugine	Invité

MINES ParisTech
CEMEF – UMR CNRS 7635
1, Rue Claude Daunesse, BP 207, 06904, Sophia-Antipolis Cedex, France

T H E S E

This page is intentionally left blank.

Acknowledgments

First of all, I would like to thank Mr. B. Legait as well as Mr. Y. Chastel, who were at the beginning of my thesis, director of Mines Paristech and director of Center for material forming (CEMEF), for giving me the opportunity to carry out my PhD thesis in this center.

I would like to express my deepest appreciation to my thesis advisers, Pierre-Olivier Bouchard and Pierre Montmitonnet, for their guidance, encouragement, support and patience during my three years at Cemef. My special thanks to Pierre-Olivier for the encouragement during the difficult periods, for the "humiliate" ping-pong match that helped me to restart my sporting program. My sincere gratitude to Pierre, who inspired me the passion of research, for his presence, his inspiration and his knowledge.

I wish to express my sincere gratefulness to the members of my PhD thesis committee, Mr. José Cesar De Sa, Mr. Pierre-Yves Manach, Mr. Jacques Besson, Mme Anne-Marie Habraken and Mr. Eric Maire, for taking time to assess my work. It is my great honor to have you in this committee. I would like to thank my industrial advisers, Mr. Christian Bobadilla, Mr. Alexis Gaillac and Mr. Christophe Vachey for attending my thesis defense.

During my 3 years, many people helped me to achieve my work. I gratefully acknowledge the help of Gilbert, Francis and Marc in performing mechanical tests at Cemef; Didier, Christophe, and Alexis for their helps during my stay at Cezus and Ugitech research centers. I would like also to acknowledge the people at ArcelorMittal Gandrange research center for their helps during my stays, thank Agathe Gillet, Antoine Cailliez, for the metallurgical training, Christian Bobadilla, Nicolas Persem for supplying the processes simulations. I want to thank Sylvain Foissey's team in ArcelorMittal Bourg-en-Bresse research center, for showing me the real industrial processes and passing their knowledge on steel forming. I do not forger, for sure, Patrice Lasne at Transvalor, for his helps in numerical implementation work in Forge2009®.

I would like to thank all the administrative staffs for their helps and administrative advices, especially Marie-Françoise Guenegan for her special attention to PhD students, Françoise Trucas for helping me each year to complete my visa renewal procedure, Genevieve Anseeuw for her helps for all the travels during my 3 years, Patrick Coels for his kind advices about life and career. I also want to thank all my friends at Cemef: Jean-Marie, who helped me a lot at the beginning; Siham, Ana Laura, Takao, my "lunch" friends; Benjamin and Stefen for the memorable Esaform conference; Fadi, Rebecca, Ugo, Michel, Koffi for the funny time together and unforgettable souvenir at Giens. Special thanks to my two office-mates: Ziad and Matthieu, two funny guys. Thanks to you two, my time in office was not just working time. I also would like to thank the bus 230 Nice-Sophia Antipolis, in which I spent two hours per day to go and return from work. These two valuable hours each day helped me to complete most of my bibliographical study.

Special thanks are due to professor Kim Son Doan at Ecole National Supérieure de Mécanque et d'Aérotechnique (Ensma) who interviewed me and gave me the occasion to carry out my study in France; to Jean-Michel Stephan, former researcher at Renardière research center, EDF R&D, who encouraged and recommended me to do a PhD.

Finally, I would like to express my deepest thanks to my father, my elder sister and brother for their continuing support of my study from elementary school all the way to PhD degree. At this time, I think about my Mother, who passed away since I was a child, who could not see the day I became a student, an engineer, and now, a PhD. This thesis is dedicated to her. Last but not least, my "fiancée", Minh Thu, who gave me love, strength and time to complete this work, who was always present whenever I needed. Thanks to her Vietnamese food, I have gained 5 kg in three years ◡̈.

Contents

List of Figures

List of Tables

Notation

In the present manuscript, the references were constructed in a friendly way so that readers can easily access to. For the electronic version, readers can click directly on the title of the documents, which are in blue, to access directly to the electronic version of that reference (with internet connection and journals subscription evidently). The references with the normal color title are the documents that the present author could not find any of their copies via the internet.

Throughout the manuscript, the following notations are employed. These notations might be recalled in each section involved.

- The bold-face symbols are used for second order tensor (e.g. $\boldsymbol{\sigma}$: stress tensor); the underlined bold-face symbols or underlined symbols are used for vector (e.g. $\underline{\boldsymbol{H}}^{\boldsymbol{\alpha}}$: vector of internal state variables); the undertilded bold-face symbols are used for 4^{th} order tensor (e.g. $\underset{\sim}{\underset{\sim}{\boldsymbol{D}}}$: the 4^{th} order tangent tensor); the **(:)** symbol represents the doubly contracted tensor product (e.g. $(\underset{\sim}{\underset{\sim}{\boldsymbol{D}}} : \boldsymbol{\epsilon})_{ij} = D_{ijkl}\epsilon_{kl}$); the $\bullet$ symbol represents the matrix product; the $\otimes$ symbol represents the tensor product or the dyadic product (e.g. $(\boldsymbol{I} \otimes \boldsymbol{I})_{ijkl} = \boldsymbol{I}_{ij}\boldsymbol{I}_{kl}$).
- For all the variables X, the notation $\dot{X}$ represents the material derivative of X with respect to the physical time t.

Remark The present study only deals with ductile damage. All the terms linked with damage (e.g. damage models, mechanisms, etc.) must be interpreted as *ductile damage* (e.g. ductile damage models, ductile damage mechanisms, etc.), unless otherwise indicated.

Nomenclature

$A, m_i, i = 1,..,9$ material constants in the Hansel-Spittel constitutive equation

$C, v^*, g, \overline{\kappa}, \alpha_2$ GLD model parameters

$C_s, C_{ax}, C_t, C_c, \gamma_{\overline{\theta}}$ parameters of the Lode dependent yield criterion

$D_1, D_2, D_3, D_4, D_5, D_6$ material constants in the Bai & Wierzbicki model

D_f final diameter (e.g. after drawing)

D_i initial diameter (e.g. before drawing)

D_{LC} Latham-Cockroft damage variable

D_{OY} Oyane damage variable

D_{Xue} Xue damage model indicator

E Young's modulus

E_M, σ_M Young's modulus and flow stress of undamaged material

F dissipation potential

F_D damage dissipative potential

F_X nonlinear kinematic hardening dissipative potential

K, ϵ_0, n material constants in the Swift hardening model

K, a, n material constants in the Ludwik hardening model

N Number of turns

$N_i^b (i = 1,..,4)$ interpolation functions of the bubble velocity associated with element i

$N_i^l (i = 1,..,4)$ interpolation functions of the linear velocity and pressure field associated with node i

N_r Number of rotations to fracture in torsion test

X_{ij} component of the back stress deviatoric $\mathbf{X}$ (kinematic hardening law)

Δ shape factor of die

Γ Torque

$\Omega\left(\frac{\sigma_h}{\sigma_{eq}}\right)$ stress dependent factor

$\alpha_1, \alpha_2, \eta_1, \eta_2$ additional material constants in the enhanced Lemaitre model

α_{Huang} Huang void growth formulation parameter

α_{RTm} modified Rice & Tracey formulation parameter

α_{RT} Rice & Tracey void growth formulation parameter

$\boldsymbol{\epsilon}^{(2)}$ the Signorini strain

$\mathcal{E}$ n-dimensional Euclidean space

$\mathcal{U}$ n-dimensional vectors space associated with $\mathcal{E}$

$\underset{\sim}{\boldsymbol{D}}^{\boldsymbol{e}}$ elastic continuum tangent modulus

$\underset{\sim}{\boldsymbol{D}}^{\boldsymbol{ep}}$ elastoplastic consistent tangent modulus

$\dot{\omega}_s$ stored energy density rate

$\dot{p}$ accumulated plastic strain rate

ϵ uniaxial total strain

ϵ^e uniaxial elastic strain

ϵ^p uniaxial plastic strain

$\epsilon_{f0}, p_L, q, k, m, \beta, \gamma, D_c, \epsilon_{DX}$ material constants in the enhanced Xue model

ϵ_{ij}, $\boldsymbol{\epsilon}$ tensorial total strain

ϵ_{ij}^e, $\boldsymbol{\epsilon}^{\boldsymbol{e}}$ tensorial elastic strain

ϵ_{ij}^p, $\boldsymbol{\epsilon}^{\boldsymbol{p}}$ uniaxial, tensorial plastic strain

ϵ_{loc} true strain

$\eta, \eta_{ini}, \eta_{av}$ stress triaxiality, initial and average stress triaxialities

κ, K bulk modulus

μ Coulomb's friction coefficient

ν Poisson ratio

$\overline{\epsilon}_f$ equivalent plastic strain at fracture

$\overline{\epsilon}_p$ or $\overline{\epsilon}^p$ equivalent plastic strain

$\overline{\theta}$ Lode parameter

$\overline{\theta}_{ini}, \overline{\theta}_{av}$ initial Lode parameter and average Lode parameter

$\overline{m}$ Tresca's friction coefficient

ϕ plastic potential/yield function

ϕ_D the damage objective function

ϕ_F the reduced drawing force objective function

$\phi_{F,D}$ the multi-objective function

ψ Helmholtz specific free energy

ψ^* Gibbs specific free enthalpy

ψ_p plastic state potential

ψ_T thermal state potential

ψ_e elastic state potential

ψ_e^* elastic specific free enthalpy

$\sigma_1, \sigma_2, \sigma_3$ 3 principal stresses, $\sigma_1 \geq \sigma_2 \geq \sigma_3$

σ_D drawing stress

σ_b back tension stress

σ_n normal contact stress

σ_y uniaxial yield stress

σ_0 flow stress

$\sigma_{eq}, \overline{\sigma}$ von Mises equivalent stress

$\sigma_{p0}, \sigma_{ps}, n$ material constants in the Voce hardening model

$\sigma_{p0}, \sigma_{ps}, n, K_2$ material constants in the modified Voce hardening model

σ_{true} true stress

$\vec{q}$ thermal flux

τ_y shear yield stress

θ_L, θ Lode angle

$\tilde{E}^+$ effective elasticity modulus in tension

$\tilde{E}^-$ effective elasticity modulus in compression

$\widetilde{m}, \widetilde{n}$ Fields-Backofen method parameters

d_{pen} authorized penetration distance

f, f^* void volume fraction and modified void volume fraction in the GTN model

f_N, s_N, ϵ_N GTN model nucleation parameters

f_c, f_f GTN model coalescence parameters

$f_{shear}, s_{shear}, \epsilon_{shear}$ GTN model nucleation parameters due to shearing

h microdefects closure parameter

k_ω rate of damage development under shear loading

p hydrostatic pressure

q_1, q_2, q_3 constitutive parameters in the GTN model

q_3^*, q_4 material constants in the modified GTN model by Xue

r reduction

s, S, D_c, h, ϵ_D material constants in the Lemaitre model

$J(\vec{x}), J'(\vec{x})$ determinants of volumetric and surface Jacobian transformation matrices

$\boldsymbol{\sigma}$ Cauchy stress tensor

$\boldsymbol{S}$ or $\boldsymbol{s}$ deviatoric part of Cauchy stress tensor

I_1, I_2, I_3 invariants of Cauchy stress tensor

J_1, J_2, J_3 invariants of the deviatoric part of Cauchy stress tensor

α die semi angle

μ Coulomb friction coefficient

$\overline{m}$ Tresca friction coefficient

L_D die bearing length or die land

RVE Representative Volume Element

X kinematic back stress (kinematic hardening law)

Introduction

Scientific background and motivation

Fracture prediction in real size structures subjected to complex loading conditions has been of utmost interest in the scientific and engineering community in the past century. With the increasing computational power of latest computers, numerical simulations with non-linear finite element (FE) codes allow investigating various complicated problems for damage and fracture prediction in real scale models, which is an important topic in many industries, such as aerospace, automotive, nuclear and forming industries. For all industrial cold forming processes, understanding and modeling ductile damage mechanisms remains a major issue in view of obtaining defects-free products. The ability of numerical modeling to predict ductile fracture is indeed crucial. However, this ability is still limited because of the complex loading paths (multi-axial and non-proportional loadings) and important shear effects in several forming processes where the stress triaxiality is nearly zero. Moreover, since forming processes involve large strain, the use of a suitable FE code with robust damage and fracture prediction models is essential to obtain realistic results both for geometry precision and mechanical properties.

Regarding ductile damage models, three main approaches have been extensively used and developed since 50 years: uncoupled phenomenological damage models (or fracture criteria), coupled phenomenological model and micromechanical models. The applicability of these approaches to non-proportional and multiaxial loading configurations involving finite deformation is still a subject for numerous debates in the ductile fracture community. In addition, among all the numerous ductile damage models defined in the literature, very few were actually applied and validated on complex industrial applications, such as multi-stages forming processes. The comparison of the three above-mentioned damage approaches on real "complex" multi-stages manufacturing processes has been studied here to clarify the advantages and drawbacks of each approach.

Industrial context

The METAL project, also the present PhD project, regrouping three industrial partners (ArcelorMittal, AREVA/CEZUS and Ugitech) and the Center for material forming (Cemef) was initiated to improve modeling of ductile damage and fracture occurring during cold metal forming processes for complex loading paths involving important shear effects. In the following, brief introductions about the issues of three industrial partners are given.

ArcelorMittal ArcelorMittal

Among many products, ArcelorMittal produces flat and shaped wires with quite a few different steel grades. Flat-rolled steel wires are commonly used in automotive industries and thus have to be precise in terms of final geometry and mechanical properties expected. Moreover, flawlessness is a major point of technical specifications to avoid breaking in use or during production. In terms of processes, after patenting, the material is subjected to several drawing passes, followed by cold rolling.

In the thesis of Thomas Massé [Massé, 2010], the author performed detailed experimental observations of damage on C72 steel grade (inclusion state, voids) during wire drawing and rolling using Scanning Electron Microscope (SEM). Numerical simulations were also performed using several existing damage models in Forge2009® (Latham& Cockcroft, Lemaitre) but these models totally failed to predict damage initiation and localization in the wire flat rolling (Fig. 1).

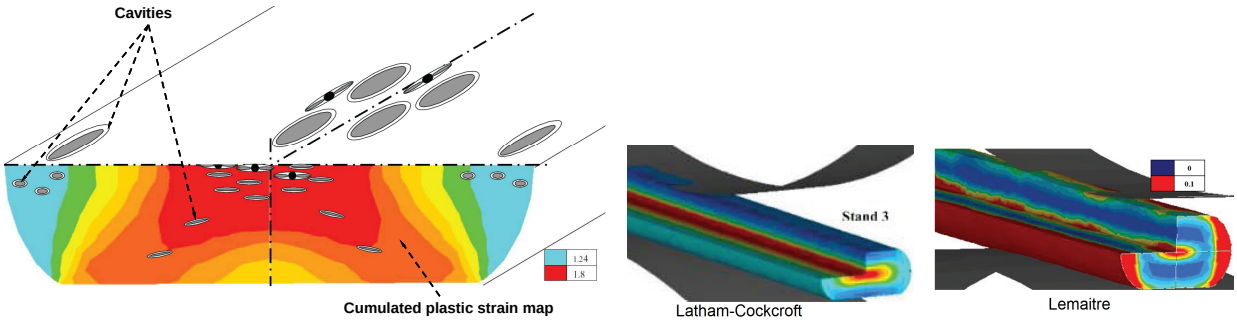

(a) *Experimental results of cavities (sketch) superimposed to the strain map (color).*

(b) *Numerical result with Latham-Cockcroft and Lemaitre models.*

Fig. 1: *Results of Massé [Massé, 2010] showing the disagreement between damage localization observed in experiment (a) and the numerical simulations (b) with two existing damage models in Forge®2009.*

This was due to several reasons: these damage models were not able to capture some of the damage mechanisms for such a process (shear localization); and the method to identify damage models parameters was not well established.

AREVA/CEZUS

AREVA/CEZUS is interested in forming cladding tubes, rods or flat products in zirconium alloys. Cold pligering is commonly used to make cladding tubes for nuclear application. Due to their specific application, these tubes require a high level of quality and dimensional precision. Avoiding defects and damage during their forming is indeed crucial. Initial work on the damage mechanisms of zirconium alloys was carried out by Alexis Gaillac ([Gaillac, 2007]). Porosities were observed mainly near the inner and outer surfaces of the tube. The existing damage models cannot capture the damage localization. In these areas, the material is subjected to almost zero or even negative stress triaxiality. There is thus a real need to understand why porosities appear locally for this type of process. Following this study, AREVA/CEZUS wants to improve the prediction of damage via numerical simulations of cold pilgering process using richer damage models, which can be adapted to complex loading history. It is worth noting that the simulation of this process is extremely time consuming and the simulation of the whole process is thus not possible (see [Lodej et al., 2006]). Moreover, few studies in literature focused on fracture of this material for different loading configurations. Performing different fracture tests and comparing different recently developed damage models on such a material is of great interest.

Ugitech

Ugitech produces stainless bars (round or profile sections) through wire drawing and cold rolling. The current damage models cannot explain some failures observed experimentally (chevron-type defects or chipping in drawing, or breaks in the rolls exit). Cracks observed in wire drawing could initiate on the wire surface (high shear zone) due to the presence of defects or in the wire core to form a cup-cone fracture (high triaxiality zone - see Fig. 2).

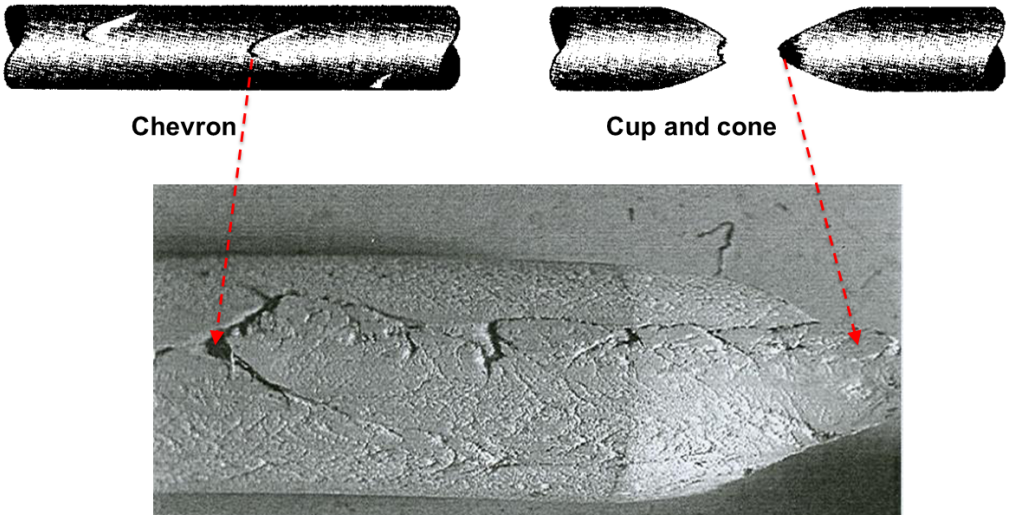

Fig. 2: *Cracks observed during wire drawing on the studied stainless steel [Vachey, 2011].*

Common issues

Throughout the above summary, apart from the fact that each industrial partner uses a specific material, the common issue is to predict ductile damage and fracture in multiaxial and non-proportional loadings, in which the damage may localize away from the maximum plastic strain location. Moreover, the shear effect in these processes seems important and damage models must be able to capture shear damage mechanism. There is thus real need to define *robust* damage models for industrial applications. By "robustness", the challenges for a good model are three-fold: (1) physical mechanisms of the onset of damage and fracture must be captured; (2) the models have to be suitable for numerical implementation and applicable for real size structure simulations; and (3) models parameters should be convenient for identification. Solving these problems is the strongest driving force of the present study.

Objectives and approaches

The present PhD thesis aims at a better understanding and modeling of ductile damage mechanisms during cold forming processes, with wire drawing, rolling and cold pilgering as examples. The principal objective is to develop in the commercial finite element (FE) code Forge2009® richer damage models, capable of predicting the damage associated with these mechanisms for large plastic strains. In addition, special attention is paid to these models' parameters identification methodology.

All three approaches of ductile damage are investigated in the present study: uncoupled phenomenological fracture criteria; coupled phenomenological models and micromechanical models. Different damage models have been enhanced and implemented in Forge2009®, which required adaptation of algorithms to its mixed velocity-pressure formulation and to its finite element ($P1 + /P1$).

Parallel to the numerical work, various mechanical tests on three different materials (high carbon steel, stainless steel and zirconium alloy) are conducted for strain hardening and damage models parameters identification based on their hybrid numerical-experimental analyses. In situ X-ray micro-tomography tensile tests (carried out by MATEIS laboratory at ESRF) are also exploited for the identification of ductile damage mechanisms (nucleation, growth and coalescence) as well as the identification of micromechanical model parameters.

Finally, comparative studies of these models are carried out on the three above-mentioned forming processes and materials. These comparisons help, on the one hand, revealing the applicability of the three ductile damage approaches to real complex loading configurations, and on the other hand, supplying "robust" predictive tools for industrial applications.

Outline of the dissertation

The present dissertation consists of seven chapters.

In the first chapter, a literature review is presented, which constitutes a background for the whole dissertation. First, some mechanical analyses of forming process are given, followed by a summary of numerical method for mechanical problem solving. Details on weak formulation construction and solving using mixed velocity-pressure finite element method are then given. Then, elastoplasticity as well as damage mechanisms and models are presented. Finally, the mechanical tests used for damage study are revised, followed by a revision of damage and fracture occurring in forming processes.

Chapter 2 and Chapter 3 constitute the first part of the present work, which deals with the phenomenological approach of ductile damage. In Chapter 2, experimental results of mechanical tests (axisymmetric tensions, axisymmetric compression and torsion) performed on 3 materials: high carbon steel, zirconium alloy and stainless steel are presented successively. Methods for exploiting experimental results are also discussed in detail. These experimental results are then used to identify the plastic behavior of all these three materials. For hardening models identification, the method to identify the parameters of a non-linear friction law in a compression test is given. Different hardening models are tested and enhanced to better describe the hardening of the three materials studied.

Chapter 3 presents the implementation, development, and identification of phenomenological damage models. First, different damage models are presented and implemented in Forge2009®, including both coupled models (enhanced Lemaitre, Xue) and recently developed fracture criteria (Bai & Wierzbicki - B&W, Modified Mohr-Coulomb - MMC). Except for the Lemaitre model, the other models account for the influence of the Lode parameter in their formulations. For the high carbon steel, Lemaitre, Xue and B&W models are used and identified. Furthermore, additional tensile tests on flat grooved specimen are performed on this material to identify the B&W model. For zirconium alloy, two uncoupled models (B&W, MMC) and the coupled Lemaitre model are identified and compared in terms of ability to predict fracture in the mechanical tests. The results show that the Lemaitre model fails to predict fracture in torsion test, this model is thus enhanced by the present author to incorporate the influence of third deviatoric stress invariant through the Lode parameter. The proposed enhanced Lemaitre model is then identified and the results show that this model gives best results in terms of fracture prediction for the studied mechanical tests. For the stainless steel, the Lemaitre and the B&W models are identified.

Chapter 4 and Chapter 5 constitute the second part, which deals with the micro-mechanical approach of ductile fracture, more precisely, the development and identification of the Gurson type models. Chapter 4 details the implementation of the GTN model within the framework of a mixed velocity-pressure finite element formulation (Forge2009®). Comparison simulations are carried out with Abaqus to validate the present implementation.

Chapter 5 is devoted to the identification of the GTN model for the high carbon steel based on in situ X ray tomography tensile tests (conducted by INSA Lyon) and our mechanical tests. The damage mechanisms are also modeled using the formulations proposed in the literature (e.g. Rice and Tracey for void growth, formulation of [Bouaziz et al., 2008, Maire et al., 2008] for void nucleation). The shear extension GTN models are identified based on the torsion test.

Chapter 6 and Chapter 7 constitute the third and last part of the present dissertation, which presents the industrial applications and discussions. In Chapter 6, the industrial applications for 3 materials are performed to validate the identified damage models in terms of fracture prediction (both qualitatively and quantitatively). Finally, Chapter 7 addresses the discussions, conclusions and perspectives of the present study.

Appendix A contains some additional element of material mechanics, which are necessary for the readers to understand certain points of the present dissertation. Appendix B presents all the necessary equations and derivations for the implementation of the GTN model presented in Chapter 4. Appendix C presents some additional results of the present study and the interesting "ways" to further improve the study (e.g. Lode dependent yield criterion development, damage to fracture transition). Appendix D contains the confidential information for thesis committee. This appendix will be deleted from the public version.

Chapter 1

Literature reviews

Contents

Introduction

The first chapter is dedicated to the literature review, which is used as a reference for the present study. This chapter first reviews the forming processes studied, which can be considered as a thermal-mechanical problem to be solved. This revision helps us to understand both technological and mechanical aspects of the forming processes studied. The equilibrium as well as boundary condition equations of this mechanical problem are then presented, leading to the weak formulations, in which the unknowns chosen are velocity and pressure. In order to solve these weak-form equations, mixed velocity-pressure Finite Element (FE) method is used, whose equations are presented in details in sections 1.2.5 and 1.2.6. With this method, at each time increment, a global system of equations needs to be solved to find the unknowns (i.e. velocity, pressure) at each node of the FE mesh, for which the Newton-Raphson method is adopted. This resolution leads to the local integration of constitutive equation at each integration point for each time-increment. We will therefore detail the derivation of these equations, which is used as the background for the implementation of pressure-dependent plasticity model presented in Chapter 4.

The elastoplastic equations are then presented in section 1.3, followed by a review of damage, which, with elastoplaticity, constitute the *real behavior law* of material. The damage mechanisms and models are then presented, followed by a review of mechanical tests used for damage characterization and models identifications (sections 1.4 and 1.5). These reviews help us to understand the damage mechanisms under different stress states, as well as to choose relevant damage models to implement and develop, which is the subject of Chapters 3 and 4. Moreover, review on mechanical tests helps to define an experimental campaign for plasticity and damage models identifications (Chapters 2 and 3). Finally, reviews on experimental results of damage and fracture occurring during cold forming processes (section 1.6) help us to validate our numerical results in Chapter 6.

1.1 Overview of metal forming processes

The forming process of metallic material (also called the metalworking process), generally, can be classified into two groups ([Dieter, 1976]):

1. Forming by plastic deformation, i.e. the *plastic forming process*, in which the volume and mass of material is considered to be unchanged and the material is deformed by irreversible deformation to obtain the final shape.

2. Forming by metal removal (or *machining process*), where the material is removed to obtain the required shape.

All the processes presented in this study (*wire drawing, rolling and pilgering*) are classified in the first group, where material undergoes large plastic deformations.

1.1.1 Cold working versus hot working

1.1.1.1 Hot working

Plastic forming processes are commonly classified into hot working or cold working. The main difference, as explicitly expressed by their name, is the operating temperature. The hot forming process is defined as the deformation under conditions of temperature and strain-rate such that the *recovery* process occurs simultaneously with the plastic deformation. The recovery process is related to other similar processes, most notably *recrystallization* and *grain growth*. Since recovery reduces the dislocation density, this process is normally accompanied by a reduction in materials strength and a simultaneous increase in the ductility. As the result of the recrystallization, new strain-free grains are created in the hot forming process, which then eliminates the distorted grain and the strain hardening created by plastic deformation. Moreover, the increase of temperature leads to the decrease of the critical resolved shear stress, which favors the movement

of dislocation and the activation of new slip systems. Very large deformation therefore can be obtained with hot forming process, with essentially *no strain hardening*. Since the flow stress decreases with increasing temperature (temperature softening), *the energy necessary for* ***deformation*** *is less for hot working than for cold working*. The distinction between cold and hot working does not depend on any arbitrary temperature. Generally, hot working is carried out at a temperature which is higher than the recrystallization temperature *of the studied material* (T_r). This temperature is not fixed for all materials: for lead and tin, it is equivalent to the room temperature, while for tungsten, the recrystallization temperature is about 1000°C ([Dieter, 1976]). The main disadvantages of hot working are the surface quality and dimensional tolerance. At high temperature, due to the expansion and contraction, the dimensional tolerance is higher than in cold working. Moreover, as the consequence of oxidation, extensive surface treatment is required to remove the decarburized and oxide layers.

1.1.1.2 Cold working

The cold forming operates at room temperature, which results in *an increase in material strength and a decrease in material ductility*. Cold forming processes are often divided into different steps, with intermediate annealing which allows softening the cold-worked material and restoring the ductility. In addition, better surface qualities as well as geometrical precision can be acquired with cold forming. The cold-working processes are often used to produce high strength material (e.g. high strength steel used in automobile) or products that require high surface precision (e.g. cladding tube of zirconium alloy in nuclear application).

All the processes studied in the present PhD thesis (wire drawing, wire rolling and pilgering) are cold forming processes, which operate at room temperature.

1.1.2 Cold rolling process

Cold rolling is used to produce flat products like sheet and strip, or on exception long products (sections from wire), by decreasing the section of a long metal part, through two or more axisymmetric tools (rolls) rotating around their axes (see Fig. 1.1). A rolling mill consists of rolls, bearings, housings containing all these parts and a drive to control rolling speed and to supply power. Rolling mills are classified by the number of rolls (e.g. two-high mill consists of two rolls, four-high mill consists of four rolls with coplanar axes, etc.).

During the rolling process, the material is subjected to *high compressive stresses* from the rolls action and to *shear stress on surface*, as a result of friction between rolls and material. This process results in better surface finish and dimensional tolerances compared with hot rolling. The strain hardening occurring during the process *increases strength* of product but *decreases its ductility*. Since each pass of rolling has a limit of reduction, multiple passes are required to obtain the final product. It is indeed desirable to distribute the work as uniformly as possible over different passes. Frequently, the last pass has the smallest reduction, with the role of controlling the quality of final product (flatness, surface finish, etc.).

In the next paragraphs, we summarize in the first part some mechanical analyses of rolling process, based on an example of sheet rolling, then some problems and defects occurring in rolling are discussed in section 1.6.1.

1.1.2.1 Mechanical analyses of cold rolling

In Fig. 1.1, the metal sheet with initial thickness h_i enters the rolls at velocity v_i.

The rolls rotate with a constant rotation speed or constant tangential velocity $v_r = R\omega$ ($v_r > v_i$). Due to the conservation of "metal flux" and the height reduction, the exit velocity v_o is generally greater than v_i. The sheet velocity therefore increases from entrance to exit. There exists a point - the so-called *"neutral point"*[1] - where the velocity of material at this point equals the roll velocity v_r (point N in Fig. 1.1). The force acting on each contact point can be decomposed into two components: the tangential component (frictional force) F and the "radial" component P_r (or into the vertical force - often called the *rolling load* P, and the horizontal

[1] In reality, the set of neutral points is not really a line but rather an area on the roll surface, see section 6, chapter 17 of [Dieter, 1976] for more details.

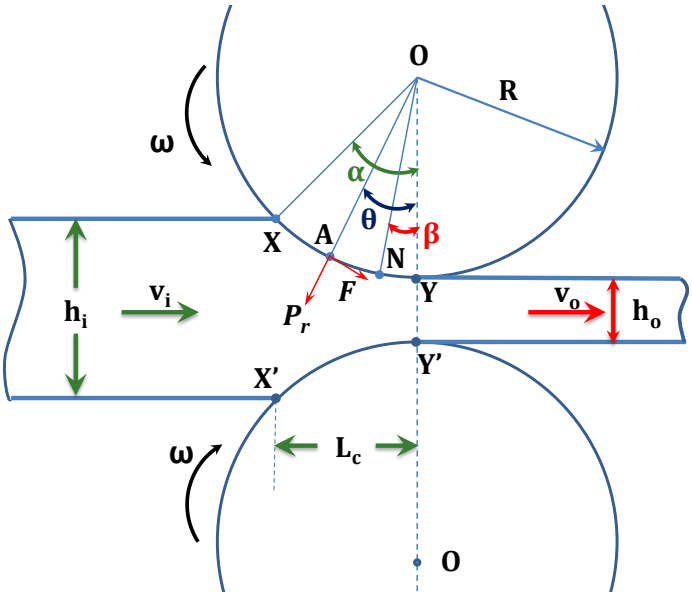

Fig. 1.1: *Schema of sheet rolling with acting forces.*

one). The rolling load is equal to the reaction force exerted by the material on rolls, which tends to separate the two rolls. For this reason, this force is frequently called the *separating force*. The average contact pressure (or roll pressure) is an important parameter, which is required to estimate the torque and power to achieve the reduction. This pressure is equal to the rolling load divided by the contact surface. For a sheet of width b, the contact area is approximated by the product of b with the projection of the arc of contact L_c, which can be determined by Pythagorean theorem and rearranged as:

$$L_c \approx \sqrt{R(h_i - h_o)} = \sqrt{R\Delta h} \tag{1.1}$$

where $\Delta h = h_i - h_o$ is the height reduction. The formula for average contact pressure can be deduced:

$$p = \frac{P}{bL_c} \tag{1.2}$$

The angle α in Fig. 1.1 is called the *angle of contact* or *angle of bite*. In order to ensure the forward movement of material, the horizontal component of frictional force $Fcos(\alpha)$ (or $\tau cos(\alpha)$) must be higher than the horizontal component of normal force $P_r sin(\alpha)$ (or $\sigma_n sin(\alpha)$), which leads to:

$$\tau cos(\alpha) \geq \sigma_n sin(\alpha) \rightarrow \mu = \frac{\tau}{\sigma_n} \geq tan(\alpha) \approx \sqrt{\frac{\Delta h}{R}} \tag{1.3}$$

From this equation, one can deduce that, to obtain a height reduction Δh, the friction between sheet and rolls must be high enough, which leads to a high rolling load and many other issues (tool wear and degradation, rolls deformation). Multiple passes are thus necessary to acquire a high reduction as mentioned above. The multiple passes can be performed either on single-stand reversing mills (lower investment cost) - Fig. 1.2a, or on multiple tandem mills (higher productivity) - Fig. 1.2b and Fig. 1.2c.

Front and back tensions For the tandem mills, the speed of each rolling stand must be controlled carefully to synchronize with its preceding stand. Additional back tensions as well as front tensions are often supplied by the decoiler and the windup reel to control the speed (Fig. 1.2c). The influence of front and back tensions can be summarized in Fig. 1.3.

As one can observe in Fig. 1.3, the back and front tensions help reducing the roll pressure (due to the result of von Mises plasticity criterion in plane strain condition) and thus reduce the rolling force. This reduction in rolling pressure results in less wear of tools and higher dimensional precision of products. In addition, these tensions shift the neutral point backward, i.e. towards the entrance, (front tension) or forward, i.e. towards the exit (back tension).

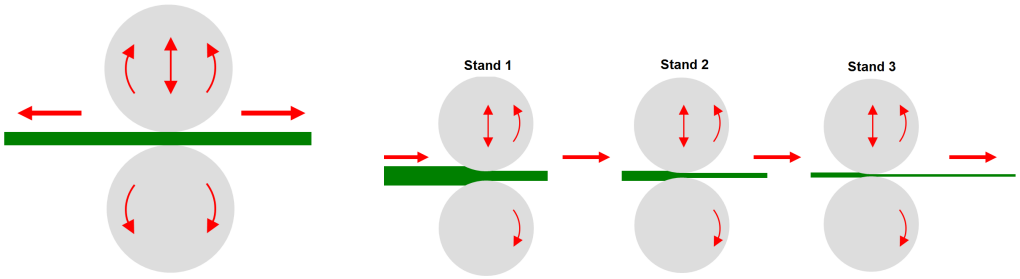

(a) *Single-stand reversing mill.*

(b) *Multi-stands mills.*

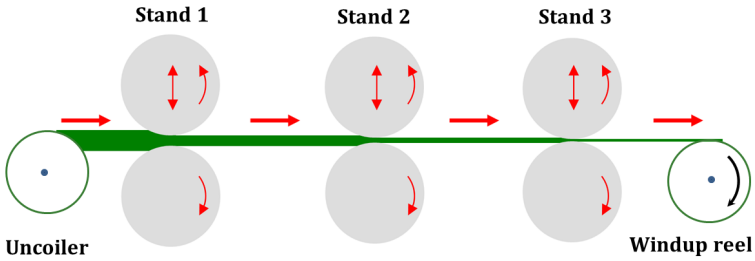

(c) *Tandem mills of strip rolling, with the uncoiler and windup reel to supply the back and front tensions.*

Fig. 1.2: *Different multiple passes rolling configurations [Montmitonnet, 2011].*

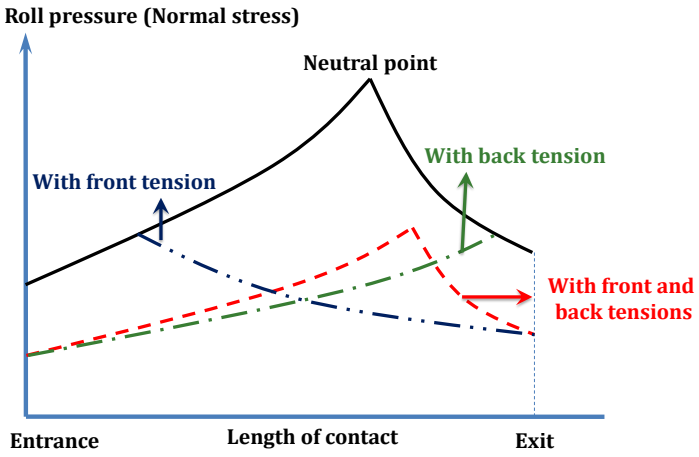

Fig. 1.3: *Effect of front and back tensions (i.e. horizontal tensions) on normal stress distribution and the position of the neutral point.*

Friction between rolls and workpiece As above-mentioned, the friction force is of great importance to pull the metal into the roll bite (Eq. 1.3). High friction leads to high rolling force and high risk of edge cracking ([Dieter, 1976]). In [Capus and Cockcroft, 1962], the authors showed that the friction varies along the contact arc between roll and workpiece. However, measurement of this variation is not straightforward, the friction is frequently assumed constant. In addition, "from the entry plane to the neutral point, the friction force acts in the direction of roll rotation, while on the exit side of the neutral point it reverses direction" ([Dieter, 1976]), and the back/front tensions modify the position of this point, the control of these tensions affects the frictional force between rolls and workpiece.

1.1.3 Wire drawing process

Wire drawing is one of the most commonly used processes to obtain wire used in many mechanical applications. Fine wires with high strength are produced through a multi-pass wire drawing process.

1.1.3.1 General definition

"Drawing consists in reducing a long product cross-section by forcing it through a die-hole of the same shape as the final product section, by a tension applied on the product from beyond the fixed die exit" ([Montmitonnet, 2011]). Wire drawing is the drawing process of round wires, whose diameters vary from 10 μm to 20 mm. In this process, most of the plastic flow is generated by compression force, which arises from the reaction of the metal with the dies (see Fig. 1.4 for the description and die geometry).

The cross section through a conical die is presented in Fig. 1.4d. The entrance of the die (bell) is shaped so that the wire entering the die will draw lubricant with it, thus increasing its hydrostatic pressure to form a continuous lubricant film. The approach angle is the part of die section where the reduction in diameter occurs (the semi-angle α). The bearing region (die land) permits the conical approach surface to be refinished (to remove the surface defects due to die wear). This region does not cause the reduction in wire dimension. The back relief allows the metal to expand slightly as the wire leaves the dies. Wire drawing usually starts with hot-rolled rod, which is cleaned by pickling to remove any scale (i.e. iron oxide) which would lead to surface defects. Almost all of rod and wire drawing processes are done "cold" (with the exception of refractory metals like W or Mo, and high speed steels), but plastic deformation and friction can heat up the drawn wire several hundred degrees Celsius. Inter-pass cooling may remove partly this heat. Furthermore, intermediate anneals may be necessary depending on the metal and the reductions involved.

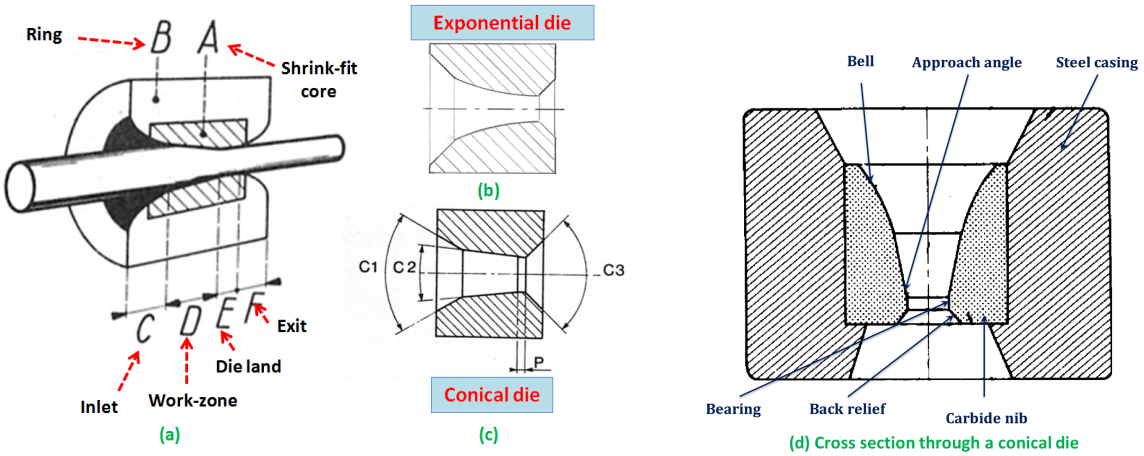

Fig. 1.4: *Drawing die (a) with different geometries: exponential die (b) and conical die (c). The cross section through a conical die is shown in (d)*

1.1.3.2 Process parameters effect on mechanical properties and damage

In wire drawing process, the major variables are cross-sectional area reduction, drawing speed, die angle and friction between the drawn wire and die interfaces. The semi-angles are often chosen in the range of 4-8° (for a minimum drawing force) with a moderate reduction (commonly $20 - 30\%$) to avoid wire break. The drawing speed depends on the *area reduction*, *wire material* as well as *friction* between interfaces. This parameter is a source of the increase of temperature during the process. The wire drawing process is always a multi-pass operation and under "cold" condition, with a drawing speed about 6 to 14 m/s (Fig. 1.5 shows an example of multi-pass machine). Moreover, for the multi-pass wire drawing, the drawing schedule, i.e. the magnitude and distribution of area reduction per pass, is an important factor.

Theoretical and analytical solutions in the literature principally concern the minimization of drawing force during drawing process. In this approach, several studies on the influence of different process parameters have been carried out. Avitzur [Avitzur, 1968] proposed the relation between relative drawing stress and various variables of process:

- For Coulomb friction law:

Fig. 1.5: *Multi-pass wire drawing machine (Ugitech).*

$$\frac{\sigma_D}{\sigma_0} = \frac{\frac{\sigma_b}{\sigma_0} + 2f(\alpha)ln\left(\frac{R_i}{R_f}\right) + \frac{2}{\sqrt{3}}\left(\frac{\alpha}{sin^2\alpha} - cot\alpha\right) + 2\mu\left(cot\alpha\left[1 - \frac{\sigma_b}{\sigma_0} - ln\left(\frac{R_i}{R_f}\right)\right]ln\left(\frac{R_i}{R_f}\right) + \frac{L_D}{R_f}\right)}{1 + \frac{2\mu L_D}{R_f}} \tag{1.4}$$

- For Tresca friction law:

$$\frac{\sigma_D}{\sigma_0} = \frac{\sigma_b}{\sigma_0} + 2f(\alpha)ln\left(\frac{R_i}{R_f}\right) + \frac{2}{\sqrt{3}}\left(\frac{\alpha}{sin^2\alpha} - cot\alpha + \overline{m}(cot\alpha)ln\left(\frac{R_i}{R_f} + \overline{m}\frac{L_D}{R_f}\right)\right) \tag{1.5}$$

where σ_D is the drawing stress, σ_b is the back tension stress, L_D is the die bearing length or die land, α is the die semi angle, μ is the Coulomb friction coefficient, $\overline{m}$ is the Tresca friction coefficient, and $f(\alpha)$ is defined as:

$$f(\alpha) = \frac{1}{sin^2(\alpha)}\left[1 - cos(\alpha)\sqrt{1 - \frac{11}{12}sin^2\alpha} + \frac{1}{\sqrt{132}}ln\frac{1 + \sqrt{\frac{11}{12}}}{\sqrt{\frac{11}{12}}cos\alpha + \sqrt{1 - \frac{11}{12}sin^2\alpha}}\right] \tag{1.6}$$

[Dixit and Dixit, 1995] found that an increase in reduction or a decrease in die semi-angle or a decrease in friction coefficient tends to make the drawn wire more homogeneous in terms of mechanical properties. Lin ([Lin et al., 2008]) investigated the influence of parameter Δ on strain homogeneity and residual stress by varying the semi-angle and reduction. In forming processes, the parameter Δ characterizes the geometry of deformation zone (some authors use the term "shape factor" to name this parameter) and is defined as: $\Delta = \frac{h}{L_D}$ (with h is the mean diameter and L_D is the contact length). In wire drawing process, Δ is calculated via Eq. 1.7:

$$\Delta = \frac{D_i + D_f}{D_i - D_f}sin(\alpha) = \frac{\left(1 + \sqrt{1 - r}\right)^2}{r}sin(\alpha) \tag{1.7}$$

where D_i, D_f are initial and final diameters of wire, r is the reduction ratio. From this last equation, one can observe that Δ **increases with** α **and decreases when** r **increases**. The author concluded that the strain inhomogeneity increases with Δ (more precisely when α or friction increases). These results are consistent with that of [Dixit and Dixit, 1995]. [Vega et al., 2009] studied the influence of different parameters such as semi-angle and friction on mechanical properties of drawn wire. **Drawing force increases with friction coefficient and section reduction** r. In addition to the drawing force, there are many other properties, which need to be brought into consideration such as damage evolution and residual stress on drawn wire. Massé ([Massé, 2010]) carried out his studies on wire drawing process optimization, which aimed at minimizing the drawing force or damage or the coupling of these two "objectives". The author observed an increase of optimum semi-angle (which minimized the drawing force) when the reduction or friction increases (same as the results obtained by [Wistreich, 1955] - Fig. 1.6 and [Vega et al., 2009]).

By using the simplified Latham-Cockcroft (L-C) uncoupled damage model, the author showed a negligible influence of die land L_D on damage and the increase of reduction or friction leads to the increase of damage. For a multi-objective optimization, the objective function is defined as:

$$\phi_{F,D} = \beta\phi_D + (1 - \beta)\phi_F \tag{1.8}$$

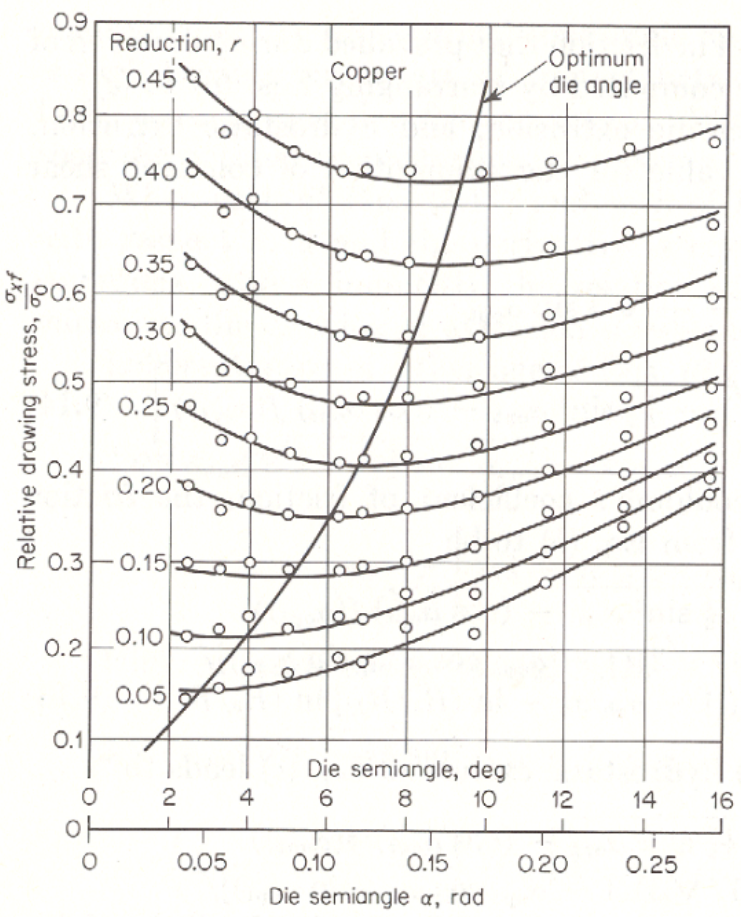

Fig. 1.6: *Variation of relative drawing stress with die angle and the representation of optimum die semi-angle [Wistreich, 1955].*

where β is a weight coefficient, ϕ_D is the damage objective function and ϕ_F is the reduced drawing force objective function. The multi-objective optimization results were then superposed to the mono-objective optimization, which aimed at minimizing either the reduced drawing force or the damage in the center line of wire (Fig. 1.7).

In this figure, each point corresponds to a set of optimal parameters and the choice of the best compromise between the minimization of reduced drawing force or damage is left to the user, accounting for other constraints (e.g. die manufacturing). The concept of optimal semi-angle is strongly objective-dependent. Moreover, from this figure, one can conclude that, **a strong decrease of damage could be obtained at the expense of a small increase of drawing force only when $\alpha > 3.5^o$ (industrially used angle)**.

Remark This conclusion is obtained with the L-C model, which is a very simplified damage model without any coupling with material elastoplastic behavior. The damage variable of this model is defined as a function of maximal principal stress: $D_{LC} = \int_0^{\bar{\epsilon}_f} max(\sigma_I,0)d\bar{\epsilon}$. In the wire drawing process, the axial direction is the dominant direction and nearly the first principal direction of stress tensor (see section 6.1.1 for processes analysis). Therefore, the damage indicator of L-C model depends strongly on the reduced drawing force.

1.1.4 Cold pilgering process

Cold pilgering is a seamless tube forming process, where the inner radius and wall thickness are both progressively reduced by a fixed axisymmetric mandrel and forward and backward-rolling grooved dies ([Montmitonnet et al., 2002], [Lodej et al., 2006], Fig. 1.8). The basic idea of this process is to cold work

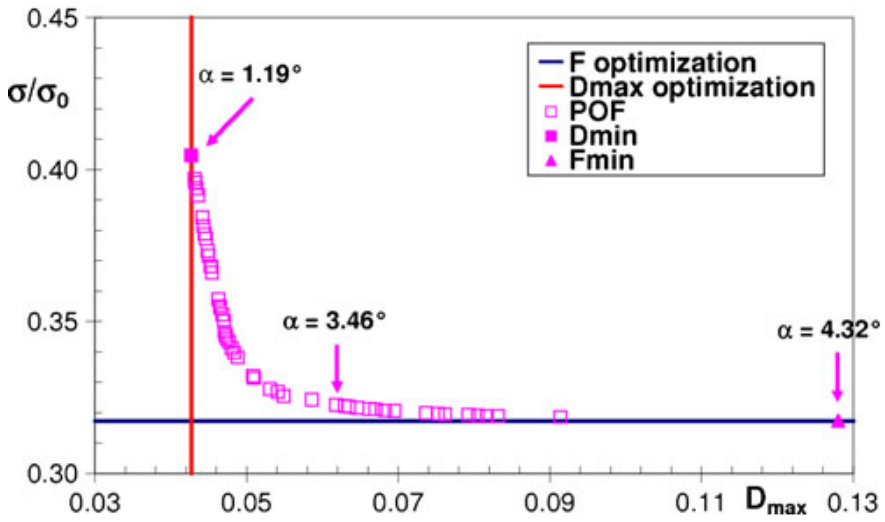

Fig. 1.7: *Multi-objective optimization of a single drawing pass with r= 20% and $\overline{m}$ = 0.02 [Massé, 2010]. F_only and D_only are the two mono-objective curves obtained by minimizing the reduced drawing force and the damage variable respectively.*

the tube by reducing simultaneously the diameter and the wall thickness by compressive forces, while the horizontally displaced material lengthens the tube.

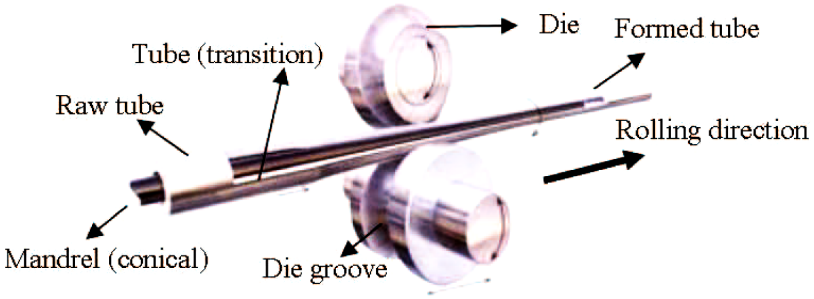

Fig. 1.8: *The cold pilgering process relies on four main actions: the tube moves forward and it rotates while the ring dies move back and forth and rotate [Strehlau, 2006].*

Generally, there are two ways to produce tube by this process: one uses the HTPR (High-Precision Tube Roller) mills, the other uses pilger mills (or VMR mills[2]). The former is out of scope of the present study, interested readers can refer to [Nerino et al., 2011] and [Vanegas Marquez, 2011] for more details.

In comparison with other tube producing processes (e.g. tube drawing process, where the tensile force is dominant), the cold pilgering process is more effective with excellent final characteristics ([Strehlau, 2006], [Nerino et al., 2011]):

- Practically, no material loss occurs during the pilgering process, while with tube drawing, the process wastes material in every pass because the ends must be cropped (for pligering process, the cropped length is negligible).
- Rather than pulling the tube through a die (as in tube drawing), the pilgering process uses rollers to compress the tube and mandrel to fix the interior diameter, the tube is therefore subjected to compressive force on both inner and outer sides. Compared with tension, compression can achieve greater reductions per pass, the cross-section reduction acquired with pilgering process is thus higher.

[2]VMR=Vertikaler Massenausgleich Ringwalze - in German, is used by several authors to refer to this mill. Throughout our study, "pilger mills" refers to the VMR mills.

- Desired textures and properties can be obtained with cold pilgering (by controlling the ratio of diameter to thickness reduction), but not with drawing. Moreover, "the homogenizing material flow in a circumferential direction facilitates substantial reductions in eccentricity. Experience has shown that the higher the eccentricity of the starting tube, the greater is the improvement in eccentricity by cold pilgering" [Strehlau, 2006].

The main drawback of the process may be the complex design and manufacturing technology for both dies and mandrel (Fig. 1.9a). The grooves of pilger mill tooling have a varying cross-section (Fig. 1.9a). With each cycle, the tooling does a partial rotation as the tube advances then returns to its starting position. Note that dies never complete a 360-degree rotation due to the variable cross-sectional forming groove. A rack-and-pinion system (Fig. 1.10a) links the mandrel and die sections, which allows a rolling-without-sliding movement, pressing the tube between the die grooves and the mandrel ([Montmitonnet et al., 2002]).

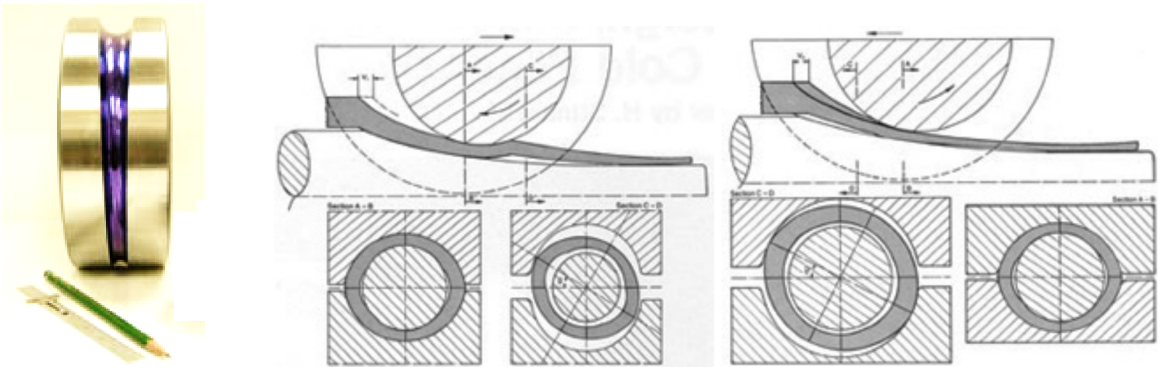

(a) *The variable groove of pilger die [Nerino et al., 2011].*

(b) *The cold pilger mill's forward motion (left) and backward motion (right) rely on the tapered cross section between the dies and the mandrel to reduce tube diameter and wall thickness simultaneously [Strehlau, 2006].*

Fig. 1.9: *Complex design of the pilger die and complex mechanism of the process.*

Fig. 1.9b shows the rolling action. During the forward and backward strokes, the dies reduce the tube in the same way that a rolling pin rolls out pastry. The grooves' cross sections decrease along the circumference and are nearly circular. In the dead-center positions of the mill saddle, the dies briefly disengage the tube. During these end-of-stroke periods, the tube advances and rotates. Note that both the forward and return strokes contribute to form the tube. Depending on the groove design, the forming process requires many steps, feeding and rotating the tube. The large number of small forming steps helps to ensure a constant wall thickness and nearly homogeneous material characteristics in the rolled tube.

In the present study, the cold pilgering of zircaloy cladding tubes for nuclear industry is addressed (Fig. 1.10b).

This process is quasi-periodic, which consists of several tens of "strokes"[3]. Between each stroke, the tube is turned by 51° and moved forward by a small distance of 2 mm (the "feed rate"). At each stroke, a material particle progresses by a few mm down the 300 mm long deformation zone of the mandrel: it takes thus about 80-100 strokes before the deformation is completed ([Montmitonnet et al., 2002]). **The metal therefore undergoes a series of small incremental plastic strains, alternatively under tensile and compressive stresses (due to the tube rotation at the end of each stroke)**[4].

Due to complex mechanical and geometrical aspects of this process (non-proportional, multi-axial loading; non-periodic strain cycling; geometrical complexity), it has been extensively analyzed and modeled since the 1950s. An overview of pilgering process studies and modelings can be found in [Vanegas Marquez, 2011].

[3]This process can be considered cyclic in Eulerian viewpoint (i.e. machine frame) but not in Lagrangian viewpoint (i.e. material frame) [Montmitonnet, 2007].

[4]This conclusion is important to choose suitable mechanical tests for plasticity behavior parameters identification, presented in section 2.3.3 of Chapter 2.

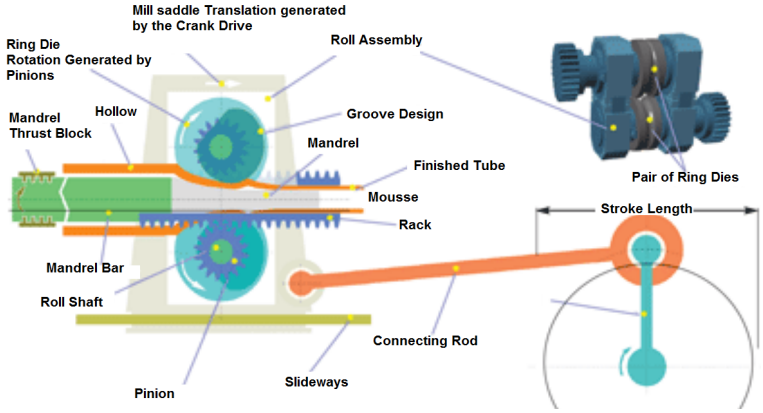

(a) *A connecting rod drives the mill saddle back and forth that causes the ring dies to rotate. Pinions mounted on each roll shaft engage two racks that are fixed to the machine housing. This arrangement uses the mill saddle's oscillating motion to generate the ring dies' oscillating rotary motion. [Strehlau, 2006]*

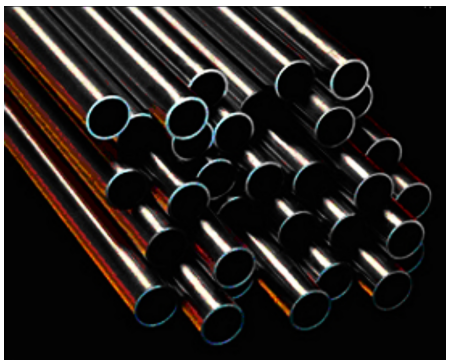

(b) *Cladding tubes (http://www.world-nuclear.org/sym/2005/doublet.htm)*

Fig. 1.10: *The arrangement of machine components (a) and cladding tubes (b).*

Remark The above sections give an overview of different mechanical aspects of three forming processes studied. The simulation of these processes can be considered as a thermo-mechanical problem to be solved using numerical methods. In the following section, details on the numerical method used are given.

1.2 Numerical method for mechanical problem solving

Throughout this study, the FE software Forge2009®, which is based on the mixed formulation of velocity and pressure, is used. In this software, the updated Lagrangian formulation is adopted, which allows using the small strain approach. The local integration of constitutive equations is solved by the backward Euler method (return mapping algorithm). Since the mesh gets distorted at large deformation, an automatic adaptive remesher ([Coupez et al., 2000]) allows Forge2009® to deal with large strain simulations (e.g. forming processes simulations). The present simulations are carried out with the 3D solver (Forge3), in which the so-called MINI element ($P1^+/P1$) is used. This linear isoparametric tetrahedron element has a velocity node added at its center, which ensures the stability condition - the Brezzi/Babuska condition of existence and uniqueness of solution [Arnold et al., 1984] (see section 1.2.6.1).

This section summarizes some theoretical background of thermal-mechanical formulations used in Forge2009®. The spatial discretization by FE method is detailed in a context of mixed velocity-pressure formulation and incompressible plasticity, which is then adapted for a compressible plasticity case (GTN model - see Chapter 4).

1.2.1 Mechanical problem definition

The forming process by plastic deformation involves two types of objects: the "undeformable" objects (tools or dies [5]) whose deformations during the process are negligible; and the deformable objects (wires, plates, etc.). From a mechanical point of view, the deformable solids are considered as the finite domains, which consist of a homogeneous and continuous media. The problem is therefore in the context of continuum mechanics.

Let $\Omega \subset R^3$ be a domain occupied by the deformable object $\mathcal{B}$ in its *reference* configuration, which is bounded by the border $\partial\Omega \subset R^2$. Studying the mechanical problem consists in developing the equations that allow describing the displacement, stress and strain fields at each instant. After introducing the formulas which define the motion of any point $\vec{x}$ of Ω, the conservative equations as well as the boundary conditions

[5] In reality, tools and dies are deformed during the process. Here, we assume that these deformations are negligible.

will be developed. This mechanical problem will then be solved by the mixed velocity-pressure finite element formulation (mixed FEM).

1.2.2 The descriptions of motion

There are two principal approaches to describe the motion: the Lagrangian approach and the Eulerian approach[6]. In the first approach, the motion of a material point is followed at each instant while the second approach consists in positioning at a fixed point in space and in observing the material point that goes by. In Forge®, the so-called "updated Lagrangian" approach is used. In the following section, the Lagrangian approach as well as the Eulerian approach will be detailed. The notion of updated Lagrangian is also given.

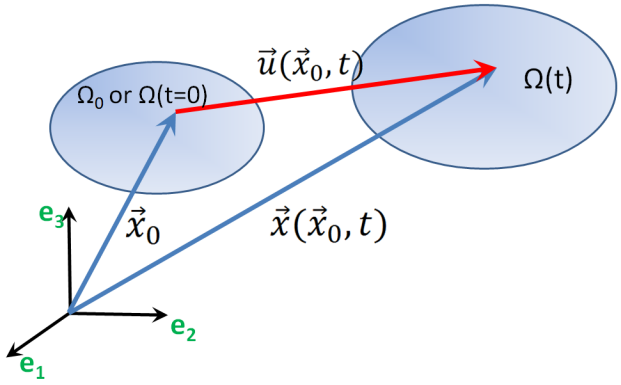

Fig. 1.11: *Lagrangian description of motion.*

1.2.2.1 The Lagrangian and Eulerian approaches

At the initial moment ($t = 0$), the solid occupies the area noted Ω_0 and then the deformed solid occupies the domain $\Omega(t)$ at time t (Fig. 1.11). There exists a function φ, which is a bijection of $\Omega(t_0)$ on $\Omega(t)$ (or $\varphi(\Omega(t_0))$), from which the expression of position vector $\vec{x}(t)$ [7] can be defined (Eq. 1.9).

$$\vec{x}(t) = \varphi(\vec{x}_0,t) \tag{1.9}$$

where $\vec{x}_0$ is the initial position at time t_0. Note that the above relation can be written as:

$$\underline{\boldsymbol{x}} = \vec{x}(t) = \varphi(\underline{\boldsymbol{p}},t) \tag{1.10}$$

where $\underline{\boldsymbol{p}}$ represents the material point p, which was initially located at the position defined by vector $\vec{x}_0$ in the reference frame. The displacement of a material point is defined as the difference between its position at current time t and its initial position:

$$\vec{u}(\vec{x}_0,t) = \vec{x}(t) - \vec{x}_0 = \varphi(\vec{x}_0,t) - \vec{x}_0 \tag{1.11}$$

With this approach, the motion of a material point is completely defined by its initial and current states. The displacement field $\vec{u}$ includes the translation, rotation and deformation of material. A rigid motion of $\mathcal{B}$ is a motion that preserves the distances between all material particles of $\mathcal{B}$, which is a rotation or a translation (or a combination of both). During a motion φ, the material velocity (Lagrangian) is defined by:

$$\dot{\vec{x}}(\vec{x}_0,t) = \frac{\partial\varphi(\vec{x}_0,t)}{\partial t} \tag{1.12}$$

whereas the spatial velocity (Eulerian), which gives the velocity of the material particle positioned at $\vec{x}$, at time t, is defined by:

$$\vec{v}(\vec{x},t) = \dot{\vec{x}}(\varphi^{-1}(\vec{x}(t)),t) \tag{1.13}$$

[6] There exists a method, the "Arbitrary Lagrangian Eulerian" (ALE) method, which is the intermediate between the Lagrangian and Eulerian methods. This method is rather linked with the meshing technique, in which the velocity of material and the velocity of mesh are dissociated. This method is often used in fluid mechanics.

[7] In more rigorous notation, the position at time t of a material point initially at $\vec{x}_0$ would be $\vec{x}(t,\vec{x}_0)$.

1.2.2.2 The updated Lagrangian approach

Forge® is based on a description of motion that follows the updated Lagrangian approach. This method consists in dividing time into different intervals $[t_0, t_0 + \Delta t,...,t]$. In each interval, the motion is defined as a function ϕ^t (same definition as Eq. 1.9):

$$\vec{x}_{t+\Delta t} = \varphi^t(\vec{x}_t, t + \Delta t) \tag{1.14}$$

Remark Throughout the present study, the terms stress and strain refer to the **Cauchy stress** and **Cauchy strain** unless otherwise indicated. For a detailed review of stress and strain measures, interested readers can refer to Appendix A.2.

1.2.3 The fundamental equations of mechanics

The behavior of a deformed solid, which occupies the domain $\Omega(t)$ at time t, are governed by some conservation equations. The first one is the mass conservation equation (Eq. 1.15) and the second one is the momentum balance (Eq. 1.16):

Fundamental equations

$$\frac{\partial \rho}{\partial t} + \vec{\nabla}.(\rho\vec{v}) = 0 \quad \text{Mass conservation} \tag{1.15}$$

$$\vec{\nabla}.\boldsymbol{\sigma} + \rho\left(\vec{f} - \vec{\gamma}\right) = \vec{0} \quad \text{Momentum balance} \tag{1.16}$$

where ρ is the mass density, $\vec{f}$ is the volumetric force (gravity), $\vec{\gamma}$ is the acceleration vector. For **incompressible materials**, the mass conservation equation becomes:

$$\vec{\nabla}.(\vec{v}) = 0 \tag{1.17}$$

This equation is only valid for a pure plastic deformation. The elastic behavior is considered compressible, which leads to another expression of Eq. 1.17:

$$\vec{\nabla}.(\vec{v}) = -\frac{\dot{p}}{\kappa} \tag{1.18}$$

where κ is the bulk modulus: $\kappa = \frac{E}{3(1-2\nu)}$. In forming processes simulations, the gravitational and inertial forces are often neglected in comparison with internal forces. The momentum balance equation thus becomes:

$$\vec{\nabla}.\boldsymbol{\sigma} = 0 \tag{1.19}$$

Note that the above equation is formulated in deformed configuration with Cauchy stress tensor. It can also be expressed in reference frame by using the Piola-Kirchoff stress tensor.

The principles of thermodynamics The first principle of thermodynamics postulates the *energy conservation* while the second states the *irreversibility of entropy production*. By combining these two principles, the Clausius-Duhem inequality can be obtained, which describes the dissipation mechanism (see Appendix A.4).

1.2.4 The boundary conditions

The above-mentioned equilibrium equations are satisfied at any point in the solid while the boundary conditions are applied on the outer surface of the volume. The boundary $\partial\Omega(t)$ is decomposed in different parts ($\partial\Omega = \partial\Omega_v + \partial\Omega_t + \partial\Omega_c + \partial\Omega_f$) as described in Fig. 1.12. There are four types of boundary conditions:

1. Free boundary condition: $\boldsymbol{\sigma}.\underline{n} = \underline{0}$ on $\partial\Omega_f$.

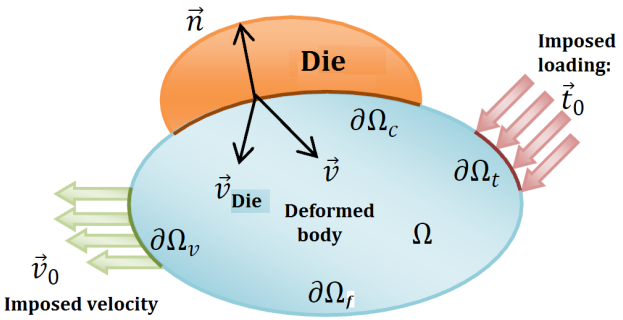

Fig. 1.12: *Representation of boundary conditions of deformed solid.*

2. Imposed velocity boundary condition: $\underline{v} = \underline{v}_0$ on $\partial\Omega_v$.
3. Stress imposed boundary condition: $\boldsymbol{\sigma}.\underline{n} = \underline{t} = \underline{t}_0$ on $\partial\Omega_t$.
4. Contact condition on $\partial\Omega_c$: the essential condition in forming processes, which can be decomposed into two types: the unilateral contact condition (deals with the normal component of the stress vector) and the friction condition (deals with the tangential component of the stress vector).

   - Unilateral contact between die and solid, which ensures the non-penetration condition (the Signorini condition):

$$\begin{cases} (\underline{v} - \underline{v}_{Die}).\underline{n} \leq 0 \\ \sigma_n = (\boldsymbol{\sigma}.\underline{n}).\underline{n} \leq 0 \\ \sigma_n.(\underline{v} - \underline{v}_{Die}).\underline{n} = 0 \end{cases} \tag{1.20}$$

   where σ_n is the normal stress (the contact pressure), $\underline{v}_{Die}$ is the die velocity. If σ_n is zero, there is no contact. The deformable solid and the rigid tool therefore can have different velocities. If contact exists, the normal speed of the solid at the contact point becomes equal to that of the tool, the contact pressure is non-zero.
   In Forge2009®, the contact between rigid dies and deformable objects[8] is controlled incrementally, by investigating the distance $d(t)$ between a node involved and its projection onto the die at a given instant (t). In order to numerically determine the zone involved in contact analysis, a minimum distance d_{out} is used, which depends on the mesh size by default (see Fig. 1.13).

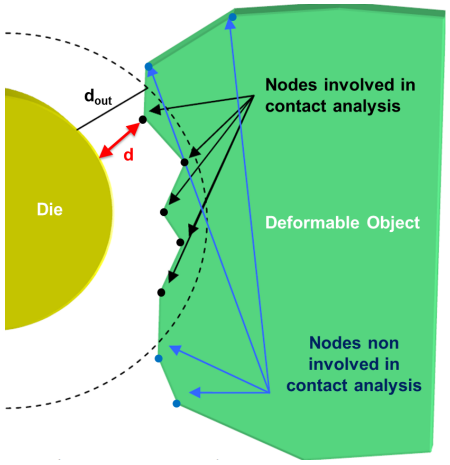

Fig. 1.13: *Zone for contact analysis defined by d_{out} and definition of contact distance d [Forge2009®, 2009].*

The unilateral contact condition for the next increment $t + \Delta t$:

$$d(t + \Delta t) + d_{pen} \approx d(t) + \frac{\partial d(t)}{\partial t}\Delta t = d(t) + (\underline{v}_{Die} - \underline{v}).\underline{n}(t)\Delta t \geq 0 \tag{1.21}$$

[8]The methodology in the case of "auto-contact" (i.e. contact between different parts of a deformable object) and contact between different deformable objects is detailed in [Forge2009®, 2009].

or:

$$(\underline{v} - \underline{v}_{Die}).\underline{n}(t) - \frac{d(t) - d_{pen}}{\Delta t} \geq 0 \tag{1.22}$$

where d_{pen} is the authorized penetration distance to be chosen, generally $\approx$ 1% of the mesh size. Note that with this method, the normal vector $\underline{n}$ is calculated at the beginning of increment and supposed to be constant during the increment. For more details concerning the contact management in Forge2009®, interested readers can refer to [Fourment et al., 1999, Forge2009®, 2009].

- The friction condition in the tangential direction:

$$\underline{\tau} = \boldsymbol{\sigma}.\underline{n} - \sigma_n.\underline{n} \tag{1.23}$$

where $\underline{\tau}$ is the tangential stress vector. The chosen tribological laws to model the friction are the Tresca and the Coulomb laws. These two laws are both based on the ***"threshold type"*** model, i.e. we suppose that there exists a critical shear stress τ_c at the contact point, which governs the friction:

$$\begin{cases} \text{If } \tau < \tau_c & \text{no sliding between the solid and die} \\ \text{If } \tau = \tau_c & \text{sliding occurs} \end{cases} \tag{1.24}$$

Tresca's friction law: the Tresca law defines the critical shear component as a function of von Mises equivalent stress:

$$\tau_c = \overline{m}\frac{\overline{\sigma}}{\sqrt{3}} \tag{1.25}$$

where $\overline{m}$ is a parameter ($0<\overline{m}<1$).

Coulomb's friction law (limited by Tresca): the Coulomb friction law defines a relation between the normal and the critical tangential contact stresses:

$$\tau_c = \mu\sigma_n \tag{1.26}$$

where μ is Coulomb's friction coefficient.

The Coulomb limited by Tresca law (Fig. 1.14) combines the two above-mentioned friction laws:

$$\tau_c = min(\mu\sigma_n, \overline{m}\frac{\overline{\sigma}}{\sqrt{3}}) \tag{1.27}$$

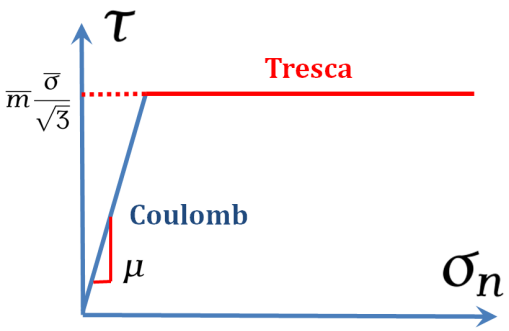

Fig. 1.14: *The Coulomb limited Tresca criterion.*

Remarks: The above equilibrium equations are written at any point in the solid (strong form). The system of equilibrium equations coupled with boundary conditions define a system of equations to be solved. In the next sections (1.2.5, 1.2.6, 1.2.7), a method for solving this system is presented in detail. These theoretical reviews help to understand the method using in Forge® for a general mechanical problem, which is then modified in Chapter 4 for the work concerning the implementation of a pressure-dependent plasticity model in Forge2009®.

1.2.5 Weak formulation for mechanical problem

In order to simplify the presentation, hereinafter, the free boundary condition as well as the contact condition is not taken into account in the formulation developments, the boundary is therefore considered as: $\partial\Omega = \partial\Omega_t + \partial\Omega_v$. The strong form of mechanical problem is defined by the set of equilibrium equations and accounting for the boundary conditions.

$$\begin{cases} \vec{\nabla}.(\boldsymbol{\sigma}) = \vec{\nabla}.(\boldsymbol{s}) - \vec{\nabla}(p) = \vec{0} \\ \vec{\nabla}.(\vec{v}) = -\frac{\dot{p}}{\kappa} + trace(\dot{\boldsymbol{\epsilon}}^{\boldsymbol{p}}) \\ \vec{v} = \vec{v}_0 \text{ on } \partial\Omega_v \\ \vec{t} = \vec{t}_0 \text{ on } \partial\Omega_t \end{cases} \tag{1.28}$$

Consider that the two variables velocity and pressure are totally independent. Let us define the following functional spaces of kinematically admissible velocity field $\mathcal{V}$ and $\mathcal{V}^0$ as well as the functional space of pressure $\mathcal{P}$:

$$\mathcal{V} = \left[\vec{v} \in (H^1(\Omega))^3, \vec{v}|_{\partial\Omega_v} = \vec{v}_0\right] \tag{1.29}$$

$$\mathcal{V}^0 = \left[\vec{v} \in (H^1(\Omega))^3, \vec{v}|_{\partial\Omega_v} = \vec{0}\right] \tag{1.30}$$

$$\mathcal{P} = L^2(\Omega) \tag{1.31}$$

where $H^1(\Omega)$ is the *Sobolev space*, $L^2(\Omega)$ is the *Lebesgue space* (or L^p space), which are detailed in the following paragraphs.

The L^2 space: given Ω is a regular and bounding region in R, the $L^2(\Omega)$ space is defined as:

$$L^2(\Omega) = \left[u : \Omega \to R, \int_\Omega u^2 d\Omega < \infty\right] \tag{1.32}$$

The Sobolev space:

$$H^1(\Omega) = \left[u \in L^2(\Omega), \frac{\partial u}{\partial x_i} \in L^2(\Omega)\right] \tag{1.33}$$

The weak formulations can be obtained by multiplying the above formulations by the *test functions* $\vec{v}^*$ *and* p^* and by integrating through the whole domain Ω (using the Green-Riemann formula). Take the momentum balance equation (Eq. 1.19), multiply by the test function $\vec{v}^* \in \mathcal{V}^0$ and integrate on the domain Ω:

$$\int_\Omega \vec{\nabla}.(\boldsymbol{\sigma}).\vec{v}^* d\Omega = \underbrace{\int_\Omega \boldsymbol{\sigma} : (\vec{\nabla}\vec{v}^*) d\Omega}_{1} - \underbrace{\int_\Omega \vec{\nabla}.(\boldsymbol{\sigma}.\vec{v}^*) d\Omega}_{2} = 0 \tag{1.34}$$

The second integration can be written as:

$$\int_\Omega \vec{\nabla}.(\boldsymbol{\sigma}.\vec{v}^*) d\Omega = \int_{\partial\Omega} \boldsymbol{\sigma}.\vec{v}^*.\vec{n} d\Gamma = \int_{\partial\Omega_t + \partial\Omega_v} \boldsymbol{\sigma}.\vec{v}^*.\vec{n} d\Gamma = 0 + \int_{\partial\Omega_t} \vec{t}_0.\vec{v}^* d\Gamma \tag{1.35}$$

By decomposing the stress tensor into deviatoric ($\boldsymbol{s}$) and volumetric parts ($p\boldsymbol{I}$), the first integration can be expressed as:

$$\int_\Omega \boldsymbol{\sigma} : (\vec{\nabla}\vec{v}^*) d\Omega = \int_\Omega \boldsymbol{s}(\vec{\boldsymbol{v}}) : \dot{\boldsymbol{\epsilon}}(\vec{\boldsymbol{v}}^*) d\Omega - \int_\Omega p(\vec{\nabla}.\vec{v}^*) d\Omega \tag{1.36}$$

Eq. 1.34 then becomes:

$$\int_\Omega \boldsymbol{s}(\vec{\boldsymbol{v}}) : \dot{\boldsymbol{\epsilon}}(\vec{\boldsymbol{v}}^*) d\Omega - \int_\Omega p(\vec{\nabla}.\vec{v}^*) d\Omega - \int_{\partial\Omega_t} \vec{t}_0.\vec{v}^* d\Gamma = 0 \tag{1.37}$$

Similarly, one can obtain the weak form of mass conservation equation (Eq. 1.18). The problem is thus:

$$\text{Find } (\vec{v},p) \in \mathcal{V} \times \mathcal{P} \begin{cases} \int_\Omega \boldsymbol{s}(\vec{\boldsymbol{v}}) : \dot{\boldsymbol{\epsilon}}(\vec{\boldsymbol{v}}^*) d\Omega - \int_\Omega p(\vec{\nabla}.\vec{v}^*) d\Omega - \int_{\partial\Omega_t} \vec{t}_0.\vec{v}^* d\Gamma = 0 \\ \int_\Omega p^* \left(-\vec{\nabla}.(\vec{v}) - \frac{\dot{p}}{\kappa} + trace(\dot{\boldsymbol{\epsilon}}^{\boldsymbol{p}})\right) d\Omega \\ \forall (\vec{v}^*,p^*) \in \mathcal{V}^0 \times \mathcal{P} \end{cases} \tag{1.38}$$

The existence and uniqueness of the solution to this problem are obtained under the conditions of Brezzi theorem ([Arnold et al., 1984]).

1.2.6 Spatial discretization by the FE method

The above weak-form equations are solved by the FE method, which consists in approximating the infinite dimensions, continuous spaces $\mathcal{V}$ and $\mathcal{P}$ by the corresponding discrete spaces $\mathcal{V}_h$ and $\mathcal{P}_h$ (the h index is related to the elements mesh size in underlying). This approximation is internal, which means the approximation spaces are usually included in $\mathcal{V}$ and $\mathcal{P}$:

$$\mathcal{V}_h \subset \mathcal{V}, \mathcal{P}_h \subset \mathcal{P}, \lim_{h\to 0} \mathcal{V}_h = \mathcal{V}, \lim_{h\to 0} \mathcal{P}_h = \mathcal{P} \tag{1.39}$$

The domain Ω is decomposed into different simple elements and the combination of these elements forms the *"triangulation"* of the domain, which defines the discretized domain Ω_h:

$$\Omega_h = \bigcup_e \Omega_e, \text{ with } e \in \mathcal{E} \tag{1.40}$$

where Ω_e represents an element and $\mathcal{E}$ is the set of elements. Eq. 1.38 can be written in the discretized space as:

$$\text{Find } (\vec{v}_h, p_h) \in \mathcal{V}_h \times \mathcal{P}_h \quad \begin{cases} \int_{\Omega_h} \boldsymbol{s}(\vec{\boldsymbol{v}}_{\boldsymbol{h}}) : \dot{\boldsymbol{\epsilon}}(\vec{\boldsymbol{v}}_{\boldsymbol{h}}^*) d\Omega_h - \int_{\Omega_h} p_h (\vec{\nabla}.\vec{v}_h^*) d\Omega_h - \int_{\partial\Omega_{ht}} \vec{t}_0.\vec{v}_h^* d\Gamma_h = 0 \\ \int_{\Omega_h} p_h^* \left(-\vec{\nabla}.(\vec{v}_h) - \frac{\dot{p}_h}{\kappa} + trace(\dot{\boldsymbol{\epsilon}}^{\boldsymbol{p}}) \right) d\Omega_h = 0 \\ \forall (\vec{v}_h^*, p_h^*) \in \mathcal{V}_h^0 \times \mathcal{P}_h \end{cases} \tag{1.41}$$

The discretization operation consists in passing from the weak problem of partial differential equations (PDEs - Eq. 1.38) to the discrete problem (Eq. 1.41). The efficiency and accuracy of the results obtained from solving the discrete problem are directly related to the choice of approximation spaces $\mathcal{V}_h$ and $\mathcal{P}_h$, i.e. to the choice of interpolation functions associated with the unknown velocity and pressure. Moreover, the interpolation space of pressure and the interpolation space of velocity cannot be chosen independently, there exists a relation which assures the compatibility between the two spaces: the Brezzi Babuska condition:

$$inf_{p_h \in \mathcal{P}_h} sup_{\vec{v}_h \in \mathcal{V}_h} \frac{\int_{\Omega_h} p_h (\vec{\nabla}.\vec{v}_h) d\Omega_h}{\|p_h\|_{\mathcal{P}_h} \|v_h\|_{\mathcal{V}_h}} > C > 0 \tag{1.42}$$

where C is a constant which does not depend on the mesh. This condition imposes the interpolation degree for the two variables velocity and pressure, and assures the ***existence and uniqueness*** of solutions. The non-respect of this condition leads to a number of unacceptable numerical solutions, such as *shear locking*. The detailed demonstrations can be found in [Arnold et al., 1984], [Brezzi and Fortin, 1991].

1.2.6.1 Element type

In Forge3®, tetrahedral elements are the only ones used (triangular elements in Forge2®). This element favors the 3D mesh generation and simplifies the 3D interpolation (by using the barycentric coordinates). In [Aliaga, 2000], the author presented different tetrahedral elements which are summarized in Table 1.1 and Fig. 1.15.

Element	Deg(v)	Deg(p)	Precision
$P1^+/P1$	1	1	$O(h)$
$P2/P1_{cont}$	2	1	$O(h^2)$
$P2+/P1_{disc}$	2	1	$O(h^2)$
$P1/P1$	1	1	Incompatible

Table 1.1: *Tetrahedral elements ([Aliaga, 2000]).*

The FE software Forge® uses the $P1^+/P1$ mixed velocity-pressure element (the smallest interpolation degree among the compatible elements - the so-called MINI element), where the velocity and pressure fields are defined as:

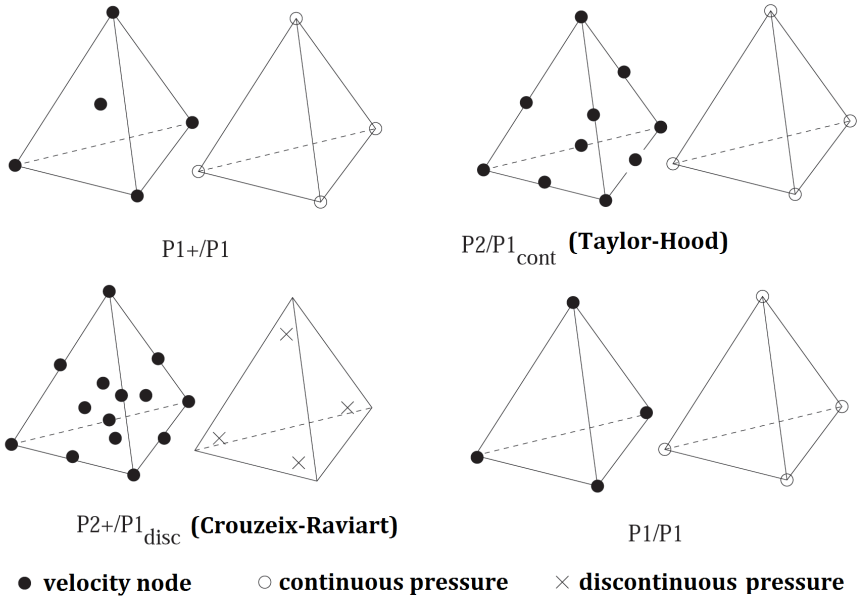

Fig. 1.15: *The tetrahedral mixed velocity-pressure elements. On each element the function is interpolated by a polynomial of a given degree. This interpolation can be entirely determined by the values at element's nodes, shared by neighboring elements (continuous); or it can be independent from one element to another (discontinuous).*

- the pressure is linear and continuous;
- the velocity field is composed of a linear part $\vec{v}^l$ and a "bubble" part $\vec{b}$ corresponding to the additional internal degree of freedom (DOF): $\vec{v}_h = \vec{v}^l + \vec{b}$. This decomposition is *unique*.

The discrete spaces are defined as:

$$\mathcal{V}_h = \mathcal{L}_h + \mathcal{B}_h \tag{1.43}$$

$$\mathcal{L}_h = \left[\vec{v}^l \in (C^0(\Omega_h))^3, \vec{v}^l|_{\Omega_e} \in (P^1(\Omega_e))^3, \vec{v}^l|_{\partial\Omega_e} = \vec{v}_0, \forall e \in \mathcal{E}\right] \tag{1.44}$$

$$\mathcal{L}_h^0 = \left[\vec{v}^{l*} \in \mathcal{V}^0 \cap (C^0(\Omega_h))^3, \vec{v}^{l*}|_{\Omega_e} \in (P^1(\Omega_e))^3, \vec{v}^{l*}|_{\partial\Omega_e} = \vec{0}, \forall e \in \mathcal{E}\right] \tag{1.45}$$

$$\mathcal{P}_h = \left[L^2(\Omega_h) \cap C^0(\Omega_h), p_h|_{\Omega_e} \in (P^1(\Omega_e))^3 \forall e \in \mathcal{E}\right] \tag{1.46}$$

where $C^0(\Omega_h)$ is the space of continuous functions on the domain Ω_h, $P^1(\Omega_e)$ is the space of linear functions on element Ω_e. Note that the $P1/P1$ element (linear in both $\vec{v}$ and p) does not satisfy the *inf-sup* condition (Eq. 1.42), the extra "bubble" is thus added in $\vec{v}$ to give an extra DOF. The use of this extra bubble is one of the stabilization techniques, which makes the $P1/P1$ element become compatible. For further discussions of stabilization techniques, interested readers can refer to [Aliaga, 2000], [Perchat, 2000]. The bubble part is an additional term for the interpolation of the velocity, which equals unity at element center and zero at element borders. This interpolation function can be constructed as a polynomial of degree 4 in the reference tetrahedron ([Fortin, 1981]):

$$N^b(\xi, \eta, \zeta) = 256(1 - \xi - \eta - \zeta)\xi\eta\zeta \tag{1.47}$$

In [Coupez, 1995] the $\mathcal{B}_h$ space is defined with a piecewise linear function on four sub-tetrahedron to avoid the difficulties in integrating the polynomial of degree 4 (Fig. 1.16):

$$\mathcal{B}_h = \left[\vec{b} \in (C^0(\Omega_h))^3, \vec{b}|_{\partial\Omega_e} = \vec{0}, \vec{b}|_{\Omega_{e_i}} \in (P^1(\Omega_{e_i}))^3, \forall e \in \mathcal{E}, i = 1,...,4\right] \tag{1.48}$$

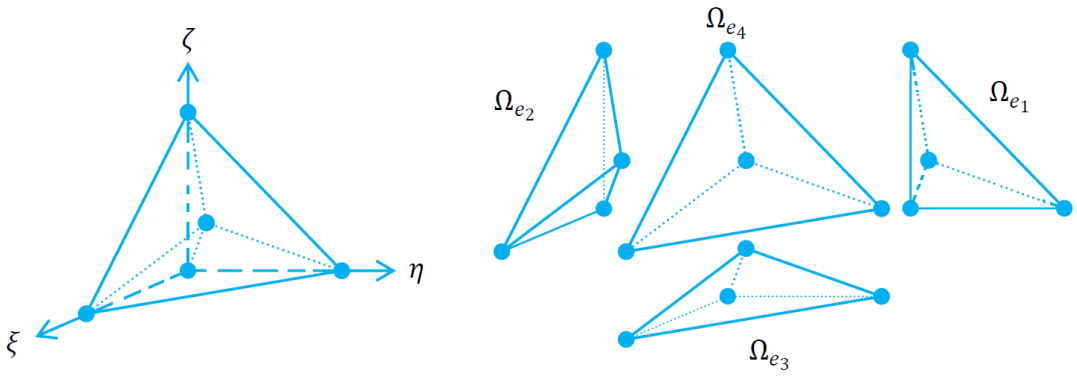

Fig. 1.16: *Decomposition of reference tetrahedron element ($P1^+/P1$) into 4 sub-tetrahedrons Ω_{ei} ([Fayolle, 2008]).*

The velocity and pressure fields at a point $\vec{x}$ can be expressed as:

$$\vec{v}_h(\vec{x}) = \sum_{k=1}^{NBNO} N_k^l(\vec{x})\vec{v}_k^l + \sum_{j=1}^{NBEL} N_j^b(\vec{x})\vec{b}_j \tag{1.49}$$

$$p_h(\vec{x}) = \sum_{k=1}^{NBNO} N_k^l(\vec{x})p_k \tag{1.50}$$

where $NBNO$ and $NBEL$ are the number of nodes and the number of elements respectively; $N_k^l(\vec{x}) \in \mathcal{L}_h$ are the interpolation functions of the linear velocity and pressure fields associated with the node k; $N_j^b(\vec{x}) \in \mathcal{B}_h$ is the interpolation function of bubble velocity associated with the element j (which will be called the bubble function hereinafter); $\vec{v}_k^l$ and p_k are the *linear* velocity and pressure at node k; $\vec{b}_j$ is *associated* with the velocity of central node (bubble part) of element j [9]. Accounting for the decomposition into sub-tetrahedra, the velocity and pressure for each element Ω_e can be obtained:

$$\vec{v}_h(\vec{x}) = \sum_{k=1}^{4} N_k^l(\vec{x})\vec{v}_k^l + N^b(\vec{x})\vec{b} \tag{1.51}$$

$$p_h(\vec{x}) = \sum_{k=1}^{4} N_k^l(\vec{x})p_k \tag{1.52}$$

For the reference element presented in Fig. 1.16, the associated velocity and pressure interpolation function are defined as:

$$\begin{cases} N_1^l = \xi \\ N_2^l = \eta \\ N_3^l = \zeta \\ N_4^l = 1-\xi-\eta-\zeta \end{cases} \quad \text{and} \quad \begin{cases} N^b = 4\xi & \text{in } \Omega_{e1} \\ N^b = 4\eta & \text{in } \Omega_{e2} \\ N^b = 4\zeta & \text{in } \Omega_{e3} \\ N^b = 4(1-\xi-\eta-\zeta) & \text{in } \Omega_{e4} \end{cases} \tag{1.53}$$

Finally, the discrete problem (Eq. 1.41) can be written as:

$$\text{Find } (\vec{v}^l, \vec{b}, p_h) \in \mathcal{V}_h \times \mathcal{B}_h \times \mathcal{P}_h \quad \begin{cases} \int_{\Omega_h} \boldsymbol{s}(\vec{\boldsymbol{v}}^{\boldsymbol{l}} + \vec{\boldsymbol{b}}) : \dot{\boldsymbol{\epsilon}}(\vec{\boldsymbol{v}}^{\boldsymbol{l}*}) d\Omega_h - \int_{\Omega_h} p_h(\vec{\nabla}.\vec{v}^{l*}) d\Omega_h - \int_{\partial\Omega_{ht}} \vec{t}_0.\vec{v}^{l*} d\Gamma_h = 0 \\ \int_{\Omega_h} \boldsymbol{s}(\vec{\boldsymbol{v}}^{\boldsymbol{l}} + \vec{\boldsymbol{b}}) : \dot{\boldsymbol{\epsilon}}(\vec{\boldsymbol{b}}^{*}) d\Omega_h - \int_{\Omega_h} p_h(\vec{\nabla}.\vec{b}^{*}) d\Omega_h = 0 \\ \int_{\Omega_h} p_h^* \left(-\vec{\nabla}.(\vec{v}^l + \vec{b}) - \frac{\dot{p}_h}{\kappa} + trace(\dot{\boldsymbol{\epsilon}}^{\boldsymbol{p}}) \right) d\Omega_h = 0 \\ \forall (\vec{v}^{l*}, \vec{b}^*, p_h^*) \in \mathcal{L}_h^0 \times \mathcal{B}_h \times \mathcal{P}_h \end{cases} \tag{1.54}$$

Due to the dependence of the stress deviator in total velocity field ($\vec{v}_h^* + \vec{b}^*$, which is the result of the local integration of behavior law), the system of equations to solve is a coupled system of two unknown field variables $\vec{v}_h^*$ and $\vec{b}^*$. By using a specific property of the bubble, [Aliaga, 2000] decoupled these equations to obtain a simplified form for the $P1^+/P1$ element, which is detailed in the following paragraph.

[9] Not to be confused $\vec{b}$ with the velocity at central node. In fact, the nodal value $\vec{b} = \vec{v}^b - \sum_{k=1}^{4} N_k^l(1/4;1/4;1/4)\vec{v}_k^l$, stands for the difference between the velocity at center of enriched linear tetrahedron element and the "normal" one (i.e. the normal linear tetrahedron).

1.2.6.2 Weak formulations of Mini-element

The "bubble" properties

- $\vec{b} = \vec{0}$ on $\partial\Omega_e$, which allows eliminating the "bubble" from all the integrations on $\partial\Omega_e$;
- For all constant tensor $\mathbf{C}$ in Ω:

$$\int_{\Omega} \mathbf{C} : (\vec{\nabla}\vec{b}) d\Omega = 0 \tag{1.55}$$

This equation leads to the orthogonal property:

$$\int_{\Omega_h} (\vec{\nabla}\vec{v}^l) : (\vec{\nabla}\vec{b}) d\Omega_h = 0, \forall \vec{b} \in \mathcal{B}_h, \forall \vec{v}^l \in \mathcal{L}_h \tag{1.56}$$

The weak formulations for the MINI-element is thus obtained:

$$\text{Find } (\vec{v}^l, \vec{b}, p_h) \in \mathcal{V}_h \times \mathcal{B}_h \times \mathcal{P}_h, \begin{cases} \int_{\Omega_h} \boldsymbol{s}(\vec{\boldsymbol{v}}^{\boldsymbol{l}}) : \dot{\boldsymbol{\epsilon}}(\vec{\boldsymbol{v}}^{\boldsymbol{l}*}) d\Omega_h - \int_{\Omega_h} p_h (\vec{\nabla}.\vec{v}^{l*}) d\Omega_h - \int_{\partial\Omega_{ht}} \vec{t}_0.\vec{v}^{l*} d\Gamma_h = 0 \\ \int_{\Omega_h} \boldsymbol{s}(\vec{\boldsymbol{b}}) : \dot{\boldsymbol{\epsilon}}(\vec{\boldsymbol{b}}^{*}) d\Omega_h - \int_{\Omega_h} p_h (\vec{\nabla}.\vec{b}^{*}) d\Omega_h = 0 \\ \int_{\Omega_h} p_h^* \left(-\vec{\nabla}.(\vec{v}^l + \vec{b}) - \frac{\dot{p}_h}{\kappa} + trace(\dot{\boldsymbol{\epsilon}}^{\boldsymbol{p}}) \right) d\Omega_h = 0 \\ \forall (\vec{v}^{l*}, \vec{b}^*, p_h^*) \in \mathcal{L}_h^0 \times \mathcal{B}_h \times \mathcal{P}_h \end{cases} \tag{1.57}$$

In the above equations, the $trace(\dot{\boldsymbol{\epsilon}}^{\boldsymbol{p}})$ term, which characterizes the plastic compressibility of material, is kept throughout the development of the formulations. In the following paragraphs, this term will be neglected, the material is therefore considered incompressible. The compressible case will be treated separately as a special case (see section 4.2.5).

By adopting the Galerkin standard method, where **the shape functions are chosen as the test functions**, 1.57 defines a non-linear system of equations of the unknown variables $\vec{v}^l, \vec{b}, p_h$, which can be written under algebraic form:

$$\begin{cases} \underline{\mathbf{R}}_e^l(\vec{v}_e^l, p_{he}) & = \underline{\mathbf{R}}_e^{ll} + \underline{\mathbf{0}} + \underline{\mathbf{R}}_e^{lp} & = \underline{\mathbf{0}} \\ \underline{\mathbf{R}}_e^b(\vec{b}_e, p_{he}) & = \underline{\mathbf{0}} + \underline{\mathbf{R}}_e^{bb} + \underline{\mathbf{R}}_e^{bp} & = \underline{\mathbf{0}} \\ \underline{\mathbf{R}}_e^p(\vec{v}_e^l, \vec{b}_e, p_{he}) & = \underline{\mathbf{R}}_e^{pl} + \underline{\mathbf{R}}_e^{pb} + \underline{\mathbf{R}}_e^{pp} & = \underline{\mathbf{0}} \end{cases} \tag{1.58}$$

Note that the underlined bold face symbols in these equations represent vector quantities and the bold face symbols represent tensor quantities. The index e signifies that these terms are calculated at each element. To simplify the writing, this e index will be dropped and these terms are understood to be calculated at element level, unless otherwise indicated. Moreover, the following conventions are used:

- The i,j,k,l indexes are used for the vector components index (i.e. $i,j,k,l \in \{1,2,3\}$).
- The n,m indexes are used for the element nodes numbers (i.e. $n,m \in \{1,2,3,4\}$).

With the above notations, let us define two tensors $\mathbf{B}^b$ and $\mathbf{B}^l$ with the components:

$$B_{ijkn}^l = \frac{1}{2} \left(\frac{\partial N_n^l}{\partial x_j} \delta_{ik} + \frac{\partial N_n^l}{\partial x_i} \delta_{jk} \right) \tag{1.59}$$

$$B_{ijk}^b = \frac{1}{2} \left(\frac{\partial N^b}{\partial x_j} \delta_{ik} + \frac{\partial N^b}{\partial x_i} \delta_{jk} \right) \tag{1.60}$$

By expanding Eq. 1.59 and Eq. 1.60, one can obtain:

$$B_{ijkn}^l v_{k,n}^l = \frac{1}{2} \sum_{n=1}^{4} \left(\frac{\partial N_n^l}{\partial x_j} v_{i,n}^l + \frac{\partial N_n^l}{\partial x_i} v_{j,n}^l \right) \tag{1.61}$$

$$B_{ijk}^b b_k = \frac{1}{2} \left(\frac{\partial N^b}{\partial x_j} b_i + \frac{\partial N^b}{\partial x_i} b_j \right) \tag{1.62}$$

The component of strain-rate tensor is determined as:

$$\dot{\epsilon}_{ij} = B_{ijkn}^l v_{k,n}^l + B_{ijk}^b b_k \tag{1.63}$$

The expressions of all the components of matrix defined in 1.58 are detailed:

$$R^{ll}_{k,n} = \int_{\Omega_e} s^l_{ij} B^l_{ijkn} J(\vec{x}) d\Omega_e - \int_{\partial\Omega_e} t_{0,k} N^l_n(\vec{x}) J'(\vec{x}) d\Gamma_e \tag{1.64}$$

$$R^{lp}_{k,n} = -\int_{\Omega_e} p_m N^l_m \frac{\partial N^l_n}{\partial x_k} J(\vec{x}) d\Omega_e \tag{1.65}$$

$$R^{bb}_{k} = \int_{\Omega_e} s^b_{ij} B^b_{ijk} J(\vec{x}) d\Omega_e \tag{1.66}$$

$$R^{bp}_{k} = -\int_{\Omega_e} p_m N^l_m \frac{\partial N^b}{\partial x_k} J(\vec{x}) d\Omega_e \tag{1.67}$$

$$R^{pl}_{n} = -\int_{\Omega_e} N^l_n \frac{\partial N^l_m}{\partial x_k} v^l_{k,m} J(\vec{x}) d\Omega_e \tag{1.68}$$

$$R^{pb}_{n} = -\int_{\Omega_e} N^l_n \frac{\partial N^b}{\partial x_k} b_k J(\vec{x}) d\Omega_e \tag{1.69}$$

$$R^{pp}_{n} = -\int_{\Omega_e} N^l_n N^l_m \frac{p_m - p_{m,0}}{\kappa \Delta t} J(\vec{x}) d\Omega_e \tag{1.70}$$

where $J(\vec{x}), J'(\vec{x})$ are the determinants of volumetric and surface Jacobian transformation matrices from the tetrahedral reference element to the current element; $p_{m,0}$ denotes the pressure at node m at the beginning of time increment. By assembling the local systems, the non-linear global system is obtained:

$$\underline{\mathbf{R}} = \begin{cases} \underline{\mathbf{R}}^l(\vec{v}^l, p_h) & = \underline{0} \quad \text{(3xNBNO equations)} \\ \underline{\mathbf{R}}^b(\vec{b}, p_h) & = \underline{0} \quad \text{(3xNBEL equations)} \\ \underline{\mathbf{R}}^p(\vec{v}^l, \vec{b}, p_h) & = \underline{0} \quad \text{(1xNBNO equations)} \end{cases} \tag{1.71}$$

1.2.7 Temporal discretization

At the instant t, the system is supposed to be at equilibrium. The equilibrium state is then disturbed by updating the external loads and the new problem is to determine the velocity and pressure fields that respect the equilibrium at $t+\Delta t$. The system is solved by the Newton-Raphson method, which linearizes the equations by the first order Taylor's development.

Let us consider an element, in which the system 1.58 can be written as:

$$\underline{\mathbf{R}}_e = \begin{cases} \underline{\mathbf{R}}^l_e(\vec{v}^l_e, \vec{p}_{he}) & = \underline{\mathbf{R}}^{ll}_e + \underline{0} + \underline{\mathbf{R}}^{lp}_e & = \underline{0} \\ \underline{\mathbf{R}}^b_e(\vec{b}_e, \vec{p}_{he}) & = \underline{0} + \underline{\mathbf{R}}^{bb}_e + \underline{\mathbf{R}}^{bp}_e & = \underline{0} \\ \underline{\mathbf{R}}^p_e(\vec{v}^l_e, \vec{b}_e, \vec{p}_{he}) & = \underline{\mathbf{R}}^{pl}_e + \underline{\mathbf{R}}^{pb}_e + \underline{\mathbf{R}}^{pp}_e & = \underline{0} \end{cases} \tag{1.72}$$

Note that in this expression, the unknown pressure variable $\vec{p}_{he}$ *is written under vector form* since we want to solve for the pressure values at *4 nodes* of each tetrahedral element ($\vec{p}_{he}$ is thus a 4 components vector). At each iteration of the algorithm, solving this system of equations reduces to solving the following linear system:

$$\begin{bmatrix} \mathbf{H}^{ll}_e & \mathbf{0} & \mathbf{H}^{lp}_e \\ \mathbf{0} & \mathbf{H}^{bb}_e & \mathbf{H}^{bp}_e \\ \mathbf{H}^{pl}_e & \mathbf{H}^{pb}_e & \mathbf{H}^{pp}_e \end{bmatrix} \begin{pmatrix} \delta\vec{v}^l_e \\ \delta\vec{b}_e \\ \delta\vec{p}_{he} \end{pmatrix} = - \begin{pmatrix} \underline{\mathbf{R}}^l_e \\ \underline{\mathbf{R}}^b_e \\ \underline{\mathbf{R}}^p_e \end{pmatrix} \tag{1.73}$$

The $\mathbf{H}^{xy}_e$ forms the stiffness matrix (or Hessian matrix), which is defined as:

$$\mathbf{H}^{xy}_e = \frac{\partial \underline{\mathbf{R}}^{xy}_e}{\partial z} \tag{1.74}$$

where: $(xy) \in \{(ll),(lp),(bb),(bp),(pl),(pb),(pp)\}$, and $z \in \{\vec{v}^l_e, \vec{b}_e, p_{he}\}$. Generally, for an incompressible case, this system is symmetric (i.e. $\mathbf{H}^{pl}_e = (\mathbf{H}^{lp}_e)^T$, $\mathbf{H}^{pb}_e = (\mathbf{H}^{bp}_e)^T$).

1.2.7.1 The Hessian matrix

The expression of Hessian matrix components is developed in the following:

$$H^{ll}_{e,knlm} = \frac{\partial R^{ll}_{e,kn}}{\partial v^{l}_{e,lm}} = \int_{\Omega_e} B^{l}_{ijkn} \frac{\partial s^{l}_{ij}}{\partial v^{l}_{e,lm}} J(\vec{x}) d\Omega_e - \int_{\partial\Omega_e} \frac{\partial t_{0,k}}{\partial v^{l}_{e,lm}} N^{l}_{n}(\vec{x}) J'(\vec{x}) d\Gamma_e \tag{1.75}$$

By using Eq. 1.63, the first derivation can be written as:

$$\frac{\partial s^{l}_{ij}}{\partial v^{l}_{e,lm}} = \frac{\partial s^{l}_{ij}}{\partial \dot{\epsilon}_{pq}} \frac{\partial \dot{\epsilon}_{pq}}{\partial v^{l}_{e,lm}} = D^{l}_{ijpq} B^{l}_{pqlm} \tag{1.76}$$

where B^{l}_{pqlm} is defined in Eq. 1.59 and D^{l}_{ijpq} is the component of the fourth order matrix $\frac{\partial \mathbf{s}^{l}}{\partial \dot{\epsilon}}$. Finally, the component of matrix $\mathbf{H}^{ll}_{e}$ is expressed as:

$$H^{ll}_{e,knlm} = \int_{\Omega_e} B^{l}_{ijkn} D^{l}_{ijpq} B^{l}_{pqlm} J(\vec{x}) d\Omega_e - \int_{\partial\Omega_e} \frac{\partial t_{0,k}}{\partial v^{l}_{e,lm}} N^{l}_{n}(\vec{x}) J'(\vec{x}) d\Gamma_e \tag{1.77}$$

Note that at element level, $\mathbf{H}^{ll}_{e}$ is a 12x12 matrix. Similarly to the above demonstration, the expressions of other matrices can be listed as below:

$$H^{lp}_{e,knm} = \frac{\partial R^{lp}_{e,kn}}{\partial p_m} = -\int_{\Omega_e} N^{l}_{m} \frac{\partial N^{l}_{n}}{\partial x_k} J(\vec{x}) d\Omega_e \tag{1.78}$$

$$H^{bb}_{e,kl} = \frac{\partial R^{bb}_{e,k}}{\partial b_l} = \int_{\Omega_e} B^{b}_{ijk} D^{b}_{ijpq} B^{b}_{pql} J(\vec{x}) d\Omega_e \tag{1.79}$$

$$H^{bp}_{e,km} = \frac{\partial R^{bp}_{e,k}}{\partial p_m} = -\int_{\Omega_e} N^{l}_{m} \frac{\partial N^{b}}{\partial x_k} J(\vec{x}) d\Omega_e \tag{1.80}$$

$$H^{pl}_{e,knm} = \frac{\partial R^{pl}_{e,n}}{\partial v_{le,km}} = -\int_{\Omega_e} N^{l}_{n} \frac{\partial N^{l}_{m}}{\partial x_k} J(\vec{x}) d\Omega_e \tag{1.81}$$

$$H^{pp}_{e,nm} = \frac{\partial R^{pp}_{e,n}}{\partial p_m} = -\int_{\Omega_e} \frac{N^{l}_{n} N^{l}_{m} J(\vec{x})}{\kappa \Delta t} d\Omega_e \tag{1.82}$$

1.2.7.2 Bubble elimination

From the second equation of system 1.73, one can derive:

$$\vec{b}_e = -(\mathbf{H}^{bb}_{e})^{-1} (\underline{\mathbf{R}}^{b}_{e} + \mathbf{H}^{bp}_{e} \delta\vec{p}_{he}) \tag{1.83}$$

We can thus eliminate the bubble part from the system, by replacing $\vec{b}_e$ as in Eq. 1.83 in the system 1.73 and by reordering the equations:

$$\begin{bmatrix} \mathbf{H}^{ll}_{e} & \mathbf{H}^{lp}_{e} \\ \mathbf{H}^{pl}_{e} & \mathbf{H}^{pp}_{e} - \mathbf{H}^{pb}_{e} (\mathbf{H}^{bb}_{e})^{-1} \mathbf{H}^{bp}_{e} \end{bmatrix} \begin{pmatrix} \delta\vec{v}^{l}_{e} \\ \delta\vec{p}_{he} \end{pmatrix} = - \begin{pmatrix} \underline{\mathbf{R}}^{l}_{e} \\ \underline{\mathbf{R}}^{p}_{e} - \mathbf{H}^{pb}_{e} (\mathbf{H}^{bb}_{e})^{-1} \underline{\mathbf{R}}^{b}_{e} \end{pmatrix} \tag{1.84}$$

From Eqs. 1.66, 1.67, 1.69, one can see that the terms $\underline{\mathbf{R}}^{bb}_{e}$, $\underline{\mathbf{R}}^{pb}_{e}$ are linear with respect to the bubble velocity; and the term $\underline{\mathbf{R}}^{bp}_{e}$ is linear with respect to the pressure. From this observation, these terms can be expressed as:

$$\underline{\mathbf{R}}^{bb}_{e} = \mathbf{H}^{bb}_{e} \vec{b}_e, \quad \underline{\mathbf{R}}^{bp}_{e} = \mathbf{H}^{bp}_{e} \vec{p}_{he}, \quad \underline{\mathbf{R}}^{pb}_{e} = \mathbf{H}^{pb}_{e} \vec{b}_e \tag{1.85}$$

By noting $\mathbf{C}_e = \mathbf{H}^{pb}_{e} (\mathbf{H}^{bb}_{e})^{-1} \mathbf{H}^{bp}_{e}$ and using the above equations, the system 1.84 can be reduced to:

$$\begin{bmatrix} \mathbf{H}^{ll}_{e} & \mathbf{H}^{lp}_{e} \\ \mathbf{H}^{pl}_{e} & \mathbf{H}^{pp}_{e} - \mathbf{C}_e \end{bmatrix} \begin{pmatrix} \delta\vec{v}^{l}_{e} \\ \delta\vec{p}_{he} \end{pmatrix} = - \begin{pmatrix} \underline{\mathbf{R}}^{l}_{e} \\ \underline{\mathbf{R}}^{pl}_{e} + \underline{\mathbf{R}}^{pp}_{e} - \mathbf{C}_e \vec{p}_{he} \end{pmatrix} \tag{1.86}$$

Finally, the global linear system to be solved at each iteration k is:

$$[\mathbf{H}] \begin{pmatrix} \delta\vec{v}^{l} \\ \delta\vec{p}_{h} \end{pmatrix} = \underline{\mathbf{R}} \tag{1.87}$$

At each iteration, this system is solved and the values of velocity and pressure are updated: $\vec{v}^l + \delta\vec{v}^l \rightarrow \vec{v}^l$, $p_h + \delta p_h \rightarrow p_h$. This iterative loop is carried out until the converged solutions are obtained: δp_h and $\delta\vec{v}^l <$ TOLERANCE. For the details of this procedure, see [Aliaga, 2000] and [Fayolle, 2008]. In the first reference, the author presents this procedure for a thermo-viscoplastic behavior law with von Mises plasticity, while in the second reference, the author presents the implementation of Lemaitre damage model with von Mises plasticity. For the implementation of a pressure-dependent plasticity model into a mixed velocity-pressure FE formulation, the difficulty lies on the consistency of the two pressure fields: at nodes and at integration points. The modifications of the global stiffness matrix allow obtaining a correct result for pressure, which is detailed in section 4.2.5.

1.2.7.3 Local integration of behavior equations

The integration of the constitutive equations for a incompressible case (i.e. pressure independent case) is quite simple since at each iteration, only the deviatoric parts of stress and strain tensors are calculated. For more details, see chapter 3 of [Fayolle, 2008]. A complete procedure for a compressible case (pressure dependent plasticity) is presented in section 4.2.

1.3 Elastoplasticity

Elastoplastic constitutive equations can be summarized as:

1. Elastic behavior (Eq. 1.93):
$$\boldsymbol{\sigma} = \underset{\sim}{\boldsymbol{D}}^{\boldsymbol{e}} : \boldsymbol{\epsilon}^{\boldsymbol{e}} \tag{1.88}$$

2. Strain-rate decomposition:
$$\dot{\boldsymbol{\epsilon}} = \dot{\boldsymbol{\epsilon}}^{\boldsymbol{e}} + \dot{\boldsymbol{\epsilon}}^{\boldsymbol{p}} \tag{1.89}$$

3. Yield criterion with the use of a yield function :
$$\phi = \phi\left(\boldsymbol{\sigma}, \underline{\boldsymbol{A}}\right) \tag{1.90}$$
where $\dot{\boldsymbol{\epsilon}}^{\boldsymbol{e}}$, $\dot{\boldsymbol{\epsilon}}^{\boldsymbol{p}}$, $\dot{\boldsymbol{\epsilon}}$ denote the elastic, plastic and total strain rate tensors respectively; $\boldsymbol{\sigma}$ is the Cauchy stress tensor ($-\boldsymbol{\sigma}$ is the thermodynamical force associated with the plastic strain); $\underline{\boldsymbol{A}} = \{A_k\}$ is a set of *conjugate thermodynamical forces* associated with the set of *internal scalar state variables* $\underline{\boldsymbol{\alpha}}=\{\alpha_k\}$. In this section, only the internal state variables that are associated with the phenomenon of hardening are considered. For the general case with the influence of damage, see Appendix A.4.

4. Plastic flow rule and hardening law :
$$d\boldsymbol{\epsilon}^{\boldsymbol{p}} = d\lambda \frac{\partial g}{\partial \boldsymbol{\sigma}} \quad \text{and} \quad d\underline{\boldsymbol{\alpha}} = -d\lambda \frac{\partial g}{\partial \underline{\boldsymbol{A}}} \tag{1.91}$$
where $d\lambda$ is a positive scalar, the so-called *plastic multiplier*; $g\left(\boldsymbol{\sigma}, \underline{\boldsymbol{A}}\right)$ is the flow potential (with assumption that the hardening is derived from the same potential, which requires that $g\left(\boldsymbol{\sigma}, \underline{\boldsymbol{A}}\right)$ is non-negative, convex and $g\left(\boldsymbol{0}, \underline{\boldsymbol{0}}\right) = 0$). For an associative flow, the yield function and the flow potential are the same: $g = \phi$.

5. Plastic consistency condition:
$$\dot{\phi}\left(\boldsymbol{\sigma}, \underline{\boldsymbol{A}}\right) = 0 \tag{1.92}$$
This condition assures that the current stress state lies on the yield surface even though the shape and size of the surface may change during plastic loading (i.e. when $\dot{\lambda} \neq 0$). It is used to obtain the plastic multiplier at each increment.

In each following subsections, details of these above equations are given.

1.3.1 Elasticity

The elastic deformation is reversible (in comparison with irreversible plastic deformation). Throughout the present manuscript, the hypothesis of small elastic deformation is adopted. An elastic law represents the relation between the Cauchy stress tensor $\boldsymbol{\sigma}$ and the elastic strain tensor $\boldsymbol{\epsilon}^{\mathbf{e}}$ through the fourth order elasticity tensor (or the elastic tangent modulus) $\underset{\sim}{\boldsymbol{D}}^{\mathbf{e}}$:

$$\boldsymbol{\sigma} = \underset{\sim}{\boldsymbol{D}}^{\mathbf{e}} : \boldsymbol{\epsilon}^{\mathbf{e}} \tag{1.93}$$

Throughout the present dissertation, linear isotropic elasticity is assumed and follows Hooke's law. The elastic tangent modulus $\underset{\sim}{\boldsymbol{D}}^{\mathbf{e}}$ is defined as:

$$D^e_{ijkl} = \left(K - \frac{2}{3}G\right)\delta_{ij}\delta_{kl} + 2G\delta_{ik}\delta_{jl} \tag{1.94}$$

where δ is the Kronecker symbol; $G = \frac{E}{2(1+\nu)}$ and $K = \frac{E}{3(1-2\nu)}$ are the elastic shear and bulk moduli respectively.

1.3.2 Yield criterion

For the materials used in the present study, we have adopted isotropic yield functions to describe the yield criterion. The yield function can depend on the hydrostatic pressure (e.g. GTN yield function) or may be pressure insensitive (von Mises function). In both cases, associative plasticity has been assumed. For a detailed review of yield criteria, interested readers can refer to Appendix A.3.

1.3.3 Hardening law

The hardening laws describe the change of yield stress or of the yield surface in the stress space during loading, including the dilatation and the translation of this surface. The isotropic hardening laws describe the dilatation while the kinematic hardening laws describe the translation. It has been shown that generally, the kinematic hardening is negligible for large deformation, which is the case of forming processes. For this reason, throughout the present study, kinematic hardening has not been considered. It is worth noting that the hardening model plays an important role to obtain accurate damage parameters in the identification process (see Chapters 2 and 3). A short review of several isotropic hardening laws is given, where the models are divided into two groups.

1.3.3.1 Isotropic strain hardening law

In this group, the influence of strain rate and temperature on the flow stress is not considered in the equations. These constitutive equations can be used to describe the flow stress at room temperature and at low strain-rate. We can list several models in this group:

$$\text{Hollomon's equation [Hollomon, 1944]} \quad \sigma_0 = C\overline{\epsilon}_p^{\,n} \tag{1.95}$$

$$\text{Swift's equation [Swift, 1952]} \quad \sigma_0 = \sqrt{3}K(\epsilon_0 + \overline{\epsilon}_p)^n \tag{1.96}$$

$$\text{Ludwik's equation [Ludwik, 1996]} \quad \sigma_0 = \sqrt{3}K(1 + a\overline{\epsilon}_p{}^n) \tag{1.97}$$

$$\text{Voce's equation [Voce, 1955]} \quad \sigma_0 = \sigma_{ps} - \left(\sigma_{ps} - \sigma_{p0}\right) exp(-n\overline{\epsilon}_p) \tag{1.98}$$

where σ_0 is the flow stress of the material; $\overline{\epsilon}_p$ is the equivalent plastic strain; other variables are material parameters. Evidently, none of these equations can be adapted for all materials and loading conditions (which is shown later in Chapter 2). At small strain, Eqs. 1.95, 1.96, 1.97 were used to describe the stress-strain relation of several materials, such as steels or copper. The Voce equation was shown to give satisfactory result for aluminum and for large strain application since it leads to a steady state flow at high strain. For more constitutive equations in this group, interested readers can refer to [Gronostajski, 2000] for a detailed discussion.

1.3.3.2 Isotropic constitutive law with strain-rate and temperature influences

Eqs. 1.95, 1.96, 1.97 can be modified to account for the temperature and strain-rate influences by adding a multiplicative term (or an additive term) in the right hand side (e.g. Hollomon's equation → Fields and Backofen's equation: $\sigma_0 = C\bar{\epsilon}^n\dot{\bar{\epsilon}}^m$ [Fields and Backofen, 1957], where m is the strain-rate sensitivity coefficient).

A more complicated phenomenological equation was proposed by Hansel and Spittel [Hansel and Spittel, 1979], where both strain hardening coefficient and strain-rate sensitivity coefficient were taken as functions of temperature:

$$\sigma_0 = Aexp(m_1T + m_4/\bar{\epsilon} + m_7\bar{\epsilon})\dot{\bar{\epsilon}}^{m_3+m_8T}\bar{\epsilon}^{m_2}(1+\bar{\epsilon})^{m_5T}T^{m9} \tag{1.99}$$

where $A(MPa)$, $m_i(i = 1,..,9)$ are material parameters. Other hardening models that are linked with microstructure properties (e.g. phase change, dynamic recovery, recrystallization) can be found in [Gronostajski, 2000], [Krauer and Hora, 2012], [Beese and Mohr, 2012].

1.3.3.3 Conclusion of the choice of hardening model

In the present study, only isotropic hardening models are used since our applications in forming processes involve large strain, where kinematic hardening has limited influences. Moreover, the influence of strain-rate and temperature are not accounted for. For this reason, all the mechanical calibration tests were carried out at the same strain rate and temperature.

1.4 Ductile damage mechanisms and models

1.4.1 Introduction

Ductility is understood as an intrinsic ability of materials to undergo a certain amount of plastic deformation without fracture (or without *mesocrack* formation). The fracture of ductile material occurs after microvoids or shear bands develop in the metal matrix, around inclusions or other discontinuities such as grain boundaries. The damage occurring under large plastic strain is called ductile damage (in opposition to brittle damage), and is frequently observed in metal forming failure.

Microscopically, damage is associated with voids nucleation, growth and coalescence under high and moderate stress triaxiality, or shear band formation under low stress triaxiality. Macroscopically, damage is represented as the progressive degradation of a material, which exhibits a decrease in material stiffness and strength. The role of microvoids in ductile failure was first modeled by McClintock ([McClintock et al., 1966]), who analyzed the evolution of an isolated cylindrical void in a ductile elastoplastic matrix. Rice and Tracey ([Rice and Tracey, 1969]) studied the evolution of spherical voids in an elastic-perfectly plastic matrix. In these studies, the interaction between microvoids, the coalescence process and the hardening effects were neglected and failure was assumed to occur when the cavity radius would reach a critical value specific for each material. These results showed that void growth is governed by stress triaxiality. Gurson ([Gurson, 1977]), in an *upper bound analysis*[10] of a finite sphere containing an isolated spherical void in a rigid perfectly plastic matrix, employed the void volume fraction f (or porosity) as an internal variable to represent damage and its softening effect on material strength. This model was then improved to account for different aspects: prediction accuracy ([Tvergaard, 1981]), void nucleation ([Chu and Needleman, 1980]), void coalescence ([Needleman and Tvergaard, 1984, Tvergaard and Needleman, 1984]), void shape effect (e.g. [Gologanu et al., 1993, Pardoen and Hutchinson, 2000]), void size effect (e.g. [Wen et al., 2005], [Monchiet and Bonnet, 2013]), void/particle interaction (e.g. [Siruguet and Leblond, 2004]), isotropic strain hardening ([Leblond et al., 1995]), kinematic hardening (e.g. [Leblond et al., 1995],

[10] The upper bound method consists of two stages: (1) find a kinematically admissible velocity field (or a family of velocity fields that is compatible with the boundary conditions); (2) within the proposed family, find the one that minimizes the plastic dissipation.

[Muhlich and Brocks, 2003]), plastic anisotropy (e.g. [Benzerga and Besson, 2001, Benzerga et al., 2004]), rate dependency (e.g. [Tvergaard, 1989]), shear effect (e.g. [Nahshon and Hutchinson, 2008, Xue, 2008]).

1.4.2 Damage mechanisms

1.4.2.1 Characterization of stress states

For an isotropic material, the stress state is characterized by the symmetric stress tensor (6 components) or its eigenvalues (3 principal stresses: $\sigma_1, \sigma_2, \sigma_3$). Material models can also be formulated in terms of the 3 invariants of the stress tensor, which are defined as:

$$p = -\sigma_h = -\frac{1}{3}tr(\boldsymbol{\sigma}) = -\frac{1}{3}(\sigma_1+\sigma_2+\sigma_3) = -\frac{I_1}{3} \tag{1.100}$$

$$q = \overline{\sigma} = \sqrt{\frac{3}{2}\boldsymbol{S}:\boldsymbol{S}} = \sqrt{\frac{1}{2}\left[(\sigma_1-\sigma_2)^2+(\sigma_2-\sigma_3)^2+(\sigma_3-\sigma_1)^2\right]} = \sqrt{3J_2} \tag{1.101}$$

$$r = \left(\frac{27}{2}det(\boldsymbol{S})\right)^{1/3} = \left(\frac{27}{2}(\sigma_1-\sigma_h)(\sigma_2-\sigma_h)(\sigma_3-\sigma_h)\right)^{1/3} = \left(\frac{27}{2}J_3\right)^{1/3} \tag{1.102}$$

where I_1 is the first invariant of the stress tensor; J_2 and J_3 are the second and the third invariants of the deviatoric stress tensor. In the ductile fracture community, the dimensionless hydrostatic pressure ($\eta = \frac{\sigma_h}{\overline{\sigma}}$) and the Lode angle θ are often used. The latter parameter is defined through the normalized third stress invariant:

$$\xi = \left(\frac{r}{q}\right)^3 = cos(3\theta) \tag{1.103}$$

The geometrical representation of Lode angle θ is shown in Figs. 1.17a and 1.17b ($0 < \theta < \frac{\pi}{3}$ - for each sextant of the octahedral plane, the azimuth angle θ and the value of $\frac{27}{2}\frac{J_3}{\overline{\sigma}^3}$ can be one-to-one mapped).

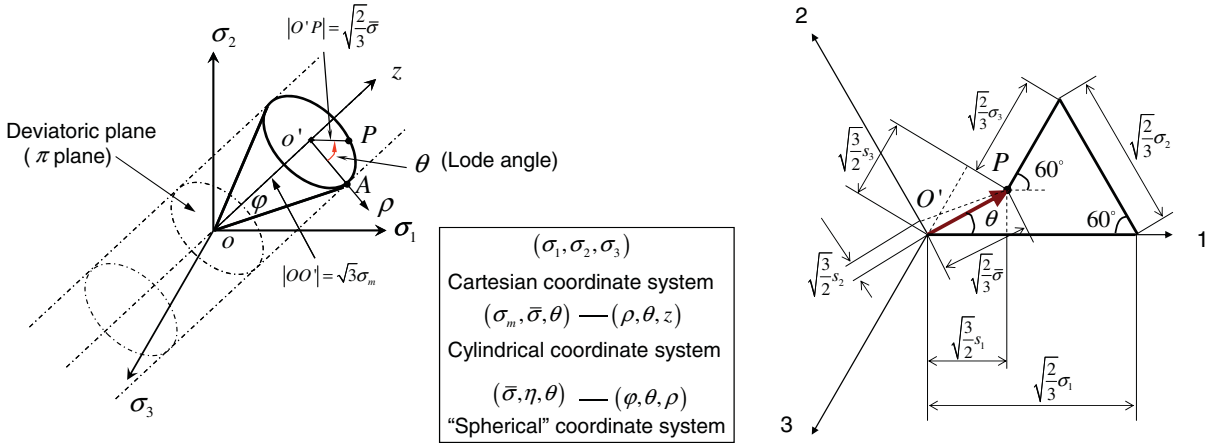

(a) *The Lode angle (azimuth angle of the octahedral plane) in the space of principal stresses.*

(b) *Geometrical interpretation in π plane.*

Fig. 1.17: *Representation of the Lode angle (a) in the stress space and on the deviatoric plane (b). In these figure $\sigma_m = \sigma_h$ (figure adapted from [Bai and Wierzbicki, 2008]).*

A stress state can therefore be expressed in the spherical coordinate system of $(\overline{\sigma}, \eta, \theta)$ (see Fig. 1.17a [Bai and Wierzbicki, 2008]). The φ angle in Fig. 1.17a is related to the stress triaxiality by:

$$\eta = \frac{\sqrt{2}}{3}tan^{-1}(\varphi) \tag{1.104}$$

Unless otherwise indicated, the term "triaxiality" refers to the "stress triaxiality ratio" hereinafter. The normalized Lode angle $\overline{\theta}$ is defined as:

$$\overline{\theta} = 1 - \frac{6\theta}{\pi} = 1 - \frac{2}{\pi}arccos\left(\left(\frac{r}{q}\right)^3\right) \tag{1.105}$$

where r and q are defined in Eqs. 1.101 and 1.102, and the parameter $\overline{\theta}$ ($-1 \leq \overline{\theta} \leq 1$) will be called the Lode angle parameter hereinafter (or the Lode parameter). Some authors used another formula to calculate the Lode angle (e.g. [Xue and Wierzbicki, 2009]) and the Lode parameter μ (e.g. [Barsoum and Faleskog, 2007a]):

$$\theta_L = tan^{-1}\left(\frac{1}{\sqrt{3}}\frac{2\sigma_2 - \sigma_1 - \sigma_3}{\sigma_1 - \sigma_3}\right) \tag{1.106}$$

$$\mu = \frac{2\sigma_2 - \sigma_1 - \sigma_3}{\sigma_1 - \sigma_3} \tag{1.107}$$

where $-\frac{\pi}{6} < \theta_L < \frac{\pi}{6}$. These definitions and the definitions in Eq. 1.103 and Eq. 1.105 are totally equivalent, which are linked by the following relation:

$$\theta_L = \theta - \frac{\pi}{6} \text{ (for all stress states, see Fig. 1.18a)} \tag{1.108}$$

$$\mu = -\overline{\theta} \text{ (for some conventional stress states, see Fig. 1.18b)} \tag{1.109}$$

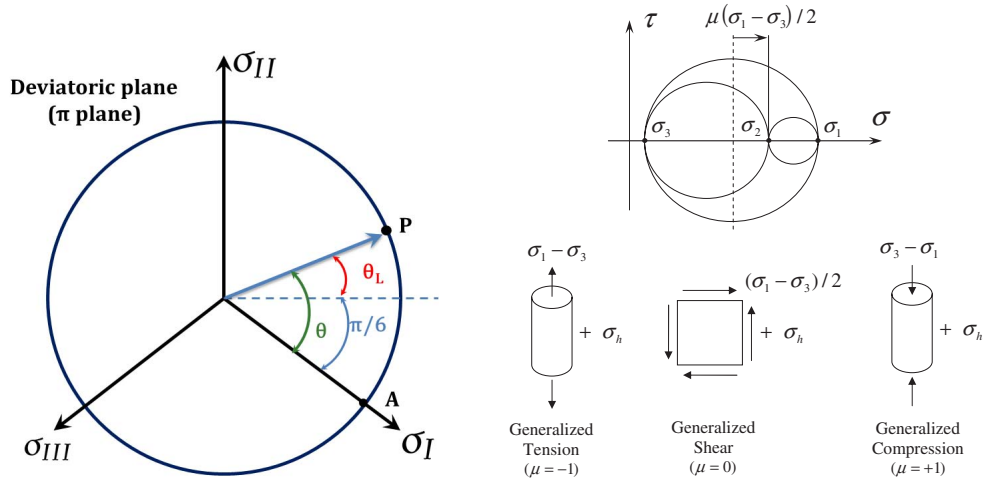

(a) *The Lode angle (azimuth angle of the octahedral plane) in the space of principal stresses.*

(b) *The Lode angle parameter in the Mohr circle [Barsoum and Faleskog, 2007a]*

Fig. 1.18: *Other definitions of Lode angle θ_L (a) and Lode parameter μ (b).*

Throughout the present manuscript, the definitions in Eq. 1.103 and Eq. 1.105 are used to represent the Lode angle (θ) and the Lode parameter ($\overline{\theta}$), unless otherwise indicated (e.g. section 3.1.1.2 of Chapter 3, section 6.1.1 of Chapter 6).

1.4.2.2 Mechanisms dominating at positive stress triaxiality ratio

Stress triaxiality ratio is a dimensionless parameter, which is defined as: $\eta = \frac{\sigma_h}{\sigma_{eq}}$, where σ_h is the hydrostatic stress and σ_{eq} is the von Mises (vM) equivalent stress. In the high stress triaxiality range, damage is governed by void nucleation, growth and coalescence (or linkage) mechanisms (in a elastoplastic/elastic matrix), which have been extensively studied in the literature. The description of the sequence of damage mechanisms during a tension test on an axisymmetric notched specimen is presented in Fig. 1.19, through the true stress-true strain curve. It is shown for 2 cases: (1) damage impacts plastic behavior (damage / plasticity coupling), (2) plasticity is not changed by damage (uncoupled approach).

Voids nucleation Unlike void growth, which would be treated independently of material hardening, the void nucleation process is *strongly material-dependent*. Generally, it depends on the particle strength, size and shape, as well as hardening of matrix material. Voids can be nucleated either by matrix-particle decohesion (Fig. 1.20a) or by particle cracking (Figs. 1.20b). The decohesion mode of nucleation is favored in the case of soft matrices while the particle cracking mode is often observed in hard matrices

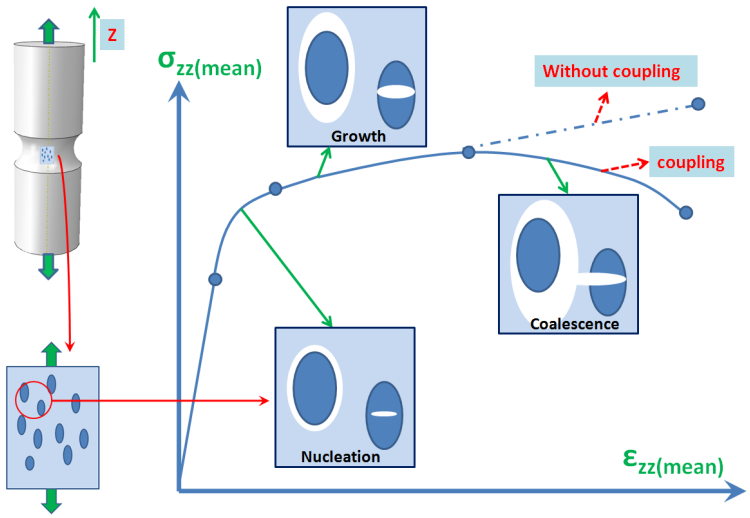

Fig. 1.19: *The sequence of damage mechanisms in the tension test on notched specimen.*

([Benzerga and Leblond, 2010]). Voids nucleate preferentially at large particles due to a higher probability of defects and local stress fields generated when the matrix undergoes plastic deformation. However, the voids created during this stage are small so they still do not have a visible influence on the material macroscopic behavior.

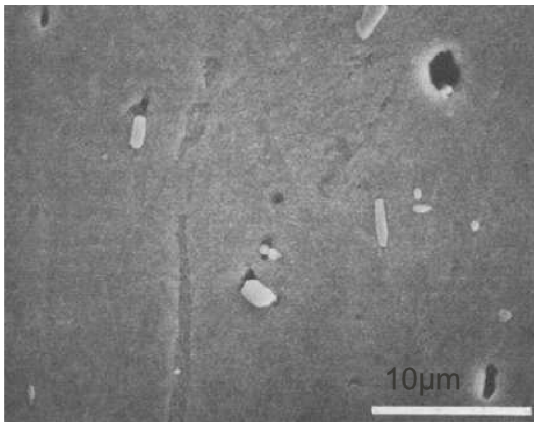

(a) *Nucleation by matrix-particle decohesion in a copper matrix Cu-0.6 pct Cr alloy containing Cu-Cr particle ([Argon and Im, 1975]).*

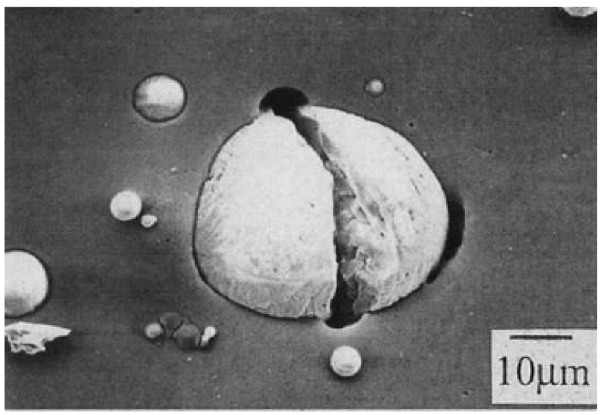

(b) *Nucleation from particle fracture in aluminum 6061 matrix, with Al_2O_3 inclusions ([Kanetake et al., 1995]). Loading is horizontal.*

Fig. 1.20: *Voids nucleation mechanisms: (a) interface decohesion, (b) particle cracking (figure adapted from [Landron, 2011]).*

One of the pioneers of voids nucleation modeling was [Gurland and Plateau, 1963], who employed the energetic method (which was formulated from the balance of stored elastic strain energy and crack surface energy), to study the voids nucleation due to the cracking of spherical particle. [Goods and Brown, 1979] proposed another energy criterion to define nucleation by matrix-particle decohesion. These energetic approaches are not discussed here, interested readers can refer to [Gurland and Plateau, 1963] and [Goods and Brown, 1979] for more details. Other criteria are often based on critical stress; some of them are listed below:

- [Argon et al., 1975] proposed a phenomenological critical stress condition based on a continuum plasticity approach, which involves the first stress and the second deviatoric stress invariants:

$$\sigma_I^{max} + \Sigma_h = min(\sigma_c^I, \sigma_c^p) \tag{1.110}$$

where σ_I^{max} is the maximum principal stress (local); Σ_h is the hydrostatic stress (remote) (see Fig. 1.21 for loading description); σ_c^I is the maximum stress that the matrix-particle interface can undergo without decohesion; σ_c^P is the particle strength. This formulation was obtained by analyzing non-deformable inclusions in a perfectly plastic or elastic matrix. In addition, there was no particle size or inclusions interaction effects.

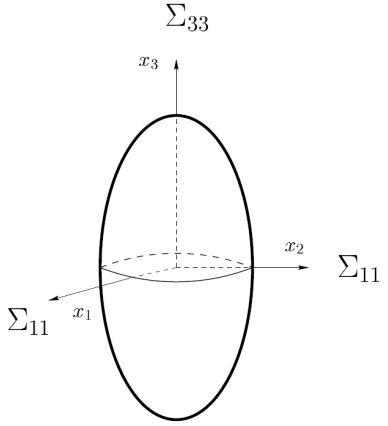

Fig. 1.21: *The sketch of an ellipsoidal particle, subjected to the remote stresses Σ_{ii} (e.g. stresses at boundary of the RVE). The shape factor (ω_P) is defined by the ratio between the major axis and the minor axis (figure adapted from [Benzerga, 2000]).*

- [Beremin, 1981] proposed an improved stress-based criterion, which accounts for the plastic strain incompatibility between matrix and particle as well as the particle shape effect. This criterion is based on the generalization to an elastoplastic matrix of the Eshelby solution (initially for the elastic case [Eshelby, 1957]) by [Berveiller and Zaoui, 1978]. This study was carried out on an A508 steel containing *elongated* MnS inclusions[11]:

$$\Sigma_I^{max} + k_s(\Sigma_{eq} - \sigma_0) = min(\sigma_c^I, \sigma_c^P) \tag{1.111}$$

where Σ_I^{max} is the remote maximum principal stress; σ_0 is the matrix initial yield strength; k_s is a factor depending on particle shape and loading direction (see Fig. 1.22 for different values of this variable for different particle shapes and loading cases); $k_s(\Sigma_{eq} - \sigma_0)$ defines the internal stress, which arises from strain inhomogeneity between inclusion and matrix. Note that in [Beremin, 1981], the author used this criterion to predict the decohesions both by inclusions failure (in longitudinal direction - loading direction of his tensile test on notched round bar) and by interface debonding (in transverse direction). The stress fields are considered as homogeneous within the particle both in Eq. 1.110 and Eq. 1.111.

- More accurate prediction can be obtained by the studies of [Lee and Mear, 1999, Lee and Mear, 1999a], in which the stress concentration factors at interface and inside the particle were employed to formulate the nucleation criteria:

$$\kappa_I = \frac{max(\sigma_{\eta\eta}|_{\eta=\eta_0})}{\Sigma_{33}}; \quad \kappa_P = \frac{max(\sigma_I^P|_{\eta\leq\eta_0})}{\Sigma_{33}} \tag{1.112}$$

where Σ_{33} is the remote axial stress (see Fig. 1.21); $\sigma_{\eta\eta}|_{\eta=\eta_0}$ is the normal stress at the matrix-particle interface ($\eta = \eta_0$, where η defines a spheroidal coordinate, which allows locating the confocal ellipses); $\sigma_I^P|_{\eta\leq\eta_0}$ is the maximum principal stress in the particle volume ($\eta \leq \eta_0$). The two factors κ_I and κ_P depend on different factors, such as rheology parameters (e.g. Poisson's ratio[12], rigidity mismatch, hardening coefficient of matrix, matrix yield strength), morphology parameters (e.g. particle aspect

[11] MnS inclusions are soft inclusions, which are two times softer than steel matrix. The inclusion in a matrix is said *soft* when its yield stress is smaller than that of matrix. In the other case, it is said *hard*. The ratio between the particle yield stress and the matrix yield stress is called the *relative plasticity* [Benzerga, 2000].

[12] Poisson's ratio was shown to have minor influence [Lee and Mear, 1999].

ratio, particle size), loading (the remote stress triaxiality). *Stress concentration inside the particle is always greater than that at matrix-particle interface as soon as plastification occurs.*

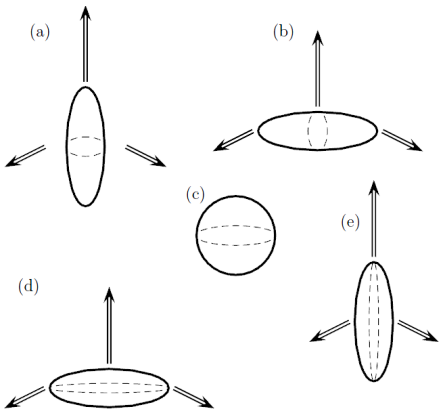

Particle shape	ωp	Loading direction	k_s	Sketch
Fiber	$\gg 1$	axial	$\frac{2}{3}\left(-1+\frac{1}{3}\frac{1+2w^{p2}}{2\ln(2w^p-1)-1}\right)$	(a)
		transverse	$\frac{1}{2}\left(1+\frac{1}{9}\frac{1+2w^{p2}}{2\ln(2w^p-1)-1}\right)$	(b)
Sphere	1		1	(c)
Disk	$\ll 1$	axial	$\frac{2}{3}\left(-1+\frac{4}{3\pi}\frac{1}{w^p}\right)$	(d)
		transverse	$\frac{2}{3}\left(-1+\frac{10}{3\pi}\frac{1}{w^p}\right)$	(e)

Fig. 1.22: *Different loading configurations for prolate particles (a,b), spherical particle (c) and for oblate particles (d,e) and the corresponding value of function k_s (figure adapted from [Benzerga and Leblond, 2010]).*

A review of the nucleation aspect in ductile fracture based on micromechanical approach can be found in Appendix A of [Benzerga, 2000], in which the influence of different factors (*relative plasticity*, *particle size*, *rigidity mismatch*, etc.) were discussed in detail. The main conclusions are summarized below:

- Matrix hardening: the increase of matrix hardening (i.e. a more hardenable matrix) favors the decohesion mode of nucleation. For spherical particles, this influence is negligible in the domain $n \in [0.1-0.2]$ for ferritic-pearlitic steel (n is the hardening coefficient).
- Particle size influence: more precisely, the influence of particle volume fraction, which leads to the interactions among particles. As also stated in [Benzerga and Leblond, 2010], for the nucleation by debonding, above a certain particle size, there is no particle size effect on the plastic strain required for nucleation.
- Rigidity mismatch: the rigidity mismatch is defined by the ratio of Young's modulus of particle to Young's modulus of matrix (E^P/E). Generally, the two stress intensity factors (κ_I and κ_P) increase with E^P/E, which means that the more rigid particle favors the nucleation.
- The influence of the stress triaxiality was also discussed in [Benzerga, 2000]. Divergent tendencies were obtained by different studies in the literature [Cox and Low, 1974] and [Argon et al., 1975, Argon and Im, 1975, Beremin, 1981], which employed the critical stresses approaches (Eq. 1.110 and Eq. 1.111) and [Lee and Mear, 1999] (which employed the factors of stress concentration). The reason is that for the analyses of nucleation, it is more important to study the *stress distribution at interface* than the *stress concentration*, especially in case of nucleation by decohesion (see [Benzerga, 2000] for the detailed and interesting discussion). The results of [Lee and Mear, 1999] showed that both stress concentration factors decrease at different "rates" when the stress triaxiality increases. The ratio κ_P/κ_I is a decreasing function of the stress triaxiality, the debonding mode is thus favored.

Besides the energy and stress-based criteria, strain-based criteria for nucleation have also been extensively developed. [Needleman and Rice, 1978] developed a phenomenological model of nucleation, where the void nucleation is governed by the equivalent plastic strain of matrix and the macroscopic hydrostatic stress:

$$\dot{f}_{nucleation} = A\dot{\bar{\epsilon}}^p + B\dot{\bar{\sigma}}_h \tag{1.113}$$

where A and B are two parameters, which are non-constant, $\dot{f}_{nucleation}$ is the rate of voids change due to nucleation. If the nucleation is only due to macroscopic stress, $A = 0$ and $B > 0$. With this approach,

[Needleman and Rice, 1978] proposed a normal distribution formulation for B:

$$B = \frac{f_N}{S_N\sqrt{2\pi}} exp\left[-\frac{1}{2}\left(\frac{(\overline{\sigma}+\sigma_h)-\sigma_N}{S_N}\right)^2\right] \tag{1.114}$$

where f_N is the total void volume fraction created by nucleation, σ_N is the average stress at maximal nucleation, S_N is the standard deviation of normal distribution, $\overline{\sigma}$ is the flow stress of matrix. If the void nucleation is only controlled by plastic strain, $B = 0$ and $A > 0$. [Chu and Needleman, 1980] defined A as a normal distribution and B equals to 0:

$$A = \frac{f_N}{S_N\sqrt{2\pi}} exp\left[-\frac{1}{2}\left(\frac{\overline{\epsilon}^p-\epsilon_N}{S_N}\right)^2\right] \tag{1.115}$$

where ϵ_N is the average plastic strain at maximal nucleation; f_N and S_N have the same meaning as above. As stated in [Zhang et al., 2000], the main difference between the strain and stress driven nucleation is that the hydrostatic pressure has been accounted for in the latter formulation. The proposed values of [Chu and Needleman, 1980] for A and B were then taken to describe the voids nucleation in the Gurson-type models (see section 4.1 for more details).

Voids growth After nucleation, voids will grow by plastic deformation and hydrostatic stress (Figs. 1.23a and 1.23b), then finally link.

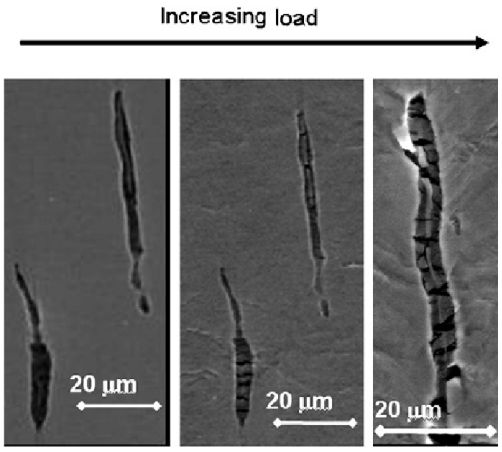

(a) *Ductile steel [Bouchard et al., 2008].*

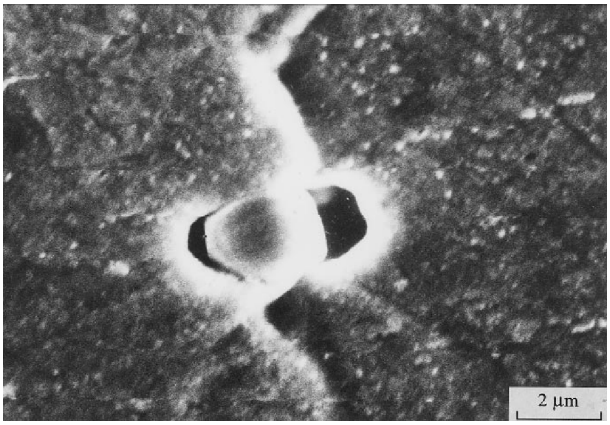

(b) *Copper matrix containing copper oxide inclusion [Pardoen et al., 1998].*

Fig. 1.23: *SEM observations during in situ tensile test, showing void growth.*

Several models have been proposed in the literature to model the void growth process within a *perfect plastic matrix*, e.g. Rice's formulation [Rice and Tracey, 1969] (Eq. 1.116), which was then modified by Huang [Huang, 1991] (Eq. 1.117), or Gurson constitutive model [Gurson, 1977] (see section 4.1).

$$\frac{dR}{R} = 0.272exp\left(\frac{3}{2}\eta\right)d\overline{\epsilon}_p \tag{1.116}$$

$$\frac{dR}{R} = \begin{cases} 0.427\eta^{0.25}exp\left(\frac{3}{2}\eta\right)d\overline{\epsilon}_p & if \quad \eta \leq 1 \\ 0.427exp\left(\frac{3}{2}\eta\right)d\overline{\epsilon}_p & if \quad \eta > 1 \end{cases} \tag{1.117}$$

The growth and coalescence processes depend on loading conditions and materials microstructure. Thomason ([Thomason, 1990]) showed that for low stress triaxiality cases, *"ductile fracture is due to large shape changing growth and relatively small volume changing growth"*. From the fact that voids nucleate over a strain range, the nucleation and growth stages occur simultaneously, which leads to the formation of voids with different sizes and shapes. Moreover, when a very small void is located near a much larger void, the growth rate of the small void is significantly increased due to the strain concentration developing around the neighbor larger void ([Tvergaard, 1998]).

Voids coalescence Voids coalescence is the final stage of damage and ductile failure. Three modes of coalescence have been observed: (1) the "internal necking mode" (necking of matrix between two voids - see Fig. 1.24a); (2) the "shear localization mode" (reduction of the inter-particle spacing during large rotation of matrix under "relatively low" stress triaxiality - see Fig. 1.24b), "necklace coalescence" (a less common mode, which is caused by localization process in the main loading axis direction [Pardoen et al., 2010] - see Fig. 1.24c). For ductile metals, voids can double or even triple in size before their coalescence, while for less ductile materials, this process starts immediately after nucleation.

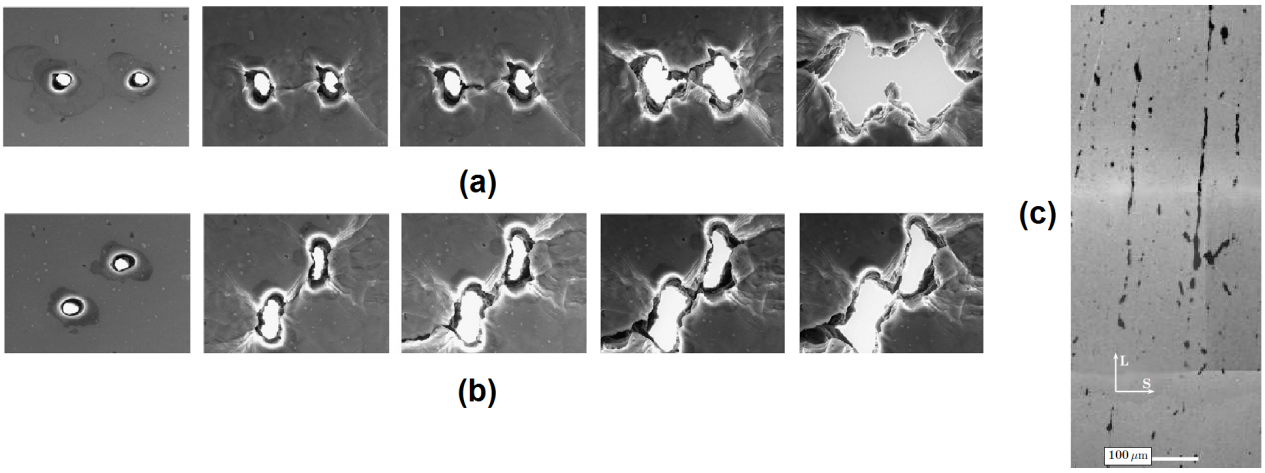

Fig. 1.24: *Illustration of 3 modes of coalescence: (a) internal necking; (b) shear localization [Weck and Wilkinson, 2008]; (c) necklace coalescence [Benzerga, 2000].*

Several models were developed in the literature to simulate the coalescence as well as post-coalescence behavior. These models are based principally on cell computations with the presence of initial voids, which are generally 2D (Fig. 1.25).

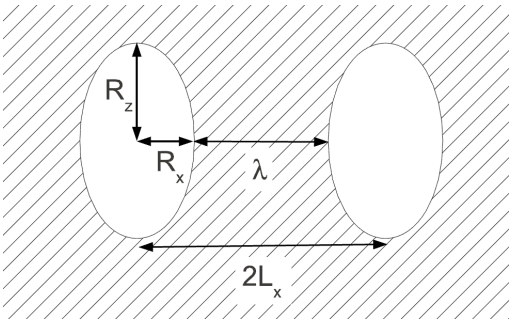

Fig. 1.25: *Illustration of geometrical parameters involved in cell simulation (figure adapted from [Landron, 2011]).*

The geometrical parameters involved are: (1) void aspect ratio $\omega^V = R_z/R_x$ and (2) relative inter-voids distance: $\chi = R_x/L_x$. Detailed analytical formulations are not recalled here, interested readers can refer to [Weck, 2007] or [Benzerga and Leblond, 2010] for the reviews of different coalescence models in the literature. It is worth noting that the models with the presence of voids (e.g. Thomasson model [Thomason, 1990]) are not straightforward to use in macroscopic simulations (e.g. structure modeling or forming process simulation). [Zhang et al., 2000] employed the Thomasson coalescence criterion, the GTN yield surface and the post-coalescence response proposed by Tvergaard and Needleman ([Tvergaard and Needleman, 1984, Needleman and Tvergaard, 1984]) to achieve the so-called "complete Gurson model"[13]. In the present study, ***the simple critical void volume fraction criterion proposed by***

[13]The word "complete" refers to the capacity of this model to simulate the whole process of ductile fracture, from void nucleation to void coalescence.

Tvergaard and Needleman is employed within the framework of the GTN model (see section 4.1).

Authors	Criteria	Limitations
[McClintock, 1968]	Hole impingement	Cylindrical holes; No interaction between holes; No localization
[Brown and Emburry, 1973]	Void length equals inter-void spacing	Regular array of voids; No influence of the stress triaxiality; Overestimation of fracture strain
[Tvergaard and Needleman, 1984]	Critical void volume fraction	Average measurement; Phenomenological method
[Thomason, 1968]	Limit plastic load	Damage growth neglected; Non hardening matrix
[Pardoen and Hutchinson, 2000]	Thomason's model with strain hardening GLD model for void growth	No shear localization

Table 1.2: *Several coalescence models in the literature (adapted from [Weck, 2007] and [Besson, 2010]).*

Remark: In the above analyses, the results were obtained by the studies of isolated voids or a limited number of voids. In reality, the presence of numerous voids can modify the overall behavior. [Pardoen et al., 2010] showed that the voids distribution has a strong influence on the void coalescence onset while this effect can be neglected during the void growth process. The coalescence phase depends not only on the overall voids volume fraction, but especially the distance between voids. The latter parameter has been shown to have significant influence on ductile fracture by some recent experimental results (e.g. [Landron, 2011]).

1.4.2.3 Mechanisms dominating at negative or low stress triaxiality ratio

There are very few studies in the literature dealing with ductile damage under negative stress triaxiality range. The upsetting test is often used to study the ductile crack formation in the negative stress triaxiality range as in the work of [Bao and Wierzbicki, 2004]. From the examination of fracture surface, "there are no evidence showing cracked particles and nucleated voids" (the fracture surface is relatively smooth in comparison with dimpled surface under high stress triaxiality). The damage process and crack formation is clearly due to a different mechanism from the well known mechanisms of voids nucleation, growth and coalescence (see Fig. 1.29 in section 1.5.1).

Kweon and co-workers ([Kweon et al., 2010, Kweon, 2012]) used combined Digital Image Correlation (DIC) experiment and crystal-plasticity simulations to reveal the damage mechanisms at zero and negative stress triaxiality at mesoscale (i.e. grain level). According to these authors, damage at this triaxiality regime is due to grain to grain interaction, which leads to the development of hydrostatic tensile stress inside grain. They incorporated this mechanism into a crystal-plasticity-based damage model.

Recently, [Achouri et al., 2013] carried out detailed SEM observations of voids development in a shear-dominated stress state region obtained with a shear test on a high-strength low-alloy steel (HSLA steel), where the stress triaxiality is low or zero. The authors observed the void nucleation due to different mechanisms: (1) debonding around an inclusion (Fig. 1.26a), (2) cracking inside a particle (Fig. 1.26b) or (3) mixed mode (i.e. both matrix-particle debonding and particle cracking took place - Fig. 1.26c).

From Fig. 1.26a, one can observe that in the undeformed state (i.e. 0%), the matrix and the inclusion were "coherent". Then, under shear loading, matrix-particles debonding occurred at interface and then void grew in a non-uniform manner in both shear directions, forming "corners" (in comparison with elongated void in loading direction, developed under tensile loading). The authors also mentioned the void rotation,

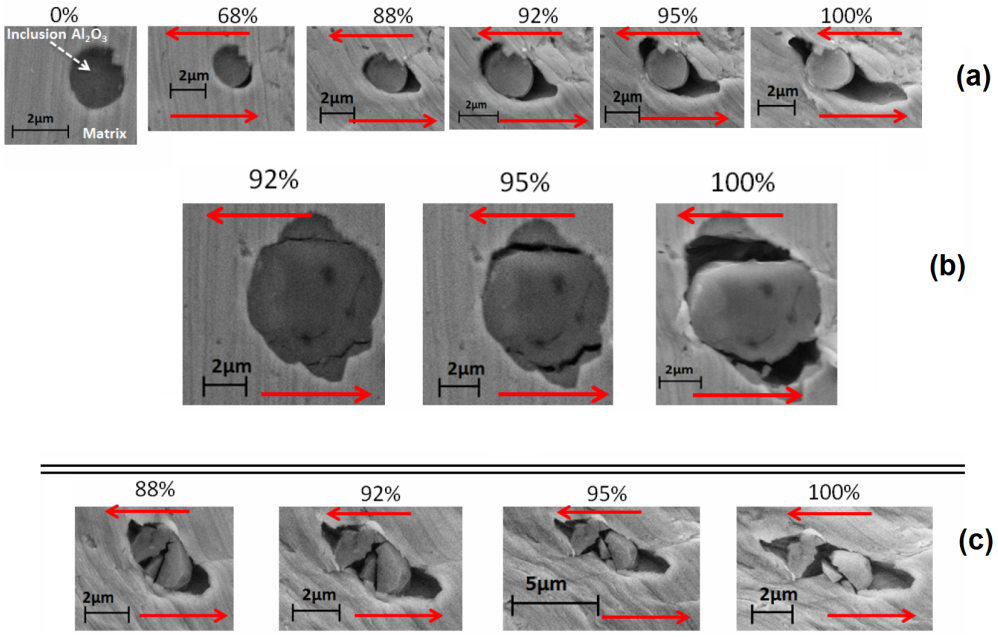

Fig. 1.26: *SEM observations of the development of voids due to (a) matrix-particle decohesion; (b) particle cracking; (3) mixed mode. The percentages correspond to the percentage of displacement to fracture and the red arrows represent the loading direction (figure adapted from [Achouri et al., 2013]).*

depending on loading level, which was not observed in their tensile test.

1.4.2.4 Remarks

For low stress triaxiality cases, the ductility or the strain to fracture can be approximated as the strain corresponding to the void coalescence onset, while this approximation must be used with caution for high triaxiality range. The ductile fracture process due to the development of voids can be split into two stages: homogenous deformation (nucleation and growth) and localized deformation due to the voids coalescence ([Zhang et al., 2000]). Since the void growth rate is proportional to the exponential of stress triaxiality ([Rice and Tracey, 1969]), *the strain to fracture decreases with the increase of stress triaxiality*. This statement is not strictly true since the stress triaxiality itself is not enough to characterize the stress state. Recent experimental evidences showed that the strain to fracture also depends on another parameter, which involves the third invariant of the deviatoric stress (see section 1.5).

1.4.3 Classification of damage models

Many different models were proposed in the literature and can be classified into three main approaches:

1. failure criteria,
2. continuum damage mechanics (CDM),
3. porous solid plasticity.

The details of advantages and drawbacks of these approaches were given in several studies (e.g. [Bonora et al., 2005]) and are summarized in the following paragraph.

1.4.3.1 Failure criteria - Uncoupled damage model

In the first approach, failure is predicted to occur when one external variable (uncoupled from other internal variables, e.g: plastic strain) reaches a critical value. The uncoupled approach is based on models that take into account an external variable, which predicts the failure when its critical value is reached.

However, the calculated damage does not interact with materials elastoplastic properties. Damage variable is therefore just a "warning" for the approach of failure. Thanks to its simplicity, this approach was increasingly developed, especially for industrial applications.

Initially, the uncoupled damage models were based on physical assumptions, in which the damage parameters were linked with void growth (e.g. [McClintock, 1968], [Rice and Tracey, 1969], [Budiansky et al., 1982]. These models differ by the shape as well as material behavior law and do not take into account the presence of inclusions. Moreover, the Mc Clintock and Rice & Tracey models are based on the analysis of an isolated cavity in an elastoplastic matrix and neglect the interaction between different cavities. Table 1.3, extracted from [Massé, 2010], gives an overview of these models.

Model	Matrix rheology	Void shape	Stress state	Formulation
McClintock (1968)	Plastic hardening	Cylinders with circular or elliptic sections minor axis a and major axis b	Principal axis of stress coincide with inclusion ones	$D=\int_0^{\varepsilon_{eq}^f}\left[\frac{\sqrt{3}}{2(1-n)}\sinh\left(\frac{\sqrt{3}(1-n)}{2}\frac{\sigma_1+\sigma_2}{\sigma_{eq}}\right)+\frac{3}{4}\frac{\sigma_1-\sigma_2}{\sigma_{eq}}\right]d\varepsilon_{eq}$
Rice and Tracey (1969) general formulation	Rigid perfectly plastic	Spherical	$\dot{\varepsilon}_{ij}, s_{ij}$ and σ_H imposed	$D=\int_0^{\varepsilon_{eq}^f}\left[0{,}558\sinh\left(\frac{3}{2}\frac{\sigma_H}{\sigma_{eq}}\right)+0{,}008\,\upsilon\cosh\left(\frac{3}{2}\frac{\sigma_H}{\sigma_{eq}}\right)\right]d\varepsilon_{eq}$
Rice and Tracey (1969)	Rigid perfectly plastic	Spherical	High stress triaxiality hypothesis $\frac{\sigma_H}{\sigma_{eq}}>1$	$D=\int_0^{\varepsilon_{eq}^f}\left[0.283\,\exp\left(\frac{3}{2}\frac{\sigma_H}{\sigma_{eq}}\right)\right]d\varepsilon_{eq}$
Budiansky, Hutchinson and Slutsky (1982)	Pseudo-plastic Velocity sensitivity (m)	Spherical	Axisymmetric loading, high triaxiality case $\frac{\sigma_H}{\sigma_{eq}}>1$	$D=\int_0^{\varepsilon_{eq}^f}\left(\frac{\chi}{2}\left[\frac{3m}{2}\left\lvert\frac{\sigma_H}{\sigma_{eq}}\right\rvert+(1-m)(1+0.418m+0.014\chi m)\right]^{1/m}\right)d\varepsilon_{eq}$

Table 1.3: *Void growth models formulation and hypotheses (from [Massé, 2010]).*

[Bao and Wierzbicki, 2004a], in a comparative study, showed that different functions are necessary to predict crack initiation for different ranges of stress triaxiality, and that it is impossible to capture all features of ductile fracture for different stress states with a single stress triaxiality-based criterion. The above-mentioned models were shown to be valid for specific loadings and depend strongly on the strain path.

Beside the physically-inspired uncoupled models, many other models were phenomenologically constructed and the damage indicator was not linked with any physical properties. The damage parameter was often defined as a cumulative function along the strain path:

$$\int_0^{\bar{\epsilon}_f} f\,(\text{stress state})\,d\bar{\epsilon}_p = C_D \tag{1.118}$$

where f (stress state) is a function of the stress state; and C_D is a material constant. We can name here some criteria: hydrostatic stress ($f = \frac{\sigma_h}{\sigma_{eq}}$) and Oyane ($f = a + b\frac{\sigma_h}{\sigma_{eq}}$) among others. These criteria are reliable in predicting fracture only if the parameters of function f are measured from mechanical tests which are close to the studied processes, regardless of damage anisotropy. The implementation and development of several recent uncoupled damage models are detailed in Chapter 3.

Remark Generally, the uncoupled models have the advantages of being easy to implement in FE software and having few parameters to identify. The application to complex loading paths and large plastic deformations is their major weakness. It is the subject of a discussion in section 3.5 of Chapter 3.

1.4.3.2 Continuum damage mechanics (CDM)

In the second approach, damage is associated with one of the internal constitutive variables that accounts for the influence of the irreversible process which occurs in materials microstructure. This approach is a phenomenological representation of the CDM which was first initiated by Kachanov [Kachanov, 1958], who used a damage parameter for describing creep damage. They are considered as "phenomenological" because their developments are essentially based on macroscopic considerations. However, these models are based on a consistent thermodynamic framework, which ensures a positive dissipation. This framework for ductile damage was later developed by Chaboche [Chaboche, 1984] and Lemaitre [Lemaitre, 1986,

Lemaitre and Desmorat, 2005]. Several models relative to the initial framework of Lemaitre, based on the use of special expressions for the damage dissipation potential, were developed by several authors ([Tai and Yang, 1986], [Tai, 1990], [Chandrakanth and Pandey, 1993], [Bouchard et al., 2011]). These models have also some limitations:

(i) some material constants are not physically based;

(ii) mesh size dependencies due to damage localization and softening, where the use of a regularization technique (e.g. non-local models) is necessary (see ([Peerlings et al., 1996, Peerlings et al., 2001], [Engelen et al., 2003], [Fayolle, 2008]);

(iii) the choice of the damage dissipation potential is specific for each material. Consequently, a new determination of the damage dissipation potential is necessary when moving from one material to another;

(iv) damage evolution law is often validated only for experimental data obtained from uniaxial test so that the transferability of parameters to complex loading paths is not proven.

A detailed review of the formulation in Lemaitre's framework of continuum damage mechanics is presented in Appendix A.4. ***A modification of the Lemaitre model for complex loading case by accounting for the Lode parameter is proposed in section 3.3.4.***

1.4.3.3 Porous solid plasticity

In the third approach, the influence of ductile damage in the yield condition is taken into account by a porosity term that progressively shrinks the yield surface, which was first proposed by Gurson ([Gurson, 1977]). Later, [Tvergaard and Needleman, 1984, Needleman and Tvergaard, 1984] extended the Gurson model to include the void coalescence mechanism (the GTN model). In spite of a lot of extensions of the GTN model based on micromechanical studies (e.g. [Acharya and Bassani, 2000], [Schacht et al., 2003], [Tvergaard and Niordson, 2004], [Bonfoh et al., 2004]), this model is also known to suffer a number of limitations:

(i) a large number of material constants needs to be identified, which causes a difficulty to evaluate the mutual influences of the parameters. This would be an obstacle for industrial applications, although some parameters can be chosen from literature or based on microstructure observations;

(ii) some material constants (e.g. q_1, q_2, q_3 in GTN model - see Chapter 5) are not physically based and their measurement from conventional mechanical tests is not straightforward;

(iii) the transferability to other geometries (different stress states) is not always satisfactory: one cannot use the parameters identified from the uniaxial tensile test with cylindrical specimen to predict the response of notched or cracked components (or flat specimen) under the same loading condition;

(iv) the damage model parameters depend on the mesh size, which is the common drawback of all the local coupled damage models (like CDM approach);

(v) there is no coupling between damage growth and the elastic behavior. However, for material forming processes, the material undergoes large plastic strain so that this "drawback" [14] has a limited impact on results.

A detailed review and implementation of models of the Gurson family is presented in section 4.1.

1.4.4 Damage measurement

In conjunction with the definition of variables, it is necessary to have an accurate and efficient damage measurement method. Several methods proposed in the literature can be summarized as:

[14] It should be considered as a "simplification" instead of a "limitation".

1. Measurement by the remaining lifetime: by reference to a test (with a given load) whose lifetime to fracture is known, the damage induced by any prior load can be measured by loading with the same reference load. The ratio of the lifetimes gives a damage measurement. However, this method requires the linear damage hypothesis which is not true for most damage models. This method is therefore not accurate but can give a quick estimation of damage for engineer applications ([Besson et al., 2010]).

2. Measurement using physical parameters: the evolution of parameters such as density, resistivity, micro hardness ([Mashayekhi et al., 2011]) or acoustic emission can be measured to characterize the evolution of damage. However, these techniques require sophisticated equipment and the accuracy is sometimes still questionable.

3. Microstructural measurements: a physical measurement of actual defects (the cavity volume fraction in ductile damage, the surface density of broken grain boundaries - creep, the number of microcracks area summation per unit volume - fatigue). These measurements give accurate results but they are destructive ([Hor, 2011]), very time consuming and difficult to integrate directly into a mechanical model. Recently, non-destructive measurements with X-ray micro-tomography gave both quantitative and qualitative information on damage ([Maire et al., 2008], [Landron, 2011]). However, this type of measurement requires specific experimental device and is quite sensitive to experimental setup. Another drawback is that the studied material must have a good X-ray absorption capacity.

4. Measurement of mechanical behavior evolution: the best adapted to mechanical modeling. Two methods are distinguished: one based on the notion of "net section" and another based on the notion of "effective stress" ([Lemaitre and Desmorat, 2005] and see Appendix A.4).

In the present study, both the microstructure measurement (using X-ray micro-tomography) and the measurement of mechanical behavior evolution are used to quantify damage. Details on the use of mechanical tests to calibrate damage models are presented in the following section.

1.5 Damage-fracture tests and the fracture loci

In this section, a brief review of mechanical tests used for material characterization and damage studies is given. In order to investigate damage under complex loading paths, one has to carry out suitable calibration tests for damage models identification. Various stress states may be obtained by using either a series of uniaxial tests, such as uniaxial tensile tests, compression test and torsion test, or multiaxial tests, such as combined torsion and tension on tube (for bulk materials), combined shear and tension on butterfly specimen (for sheet materials). From the experimental results of these tests, the analysis followed was initially based only on stress triaxiality. Several recent studies revealed the strong influence of the third deviatoric stress invariant on material ductility, which leads to the necessity of accounting for this stress component in the analysis of damage and fracture experiments.

1.5.1 Triaxiality based analyses

Bridgman, one of the first researchers who carried out damage and fracture tests, in his famous book ([Bridgman, 1952]), presented all the experimental data obtained from axisymmetric tensile tests under hydrostatic pressure for 20 different types of steels. To reveal the nature of fracture in these tests, it is convenient to work with the stress triaxiality ratio. The statistics of the average stress triaxiality of all these tests provided a global view of the limit between fracture and non-fracture zones (see Fig. 1.27).

One can notice the difference between the average and the final stress triaxialities, which is caused by the evolution of the stress triaxiality at the neck center (approximately a linear function). The average of stress

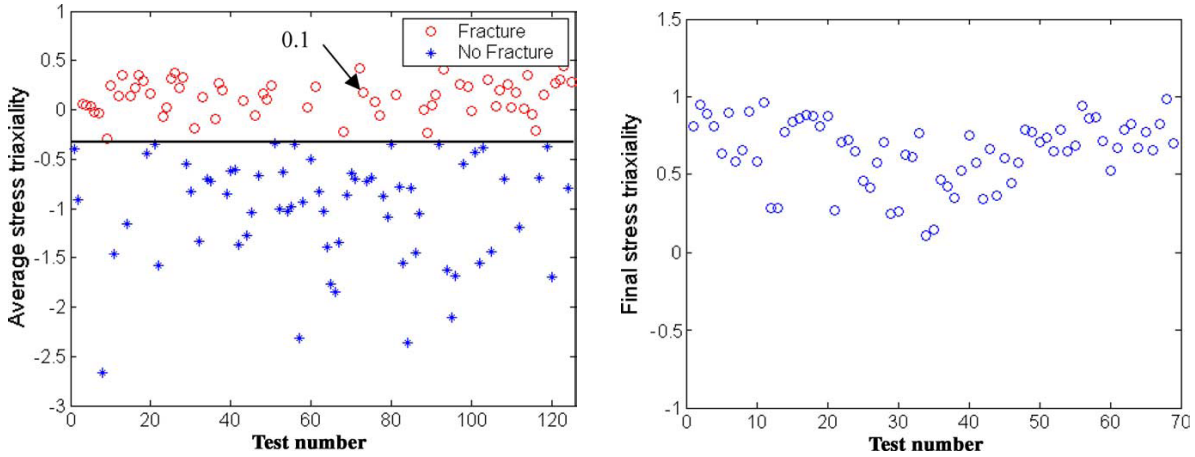

(a) *Average stress triaxiality.* **(b)** *Final stress triaxiality (fractured specimens).*

Fig. 1.27: *Tensile tests with superimposed hydrostatic pressure [Bridgman, 1952].*

triaxiality was defined as one half of the sum of its initial and final values[15]:

$$\left(\frac{\sigma_h}{\bar{\sigma}}\right)_{average} = \frac{1}{2}\left[\left(\frac{\sigma_h}{\bar{\sigma}}\right)_{initial} + \left(\frac{\sigma_h}{\bar{\sigma}}\right)_{final}\right] \tag{1.119}$$

$$\left(\frac{\sigma_h}{\bar{\sigma}}\right)_{initial} = \frac{-p}{\bar{\sigma}} + \frac{1}{3} \tag{1.120}$$

$$\left(\frac{\sigma_h}{\bar{\sigma}}\right)_{final} = \frac{-p}{\bar{\sigma}} + \frac{1}{3} + ln\left(1 + \frac{a}{2R}\right) \text{ (Bridgman correction)} \tag{1.121}$$

$$\left(\frac{\sigma_h}{\bar{\sigma}}\right)_{final} = \frac{-p}{\bar{\sigma}} + \frac{1}{3} + 1.4ln\left(1 + \frac{a}{2R}\right) \text{ (Calibration by [Bao, 2005])} \tag{1.122}$$

where p, in this context, is the magnitude of superimposed hydrostatic pressure; a and R are respectively the radius of the minimum cross-section and the radius of the circumferential notch. Furthermore, from Fig. 1.27, a limit of average stress triaxiality can be observed (about -0.33), which means the stress triaxiality must overcome this "cut-off value" to make fracture occur. Bao ([Bao, 2005]), by assuming the independence of yielding surface with hydrostatic pressure (the classical J_2 plasticity theory), showed that equivalent strain and stress triaxiality are the two most important factors governing crack formation. Table 1.4 represents the initial values of the stress triaxiality ratio for several mechanical tests (these values can vary with the plastic strain during the tests).

Test number	Loading	Specimen description	Stress triaxiality $\sigma_H/\bar{\sigma}$
1	Compression	Cylinder $(D/H = 0.5)$	-0.33 to -0.12
2	Compression	Cylinder $(D/H = 0.8)$	-0.32 to -0.05
3	Compression	Cylinder $(D/H = 1.0)$	-0.32 to -0.05
4	Compression	Cylinder $(D/H = 1.5)$	-0.32 to -0.05
5	Compression	Asymmetric	-0.4 to -0.09
6	Shear	Flat	0 to 0.02
7	Combined shear /tension	Flat	0.04 to 0.15
8	Tension	Plate with a circular hole	0.33
9	Tension	Round, smooth	0.33 to 0.5
10	Tension	Round, large notch	0.6 to 0.7
11	Tension	Round, small notch	0.9 to 1

Table 1.4: *List of the tests carried out by [Bao and Wierzbicki, 2004].*

Bao ([Bao and Wierzbicki, 2005]) then analyzed the upsetting test of short cylinders of Al2024-T351 with

[15] In the following paragraph, a more precise integrate formula to calculate the average stress triaxiality will be presented.

different aspect ratio to validate this observation. A series of virtual tensile tests under hydrostatic pressure were then carried out to see if the applied hydrostatic pressure increases the ductility of the specimen (much deeper neck). The results showed that fractures initiated at the center of the neck in tensile test under hydrostatic pressure while they initiated at the equatorial area in upsetting test (effect of friction). Furthermore, the differences between two damage mechanisms were highlighted. In the tension tests (with high stress triaxialities), the fracture surface was quite rough and dimples with cracked inclusions could be observed (Fig .1.28), while in the case of upsetting tests, the fracture surface was relatively smooth and no dimples could be seen (Fig .1.29). The well-known void nucleation, growth and coalescence mechanism monitored the high stress triaxialities fracture, while for low value of stress triaxialities region, the main cause of fracture is the "shear decohesion" mechanism.

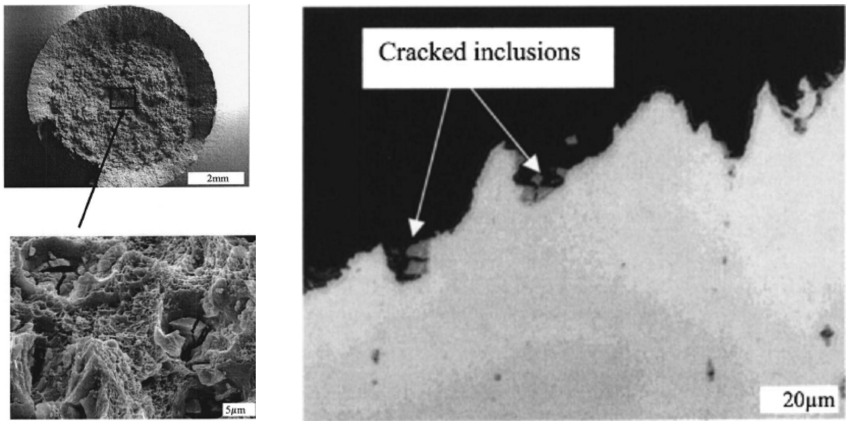

(a) (b)

Fig. 1.28: *Dimple fracture in the notched tensile specimen [Bao and Wierzbicki, 2004a].*

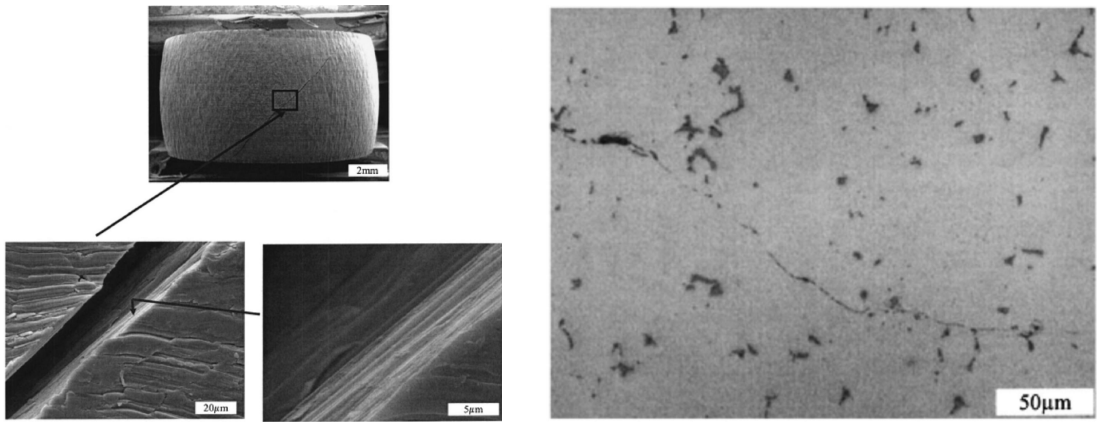

(a) (b)

Fig. 1.29: *Fractograph showing flat fracture surface in the upsetting specimen [Bao and Wierzbicki, 2004a].*

A limit value of stress triaxiality: $\frac{\sigma_h}{\bar{\sigma}} = -\frac{1}{3}$, below which the fracture never occurs, can be obtained by analyzing the compression tests.

[Kao et al., 1990], with the same type of tests, in the study on tensile fracture of 1045 spheroidized steel under hydrostatic pressure, clearly demonstrated that the *influence of superimposed hydrostatic pressure of tensile fracture of 1045 spheroidized steel was such that void nucleation was suppressed*, leading to larger *post-uniform strain* under pressure and a transition of the fracture surface from cup-cone mode under atmospheric pressure to a slant mode under high pressure (Fig. 1.30a). However, according the authors, the maximum pressure applied (1120 MPa) was not high enough to completely suppress void nucleation around carbide

particles. The authors revealed that the increase of the superimposed hydrostatic pressure (or the decrease of the stress triaxiality) may lead to the increase of "nucleation strain" (Fig. 1.30b). This study also demonstrated that the increase of pressure led to a significant increase in ductility and a slight increase in flow stress. [Peng et al., 2009] numerically studied the effect of superimposed hydrostatic pressure on fracture in round bar, using the finite element method based on the Gurson damage model and validated the conclusion in the [Kao et al., 1990] study.

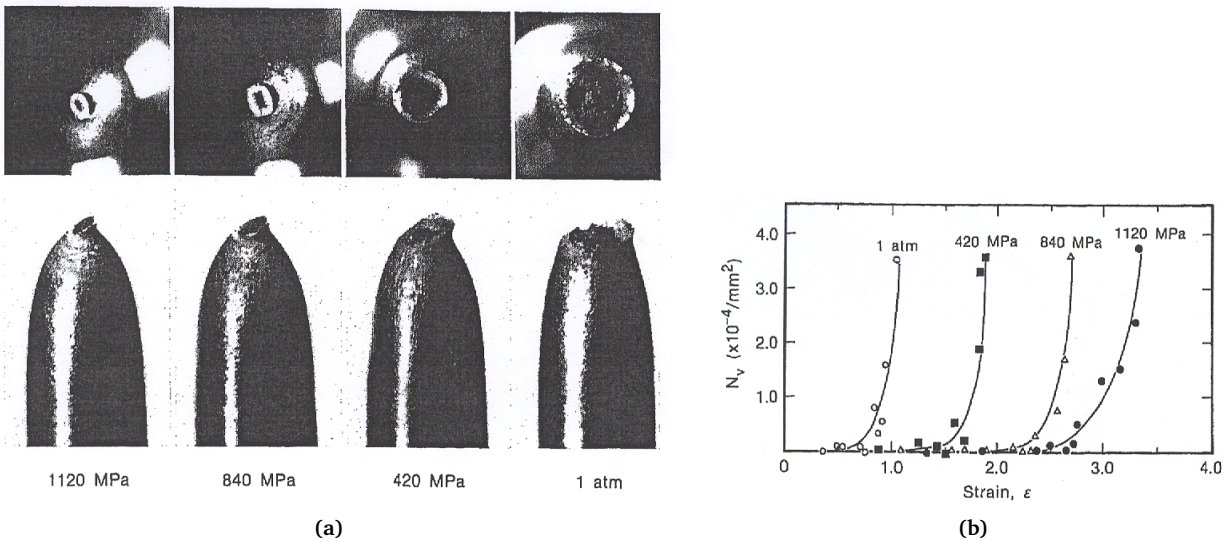

Fig. 1.30: *(a) The appearance of the fractured tensile bar under applied pressure. The transition of fracture surfaces from cup-cone mode to slant mode can be observed when the applied pressure increases. (b) The void density is plotted again the local plastic strain with different levels of superimposed pressure (figures adapted from [Kao et al., 1990]).*

Remark The tensile test under hydrostatic pressure can generate a large range of triaxiality values, from negative to highly positive, which is interesting for the study of its influence on the damage and fracture of material. Many numerical studies were carried out (such as [Bao and Wierzbicki, 2004a], [Bao, 2005], [Peng et al., 2009]) to validate these experimental results. However, this test, which requires very high pressure states, is not easy to conduct.

[Bao and Wierzbicki, 2004] performed a series of tests including upsetting tests, shear tests and tensile tests on 2024-T351 aluminum alloy to investigate the fracture locus in the equivalent strain and stress triaxiality space ($\bar{\epsilon}$–$\frac{\sigma_h}{\bar{\sigma}}$ space), with a wide range of stress triaxiality values. For each test, the authors determined first the location of fracture initiation and displacement to fracture, then calculated the evolution of the equivalent strain and stress triaxiality at the fracture initiation location. The strain to fracture was then calculated and represented in the ($\bar{\epsilon}$–$\frac{\sigma_h}{\bar{\sigma}}$) space to construct the limiting fracture curve. Table 1.4 shows the list of all the tests with different types of specimens.

To generate a low stress triaxiality state, new specimens were used in pure shear configurations ($\frac{\sigma_h}{\bar{\sigma}} = 0$) and combined loading test, while two types of compressive specimens were used to obtain negative stress triaxiality states. The new type of compression test specimen (Fig. 1.31a) helped removing the undesirable effect of friction and the fracture could always be observed on the surface. With the new specimen configuration with different gauge section shapes, one can create a low stress triaxiality state that takes into account the shear effect (Figs. 1.31b and 1.31c).

The 2D fracture locus in the ($\bar{\epsilon}$-$\frac{\sigma_h}{\bar{\sigma}}$) space shown in Fig. 1.32a revealed that the equivalent strain to fracture varied differently under different stress triaxialities and this dependency was not monotonic. Note that the average of stress triaxiality was used to construct this curve[16]. The results showed the strong depen-

[16]The average of stress triaxiality is defined as: $(\frac{\sigma_h}{\bar{\sigma}})_{av} = \frac{1}{\bar{\epsilon}^f}\int_0^{\bar{\epsilon}^f_{eq}} \frac{\sigma_h}{\bar{\sigma}} d\bar{\epsilon}$.

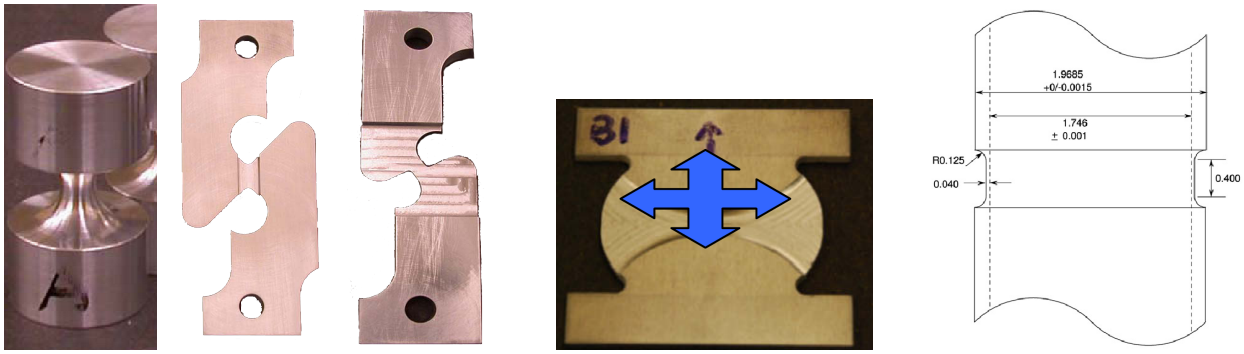

(a) (b) (c) (d) (e)

Fig. 1.31: *New specimens used for compression (a), pure shear (b) and combined shear tests (c) [Bao and Wierzbicki, 2004]; butterfly specimen for combined tension-shear tests (d) [Beese et al., 2010]; tube specimen for combined tension-torsion tests (e) [Haltom et al., 2013].*

dency of fracture ductility on the stress triaxiality. The shear fracture dominates in the range of negative stress triaxialities while in the range of high stress triaxialities, the fracture occurs due to voids nucleation and growth. In the transition zone between the above two regimes, fracture might develop as a combination of these two mechanisms. The analytical expressions of the 3 branches of this curve can be found in [Bao and Wierzbicki, 2004].

More recently, [Beese et al., 2010] constructed the fracture locus for an aluminum 6061-T6 alloy using series of "uniaxial tests" as well as combined shear-tension tests on the butterfly specimen (Fig. 1.31d). The authors observed the same tendency as in [Bao and Wierzbicki, 2004] (Fig. 1.32b). However, with the same material, [Haltom et al., 2013] obtained a different fracture locus by using the combined tension-torsion test (Fig. 1.31e). The strain to fracture monotonically decreased with the increase of the stress triaxiality (Fig. 1.32c), which was not materialized by the studies of [Bao and Wierzbicki, 2004] and [Beese et al., 2010] (Figs. 1.32a and 1.32b). According to the authors, the difference observed could be explained by the differences in the testing procedures and in the ways the stresses and strains measurements were performed. These authors also indicated that to obtain correct results, the experiments had to respect several characteristics such as: uniform stress in the test section; no stress concentration; no geometric constraints (i.e. the test section must be wide enough for the localization to develop); the deformation must be accurately measured both in uniform regime (relatively large zone) and localized regime (often in narrow zone).

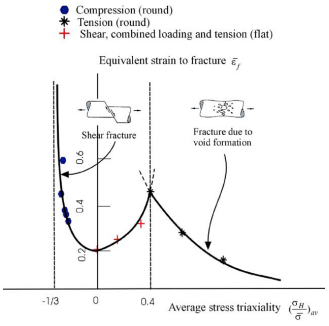

(a) *Fracture locus for aluminum alloy 2024-T351 obtained from series of conventional tests [Bao and Wierzbicki, 2004].*

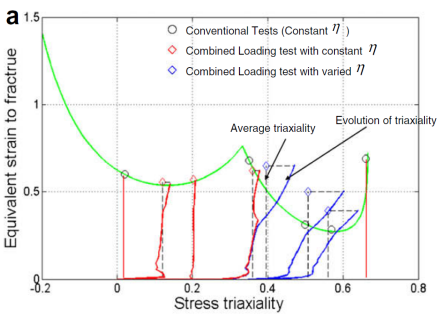

(b) *Fracture locus for aluminum alloy 6061-T6 obtained from conventional tests and combined shear-tension test on butterfly specimen [Beese et al., 2010].*

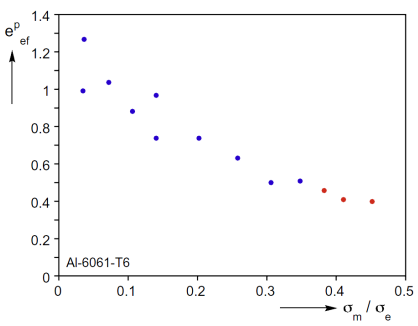

(c) *Fracture locus for aluminum alloy 6061-T6 obtained from the combined tension-torsion tests [Haltom et al., 2013].*

Fig. 1.32: *Dependency of the equivalent strain to fracture on the stress triaxiality.*

Remarks Throughout these studies, one can observe that the analysis based only on the stress triaxiality is not capable of describing the damage and fracture behaviors in a wide range of stress states since the stress triaxiality itself is not sufficient to characterize a stress state (multiples stress states can result in the same stress triaxiality ratio). Several recent studies demonstrated the significant influence of the third stress invariant on damage prediction, especially at low stress triaxiality ([Barsoum and Faleskog, 2007a]); the Lode angle parameter has been often used to include it. This parameter helps distinguishing different stress states having the same stress triaxiality ratio (see Fig. 1.33a).

1.5.2 Triaxiality and Lode angle based analyses

[Bai and Wierzbicki, 2008] constructed a 3D fracture locus (see Fig. 1.33b) that accounted for the effect of the **Lode angle** θ (or the effect of the third invariant of stress tensor). From Fig. 1.33b, for each value of the stress triaxiality, one can observe the evolution of fracture strain with the Lode angle: the lower the stress triaxiality, the stronger the sensitivity to Lode angle. Since the stress triaxiality in forming processes is usually weakly positive or negative, accounting for the influence of the Lode angle is indeed necessary.

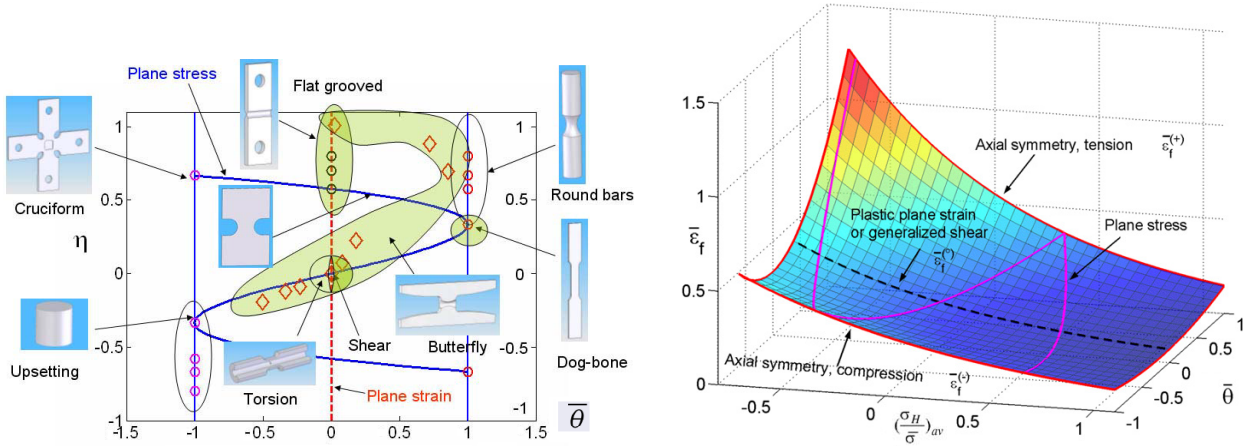

(a) *"Positions" of some conventional mechanical tests in* $(\eta, \bar{\theta})$ *space.* **(b)** *3D asymmetric fracture locus [Bai and Wierzbicki, 2008].*

Fig. 1.33: *Conventional mechanical tests in* $(\eta, \bar{\theta})$ *space (a) and 3D fracture locus accounting for the effect of the third invariant of deviatoric stress tensor (b) (figures adapted from [Bai and Wierzbicki, 2008]).*

A series of fracture tests using classical specimens and the butterfly specimen (Fig. 1.34) was then carried out to obtain the fracture locus in the $(\bar{\varepsilon}–\frac{\sigma_h}{\bar{\sigma}}–\bar{\theta})$ space (Fig. 1.33b). Table 1.5 presents ten types of classical specimens for plasticity and fracture calibration.

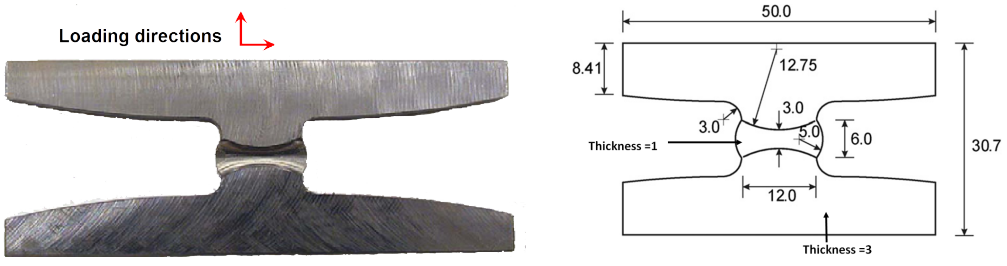

(a) *butterfly shape specimen (A710) steel [Bai and Wierzbicki, 2008]* **(b)** *principal dimensions of the butterfly specimen used in [Mae et al., 2007]*

Fig. 1.34: *The butterfly specimens.*

This butterfly specimen was then optimized such that fracture initiated far from the free specimen boundaries [Dunand and Mohr, 2011]. It was used for many recent studies [Dunand and Mohr, 2011],

No.	Specimen type	Analytical expressions for stress triaxiality η[a]	The Lode angle parameter $\bar{\theta}$
1	Smooth round bars, tension	$\frac{1}{3}$	1
2	Notched round bars, tension (Bridgman, 1952)	$\frac{1}{3}+\sqrt{2}\ln\left(1+\frac{a}{2R}\right)$	1
3	Plastic plane strain, tension	$\frac{\sqrt{3}}{3}$	0
4	Flat grooved plates, tension (Bai et al., 2006b)	$\frac{\sqrt{3}}{3}\left[1+2\ln\left(1+\frac{t}{4R}\right)\right]$	0
5	Torsion or shear	0	0
6	Cylinders, compression	$-\frac{1}{3}$	-1
7	Equi-biaxial plane stress tension	$\frac{2}{3}$	-1
8	Equi-biaxial plane stress compression	$-\frac{2}{3}$	1
9	Plastic plane strain, compression	$-\frac{\sqrt{3}}{3}$	0
10	Notched round bars, compression	$-\left[\frac{1}{3}+\sqrt{2}\ln\left(1+\frac{a}{2R}\right)\right]$	-1

[a] In the expressions of η, R is the radius of a notch or a groove, a is the radius of a round bar at the notch, t is the thickness of a flat grooved plate at the groove.

Table 1.5: *List of the tests carried out by Bai [Bai and Wierzbicki, 2008].*

[Luo et al., 2012], [Gachet, 2013] (see section 4.4.2.3 for the numerical studies of shear test with the modified GTN model).

Remarks In [Bao and Wierzbicki, 2004], [Bao and Wierzbicki, 2004a], [Bao and Wierzbicki, 2005], [Bai and Wierzbicki, 2008], the experimental results were all compared with the simulation results using FE models. However, the damage evolution rule is quite simple and is not coupled with the material behavior law, with a relationship between the damage indicator D and the equivalent plastic strain $\bar{\epsilon}_p$:

$$D(\bar{\epsilon}_p)=\int_0^{\bar{\epsilon}_p}\frac{d\bar{\epsilon}_p}{f} \tag{1.123}$$

where $f=f(\frac{\sigma_h}{\bar{\sigma}})$ or $f(\frac{\sigma_h}{\bar{\sigma}},\bar{\theta})$. Many further studies developed this method and the butterfly specimen to establish fracture loci for different materials: cast aluminum alloy ([Mae et al., 2007]), aluminum alloy 6060-T6 [Beese et al., 2010], advanced high strength steels (AHSS) [Li and Wierzbicki, 2010], using the Modified Mohr-Coulomb (MMC) ductile failure criterion ([Bai and Wierzbicki, 2010] see 3.1.2.2 for more details). The butterfly specimen is a very good candidate to carry out fracture tests for a wide range of stress triaxialities. This specimen has several advantages including the same fracture initiation location under different loading combinations. It is also able to remove partly the effect of mesh size (due to the fact that only one finite element model is needed for different loading conditions). However, this specimen has been shown suitable for metal sheet applications (with a special geometry which is not easy to machine) but the applicability to metal wire or metal bar still needs to be proven by future researches.

In addition to the butterfly specimen, the new double notched tube specimens were presented in [Barsoum and Faleskog, 2007a] to carry out experiments under tension and torsion combined loading. In this study, Barsoum and Faleskog defined the Lode parameter as $\mu=\frac{2\sigma_2-\sigma_1-\sigma_3}{\sigma_1-\sigma_3}$ - Fig. 1.18b ($\mu=-1$ in generalized tension, $\mu=0$ in generalized shear and $\mu=1$ in generalized compression, which is opposed to the definition of [Bai and Wierzbicki, 2008] - see section 1.4.2.1). During each test, the load ratio $\kappa=\frac{Nr_m}{M}$ was kept constant (where N, M are axial tension force and torsional loading, r_m is the radius to the center of the notch - Fig. 1.35a). The authors then carried out a micromechanical modeling of fracture mechanisms in combined tension and shear using the unit cell method [Barsoum and Faleskog, 2007]. The results revealed that the influence of the Lode parameter on void growth and coalescence can be significant. One can generate two different fracture mechanisms with the double notched tube specimen, which can be predicted by the micromechanical models. This specimen might be employed to carry out experiments in low to intermediate triaxiality regime but cannot create negative stress triaxiality states.

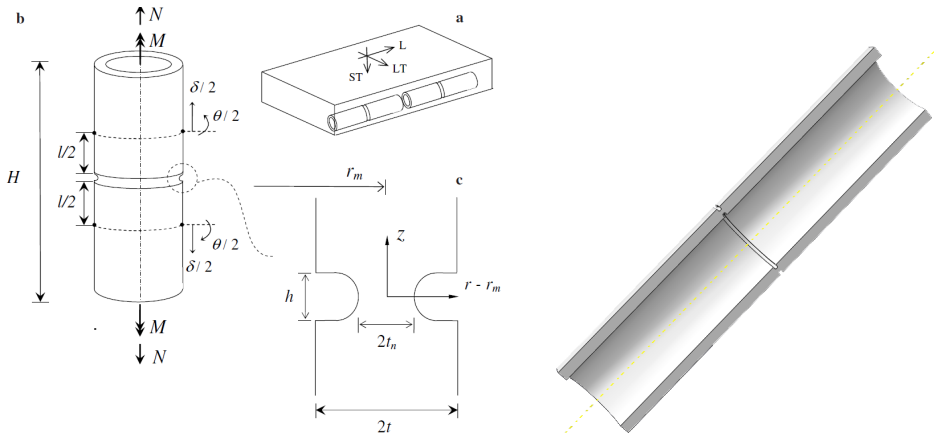

(a) *Double notched specimen configuration* **(b)** *Cutting surface along the tube axis.*

Fig. 1.35: *Double notched tube specimen [Barsoum and Faleskog, 2007a].*

1.5.3 Mechanical tests suitable for forming processes

In order to better predict damage and fracture occurring during forming processes using FEM simulation, the use of representative mechanical tests is necessary to identify the model parameters. In [Vanegas Marquez, 2011], the author demonstrated the influence of calibration tests (compression, cyclic tension-compression) on damage prediction during the simulation of cold pilgering process.

For the wire drawing process, the tensile test might be used for the model calibration since the stress state experienced by a material point located in the wire core is equivalent to uniaxial tensile stress state with some superimposed pressure.

Tang and co-workers ([Tang and Lee, 1995], [Tang et al., 2003]) carried out shear tests using the Iosipescu specimen (see Fig. 1.36) to study the shear damage of aluminium alloy 2024-T3. After shear fracture, the Iosipescu specimen was then polished for microscopic examination (these Iosipescu specimens were machined from pre-tension specimens - Fig. 1.36).

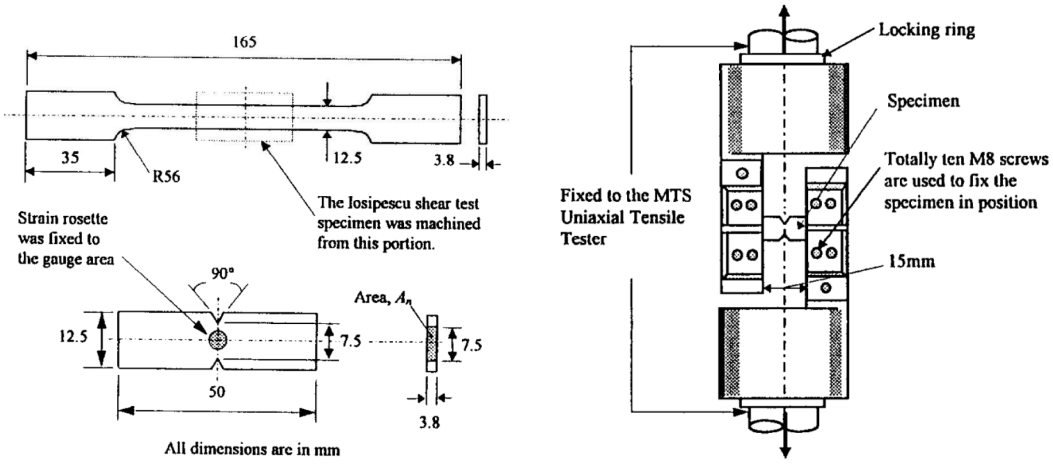

(a) *Geometry of the Iosipescu shear test specimen.* **(b)** *Connection between the specimen and the shear fixture.*

Fig. 1.36: *Shear test with Iosipescu specimen [Tang and Lee, 1995], [Tang et al., 2003].*

Parallel to this study, the author used the load-and-unload torsion test to measure the shear damage variable $D_G = 1 - \frac{\tilde{G}}{G}$ (G is the shear modulus and $\tilde{G}$ is the effective shear modulus), which quantified the level of damage. In these torsion tests, the torsion specimen was loaded to below the yield limit. The author

concluded that the shear damage was localized in the shear band region where the deformation and rotation of grains were intense.

Starck [Starck, 1992] carried out the study of the same type of loading (tension then torsion tests on round specimen). This type of test is interesting for the study of the influence of loading path change (uniaxial tensile state to shear state) on material ductility, which is suitable for the application to processes with the same type of loading path (e.g. wire drawing followed by cutting).

In order to generate the stress state during rolling of flat products, there are two simple ways to make plane-strain compression tests: one is to put the specimen in a well-lubricated channel that prevents the lateral spreading (channel-die test - see Fig. 1.37a); the other is to indent a thin, wide specimen with overlapping dies (see Fig. 1.37b). The influence of friction in these two tests is very important. These tests are used to characterize flat products during rolling and to the best of the present author's knowledge, they are not yet validated for the wire-flat rolling process.

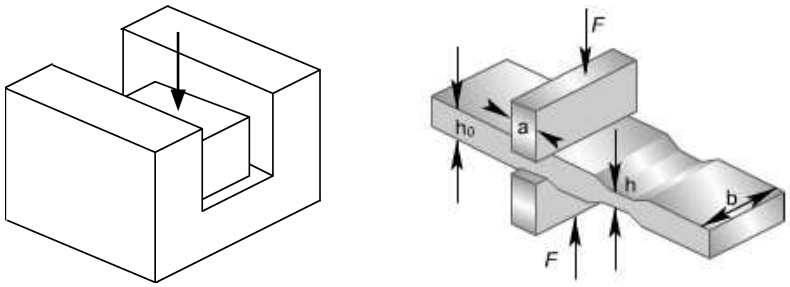

(a) *Channel-die test.* **(b)** *Plane strain compression test.*

Fig. 1.37: *Two ways of performing plane-strain compression test.*

Farrugia [Farrugia, 2006] carried out series of mechanical tests including double collar and "flying saucer" axisymmetric tests, U-bending and revised plane strain compression tests using a Gleeble thermo-mechanical simulator to vary the stress triaxiality ratio, principal stress (SPR) and principal strain (PSR)[17] ratios during hot rolling. The author then developed a multi-scale modeling approach to represent the various physical length scales encountered during rolling and mechanical tests. From the experimental and numerical results, the double collar (see Fig. 1.38), flying saucer and mostly revised plane strain (see Fig. 1.39) compression tests seem to be the most relevant to rolling. However, according to the author, this conclusion, which was obtained by studying only one parameter (stress triaxiality), is strongly sensitive to steel grades.

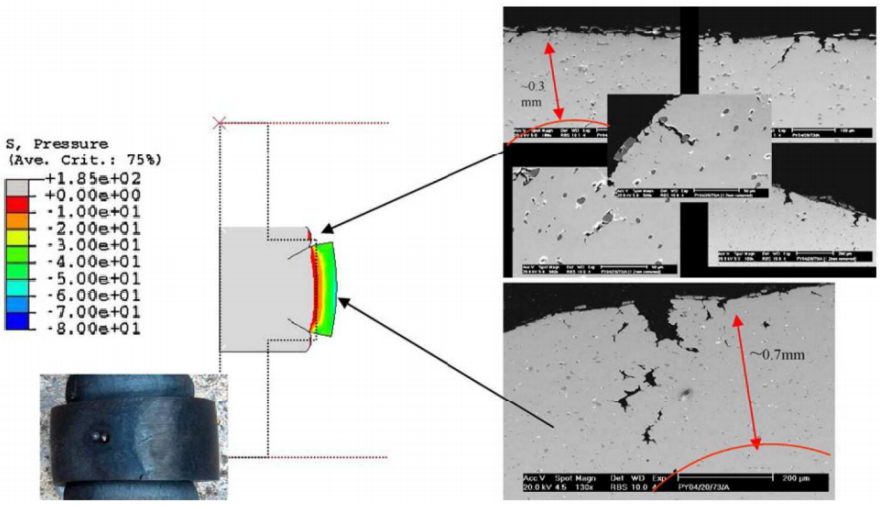

Fig. 1.38: *Double collar damage assessment at both inner and outer ring [Farrugia, 2006].*

[17] SPR= $\frac{\sigma_3}{\sigma_1}$, PSR = $\frac{\epsilon_3}{\epsilon_1}$.

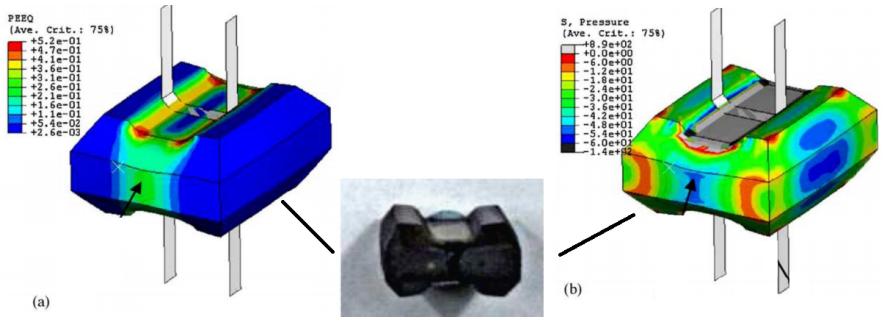

Fig. 1.39: *New revised plane strain specimen and its model in Abaqus [Farrugia, 2006].*

1.5.4 Conclusion on the choice of mechanical tests

In order to investigate the damage under complex loading paths, one has to carry out suitable calibration tests for damage models identification. Various stress states may be obtained by using either a series of uniaxial tests such as uniaxial tensile test, compression test and torsion test, or multiaxial tests, such as combined torsion and tension on tube (for bulk materials), combined shear and tension on butterfly specimen (for sheet materials). In the present study, bulk materials were used (rod or tube), the combined torsion and tension test may be suitable to generate multi-axial stress state. Exploiting the result of this test needs special attention. However, due to the lack of experimental device to perform this type of test, we used the series of uniaxial tests to study damage for different loading conditions. These uniaxial tests are straightforward to be exploited and have been shown to be accurate for damage/fracture models identification (see [Bao and Wierzbicki, 2004, Bai and Wierzbicki, 2008]). The major drawback of this approach is that one cannot obtain intermediate stress states between the three limits: uniaxial compression, pure shear and uniaxial tension. Moreover, the influence of strain path change cannot be studied with the series of uniaxial tests. For this reason, in the present study, the applications simulations of different forming processes will help us to validate the identified damage models from the mono-axial tests. Detailed descriptions of mechanical test and their application to the identification of plasticity and damage models parameters for different materials are presented in Chapters 2 and 3.

1.6 Damage in studied forming processes

1.6.1 Defects, damage and fracture in cold rolling

A type of crack observed in sheet or thin strip rolling is often the edge crack ([Dieter, 1976], [Dodd and Boddington, 1980], [Xie et al., 2011]). In the present study, we concentrate on the rolling of long products (the wire flat rolling). The interested readers can refer to the above-mentioned references for different aspects of edge crack analyses, and to [Banabic, 2010] for more details on constitutive modeling of sheet metal forming.

[Filipovic et al., 2006], [Son et al., 2008] studied the behavior of surface defects in wire rod *hot rolling*. In [Farrugia et al., 2009], different factors that affect the damage and fracture in long product hot rolling are discussed. The influences of different properties on material ductility, such as inclusion spacing, strain rate and temperature, strain path, dynamic recrystallization and thermal gradients are presented in details in this reference. A summary of the main parameters and their sensitivities is reported in Table 5 of [Farrugia et al., 2009]. However, these studies ([Filipovic et al., 2006], [Son et al., 2008], [Farrugia et al., 2009]) concern the hot rolling process, in which high strain rate and temperature as well as different microstructure processes occur simultaneously with deformation (see section 1.1.1.1).

To the best of the present author's knowledge, there are not many researches in the literature dealing with the damage and fracture during *cold rolling* of long products, especially the *wire flat rolling*. The reason is

that few long products are made by cold rolling. Fig. 1.40 represents the schematic of the wire flat rolling.

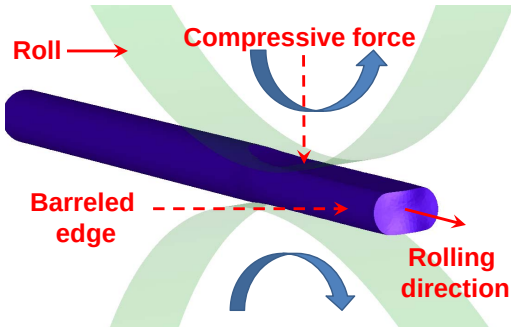

Fig. 1.40: *Schematic of wire flat rolling.*

As the wire passes through the rolls, all material points across the width experience some tendency to expand laterally (transverse direction); this is called *"spread"*. The edges are thus strained in tension, which may lead to edge cracking. The edge center tends to expand laterally more than the upper and lower surfaces, which produces barreled edges similar to those observed in compression of a cylinder. Therefore, theoretically, in this process, the barreled areas are critical zones where cracks tend to initiate first. Recently, Massé ([Massé, 2010]) carried out an experimental study of damage in rolling process. Damage had been identified at a microscopic scale through SEM observation, which showed decohesion around non deformable inclusions (matrix-inclusion debonding) and fragmentation of deformable inclusions. The FEM analyses of the strain map was also presented, which showed a localization area called the *"blacksmith cross"*. This strain localization may explain the evolution of microstructure during rolling (see [Massé, 2010] for more details). The author then carried out SEM observations of the transverse as well as the longitudinal cutting planes to obtain the 3D view of damage localization at the end of rolling. The 3D experimental sketch of damage, superposed on a strain map obtained with FEM analysis, is presented in Fig. 1.41a.

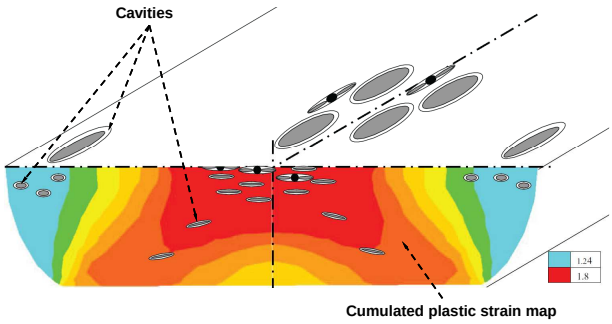

(a) *The sketch shows the decohesion in axial direction due to the wire drawing process and in axial direction due to the rolling process. Moreover, void rotation can be observed in the blacksmith cross.*

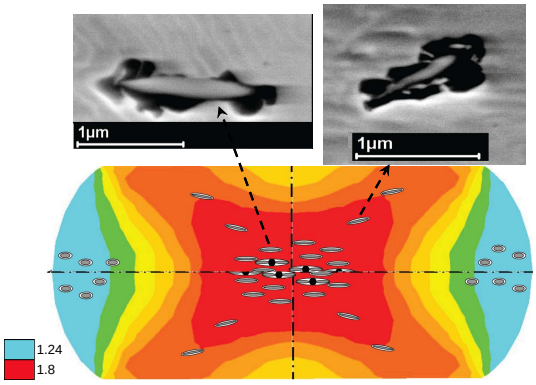

(b) *The zoomed pictures show flattened deformable inclusions in the wire core and in the blacksmith cross (SEM pictures).*

Fig. 1.41: *3D-sketch of the damage state at the end of rolling superimposed to strain map obtained by FEM analysis (color) (figure adapted from [Massé, 2010]).*

As stated above, the rolling process is defined by a global vertical compression with a significant transverse flow, the expansion of decohesion thus follows the transverse direction. In this figure, one can observe that the decohesion is opened partly in the axial direction, a result of the previous wire drawing. Moreover, the inclusions located in the branches of the blacksmith cross seem to have a preferential orientation due to rotation associated with shear strain in this area. The author mentioned a higher void density as well as a higher flattening of cavities in the wire core than in the edge. Therefore, from this experimental observation, **the rolling process principally affects the voids in the wire core and on the blacksmith cross**. Voids

located in the barreled zone were also expanded laterally due to rolling, but the expansion is less significant.

1.6.2 Damage and fracture in wire drawing process

Defects in drawn wire come from both the initial defects from the preform and the deformation process itself. The common defect observed in drawing is chevron cracking or center burst (also called "cupping" - cup and cone fracture [Dieter, 1976], see Figs. 1.42a and 1.42b).

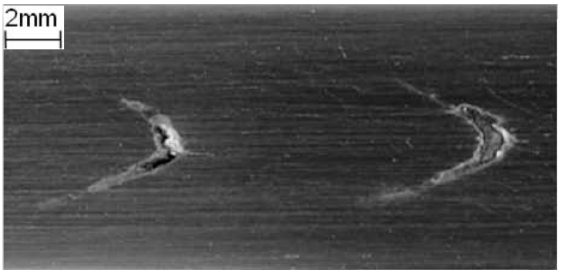

(a) *Chevron observed on the longitudinal cutting surface in drawing direction.*

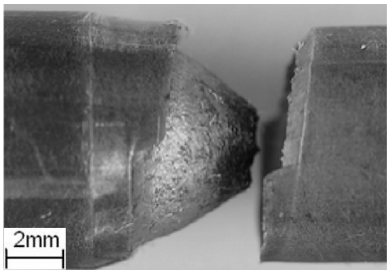

(b) *Cup-cone fracture.*

Fig. 1.42: *Cup-cone fracture observed in wire drawing of high carbon steel (figure adapted from [Komori, 2008]).*

Avitzur ([Avitzur, 1968, Avitzur, 1980]) carried out an upper-bound analysis to investigate this type of fracture. According to the author, for a given semicone angle of die, the reduction must be high enough to avoid the central burst (see Fig. 1.43 for an example of a criterion proposed by Avitzur).

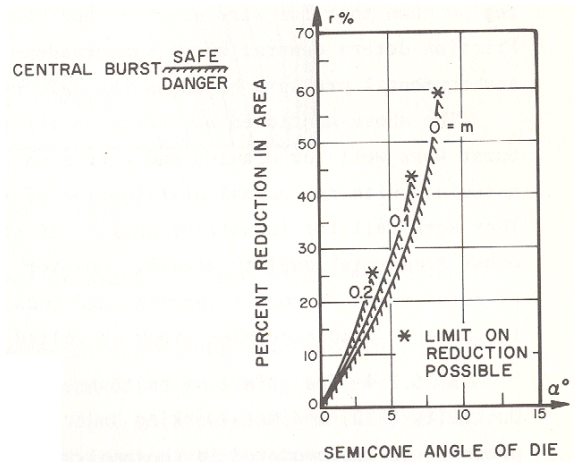

Fig. 1.43: *Criterion to prevent central burst in metals. In this figure: m is the Tresca friction coefficient; r is the reduction ratio; α is the semi-angle. The "safe" region is the region above each curve (figure adapted from [Avitzur, 1980]).*

If the die angle increases, the critical reduction also increases, but it cannot be higher than some values, represented by the asterisk symbols at the end of each curve in Fig. 1.43. The reason is, when the reduction is too high, the average stress at the exit is high and crack might occur (but not the central burst). Moreover, for a fixed die angle, the critical reduction increases with friction. In summarizing, to avoid central burst, a configuration of *low angle and high reduction* is preferred (but in this case, there is more risk of "total" crack at die exit).

Venkata Reddy and coworkers[Venkata Reddy et al., 2000] compared three ductile fracture criteria for the prediction of the chevron crack in axisymmetric drawing: hydrostatic stress criterion, the Thomason's fracture criterion ([Thomason, 1968, Thomason, 1990]) and the critical damage criterion[18]. The hydrostatic

[18]This criterion is a modification of Lemaitre model to account for *"void nucleation"* [Dhar et al., 1996].

stress criterion (proposed by [Venkata Reddy et al., 1996]) states that *"whenever hydrostatic stress at a point on the centerline in the deformation zone becomes zero and is compressive elsewhere, there is fracture initiation leading to central burst"*. In [Venkata Reddy et al., 2000], this criterion (among the three above-mentioned criteria), was proved to be the best adapted to central burst prediction during drawing.

McAllen and Phelan ([McAllen and Phelan, 2007]) analyzed the occurrence of central burst defects in single and multipass wire drawing by using a modified damage work model for damage study, and the GTN model to define the flow rule and the yield function. In this damage model, the incremental plastic work is defined as:

The incremental plastic work:

$$\delta W_d = \begin{cases} \sigma_{eq}\delta\bar{\epsilon}^p \left[1 + 3\frac{\sigma_h}{\sigma_{eq}} 0.487 \left(\frac{\sigma_h}{\sigma_{eq}}\right)^{0.25} exp\left(\frac{3}{2}\frac{\sigma_h}{\sigma_{eq}}\right)\right] & ,for \quad \frac{\sigma_h}{\sigma_{eq}} \leq 1 \\ \sigma_{eq}\delta\bar{\epsilon}^p \left[1 + 3\frac{\sigma_h}{\sigma_{eq}} exp\left(\frac{3}{2}\frac{\sigma_h}{\sigma_{eq}}\right)\right] & ,for \quad \frac{\sigma_h}{\sigma_{eq}} > 1 \end{cases} \tag{1.124}$$

The damage development over strain path is then calculated as:

$$D = \int_0^{\bar{\epsilon}_p} max(0, \delta W_d) \tag{1.125}$$

With this approach and using the element removal technique (i.e. the element was removed when its damage variable reached a critical value), the authors investigated the influence of central burst formation on the distribution of die pressure, hydrostatic pressure and the effective stress along the central line. The results showed a fluctuation of these parameters along the central line, with the "wavelength" equals to the distance between two consecutive central bursts. This oscillation came from the fact that the fracture relaxed the tensile stress, which took a certain time to recover. Moreover, again, **the die land is demonstrated to have a negligible effect** on damage and mechanical properties such as stress and strain state.

[Tang et al., 2011] used the GTN model for the numerical simulation of damage evolution in multi-pass drawing. Their results showed a good agreement with the real drawing process. Moreover, an optimization procedure, based on least damage accumulation principle, was proposed to define an optimal area reduction in a single pass drawing, with a constant semi-angle ($\alpha = 4°$). The authors then proposed the potential replacement of the standard 8-pass process with a 7-pass one, for the same total area reduction through the following drawing schedule: reduction should be low in the first pass, then increases in second pass and gradually decreases in the following passes. However, these results have not been validated yet by experimental study.

[Lapovok and Hodgson, 2009] studied the characterization of strain path with respect to the directionality of defect formation, using the hypothesis of "dominant" direction and strain-rate-change criterion. Two formulations were proposed, one was based on the scalar damage and the other used the damage tensor. These models were implemented to carry out the simulation of a two-stage metal forming process: wire drawing followed by constrained upsetting (bulge test). The results showed that the tensor damage criterion predicts the defect formation earlier than the scalar criterion. Moreover, the direction of defect development can also be calculated.

[Son et al., 2011] studied the influence of inclusions on gold wire drawing stress with different types of inclusions. The results show that different inclusions have different effects on drawing stress through their yield stresses. If the yield stress of inclusion is lower than that of wire, the drawing force will decrease, while inclusions with higher yield stress than wire cause an increase in drawing stress. These results can be used to detect the inclusions in drawn wire. However, this study did not show the influence of *inclusion size* on damage as well as on drawing force.

1.6.3 Cracks observed in cold pilgering

There are few studies in the literature dealing with crack initiation during the cold pilgering process. Abe [Abe, 2010] used the compression test to investigate the workability of zirconium alloy tube (Zr4) in cold

pilgering process. The author mentioned the crack initiation on the **inner surface** of tube, without showing any experimental evidence. In [Gaillac, 2007], the author showed the photo of cracks, which revealed that crack initiated more frequently on the **external surface** of tube and the crack was perpendicular to the rolling direction. Fig. 1.44 shows an example of several cracks observed.

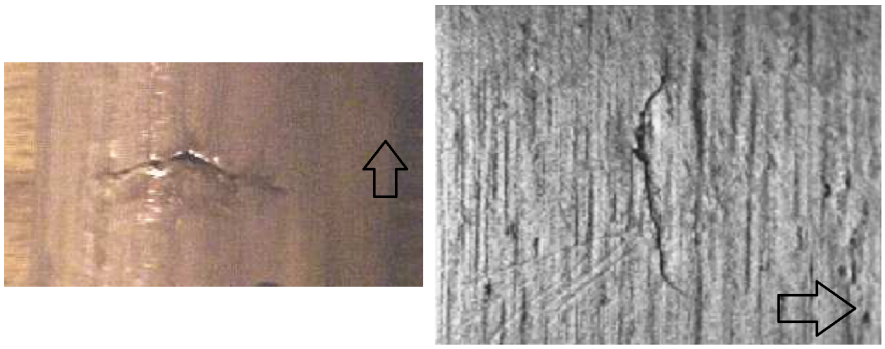

Fig. 1.44: *Crack observed on external surface of tube during cold pilering. The arrows in the images indicate the rolling direction (figure adapted from [Gaillac, 2007]).*

Since Gaillac carried out his study on the same process and material as the present study, the danger zone is *assumed* on the external surface of tube, where the risk of crack initiation is higher

1.7 Summary of Chapter 1

This chapter is dedicated to the bibliographical background for the present study. Six principal parts were presented.

First, the forming processes used were revisited. The mechanical analyses of cold rolling process were shortly presented. The frictions as well as the back/front tension forces were proved to have an important influence on the rolling force. Concerning the wire drawing process, the reviewed studies principally concentrated on drawing force and damage prediction (central bursts, chevron defects). However, these studies did not address the influence of residual stresses at the end of wire drawing, another important factor for the next step of metal forming process. Results in the literature on other processes showed the strong influence of these residual stresses and strain, as well as damage accumulation in previous processes on the damage evolution in the next step forming process. Short review on cold pilgering process was then given, which reveals the complexity of such a process, both in tools design and mechanical aspect.

In the second section, a review on continuum mechanics as well as the mixed velocity-pressure FE method used to solve the thermo-mechanical problem was given. A short review of elastoplasticity has been presented in the third section. These reviews help to clarify the development work presented in Chapter 4 for the implementation of a pressure-dependent plasticity model in Forge2009®.

In the fourth section, ductile damage mechanisms were presented in detail. At positive stress triaxiality, ductile damage is governed by nucleation, growth and coalescence of voids. Details on mechanisms as well as modeling of each stage were presented. For low stress triaxiality with shear dominated-loading, recent experimental observations of [Achouri et al., 2013] revealed the same mechanisms of ductile damage as in high stress triaxiality. Moreover, under shear loading, deformed voids also underwent a rotation, depending on the loading level. At negative stress triaxiality, experimental results of [Bao and Wierzbicki, 2004] showed no cracked particles and nucleated voids on the fracture surface, and this surface was relatively smooth in comparison with dimpled surface under high stress triaxiality. Macroscopically, damage results in a softening of material, which is an important observation to identify damage models parameters. Short reviews of damage models were then given, which were classified into three groups: uncoupled phenomenological models, coupled phenomenological models and micro-mechanical models. Methods for damage quantification were also introduced, which could be based on either macroscopic properties (e.g. softening effect) or microscopic observations (e.g. evolution of voids).

In the fifth section, experimental tests for damage and fracture quantification were presented. For an application to complex loading configurations, damage has to be quantified under different loading configurations (i.e. stress states), using either multi-axial experiments (e.g. combined tensile and shear test [Bai and Wierzbicki, 2008, Beese et al., 2010], combined tensile and torsion test [Barsoum and Faleskog, 2007a, Haltom et al., 2013]) or series of mono-axial experiments (e.g. uniaxial compression, uniaxial tension, torsion). Moreover, successive loading tests (e.g. tensile test then shear test [Tang and Lee, 1995, Tang et al., 2003], tensile test then torsion test [Starck, 1992], shear then tension test [Gachet, 2013]) were also used to investigate the influence of loading path change on material ductility. From these tests, authors in the literature carried out analyses based only on the stress triaxiality or both the stress triaxiality and the Lode parameter. In the present study, a set of mono-axial mechanical tests has been used for ductile damage study and hardening and damage models identifications. They are the subjects of Chapters 2 and 3.

In the final section, reviews on experimental results of damage and fracture during forming processes were presented. Literature reviews of damage occurring during the rolling process were first given, which showed a limited research on damage in wire flat rolling. Massé ([Massé, 2010]) carried out an experimental study of damage in cold rolling of wire, which showed strong localization of damage in the wire core and in the blacksmith cross. The ability of FE simulation to predict such localization is the key point to avoid cracking in the real industrial process. Regarding damage in wire drawing process, several important results are summarized as:

- A negligible influence of die land length on damage evolution was demonstrated.
- The increase of reduction or friction leads to the increase of damage and drawing force. Furthermore, with the Latham & Cockcroft fracture criterion, the results of Massé showed that a strong decrease of damage could be obtained with a limited increase of the drawing force.
- Generally, a high value of the shape factor Δ increases strain inhomogeneity.

For the cold pilgering process, cracks are often observed on the external surface of pilgered tube as shown in [Gaillac, 2007]. These experimental evidences will enable us to validate our numerical results obtained with our developed damage models presented in Chapter 6.

1.8 Résumé en français

Ce chapitre est consacré à une revue bibliographique pour la présente étude. Six parties principales ont été présentées. Dans la première partie, les procédés de mise en forme à froid utilisés dans cette étude ont été revisités.

Tout d'abord, une analyse mécanique du laminage a été présentée. Le frottement ainsi que les forces de traction et de contre-traction a été montré important sur la force de laminage. Concernant le tréfilage, les études bibliographiques ont porté sur la force de tréfilage et la prédiction de l'endommagement (e.g. les fissures de type chevron). Pourtant, les études abordées n'ont pas envisagé l'influence de la contrainte résiduelle à la fin du tréfilage sur les étapes de mise en forme suivantes (e.g. le tréfilage suivi par le laminage). Les résultats dans la littérature sur d'autres procédés ont montré une forte influence de la contrainte, de la déformation et aussi de l'endommagement résiduels du procédé précédant sur le procédé suivant. Ensuite, une brève revue du laminage à pas de pèlerin a été présentée, qui a montré la complexité de ce procédé, à la fois sur la conception d'outil et sur l'aspect mécanique.

Dans la seconde partie, une revue sur la mécanique des milieux continus et la méthode des éléments finis mixtes utilisée pour résoudre le problème thermomécanique a été présentée. Un rappel sur l'élastoplasticité a été donné dans la troisième partie. Ces revues bibliographiques aident à clarifier le travail de développement présenté au chapitre 4 où l'implémentation d'un modèle de plasticité compressible dans le logiciel Forge2009® est détaillée.

Dans la quatrième partie, les mécanismes de l'endommagement ductile ont été présentés en détail. Quand la triaxilité des contraintes est positive, l'endommagement ductile est gouverné par la germination, la croissance et la coalescence des porosités. Les détails de chaque mécanisme ainsi que la modélisation de chaque stade ont été présentés. Pour les faibles niveaux de triaxialité où le cisaillement est dominant, les résultats expérimentaux de [Achouri et al., 2013] ont montré les même mécanismes qu'à plus forte triaxialité. En outre, en cisaillement, les porosités déformées peuvent également subir une rotation. Kweon et ses collègues ([Kweon et al., 2010, Kweon, 2012]) ont expliqué que l'endommagement à triaxialité négative ou nulle était dû à l'interaction entre les grains, qui fait augmenter la traction hydrostatique à l'intérieur du grain. Cette observation a été introduite dans leur modèle d'endommagement basé sur la plasticité cristalline et la théorie de croissance de porosité. Des essais mécaniques réalisés par Bao ([Bao and Wierzbicki, 2004]) ont montré des ruptures plutôt lisses, où les cupules n'ont pas été observées. Macroscopiquement, l'endommagement se traduit par un adoucissement du matériau, ce qui est une observation importante afin d'identifier les modèles d'endommagement. Une brève revue des modèles d'endommagement a été proposée. Ces modèles ont été classés en trois groupes : les modèles phénoménologiques découplés, les modèles phénoménologiques couplés et les modèles micromécaniques. Les méthodes de quantification de l'endommagement ont été également abordées, en se basant sur des propriétés macroscopiques (e.g. l'effet adoucissant) ou des observations microscopiques (e.g. l'évolution de la fraction volumique des vides).

Dans la cinquième partie, des essais expérimentaux pour quantifier l'endommagement et la rupture ductile ont été présentés. Pour une application aux chargements complexes, l'endommagement doit être quantifié pour différentes configurations de chargement (i.e. état de contrainte), en utilisant soit des expériences multiaxiales (par exemple traction-cisaillement combiné [Bai and Wierzbicki, 2008, Beese et al., 2010], traction-torsion combinée [Barsoum and Faleskog, 2007a, Haltom et al., 2013]) soit une série d'expériences mono-axiales (e.g. compression uniaxiale, traction uniaxiale, torsion). En outre, les essais avec changement de chargement (e.g. essai de traction puis de cisaillement [Tang and Lee, 1995, Tang et al., 2003], essai de traction puis torsion [Starck, 1992], essai de cisaillement puis traction [Gachet, 2013]) ont été également utilisés pour étudier l'influence du changement de chargement sur la ductilité du matériau. A partir de ces essais, des auteurs dans la littérature ont réalisé des analyses basées uniquement sur la triaxialité des contraintes ou en combinant triaxialité des contraintes et angle de Lode. Dans la présente étude, une série des essais mono-axiaux a été utilisée pour étudier l'endommagement ductile ainsi que pour identifier les paramètres des lois d'écrouissage. Ils font l'objet des Chapitres 2 et 3.

Dans la dernière partie, une revue sur l'endommagement au cours des procédés de mise en forme a été donnée. Concernant le laminage de fil, il y avait peu d'études dans la littérature. Massé [Massé, 2010] a réalisé des observations expérimentales sur le fil tréfilé puis laminé, qui ont montré une forte localisation de l'endommagement ductile (des porosités) au cœur du fil ainsi que sur la croix du forgeron. La capacité des modèles d'endommagement à prédire cette localisation est un point clé afin d'éviter les risques de fissure au cours du procédé. Pour le procédé de tréfilage, les résultats principaux concernant l'étude de l'endommagement peuvent être résumés comme suite :

- Une influence négligeable de la portée sur l'évolution de l'endommagement a été démontrée.
- L'augmentation de la réduction ou du frottement conduit à l'augmentation de l'endommagement et de la force de tréfilage. En outre, avec le modèle d'endommagement de Latham & Cockcroft, Massé [Massé, 2010] a montré qu'une forte diminution de l'endommagement pourrait être obtenue avec une légère augmentation de la force de traction.
- En général, une valeur élevée du facteur de forme Δ augmente l'hétérogénéité des propriétés mécaniques.

Pour le laminage à pas de pèlerin, des fissures sont souvent observées sur la surface externe du tube comme indiqué dans [Gaillac, 2007]. Ces résultats expérimentaux vont nous permettre de valider les résultats numériques obtenus avec les modèles d'endommagement que nous avons développé (dans le chapitre 6).

Part I

Ductile damage: phenomenological approach

Chapter 2

Materials characterization - Identification of hardening laws

Contents

Introduction

This chapter and Chapter 3 constitute the first part of the present dissertation, which deals with the phenomenological approach of ductile damage. More precisely, several models in this approach were developed and implemented in FE software Forge®2009 to compare their ability to predict fracture. To reach this goal, their parameters have to be identified first, based on different mechanical tests. In order to obtain accurate damage parameters, the elastoplasticity parameters have to be calibrated first, which is the objective of the present chapter. The identification of phenomenological damage models parameters is the subject of Chapter 3.

For the identification of plasticity parameters, homogeneous deformation tests have to be used to have a correct [flow stress - equivalent plastic strain] curve. For this reason, the tensile test on smooth round bar (before necking) and the compression test on cylinder were chosen for this identification procedure. The latter requires preliminary identification of friction effect.

2.1 Mechanical tests

The objectives of the experimental campaign are to identify the plasticity and damage parameters with a series of mechanical tests that cover a large range of stress triaxiality and Lode angle parameter. Fig. 2.1 represents all the tests used in the present study in the space of initial stress triaxiality and initial Lode parameter.

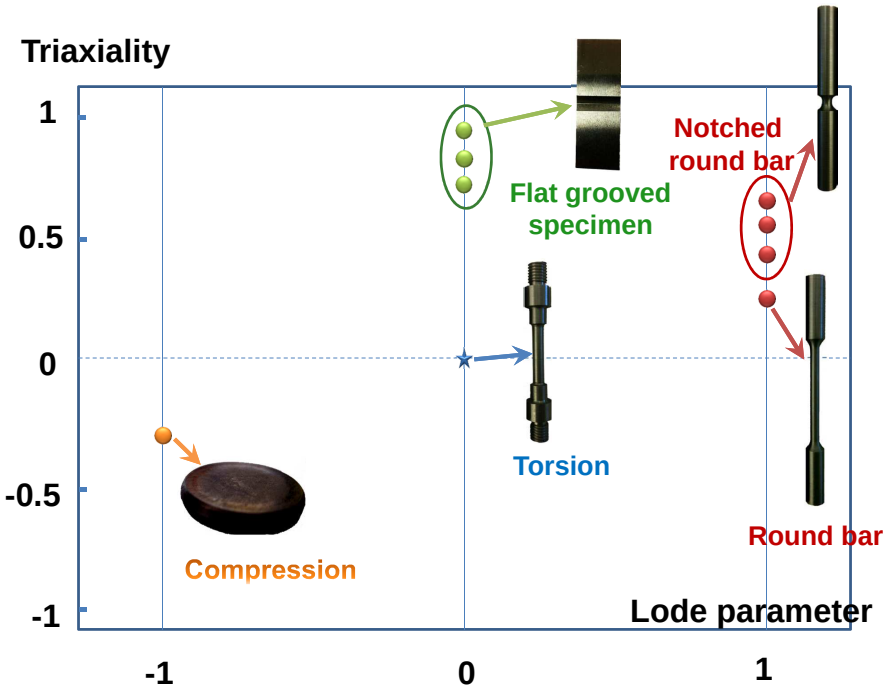

Fig. 2.1: *Representations of mechanical tests carried out in the space of initial stress triaxiality and Lode parameter.*

The formulations to calculate the stress triaxiality and the Lode parameter for each test and each geometry are given in Table 2.1.

In Table 2.1, a_0 and a_f are respectively initial and fracture radii in tensile test on RB and NRB specimens; t_0 and t_f are respectively initial and fracture thicknesses in tensile test on FG specimen[1]; R_0 is the initial notch radius; R and L are the radius and the length of gauge section of torsion specimen; N_r is the number of rotations to fracture; h_0 and h_f are initial and final heights of cylinder used in compression test.

[1]The formulations for FG specimen were developed in [Bai and Wierzbicki, 2008].

Tests/Specimens	Initial triaxiality	Lode parameter $\bar{\theta}$	Fracture strain
Tension on smooth round bar (RB)	1/3	1	$2\ln(a_0/a_f)$
Tension on notched round bar (NRB)	$1/3+ln(1+a_0/2R_0)$	1	$2\ln(a_0/a_f)$
Torsion on round bar	0	0	$2\pi RN_r/\sqrt{3}L$
Compression on cylinders	-1/3	-1	$\ln(h_0/h_f)$
Tension on flat grooved specimen (FG)	$1/\sqrt{3}[1+2ln(1+t_0/4R_0)]$	0	$2/\sqrt{3}\ln(t_0/t_f)$

Table 2.1: *Specimens and tests for fracture calibration.*

2.2 High carbon steel

2.2.1 Material

Steel wires with carbon content greater than 0.25 % are often submitted to a special heat treatment process before being drawn: the patenting process. It consists in heating the steel wire above the austenitizing temperature (900-1000°C) and then cooling at a controlled rate in a lead bath at a temperature greater than 500°C to achieve fine pearlite structure formation. Moreover, it both increases material ductility and strength. The studied material is a high carbon steel grade C62, with the carbon weight percentage near the eutectoid point in the Iron-Iron carbide phase diagram. The structure is therefore pearlitic: ferrite with lamellae of cementite (see Fig. 2.2, which shows cementite lamellae in white and ferrite in dark).

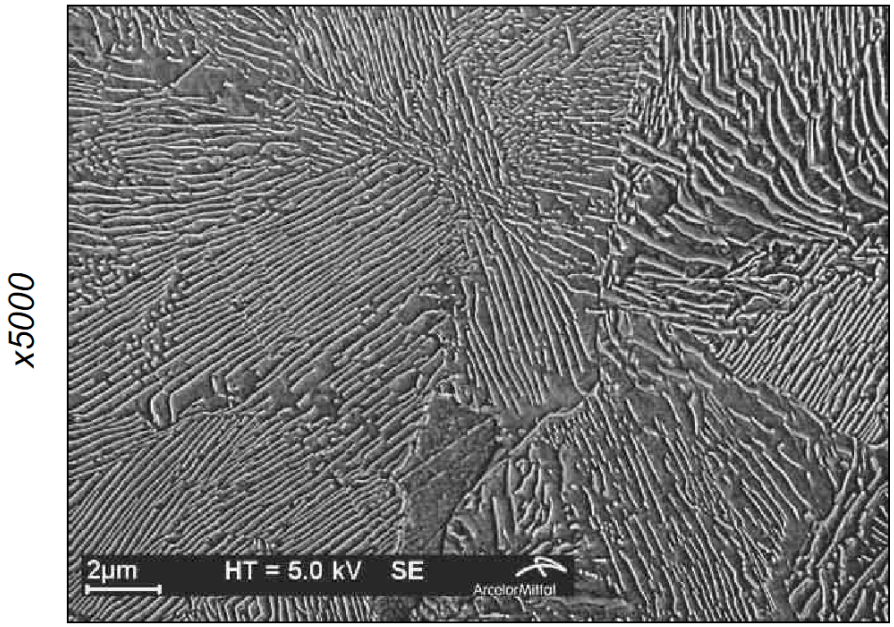

Fig. 2.2: *Initial microstructure of steel wire at patenting state [Cailliez, 2012].*

As shown in Fig. 2.2, the material microstructure at this state is homogeneous, with equiaxial grains and random crystallographic texture. Within a grain, lamellae *seem* have the same orientation due to a relationship between ferrite and cementite [Zhou and Shiflet, 1992]. However, the random grain texture gives overall random lamellae and ferrite orientation [Massé, 2010].

2.2.2 Mechanical tests for model calibration

Table 2.1 summarizes the mechanical tests with the value of initial stress triaxiality and Lode parameter. The machines at CEMEF are limited by a maximum force about **100kN**. The displacement speed varies from 0.1 mm/s to 250 mm/s and the maximum diameter for tension on axisymmetric specimen is **12 mm**. From the

limitation of the maximum force and diameter, the notched radius and specimen radius have to be dimensioned by analytical calculations as well as FE simulations (due to the complexity of strain field in the notched regions). The following sections present the analytical review of these tests.

2.2.2.1 Experimental setup

In order to have the same strain rate for different tests (about 0.7 s^{-1} to $1s^{-1}$), preliminary analytical as well as finite elements analyses were carried out. For tensile test on notched round bar, the strain rate in the notched zone is complex and strongly heterogeneous, the finite element analysis is thus necessary to obtain the average strain rate. Nine simulations (compression (1), tension on smooth bar (2), tensions on notched round bars with three different notch radii (3,4,5), tensions on FG specimens with three different radii (6,7,8), torsion (9)) were carried out to investigate the influence of crosshead speed on the strain rate. Table 2.2 presents the machine speed necessary to have a strain rate about 0.7 to $1s^{-1}$. These results are approximate since they were obtained with coarse meshes. The Bridgman correction ([Bridgman, 1952]) is often used to calculate the stress triaxiality of notched round bar (Eq. 2.1). In [Bao and Wierzbicki, 2005], based on "virtual" tensile tests results, the authors proposed a calibration formulation by adding a multiplicative term of $\sqrt{2}$ (Eq. 2.2). In order to verify these formulations, a series of simulation was carried out on notched round bars models, with different ratios a/R. The simulation results as well as the values obtained by the two above-mentioned formulations are presented in Fig. 2.3.

$$\left(\frac{\sigma_h}{\sigma_{eq}}\right) = \frac{1}{3} + ln\left(1 + \frac{a}{2R}\right) \text{ (Bridgman correction)} \tag{2.1}$$

$$\left(\frac{\sigma_h}{\sigma_{eq}}\right) = \frac{1}{3} + 1.4ln\left(1 + \frac{a}{2R}\right) \text{ (Calibration by [Bao and Wierzbicki, 2005])} \tag{2.2}$$

The results show the consistency between the Bridgman's formulation and our numerical results. Conversely, Bao's modification obtained from simulations with Abaqus is not in agreement with our result with Forge2009®. The difference between the present study and the result of Bao may be linked with mesh size effect since the softening behavior is sensitive to mesh size. The Bridgman formulation is adopted to calculate the *initial* stress triaxialities for different notched round bar specimens.

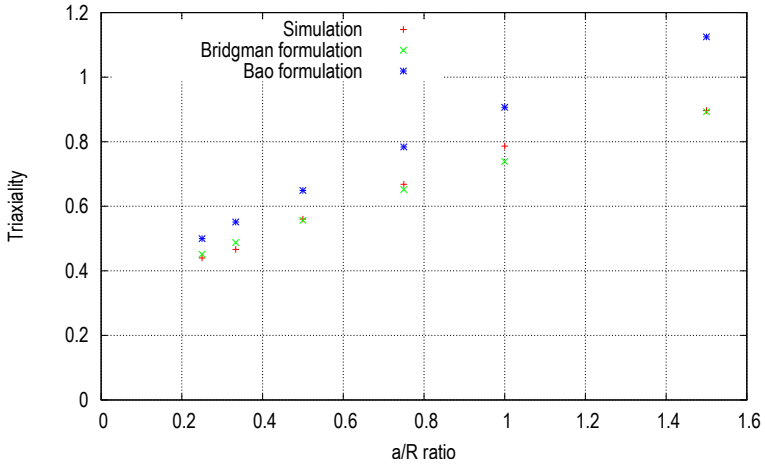

Fig. 2.3: *Evolution of stress triaxiality with the a/R ratio: comparison between the simulation; Bridgman's formulation and Bao's formulation.*

2.2.2.2 Torsion test

Two torsion specimens (Fig. 2.4a) have an effective gauge length (L) of 30 mm and a radius (R) of 3 mm. These torsion tests were carried out at Cemef, Sophia Antipolis. In this test, the specimen is deformed in shear, which allows high deformation because no plastic instabilities (e.g. necking in tensile test) is involved. The fractured specimen is presented in Fig. 2.4b, which shows a flat fracture surface (the scratch on the fracture surface was formed because of friction between two parts of fractured specimen).

Tests/Specimens	Velocity (mm/s)	Lode parameter	Triaxiality	Fracture strain
Tension on smooth RB	50 (30)	1	1/3	0.6539
Tension on NRB, R=4mm	4 (0.86)	1	0.6517	0.2865
Tension on NRB, R=6mm	3 (1.12)	1	0.5565	0.3467
Tension on NRB, R=9mm	2.8 (1)	1	0.4875	0.4
Tension on FG, R=2mm	4 (0.382)	0	0.7758	0.147
Tension on FG, R=5mm	3.95 (0.55)	0	0.6609	0.156
Tension on FG, R=7mm	3.92 (0.586)	0	0.6376	0.159
Torsion on RB	2.75 (2.75) (rounds/sec)	0	0	0.5946
Compression on cylinders	10 (8)	-1	-1/3	No fracture

Table 2.2: *Experimental setup with machine speeds (e.g. crossheads speed in tensile tests) and initial, theoretical values of the stress triaxiality and the Lode parameter. For the "velocity" column, the numbers in parentheses represent the "real" displacement speed of the specimen (see Fig. 2.12 for the difference between crosshead displacement and real displacement of tensile specimens).*

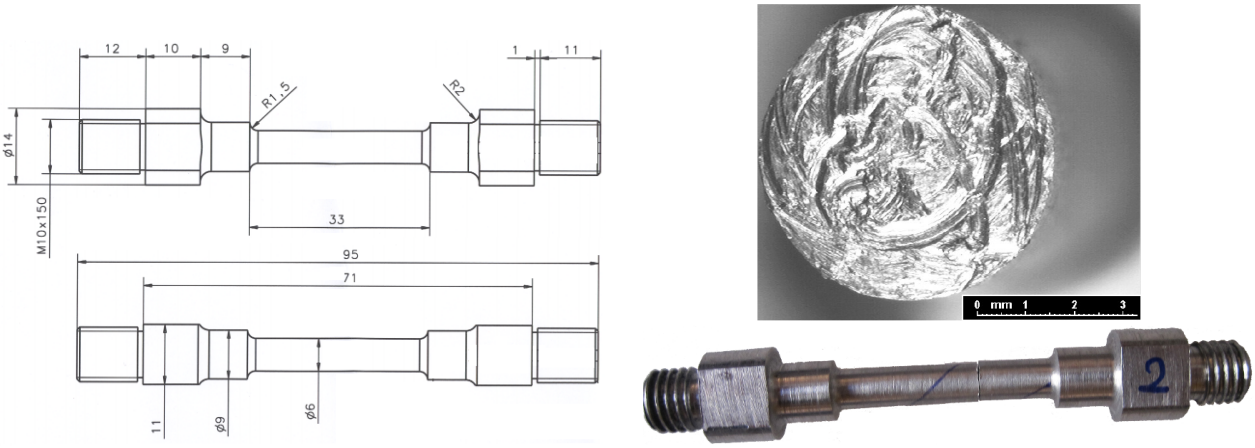

(a) (b)

Fig. 2.4: *Torsion specimens: geometry and dimensions (a) and fractured state (b). All dimensions are in mm.*

The data obtained from this test are the applied torque (Γ) and the number of turns (N) (Fig. 2.5a). There is a slight difference between these two curves but the error is negligible. The first curve, whose correction is presented in Fig. 2.5b, was chosen for further analysis. A conversion was carried out to obtain the stress-strain curve from the ($\Gamma - N$) curve.

Elastic region The applied torque (Γ) to the specimen and the resulting deformation (twist angle, ϕ) were converted to shear stress (τ) and shear strain (γ) by the following respective equations[2]:

$$\tau(R) = \frac{\Gamma R}{J} \tag{2.3}$$

$$\gamma(R) = \frac{\phi R}{L} \tag{2.4}$$

where L is the effective length of specimen; J is the polar moment of inertia, which is defined as: $J = \frac{\pi}{2}R^4$. The effective stress ($\overline{\sigma}$) and the effective strain ($\overline{\epsilon}$) were then obtained through the relations: $\overline{\sigma} = \tau\sqrt{3}$ and $\overline{\epsilon} = \frac{\gamma}{\sqrt{3}}$. These relations have been shown to be valid either in elastic region or at large strain [Shrivastava et al., 1982]. The shear modulus G is defined as the linear slope of the shear stress-shear strain curve.

[2]The shear stress and the shear strain are both calculated on the surface where these values are maximum.

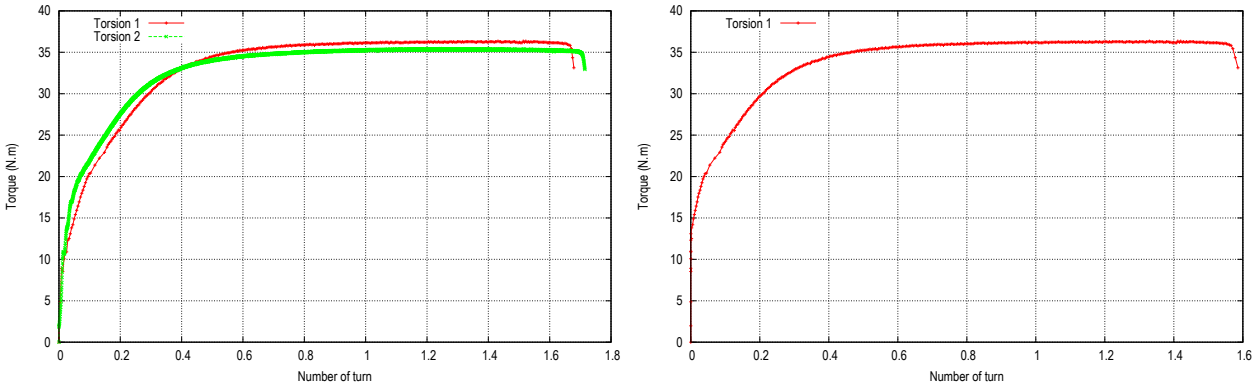

(a) *The original (Torque/Number of turn) curves obtained from the two torsion tests.*

(b) *The first curve with machine stiffness correction, which is chosen for further study.*

Fig. 2.5: *The (Torque/Number of turn) curves before and after correction of machine stiffness.*

Plastic region The Fields-Backofen method ([Fields and Backofen, 1957]) has been employed to construct the (shear stress - shear strain) curve in the plastic region. This method is detailed in Appendix A.5, and the formulation for shear stress is defined as follows:

$$\tau(R) = \frac{\Gamma(\widetilde{m} + \widetilde{n} + 3)}{2\pi R^3} \tag{2.5}$$

where $\widetilde{m}$ and $\widetilde{n}$ are two material parameters (which coincide with the strain-rate sensitivity and the hardening coefficient if the Fields-Backofen constitutive equation is used). These parameters can be calculated as:

$$\widetilde{n} = \left(\frac{\partial ln(\Gamma)}{\partial ln(N)}\right)_{\dot{N},T} \tag{2.6}$$

$$\widetilde{m} = \left(\frac{\partial ln(\Gamma)}{\partial ln(\dot{N})}\right)_{N,T} \tag{2.7}$$

From Appendix A.5, the effective strain-rate and the effective strain are calculated according to von Mises (see Appendix A.5 for more details):

$$\dot{\overline{\epsilon}} = \frac{2\pi R\dot{N}}{\sqrt{3}L} \tag{2.8}$$

$$\overline{\epsilon} = \frac{2\pi RN}{\sqrt{3}L} \tag{2.9}$$

To obtain the true stress-true strain curve in the full range of deformation, the two conversion curves (for elastic region and plastic region respectively) are plotted in the same graph (see Fig. 2.6).

From these two curves, the total stress-strain curve can be obtained by combining the two regions, which is not different from the approximate curve by F-B method.

2.2.2.3 Compression test

In compression tests, homogeneous strain is difficult to achieve due to the friction effect. From analytical analysis, true stress-true strain curve can be obtained from the force-displacement one by using the following formulas:

$$\overline{\sigma} = \frac{4P}{\pi d^2} = \frac{4Ph}{\pi d_0^2 h_0} \tag{2.10}$$

$$\overline{\epsilon} = ln\left(\frac{h_0}{h}\right) \tag{2.11}$$

where P is the applied load; d_0, h_0, d, h are initial and current diameters and heights respectively. Bao [Bao, 2003] carried out upsetting tests on cylinders with different ratios of initial diameter to initial height

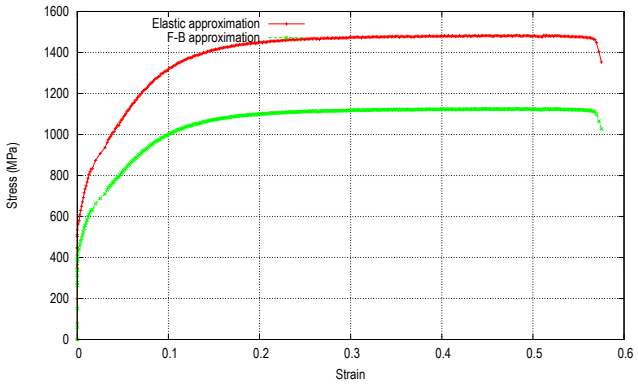

Fig. 2.6: *The stress-strain curve obtained by two methods: the red curve is valid only in elastic region while the green one is valid in plastic region.*

and then used the extrapolation method to obtain the true stress-true strain curve. The idea of this method is to extrapolate the curves obtained with different aspect ratios to the ratio of zero (i.e. $d_0/h_0 = 0$, which is the condition for no barreling effect). This method was validated by different authors (e.g. [Johnson and Mellor, 1962]), for determining the stress-strain curves in uniaxial compression. The result of Bao [Bao, 2003] showed that the stress-strain curve obtained with the specimen whose ratio d_0/h_0 is between 0.65 and 0.8, is the best approximation of the extrapolated curve. In our studies, this range of ratio was chosen.

(a) (b)

Fig. 2.7: *(a) The compression specimens before and after deformation, and (b) the end of the compression specimen. The darker central region was the original end. The lighter region outside was originally part of the cylindrical wall that folded up due to severe barreling.*

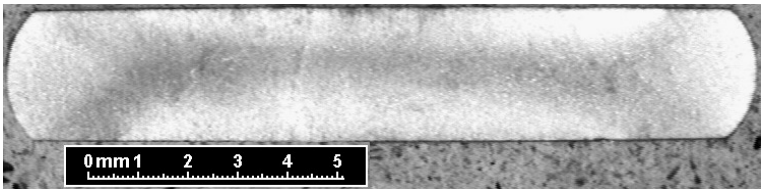

Fig. 2.8: *Strain localization band on the polished and etched cross section.*

Three compression tests were carried out with initial diameter and height of 8 mm and 11 mm respectively. The deformed specimens are shown in Fig. 2.7. There was no fracture during these tests but strong strain localization in shear bands could be observed on the cut section (Fig. 2.8).

The force-displacement curves obtained directly from the machine software take into account the influence

of the machine stiffness. In order to have the force-displacement curve of specimen, the former curve has to be corrected by eliminating the machine stiffness. The result after correction is represented in Fig. 2.9a.

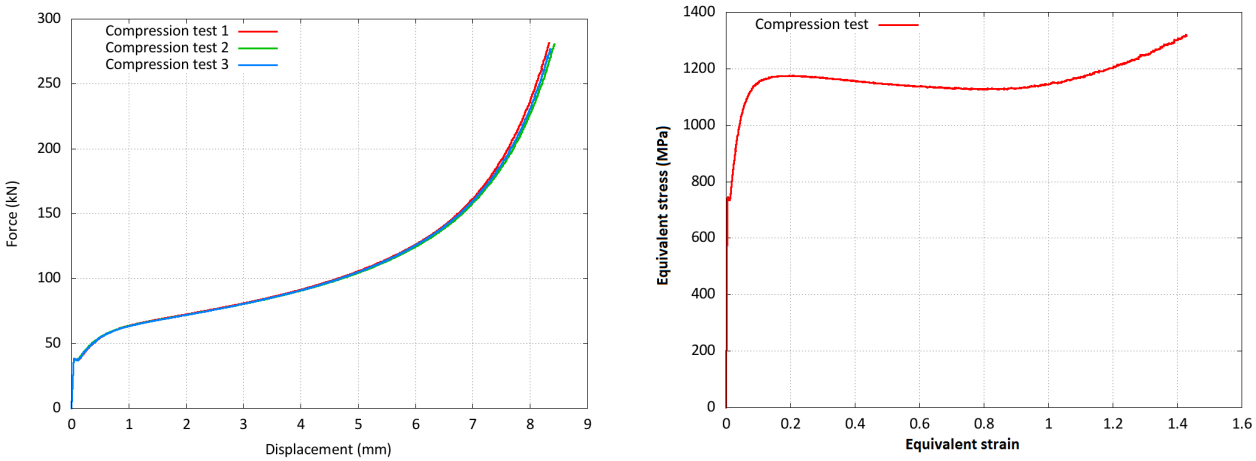

(a) *Force-displacement curves from compression tests.*

(b) *Approximated stress-strain curve.*

Fig. 2.9: *Experimental result from compression tests.*

The plastic zone can be divided into 3 regions: the first (displacement $< 0.8\ mm$), a strong increase of force with displacement can be observed; the second region (displacement from 0.8 to 5.5 mm): the applied force increases linearly with the displacement; and in the last region (displacement $> 5.5\ mm$): the applied force increases sharply with displacement (which is principally due to the increase of diameter and also the friction effect). The approximated stress-strain curve (Fig. 2.9b) could be derived from Eqs. 2.10 and 2.11. Clearly, this curve is correct only if the barreling is small and homogenous deformation is respected. In the present compression test, since the barreling is effect is remarkable, this curve is thus unreliable. The analyses will be referred in section 2.2.3.2.

2.2.2.4 Tensile tests on round bars and notched round bars

A series of tensile specimens were cut in the longitudinal direction of patenting steel wire. The geometry and dimensions of these specimens are presented in Fig. 2.10. Example of fractured specimen is presented in Fig. 2.11 (NRB-R4 specimen), which reveals cup-cone fracture mode.

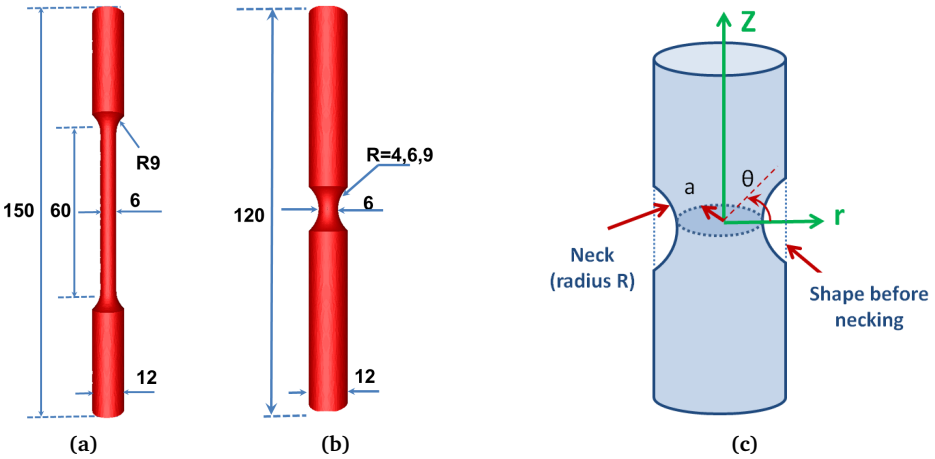

(a) **(b)** **(c)**

Fig. 2.10: *Dimensions of smooth RB (a) and NRB (b) with notch radii equal to* 4 mm, 6 mm, 9 mm *respectively; (c) illustration of necking of round bar under tension. All dimensions are in* mm.

The load-displacement curves for the smooth and notched round bar tensile tests are plotted together in

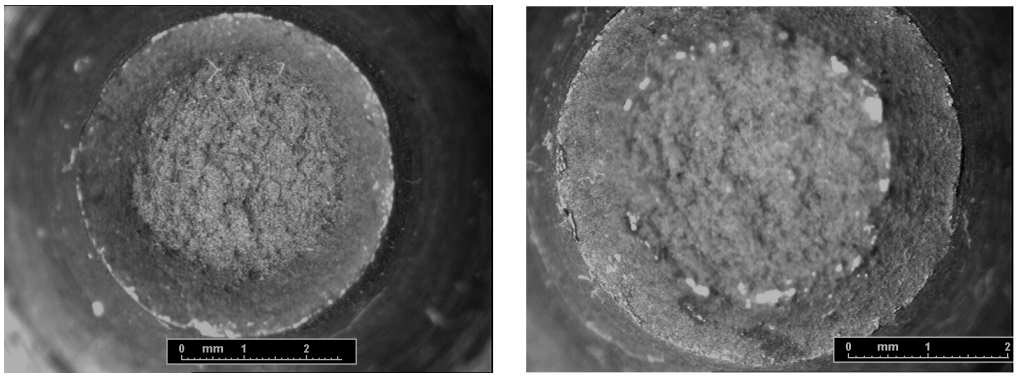

Fig. 2.11: *Cup-cone fracture observed on NRB-R4 specimen. Cracks initiated at the center then propagated outward to form shear lips (flat to slant fracture modes).*

Fig. 2.12. For the notched round bar, the reduction of ductility due to a higher stress triaxiality leads to the decrease of displacement to fracture (this well-known behavior of ductile fracture is often called *"the notch sensitivity"*).

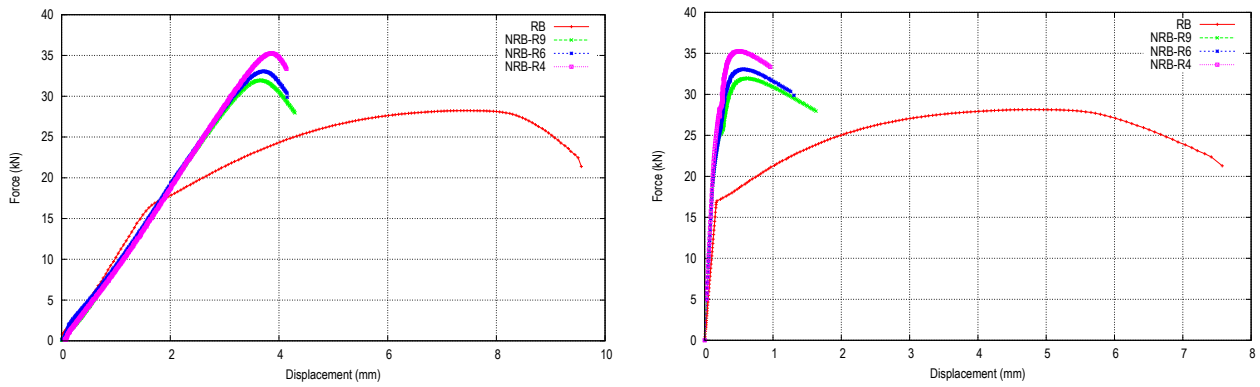

Fig. 2.12: *The force-displacement curves from tensile tests: (a) before the correction of machine stiffness, (b): after correction.*

The true stress-true strain curve up to necking can be determined as follows:

$$\overline{\sigma} = \frac{P}{\pi a^2} \tag{2.12}$$

$$\overline{\epsilon} = ln\left(\frac{l}{l_0}\right) \tag{2.13}$$

After necking occurs, these equations are no longer valid. Bridgman [Bridgman, 1952], developed a semi-empirical analysis to obtain the local stress and strain in the necked zone. This analysis assumes that the equivalent stress is uniform across the minimum cross section while the radial, hoop, and axial stresses vary as a function of radial position. The stress and strain are determined by the following equations (refer to Fig. 2.10c for notations)

$$\overline{\epsilon} = 2ln\left(\frac{a_0}{a}\right) \tag{2.14}$$

$$\sigma_{zz} = \overline{\sigma}\left[1 + ln\left(\frac{a^2 + 2aR - r^2}{2aR}\right)\right] \tag{2.15}$$

$$\sigma_{rr} = \sigma_{\theta\theta} = \overline{\sigma} ln\left(\frac{a^2 + 2aR - r^2}{2aR}\right) \tag{2.16}$$

$$\frac{\sigma_h}{\overline{\sigma}} = \frac{1}{3} + ln\left(\frac{a^2 + 2aR - r^2}{2aR}\right) \tag{2.17}$$

where a_0 is initial specimen radius. The displacement speeds are also corrected because the total displacement (crosshead displacement) is the sum of the real displacement of specimen and the "machine" displacement. The final applied speeds for the numerical simulations are also reported in Table 2.2 (numbers in parentheses).

2.2.2.5 Summary

The stress-strain curves for compression and tension tests can only be obtained approximately due to the inhomogeneity of deformation. For this reason, converted force-displacement curves are used instead of stress-strain curves to identify hardening law and damage model parameters.

2.2.3 Isotropic strain hardening law identification

In this section, the matrix material is considered to be isotropic and volumetrically conservative in plastic deformation[3]. The material therefore obeys the J_2 plasticity theory: there are no influence of hydrostatic pressure, nor of the third invariant of stress tensor (see Appendix A.3 for a detailed review of yield criteria). Generally, the load-displacement curve of compression test is preferred for identification of isotropic strain hardening law because of the following two reasons: first, the influence of damage process is less significant in upsetting test. Secondly, the fracture strain for this type of test is remarkably higher than that in the tensile test, which allows a more accurate curve fitting and the applicability of the hardening model for large strain[4].

2.2.3.1 Identification by inverse analysis.

Solving the problem of inverse analysis consists in minimizing a cost function representing the discrepancy between data from a numerical model $\underline{\boldsymbol{F}}$ and data obtained experimentally $\underline{\boldsymbol{F}}^e$ (e.g. the load-displacement curves of tensile tests described in Table 2.1). For an elasto-plastic model with damage, the mechanical behavior is fully described when all the elastic, plastic and damage parameters are known. In our study, the unknowns are the hardening law parameters and the damage model parameters. They define a set $\mathcal{P}$ which needs to be identified. The parameters identification problem is then expressed as an optimization problem: *Find the optimum set of parameters that minimizes the difference between experimental values and numerical values*. The normalized least squares error is chosen as the cost function (ϕ):

$$\begin{cases} \text{Find } \mathcal{P}* & \phi(\mathcal{P}*) = min\,(\phi(\mathcal{P})) \\ \text{With} & \phi(\mathcal{P}) = \frac{\|\underline{\boldsymbol{F}}^e - \underline{\boldsymbol{F}}(\mathcal{P})\|}{\|\underline{\boldsymbol{F}}^e\|} = \sqrt{\frac{\sum_{i=1}^{N}(F_i^e - F_i(\mathcal{P}))^2}{\sum_{i=1}^{N}(F_i^e)^2}} \end{cases} \tag{2.18}$$

The process is completed with the choice of optimization method. In Forge2009®, the Evolution Strategy (ES) algorithm has been adopted for the optimization procedure, which ensures that the global minimum can be obtained ([Schwefel, 1993], [Beyer, 2001]). In the present study, the identification procedure is divided into two steps: (1) isotropic hardening law identification, and (2) damage models identification using the identified hardening law.

2.2.3.2 Identification of friction coefficient in the compression test

During the compression test, the influence of friction on the load-displacement curves due to the loss of lubricant is remarkable. In order to obtain the correct parameters of hardening law, the average friction coefficients need to be identified first, which is based on the variation of specimen's geometry. The friction law involves two coefficients: the Coulomb's friction coefficient μ and the limiting friction parameter $\overline{m}$ (Eq. 6.2). They are supposed constant all along the numerical simulation:

$$\tau = min(\overline{m}\frac{\overline{\sigma}}{\sqrt{3}}, \mu\sigma_n) \tag{2.19}$$

where σ_n is the normal contact stress. Three geometry parameters are considered to identify these coefficients:

[3] There is a confidential study of ArcelorMittal on the anisotropy of this material (C62), which shows the validity of isotropy hypothesis.

[4] The fracture strains of tension and compression tests are obtained by measuring the diameter of tensile specimen and the height of compressed specimen at fracture, and using Eq. 2.11 and Eq. 2.13.

1. The approximate radius R_d of darker central region, which was the original end of specimen (see Fig. 2.13b); the higher friction is, the less this surface expansion;
2. the radius R_u of the upper surface (the original end and a part of cylindrical wall that folded up);
3. the maximum radius R_m of specimen (which corresponds to the maximum barreled region).

Exploiting the symmetry of the specimen geometry and loading conditions, only one-fourth of cylinder is modeled. In the numerical simulation, a marking grid was set up to obtain the variation of the specimen geometry (Fig. 2.13a). Fig. 2.13b shows the marking grid at the end of test. We can observe that a part of cylindrical wall folded up and created a rear zone on the two ends (upper and lower surfaces). This picture also shows the concentration of "material" in the cross and the rotation of the initial rectangular elements.

The friction coefficients ($\overline{m}$ and μ) are varied to obtain an equivalent geometry between the numerical simulation and experimental observation at the end of the test. With $\overline{m} = 0.31$ and $\mu = 0.2$, the observed dimensions (R_u,R_d,R_m) match the experimental results (see Fig. 2.13b).

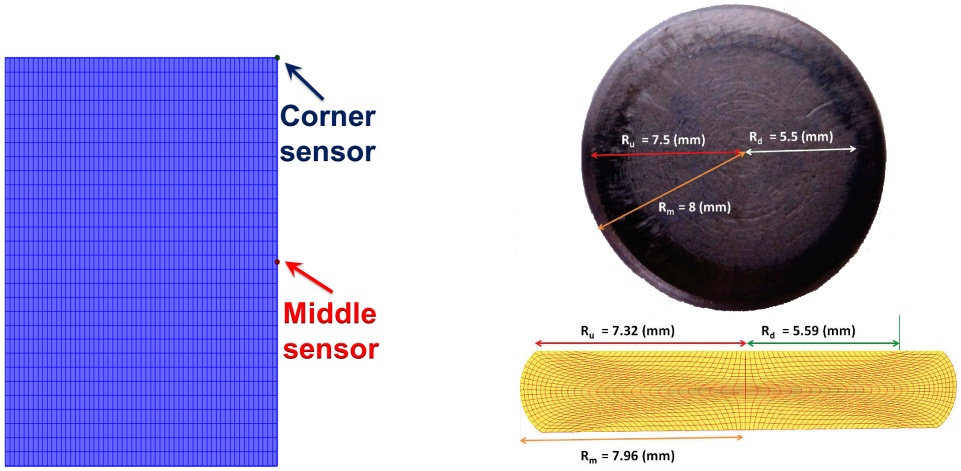

(a) (b)

Fig. 2.13: *(a) The marking grid attached to the cross section as well as two sensors to follow the geometrical variation; (b) the characteristic dimensions: central, lighter region (R_d), which was the original upper end of specimen; upper surface (R_u) and maximum barreling (R_m). The outside darker region ($R_d < R < R_u$) comes from the initial wall material folded up. The numerical model (below) with the marking grids (Lagrangian grids) shows dimensional agreement with the identified friction parameters: $\overline{m} = 0.31$ and $\mu = 0.2$.*

2.2.3.3 Mesh size sensitivity

The influence of mesh size on the numerical results has been studied. It is illustrated here by the comparison of 3 different meshes, which was carried out on the tensile test on NRB-R4 (Fig. 2.14a). Exploiting the symmetry of the specimen geometry and loading conditions, only one eighth of tensile specimens are modeled. The characteristics of meshes used as well as the simulations performed are reported in Table 2.3. Note that all the simulations are performed with the maximum time increment equal to 0.05s (a compromise between accuracy and CPU time).

As one can observe in Fig. 2.14b, the load-displacement curve is nearly insensitive when changing from coarse mesh to fine mesh, while CPU time sharply increases (Table 2.3). In addition, the predicted local strain at specimen center is noticeably influenced by the mesh size (Table 2.3), but the variation is still acceptable (4.77% when passing from coarse mesh to fine mesh). In the following, all the simulations of tensile tests are carried out using the local mesh size of 0.25 mm (mesh 1) for a compromise between CPU time and precision.

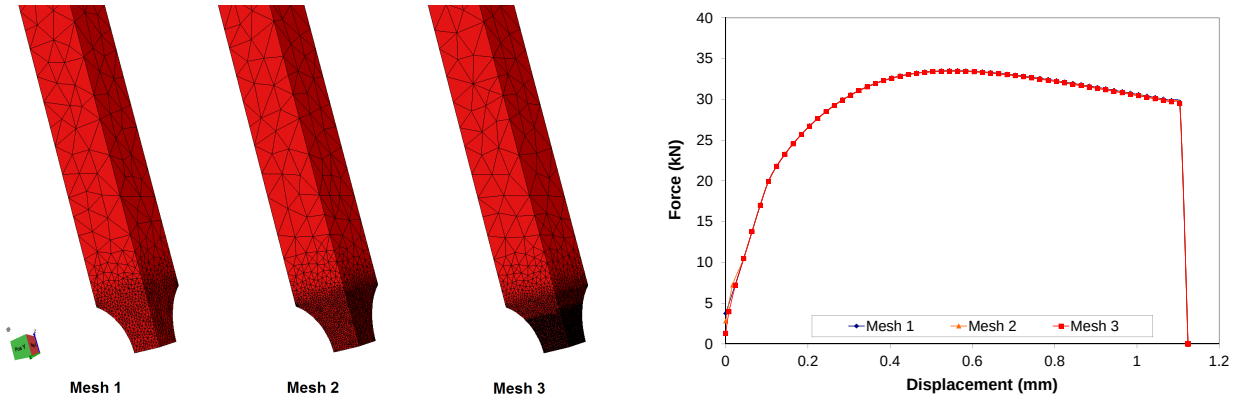

(a) *Meshes of notched round bar specimen (NRB-R4): coarse (mesh 1), medium (mesh 2) and fine (mesh 3).*

(b) *Global load-displacement curves obtained with three different mesh sizes.*

Fig. 2.14: *Comparison of load-displacement curves obtained with 3 types of meshes.*

Property	Mesh 1	Mesh 2	Mesh 3
Mesh size - gauge section (mm)	0.25	0.15	0.075
Number of elements	29250	69500	188000
CPU time - 4 processors (minute)	3	7	25.5
Necking radius (mm)	2.555	2.551	2.548
Strain at specimen center	0.351	0.362	0.369

Table 2.3: *Comparison between the simulations of the tensile test on NRB with different mesh sizes, using identified hardening law (see the following section - Table 2.4).*

2.2.3.4 Strain hardening law identification

The hardening law is then identified from both the whole compression load-displacement curve and the plastic part (before necking) of load-displacement curve with the tensile test on round bar. The studied hardening laws are Swift [Swift, 1952] (E.q. 2.20), Ludwik [Ludwik, 1996] (E.q. 2.21), and Voce [Voce, 1955] (E.q. 5.8), which were widely used for metals:

$$\sigma_0 = \sqrt{3}K(\epsilon_0 + \overline{\epsilon}^p)^n \tag{2.20}$$

$$\sigma_0 = \sqrt{3}K(1 + a\overline{\epsilon}^{pn}) \tag{2.21}$$

$$\sigma_0 = \sigma_{p0} + \left(\sigma_{ps} - \sigma_{p0}\right)\left(1 - exp(-n\overline{\epsilon}^p)\right) \tag{2.22}$$

where σ_0 is the flow stress; $\overline{\epsilon}^p$ is the equivalent plastic strain; K, a, n, ϵ_0 are material parameters; $\sigma_{p0} = \sigma_0(\overline{\epsilon}^p = 0)$; $\sigma_{ps} = \sigma_0\,(\overline{\epsilon}^p \to \infty)$. The unity of $K, \sigma_{p0}, \sigma_{ps}$ is the unity of stress (MPa), while other parameters are dimensionless quantities.

The results are represented in Fig. 2.15 with the identified parameters reported in Table 2.4. The results show that the Swift and the Ludwik laws cannot describe the hardening of the studied material for both compression and tensile tests, while with the Voce law, the flow stress saturates rapidly. The Voce law gives a very good result in compression test, but fails to describe the behavior in tensile test. This fact shows the importance of the number of objective functions: for an accurate result in complex loading cases, the parameters must be identified simultaneously from different loading paths. In order to better describe the hardening, we modified the Voce law to account for material hardening at large strain:

$$\sigma_0 = \sigma_{p0} + \left(\sigma_{ps} - \sigma_{p0} + K_2\overline{\epsilon}^p\right)\left(1 - exp(-n\overline{\epsilon}^p)\right) \tag{2.23}$$

where K_2 (MPa) is an additional parameter. The results with the modified Voce law are shown in the same figures (Fig. 2.15a and Fig. 2.15b - black curves). This modified formulation gives a better description

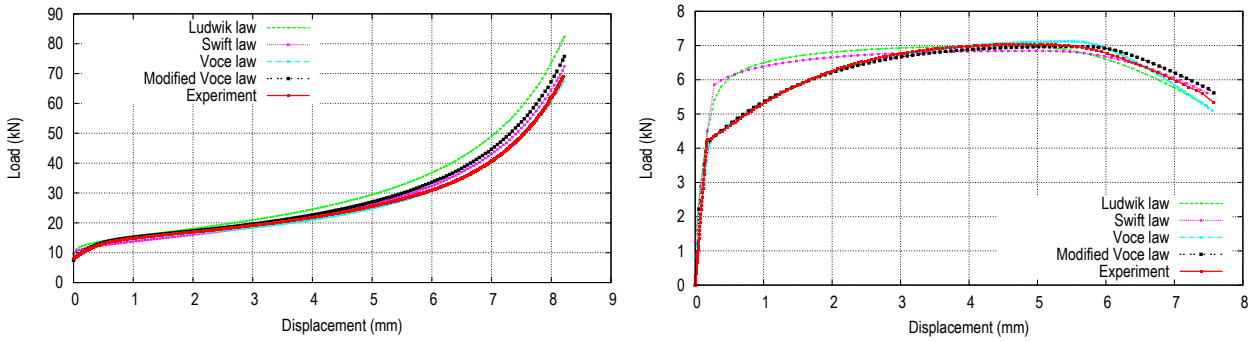

(a) *Compression curves .* **(b)** *Tensile curves.*

Fig. 2.15: *Load-displacement curves with different identified hardening laws for compression test (a) and tensile test on smooth round bar (b). Only 1/4 of specimens are modeled.*

of material hardening, in both tensile and compression tests. Moreover, the necking in tension is also well predicted with this modified law: softening due to necking was well described thanks to this hardening model used (Fig. 2.15b - black curve).

Ludwik			Swift			Voce			Modified Voce			
K	a	n	K	ϵ_0	n	σ_{p0}	σ_{ps}	n	σ_{p0}	σ_{ps}	n	K_2
96	7	0.087	675.377	0.004	0.069	601.146	1163.2	33	601.146	1113.2	37	100

Table 2.4: *Identified hardening parameters (refer to the text for parameters unit).*

Fig. 2.16a represents the comparison between the experimental and the numerical results in terms of geometrical variation prediction as well as local strain prediction[5]. For the geometrical variation prediction, the minimum radii in the cross section of tensile specimens as well as the radius of torsion specimen at the end of tests are compared. The results show that the simulations reproduce quite accurately the specimen dimensions at the end of tests. Moreover, the local strains at the minimum cross section for tensile tests and at the surface for torsion test (the maximum strains for each test) are also compared. For the torsion test, the difference is negligible. However, for the tensile tests, the difference between the "experimental" logarithmic plastic strains and the numerical local strains at the center of specimen minimum cross section is significant, especially for the RB and NRB-R9 ($> 10\%$). This difference may be explained by the heterogeneity of the numerical plastic strains over the minimum cross section (Fig. 2.16b), while for the analytical calculation of logarithmic plastic strain, the assumption of constant strain over cross-section is employed. As one can see in Fig. 2.16b, the strain distributions over cross-section in the case of tensile tests on NRB-R9 and RB are strongly heterogeneous, the errors are thus high. Another source of error may be due to the fact that the identified hardening law is not "perfect" enough to cover all the performed tests. However, the overall error of dimension is still acceptable.

2.3 Zirconium alloy - M5®

2.3.1 Material

Zirconium alloys have several attractive properties such as excellent corrosion resistance, low absorption cross-section for thermal neutrons, good mechanical properties at operating temperature of nuclear reactor. They have a distinctive position among all structural materials in nuclear applications ([Banerjee, 2001]).

[5]In the present study, the term **"experimental strain"** must be understood as the **logarithmic strain** calculated from the **experimental measurement** of specimen diameter. See the discussion in section 3.1.3

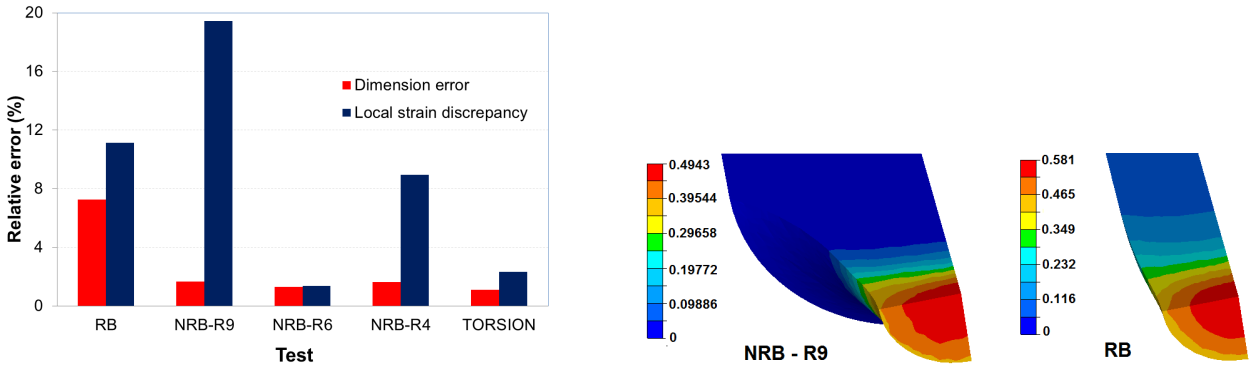

(a) *Relative errors in terms of the prediction of minimum radii of specimens and maximum local strains*

(b) *Numerical iso-value of equivalent plastic strains showing their heterogeneity over cross section.*

Fig. 2.16: *Comparison between numerical and experimental results with identified hardening law.*

In the same reference, the authors briefly discuss different aspects of zirconium alloys (physical metallurgy, chemical properties under operating conditions, etc.). For these excellent qualities, these alloys have been used for the fabrication of fuel cladding tubes. The last step of their forming is cold pilgering (see section 1.1.4 for the review of this process and Chapter 6 for its simulation). Due to their specific application, these tubes require a high level of quality and dimensional precision. Avoiding of defects and damage occurring during their forming is indeed vital.

Pure zirconium has a hexagonal close-packed crystallographic structure at a temperature lower than 865^oC ([Gaillac, 2007]). In the pressurized water reactor, there are different zirconium alloys which are used to produce fuel cladding tube and AREVA / CEZUS produces three main zirconium alloys for this purpose: Zircaloy 2, Zircaloy 4 and M5® [6] (see Table 2.5 for the chemical composition of these alloys)

	Fe	Cr	Sn	Nb	Ni	O
Zircaloy 2	0.2	0.1	1.3	-	0.05	0.13
Zircaloy 4	0.2	0.1	1.3	-	-	0.13
M5®	-	-	-	1	-	0.14

Table 2.5: *Composition of the principal zirconium alloys (% weight) [Gaillac, 2007].*

All specimens are prepared from the same batch of zirconium alloy (M5®) and from the same location and direction. It is a recrystallized bar, whose microstructure and grain size are comparable with the tube before rolling. Grains are equiaxial and the average size is about 8 μm ([Gaillac, 2007]). For more details concerning the chemical properties as well as crystallographic properties of this material, interested readers can refer to [Gaillac, 2007, Gaillac and Barberis, 2007].

2.3.2 Experimental setup

All the mechanical tests were conducted at Cezus Research Center, in Ugine, France. The configurations of all these tests were defined to have the same order of strain rate, about $0.1 - 0.15s^{-1}$ (obtained from the preliminary analytical as well as finite elements analyses) and at room temperature. Because of the limited diameter of the recrystallized bar, flat-grooved specimens could not be machined (see Fig. 2.1). Therefore, these specimens were not used for this material. The geometry and dimensions of specimens are presented in Fig. 2.17. All the tests performed are summarized in Table 2.6.

The objective of the experimental campaign is to perform mechanical tests which can "cover" the whole range of Lode parameter ($\bar{\theta}$ from -1 to 1) and a large range of stress triaxiality (η from -1/3 to 0.65) for damage study (see Fig. 2.17). The analytical formulations as well as the signification of these two parameters

[6] M5® is a trademark of AREVA NP registered in France, in the USA and in other countries.

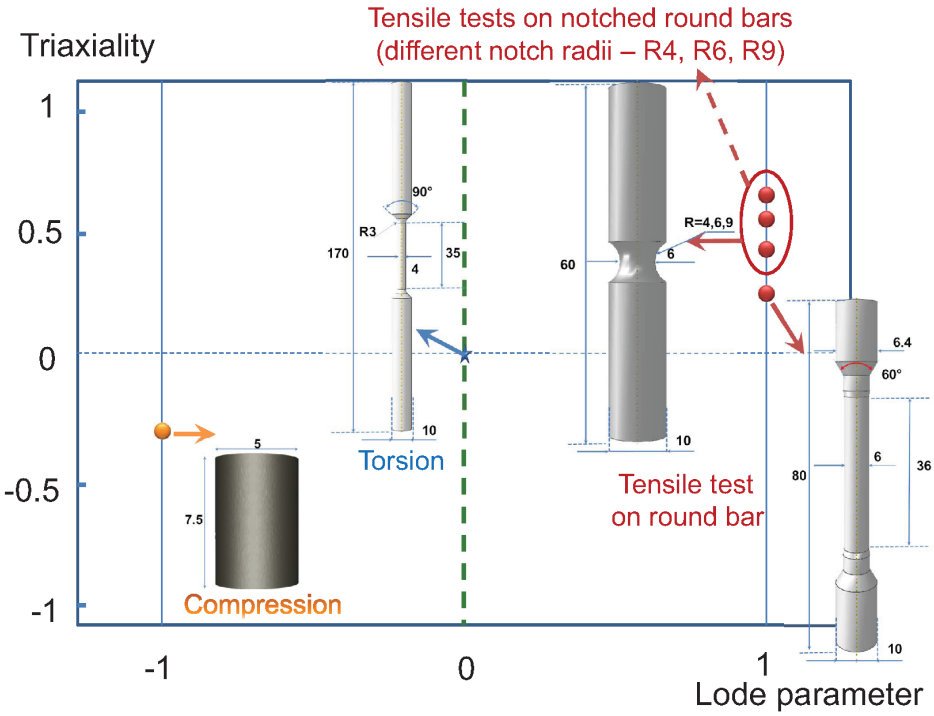

Fig. 2.17: *Representation of performed mechanical tests with axisymmetric specimens used in the space of initial stress triaxiality and Lode parameter. All dimensions are in mm. The loading paths are supposed to be proportional.*

are presented in 1.4.2.1. This range of stress triaxiality seems suitable since -1/3 is the cut-off value of the stress triaxiality, below which damage does not occur, as shown in [Bao and Wierzbicki, 2005]. Moreover, the final applications of the present study are the forming processes, in which the stress triaxiality is negative or slightly positive, well below 0.65.

Tests/Specimens	Velocity (mm/s)	$\overline{\theta}$	η	Fracture strain
Tension on RB	3.68	1	1/3	0.717
Tension on NRB, R=4mm	0.24	1	0.652	0.441
Tension on NRB, R=6mm	0.316	1	0.557	0.482
Tension on NRB, R=9mm	0.44	1	0.488	0.513
Torsion on RB	0.5 (rps)	0	0	0.594
Compression on cylinders	0.32	-1	-1/3	No crack

Table 2.6: *Experimental results in terms of the initial stress triaxiality and Lode parameter as well as the fracture strains for all mechanical tests. The velocities are calculated from the real displacements of specimens. For the compression test, no crack was observed at the end of test (final height = 1.63 mm).*

For the compression test, the cylinder was lubricated both on top and bottom faces before the test. Two specimens were used and the results in terms of load-displacement curves are superimposed. Variation in terms of maximum torque was observed in the three torsion tests performed ($\pm 5\%$). For experimental tensile tests on notched round bars, extensometers were set up to measure the displacement on 15 mm length of specimens (25 mm for tensile test on round bar), while the tensile forces were measured at the driven crosshead. For each test, three specimens were used and the results were quite reproducible ($< 1\%$ of maximum load variation, $< 3\%$ displacement to fracture).

2.3.3 Isotropic hardening law identification

The matrix material is considered to be isotropic and the plastic deformation is isochoric, obeying the J_2 plasticity theory: isotropic yield surface, associated flow rule and isotropic hardening law. Examples of fractured surfaces of tensile test on NRB-R4 and torsion test are presented in Fig. 2.18, which shows that the specimens kept their circular forms. It suggests that the behavior of this material is isotropic on the cross section.

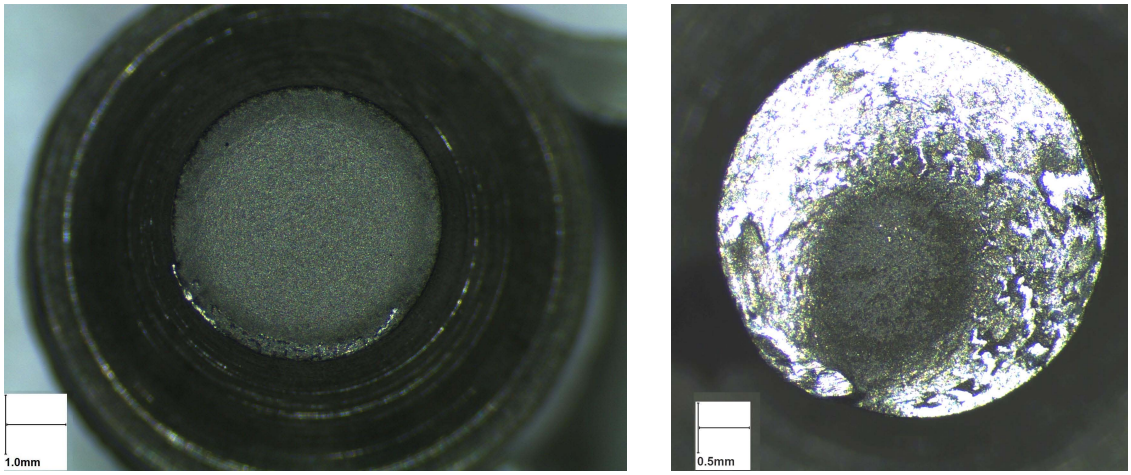

(a) (b)

Fig. 2.18: *Example of fractured surfaces of NRB-R4 tensile specimen (a) and torsion specimen (b), showing circular fractured surfaces.*

2.3.3.1 Friction identification for compression

The same method as in section 2.2.3.2 was employed to identify the friction coefficients of a non-linear friction law.

Based on the three characteristic dimensions (Fig. 2.19), the values of $\overline{m} = 0.85$ and $\mu = 0.5$ are identified. Note that the results of friction coefficients obtained by the present methods do not depend significantly on the hardening law used.

2.3.3.2 Strain hardening law identification

As in section 2.2.3.4, the hardening law is thus identified from both the whole compression load-displacement curve and the plastic part before necking of the load-displacement curve in the tensile test on round bar (to avoid post-necking instabilities). The studied strain hardening law is the Swift law [Swift, 1952] (Eq. 2.24):

$$\sigma_0 = \sqrt{3}K(\epsilon_0 + \overline{\epsilon}_p)^n \tag{2.24}$$

where σ_0 is the flow stress of material; $\overline{\epsilon}_p$ is the equivalent plastic strain; $K(MPa), n, \epsilon_0$ are material parameters. An automatic optimization process by inverse analysis was carried out to identify the 3 material parameters by minimizing the discrepancy between numerical load-displacement curves and the experimental ones ([Bouchard et al., 2011]).

2.3.3.3 Mesh size sensitivity

As in section 2.2.3.3, the influence of mesh size on numerical results was studied. The comparison of three different meshes were carried out on the tensile test on smooth round bar (Fig. 2.20a). The characteristics of meshes used as well as the simulations performed are reported in Table 2.7. Note that all the simulations were carried out with the upper limit of the time increment equal to $0.05s$.

As can be observed in Fig. 2.20b and Table 2.7, the coarse mesh (mesh 1) gives incorrect results for both global quantity (load) and local quantity (strain). Furthermore, the load-displacement curve is nearly

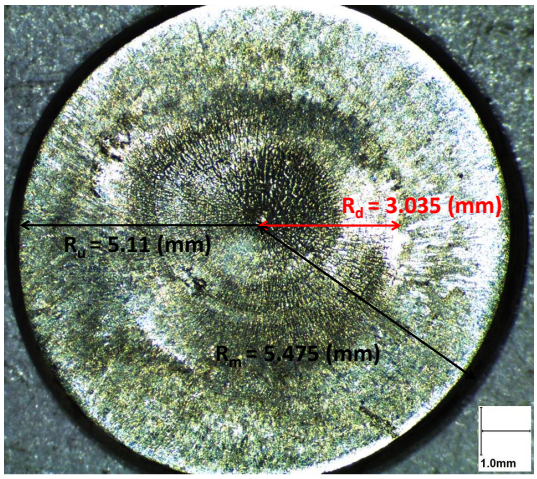

(a)

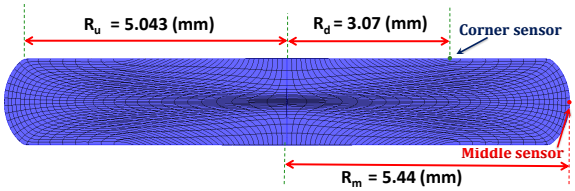

(b)

Fig. 2.19: *The characteristic dimensions (a): central, lighter region (R_d), which was the original upper end of specimen; upper surface (R_u) and maximum barreling (R_m). The numerical model (b), with the marking grids (Lagrangian grids) and sensors, shows dimensional agreement with the identified friction parameters: $\overline{m} = 0.85$ and $\mu = 0.5$.*

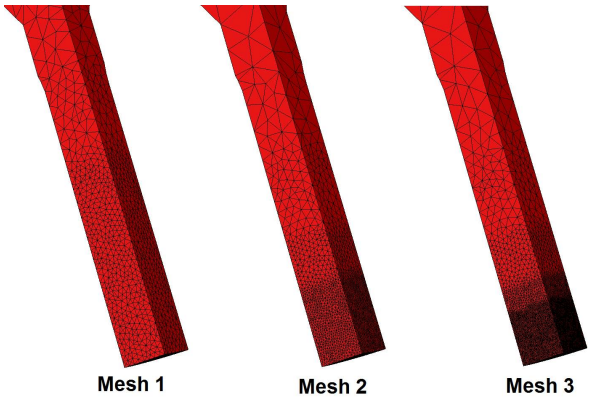

(a) *Meshes of round bar specimen: coarse (mesh 1), medium (mesh 2) and fine (mesh 3).*

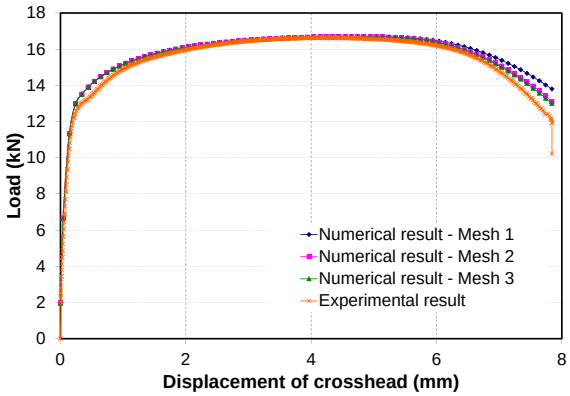

(b) *Global load-displacement curves obtained with three different mesh sizes.*

Fig. 2.20: *Comparison of load-displacement curves (b) obtained with 3 types of mesh (a). Note that in (b), the decrease of load is due to specimen necking, there is no damage introduced at this stage.*

insensitive when changing from medium mesh to fine mesh, while CPU time sharply increases (Table 2.7). In addition, the predicted local strain at specimen center is noticeably influenced by the mesh size (Table 2.7), but the variation is still acceptable (3.48%). In the following, all the simulations of tensile tests are carried out using the local mesh size of 0.12 mm (mesh 2) as a compromise between CPU time and precision.

2.3.3.4 Identification result

Fig. 2.21a and Fig. 2.21b show the comparison between the experimental and the numerical load-displacement curves for the compression and the tensile tests. The identified parameters are reported in Table

Property	Mesh 1	Mesh 2	Mesh 3
Mesh size (mm)	0.3	0.12	0.06
Number of elements	19600	69000	238600
CPU time (minute)	2	9	40
Necked radius (mm)	2.20	2.11	2.09
Strain at specimen center	0.660	0.767	0.795

Table 2.7: *Comparison of tensile tests on round bar with different mesh sizes using identified hardening law (see the following section). The values of dimension and the equivalent plastic strain are extracted at the end of simulation.*

2.8.

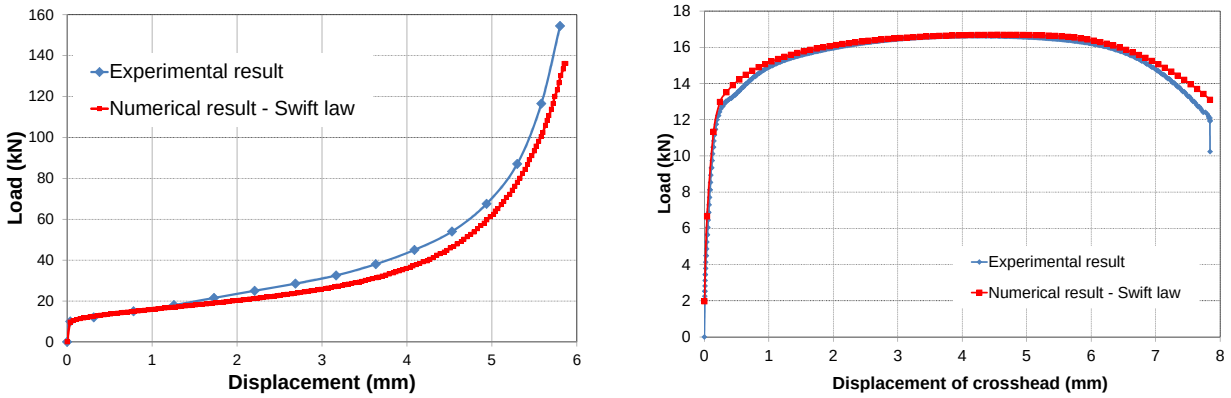

(a) *Compression test on cylinder.* **(b)** *Round bar tensile test.*

Fig. 2.21: *Comparison between experimental and numerical load-displacement curves for compression and tensile tests with Swift hardening law.*

Elasticity		**Plasticity-Swift**		
E (GPa)	ν	K (MPa)	n	ϵ_0
99.3	0.37	505.92	0.12	0.0038

Table 2.8: *Identified elasticity and plasticity parameters.*

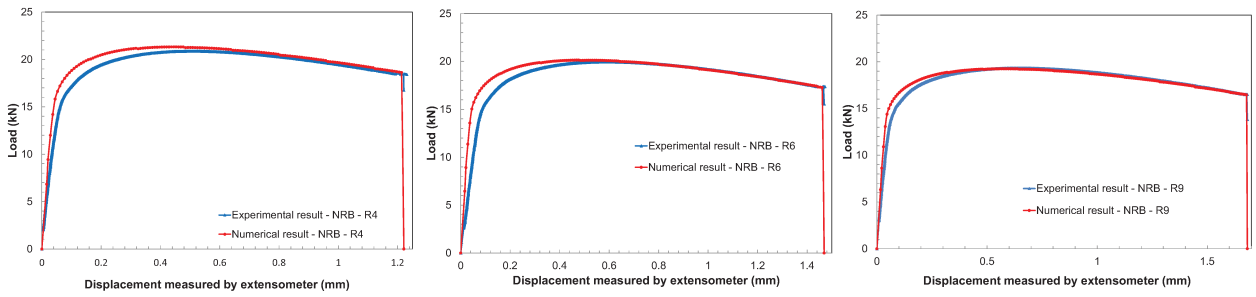

(a) *NRB-R4.* **(b)** *NRB-R6.* **(c)** *NRB-R9.*

Fig. 2.22: *Comparisons between the experimental and numerical load-displacement curves of tensile tests on notched round bars.*

Specimen	NRB-R4	NRB-R6	NRB-R9	RB
Numerical necking radius (mm)	2.389	2.331	2.302	2.111
Experimental necking radius (mm)	2.405	2.355	2.320	2.096
Numerical local fracture strain	0.442	0.515	0.558	0.768
Experimental local fracture strain	0.44	0.48	0.51	0.72
Error % (radius)	0.66	1.0	0.797	0.701
Strain discrepancy (%)	0.4	7.26	9.43	7.02

Table 2.9: *Comparison between the numerical and experimental necking radii and local fracture strains for different tensile tests. The numerical fracture strains were extracted from a numerical sensor located at the center axis of notch (onset of fracture). The "experimental" fracture strains were calculated from the necking section with an assumption of constant strain over cross section.*

2.3.3.5 Discussions

Since the identified parameters of Swift's law give relatively good results both in compression and tension test on round bar, they were chosen for the simulation of tensile tests on notched round bars with different notch radii. The comparative results are presented in Fig. 2.22, which also shows the validity of this identified Swift's law to describe the hardening of the studied material for different states of stress.

In Table 2.9, the comparisons between numerical and experimental necking radii and fracture strains are reported. In terms of geometry (necking radii), the errors between the simulation results and the experimental results are very small ($< 1\%$). Although the simulations can capture accurately the geometry variation of notched round bar specimens, the differences of local fracture strains are relatively high except for the tensile test on NRB-R4 (but still $< 10\%$). These differences are due to the assumption of constant strain over cross section when calculating the experimental logarithmic fracture strains based on the cross section of neck. Fig. 2.23a shows the strain map of half specimens at the end of simulations. As one can observe, for the NRB-R4 specimen, the equivalent plastic strain is nearly constant in the cross section; the error between numerical and "experimental" strains[7] is thus small. However, for other cases, the strain localization can be observed in the center of specimens. Fig. 2.23b shows the variation of the equivalent plastic strain as the function of relative position in the minimum cross section (a denotes radial position, i.e. $a = 0$ is the center and $a = R$ is the border). The variation in the case of RB, NRB-R6 and NRB-R9 is noticeable while for NRB-R4, the equivalent plastic strain varies slightly. Therefore, the local values of numerical simulations for the three former cases are different from the "experimental" average values across the cross section.

In addition, since the identification of hardening law was based on the pre-necking part of the load-displacement curve of tensile test on smooth round bar, the post-necking behavior was not well captured (Fig. 2.21b). Before necking, the bar is subjected to uniaxial tension, then the necking formation introduces triaxial loading. The identified hardening law overestimates the force level (the red curve in Fig. 2.21b). The difference between the experimental and numerical curves in Fig. 2.21b can be explained by the coupling between damage and necking: ductile damage (voids) increases rapidly after necking, which has not been taken into account in this section. Another explanation might be the questionable validity of the Swift law after necking, which needs a special treatment. In [Xue et al., 2010], the authors varied the hardening coefficient n to reproduce the experimental stress-strain curve in post-necking area. However, since these authors used only the tensile test on round bar for identification and validation, the influence of this modification on other strain levels (e.g. tensile tests on notched round bars) was not studied. In [Dunand and Mohr, 2010], an extrapolation technique was adopted to modify the Swift hardening law after necking occurs. In order to obtain a better extrapolation of the measured stress-strain curve, the authors defined two segments of constant slope H_1 and H_2; where H_1 corresponds to the range of intermediate plastic strains (from 0.2 to 0.35),

[7] In the present study, the term *"experimental strain"* must be understood as the *logarithmic strain* calculated from the *experimental measurement* of specimen diameter: $\overline{\epsilon} = 2ln(R_0/R_f)$, where R_0 and R_f are the initial and the fracture radii. For the torsion test $\overline{\epsilon} = \frac{2\pi R N_f}{\sqrt{3}L}$, where N_f is the number of rotations to fracture; L is specimen length.

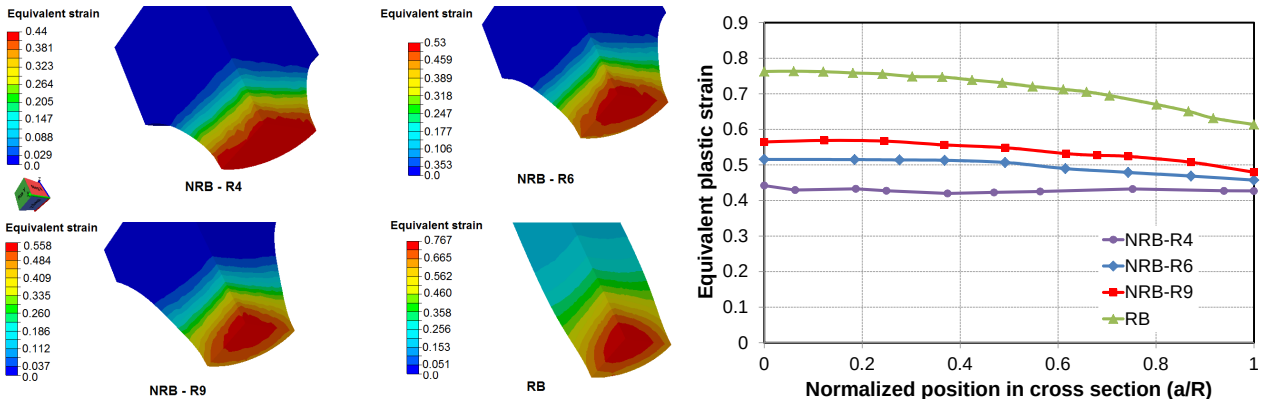

(a) (b)

Fig. 2.23: *(a) The strain map on the cross section of specimens at the end of different tensile tests. For the NRB-R4 specimen, the equivalent plastic strain is nearly constant in the cross section. However, for other cases, the strains are localized in the centers of specimens. (b) Variation of numerical equivalent plastic strain with relative position in the cross section.*

H_2 to the range of high plastic strains (higher than 0.35) (note that in [Dunand and Mohr, 2010], the strain level of 0.2 corresponds to the onset of necking). These two parameters H_1 and H_2 were then identified to reproduce the experimental load-displacement curves. In the present author's point of view, with this method, one could introduce not only two parameters H_1 and H_2, but also a set of parameter H_i (i.e. successively constant slopes), which would be calibrated with experimental results. The flow curve is thus reduced to point-to-point type (i.e. the table of one to one mapping of equivalent plastic strain and yield stress). Furthermore, since these approaches ([Xue et al., 2010, Dunand and Mohr, 2010]) neglect the influence of damage on material strength, their physical origins were not well established. A systematic methodology to obtain hardening law valid up to large strain was presented in [Tardif and Kyriakides, 2012], in which the authors used the force-elongation curves combined with an accurate measurement of the deformation in the necked region. In the present study, the hardening law is also identified from compression test, in which the nominal strain at the end of test reaches a high value ($\overline{\epsilon} \approx ln\left(\frac{H_0}{H_f}\right) = 1.53$). The hardening law is thus valid for a relative large range of strain.

In the present study, applying such modifications proposed by [Dunand and Mohr, 2010] or [Xue et al., 2010] may give better result in the tensile test on round bar, but at the same time modifies the results of the tensile test on notched round bars and the compression test: the load levels in these tests are underestimated. For this reason, the identified Swift law (Table 2.8), which gives relatively accurate results for different tests, is used hereafter to describe the hardening law of the studied material. The difference at the end of the two curves can be considered as the influence of damage at this strain level. Identification of this influence and accounting for it is the purpose of the next chapter (Chapter 3).

2.3.4 Remark on plasticity and hardening for the studied zirconium alloy

In this section, the hardening law was assumed isotropic and the J_2 plasticity theory was adopted. The identified strain hardening law gave relatively good results in terms of global behavior of material for different tests (load-displacement curves). However, for the material studied with hexagonal compact crystal structure, the texture has been demonstrated to have a strong influence on material mechanical properties ([Gaillac, 2007]). A more physical model, accounting for the evolution of microstructure and/or an anisotropic plasticity criterion, might be used in future studies.

2.4 Austenitic stainless steel

2.4.1 Material

All specimens are prepared from metal rods of austenitic stainless steel (on the basis of 304 steel grade) and from the same location and direction. The rod metal used is composed of austenitic matrix and sulfide inclusions [Vachey, 2011].

2.4.2 Experimental setup

The tests used and the configuration are the same as presented in section 2.3.2. For the compression test, the cylinder was lubricated on both top and bottom faces before the test. Two specimens were used and the load-displacement curves were superimposed. Variation of maximum torque as well as number of rotations to fracture was observed in the three torsion tests performed ($\pm 6\%$). For experimental tensile tests on notched round bars, extensometers were set up to measure the displacement on 15 mm length of specimens (25 mm for tensile test on round bar), while the tensile forces were measured at the driven crosshead. For each test, three specimens were used and the results were quite reproducible ($< 1\%$ of maximum load variation, $< 3\%$ of displacement to fracture).

2.4.3 Isotropic hardening law identification

The matrix material is considered to be isotropic and the plastic deformation is isochoric, obeying the J_2 plasticity theory: isotropic yield surface, associated flow rule and isotropic hardening law.

2.4.3.1 Friction identification for compression

The same method as in section 2.2.3.2 was employed in order to identify the friction coefficient. Based on the three characteristic dimensions (Fig. 2.24a), the values of $\overline{m} = 0.8$ and $\mu = 0.4$ are identified.

2.4.3.2 Strain hardening law identification

We followed the same procedure as in section 2.3.3. The studied strain hardening law are the Swift law [Swift, 1952] (Eq. 2.25) and the Hansel-Spittel law [Hansel and Spittel, 1979]:

$$\sigma_0 = \sqrt{3}K(\epsilon_0 + \overline{\epsilon}_p)^n \tag{2.25}$$

$$\sigma_0 = Aexp(m_1 T + m_4/\overline{\epsilon}_p + m_7\overline{\epsilon}_p)\dot{\overline{\epsilon}}_p^{m_3+m_8 T}\overline{\epsilon}_p^{m_2}(1+\overline{\epsilon}_p)^{m_5 T}T^{m9} \tag{2.26}$$

where σ_0 is the flow stress of material; $\overline{\epsilon}_p$ is the equivalent plastic strain; $A, K(MPa), n, \epsilon_0, m_i(i = 1,..,9)$ are material parameters. In the present study, the influences of the temperature and the strain-rate have not been considered, the hardening is assumed to be the consequence of plastic deformation (i.e. strain hardening). Therefore, all the terms concerning the temperature and strain-rate influence in Eq. 2.26 are set to zero. The Hansel-Spittel law is reduced to the Hollomon law (Eq. 1.95):

$$\sigma_0 = A\overline{\epsilon}_p^{m_2} \tag{2.27}$$

2.4.3.3 Mesh size sensitivity

As one can observe in Fig. 2.25b the result obtained with the coarse mesh is slightly different from the other two results and the load-displacement curve is nearly insensitive when changing from medium mesh to fine mesh, while CPU time sharply increases (Table 2.10). In addition, the predicted local strain at specimen center is noticeably influenced by the mesh size (Table 2.10), but the variation is still acceptable (4.23%) when changing from medium mesh to fine mesh. In the following, all the simulations of tensile tests are carried out using the local mesh size of 0.3 mm (mesh 2) as a compromise between CPU time and precision.

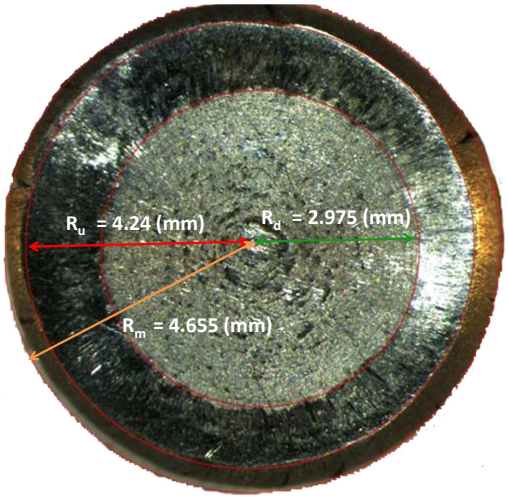

(a)

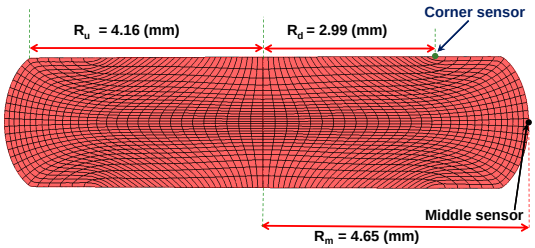

(b)

Fig. 2.24: *The characteristic dimensions (a): central, lighter region (R_d), which was the original upper end of specimen; upper surface (R_u) and maximum barreling (R_m). The numerical model (c), with the marking grids (Lagrangian grids) and sensors, shows dimensional agreement with the identified friction parameters: $\overline{m} = 0.8$ and $\mu = 0.4$.*

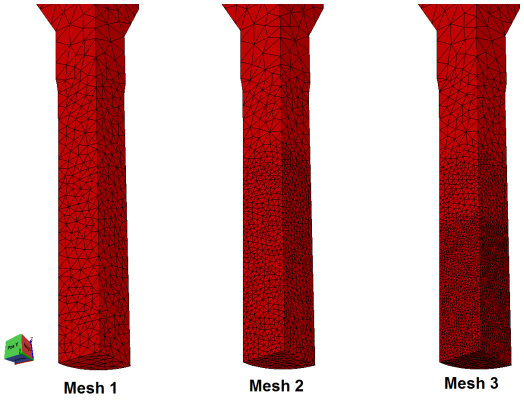

(a) *Meshes of round bar specimen: coarse (mesh 1), medium (mesh 2) and fine (mesh 3).*

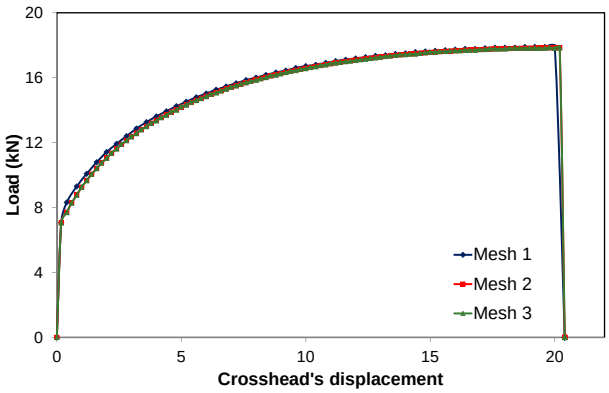

(b) *Global load-displacement curves obtained with three different mesh sizes.*

Fig. 2.25: *Comparison of load-displacement curves (b) obtained with 3 types of meshes (a).*

2.4.3.4 Identification result

Figs. 2.26a, Fig. 2.26b and 2.27 show the comparison between the experimental and the numerical load-displacement curves for the compression test, the tensile tests on RB and NRB. The identified parameters are reported in Table 2.11.

Property	Mesh 1	Mesh 2	Mesh 3
Mesh size (mm)	0.5	0.3	0.15
Number of elements	8650	19680	72300
CPU time (minute - 4 CPUs)	1	3.5	13
Local strain (center)	0.421	0.430	0.449

Table 2.10: *Comparison of tensile tests on round bar with different mesh sizes using identified Hansel-Spittel hardening law (see the following section).*

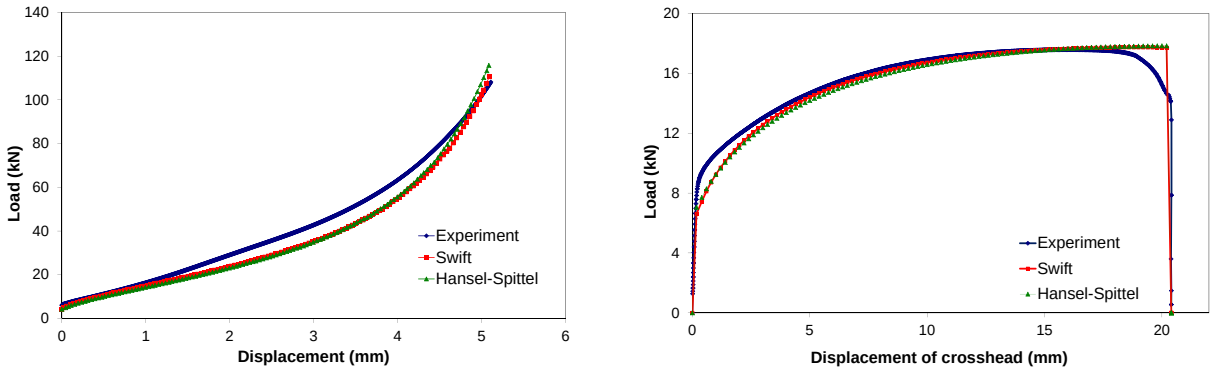

(a) *Compression test on cylinder.* **(b)** *Round bar tensile test.*

Fig. 2.26: *Comparison between experimental and numerical load-displacement curves for compression and tensile tests with identified Swift and Hansel-Spittel hardening laws.*

Elasticity		**Swift**			**Hansel-Spittel (Hollomon)**	
E (GPa)	ν	K (MPa)	n	ϵ_0	A (MPa)	m_2
193	0.3	803.28	0.398	0.004	1401.7	0.423

Table 2.11: *Identified elasticity and plasticity parameters for the stainless steel.*

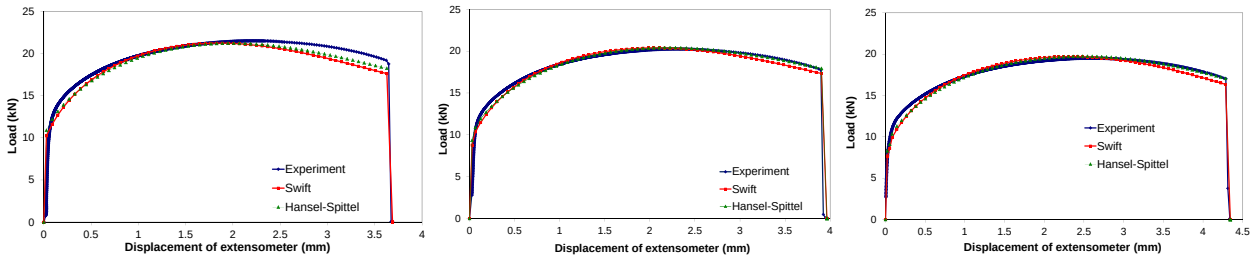

(a) *NRB-R4.* **(b)** *NRB-R6.* **(c)** *NRB-R9.*

Fig. 2.27: *Comparisons between the experimental and numerical load-displacement curves of tensile tests on notched round bars. The drop at the end of these curves correspond to the instant of fracture.*

2.4.3.5 Discussion

Between the two studied hardening laws, the Hansel-Spittel law gives slightly better results in terms of the predictions of macroscopic observations (load-displacement curves). With the identified hardening laws, the results of tensile tests are well reproduced except the tensile test on round bar, in which the necking of the specimen is not predicted. Moreover, we can observe that, at the beginning of plastification (beginning of all curves), the identified hardening laws underestimate the hardening of the material. At relatively small strains, (i.e. before necking in tensile tests, compression with displacement $< 1.3\ mm$), these laws describe

quite accurately hardening (the important difference observed in the case of NRB-R4 is mainly due to fast necking development in numerical simulations). For higher strains (e.g. compression test with displacement $> 1.3\ mm$), the identified laws *underestimate the hardening in compression test* and *overestimate the hardening in tensile test on RB*. These opposite tendencies reveal that the identified hardening laws are not *rich* enough to account for all the mechanisms leading to the hardening (or softening) of the studied material.

In the present study, different dynamic compression tests at different strain rates were also performed. The results obtained showed the possible influence of strain rate (and also temperature, due to the increase of temperature when the velocity increases) on the hardening of the studied stainless steel grade. Nevertheless, all the tests used for the identification process in the above section were carried out at the same strain rate and at room temperature. Therefore, the difference between the hardening in compression test and tensile tests, in this case, depends neither on the strain-rate nor on the temperature. We believe that accounting for other mechanisms (e.g. austenite-martensite transformation, as reviewed in section 2.4.3.6) can help better describing the behavior of this material under different stress states. However, such a mechanism (e.g. austenite-martensite transformation) needs experimental evidence, which unfortunately could not be performed in the present study. Nevertheless, in terms of overall results of different tests, the identified hardening laws gave relatively good predictions for different stress-states.

2.4.3.6 Toward a more physically sound hardening model

It has been shown in the literature, for unstable austenitic stainless steels, that austenite-martensite transformation plays an important role in hardening ([Krauer and Hora, 2012], [Beese and Mohr, 2012]). One of the first works on modeling of phase transformation kinetic was carried out by [Olson and Cohen, 1975], who proposed a model to the martensite formation as a function of plastic strain and temperature. Stringfellow and co-workers [Stringfellow et al., 1992] assumed that this transformation could depend also on the rate of the stress triaxiality :

$$\dot{c} = (1 - c)(A\dot{\gamma}_a + B\dot{\eta}) \tag{2.28}$$

where c is the rate of martensite formation; $\dot{\gamma}_a$ is the plastic shear strain rate in the austenite; A and B are functions of stress state and temperature. Under isothermal condition, this model represents a monotonic relationship between the rate of martensite formation and the stress triaxiality rate. This result was confirmed by the experimental work of [DeMania, 1995]. However, [Beese and Mohr, 2011], who worked on 301LN steel grade, showed that for this material, the rate of transformation is not a monotonic function of the stress triaxiality and one needs to account for the Lode parameter as well. Starting from the model of [Santacreu et al., 2006], Beese and Mohr proposed the following set of equations to describe the transformation kinetics:

$$\dot{c} = (c_{max} - c)nD^n\bar{\epsilon}^{n-1}\dot{\bar{\epsilon}}_p \tag{2.29}$$

where: $D = D(\eta, \bar{\theta}) = max(0, D_0 + a_\theta\bar{\theta} + a_\eta\eta)$. The contribution of phase change kinetics to the hardening of the material is taken as:

$$\sigma_0 = \sigma_0(\bar{\epsilon}_p) + H_c c(\eta, \bar{\theta}, \bar{\epsilon}_p) \tag{2.30}$$

where $\sigma_0(\bar{\epsilon}_p)$ is the strain hardening term which can be defined by some classical strain hardening laws (e.g. Swift or Ludwik); $c(\eta, \bar{\theta}, \bar{\epsilon}_p)$ is the percentage of martensite formation, whose evolution is given in Eq. 2.29; H_c a material parameter, which is assumed constant. In the present study, the difference between the hardening under different stress states could be described by the Beese and Mohr approach, which differentiates the hardening under different stress states via the contribution of phase transformation kinetic. This model was implemented in the FE software Forge2009® by the present author and can be used in future studies once we can perform the measurement of the martensite transformation under different stress states.

2.5 Summary of Chapter 2

This chapter presents the mechanical tests and the identification of isotropic strain hardening models for three materials: high carbon steel, zirconium alloy and stainless steel. The objective of the experimental

campaign is to identify both hardening laws and damage models. These mechanical tests cover different stress states (characterized by the stress triaxiality and the Lode parameter), which allows better calibrating damage parameters for complex loadings. Moreover, velocities for all the mechanical tests were chosen to give similar strain rates. Methods for exploiting the experimental results were detailed for the case of high carbon steel.

Concerning the identification of hardening parameters, load-displacement curves of compression test and tensile test on RB (before necking) are chosen. For the former test, method for non-linear friction law parameters identification was also presented to minimize the influence of friction on load-displacement curve. An automatic optimization process by inverse analysis was carried out with the FE software Forge2009®, which aimed at minimizing the discrepancy between the load-displacement curves obtained with numerical simulations and the experimental ones.

In the first section, for high carbon steel, after testing several isotropic hardening models, the Voce model was selected and modified to better describe the hardening of this material. The identification procedure has been detailed. The same methods were applied for the other two materials in the following sections. The mesh size was chosen for a compromise between the CPU time and the precision of simulations. Moreover, although the identification was based on the load-displacement curves, local strains and minimum diameters of specimens were also compared between numerical and experimental results.

In the second and third sections, the same procedure as in section 1 was used for a zirconium alloy (M5) and a stainless steel. For the first material, since its application is for the cold pilgering process, where a material point is subjected to successive tensile and compressive forces, the torsion test was not used for the identification of hardening. Identification results with the Swift hardening law were in good agreement with experimental tests, for both macroscopic observations (load-displacement curves) and local plastic strains. For the stainless steel, the Swift and the Hansel-Spittel laws were used. Moreover, since the influence of strain rate and temperature was neglected, the Hansel-Spittel law was simplified into the Hollomon equation (Eq. 1.95). The Hollomon law gave better results than the Swift law, but the necking in tensile test on RB was not captured. An explanation was that the influence of damage was not accounted for. A more physically sound model, which accounts for the microstructure change (austenite - martensite transformation) may help better describing the hardening of this material for different loading conditions. Nevertheless, the overall error for all tests is acceptable with the simple Hollomon law.

2.6 Résumé en français

Ce chapitre présente des essais mécaniques et l'identification des modèles d'écrouissage isotrope pour les trois matériaux : acier haut carbone, alliage de zirconium et acier inoxydable. L'objectif de la campagne expérimentale est d'identifier à la fois des paramètres des lois d'écrouissage et d'endommagement. Ces essais mécaniques couvrent différents états de contrainte (caractérisés par la triaxialité des contraintes et le paramètre de Lode), ce qui permet de mieux calibrer les paramètres d'endommagement pour les applications aux chargements complexes. En outre, la vitesse de ces essais a été sélectionnée pour aboutir à des vitesses de déformation comparables. La méthode d'exploitation des résultats expérimentaux a été détaillée pour l'acier haut carbone.

Pour l'identification des paramètres d'écrouissage, les courbes force-déplacement des essais de compression et de traction sur éprouvette lisse (la partie avant la striction, où la déformation est homogène) ont été choisies. Pour le premier test, une méthode permettant de quantifier l'influence du frottement en compression a été introduite. Puis, une identification basée sur l'optimisation automatique par analyse inverse a été réalisée avec Forge2009®. Cette identification s'appuie sur la minimisation de l'écart entre la courbe force-déplacement expérimentale et celle de la simulation.

Dans la première section, pour l'acier haut carbone, après avoir testé plusieurs modèles d'écrouissage isotrope, le modèle de Voce a été sélectionné et modifié pour mieux décrire l'écrouissage de ce matériau. La procédure d'identification a été détaillée. La même méthode a été appliquée pour les deux autres matériaux

dans les sections suivantes. Le maillage a été choisi de manière à assurer un bon compromis entre le temps de calcul et la précision des simulations. En outre, bien que l'identification fût basée sur les courbes force-déplacement, les déformations locales et les diamètres minimaux des éprouvettes ont aussi été comparés entre les résultats numériques et expérimentaux.

Dans les deuxième et troisième sections, la même procédure que dans la section 1 a été utilisée pour un alliage de zirconium (M5) et un acier inoxydable. Le premier matériau est mis en forme par laminage à pas de pèlerin, où un élément de matière est soumis à des chargements de "traction" et "compression" successifs. L'essai de torsion n'a donc pas été utilisé pour l'identification de la loi d'écrouissage. Les résultats de l'identification avec la loi de Swift sont en bon accord avec les essais expérimentaux, à la fois pour les observations macroscopiques (courbes effort-déplacement) et les déformations locales. Pour l'acier inoxydable, les lois de Swift et de Hansel-Spittel ont été utilisées. En outre, puisque nous avons négligé l'influence de la vitesse de déformation et de la température, la loi Hansel-Spittel a été simplifiée à la loi de Hollomon (Eq. 1.95). La loi d'Hollomon a donné un meilleur résultat que la loi de Swift, mais la striction en essai de traction sur l'éprouvette lisse n'a pas été bien capturée. La raison peut provenir du fait que l'influence de l'endommagement n'a pas été prise en compte. L'utilisation d'un modèle plus physique, qui pourrait expliquer le changement de microstructure (transformation austénite - martensite) aiderait à mieux décrire le durcissement/adoucissement de ce matériau pour différentes conditions de chargement. En tous cas, l'erreur globale pour tous les tests est acceptable avec la loi simple de Hollomon.

Chapter 3

Phenomenological damage models implementation and identification

Contents

Introduction

Following the identification of hardening parameters for the 3 studied materials presented in the previous chapter, the present one aims at identifying the parameters of phenomenological ductile damage models. An overview of several existing and implemented models is given in Table 3.1 (in this table, the • symbol indicates the full dependence).

Models	Pressure	Lode angle	Coupling
Gurson [Gurson, 1977], GTN [Tvergaard and Needleman, 1984] (*)	•		•
Wilkins[Wilkins et al., 1980]	•	•	
Lemaitre [Lemaitre, 1986] (*)	•		•
Xue [Xue, 2007a] (*)	•	•	•
Modified GTN [Nahshon and Hutchinson, 2008](*)	•	•	•
Modified GTN [Xue, 2008] (*)	•	•	•
Bai and Wierzbicki (B&W)[Bai and Wierzbicki, 2008] (*)	•	•	
Modified Mohr-Coulomb (MMC)[Bai and Wierzbicki, 2010] (*)	•	•	
Enhanced Lemaitre (present study) (*)	•	•	•

Table 3.1: *Comparison of several existing damage models. Models with asterisk symbol (*) have been implemented and used in the present study.*

In the first section, a review of several phenomenological damage models used (Lemaitre, modified Xue, B&W, MMC) is given. Except the Lemaitre model, which was introduced into Forge2009® by [Bouchard et al., 2011], the other phenomenological damage models used have been implemented by the present author. In the following sections, the models identification for high carbon steel (Lemaitre, modified Xue and B&W), zirconium alloy (B&W, MMC, Lemaitre and enhanced Lemaitre), stainless steel (B&W, Lemaitre) are presented. Discussions on the results are also given, followed by the summary of the chapter.

3.1 Phenomenological damage models reviews

3.1.1 Coupled damage models

3.1.1.1 The Lemaitre damage model

The Lemaitre model is derived from the thermodynamics framework of continuum damage mechanics (CDM), which consists in 3 steps: (1) state variables definition (e.g. damage variable), which defines the present state of corresponding physical mechanism (i.e. damage); (2) state potential definition, from which one can derive the state laws, and definition of associated variables (i.e. the variables which are associated with the internal state variables); (3) dissipation potential definition: to derive the evolution law of state variables, which are associated with the dissipative mechanisms. Detailed review of the CDM approach is given in Appendix A.4. The scalar D ($0 \leq D \leq 1$), which is an internal variable, is adopted to describe the *isotropic damage* (D represents the ratio of damaged area S_D to the total surface S: $D = S_D/S$). The energy density release rate (Y), the variable associated with D, is derived from the state potential (see [Lemaitre and Desmorat, 2005] for more details):

$$Y = \frac{\overline{\sigma}^2}{2E(1-D)^2}\left[\frac{2}{3}(1+\nu) + 3(1-2\nu)\left(\frac{-p}{\overline{\sigma}}\right)^2\right] \tag{3.1}$$

where $\overline{\sigma}$ is the von Mises equivalent stress; E is the Young modulus; ν is the Poisson ratio; p is the hydrostatic pressure. Lemaitre ([Lemaitre, 1986]) defined the dissipation potential, which is a convex function of associated variables, as:

$$F = f + F_X + F_D \tag{3.2}$$

with f, F_X, F_D being respectively the plastic potential (also the yield function in associative flow), the nonlinear kinematic hardening dissipative potential (which is not considered in the present study), and the damage dissipative potential. The latter is defined as:

$$F_D = \frac{S}{(s+1)(1-D)}\left(\frac{Y}{S}\right)^{s+1} \tag{3.3}$$

S (MPa) and s are two material parameters (which might depend on temperature). Finally, the damage evolution is given by:

$$\dot{D} = \dot{\lambda}\frac{\partial F_D}{\partial Y} = \frac{\dot{\lambda}}{1-D}\left(\frac{Y}{S}\right)^{s} = \dot{\bar{\epsilon}}_p\left(\frac{Y}{S}\right)^{s} \tag{3.4}$$

where $\dot{\lambda}$ is the plastic multiplier, which can be deduced from the equivalent plastic strain rate as: $\dot{\lambda} = \dot{\bar{\epsilon}}_p(1-D)$, with $\dot{\bar{\epsilon}}_p = \sqrt{\frac{2}{3}\dot{\boldsymbol{\epsilon}}^p : \dot{\boldsymbol{\epsilon}}^p}$ ($\dot{\boldsymbol{\epsilon}}^p$ denotes plastic strain rate tensor). Lemaitre proved that there may exist a limit of equivalent strain ϵ_D below which the damage accumulation does not occur. Moreover, based on the observations of the experimental results of Bridgman ([Bridgman, 1952]), Bao ([Bao and Wierzbicki, 2005]) showed that there exists a limit of the stress triaxiality ($\frac{-p}{\bar{\sigma}}$) below which there is no damage growth. This observation was applied to the Lemaitre model by Bouchard and co-workers ([Bouchard et al., 2011]). The damage evolution is therefore modified as:

$$\dot{D} = \begin{cases} \dot{\bar{\epsilon}}_p\left(\frac{Y}{S}\right)^{s} & \text{, if } \bar{\epsilon}_p > \epsilon_D \quad \text{and} \quad \frac{-p}{\bar{\sigma}} > -\frac{1}{3} \\ 0 & \text{, otherwise} \end{cases} \tag{3.5}$$

In order to account for the softening by damage accumulation, the weakening function $w(D)$ has been adopted:

$$\begin{cases} \bar{\sigma} = w(D)\sigma_M \\ E = w(D)E_M \end{cases} \quad \text{with} \quad w(D) = \begin{cases} 1-D & \text{, if } \eta \geq 0 \\ 1-hD & \text{, if } \eta < 0 \end{cases} \tag{3.6}$$

where σ_M and E_M are the flow stress and Young's modulus of undamaged material; h is a material parameter ($0 < h < 1$), which accounts for the "micro-crack closure effect", i.e. the distinction between "compressive" and "tensile" damages ([Lemaitre and Desmorat, 2005]). By measuring the variation of Young's modulus in compression and tension, Lemaitre proposed $h = 0.2$, assumed valid for most materials.

3.1.1.2 Xue's damage model.

Xue [Xue, 2007] proposed a phenomenological damage model, which is based on the definition of the equivalent fracture strain ϵ_f as a function of hydrostatic pressure (p) and Lode angle (θ_L):

$$\epsilon_f = \epsilon_{f0}\mu_p(p)\mu_\theta(\theta_L). \tag{3.7}$$

where ϵ_{f0} is the reference fracture strain, which is determined from tension test at constant zero confinement pressure; $\mu_p(p)$ and $\mu_\theta(\theta_L)$ are the pressure-dependent function and the Lode angle-dependent function respectively. Eq. 3.7 defines a fracture envelope in three dimensional space of pressure, Lode angle and equivalent strain. Since p and θ_L are orthogonal to each other, they can have separate forms:

$$\mu_p = 1 - q\,ln(1 - \frac{p}{p_L}) \quad , \quad \mu_\theta = \gamma + (1-\gamma)\left[\frac{6\,|\theta_L|}{\pi}\right]^k \tag{3.8}$$

where p is the hydrostatic pressure, p_L is the limit pressure (above which damage does not occur), θ_L is the Lode angle, γ is the ratio between fracture strain under shear loading and fracture strain under uniaxial tension with the same imposed pressure; $k, q > 0$ are material parameters. The Lode angle ([Lode, 1925]) is defined as:

$$\theta_L = tan^{-1}\left(\frac{1}{\sqrt{3}}\frac{2\sigma_2 - \sigma_1 - \sigma_3}{\sigma_1 - \sigma_3}\right) \tag{3.9}$$

where $\sigma_1 \geq \sigma_2 \geq \sigma_3$ are the three principal stresses and $-\pi/6 \leq \theta_L \leq \pi/6$. This parameter can be normalized to obtain the so-called Lode parameter $\bar{\theta}$ ($-1 \leq \bar{\theta} \leq 1$), which is defined by:

$$\bar{\theta} = 1 - \frac{6\theta}{\pi} = -\frac{6}{\pi}\theta_L \quad \text{with} \quad \theta = \theta_L + \pi/6 \tag{3.10}$$

From the expression of μ_p, there exists a cut-off value of pressure where μ_p reduces to zero (so does ϵ_f, which means the material fails immediately):

$$p_{cutoff} = p_L(1 - e^{1/q}) < 0. \tag{3.11}$$

Note that the choice of Lode angle-dependent function as in Eq. 3.8 depending on the absolute value of θ_L, induces a symmetric fracture locus with respect to $\theta_L = 0$. The scalar damage variable D_X was used as an internal variable to represent the material degradation. The weakening function $w(D_X) = 1 - D_X^\beta$ is adopted to describe the damage effect on the macroscopic strength:

$$\dot{D}_X = m \left(\frac{\overline{\epsilon}_p}{\epsilon_f(p,\theta_L)} \right)^{m-1} \frac{\dot{\overline{\epsilon}}_p}{\epsilon_f(p,\theta_L)} \quad \text{and} \quad \overline{\sigma} = \left(1 - D_X^\beta\right) \sigma_M \tag{3.12}$$

where β is the weakening exponent, $\overline{\epsilon}_p$ is the equivalent plastic strain, $\epsilon_f(p,\theta_L)$ is the fracture strain, which depends on the current stress state (p,θ_L), σ_M is the flow stress of undamaged material.

Enhanced Xue model Based on the studies of Lemaitre [Lemaitre and Desmorat, 2005], the damage accumulation process is activated above certain "threshold" defined by a physical parameter (plastic strain or stored energy). For this reason, this observation was adopted for the Xue model by the present author by introducing the strain threshold ϵ_{DX}, from which damage begins to occur[1]. At the other end of the damage evolution, when $D_X = D_c$, a mesocrack is initiated. The damage critical value D_c is another material parameter which needs to be identified. In addition, the coupling between damage and elasticity, which does not exist in the original Xue model, is also introduced: $E = \left(1 - D_X^\beta\right) E_M$, where E_M is the Young's modulus of undamaged material[2].

3.1.1.3 Numerical implementation.

The Lemaitre model was implemented by Bouchard and coworkers [Bouchard et al., 2011]. In the present study, we introduced the Xue model in Forge2009® through a user subroutine, with a "weak coupling" of damage and material behavior: the damage variable at time step *n-1* is used to solve the mechanical equations at time step n. Concerning the identification procedure, the scalar version of the Lemaitre model has 4 parameters: S, s, ϵ_D and D_c. There are 8 parameters to be identified for the original Xue model: $\epsilon_{f0}, p_L, q, k, m, \beta, \gamma, D_c$ and the strain threshold ϵ_{DX} for the modified model (note that the two parameters m and k are often chosen fixed as proposed by Xue: $m = 2, k = 1$).

In order to validate the numerical implementation, the simulations of a compression test on a cylinder billet and a tension test on a smooth round bar were carried out, based on the experimental results of [Xue, 2007] and [Bai, 2008] on aluminum 2024-T351 ([Cao, 2011]). Only the result concerning the crack prediction for the compression test is presented.

As stated by several authors in the literature, the plastic flow in an axially compressed cylinder is not uniform due to the presence of friction between the flat specimen ends and the loading fixture. Fig. 3.1a represents the numerical result with Forge®2009. The crack observed on the surface of the compressed cylinder is in good agreement with the experimental results by [Bai, 2008] as shown in Fig. 3.1b[3]. A polished and etched cross section of the compressed cylinder shows the shear bands in the diagonal planes (Fig. 3.1c and Fig. 2.8)[4]. Note that these results were obtained with "local damage model", which were sensitive to mesh size.

[1] It will be shown in Fig. 5.9a of Chapter 5, that damage (voids) of the studied high carbon steel (on which the Xue model will be used), is only noticeable above a certain value of the equivalent plastic strain. The presence of such a threshold is thus legitimate for the coupled damage model.

[2] To simplify the writing, the term *Xue model* in the present dissertation refers to *the enhanced Xue model* which accounts for the proposed modifications.

[3] The damage to fracture transition was modeled using the element erosion and remeshing techniques. See Appendix C.4 for a detailed study on damage to fracture transition modeling for different mechanical tests.

[4] From an experimental study of ArcelorMittal, this type of shear band could also be observed on the cross section of rolled wire. For confidentiality reason, we cannot illustrate it here.

(a) *Numerical result with Forge®2009 (with option "kill element"). The damage variable D_{Xue} is represented.*

(b) *Fracture specimen in compression test - [Bai, 2008]*

(c) *Polished and etched cross section of compressed specimen showing a cross-shaped zone of severe shear [Mescall et al., 1983]*

Fig. 3.1: *Validation of the Xue model with a uniaxial compression test on cylinder ([Cao, 2011]).*

3.1.2 Uncoupled damage models

3.1.2.1 Bai and Wierzbicki's model

Bai and Wierzbicki ([Bai and Wierzbicki, 2008]) constructed the 3D fracture locus in the space $(\overline{\epsilon}_f, \eta, \overline{\theta})$, which defines the strain to fracture as a function of the stress triaxiality (η) and the Lode parameter $(\overline{\theta})$. This function is based on three limiting cases: $\overline{\epsilon}_f^-$ (corresponding to $\overline{\theta} = -1$), $\overline{\epsilon}_f^0$ (corresponding to $\overline{\theta} = 0$) and $\overline{\epsilon}_f^+$ (corresponding to $\overline{\theta} = 1$). By adopting a parabolic function to represent the effect of the Lode parameter on fracture locus, the fracture envelope $\overline{\epsilon}_f = f(\eta,\overline{\theta})$ is thus defined as:

$$\overline{\epsilon}_f(\eta,\overline{\theta}) = \left[\frac{1}{2}\left(\overline{\epsilon}_f^{(+)} + \overline{\epsilon}_f^{(-)}\right) - \overline{\epsilon}_f^{(0)}\right]\overline{\theta}^2 + \frac{1}{2}\left(\overline{\epsilon}_f^{(+)} - \overline{\epsilon}_f^{(-)}\right)\overline{\theta} + \overline{\epsilon}_f^{(0)} \tag{3.13}$$

From the early studies of [McClintock et al., 1966] and [Rice and Tracey, 1969], for each limiting bound, the influence of stress triaxiality on material ductility can be introduced through an exponential function, hence : $\overline{\epsilon}_f^{(+)} = D_1 e^{-D_2\eta}$, $\overline{\epsilon}_f^{(0)} = D_3 e^{-D_4\eta}$, $\overline{\epsilon}_f^{(-)} = D_5 e^{-D_6\eta}$. Eq. 3.13 can be rewritten as:

$$\overline{\epsilon}_f(\eta,\overline{\theta}) = \left[\frac{1}{2}\left(D_1 e^{-D_2\eta} + D_5 e^{-D_6\eta}\right) - D_3 e^{-D_4\eta}\right]\overline{\theta}^2 + \frac{1}{2}\left(D_1 e^{-D_2\eta} - D_5 e^{-D_6\eta}\right)\overline{\theta} + D_3 e^{-D_4\eta} \tag{3.14}$$

where $D_1, D_2, D_3, D_4, D_5, D_6$ are 6 material parameters which need to be identified. A linear incremental relationship is assumed between the damage variable D and the equivalent plastic strain $\overline{\epsilon}_p$:

$$D(\overline{\epsilon}_p) = \int_0^{\overline{\epsilon}_p} \frac{d\overline{\epsilon}_p}{\overline{\epsilon}_f(\eta,\overline{\theta})} \tag{3.15}$$

where the triaxiality $(\eta = \eta(\overline{\epsilon}_p))$ and the Lode parameter $(\overline{\theta} = \overline{\theta}(\overline{\epsilon}_p))$ are functions of the equivalent plastic strain. For the proportional loadings (also called radial loadings, e.g. [Mohr and Henn, 2007, Benzerga et al., 2012]), these two stress state parameters are constant during loading. If not, average values are defined as:

$$\eta_{av} = \frac{1}{\overline{\epsilon}_f}\int_0^{\overline{\epsilon}_f} \eta(\overline{\epsilon}_p)d\overline{\epsilon}_p \quad , \quad \overline{\theta}_{av} = \frac{1}{\overline{\epsilon}_f}\int_0^{\overline{\epsilon}_f} \overline{\theta}(\overline{\epsilon}_p)d\overline{\epsilon}_p \tag{3.16}$$

In the present study, depending on the proportionality of loading paths, either the average values or the current values (i.e. at each numerical increment) of the stress triaxiality and the Lode parameter are employed to construct the *fracture locus*. The advantage of the method using the average value is that, as $\overline{\epsilon}_f$ is a constant, fracture occurs when $D = 1$. The identification can be done in post-processing as in [Bai and Wierzbicki, 2008], without using the inverse analysis. This is not the case if one uses the current values of the stress triaxiality and the Lode parameter. However, in order to use the average values of the stress triaxiality and the Lode parameter, the proportionality of loading paths must be investigated (see e.g. 3.4.1). Throughout the present study, the model defined by Eqs. 3.14 and 3.15 is referred to as Bai and Wierzbicki (B&W) model. Note that all the identifications of damage models parameters in the present study were performed using inverse analysis.

3.1.2.2 Modified Mohr-Coulomb model (MMC)

The Mohr-Coulomb failure criterion ([Coulomb, 1776], [Mohr and Beyer, 1928] - see Appendix A.3.2) has been widely used in rock and soil mechanics ([Palchik, 2006]) as well as brittle materials communities ([Lund and Schuh, 2004]). This criterion, an extension of the maximum shear stress failure criterion, is a good candidate to predict "shear fracture", which is nowadays still a challenge for the ductile damage and fracture community. Recently, Bai and Wierzbicki ([Bai and Wierzbicki, 2010]) transformed the Mohr-Coulomb (M-C) model into stress triaxiality and Lode parameter dependent formulation. This modified model was then successfully used to predict fracture of different proportional loadings in several recent studies, e.g. [Luo et al., 2012], [Dunand and Mohr, 2011], and was implemented in different commercial FE software (e.g. LS Dyna, Abaqus).

Here, the analytical formulation of this model is first revisited. The starting point is the M-C fracture criterion, which postulates that the fracture occurs when the combination of shear stress (τ) and normal stress (σ_n) on a plane reaches a critical value:

$$(\tau + c_1\sigma_n)_f = c_2 \tag{3.17}$$

$c_1, c_2(MPa)$ are two parameters, which are the static "friction" coefficient and the "shear resistance" respectively; the subscript f denotes the failure. When $c_1 = 0$, the maximum shear stress failure criterion is obtained. The failure plane orientation is defined by its unit normal vector $\vec{n} = (n_1, n_2, n_3)$, and the shear and normal stresses can be obtained from the three principal stresses ($\sigma_1, \sigma_2, \sigma_3$) as:

$$\tau = \sqrt{n_1^2 n_2^2(\sigma_1 - \sigma_2)^2 + n_2^2 n_3^2(\sigma_2 - \sigma_3)^2 + n_1^2 n_3^2(\sigma_1 - \sigma_3)^2} \tag{3.18}$$

$$\sigma_n = n_1^2\sigma_1 + n_2^2\sigma_2 + n_3^2\sigma_3 \tag{3.19}$$

By substituting Eq. 3.18 and Eq. 3.19 in Eq. 3.17, the maximum value problem of the left hand side of Eq. 3.17 with the constraint $n_1^2 + n_2^2 + n_3^2 = 1$ must be solved to find the failure plane. By using the Lagrangian multiplier technique, the following results can be obtained (see [Bai and Wierzbicki, 2010] for more details):

$$n_1^2 = \frac{1}{1 + \left(\sqrt{1 + c_1^2} + c_1\right)^2} \quad , \quad n_2^2 = 0 \quad , \quad n_3^2 = \frac{1}{1 + \left(\sqrt{1 + c_1^2} - c_1\right)^2} \tag{3.20}$$

Using this result in Eq. 3.17, the M-C criterion can be written in terms of principal stresses:

$$\left(\sqrt{1 + c_1^2} + c_1\right)\sigma_1 - \left(\sqrt{1 + c_1^2} - c_1\right)\sigma_3 = 2c_2 \tag{3.21}$$

The next step is to transform this formulation into a function of the stress triaxality and the Lode parameter, for which the expressions of these latter two parameters in terms of the principal stresses are needed. As recalled by [Bai and Wierzbicki, 2010]:

$$\sigma_1 = \left(1 + \frac{2cos(\theta)}{3\eta}\right)\sigma_m \tag{3.22}$$

$$\sigma_2 = \left(1 + \frac{2cos(2/3\pi - \theta)}{3\eta}\right)\sigma_m \tag{3.23}$$

$$\sigma_3 = \left(1 + \frac{2cos(4/3\pi - \theta)}{3\eta}\right)\sigma_m \tag{3.24}$$

where θ is the Lode angle ($\theta = \theta_L + \pi/6$ - see 1.4.2.1), σ_m is the mean stress. The M-C criterion can therefore be expressed in terms of the equivalent stress, the stress triaxiality and the Lode angle as:

$$\overline{\sigma} = c_2\left[\sqrt{\frac{1 + c_1^2}{3}}cos(\frac{\pi}{6} - \theta) + c_1\left(\eta + \frac{1}{3}sin(\frac{\pi}{6} - \theta)\right)\right]^{-1} \tag{3.25}$$

For the case of proportional loadings (constant stress triaxality and Lode parameter), the equivalent stress at fracture $\overline{\sigma}_f$ can be expressed as:

$$\overline{\sigma}_f = c_2 \left[\sqrt{\frac{1+c_1^2}{3}} cos(\frac{\overline{\theta}\pi}{6}) + c_1 \left(\eta + \frac{1}{3} sin(\frac{\overline{\theta}\pi}{6}) \right) \right]^{-1} \tag{3.26}$$

with the introduction of Lode parameter: $\frac{\overline{\theta}\pi}{6} = \frac{\pi}{6} - \theta$. As an example, if the Swift hardening law is employed (Eq. 2.24) and J_2 plasticity is assumed, Eq. 3.26 then becomes:

$$\overline{\sigma}_f = \sqrt{3}K(\epsilon_0 + \overline{\epsilon}_f)^n = c_2 \left[\sqrt{\frac{1+c_1^2}{3}} cos(\frac{\overline{\theta}\pi}{6}) + c_1 \left(\eta + \frac{1}{3} sin(\frac{\overline{\theta}\pi}{6}) \right) \right]^{-1} \tag{3.27}$$

The strain to fracture for proportional loading is then defined as:

$$\overline{\epsilon}_f = \left(\frac{\sqrt{3}K}{c_2} \left[\sqrt{\frac{1+c_1^2}{3}} cos(\frac{\overline{\theta}\pi}{6}) + c_1 \left(\eta + \frac{1}{3} sin(\frac{\overline{\theta}\pi}{6}) \right) \right] \right)^{-1/n} - \epsilon_0 \tag{3.28}$$

Since ϵ_0 is very small in our study ($\epsilon_0 = 0.0038$, see Table 2.8), this term can be omitted in Eq. 3.28. This equation represents an asymmetric fracture envelope with respect to the Lode parameter, which becomes symmetric when $c_1 = 0$ (maximum shear stress criterion). There are two parameters c_1 and c_2 which need to be identified. In [Bai and Wierzbicki, 2010], the authors carried out a parametric study, which showed that when c_1 increases, the fracture strain becomes more stress-triaxiality dependent. Moreover, the fracture strain was proved to increase with c_2.

The damage indicator evolution is defined similarly to Eq. 3.15. This modified model is called the modified Mohr-Coulomb model (MMC) hereinafter.

3.1.3 On the experimental validation of fracture prediction ability: what is the reliable measurement?

In this section, before entering to the identification of the above-mentioned damage models, different measurements used to characterize the validation of fracture predictions are discussed to choose, if possible, the most relevant one.

Considering the displacement to fracture, which can be seen as a "global variable", a given damage model is said to be valid, if its counter indicates that fracture occurs at the applied displacement level, which is equal to the experimental displacement to fracture. If it is not the case, a measurement of the displacement at which fracture numerically occurs (i.e. when the damage variable reaches its critical value $D = D_c$) is performed. This displacement is then compared with the real "experimental displacement to fracture" to deduce the relative error of displacement to fracture. These measurements of displacement (numerical or experimental) can be extracted directly from experimental test and numerical simulation. Apparently, the relative error depends on the gauge length and cannot characterize the local event.

Another measurement, the local strain to fracture, can be deduced experimentally by measuring the local section and using the logarithmic formula. It is often called "experimental local fracture strain", although it is not really an experimental measurement. The experimental measurement in this case is none other than the specimen section (or its diameter). Then, an analytical formula, which is also an approximation, is used to calculate the so-called local strain. It is the first source of error. For numerical simulation, e.g. tensile tests simulations, fracture often occurs after a diffuse then a localized necking. In this softening zone, the value of "numerical local plastic strain" depends strongly on the mesh size used (even without damage coupling). In order to overcome such an influence, non-local plastic strain must be used, using non-local formulation (evidently, coupled damage variable also depends strongly on the mesh size but here the present author just focuses on the plastic strain). This topic was addressed by several authors (e.g. [Peerlings et al., 1996,

Jirásek, 1998]). In order to have a mesh-independent plastic strain using non-local formulation, the mesh size must be smaller than certain characteristic length, which is often small. To summarize, even based on this local measurement, numerical and experimental sources of error may still exist. The numerical local plastic strain cannot be considered as a strict reliable measurement if non-local formulation is not employed when softening is involved.

In the present study, the present author only presents a full comparison for the case of zirconium alloy (i.e. both errors of displacement to fracture and local strain to fracture) in section 3.3. The same tendency of error can be observed for each test by using either of these two measurements. For the two others materials (high carbon and stainless steels), only the comparison using the displacement to fracture is given.

3.2 High carbon steel

3.2.1 Coupled damage models: enhanced Xue and Lemaitre

Since the coupled damage models were employed, the identifications of these models were based on the softening behavior due to damage accumulation. This softening, however, depends on the mesh size as stated in [Jirásek, 1998] and [Fayolle, 2008]: a finer mesh leads to a faster damage accumulation. Many methods were proposed in the literature to overcome this limitation ([Peerlings et al., 1996, Peerlings et al., 2001], [Engelen et al., 2003]), the non-local formulation is among others. Two approaches were often used: (1) integration formulation, where the non-local variable is defined as an integration of local variable on a neighbor domain (whose size is an intrinsic length); (2) implicit gradient formulation, which introduces higher order gradient of local variable with a multiplicative term defining the internal length. However, these approaches need a characteristic length, which can be inferred from certain physical measurements (e.g. mean distance between voids or particles). The identification of such a physical measurement is not straightforward and it was thus often chosen as fixed (e.g. $l_c = 0.01\ mm$ as in [Fayolle, 2008]). The mesh size has to be chosen smaller than this value to avoid mesh-dependency. However, for certain materials, voids nucleated from particles with different sizes will also have different sizes. The use of different characteristic lengths might be more suitable ([Besson, 2013]). It leads to a huge CPU time for a simulation with real size structure in industrial forming processes. Although using this approach is reliable to obtain more accurate result, the identification of the intrinsic length scale and the application to industrial simulations are main drawbacks to apply such an approach in the present study. In addition, identification of damage models were based on numerous mechanical tests using inverse analysis (and for 3 different materials), which also required a large number of FE simulations. The use of non-local models might increase sharply CPU time for identification work. In the present study, no particular technique was employed, the mesh size was thus kept constant for all the simulations of mechanical tests.

For the Lemaitre model, the compression and tension tests on round bar were chosen for the curve fitting procedure, while the identifications of the Xue model were based on the axisymmetric compression and tensile tests as well as torsion test. For the latter model, the damage variable is calculated from ϵ_f (Eq. 3.12), which is the function of μ_p and μ_θ (eq. 3.8). The identification procedure was then decoupled into two phases: identification of the pressure-dependent function μ_p with the series of tensile tests on RB and NRB (in which the Lode angle-dependent function μ_θ varies slightly, $\theta_L \approx -\pi/6$ on the axis during these tests), and identification of μ_θ with torsion test (in which $\mu_p \approx 1$ since $p \approx 0$). Xue proposed $k = 1$ and $m = 2$ and these values are kept in the present inverse analysis. The multi-objective optimization based on all loading cases was used.

Identification results are reported in Table D.1 (Appendix D). Fig. 3.2 shows the comparison between the numerical load-displacement curves and the experimental ones.

From Fig. 3.2b, one can observe that both damage models give good results for tensile tests and slightly different in compression test (Fig. 3.2a). The Lemaitre model, which takes into account phenomenologically the "crack-closure" effect (by using the parameter h) and introduces a cut-off value of stress triaxiality ($-1/3$),

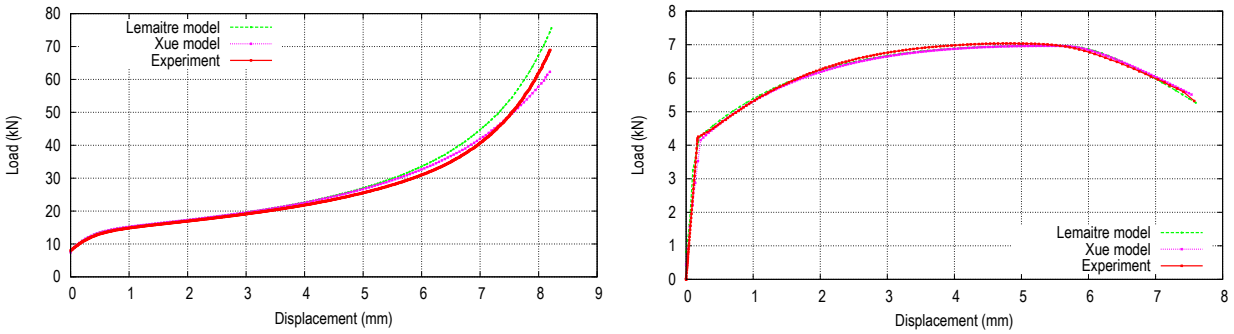

(a) *Compression curves.* **(b)** *Tensile curves.*

Fig. 3.2: *Load-displacement curves obtained with Lemaitre and Xue damage models and modified Voce hardening law. Only a quarter of each specimen is modeled.*

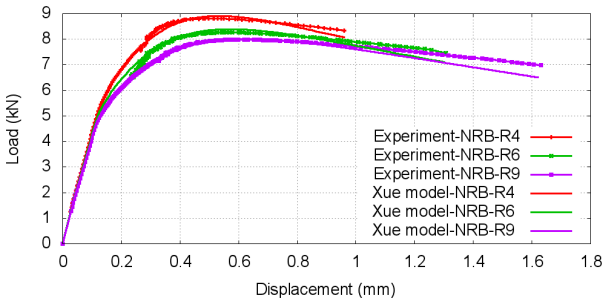

Fig. 3.3: *The comparison between experimental load-displacement curves from tensile tests with notched round bars (NRB) and the numerical ones with the Xue damage model and the modified Voce hardening law. Only a quarter of each specimen is modeled.*

has negligible influence on the load-displacement curve in compression test since the weakening function is relatively small (Fig. 3.2a). On the other hand, the damage with the Xue model has greater influence since the difference between compressive or tensile states is only accounted for in the pressure-dependent function and there is no phenomenological modification (i.e. the parameter h) for the weakening function. Fig. 3.3 shows the comparison between the experimental tensile curves on notched round bars (with different necking radii R: $4\ mm, 6\ mm, 9\ mm$) and the numerical ones obtained with the Xue model. The Xue model with modified Voce hardening law gives relatively good results although weakening is overestimated ([Cao et al., 2012]).

3.2.2 Uncoupled model: B&W model

The identification of B&W model is based on the fracture strains and the displacements to fracture of different tests, which cover the space of stress-triaxiality and the Lode parameter (see section 3.1.2.1). Having more experimental data (i.e. more values of the strain to fracture for different tests) helps to acquire more accurate calibration parameters. For this reason, besides the mechanical tests on round specimens, tensile tests on flat grooved specimens were also carried out to have more "data" in "plane strain" condition (theoretically, $\overline{\theta} = 0$ under this condition).

In this section, the result of the tensile tests on FG specimens is first presented, then the loading path of all the tests presented in Fig. 2.1 are investigated. The latter aims at studying the proportionality of loading path, which determines the precision of identified parameters.

3.2.2.1 Fracture tests: tensile tests on flat grooved (FG) specimens

Specimens' geometries as well as FE mesh are given in Figs. 3.4a and 3.4b, where 3 different radii are used to vary the stress triaxiality. Since the thickness of gauge section is small with respect to the other two

dimensions (1.5 mm), plane strain state is expected, which gives $\overline{\theta} = 0$.

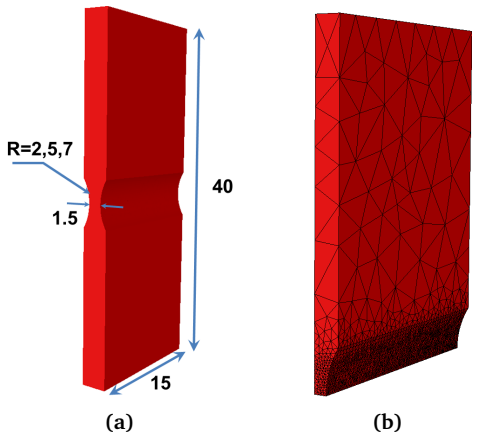

Fig. 3.4: *(a) Geometry and dimensions of flat grooved specimen with 3 different radii (all dimensions are in mm); (b) FE mesh used on a fourth of specimen due to symmetry conditions.*

Since the specimens were machined from 21 mm diameter patenting steel wire, the width was limited ($w = 15\ mm$) and the specimen height had to be high enough for machine holder ($h = 40\ mm$). The thickness of gauge section is small ($t = 1.5\ mm$), with a machining error of $\pm 0.05\ mm$. Note that the applied loading is quite sensitive to this thickness since the latter defines the load carrying surface ($= t * w$) [5]. For each test, 3 specimens were used and the variation in terms of maximum force was $\pm 5.5\%$, the variation in terms of displacement to fracture was $\pm 3.7\%$. This variation is acceptable as we notice the sensitivity of load to the minimum thickness.

In tension, this type of specimen is expected to exhibit a plane strain condition since the deformation through the width is negligible in comparison with the deformation through the thickness and in the loading direction. The average load-displacement curves are shown in Fig. 3.5a, which shows a slight difference between the FG-R5 and the FG-R7 specimens (in terms of maximum force as well as displacement to fracture). It can be explained principally by the specimen itself and the error in machining. Another source of error may be the alignment of specimen during test setup, which was carefully controlled but for such a small dimension specimen, a slight error in test setup can lead to an important error in the results.

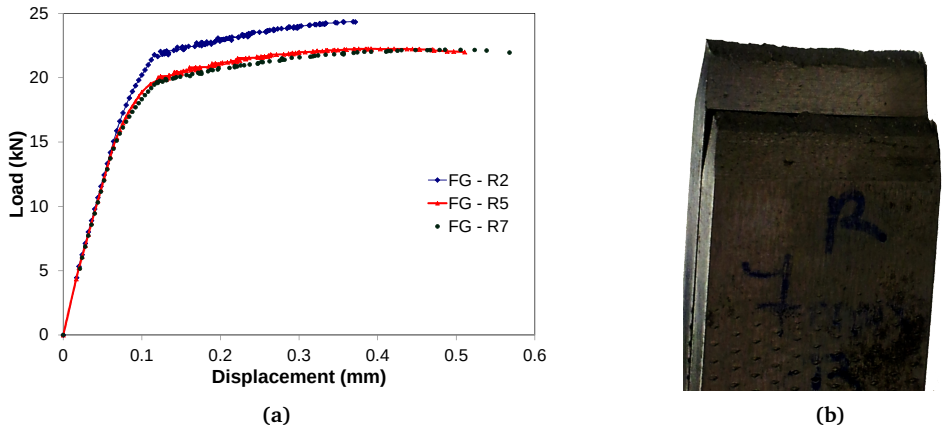

Fig. 3.5: *Results of tensile tests on FG specimens: (a) Average load-displacement curves of tensile tests on FG specimens; (b) Example of fracture surface of FG-R7 specimen, showing a slant mode of fracture and "necking" in traverse direction. Plane strain hypothesis is therefore not valid.*

[5] The same problem was stated in [Bai, 2008], in which the author observed an important variation between different specimens (Fig. 2-14 of [Bai, 2008]).

The local fracture strains for these tests were obtained by measuring the average thickness at fracture and using the formulation introduced in Table 2.2. Again, the difference between the fracture strains of FG-R5 and FG-R7 is small (0.156 for FG-R5 compared to 0.159 for FG-R7) since the difference in the theoretical initial stress triaxiality is also small (0.661 for FG-R5 compared to 0.638 for FG-R7). The fractured specimen is presented in Fig. 3.5b, showing a slant fracture surface. Moreover, one can observe the "necking" in traverse direction (i.e. through width direction), which shows that the deformation in this direction is not zero and the "expectation" of a plane strain state is not fulfilled. A simulation of crack propagation during the tensile test on FG-R7 specimen is presented in Appendix C.4.2.

Fig. 3.6 represents the plot of fracture strain for all the tests used as a function of theoretical initial stress triaxiality. As one can observe, the Lode parameter plays an important role on the strain to fracture and one cannot use a simple function of stress triaxiality to describe the experimental results[6]. Moreover, on each "branch" (i.e. $\bar{\theta} = 1$ or $\bar{\theta} = 0$), the variation of fracture strain with stress triaxiality can be approximated by exponential form functions, which is the main idea of the B&W model.

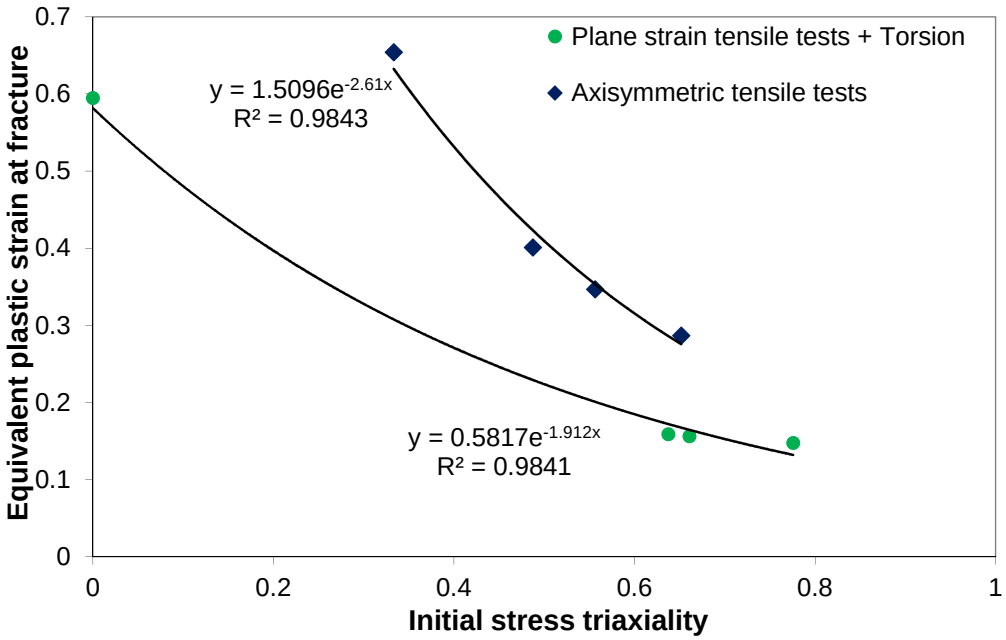

Fig. 3.6: *Strain to fracture for mechanical tests at different stress states: axisymmetric tensile tests ($\bar{\theta} = 1$); torsion + "plane strain" tensile tests ($\bar{\theta} = 0$).*

3.2.2.2 The onset of fracture

Before carrying out the identification of damage models, it is important to define *the onset of fracture*. In the present study, the fracture is defined by the instant at which one can observe the sharp drop of load-displacement curves (or torque-number of rotations curve). The corresponding displacement (or rotation) at that instant is defined as the displacement to fracture (or the rotation to fracture for the torsion test). However, in compression tests, this sudden drop is not observed. Consequently, the crack formation must be observed on the external surface during the experiment by examining the compressed specimens at different stages. In our case, for high carbon steel, there was no crack observed in the compression tests. This compression test was then not used for identification of fracture model.

3.2.2.3 Loading paths to fracture

The loading paths to fracture of the tensile tests and the torsion test are presented in Fig. 3.7a and Fig. 3.7b, where the equivalent plastic strains are plotted as functions of the stress triaxiality and the Lode

[6]It is worth noting that, for this material, the Lode parameter also plays an important role on yielding (or hardening) as shown in Appendix C.3.

parameter (the last point of these curves corresponds to the fractures in these tests). The values were extracted from the critical point, which is positioned at the axis for the tensile specimens and on the specimen surface for the torsion specimen.

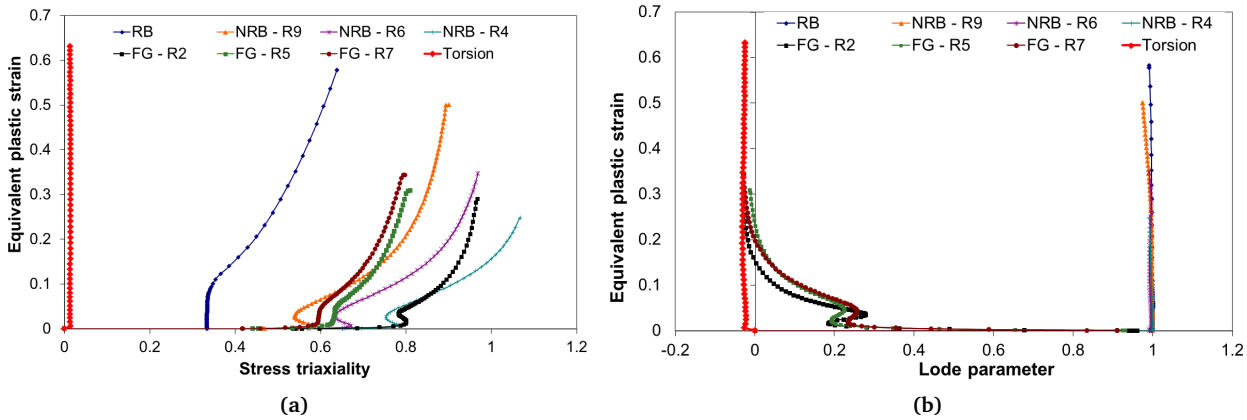

Fig. 3.7: *The loading paths to fracture: the evolution of (a) stress triaxiality and (b) Lode parameter with equivalent plastic strain.*

For the axisymmetric tensile tests, the Lode parameter is nearly constant and equal to unity (axisymmetric stress state - Fig. 3.7b). The variations of the stress triaxialities during loading can be observed in Fig. 3.7a, which shows the non-proportionality of these loading paths. For the tensile test on round bar (blue curve in Fig. 3.7a), the stress triaxiality changes sharply when necking develops: the stress state is no longer uniaxial ($\eta = 1/3$) but rather triaxial. For the torsion test, the loading is proportional and the stress triaxiality and the Lode parameter are approximately zero during the numerical simulation.

3.2.2.4 B&W model identification

There are 6 parameters to be identified (Eq. 3.14), among which the four parameters D_1, D_2, D_3 and D_4 define functions $\overline{\epsilon}_f^{(+)} = D_1 e^{-D_2\eta}$ and $\overline{\epsilon}_f^{(0)} = D_3 e^{-D_4\eta}$, which correspond to the fracture strain at $\overline{\theta} = 1$ and $\overline{\theta} = 0$ respectively. These four parameters were thus estimated *a priori* via the experimental fracture strains of tensile tests (see Fig. 3.6).

The fracture locus was then assumed to be symmetric with respect to $\overline{\theta} = 0$, i.e. $D_1 = D_5$ and $D_2 = D_6$. All the parameters estimated based on the exponential functions in Fig. 3.6 define a set of input parameters for an automatic optimization process by inverse analysis, which aims at minimizing the difference between the numerical and experimental displacements to fracture of the tensile tests and the torsion test.

In order to identify the parameters of the fracture strain-based damage models, the damage variable $D(\overline{\epsilon}_p) = \int_0^{\overline{\epsilon}_p} \frac{d\overline{\epsilon}_p}{\overline{\epsilon}_f(\eta,\overline{\theta})}$ (Eq. 3.15) is used as a fracture indicator: when $D = D_c$ (its critical value), fracture is considered to occur. For a proportional loading (i.e. $\eta, \overline{\theta}$ are constant during loading), $Dc = 1$ and $\overline{\epsilon}_f(\eta,\overline{\theta}) = \overline{\epsilon}_f(\eta_{av},\overline{\theta}_{av})$ is also constant. However, in our study on high carbon steel, most tests are non-proportional (or just nearly proportional), the value of the stress triaxiality and the Lode parameter change at each numerical time increment. For this reason, the real value of these two parameters at each increment were used to calculate $\overline{\epsilon}_f(\eta,\overline{\theta})$. Moreover, the critical value of damage is assumed equal to unity and all the parameters were identified so that the maximum value of damage reached this critical value at the end of test.

The identified parameters are grouped in Table D.2 and the error between the experimental and numerical displacements to fracture (d_{ef} and d_{nf} respectively)[7] is presented in Fig. 3.8a. Except the tensile tests on NRB-R4 and NRB-R9, the errors are relatively small (<3.5%). Moreover, the overall average error ($= 1/N \sum_{i=1}^{N} E_i = 4.32\%$, where N = 8 is the number of tests used, E_i is the relative error of the test number i)

[7]The numerical displacement to fracture is the necessary displacement in the simulation so that the maximum value of damage reaches the critical value D_c.

is acceptable.

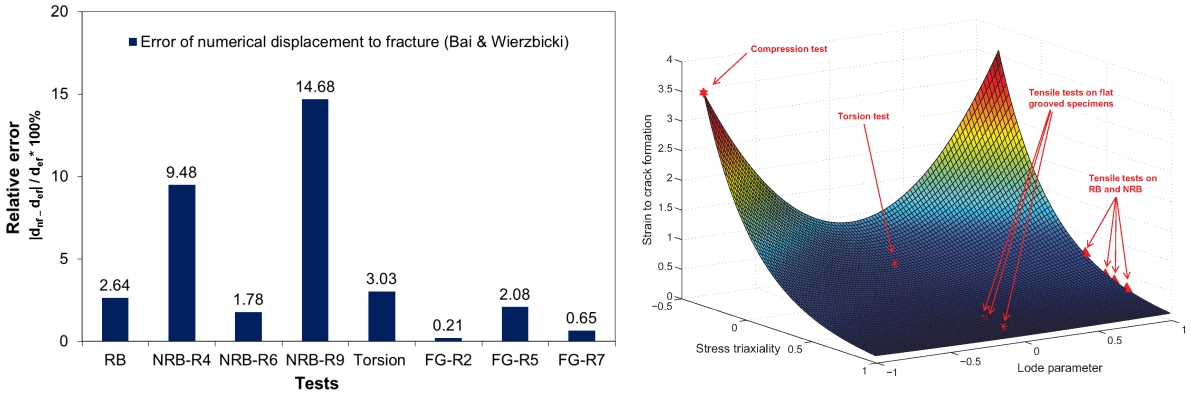

(a) *Comparison between the numerical and the experimental displacements to fracture.*

(b) *Fracture locus in the space of initial stress triaxiality and initial Lode parameter.*

Fig. 3.8: *Results of B&W models for high carbon steel.*

In addition, the "fracture locus" can be constructed, using the initial values of stress triaxiality and Lode angle parameter (see Fig. 3.8b)[8]. The red symbols represent the experimental fracture strain of mechanical tests (see Table 2.2). The 3D-surface is obtained from a post-processor optimization by minimizing the difference between the function $\overline{\epsilon}_f(\eta,\overline{\theta}) = \left[\frac{1}{2}\left(D_1 e^{-D_2\eta} + D_5 e^{-D_6\eta}\right) - D_3 e^{-D_4\eta}\right]\overline{\theta}^2 + \frac{1}{2}\left(D_1 e^{-D_2\eta} - D_5 e^{-D_6\eta}\right)\overline{\theta} + D_3 e^{-D_4\eta}$ and the experimental data of $(\overline{\epsilon}_f, \eta, \overline{\theta})$ for different tests (Fig. 3.8b). This fracture locus helps to estimate the fracture strain at a given stress state (defined by η and $\overline{\theta}$), which is interesting from an industrial point of view.

3.2.3 Concluding remark for the high carbon steel

For the high carbon steel, the coupled damage models (Xue, Lemaitre) were identified based on the softening effect of damage. The B&W uncoupled model was identified based on the strain and displacement to fracture of different tests: tensile test on axisymmetric specimens (RB, NRB), tensile tests on flat grooved specimens and torsion test. The overall error of displacement to fracture is small (<5%).

3.3 Zirconium alloy - M5®

3.3.1 Damage observation

The fractured specimens were observed under SEM and revealed dimpled surface (see Fig. 3.9) which was the result of ductile damage.

The fractured surface of torsion specimen is shown in Fig. 3.10, which show a local dimpled fractured area.

3.3.2 Loading paths to fracture

The loading paths to fracture of the tensile tests and the torsion test are presented in Fig. 3.11a and Fig. 3.11b.

[8]Note that one can use either the final value or the average value of stress triaxiality and Lode parameter to construct such a locus. Evidently, the loci obtained with different methods are different. The initial value-based fracture locus helps to give a quick estimation of strain to fracture for a given test, in which the values of stress triaxiality and Lode parameter do not change too much. This method is interesting for engineering applications.

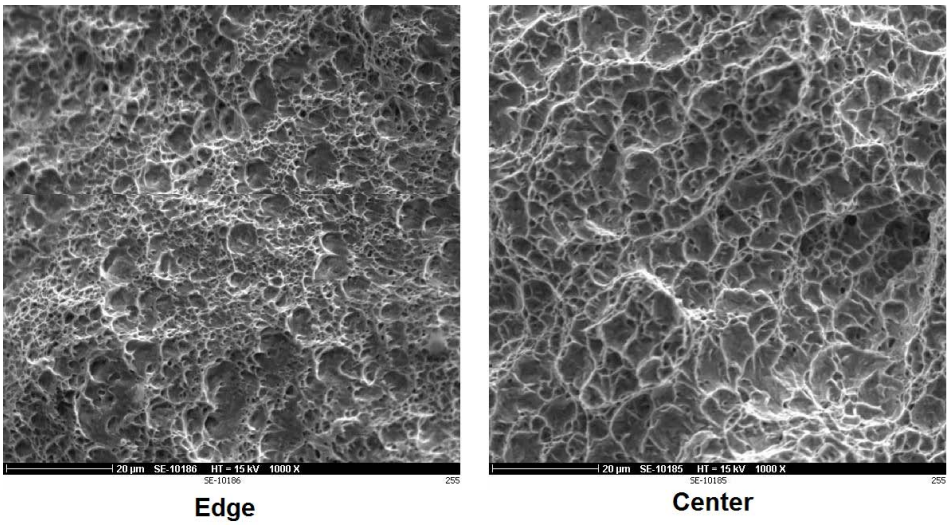

Fig. 3.9: *Dimpled fractured surface of RB specimen at the border and in the center of specimen obtained with SEM (SE mode, 15 kV). SEM observations were conducted at Cezus research center, in Ugine [Cao et al., 2013a].*

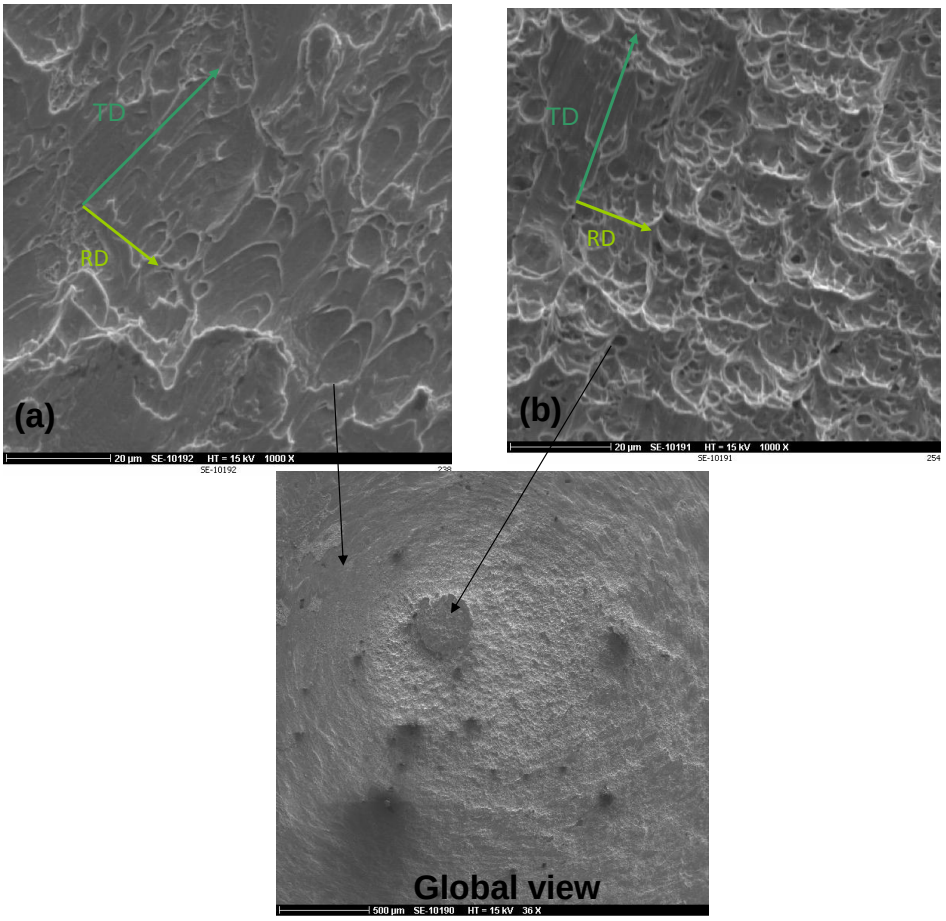

Fig. 3.10: *Fractured surface of torsion specimen showing two zones, where the dimples can be observed in zone (b) (RD is radial direction and TD is transverse direction).*

We can also observe in Fig. 3.11a, when the notch radius decreases from 9 mm to 4 mm, variation of stress triaxiality during loading is less.

For the present torsion test, the stress state of the material point located on the surface is nearly the pure shear state ($\eta = 0, \overline{\theta} = 0$). The values of the stress triaxiality and the Lode parameter are nearly constant during the experiment. This loading can be considered as proportional.

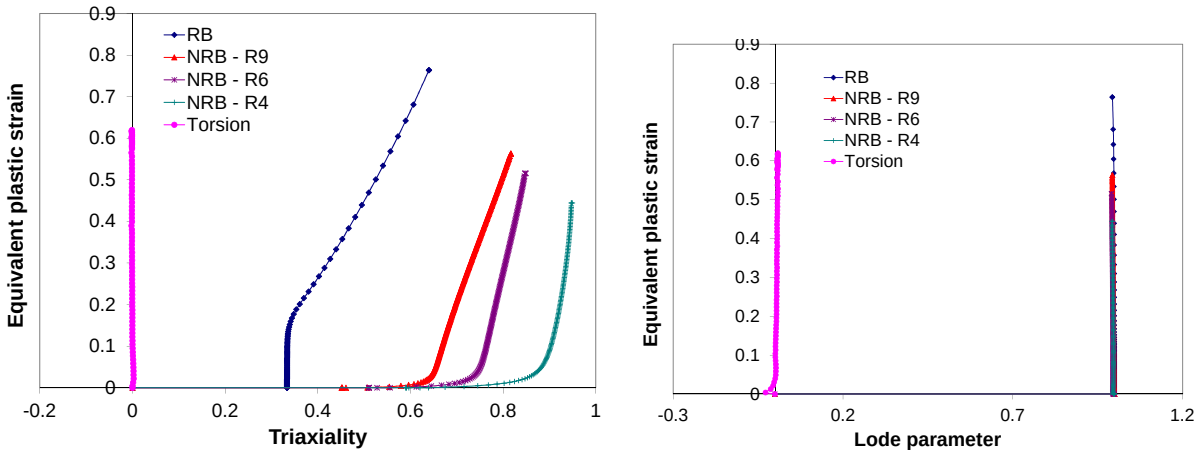

(a) *Equivalent plastic strain versus stress triaxiality.* **(b)** *Equivalent plastic strain versus Lode parameter.*

Fig. 3.11: *Loading path to fracture of tensile tests and torsion test.*

In our study, there was no crack observed on the external surface of the compressed specimen. The crack observed in the compression test is mainly due to the presence of friction, which then causes barreling: a high positive stress triaxiality region (Fig. 3.12b). A material point located at the middle of the external surface of specimen is firstly subjected to compressive stress, then tensile stress when barreling develops. The definition of fracture strain based on the average stress triaxiality and Lode parameter required *a priori* knowledge of fracture location. The value of average stress triaxiality and Lode parameter are then obtained from a material point located at this critical zone, via Eq. 3.16, as it was done in the literature, e.g. [Bai and Wierzbicki, 2010], [Dunand and Mohr, 2010], [Luo et al., 2012]. For the compression test, the loading history of a material point located at external surface middle position is presented in Fig. 3.12a. As one can observe, the loading experienced by this material point is far from proportional. The use of the averages values of the stress triaxiality and the Lode parameter in this case does not make sense since these values cannot characterize the stress state that the material point is subjected to.

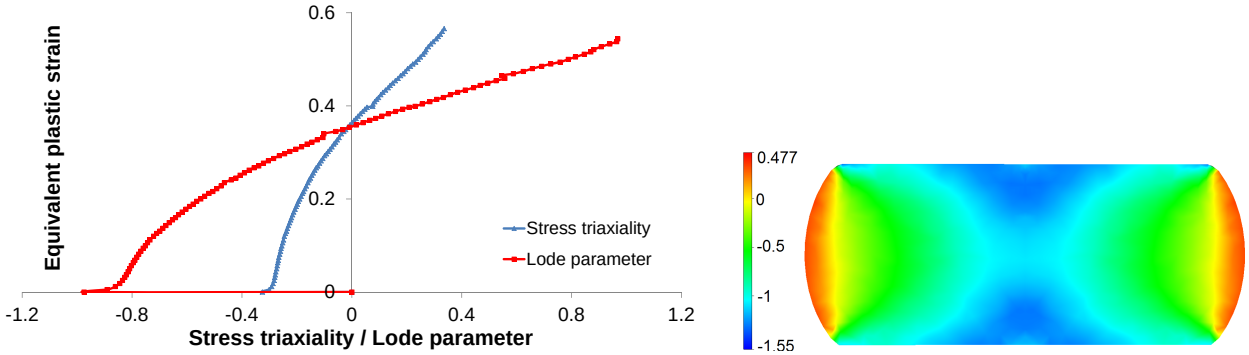

(a) *The loading path of a material point located in the barreling region, showing its non-proportionality. The calculated average stress triaxiality and Lode parameter are respectively equal to* 0.11 *and* 0.156*, which are far from the corresponding values of a uniaxial compression stress state* ($\eta = -1/3, \bar{\theta} = -1$)*.*

(b) *Stress triaxiality map on cutting surface at the end of test, showing the high triaxiality region in the barreled area.*

Fig. 3.12: *Loading path to fracture of a material point in barreling region (a) and the iso-value of stress triaxiality at the end of simulation.*

3.3.3 Calibration of the Lemaitre model

The tensile test on smooth round bar was chosen for the curve fitting procedure by inverse analysis. The comparison of experimental and numerical load-displacement curves are presented in Fig. 3.13a, while identified

parameters are reported in Table 3.2.

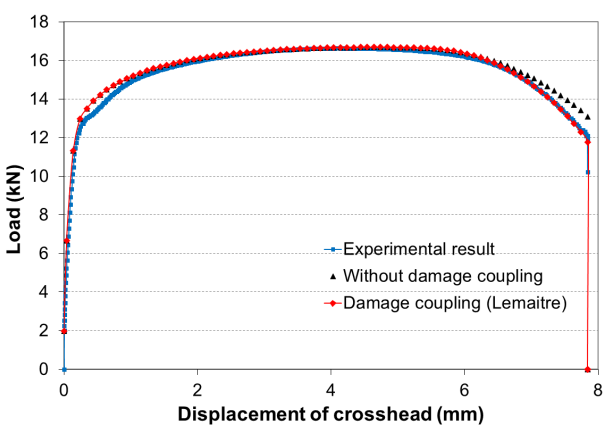

(a) *Numerical and experimental load-displacement curves of tensile test on round bar.*

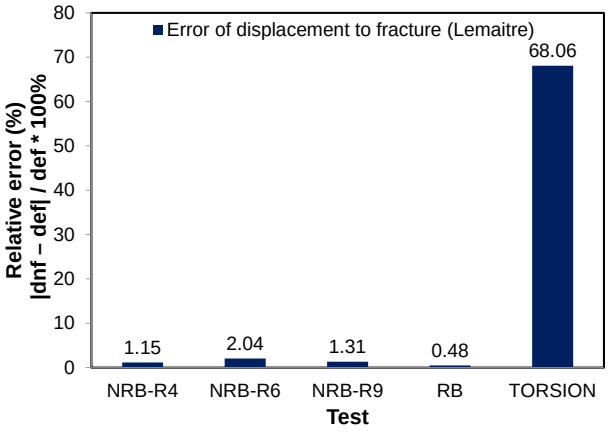

(b) *Error of displacement to fracture for all the tests predicted by the identified model.*

Fig. 3.13: *Comparison between the experimental and numerical result with Lemaitre model: (a) load-displacement curve of tensile test on round bar; (b) errors of displacement to fracture predicted by identified model.*

These identified parameters are then used to verify the prediction of fracture on other tensile tests on notched round bars and the torsion test. The relative errors between experimental and predicted displacements to fracture are presented in Fig. 3.13b; they are relatively small ($< 2.1\%$) except the torsion test. For numerical simulations, the fracture is supposed to occur when the damage parameter reaches its critical value (e.g. $D = D_c \approx 0.21$ for Lemaitre's model). The numerical results are in good agreement with experimental observations for the tensile tests. However, the identified Lemaitre model is unable to predict fracture in the torsion test. This model thus needs to be enhanced to predict the fracture in shear-dominated loading.

3.3.4 Enhanced Lemaitre model for shear loading

3.3.4.1 Modified dissipative potential and damage evolution

In this section, the Lemaitre model is improved by incorporating the influence of the third stress invariant represented by the Lode parameter in its formulation. The present authors propose to modify the damage dissipative potential (Eq. 3.3) as:

$$F_D = \frac{S}{(s+1)(1-D)} \left(\frac{Y}{S}\right)^{s+1} \frac{1}{\alpha_1 + \alpha_2 \bar{\theta}^2} \tag{3.29}$$

where α_1 and α_2 are two new parameters ($\alpha_1 > 0$ and $\alpha_2 \geq 0$). Note that with a simple choice: $\alpha_2 = 1 - \alpha_1$, for $\bar{\theta} = 1$, the original Lemaitre model is obtained, which means the modified model coincides with the original model in uniaxial tension (which has often been used to identify the Lemaitre model). In this case, the parameters identified of the Lemaitre model can be used for the modified Lemaitre model and there is only one additional parameter to be identified (since $\alpha_2 = 1 - \alpha_1$).

With this modified potential, the damage evolution can be deduced:

$$\dot{D} = \dot{\lambda} \frac{\partial F_D}{\partial Y} = \dot{\bar{\epsilon}}_p \left(\frac{Y}{S}\right)^{s} \frac{1}{\alpha_1 + \alpha_2 \bar{\theta}^2} \tag{3.30}$$

where Y is defined in Eq. 3.1.[9]

[9] Since the term added is a positive multiplicative term ($\frac{1}{\alpha_1+\alpha_2\bar{\theta}^2}$), the product $Y\dot{D}$ does not change sign and the positive damage dissipation is maintained.

3.3.4.2 Coupling function

For the Lemaitre model, the coupling function was defined as in Eq. 3.6. Lemaitre proposed such a coupling function based on his uniaxial compression ($\eta_{ini} = -1/3$) and tension ($\eta_{ini} = 1/3$) tests. The coupling function thus may be valid for these two limits of stress triaxiality but nothing proves its validity for the intermediate values of the stress triaxiality. The present authors propose a phenomenological coupling function as:

$$w(D) = \begin{cases} 1 - D & \text{, if } \eta \geq \eta_1 \\ 1 - \frac{(1-h)\eta + h\eta_1 - \eta_2}{\eta_1 - \eta_2} D & \text{, if } \eta_1 > \eta \geq \eta_2 \\ 1 - hD & \text{, if } \eta < \eta_2 \end{cases} \tag{3.31}$$

where η_1 and η_2 are two parameters to be identified, which can be chosen as $\eta_1 = 1/3$ and $\eta_2 = -1/3$ as a first approximation[10]; h can also be chosen equal to 0.2 as proposed by Lemaitre.

3.3.4.3 Identification

For the modified model, $\alpha_2 = 1 - \alpha_1$ was chosen and $\eta_1 = 1/3$, $\eta_2 = -1/3$, $h = 0.2$ as discussed above. The parameters of the original model were identified above. In principle, these parameters can be kept for the modified model. However, in the inverse analysis procedure, we allow slight variations of these parameters for a better result. The complete set of parameters for the modified Lemaitre model is presented in Table 3.2 while the comparison of the load-displacement curves for tensile test on RB and relative error of displacements to fracture for all tests are shown in Fig. 3.14.

Lemaitre				**Modified Lemaitre**				
$S(MPa)$	s	ϵ_D	D_c	$S(MPa)$	s	ϵ_D	D_c	α_1
6	3.2	0.202	0.208	6	3.8	0.202	0.208	0.27

Table 3.2: *Identified Lemaitre and modified Lemaitre models parameters.*

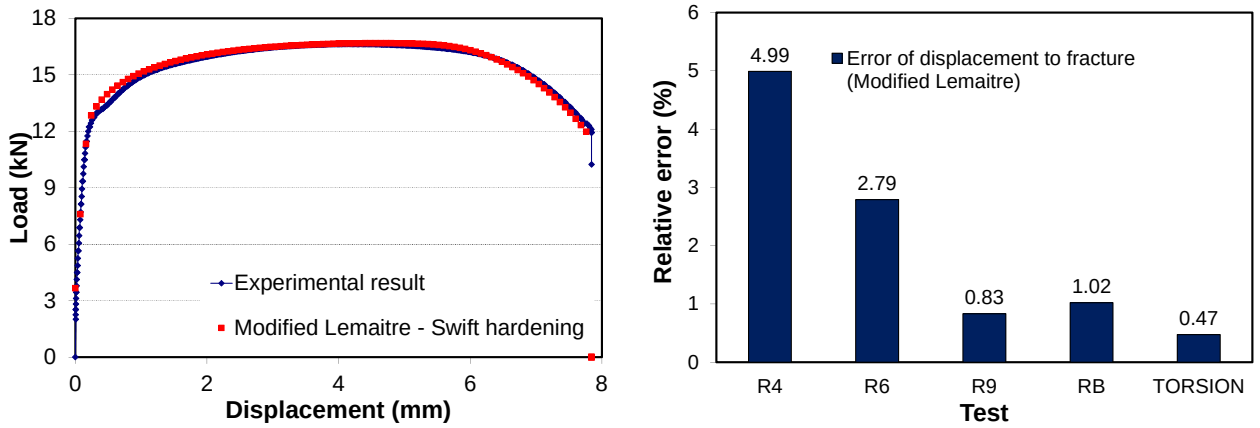

(a) *Comparison of experimental and numerical load-displacement curve of tensile test on RB.*

(b) *Relative errors of displacement to fracture for all tests performed.*

Fig. 3.14: *Results with the modified Lemaitre model.*

With the modified Lemaitre model, the displacement to fracture of all tests can be accurately predicted with only one additional parameter in the present study. The maximum error of displacement to fracture is about 5% for tensile test on NRB-R4.

[10]With the choice: $\eta_1 = \eta_2 = 0, \alpha_2 = 0, \alpha_1 = 1$, the Lemaitre model is resumed.

3.3.5 Calibration of the uncoupled models: B&W and MMC

The two uncoupled models B&W and MMC were calibrated via the strain to fracture of different tests. Fracture is assumed to occur when the damage variable reaches unity.

3.3.5.1 B&W model

The same method as in section 3.2.2.4 was used to identify the B&W model parameters for zirconium alloy.

3.3.5.2 MMC model

For this model, there are just 2 parameters c_1, c_2 which need to be calibrated. An identification process by inverse analysis was also carried out to identify these two parameters.

3.3.5.3 Results and discussions

The identified parameters of B&W and MMC models are reported in Table 3.3. Fig. 3.15a shows the relative errors between the experimental and the numerical displacements to fracture predicted by these two models. Globally, the errors are small ($< 5\%$) except the result of MMC model for torsion test (error of 6.79%). This difference, however, could be expected since the MMC model has just only two parameters to be calibrated from five different tests.

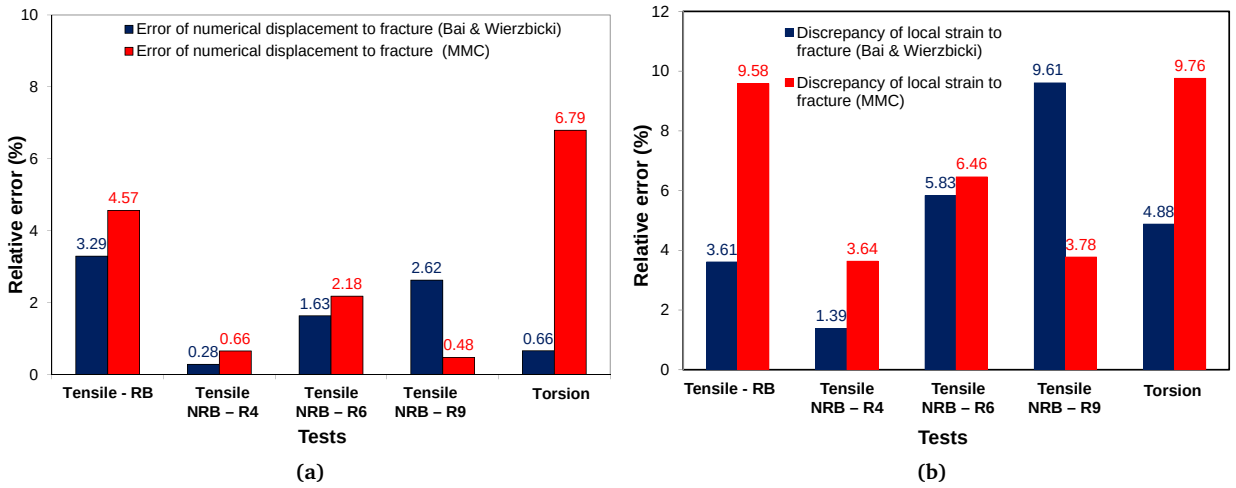

Fig. 3.15: *The relative errors between experimental and numerical displacements to fracture (a) and strain to fracture (b) of different tests, with the two uncoupled damage models B&W and MMC. Note that for the torsion test, the "displacement to fracture" corresponds to the "number of rotations to fracture".*

The discrepancy between the "experimental" and the numerical local plastic strains to fracture are also presented (Fig. 3.15b). The same tendency as for the displacement to fracture can be observed: the B&W model is better than the MMC model since it has more calibrated parameters. For all cases, the local strain maximum error is still smaller than 10%. These results show that, if one uses either the error of displacement to fracture or the discrepancy of local strain to fracture, the same tendency is observed, the B&W is still globally better[11].

From the identified parameters, the fracture loci obtained with these two models can be constructed. They correspond to the plots of strains to fracture as the function of the stress triaxiality and the Lode parameter (Fig. 3.16a and Fig. 3.16b)).

[11]None of these two above-mentioned measurements (displacement to fracture or "experimental" local strain to fracture) are the real observable variables during the experiments. The "experimental strain" is calculated from the real specimen *dimension* using an *approximate* formula, see the discussion in section 3.1.3.

Bai and Wierzbicki						MMC	
D_1	D_2	D_3	D_4	D_5	D_6	c_1	$c_2(MPa)$
1.5	1.395	0.7	1.579	1.5	1.395	0.1124	481.2

Table 3.3: *Identified uncoupled damage models' parameters for M5® zirconium alloy.*

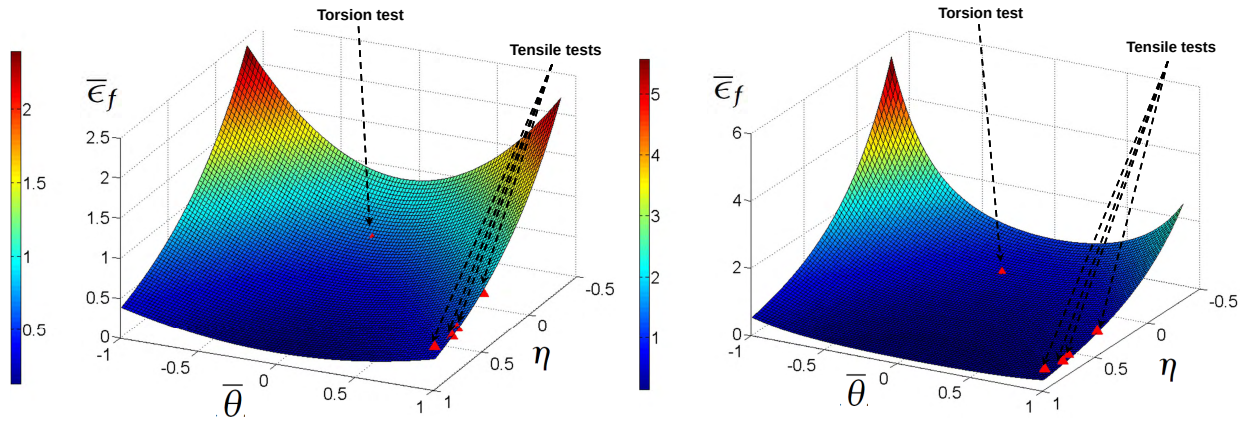

(a) *B&W fracture locus.* **(b)** *MMC fracture locus.*

Fig. 3.16: *Fracture loci obtained with uncoupled damage models for M5® zirconium alloy (note that the scales are different in these two figures).*

The triangle symbols represent the experimental fracture strains of the tests, with their corresponding average stress triaxiality and Lode parameter. Since the loading paths of our tensile experiments are non-proportional, these points are not expected to lie exactly on the identified fracture envelopes. However, the difference is small and these loci help estimating the strain to fracture for a given proportional loading.

Remark The MMC model with only two parameters gives satisfactory results for 5 mechanical tests. Moreover, the fracture locus is "naturally" not symmetric with respect to $\overline{\theta} = 0$ (if $c_1 \neq 0$): at a given value of the stress triaxiality, the strain to fracture can be approximated by a parabolic function and the value of fracture strain at $\overline{\theta} = -1$ is higher than that at $\overline{\theta} = 1$ (see Fig. 3.16b). Fig. 3.17a represents the plot of the fracture strain as a function of the Lode parameter at 3 different values of the stress triaxiality: $\eta = 0$ and $\eta = \pm 1/3$ with the identified parameters c_1 and c_2.

From Fig. 3.17a, one can observe the asymmetry of the strain to fracture with respect to $\overline{\theta} = 0$. Moreover, the influence of the Lode parameter on the ductility is more noticeable at low stress triaxiality. Barsoum and Faleskog ([Barsoum and Faleskog, 2011]) studied the influence of the Lode parameter on void growth and coalescence as well as the localization plastic strain, using micromechanical analyses of a single unit cell. This cell was subjected to a combination of an axisymmetric and a pure shear stress state, with fully periodic boundary conditions. These authors found an analogical tendency of the dependency of the localization equivalent plastic strain on the Lode parameter (see Fig. 3.17b). Note that in the study of Barsoum and Faleskog, the Lode parameter (L) is defined as in Eq. 1.107 (Chapter 1) and $L \approx -\overline{\theta}$. Although these two measurements of deformation are not the same, the same tendency of the Lode dependency suggests the validity of the underlined assumption of Lode dependency in the MMC model. Moreover, as shown in section 3.3.6.1, the MMC model also assumes a "natural" cut-off value of the stress triaxiality. Throughout these above-mentioned points, the MMC model seems interesting with only two parameters to be identified and contains relatively accurate physical assumptions.

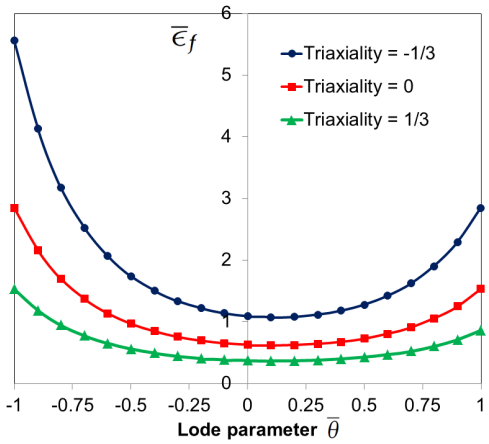

(a) *Plastic strain to fracture.*

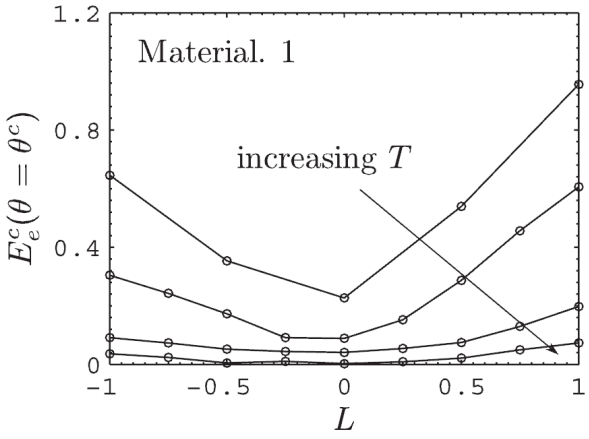

(b) *Localization equivalent plastic strain (figure adapted from [Barsoum and Faleskog, 2011]). T is the stress triaxiality and L is another definition of the Lode parameter: $L \approx -\overline{\theta}$.*

Fig. 3.17: *Influence of the Lode parameter (a) on the equivalent plastic strain at fracture (with the MMC model); (b) on the localization equivalent plastic strain ([Barsoum and Faleskog, 2011]).*

3.3.6 Discussions and recommendations for the zirconium alloy - M5®

3.3.6.1 Cut-off value of fracture

From the famous series of tests under pressure of Bridgman ([Bridgman, 1952]), Bao proposed a cut-off value of stress triaxiality of -1/3, below which fracture does not occur. As presented in section 3.1.1.1, this cut-off value was introduced into the Lemaitre model in Forge2009® by [Bouchard et al., 2011]. For the MMC model, the cut-off region is defined by a combination of the Lode parameter and the stress triaxiality. Starting from Eq. 3.28, the cut-off region is obtained by setting the denominator to zero:

$$\sqrt{\frac{1+c_1^2}{3}}cos(\frac{\overline{\theta}\pi}{6}) + c_1\left(\eta + \frac{1}{3}sin(\frac{\overline{\theta}\pi}{6})\right) \leq 0 \tag{3.32}$$

This equation can be expressed in terms of stress triaxiality condition:

$$\eta \leq \frac{-1}{c_1}\sqrt{\frac{1+c_1^2}{3}}cos(\frac{\overline{\theta}\pi}{6}) - \frac{1}{3}sin(\frac{\overline{\theta}\pi}{6}) \tag{3.33}$$

Fig. 3.18a represents the cut-off regions in 2D space of $(\overline{\theta}, \eta)$ obtained with the Lemaitre model and the identified MMC model. As one can observe, the cut-off value of stress triaxiality obtained with the identified MMC model is significantly smaller than that obtained by the study of [Bao and Wierzbicki, 2005], which was introduced into the Lemaitre model.

[Bai and Wierzbicki, 2010] showed that the cut-off region of the MMC model can be linked with the "friction-cone" concept, which is an interesting physical interpretation (Fig. 3.18b). When the stress triaxiality is smaller than a given value, the combination of shear and normal stresses will be contained within a cone similar to the "friction-cone". The value of cut-off stress triaxiality of $-1/3$ found by Bao ([Bao and Wierzbicki, 2005]) was deduced from empirical observations, which was based on the work of Bridgman ([Bridgman, 1952]) and confirmed by the work of Teng on dynamic impact fracture ([Teng, 2005]). Although the cut-off region obtained with the MMC model is more physically sound, its predicted value of cut-off stress triaxiality is too low compared with experimental evidence (about -4.3 to -5.18 in our study - Fig. 3.18a). The reason might be linked with the fact that the Mohr-Coulomb model has often been used for brittle material, whose "cut-off" value of stress triaxiality might be small in comparison with that of ductile material.

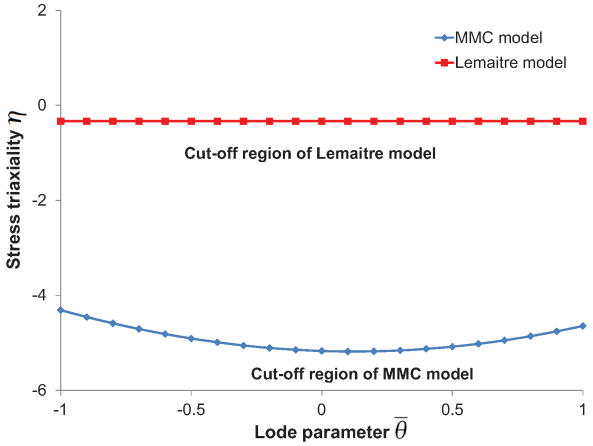

(a) *The cut-off regions of Lemaitre model (using the result of [Bao and Wierzbicki, 2005]) and MMC model, which are defined by the area below each curve respectively.*

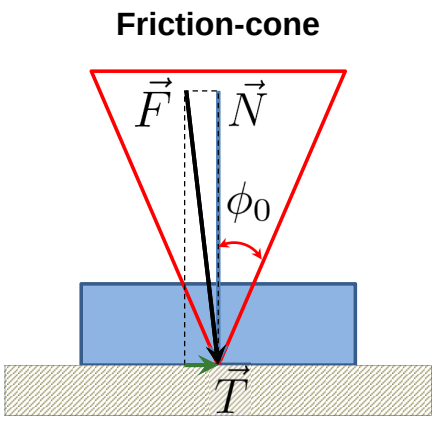

(b) *In friction, there is no sliding when the total force $\vec{F}$ of normal force $\vec{N}$ and shear force $\vec{T}$ is contained within the friction-cone, which is defined by the angle ϕ_0.*

Fig. 3.18: *(a) The comparison between the cut-off regions of the stress triaxiality obtained with the MMC model and the Lemaitre model; (b) the friction cone, from which the cut-off region of the MMC model can be inferred.*

Another shortcoming of the MMC model is its derivation from a stress-based MC criterion to a mixed strain/stress-based criterion. This transformation is only valid for proportional loading. The use of the MMC criterion for a non-radial loading loses its initial meaning and this criterion in this case must be considered as a general uncoupled formulation (see section 3.5).

3.3.6.2 Lode dependent function

Between the coupled damage model (Lemaitre) and the two uncoupled formulations (B&W and MMC), one can observe that the identified Lemaitre model predicts quite accurately the displacement to fracture of the tensile tests with just 3 parameters to be identified. All the relative errors between the experiments and the results obtained with the Lemaitre model are quite small, in comparison with the two uncoupled models studied. However, the Lemaitre model, which is based only on the stress triaxiality, fails to predict damage under shear dominated loading, which can be captured by the Lode parameter and the triaxiality based models (e.g. B&W, MMC and enhanced Lemaitre models in the present study). The B&W model assumed a parabolic form of Lode dependent function. Bai and Wierzbicki [Bai and Wierzbicki, 2010] also showed that at a given value of the stress triaxiality, the Lode dependent function of the MMC model can also be approximated by a parabolic curve (see Fig. 3.17a). In [Xue, 2007], the author proposed a linear function of the absolute value of Lode angle, the form of Lode dependent function is thus bilinear and symmetric with respect to $\bar{\theta} = 0$. The Lode-dependent term in the proposed enhanced Lemaitre model is also taken as a parabolic function. In order to accurately identify the form of this function, one needs to carry out different mechanical tests at a fixed value of the stress triaxiality and different Lode parameter. This configuration is still a challenge and to the best of our knowledge, this problem has not been addressed yet.

3.3.6.3 Synthesis on studied damage models for the zirconium alloy M5®

The Lemaitre model gives the best results for “high” stress triaxiality region (tensile tests on round bar and notched round bars), which also shows the importance of the coupling between damage and elastoplasticity (not taken into account in the uncoupled models). Nevertheless, it fails to predict the ductile fracture in the present torsion test.

Among the studied damage models, the proposed enhanced Lemaitre model gives the overall best result for all the studied tests in terms of fracture prediction (via the displacement to fracture). This proposed model is also user-friendly since one can use the parameters of the original model (which are often identified from uniaxial tensile test) for this modified model with the choice: $\alpha_2 = 1 - \alpha_1$; only one additional parameter

needs to be identified. Moreover, the proposed modified coupling function enables a more flexible interaction between damage and material strength.

Regarding the two uncoupled models, the B&W model gives a better result for all the tests studied in terms of fracture prediction (via the displacement to fracture). This model, which is based on the three limiting curves, is also easy to identify and friendly to use and implement. However, the identification of this model (as well as the MMC model) is based on the strong assumption of proportional loadings. In our experiments, the stress triaxiality and the Lode parameter vary moderately, the error is thus small. For a non-proportional loading (e.g. upsetting test), using the average values of the stress triaxiality and the Lode parameters may lead to unrealistic results. On the other hand, the fracture envelope is supposed to be symmetric in the present study since we do not have sufficient data in negative Lode parameter region. This assumption must be justified in future studies.

The MMC model itself predicts relatively exact fracture displacements for different tests, except for the torsion test (error of 6.79%). Since this model consists of two parameters, which are calibrated from 5 different tests, this shortcoming is expectable. Using another form of hardening law to account for the influence of Lode parameter and hydrostatic pressure (as in [Bai and Wierzbicki, 2008]) may introduce more parameters in the left hand side of Eq. 3.27 to be calibrated. It might give better results, but it would be more expensive in terms of identification work. Moreover, as discussed in section 3.3.5.3, this model is of great interest since it seems to contain "reliable" physical assumption.

3.3.7 Concluding remarks for the zirconium alloy M5®

1. In terms of fracture prediction, the Lemaitre coupled damage model gives the best results for high triaxiality tests (i.e. tensile tests) in comparison with the two uncoupled models. This fact shows the importance of coupling damage and elastoplasticity in fracture prediction of high triaxiality tests, in which significant void growth can be observed. Therefore, the Lemaitre model, with few parameters to be calibrated, can be used for the fracture prediction in high triaxiality forming processes. However, this model fails to predict ductile fracture for torsion test.

2. The proposed enhanced Lemaitre model gives the overall best results in terms of fracture prediction for all tests (based on the displacement to fracture). This model is also friendly to identify with a flexible coupling function. Fracture in shear-dominated loading can be accurately predicted by the proposed model. In terms of formulation, this enhanced model also ensures a positive dissipation of damage process.

3. Between the two uncoupled models, the B&W model gives better result. These two models are friendly to implement and identify and is interesting for engineering applications. Nevertheless, the proportionality of calibration tests must be verified to avoid unrealistic identification results. Moreover, the application of these models to non-proportional loading needs special attention in interpreting the signification of function $\overline{\epsilon}_f$: it is no longer the strain to fracture but rather a stress-dependent function used to defined the damage variable (see the discussion in section 3.5).

4. The identified cut-off region of the MMC model in terms of stress triaxiality, although it has an interesting physical interpretation, is too low compared with experiments from the literature. However, this model with only two parameters gives satisfactory results for all tests.

5. The loading path of a critical point of quasi-static compression test is proven to be strongly non-proportional. This test thus cannot be used in the identification process of the models that are based on the fracture envelope using the average stress triaxiality and Lode parameter.

3.4 Austenitic stainless steel

For this material, two damage models were identified: B&W and Lemaitre. Only the result of B&W model is presented here. The results obtained with the Lemaitre model (identification, processes applications) is given in Appendix C.1[12].

3.4.1 Loading paths to fracture

As in sections 3.2.2.3 and 3.4.1, the loading paths to fracture of the tensile tests and the torsion test are presented in Fig. 3.19a and Fig. 3.19b.

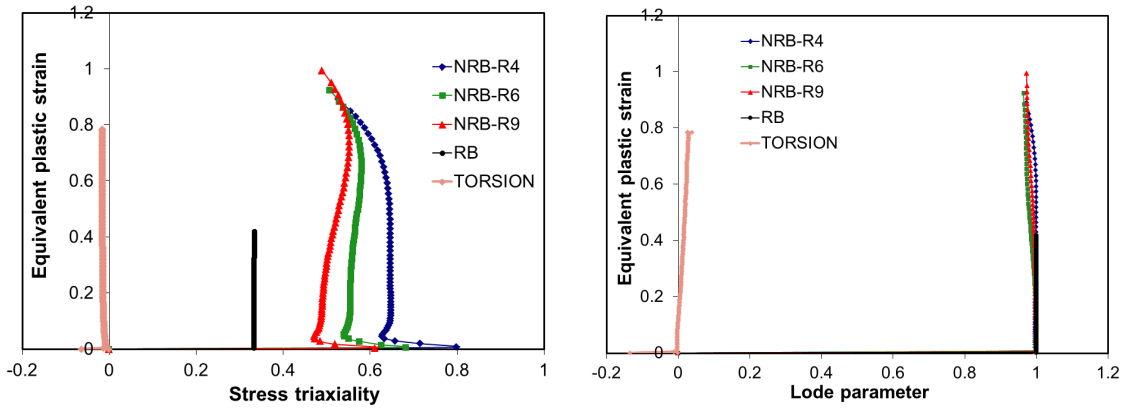

(a) *Equivalent plastic strain versus stress triaxiality.* **(b)** *Equivalent plastic strain versus Lode parameter.*

Fig. 3.19: *Loading path to fracture of tensile tests and torsion test.*

From these results, all the tests in Fig. 3.19 can be considered as proportional since only slight variations of the Lode parameter and the stress triaxiality are observed during loading.

3.4.2 Calibration of the uncoupled B&W model

Since the hardening model identified cannot capture the necking in the tensile test on smooth round bar (see Fig. 2.26b, section 2.4, Chapter 2), the local strain for this test is not precise. For this reason, this test was not used in the identification of the B&W uncoupled damage model.

The identified parameters of B&W model are reported in Table 3.4. Fig. 3.20 shows the relative errors between the experimental and the numerical displacements to fracture predicted by the B&W model. Globally, the errors are small ($< 5.3\%$)[13].

Bai and Wierzbicki					
D_1	D_2	D_3	D_4	D_5	D_6
1.276	0.594	0.74	0.594	0.85	0.594

Table 3.4: *Identified B&W model parameters for stainless steel.*

From the identified parameters, the fracture locus can also be constructed as in Fig. 3.16a.

[12]SEM observations of damage in mechanical tests were also carried out, which confirmed that all fractures were ductile. However, due to the confidential reason concerning material microstructures, these pictures cannot be shown here.

[13]It must be emphasized that the result is obtained by neglecting the tensile test on round bar. If the damage parameters identified are used for this test, the error of displacement to fracture is about 22%, which is due to the error in hardening law.

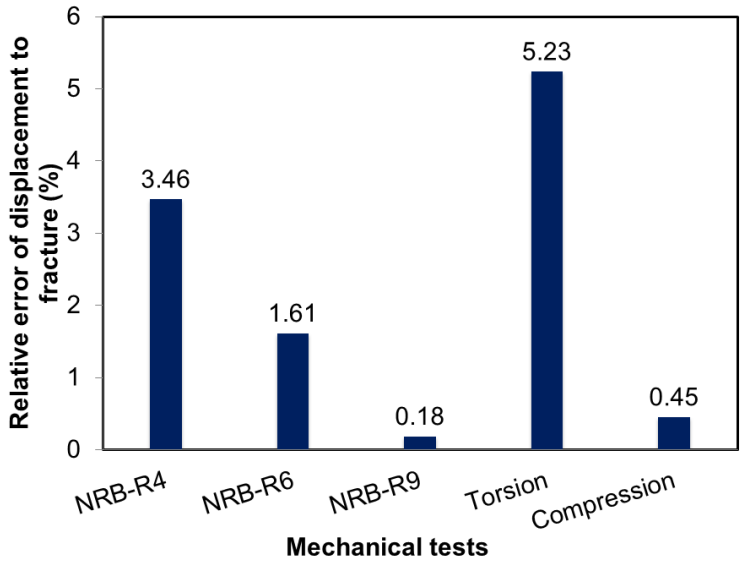

Fig. 3.20: *The relative errors between experimental and numerical displacements to fracture of different tests, with the uncoupled damage model B&W. Note that for the torsion test, the "displacement to fracture" corresponds to the "number of rotations to fracture".*

3.4.3 Concluding remark for the stainless steel

In this section, the B&W model was identified for the studied stainless steel. The error of displacement to fracture is relatively small except for the tensile test on round bar, in which the necking was not captured by the identified hardening law in section 2.4. This result reveals the important influence of the hardening model identification on damage model identification.

3.5 Closure remark: application of damage models to non-proportional loading cases, a limitation of uncoupled approach?

In this section, the application of damage models for non-proportional loadings is discussed. For the micro-mechanical based models (e.g. Gurson - see Chapter 4) or coupled phenomenological models such as Lemaitre (CDM approach) or other uncoupled formulations (e.g. Rice and Tracey), their applications to non-proportional loading configurations is not an issue since the derivation of these models is not based on the assumption of proportional loadings[14].

As mentioned above, uncoupled damage models used in the present study were initially based on an assumption of proportional or radial loadings to define the so-called strain to fracture function. For a non-proportional loading, the use of average measurements to construct a fracture locus does not make sense since these measurements cannot account for the whole loading history (e.g. a cyclic tension-compression test on axisymmetric specimen). In the study of Bai and Wierzbicki, the authors constructed the fracture loci based on their "proportional" experiments. Moreover, they transformed the stress-based M-C criterion (see section 3.1.2.2 or [Bai and Wierzbicki, 2010]), to a mixed strain/stress-based formulation to predict fracture. This transformation is valid only if the loading is proportional. Recently, Benzerga and co-workers ([Benzerga et al., 2012]) examined the influence of strain history on fracture behavior by using cell model calculation. In their simulations, the authors considered two cases: radial loading and non-radial loading. For the latter case, loading was composed of two steps. In each step, the stress triaxiality was kept constant (i.e. a piecewise constant function) and the strain-averaged value of the stress triaxiality was equivalent to the case of radial loading. By varying the stress triaxiality, these authors showed that for each value of average stress

[14]Here, the present author only mentions the ability of application, not the ability of prediction.

triaxiality, the value of "fracture strain" was not unique. For these reasons, in the present author opinion, the application of these criteria for non-proportional loading needs further consideration about the meaning of the function $\overline{\epsilon}_f$. In this case, $\overline{\epsilon}_f$ is no longer the strain to fracture function, but rather a weighting function, which accounts for the stress state.

Uncoupled damage models (or fracture criteria) can be based on physical assumptions (e.g. Rice and Tracey criterion) or pure phenomenological assumptions, in which damage parameter is defined as an integration of a stress-based function along the strain path: $D = \int_0^{\overline{\epsilon}_f} f(\boldsymbol{\sigma})\, d\overline{\epsilon}_p$. If the stress-based function $f(\boldsymbol{\sigma})$ is chosen as: $f(\boldsymbol{\sigma}) = 1/\overline{\epsilon}_f$, with $\overline{\epsilon}_f$ defined as in Eq. 3.14 (B&W model) or in Eq. 3.28 (MMC model), the damage variable of B&W and MMC models can be obtained respectively. If proportional (or nearly proportional) tests are used to calibrate these models, the function $\overline{\epsilon}_f$ *coincides* with the fracture strain. To summarize, $\overline{\epsilon}_f$ must not be considered as a fracture strain function in a strict sense. It is only a phenomenological weighting function, which *coincides* with the fracture strain for radial loadings. The fracture prediction in numerical simulation is based on the damage variable D (defined as in Eq. 3.15).

Throughout the present study, for the identification procedure, the average values were used to simplify the identification only if loadings were proportional or nearly proportional.

3.6 Summary of Chapter 3

This chapter presents the development as well as the identifications of phenomenological damage models for 3 different materials: high carbon steel, austenitic stainless steel and zirconium alloy.

Recently developed damage models (Xue, B&W and MMC) were detailed, reviewed and implemented in FE software Forge2009®. These models account for the influence of the third deviatoric stress invariant (through the Lode angle or the Lode parameter) to describe the evolution of ductile damage. Moreover, the Xue model was modified to match our experimental observations. Methods for identification process were also detailed, in which the identification of coupled models were based on the damage softening effect while the identification of uncoupled models were based on the fracture strains of different loading cases. In addition, the loading path for each test was investigated to study the proportionality of loading, and then choose a suitable identification method for uncoupled damage models.

For each material, different models were identified and compared. For high carbon steel, phenomenological coupled models (Lemaitre, Xue) and an uncoupled model (B&W) were identified. With the B&W model, besides the tests on round specimens, tensile tests on FG specimens were also carried out to enrich the data of fracture strains for "plane strain" state. Moreover, the results of these tests also reveal the difference between the variation of the fracture strain as a function of the stress triaxiality at $\overline{\theta} = 1$ and $\overline{\theta} = 0$. The result shows a small average error (<5%) of fracture prediction for all the tests carried out.

Concerning the zirconium alloy, the Lemaitre coupled model and the two uncoupled models B&W and MMC were identified and compared. Results show that for the tensile tests, Lemaitre's model gives the best results but fails to predict fracture in torsion (where the stress triaxiality is nearly zero). This model is therefore enhanced for fracture prediction under shear-dominated loading. A modification is proposed and the enhanced Lemaitre model give overall best results for fracture prediction for our mechanical tests. Between the two fracture criteria, the B&W criterion gives better results in terms of fracture prediction for all tests while the MMC model with only 2 parameters, gives satisfactory results.

For austenitic stainless steel, the B&W model was identified based on all tests, except the tensile test on RB (because the hardening model identified cannot capture the necking in this test (Fig. 2.26b, the error of local strain is thus high, which leads to the error of damage prediction). The error of displacement to fracture for all tests is small (<5.3%). However, as expected, applying the identified damage parameters on the tensile test on RB gives an unreasonable error of 22% since the uncoupled damage model and the hardening law identified cannot capture the local necking for this test. The Lemaitre coupled damage model was identified to fit the load-displacement curve for the tensile test on RB. The result is presented in Appendix C.1.1.

3.7 Résumé en français

Ce chapitre présente le développement ainsi que les identifications des modèles d'endommagement phénoménologiques pour 3 matériaux différents : acier haut carbone, acier inoxydable et alliage de zirconium.

Les modèles d'endommagement récemment développés par l'équipe du MIT (Xue, B&W, MMC) ont été détaillés, analysés et implémentés dans Forge2009®. Ces modèles prennent en compte l'influence du troisième invariant de contrainte déviatorique (à travers l'angle de Lode ou le paramètre de Lode) pour décrire l'évolution de l'endommagement ductile. En outre, le modèle de Xue a été modifié pour mieux reproduire notre résultat expérimental. La procédure d'identification a été détaillée, dans laquelle l'identification des modèles couplés a été basée sur l'adoucissement causé par l'endommagement, tandis que l'identification des modèles découplés a été basée sur les déformations et déplacements à rupture des différents trajets de chargement. En outre, les trajets de chargement des essais mécaniques ont été également étudiés pour vérifier la proportionnalité de ces chargements afin de choisir une méthode d'identification appropriée (basée sur les mesures moyennes de la triaxialité et l'angle de Lode ou leurs valeurs instantanées).

Pour chaque matériau, les différents modèles ont été identifiés et comparés. Pour l'acier haut carbone, les modèles couplés phénoménologiques (Lemaitre, Xue) et le modèle découplé (B&W) ont été identifiés. Avec le modèle de B&W, outre les tests sur les éprouvettes axisymétriques, des essais de traction sur des éprouvettes plates ont également été réalisés afin d'enrichir les données de la déformation à rupture pour des états de déformation plane. Le résultat a montré une erreur moyenne très petite sur la prédiction des ruptures de tous les essais réalisés. En ce qui concerne l'alliage de zirconium, le modèle couplé de Lemaitre et les deux modèles découplés B&W et MMC ont été identifiés et comparés. Les résultats montrent que pour les essais de traction, le modèle de Lemaitre donne les meilleurs résultats, mais qu'il ne parvient pas à prédire la rupture en torsion (où la triaxialité est proche de zéro). Ce modèle a ensuite été amélioré pour prédire l'endommagement et la rupture sous chargement de cisaillement dominant. Avec la modification proposée, le modèle de Lemaitre modifié donne le meilleur résultat global concernant la prédiction de la rupture pour nos essais mécaniques. De plus, entre les deux critères de rupture, le critère B&W donne le meilleur résultat en terme de prédiction de rupture pour tous les essais (il possède plus de paramètres à identifier) tandis que le modèle MMC avec seulement 2 paramètres, donne des résultats satisfaisants.

Pour l'acier austénitique inoxydable, le modèle de B&W a été identifié, mais l'erreur pour l'essai de traction sur l'éprouvette lisse est assez importante car le modèle d'écrouissage identifié et le modèle d'endommagement découplé ne peuvent pas prédire correctement la striction dans ce test (Fig. 2.26b). L'erreur de la déformation locale est donc élevée, ce qui conduit à une erreur de prédiction de l'endommagement (car le modèle de B&W est basé sur la déformation à la rupture). Pour cette raison, le modèle d'endommagement couplé de Lemaitre a été identifié pour mieux reproduire la courbe force-déplacement pour l'essai de traction lisse. Le résultat est présenté en Annexe C.1.1.

Part II

Ductile damage: micromechanical approach

Chapter 4

Gurson-Tvergaard-Needleman model implementation and development

Contents

Introduction

The present chapter and Chapter 5 constitute the second part of the present dissertation, which deals with the micromechanical approach of ductile damage, more precisely, the Gurson type models.

The present chapter details the implementation of the GTN model within the framework of mixed velocity-pressure ($v-p$) finite element (FE) formulation ([Cao et al., 2013c]). In the first section, a literature review on the Gurson type models is presented. Then, details on the derivation of the equations proposed by Aravas [Aravas, 1987, Govindarajan and Aravas, 1995] are given, followed by a comparison between two formulations for the analytical tangent modulus proposed by Aravas and by Zhang ([Zhang, 1995b]). This comparison is necessary to understand the origin of their formulas for a displacement-based FE formulation to adapt to the mixed $v-p$ formulation[1]. The unified analytical formulation is then compared with the "numerical one" (using perturbation technique) for a $1D$ tension. Note that the use of finite difference method to obtain the numerical tangent modulus is possible but sometimes leads to numerical instability due to the choice of perturbation factor. The use of a reliable analytical formulation helps avoiding such instability. Finally, comparisons with Abaqus were carried out to validate the present implementation.

4.1 Microscopic approach - Gurson-type models

4.1.1 Gurson model

Ductile fracture in metals could involve the generation of considerable porosity, via void nucleation and growth (and eventually the coalescence process where voids are linked together). Several classical plasticity models (e.g. von Mises, Tresca - see Appendix A.3.1) assume plastic incompressibility and therefore could not show the volume change in porous ductile materials. [Gurson, 1977] proposed a model that predicts the ductile fracture by void growth. This model was based on the spherical void growth (as in Rice & Tracey model [Rice and Tracey, 1969]) or cylindrical void growth in an elastic-perfectly plastic matrix. The material behavior is modified by the presence of porosity and the damage variable f is defined as the void volume fraction (in this definition, the void volume consists of the real void volume and the inclusion volume, the inclusion is considered as the initial void volume):

$$f = \frac{V_{void}}{V_{total}} \tag{4.1}$$

where V_{void} is the void volume of the void-containing solid. The evolution of void volume fraction due to voids growth is obtained thanks to the mass conservation and by neglecting the elastic strain:

$$\dot{f}_{growth} = (1-f)tr(\dot{\boldsymbol{\epsilon}}^p) \tag{4.2}$$

Based on numerical simulations of a single spherical void in an incompressible, perfectly plastic matrix, Gurson [Gurson, 1977] defined a function to describe the yield surface (the yield criterion - Fig. 4.1a):

$$\phi = \left(\frac{\sigma_{eq}}{\sigma_0}\right)^2 + 2f cosh(\frac{3}{2}\frac{\sigma_h}{\sigma_0}) - 1 - f^2 = 0 \tag{4.3}$$

where σ_0 is the yield stress of undamaged material (the matrix); σ_{eq}, σ_h are the macroscopic von Mises equivalent stress and the hydrostatic stress respectively ($\sigma_h = -p$). When $f = 0$ (material without porosity), the von Mises yield criterion is resumed.

The flow rule, which defines the rate of plastic strain components as a function of the stress state at yield, is obtained by the normality principle[2] from the plastic potential, which is another function of stress state.

[1] In Forge2009®, since the $P1^+/P1$ element has been used. Therefore, two tangent moduli need to be calculated instead of one, named: the linear tangent modulus and the bubble tangent modulus (see section 4.2.6).

[2] The normality for the Gurson plastic potential was discussed in appendix section of [Gurson, 1977].

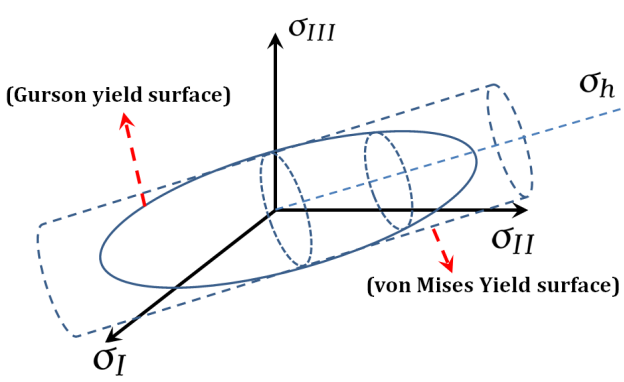

(a) *The representation of the Gurson yield surface and the von Mises yield surface in principal stresses space.*

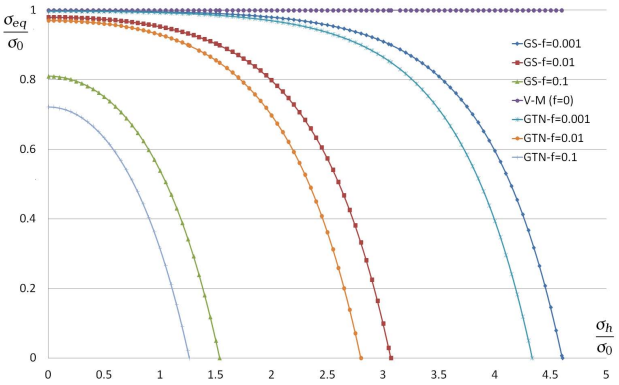

(b) *Representation of the Gurson and the GTN yield surfaces (q_1 = 1.5, q_2 = 1 and $q_3 = (q_1)^2$) in the space of normalized mean stress and normalized equivalent stress.*

Fig. 4.1: *Representations of the Gurson yield surface in 3D (a) and the GTN yield surface in 2D (b).*

For the Gurson model, the associative flow rule is assumed, which allows taking the yield function as a plastic potential:

$$d\boldsymbol{\epsilon}^{\boldsymbol{p}} = d\lambda \frac{\partial \phi}{\partial \boldsymbol{\sigma}} \tag{4.4}$$

This original model took into account the void growth mechanism but the voids interactions were neglected. This model was then improved to account for different aspects: prediction accuracy ([Tvergaard, 1981]), void nucleation ([Chu and Needleman, 1980]), void coalescence ([Tvergaard and Needleman, 1984, Needleman and Tvergaard, 1984]), void shape effect (e.g. [Gologanu et al., 1993, Pardoen and Hutchinson, 2000]), void size effect (e.g. [Wen et al., 2005], [Monchiet and Bonnet, 2013]), void/particle interaction (e.g. [Siruguet and Leblond, 2004]), isotropic strain hardening ([Leblond et al., 1995]), kinematic hardening (e.g. [Leblond et al., 1995], [Muhlich and Brocks, 2003]), plastic anisotropy (e.g. [Benzerga and Besson, 2001, Benzerga et al., 2004]), rate dependency (e.g. [Tvergaard, 1989]), shear effect (e.g. [Nahshon and Hutchinson, 2008, Xue, 2008]).

4.1.2 Gurson, Tvergaard and Needleman (GTN) model

Tvergaard ([Tvergaard, 1981]) first extended the Gurson model by adding three constitutive parameters q_1, q_2 and q_3 in the yield function ϕ since this model overestimated the critical strain for *localization* in his numerical analysis of a periodic array of voids:

$$\phi = \left(\frac{\sigma_{eq}}{\sigma_0}\right)^2 + 2q_1 f^* cosh\left(\frac{3q_2}{2}\frac{\sigma_h}{\sigma_0}\right) - 1 - q_3 f^{*2} = 0 \tag{4.5}$$

Then, in order to account for the void coalescence, Tvergaard and Needleman ([Tvergaard and Needleman, 1984]) used the modified void volume fraction f^* to describe the sharp increase of void volume fraction when void linkage occurs:

$$f^* = \begin{cases} f & ,if \quad f < f_c \\ f_c + \frac{f_u^* - f_c}{f_f - f_c}(f - f_c) & ,if \quad f > f_c \end{cases} \tag{4.6}$$

where f_c is the void volume fraction at the beginning of the coalescence phase; f_f is the value of f at fracture and f_u^* is the ultimate value of f^* (when $f{=}f_f$, $f^*{=}f_u^*{=}\frac{q_1 \pm \sqrt{q_1^2 - q_3}}{q_3} = \frac{1}{q_1}$). Zhang and coworkers ([Zhang et al., 2000]) proposed the following relation between f_f and f_0, which is a pure phenomenological relationship:

$$f_f = 0.15 + 2f_0 \tag{4.7}$$

Generally, the values of q_1, q_2, q_3 are chosen as proposed in [Tvergaard and Needleman, 1984]: $q_1 = 1.5$, $q_2 = 1$ and $q_3 = (q_1)^2$. The mechanism of micro-cavity nucleation is taken into account in the void volume fraction evolution as:

$$\dot{f} = \dot{f}_{nucleation} + \dot{f}_{growth} \tag{4.8}$$

where $\dot{f}_{growth}$ is defined as in Eq. 4.2 and $\dot{f}_{nucleation}$ was often described by a Gaussian curve which was introduced by [Chu and Needleman, 1980] (see section 1.4.2.2 for a review):

$$\dot{f}_{nucleation} = \frac{f_N}{S_N\sqrt{2\pi}} exp\left[-\frac{1}{2}\left(\frac{\overline{\epsilon}^p - \epsilon_N}{S_N}\right)^2\right]\dot{\overline{\epsilon}}^p \tag{4.9}$$

with:

- $\overline{\epsilon}^p$: the equivalent plastic strain,
- ϵ_N: value of mean plastic strain at maximal nucleation,
- S_N: standard deviation of Gaussian distribution corresponding;
- f_N: the volume fraction of inclusions at which damage can be nucleated ([Besson, 2010]). This parameter is determined so that the total void volume nucleated is consistent with the volume fraction of particles ([Chu and Needleman, 1980])[3].

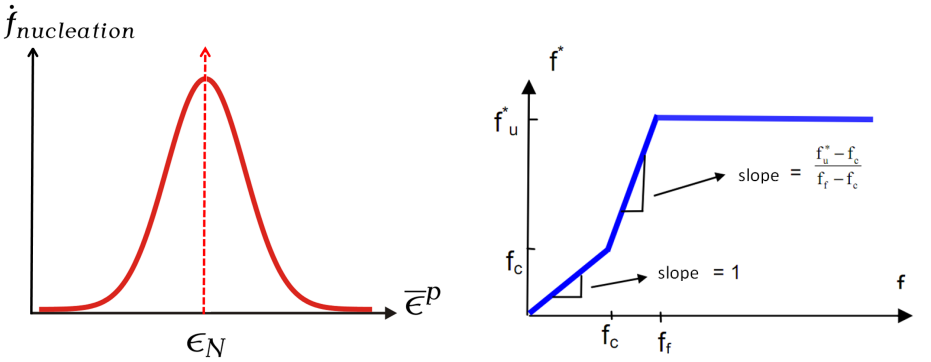

(a) *Nucleation law introduced by [Chu and Needleman, 1980].* **(b)** *Evolution of modified void volume fraction f^*.*

Fig. 4.2: *Nucleation law and modified void volume fraction.*

The increase in the void volume fraction due to coalescence can be simulated via f^*. The major problem appears in pure shear, (when the triaxiality equals zero), since damage evolution remains zero for this model. However, shear stresses appearing at the interfaces of second phase particles produce local decohesions (see experimental result of [Achouri et al., 2013] in section 1.4.2.3). Therefore, in the case of strong shear, several authors (e.g. [Croix, 2002]) introduced an additional component involving the nucleation due to shearing[4]:

$$\dot{f}_{shear} = \frac{f_{shear}}{S_{shear}\sqrt{2\pi}} exp\left[\frac{-1}{2}\left(\frac{\epsilon_{xy} - \epsilon_{shear}}{S_{shear}}\right)^2\right]\dot{\epsilon}_{xy} \tag{4.10}$$

with:

- f_{shear}: the void volume fraction created by local decohesion of second phase particles,
- ϵ_{shear}: value of mean plastic strain at maximal local decohesion,
- S_{shear}: standard deviation of Gaussian distribution corresponding.

[3]The volume fraction that can be nucleated in equal to $\int_0^\infty A(\overline{\epsilon}^p)\,d\overline{\epsilon}^p$, whereas $f_N = \int_{-\infty}^\infty A(\overline{\epsilon}^p)\,d\overline{\epsilon}^p$. If S_N is small enough with respect to ϵ_N, $f_N = \int_{-\infty}^\infty A(\overline{\epsilon}^p)\,d\overline{\epsilon}^p \approx \int_0^\infty A(\overline{\epsilon}^p)\,d\overline{\epsilon}^p$.

[4]In [Croix, 2002], the author did not explicit in which frame that ϵ_{xy} was calculated.

Although this modification introduces the nucleation due to shearing, the void growth mechanism, which is based on the trace of plastic strain rate tensor ($\dot{\epsilon}^p$), is still disabled. Note that neither the Gurson nor the GTN model considered the strain hardening in their formulas. To take the strain hardening into account, a modification of Eq. 4.27 was proposed by replacing σ_0 by $\overline{\sigma}(\epsilon^p)$, which is the yield stress which accounts for hardening (e.g. [Leblond et al., 1995]).

To summarize, the GTN model has 9 parameters: q_1, q_2, q_3, f_0, f_c, f_f, f_N, ϵ_N, S_N (or 12 parameters to account for shearing nucleation) to be identified. Some of these parameters can be identified based on microstructural observations (f_0, f_c, f_f, f_N), and inverse analysis has to be used for the others.

4.1.3 Gologanu, Leblond and Devaux (GLD) model

One of the major limitations of the GTN model is that it considers only spherical voids: voids are initially spherical and keep this shape during growing. This hypothesis is valid only for high stress triaxiality levels (about 1.5 in average). Microvoids may have elongated or flattened shapes due to the forming processes (e.g. wire drawing process). It was for these reasons that the GTN model was extended by Gologanu, Leblond and Devaux ([Gologanu et al., 1993]) to consider an incompressible matrix in which microvoids volume, shape and orientation can change during axisymmetric loading. This model is governed by the 3 following parameters (see Fig. 4.3):

- Microvoid volume fraction: $f = \frac{V_c}{V_t} = \frac{R_{y1}R_{x1}^2}{R_{y2}R_{x2}^2}$; where: R_{y1}, R_{x1} are the major semi-axis and the minor semi-axis of elliptical void; R_{y2}, R_{x2} are the major semi-axis and the minor semi-axis of elliptical matrix; V_c and V_t are the void volume and the matrix volume.
- Microvoid shape factor: $S = ln\left(\frac{R_{y1}}{R_{x1}}\right)$.
- Void orientation, defined by the $\vec{y}$ vector.

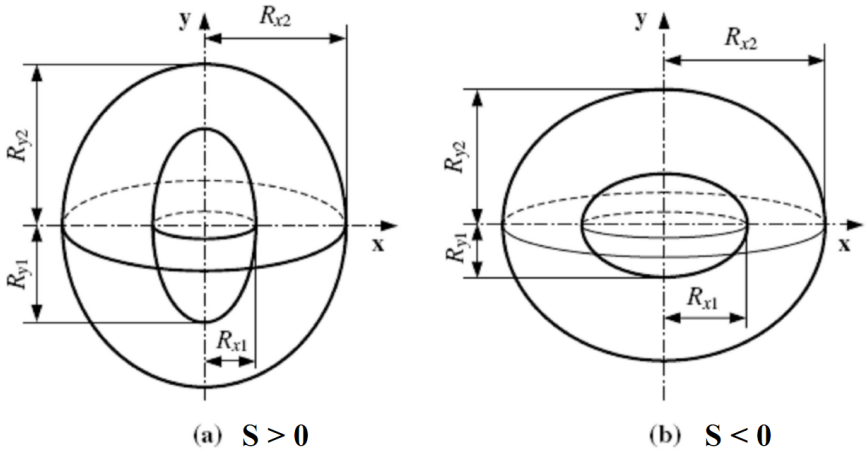

Fig. 4.3: *Geometrical representation of a representative material volume: (a) prolate void shape and (b) oblate void shape ([Gologanu et al., 1993])*

The yield criterion was then modified as:

$$\phi = \frac{C}{{\sigma_0}^2}\|\mathbf{s} + v^*\sigma_H\chi\|^2 + 2q_{GLD}(g+1)(g+f)cosh\left(\frac{\overline{\kappa}\sigma_h}{\sigma_0}\right) - (g+1)^2 - (q_{GLD})^2(g+f)^2 = 0 \qquad (4.11)$$

with:

- $\mathbf{s}$: deviatoric stress tensor.
- $\|.\|$: the von Mises norm, e.g. for a tensor $\mathbf{T}$: $\|\mathbf{T}\| = \sqrt{\frac{3}{2}T_{ij}T_{ij}}$.

- $\sigma_H = (1-2\alpha_2)\sigma_{xx} + \alpha_2(\sigma_{yy}+\sigma_{zz})$.
- $\chi = \frac{1}{3}(2\,\vec{e_y}\otimes\vec{e_y} - \vec{e_x}\otimes\vec{e_x} - \vec{e_z}\otimes\vec{e_z})$, where $(\vec{e_x}, \vec{e_y}, \vec{e_z})$ is an orthogonal reference with $\vec{e_y}$ parallel to the void axisymmetric axis.

The parameters $C, v^*, g, \overline{\kappa}$ and α_2 are defined as functions of f and the shape factor S. The parameter q_1 was modified to take into account the new form of elementary volume:

$$q_{GLD} = 1 + 2(q_1 - 1)\frac{h}{1+h^2} \tag{4.12}$$

where: $h = exp(S) = \frac{R_{y1}}{R_{x1}}$ and q_1 is the Tvergaard parameter for spherical cavity. When $h = 1$, $q_{GLD} = q_1$. The GLD model has the same evolution law as the GTN model: $\dot{f} = \dot{f}_{nucleation} + \dot{f}_{growth}$ (see Eq. 4.9).

Summary This model takes into account the damage anisotropy but damage still cannot be produced under pure shear. As the GTN model, the GLD model has a large number of parameters to be identified, which requires the combination of different studies: microscopic analysis, mechanical tests and inverse analysis. Several authors extended the GLD model by introducing the matrix anisotropy (e.g. [Croix et al., 2003]) or adding an inclusion inside the void (e.g. [Siruguet and Leblond, 2004]). However, the application in shear loading remains a major problem of using these models. In the next section, some methods of incorporating the shear effect into the Gurson based models are presented

4.1.4 Methods accounting for the effect of shear-driven microvoids coalescence

Different methods that account for the shear effect and have a limited number of material parameters have been proposed in the literature. *"Shear damage"* is caused by the voids rotation, which reduces the inter-particle spacing (see section 1.4.2.3). Under shear loading, voids are driven towards each other, decreasing the size of the ligaments between them, which reduces the load carrying section on the shear plane (similar to internal necking between voids in an uniaxial tensile test - Fig. 4.4).

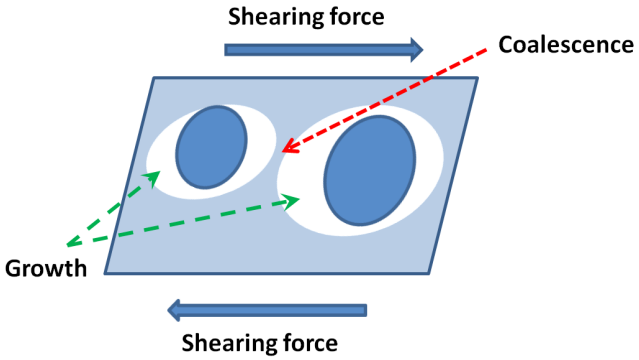

Fig. 4.4: *Shear localization mechanism.*

4.1.4.1 Model proposed by [Nahshon and Hutchinson, 2008]

Nahshon and Hutchinson [Nahshon and Hutchinson, 2008] modified the GTN model for shear dominated loading by introducing a new parameter k_ω, which sets the rate of damage development in shear. In this modified model, f **is no longer strictly attached to the void volume fraction but rather to the "effective void volume fraction" or simply to a universal damage parameter**. Accounting only for the evolution of existing voids, the damage evolution can be phenomenologically described as follows:

$$\dot{f} = (1-f)tr(\dot{\boldsymbol{\epsilon}}^p) + k_\omega f \omega_0 \frac{s_{ij}\dot{\epsilon}^p_{ij}}{\sigma_{eq}} \tag{4.13}$$

$$\omega_0 = \omega(\boldsymbol{\sigma}) = 1 - \left(\frac{27J_3(\boldsymbol{\sigma})}{2\sigma_{eq}^3}\right)^2 \tag{4.14}$$

where k_ω is a material constant ($0<k_\omega<3$ as proposed by [Nahshon and Hutchinson, 2008]); $\omega(\boldsymbol{\sigma})$ is a stress state dependent function, which ensures that the modification for shear will disappear under axisymmetric stress states. A stress state is called "axisymmetric" when two of three principal stresses are equal ([Nahshon and Hutchinson, 2008]). The measure of $\omega(\boldsymbol{\sigma})$ lies in the range $0 \leq \omega(\boldsymbol{\sigma}) \leq 1$, with $\omega(\boldsymbol{\sigma}) = 0$ for an axisymmetric stress state and $\omega(\boldsymbol{\sigma}) = 1$ for all combined pure shear and hydrostatic pressure stress states. The additional contribution was defined so that under pure shear state, the void volume fraction rate is proportional to the rate of plastic shear strain ($\dot{\gamma}^p$): $\dot{f} \propto k_\omega f \dot{\gamma}^p$ (note that $\omega_0 = 1$ in pure shear).

This modified model is capable of modeling the damage localization and fracture under shear-dominated stress states with low stress triaxiality. However, in the high stress triaxiality range (which is known to be well described by the original GTN model), the shear modification was shown to have important effects on damage evolution ([Nielsen and Tvergaard, 2009, Nielsen and Tvergaard, 2010]). In order to limit this influence, an extension was suggested by these authors, by introducing a stress dependent factor $\Omega\left(\frac{\sigma_h}{\sigma_{eq}}\right)$:

$$\omega_0 = \omega(\boldsymbol{\sigma})\Omega\left(\frac{\sigma_h}{\sigma_{eq}}\right) \tag{4.15}$$

where $\Omega\left(\frac{\sigma_h}{\sigma_{eq}}\right) = \begin{cases} 1, & if \quad \frac{\sigma_h}{\sigma_{eq}} < T_1 \\ (\frac{\sigma_h}{\sigma_{eq}} - T_2)/(T_1 - T_2), & if \quad T_1 \leq \frac{\sigma_h}{\sigma_{eq}} \leq T_2 \\ 0, & if \quad \frac{\sigma_h}{\sigma_{eq}} > T_2 \end{cases}$.

This modification means that the modified model by [Nahshon and Hutchinson, 2008] is used for $\frac{\sigma_h}{\sigma_{eq}} < T_1$; while the original GTN model is used when $\frac{\sigma_h}{\sigma_{eq}} > T_2$. A linear interpolation is applied in the range $T_1 \leq \frac{\sigma_h}{\sigma_{eq}} \leq T_2$. Nielsen and Tvergaard proposed $T_1 = 0$ and $T_2 = 0.5$, which leads to the following expression of $\Omega\left(\frac{\sigma_h}{\sigma_{eq}}\right)$:

$$\Omega\left(\frac{\sigma_h}{\sigma_{eq}}\right) = \begin{cases} 1, & if \quad \frac{\sigma_h}{\sigma_{eq}} < 0 \\ 1 - 2\frac{\sigma_h}{\sigma_{eq}}, & if \quad 0 \leq \frac{\sigma_h}{\sigma_{eq}} \leq 0.5 \\ 0, & if \quad \frac{\sigma_h}{\sigma_{eq}} > 0.5 \end{cases} \tag{4.16}$$

Fig. 4.5 represents the variation of ω_0 in principal stress space in this case.

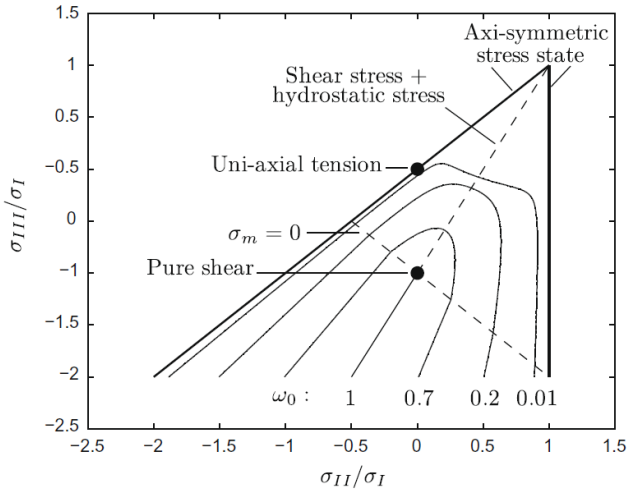

Fig. 4.5: *Variation of ω_0 in principal stress space ([Nielsen and Tvergaard, 2009]).*

With this modification, the GTN model is thereby maintained at high triaxiality.

Remark: By introducing these modifications, the modified GTN model is no longer a "micro-mechanical model" but rather a phenomenological model.

4.1.4.2 Model proposed by [Xue, 2008]

[Xue, 2008] carried out an analytical development for a shearing case in 2D, where a square cell having length L and containing a cylindrical void of radius R at the center, is subjected to a simple shear loading (Fig. 4.6).

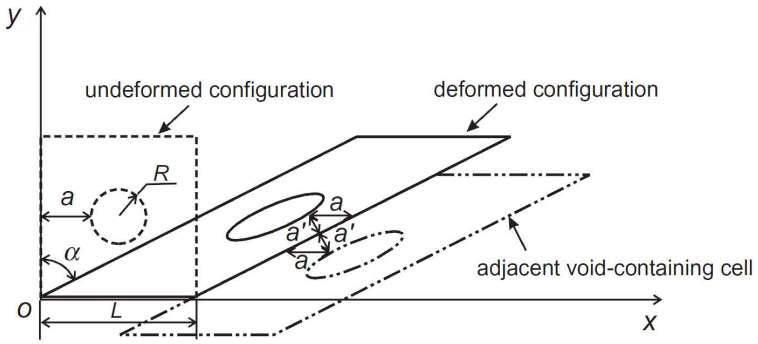

Fig. 4.6: *Illustration of the void shear mechanism in 2D ([Xue, 2008]).*

The author defined the damage associated with the void shearing as:

$$\dot{D}_{shear} = q_3^* f^{q_4} \overline{\epsilon}^p \dot{\overline{\epsilon}}^p \tag{4.17}$$

where $q_3^* = 6/\sqrt{\pi} = 1.69$, $q_4 = 0.5$ for 2D configuration, and $q_3^* = 3\left(\frac{6}{\pi}\right)^{1/3} = 3.722$, $q_4 = 1/3$ for 3D problems. For an arbitrary loading case, Xue introduced a Lode angle dependence function g_θ into the above equation:

$$\dot{D}_{shear} = q_3^* f^{q_4} \overline{\epsilon}^p \dot{\overline{\epsilon}}^p g_\theta \tag{4.18}$$

where g_θ is a linear function of the absolute value of Lode angle $|\theta_L|$:

$$\theta_L = tan^{-1}\left(\frac{1}{\sqrt{3}}\frac{2\sigma_2 - \sigma_1 - \sigma_3}{\sigma_1 - \sigma_3}\right) \tag{4.19}$$

$$g_\theta = 1 - \frac{6|\theta_L|}{\pi} \tag{4.20}$$

In generalized tension ($\theta_L = -\frac{\pi}{6}$, $g_\theta = 0$) there is no contribution of shear damage, while in generalized shear, $\theta_L = 0$, $g_\theta = 1$, Eq. 4.17 is regained. Note that the form of Lode angle dependence function was chosen phenomenologically. In fact, any function $g_\theta = 1 - \left(\frac{6|\theta_L|}{\pi}\right)^k$ could be employed (all these functions satisfy the condition $g_\theta = 0$ in generalized tension and $g_\theta = 1$ in generalized shear).

The GTN model uses a critical void volume fraction at fracture (f_f) as the fracture criterion (when $f = f_f$, $f^* = f_u^* = \frac{1}{q_1}$). The value of f_f is often identified by a uniaxial tension test. However, for different loading conditions, this value of critical void volume at fracture might be different. The damage variable associated with the GTN model can be defined as: $D_{GTN} = q_1 * f^*$ (when $f^* = f_u^*$, $D_{GTN} = 1$). Let us recall the formulation of f^* (Eq. 4.6) in the GTN model:

$$f^* = \begin{cases} f & ,if \quad f < f_c \\ f_c + \frac{f_u^* - f_c}{f_f - f_c}(f - f_c) & ,if \quad f > f_c \end{cases} \tag{4.21}$$

From this equation: $\dot{f}^* = \delta_f . \dot{f}$ or $\dot{D}_{GTN} = q_1 \delta_f . \dot{f}$, where δ_f is defined as follow:

$$\delta_f = \begin{cases} 1 & ,if \quad f < f_c \\ \frac{f_u^* - f_c}{f_f - f_c} & ,if \quad f > f_c \end{cases} \tag{4.22}$$

Xue proposed a new damage variable (D), which accounts for the shear damage:

$$\dot{D} = \delta_D \left(q_1 \dot{f} + \dot{D}_{shear}\right) \tag{4.23}$$

where δ_D is the damage rate coefficient. For the GTN model, which accounts for coalescence (i.e. using f_c to define the beginning of coalescence stage), this coefficient is defined as:

$$\delta_D = \begin{cases} 1 & ,if \quad D \leq D_c = q_1 f_c \\ \frac{f_u^* - f_c}{f_f - f_c} & ,if \quad D_c < D \leq 1 \end{cases} \tag{4.24}$$

On the other hand, if the coalescence is not accounted for in the original GTN model, this coefficient can be defined as:

$$\delta_D = \begin{cases} 1 & ,if \quad D \leq D_c = q_1 f_c^* \\ \frac{f_u^* - f_c^*}{f_f - f_c^*} & ,if \quad D_c < D \leq 1 \end{cases} \tag{4.25}$$

where $f_c^* < f_f$ is an additional parameter to be identified. Finally, Eq. 4.23 can be written as:

$$\dot{D} = \dot{D}_{GTN} + \delta_D \dot{D}_{shear} \tag{4.26}$$

The fracture is assumed to occur when $D = 1$. The modification of Xue allows the fracture to initiate at different values of void volume fraction in different loading cases (Fig. 4.7).

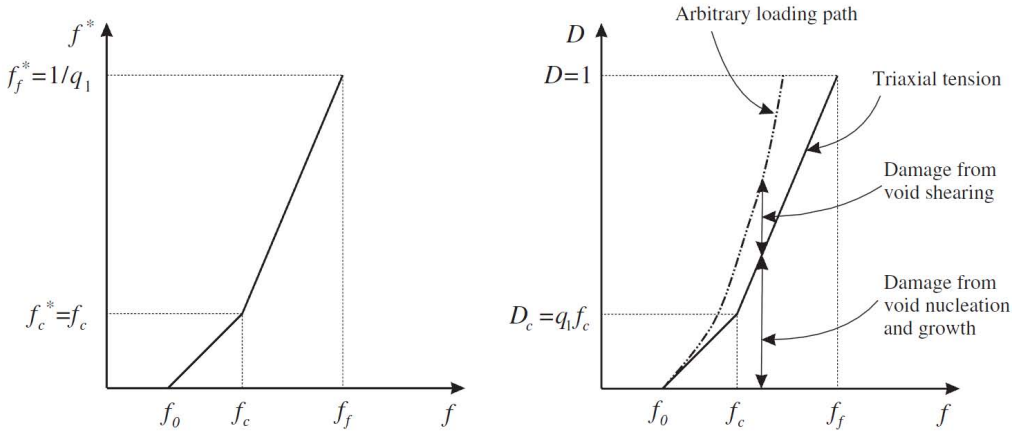

Fig. 4.7: *The void volume fraction of the GTN model (left) and the damage evolution of modified model by Xue (figure adapted from [Xue, 2008]).*

With this modification of the damage variable, Xue proposed two approaches:

1. Damage counter: in this approach, the yield function of GTN model is retained, the damage variable is defined as an independent variable, which can be considered as a fracture indicator and has no influence on yielding condition.

2. Damage yielding model: the effective void volume fraction f^* is replaced by the damage variable in the yield function. The damage variable is therefore fully coupled with material behavior.

4.1.4.3 Remarks

Both models presented above have been successfully applied to predict shear fracture in different studies, e.g. [Xue, 2008], [Nielsen and Tvergaard, 2009]. The model proposed by Nahshon and Hutchinson has only one additional parameter (k_ω) and the limited function $\Omega\left(\frac{\sigma_h}{\sigma_{eq}}\right)$ is chosen as in Eq. 4.16. Xue's extension has two parameters (q_3^* and q_4) to identify (but their values were also proposed by Xue from an analytical calculation). Concerning the numerical implementation, the N&H extension requires coupling while for the Xue extension, one can choose either coupling or uncoupling approaches. In the present study, damage counter approach is adopted for the Xue-modified GTN model. In such case, the modification of Nahshon and Hutchinson considers the yielding directly from damage indicator (f [5]) while for the Xue's modification, damage and yielding are governed by two different internal variables: D and the void volume fraction respectively

[5] It is worth noting to remind that f is no longer the void volume fraction, but the damage variable.

(in the latter case, the GTN yield function is retained). The difference between the two approaches is thus the fundamental question: are plasticity and damage controlled by a same set of internal variables? What is the consequence if damage does or does not affect yielding?

4.2 Implementation of GTN model in a context of mixed velocity-pressure FE formulation

In the finite element (FE) analysis using isoparametric elements, the integration of the constitutive equations is carried out at integration points. This process is done incrementally and the solution is assumed to be known at the start of each increment. The strain increment $\Delta\boldsymbol{\epsilon}$ is known at the beginning and one needs to calculate the stresses and state variables at the end of the increment. Ortiz and Popov ([Ortiz and Popov, 1985]) found that the stability of the integration algorithm generally depends on the curvature of the yield surface and that the backward Euler method is unconditionally stable, independently of the smoothness of the yield function. The backward Euler method therefore was chosen by many authors in the literature for the integration of the elastoplastic equations and especially the pressure-dependent plasticity ([Aravas, 1987], [Zhang, 1995b], [Muhlich and Brocks, 2003]). In [Aravas, 1987], the author proposed a general method for the integration of pressure-dependent elastoplasticity, which employed the closest-return mapping algorithm and the decomposition of strain increments into hydrostatic and deviatoric components. A formulation for the calculation of the consistent linearization moduli was also presented, where one matrix inversion was required. Zhang [Zhang, 1995b] employed the Aravas' method and proposed an explicit formulation for the tangent moduli without matrix inversion. Govindarajan [Govindarajan and Aravas, 1995] then proposed another formulation to calculate this tangent modulus. Almost all the implementation works of Gurson-type models ([Gurson, 1977], [Needleman and Tvergaard, 1984]) were based on these formulations. In an effort to implement the Gurson-type models into the FE software Forge, the algorithms proposed by [Aravas, 1987] as well as the formulations of consistent tangent modulus have been analyzed and compared to determine a unified formulation. In this study, the mathematical basis of the formulation proposed by Aravas are firstly detailed and demonstrated, then the formulation of [Zhang, 1995b] and [Govindarajan and Aravas, 1995] are discussed.

Hereinafter, to simplify the notation, the bold-face symbols are used for second order tensors (e.g. $\boldsymbol{\sigma}$: stress tensor); the underlined bold-face symbols are used for vectors (e.g. $\underline{\boldsymbol{H}}^{\alpha}$: vector of internal state variables); the undertilded bold-face symbols are used for 4^{th} order tensors (e.g. $\underset{\sim}{\boldsymbol{D}}$: the 4^{th} order tangent tensor); the **(:)** symbol represents the doubly contracted tensor product (e.g. $(\underset{\sim}{\boldsymbol{D}} : \boldsymbol{\epsilon})_{ij} = D_{ijkl}\epsilon_{kl}$); the $\bullet$ symbol represents the matrix product; the $\otimes$ symbol represents the tensor product (e.g. $(\boldsymbol{I} \otimes \boldsymbol{I})_{ijkl} = \boldsymbol{I}_{ij}\boldsymbol{I}_{kl}$).

4.2.1 The GTN model

The yield function of GTN model ([Needleman and Tvergaard, 1984]) is recalled below:

$$\phi = \phi(p,q,\underline{\boldsymbol{H}}^{\alpha}) = \left(\frac{q}{\sigma_0}\right)^2 + 2q_1 f^* cosh(-\frac{3q_2}{2}\frac{p}{\sigma_0}) - 1 - q_3 f^{*2} = 0 \tag{4.27}$$

where ϕ is the yield function, which involves the first and second invariants of the deviatoric stress tensor; p is the hydrostatic pressure; q is the equivalent stress; σ_0 is the flow stress of the matrix material[6]; $\underline{\boldsymbol{H}}^{\alpha}$ (with α=1, 2...n) is a set of scalar state variables. In the GTN model, there are two state variables: the equivalent plastic strain $\bar{\epsilon}^p$ and the void volume fraction f. The set of elastoplastic constitutive relations is summarized:

1. The linear isotropic elastic behavior [7]:

$$\boldsymbol{\sigma} = \underset{\sim}{\boldsymbol{D}}^{\boldsymbol{e}} : \boldsymbol{\epsilon}^{\boldsymbol{e}} \tag{4.28}$$

[6] In case of hardening of matrix material, the flow stress is a function of the equivalent plastic strain, one of internal state variables.
[7] Throughout this study, the influence of porosity on elastic property is considered negligible and is not taken into account.

2. The strain-rate decomposition:
$$\dot{\boldsymbol{\epsilon}} = \dot{\boldsymbol{\epsilon}}^{\boldsymbol{e}} + \dot{\boldsymbol{\epsilon}}^{\boldsymbol{p}} \tag{4.29}$$

3. The isotropic yield function:
$$\phi\left(\boldsymbol{\sigma}, \underline{\boldsymbol{H}}^{\alpha}\right) = \phi\left(p, q, \underline{\boldsymbol{H}}^{\alpha}\right) \tag{4.30}$$

4. The plastic consistency condition:
$$\dot{\phi}\left(\boldsymbol{\sigma}, \underline{\boldsymbol{H}}^{\alpha}\right) = 0 \tag{4.31}$$

5. The plastic flow rule:
$$d\boldsymbol{\epsilon}^{\boldsymbol{p}} = d\lambda \frac{\partial g}{\partial \boldsymbol{\sigma}} \tag{4.32}$$
where $d\lambda$ is a positive scalar; $g\left(p, q, \underline{\boldsymbol{H}}^{\alpha}\right)$ is the flow potential. For an associative flow: $g = \phi$. By introducing the definition of $p = -\frac{1}{3}\boldsymbol{\sigma} : \boldsymbol{I}$ and $q = \sqrt{\frac{3}{2}\boldsymbol{S} : \boldsymbol{S}}$, where $\boldsymbol{I}$ is the second order identity tensor and $\boldsymbol{S}$ is the stress deviator, the flow rule becomes:
$$d\boldsymbol{\epsilon}^{\boldsymbol{p}} = d\lambda \left(-\frac{1}{3}\frac{\partial g}{\partial p}\boldsymbol{I} + \frac{\partial g}{\partial \boldsymbol{n}} \right) \tag{4.33}$$
where
$$\boldsymbol{n} = \frac{3}{2q}\boldsymbol{S} \tag{4.34}$$

6. The evolution law of internal state variables, which includes both plasticity and damage evolutions:
$$d\underline{\boldsymbol{H}}^{\alpha} = \underline{\boldsymbol{h}}^{\alpha}\left(d\boldsymbol{\epsilon}^{\boldsymbol{p}}, p, q, \underline{\boldsymbol{H}}^{\beta}\right) \tag{4.35}$$
This equation can be stated as: the evolution of each internal state variable is a function of plastic strain tensor, stress tensor, and internal state variables.

4.2.2 Integration of the pressure dependent plasticity model

The elastoplastic problem could be treated as a strain driven problem where the stress history is obtained from the strain history by means of an integration algorithm. The return mapping algorithms (elastic predictor/plastic corrector) together with the Euler implicit method have been largely used for the numerical integration of constitutive equations. A short summary of the return mapping algorithm is given in the following paragraph (see [Simo and Taylor, 1985], [Simo and Taylor, 1986] for more details concerning the mathematical basis).

4.2.2.1 The return mapping algorithms

At the beginning of time step (a *converged* configuration or an equilibrium state), the total and incremental strains are given, then the problem is to update the known variables, which are the solution at time t: $\boldsymbol{\epsilon}_t^{\boldsymbol{p}}$, $\boldsymbol{\epsilon}_t$, $\boldsymbol{\sigma}_t$, $\boldsymbol{H}_t^{\alpha}$, into the corresponding values at time $t + \Delta t$ (which is also a *converged* configuration). The return mapping algorithm consists in defining first, the elastic predictor, with the assumption of fully elastic strain increment:
$$\boldsymbol{\sigma}_{t+\Delta t}^{T} = \underset{\sim}{\boldsymbol{D}}^{\boldsymbol{e}} : \left(\boldsymbol{\epsilon}_t^{e} + \Delta\boldsymbol{\epsilon}\right) \tag{4.36}$$
where $\underset{\sim}{\boldsymbol{D}}^{\boldsymbol{e}}$ is the elastic continuum tangent modulus. If the resulting state lies outside the yield surface, this predicted value is taken as initial condition for the plastic relaxation process (the "closest-point" projection of $\boldsymbol{\sigma}_{t+\Delta t}^{T}$ onto the yield surface):
$$\boldsymbol{\sigma}_{t+\Delta t} = \boldsymbol{\sigma}_{t+\Delta t}^{T} - \underset{\sim}{\boldsymbol{D}}^{\boldsymbol{e}} : \Delta\boldsymbol{\epsilon}^{\boldsymbol{p}} \tag{4.37}$$
In the case of von Mises yield condition with associative flow rule and isotropic hardening, the closest point projection becomes the "radial return". The basic idea of this algorithm is illustrated in Fig. 4.8. This process, in fact, enforces the plastic consistency condition at the end of each time step. The process is completed by calculating the plastic strain increment $\Delta\boldsymbol{\epsilon}^{\boldsymbol{p}}$, which can be derived from the flow rule.

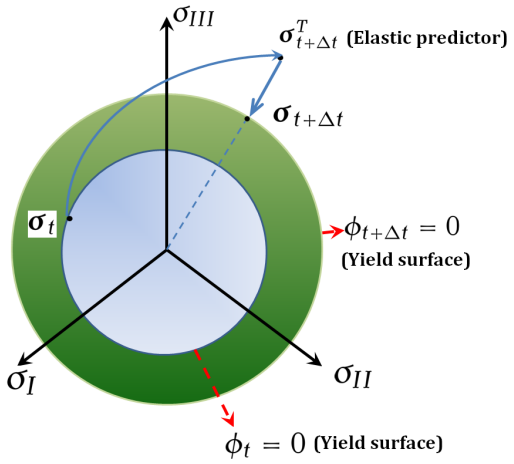

Fig. 4.8: *The return mapping algorithm with isotropic hardening in case of von Mises plasticity model. The return direction, which is normal to the yield surface, is also the radial direction in this case.*

In this algorithm, the equilibrium equations are written at the end of the time increment. Therefore, for the simplicity of notation, all the quantities not explicitly associated with time are assumed to be calculated at the end of the time increment, unless otherwise indicated. Let $\boldsymbol{S}^T$ be the deviatoric part of trial stress tensor $\boldsymbol{\sigma}^T$. Similarly to the decomposition of stress tensor into deviatoric and hydrostatic parts, plastic increment can also be decoupled into volumetric and deviatoric parts:

$$\Delta\boldsymbol{\epsilon}^p = \Delta\boldsymbol{\epsilon}^p_V + \Delta\boldsymbol{\epsilon}^p_D = \frac{1}{3}\Delta\epsilon_p\boldsymbol{I} + \Delta\epsilon_q\boldsymbol{n} \tag{4.38}$$

where $\boldsymbol{n}$ is defined in Eq. 4.34 and:

$$\Delta\epsilon_p = -\Delta\lambda\left(\frac{\partial g}{\partial p}\right) \tag{4.39}$$

$$\Delta\epsilon_q = \Delta\lambda\left(\frac{\partial g}{\partial q}\right) \tag{4.40}$$

There are two contributions to the plastic strain increment: a hydrostatic part $\frac{1}{3}\Delta\epsilon_p\boldsymbol{I}$ (which does not exist in von Mises plasticity) and a deviatoric part $\Delta\epsilon_q\boldsymbol{n}$. By eliminating $\Delta\lambda$ from Eqs. 4.39 and 4.40, a relation between $\Delta\epsilon_p$ and $\Delta\epsilon_q$ can be obtained:

$$\Delta\epsilon_p\left(\frac{\partial g}{\partial q}\right) + \Delta\epsilon_q\left(\frac{\partial g}{\partial p}\right) = 0 \tag{4.41}$$

Linear isotropic elasticity is assumed, which leads to:

$$D^e_{ijkl} = \left(K - \frac{2}{3}G\right)\delta_{ij}\delta_{kl} + 2G\delta_{ik}\delta_{jl} \tag{4.42}$$

where δ is the Kronecker symbol; $G = \frac{E}{2(1+\nu)}$ and $K = \frac{E}{3(1-2\nu)}$ are the elastic shear and bulk moduli respectively.

$$\underset{\sim}{\boldsymbol{D}}^{\boldsymbol{e}} : \Delta\boldsymbol{\epsilon}^{\boldsymbol{p}} = \underset{\sim}{\boldsymbol{D}}^{\boldsymbol{e}} : \left(\frac{1}{3}\Delta\epsilon_p\boldsymbol{I} + \Delta\epsilon_q\boldsymbol{n}\right) = K\Delta\epsilon_p\boldsymbol{I} + 2G\Delta\epsilon_q\boldsymbol{n} \tag{4.43}$$

Eq. 4.37 becomes:

$$\boldsymbol{\sigma} = \boldsymbol{\sigma}^T - \underset{\sim}{\boldsymbol{D}}^{\boldsymbol{e}} : \Delta\boldsymbol{\epsilon}^{\boldsymbol{p}} = \boldsymbol{\sigma}^T - K\Delta\epsilon_p\boldsymbol{I} - 2G\Delta\epsilon_q\boldsymbol{n} \tag{4.44}$$

The trial stress $\boldsymbol{\sigma}^T$ can be written as:

$$\boldsymbol{\sigma}^T = -p^T\boldsymbol{I} + \boldsymbol{S}^T = -p^T\boldsymbol{I} + \frac{2}{3}q^T\boldsymbol{n} \tag{4.45}$$

$$\boldsymbol{\sigma} = -p^T\boldsymbol{I} + \frac{2}{3}q^T\boldsymbol{n} - K\Delta\epsilon_p\boldsymbol{I} - 2G\Delta\epsilon_q\boldsymbol{n} \tag{4.46}$$

$$-p\boldsymbol{I} + \frac{2}{3}q\boldsymbol{n} = -p^T\boldsymbol{I} + \frac{2}{3}q^T\boldsymbol{n} - K\Delta\epsilon_p\boldsymbol{I} - 2G\Delta\epsilon_q\boldsymbol{n} \tag{4.47}$$

From the last equation, the return mapping procedure can be decoupled into two processes along $\boldsymbol{I}$ and $\boldsymbol{n}$ to update p and q:

$$p = p^T + K\Delta\epsilon_p \tag{4.48}$$
$$q = q^T - 3G\Delta\epsilon_q \tag{4.49}$$

To summarize, the problem of integrating the elastoplastic equations consists in solving the following set of non-linear equations:

$$\Delta\epsilon_p \left(\frac{\partial g}{\partial q}\right) + \Delta\epsilon_q \left(\frac{\partial g}{\partial p}\right) = 0 = \phi_1 \quad \text{(from Eq. 4.41)} \tag{4.50}$$
$$\phi\left(p,q,\underline{\boldsymbol{H}}^{\alpha}\right) = 0 = \phi_2 \quad \text{(from Eq. 4.30)} \tag{4.51}$$

with:

$$p = p^T + K\Delta\epsilon_p \tag{4.52}$$
$$q = q^T - 3G\Delta\epsilon_q \tag{4.53}$$
$$\Delta\underline{\boldsymbol{H}}^{\alpha} = \underline{\boldsymbol{h}}^{\alpha}\left(\Delta\boldsymbol{\epsilon}^{\boldsymbol{p}},p,q,\underline{\boldsymbol{H}}^{\boldsymbol{\beta}}\right) = \underline{\boldsymbol{h}}^{\alpha}\left(\Delta\epsilon_p,\Delta\epsilon_q,p,q,\underline{\boldsymbol{H}}^{\boldsymbol{\beta}}\right) \tag{4.54}$$

$\Delta\epsilon_p$ and $\Delta\epsilon_q$ are the two primary unknown variables in the system of two equations 4.50 and 4.51. These equations are solved iteratively using the Newton-Raphson algorithm.

4.2.2.2 The evolution of internal state variables

This section deals with the evolution of internal state variables $\underline{\boldsymbol{H}}^{\alpha}$ (i.e. the equivalent plastic strain $\bar{\epsilon}^p$ and the void volume fraction f for the GTN model). The equivalent plastic strain is assumed to vary according to the equivalent plastic work:

$$(1-f)\sigma_0 d\bar{\epsilon}^p = \boldsymbol{\sigma} : d\boldsymbol{\epsilon}^p \tag{4.55}$$

or:

$$\Delta\bar{\epsilon}^p = \frac{\boldsymbol{\sigma} : \Delta\boldsymbol{\epsilon}^p}{(1-f)\sigma_0} \tag{4.56}$$
$$\Delta\bar{\epsilon}^p = \frac{(-p\boldsymbol{I} + \frac{2}{3}q\boldsymbol{n}) : \Delta\boldsymbol{\epsilon}^p}{(1-f)\sigma_0} \tag{4.57}$$

By substituting $\Delta\boldsymbol{\epsilon}^p$ from Eq. 4.38:

$$\Delta\bar{\epsilon}^p = \frac{(-p\boldsymbol{I} + \frac{2}{3}q\boldsymbol{n}) : \left(\frac{1}{3}\Delta\epsilon_p\boldsymbol{I} + \Delta\epsilon_q\boldsymbol{n}\right)}{(1-f)\sigma_0} \tag{4.58}$$
$$\Delta\bar{\epsilon}^p = \frac{-p\Delta\epsilon_p + q\Delta\epsilon_q}{(1-f)\sigma_0} \tag{4.59}$$

The variation of void volume fraction is partly due to growth of existing voids and partly due to nucleation of new voids:

$$\dot{f} = \dot{f}_{nucleation} + \dot{f}_{growth} \tag{4.60}$$

From Eqs. 4.2 and 4.9

$$\dot{f}_{growth} = (1-f)tr(\dot{\boldsymbol{\epsilon}}^p) \tag{4.61}$$
$$\dot{f}_{nucleation} = \frac{f_N}{S_N\sqrt{2\pi}} exp\left[\frac{-1}{2}\left(\frac{\bar{\epsilon}^p - \epsilon_N}{S_N}\right)^2\right]\dot{\bar{\epsilon}}^p = A\left(\bar{\epsilon}^p\right)\dot{\bar{\epsilon}}^p \tag{4.62}$$

The incremental form of voids change can be written as:

$$\Delta f = \Delta f_{nucleation} + \Delta f_{growth} = (1-f)\Delta\epsilon_p + A\left(\bar{\epsilon}^p\right)\Delta\bar{\epsilon}^p \tag{4.63}$$

where the increment of equivalent plastic strain can be calculated by Eq. 4.57. Finally, the evolutions of the two internal variables are summarized as:

Evolutions of state variables

$$\Delta\bar{\epsilon}^p = \Delta H^1 = h^1 = \frac{-p\Delta\epsilon_p + q\Delta\epsilon_q}{(1-f)\sigma_0} \tag{4.64}$$

$$\Delta f = \Delta H^2 = h^2 = (1-f)\Delta\epsilon_p + A(\bar{\epsilon}^p)\Delta\bar{\epsilon}^p \tag{4.65}$$

4.2.2.3 Solution of the elastoplastic equation

By linearization of Eqs. 4.50 and 4.51, we obtain the following system of equations to solve for the corrections $\delta\epsilon_p$ and $\delta\epsilon_q$ of plastic increments at each Newton's iteration:

$$J_{11}\delta\epsilon_p + J_{12}\delta\epsilon_q = Y_1 \tag{4.66}$$

$$J_{21}\delta\epsilon_p + J_{22}\delta\epsilon_q = Y_2 \tag{4.67}$$

where: $Y_1 = -\left[\Delta\epsilon_p\left(\frac{\partial g}{\partial q}\right) + \Delta\epsilon_q\left(\frac{\partial g}{\partial p}\right)\right]$, $Y_2 = -\phi(p,q,\underline{\boldsymbol{H}}^{\alpha})$ and:

$$J_{11} = \frac{\partial\phi_1}{\partial\Delta\epsilon_p} \qquad J_{12} = \frac{\partial\phi_1}{\partial\Delta\epsilon_q}$$
$$J_{21} = \frac{\partial\phi_2}{\partial\Delta\epsilon_p} \qquad J_{22} = \frac{\partial\phi_2}{\partial\Delta\epsilon_q} \tag{4.68}$$

These coefficients are given in Appendix B.1. By solving this system of equations, the values of $\Delta\epsilon_p$ and $\Delta\epsilon_q$ are then updated:

$$\Delta\epsilon_p = \Delta\epsilon_p + \delta\epsilon_p \tag{4.69}$$

$$\Delta\epsilon_q = \Delta\epsilon_q + \delta\epsilon_q \tag{4.70}$$

The updated stress states p and q are obtained by Eqs. 4.52 and 4.53. The internal state variables are updated by solving the set of equations 4.64 and 4.65. This iterative loop is carried out until $\Delta\epsilon_p$ and $\Delta\epsilon_q$ converge (i.e. $\delta\epsilon_p$ and $\delta\epsilon_q <$ tolerance value). Note that the tolerance value of each time increment depends on the plastic strain increment. This tolerance is around (10^{-10})[8]. Moreover, additional conditions for $\Delta\epsilon_p$ and $\Delta\epsilon_q$ are applied:

$$\begin{cases} 0 \leq \Delta\epsilon_q \leq \frac{q^T}{3G} & \text{(from Eq. 4.49: } q > 0\text{)} \\ \Delta\epsilon_{p_{min}} \leq \Delta\epsilon_p \leq \Delta\epsilon_{p_{max}} & \text{(from Eq. 4.64: } \Delta\bar{\epsilon}^p > 0\text{)} \end{cases} \tag{4.71}$$

where $\Delta\epsilon_{p_{min}} = \frac{-p^T-\sqrt{\Delta}}{2K}$ and $\Delta\epsilon_{p_{max}} = \frac{-p^T+\sqrt{\Delta}}{2K}$, with $\Delta = (p^T)^2 + 4K(q^T - 3G\Delta\epsilon_q)\Delta\epsilon_q$.

Fracture management For the GTN model, when coalescence is activated, numerical problems might occur when $f > f_c$, especially when $f \to f_f$ (i.e. fracture). In order to avoid the total loss of bearing ability (when $f \to f_f$, $\boldsymbol{\sigma} \to \mathbf{0}$), we defined the fracture at $0.98f_f$ instead of f_f. Moreover, SUB-INCREMENT technique was used when $f > f_c$, which consists in dividing the *local time step* (i.e. in local integration at Gauss point) into N sub-time steps while the **global time step** is kept unchanged. The SUB-INCREMENT technique was also applied when the strain or damage increment is higher than certain values.

4.2.3 Consistent tangent modulus

In an implicit FE code, the equilibrium equations are written at the end of each time increment, resulting in a set of non-linear equations for the nodal unknowns (e.g. displacement in Abaqus; velocity, pressure in Forge2009®). As stated in [Nagtegaal, 1982] and [Simo and Taylor, 1985], if a full Newton

[8] Tolerance = $10^{-8}\max(\Delta\epsilon_p, \Delta\epsilon_q, \sigma_0(t)/E)$.

scheme is employed to solve these non-linear equations, it is necessary to use the tangent modulus consistent[9] with the integration algorithm to preserve the quadratic rate of asymptotic convergence of Newton's method. Aravas ([Aravas, 1987]) proposed a formulation to calculate the tangent modulus, which requires the inversion of matrix (see [Aravas, 1987] for more details). Such an inversion leads to numerical problems when the Euler backward algorithm is employed as stated in [Zhang, 1995b]. Govindarajan and Aravas ([Govindarajan and Aravas, 1995]) and Zhang ([Zhang, 1995b]) proposed two formulations to obtain the discrete tangent modulus where no matrix inversion is required. The linearization procedures of ([Aravas, 1987], [Govindarajan and Aravas, 1995]) and [Zhang, 1995b] are summarized below. The resulting formulations will also be compared to demonstrate a unique formulation for the tangent modulus.

4.2.3.1 Formulation of Aravas ([Aravas, 1987], [Govindarajan and Aravas, 1995])

We start from the elasticity equation:

$$\boldsymbol{\sigma}_{t+\Delta t} = \underset{\sim\sim}{\boldsymbol{D}}^{\mathbf{e}} : (\boldsymbol{\epsilon}_{t+\Delta t} - \boldsymbol{\epsilon}^{\mathbf{p}}{}_{t+\Delta t}) = \underset{\sim\sim}{\boldsymbol{D}}^{\mathbf{e}} : \left(\boldsymbol{\epsilon}_{t+\Delta t} - \boldsymbol{\epsilon}^{\mathbf{p}}{}_{t} - \frac{1}{3}\Delta\epsilon_p \boldsymbol{I} - \Delta\epsilon_q \boldsymbol{n}\right) \tag{4.72}$$

$$\partial\boldsymbol{\sigma} = \underset{\sim\sim}{\boldsymbol{D}}^{\mathbf{e}} : \left(\partial\boldsymbol{\epsilon} - \frac{1}{3}\partial\Delta\epsilon_p \boldsymbol{I} - \partial\Delta\epsilon_q \boldsymbol{n} - \Delta\epsilon_q \frac{\partial \boldsymbol{n}}{\partial \boldsymbol{\sigma}} : \partial\boldsymbol{\sigma}\right) \tag{4.73}$$

With the definition on $\boldsymbol{n}$ in Eq. 4.34, its partial derivation with respect to $\boldsymbol{\sigma}$ can be written as:

$$\frac{\partial \boldsymbol{n}}{\partial \boldsymbol{\sigma}} = \frac{1}{q}\left(\frac{3}{2}\underset{\sim\sim}{\boldsymbol{J}} - \frac{1}{2}\right) \tag{4.74}$$

where $\underset{\sim\sim}{\boldsymbol{J}}$ is the 4^{th} order identity tensor ($J_{ijkl} = \frac{\delta_{ik}\delta_{jl}+\delta_{il}\delta_{jk}}{2}$). The next step consists in calculating the variation of volumetric and deviatoric plastic strain increments in term of $\partial\boldsymbol{\sigma}$. Eqs. 4.50 and 4.51 can be written as:

$$\phi(p, q, \underline{\boldsymbol{H}^{\boldsymbol{\alpha}}}) = g_1 = 0 \tag{4.75}$$

$$\Delta\epsilon_p \left(\frac{\partial g}{\partial q}\right) + \Delta\epsilon_q \left(\frac{\partial g}{\partial p}\right) = g_2 = 0 \tag{4.76}$$

By differentiating these two equations:

$$dg_1 = \frac{\partial\phi}{\partial p}\partial p + \frac{\partial\phi}{\partial q}\partial q + \sum_{\alpha=1}^{n}\frac{\partial\phi}{\partial H^\alpha}\partial H^\alpha = 0 \tag{4.77}$$

$$dg_2 = \left(\frac{\partial g}{\partial q}\right)\partial\Delta\epsilon_p + \Delta\epsilon_p\partial\left(\frac{\partial g}{\partial q}\right) + \left(\frac{\partial g}{\partial p}\right)\partial\Delta\epsilon_q + \Delta\epsilon_q\partial\left(\frac{\partial g}{\partial p}\right) = 0 \tag{4.78}$$

The two terms $\frac{\partial g}{\partial p}$ and $\frac{\partial g}{\partial q}$ can be functions of p, q and $\underline{\boldsymbol{H}^{\boldsymbol{\alpha}}}$, so their differentiations can be developed as:

$$\partial\left(\frac{\partial g}{\partial p}\right) = \frac{\partial^2 g}{\partial p^2}\partial p + \frac{\partial^2 g}{\partial p\partial q}\partial q + \sum_{\alpha=1}^{n}\frac{\partial^2 g}{\partial p\partial H^\alpha}\partial H^\alpha \tag{4.79}$$

$$\partial\left(\frac{\partial g}{\partial q}\right) = \frac{\partial^2 g}{\partial q\partial p}\partial p + \frac{\partial^2 g}{\partial q^2}\partial q + \sum_{\alpha=1}^{n}\frac{\partial^2 g}{\partial q\partial H^\alpha}\partial H^\alpha \tag{4.80}$$

The derivation of internal state variables $\underline{\boldsymbol{H}^{\boldsymbol{\alpha}}}$:

$$\partial H^\alpha = \sum_{\beta=1}^{n} c_{\alpha\beta}\left[\frac{\partial h^\beta}{\partial\Delta\epsilon_p}\partial\Delta\epsilon_p + \frac{\partial h^\beta}{\partial\Delta\epsilon_q}\partial\Delta\epsilon_q + \frac{\partial h^\beta}{\partial p}\partial p + \frac{\partial h^\beta}{\partial q}\partial q\right] \tag{4.81}$$

where $c_{\alpha\beta}$ is the inverse matrix of $\delta_{\alpha\beta} - \frac{\partial h^\alpha}{\partial H^\beta}$. The detailed demonstration is given in Appendix B.2. Finally, the derivatives of p and q are expressed as functions of $\partial\Delta\epsilon_p$ and $\partial\Delta\epsilon_q$:

$$\partial p = \partial p^T + K\partial\Delta\epsilon_p = -K\boldsymbol{I} : \partial\boldsymbol{\epsilon} + K\partial\Delta\epsilon_p \tag{4.82}$$

$$\partial q = \partial q^T - 3G\partial\Delta\epsilon_q = 2G\boldsymbol{n} : \partial\boldsymbol{\epsilon} - 3G\partial\Delta\epsilon_q \tag{4.83}$$

[9]The consistent modulus in the linearized problem is the modulus obtained by the "consistent linearization" of the response function resulting from the integration algorithm. The procedure to obtain the consistent linearization is discussed in [Marsden and Hughes, 1983].

By substituting Eqs. 4.81, 4.82, 4.83 in Eq. 4.77, we can obtain:

$$\begin{aligned} dg_1 = 0 = \frac{\partial \phi}{\partial p}\left[-K\boldsymbol{I}:\partial\boldsymbol{\epsilon} + K\partial\Delta\epsilon_p\right] + \frac{\partial \phi}{\partial q}\left[2G\boldsymbol{n}:\partial\boldsymbol{\epsilon} - 3G\partial\Delta\epsilon_q\right] \\ + \sum_{\alpha=1}^{n}\sum_{\beta=1}^{n}\frac{\partial \phi}{\partial H^\alpha}c_{\alpha\beta}\left[\frac{\partial h^\beta}{\partial \Delta\epsilon_p}\partial\Delta\epsilon_p + \frac{\partial h^\beta}{\partial \Delta\epsilon_q}\partial\Delta\epsilon_q + \frac{\partial h^\beta}{\partial p}\partial p + \frac{\partial h^\beta}{\partial q}\partial q\right] \end{aligned} \tag{4.84}$$

or:

$$\begin{aligned} &\partial\Delta\epsilon_p\left[K\frac{\partial \phi}{\partial p} + \sum_{\alpha=1}^{n}\sum_{\beta=1}^{n}\frac{\partial \phi}{\partial H^\alpha}c_{\alpha\beta}\left(\frac{\partial h^\beta}{\partial \Delta\epsilon_p} + K\frac{\partial h^\beta}{\partial p}\right)\right] + \partial\Delta\epsilon_q\left[-3G\frac{\partial \phi}{\partial q} + \sum_{\alpha=1}^{n}\sum_{\beta=1}^{n}\frac{\partial \phi}{\partial H^\alpha}c_{\alpha\beta}\left(\frac{\partial h^\beta}{\partial \Delta\epsilon_q} - 3G\frac{\partial h^\beta}{\partial q}\right)\right] \\ &= \left[K\left(\frac{\partial \phi}{\partial p} + \sum_{\alpha=1}^{n}\sum_{\beta=1}^{n}\frac{\partial \phi}{\partial H^\alpha}c_{\alpha\beta}\frac{\partial h^\beta}{\partial p}\right)\right]\boldsymbol{I}:\partial\boldsymbol{\epsilon} + \left[-2G\left(\frac{\partial \phi}{\partial q} + \sum_{\alpha=1}^{n}\sum_{\beta=1}^{n}\frac{\partial \phi}{\partial H^\alpha}c_{\alpha\beta}\frac{\partial h^\beta}{\partial q}\right)\right]\boldsymbol{n}:\partial\boldsymbol{\epsilon} \end{aligned} \tag{4.85}$$

The last equation can be written as:

$$A_{11}\partial\Delta\epsilon_p + A_{12}\partial\Delta\epsilon_q = (B_{11}\boldsymbol{I} + B_{12}\boldsymbol{n}):\partial\boldsymbol{\epsilon} \tag{4.86}$$

Similarly, Eq. 4.78 can also be simplified as:

$$A_{21}\partial\Delta\epsilon_p + A_{22}\partial\Delta\epsilon_q = (B_{21}\boldsymbol{I} + B_{22}\boldsymbol{n}):\partial\boldsymbol{\epsilon} \tag{4.87}$$

where the coefficients A_{ij} and B_{ij} $(1 \leq i,j \leq 2)$ are given in Appendix B.3. Finally, we obtain a system of two equations 4.86 and 4.87 which can be solved for $\partial\Delta\epsilon_p$ and $\partial\Delta\epsilon_q$:

$$\begin{cases} \partial\Delta\epsilon_p &= \frac{1}{D}\left(A_{22}\left(B_{11}\boldsymbol{I} + B_{12}\boldsymbol{n}\right):\partial\boldsymbol{\epsilon} - A_{12}\left(B_{21}\boldsymbol{I} + B_{22}\boldsymbol{n}\right):\partial\boldsymbol{\epsilon}\right) \\ \partial\Delta\epsilon_q &= \frac{1}{D}\left(A_{11}\left(B_{21}\boldsymbol{I} + B_{22}\boldsymbol{n}\right):\partial\boldsymbol{\epsilon} - A_{21}\left(B_{11}\boldsymbol{I} + B_{12}\boldsymbol{n}\right):\partial\boldsymbol{\epsilon}\right) \end{cases} \tag{4.88}$$

where D is the determinant of the Jacobian matrix:

$$D = A_{11}A_{22} - A_{12}A_{21} \tag{4.89}$$

These equations can be rewritten as:

$$\begin{cases} \partial\Delta\epsilon_p &= \left(\frac{A_{22}B_{11} - A_{12}B_{21}}{D}\right)\boldsymbol{I}:\partial\boldsymbol{\epsilon} + \left(\frac{A_{22}B_{12} - A_{12}B_{22}}{D}\right)\boldsymbol{n}:\partial\boldsymbol{\epsilon} \\ \partial\Delta\epsilon_q &= \left(\frac{A_{11}B_{21} - A_{21}B_{11}}{D}\right)\boldsymbol{I}:\partial\boldsymbol{\epsilon} + \left(\frac{A_{11}B_{22} - A_{21}B_{12}}{D}\right)\boldsymbol{n}:\partial\boldsymbol{\epsilon} \end{cases} \tag{4.90}$$

or:

$$\begin{cases} \partial\Delta\epsilon_p &= \left(m_{pI}\boldsymbol{I} + m_{pn}\boldsymbol{n}\right):\partial\boldsymbol{\epsilon} \\ \partial\Delta\epsilon_q &= \left(m_{qI}\boldsymbol{I} + m_{qn}\boldsymbol{n}\right):\partial\boldsymbol{\epsilon} \end{cases} \tag{4.91}$$

where:

$$\begin{aligned} m_{pI} &= \tfrac{A_{22}B_{11} - A_{12}B_{21}}{D}, \quad m_{pn} = \tfrac{A_{22}B_{12} - A_{12}B_{22}}{D} \\ m_{qI} &= \tfrac{A_{11}B_{21} - A_{21}B_{11}}{D}, \quad m_{qn} = \tfrac{A_{11}B_{22} - A_{21}B_{12}}{D} \end{aligned} \tag{4.92}$$

By substituting $\Delta\epsilon_p$ and $\Delta\epsilon_q$ from Eq. 4.91 into Eq. 4.73, the expression of tangent modulus appearing in equation (30) of [Govindarajan and Aravas, 1995] is obtained:

$$\underset{\sim}{\boldsymbol{D}}^{ep} = C_1\underset{\sim}{\boldsymbol{J}}' + C_2\boldsymbol{I}\otimes\boldsymbol{I} + C_3'\boldsymbol{I}\otimes\boldsymbol{n} + C_3''\boldsymbol{n}\otimes\boldsymbol{I} + C_4\boldsymbol{n}\otimes\boldsymbol{n} \tag{4.93}$$

where $\underset{\sim}{\boldsymbol{J}}' = \underset{\sim}{\boldsymbol{J}} - 1/3\boldsymbol{I}\otimes\boldsymbol{I}$. The coefficients C_1, C_2, C_3', C_3'' are defined as:

$$\begin{aligned} C_1 &= 2G\tfrac{q}{q^T}, \quad C_2 = K(1 - m_{pI}), \quad C_3' = -2Gm_{qI} \\ C_3'' &= -Km_{pn}, \quad C_4 = \tfrac{4G^2\Delta\epsilon_q}{q^T} - 2Gm_{qn} \end{aligned} \tag{4.94}$$

4.2.3.2 Formulation of Zhang ([Zhang, 1995b])

Zhang developed separately the variation of $\boldsymbol{S}$ and p, and combined them to have the differentiation of $\boldsymbol{\sigma}$. From Eq. 4.49:

$$\partial q = \partial q^T - 3G\partial\Delta\epsilon_q, \text{ with: } q^T = 2G\overline{e}^T \text{ and: } \overline{e}^T = \sqrt{\frac{3}{2}(\mathbf{e}^T : \mathbf{e}^T)} \tag{4.95}$$

where $\mathbf{e}^T$ denotes the deviatoric part of $\boldsymbol{\epsilon}$. The trial deviatoric stress and its correction:

$$\boldsymbol{S}^T = 2G(\mathbf{e}_t^e + \Delta\mathbf{e}) = 2G(\mathbf{e}^T) \tag{4.96}$$

$$\boldsymbol{S} = \boldsymbol{S}^T - 2G\Delta\mathbf{e}^p = \boldsymbol{S}^T - 2G\Delta\epsilon_q\boldsymbol{n} = \boldsymbol{S}^T - \frac{3G}{q}\Delta\epsilon_q\boldsymbol{S} \rightarrow (1 + \frac{3G}{q}\Delta\epsilon_q)\boldsymbol{S} = \boldsymbol{S}^T \tag{4.97}$$

By differentiating this equation and accounting for $\partial q = 3G\left(\frac{\boldsymbol{S}^T}{q^T}\partial\mathbf{e}^T - \partial\Delta\epsilon_q\right)$ (from Eq. 4.95), one can obtain the variation of $\boldsymbol{S}$:

$$\partial\boldsymbol{S} = \left(2G\frac{q}{q^T}\underset{\sim}{\underset{\sim}{\boldsymbol{I}}} + \frac{4G^2}{q^T}\Delta\epsilon_q\boldsymbol{n}\otimes\boldsymbol{n}\right) : \partial\mathbf{e}^T - 2G\partial\Delta\epsilon_q\boldsymbol{n} \tag{4.98}$$

The differentiation of hydrostatic pressure can be deduced from Eq. 4.48:

$$\partial p = \partial p^T + K\partial\Delta\epsilon_p = -K\boldsymbol{I}\partial\boldsymbol{\epsilon} + K\partial\Delta\epsilon_p \tag{4.99}$$

From the relation: $\mathbf{e}^T = (\underset{\sim}{\underset{\sim}{\boldsymbol{I}}} - 1/3\boldsymbol{I}\otimes\boldsymbol{I})\boldsymbol{\epsilon}$ (for more details about tensor calculation, see [Itskov, 2000]) and Eq. 4.99, one can obtain:

$$\partial\boldsymbol{\sigma} = \left(2G\frac{q}{q^T}\underset{\sim}{\underset{\sim}{\boldsymbol{I}}} + \frac{4G^2}{q^T}\Delta\epsilon_q\boldsymbol{n}\otimes\boldsymbol{n} + (K - \frac{2G}{3}\frac{q}{q^T}\boldsymbol{I}\otimes\boldsymbol{I})\right) : \partial\boldsymbol{\epsilon} - K\boldsymbol{I}\partial\Delta\epsilon_p - 2G\partial\Delta\epsilon_q\boldsymbol{n} \tag{4.100}$$

Zhang then solved $\partial\Delta\epsilon_p$ and $\partial\Delta\epsilon_q$ as function of $\partial\boldsymbol{\epsilon}$ from the following system of equations (equivalent to [Aravas, 1987]):

$$A'_{11}\partial\Delta\epsilon_p + A'_{12}\partial\Delta\epsilon_q = \left(B'_{11}\boldsymbol{I} + B'_{12}\boldsymbol{n}\right) : \partial\boldsymbol{\sigma} \tag{4.101}$$

$$A'_{21}\partial\Delta\epsilon_p + A'_{22}\partial\Delta\epsilon_q = \left(B'_{21}\boldsymbol{I} + B'_{22}\boldsymbol{n}\right) : \partial\boldsymbol{\sigma} \tag{4.102}$$

then substituted into Eq. 4.100 to obtain the relation between $\partial\boldsymbol{\sigma}$ and $\partial\boldsymbol{\epsilon}$. The expression of the consistent tangent modulus could be deduced (Eq. 5.30 in [Zhang, 1995b]):

$$\underset{\sim}{\underset{\sim}{\boldsymbol{D}}}^{\boldsymbol{ep}} = d_0\underset{\sim}{\underset{\sim}{\boldsymbol{I}}} + d_1\boldsymbol{I}\otimes\boldsymbol{I} + d_2\boldsymbol{n}\otimes\boldsymbol{n} + d_3\boldsymbol{I}\otimes\boldsymbol{n} + d_4\boldsymbol{n}\otimes\boldsymbol{I} \tag{4.103}$$

where:

$$\begin{aligned} d_0 &= 2G\tfrac{q}{q^T}, \quad d_1 = K - \tfrac{2G}{3}\tfrac{q}{q^T} - 3K^2C_{11}, \\ d_2 &= \tfrac{4G^2}{q^T}\Delta\epsilon_q - 4G^2C_{22}, \quad d_3 = -2GKC_{12}, \quad d_4 = 2GKC_{21} \end{aligned} \tag{4.104}$$

and:

$$C_{11} = \left[(A'_{22} + 3GB'_{22})B'_{11} - (A'_{12} + 3GB'_{12})B'_{21}\right]/\Delta \tag{4.105}$$

$$C_{12} = \left[(A'_{22} + 3GB'_{22})B'_{12} - (A'_{12} + 3GB'_{12})B'_{22}\right]/\Delta \tag{4.106}$$

$$C_{21} = \left[(A'_{11} + 3KB'_{11})B'_{21} - (A'_{21} + 3KB'_{21})B'_{11}\right]/\Delta \tag{4.107}$$

$$C_{21} = \left[(A'_{11} + 3KB'_{11})B'_{22} - (A'_{21} + 3KB'_{21})B'_{12}\right]/\Delta \tag{4.108}$$

with:

$$\Delta = (A'_{11} + 3KB'_{11})(A'_{22} + 3GB'_{22}) - (A'_{12} + 3GB'_{12})(A'_{21} + 3KB'_{21}) \tag{4.109}$$

All the involved coefficients are reported in Appendix B.4.

4.2.4 Toward a unified formulation for calculating the consistent tangent modulus

In an effort to determine an efficient formulation for the consistent tangent modulus, the expression proposed by Aravas (Eq. 4.93) and the formulation of Zhang (Eq. 4.103) are compared here. The following proof shows that the two formulations are totally identical and one can use either of these two equations to obtain the "explicit" tangent modulus. In order to demonstrate the equivalence of these equations, the coefficients associated with the tensor cross products are compared. Starting from Eqs. B.17, B.21, B.25, B.28 one can prove that:

$$B'_{21} = B_{11}/3K \quad \text{and} \quad B'_{11} = B_{21}/3K \tag{4.110}$$

Moreover, the following relations can also be demonstrated:

$$\begin{aligned} A'_{22} + 3GB'_{22} &= A_{12} \qquad A'_{12} + 3GB'_{12} = A_{22} \\ A'_{11} + 3KB'_{11} &= A_{21} \qquad A'_{21} + 3KB'_{21} = A_{11} \end{aligned} \tag{4.111}$$

Eq. 4.109 therefore can be written as:

$$\Delta = (A'_{11}+3KB'_{11})(A'_{22}+3GB'_{22})-(A'_{12}+3GB'_{12})(A'_{21}+3KB'_{21}) = A_{21}A_{12}-A_{22}A_{11} = D \qquad \text{(Eq. 4.89)} \tag{4.112}$$

From Eqs. 4.92, 4.110 and 4.112 the coefficient C_{11} of Zhang's approach can be reduced as:

$$C_{11} = \left[(A'_{22} + 3GB'_{22})B'_{11} - (A'_{12} + 3GB'_{12})B'_{21}\right]/\Delta = -\left(\frac{B_{21}}{3K}A_{12} - \frac{B_{11}}{3K}A_{22}\right)/D = \frac{m_{pi}}{3K} \tag{4.113}$$

Similarly, one can obtain the following relations with the same procedure:

$$m_{qI} = KC_{12}, \qquad m_{pn} = 6GC_{21}, \qquad m_{qn} = 2GC_{22} \tag{4.114}$$

Finally, from Eqs. 4.94, 4.104 and 4.114, one can obtain:

$$d_0 \underset{\sim}{\boldsymbol{J}} + d_1 \boldsymbol{I} \otimes \boldsymbol{I} = C_1 \underset{\sim}{\boldsymbol{J}'} + C_2 \boldsymbol{I} \otimes \boldsymbol{I} \tag{4.115}$$

$$C'_3 = d_3 \tag{4.116}$$

$$C''_3 = d_4 \tag{4.117}$$

$$C_4 = d_2 \tag{4.118}$$

These last equations proved the equivalence between the two formulations for calculating the tangent modulus proposed by Aravas (Eq. 4.93) and Zhang (Eq. 4.103).

4.2.5 Modification of global solver

Since the default solver of Forge2009® does not account for the plastic compressibility of materials, some modifications were applied in the assembly of the global Hessian matrix. Let us recall the weak formulation for the MINI-element (see subsection 1.2.6.2):

$$\text{Find } (\vec{v}^l, \vec{b}, p_h) \in \mathcal{V}_h \times \mathcal{B}_h \times \mathcal{P}_h \quad \begin{cases} \int_{\Omega_h} \boldsymbol{s}(\vec{\boldsymbol{v}}^{\boldsymbol{l}}) : \dot{\boldsymbol{\epsilon}}(\vec{\boldsymbol{v}}^{\boldsymbol{l}*}) d\Omega_h - \int_{\Omega_h} p_h(\vec{\nabla}.\vec{v}^{l*}) d\Omega_h - \int_{\partial\Omega_{ht}} \vec{t}_0.\vec{v}^{l*} d\Gamma_h = 0 \\ \int_{\Omega_h} \boldsymbol{s}(\vec{\boldsymbol{b}}) : \dot{\boldsymbol{\epsilon}}(\vec{\boldsymbol{b}}^{*}) d\Omega_h - \int_{\Omega_h} p_h(\vec{\nabla}.\vec{b}^{*}) d\Omega_h = 0 \\ \int_{\Omega_h} p_h^* \left(-\vec{\nabla}.(\vec{v}^l + \vec{b}) - \frac{\dot{p}_h}{\kappa} + trace(\dot{\boldsymbol{\epsilon}}^{\boldsymbol{p}})\right) d\Omega_h = 0 \\ \forall (\vec{v}^{l*}, \vec{b}^*, p_h^*) \in \mathcal{L}_h^0 \times \mathcal{B}_h \times \mathcal{P}_h \end{cases} \tag{4.119}$$

The $trace(\dot{\boldsymbol{\epsilon}}^{\boldsymbol{p}})$ term in the third equation is not equal to zero (Eq. 4.39):

$$trace(\dot{\boldsymbol{\epsilon}}^{\boldsymbol{p}}) = -\frac{\Delta\lambda}{\Delta t}\left(\frac{\partial g}{\partial p}\right) = -\dot{\lambda}\left(\frac{\partial g}{\partial p}\right) \tag{4.120}$$

By accounting for this term, the residual term $\underline{\mathbf{R}}_e^p$ as well as $\mathbf{H}_e^{pl}$ and $\mathbf{H}_e^{pp}$ must be modified:

$$\underline{\mathbf{R}}_e^p \Rightarrow \underline{\mathbf{R}}_e^p + (-\int_{\Omega_e} N_n^l N_m^l \dot{\lambda} \left(\frac{\partial g}{\partial p}\right) J(\vec{x}) d\Omega_e) = \underline{\mathbf{R}}_e^p + \underline{\mathbf{R}}_e^{p'} \tag{4.121}$$

$$\mathbf{H}_e^{pl} \Rightarrow \mathbf{H}_e^{pl} + \frac{\partial \underline{\mathbf{R}}_e^{p'}}{\partial \vec{v}^l} \tag{4.122}$$

$$\mathbf{H}_e^{pp} \Rightarrow \mathbf{H}_e^{pp} + \frac{\partial \underline{\mathbf{R}}_e^{p'}}{\partial p_h} \tag{4.123}$$

All the corresponding derivations are reported in Appendix B.6.

4.2.6 Tangent moduli in the context of mixed velocity-pressure FE formulation with $P1^+/P1$ element

Consider the two terms $\mathbf{H}^{ll} = \frac{\partial \mathbf{R}^{ll}}{\partial \vec{v}^l}$ and $\mathbf{H}^{bb} = \frac{\partial \mathbf{R}^{bb}}{\partial \vec{b}}$. The calculations of these terms lead to the calculations of $\frac{\partial \boldsymbol{s}(\vec{\boldsymbol{v}}^l)}{\partial \dot{\boldsymbol{\epsilon}}(\vec{\boldsymbol{v}}^l)} = \frac{\partial \boldsymbol{s}(\vec{\boldsymbol{v}}^l)}{\partial \boldsymbol{\epsilon}(\vec{\boldsymbol{v}}^l)} dt$ and $\frac{\partial \boldsymbol{s}(\vec{\boldsymbol{b}})}{\partial \dot{\boldsymbol{\epsilon}}(\vec{\boldsymbol{b}})} = \frac{\partial \boldsymbol{s}(\vec{\boldsymbol{b}})}{\partial \boldsymbol{\epsilon}(\vec{\boldsymbol{b}})} dt$, which are called the "linear tangent modulus" (corresponding to the linear velocity) and the "bubble tangent modulus" (corresponding to the bubble velocity) respectively. In the context of mixed velocity-pressure FE formulation with $P1^+/P1$ element, one has to calculate these two tangent moduli instead of one as in standard displacement FE formulation. At each time increment, the linear tangent modulus can be deduced directly from the formulation in 4.2.3 (Eq. 4.93 or Eq. 4.103):

$$\frac{\partial \boldsymbol{s}(\vec{\boldsymbol{v}}^l)}{\partial \boldsymbol{\epsilon}(\vec{\boldsymbol{v}}^l)} = \underset{\approx}{\boldsymbol{D}}^{ep} \left[\underset{\approx}{\boldsymbol{I}} - 1/3 \boldsymbol{I} \otimes \boldsymbol{I}\right] \tag{4.124}$$

where $\underset{\approx}{\boldsymbol{I}}$ is the 4^{th} order identity tensor ($I_{ijkl} = \frac{\delta_{ik}\delta_{jl} + \delta_{il}\delta_{jk}}{2}$). Let us define:

$$\beta = \frac{2G}{1 + 6G\Delta\lambda/\sigma_0} \tag{4.125}$$

where G is the shear modulus; $\Delta\lambda = \Delta\epsilon_q \left(\frac{\partial g}{\partial q}\right)^{-1}$ (Eq. 4.40); σ_0 is the yield stress of material matrix. The formula for the bubble tangent modulus is defined as:

$$\frac{\partial \boldsymbol{s}(\vec{\boldsymbol{b}})}{\partial \boldsymbol{\epsilon}(\vec{\boldsymbol{b}})} = \beta . \underset{\approx}{\boldsymbol{I}}^{dev} \tag{4.126}$$

where $\underset{\approx}{\boldsymbol{I}}^{dev}$ is the deviatoric part of $\underset{\approx}{\boldsymbol{I}}$.

4.3 Accuracy analysis

4.3.1 Accuracy of the consistent tangent modulus formulation

In this section, a simple test is introduced to check the tangent modulus formulation by comparing the analytical tangent modulus (Eq. 4.93 or Eq. 4.103) and numerical tangent modulus obtained by the finite difference method:

$$\underset{\approx}{\boldsymbol{D}} = \frac{\partial \boldsymbol{\sigma}(\boldsymbol{\epsilon})}{\partial \boldsymbol{\epsilon}} = \frac{\boldsymbol{\sigma}(\boldsymbol{\epsilon} + \epsilon_i) - \boldsymbol{\sigma}(\boldsymbol{\epsilon} - \epsilon_i)}{2\epsilon_i} \tag{4.127}$$

A simple tensile test on a material point is carried out with a Fortran subroutine that solves the local integration of the constitutive equations. Tensile strain is applied during $0.2s$ (for a total uniaxial strain of 0.2) in one direction, with a small strain increment (5.10^{-3})[10], other components of strain tensor are zero. The analytical tangent modulus is extracted at the end of each increment and compared with the numerical tangent modulus from finite difference method (i.e. perturbation technique). A perturbation is applied to the

[10] Strain increment is the applied strain for each increment, not the perturbation factor ϵ_i.

strain tensor, then the resulting stress is measured. The choice of the perturbation factor (ϵ_i) is not straightforward because if this value is too small, numerical oscillations may occur, and if it is too large, the finite difference approximation is not precise enough (for further information, see [Dennis and Schnabel, 1996], [Burden and Faires, 2000]). In chapter 5 and chapter 7 of [Dennis and Schnabel, 1996], the authors discussed the perturbation factor and proposed a formula to estimate this value, which involves different factors (see Eq. 5.4.10 of [Dennis and Schnabel, 1996]). After testing several values, $\epsilon_i = 10^{-5}$ was chosen.

The Ludwik hardening law is employed (Eq. 1.97) with $K = 210$ (MPa), $a = 7.8$, $n = 0.16$; and the elastic constants: $E = 210$ (GPa), $\nu = 0.3$. Two comparisons were carried out: an incompressible case ($q_1 = q_2 = q_3 = 0$ in Eq. 4.27), and a compressible case with the GTN yield function ($q_1 = 1.5, q_2 = 1, q_3 = 2.25$ in Eq. 4.27). The relative error between numerical and analytical tangent moduli is obtained according to the following equation:

$$error = \frac{\|\underset{\sim}{\underset{\sim}{\boldsymbol{D_n}}} - \underset{\sim}{\underset{\sim}{\boldsymbol{D_a}}}\|}{\|\underset{\sim}{\underset{\sim}{\boldsymbol{D_a}}}\|} \tag{4.128}$$

where $\|.\|$ represents the norm of tensor; $\underset{\sim}{\underset{\sim}{\boldsymbol{D_n}}}$ and $\underset{\sim}{\underset{\sim}{\boldsymbol{D_a}}}$ are the numerical and analytical consistent tangent moduli respectively. The evolution of the relative error is presented in Fig. 4.9a, in which some fluctuations can be observed. These fluctuations are principally due to the choice of the perturbation term (ϵ_i).

Overall, the error is relatively small, which confirms the accuracy of the implemented analytical formulation.

4.3.2 Approximation of the tangent matrix by its symmetric part

As stated in [Aravas, 1987], the tangent modulus is symmetric when $C_3' = C_3''$ (Eq. 4.94), which means $m_{pn} = \frac{2G}{K} m_{ql}$, where m_{pn} and m_{ql} represent the "coupling" between the deviatoric and hydrostatic behaviors. The author also showed that, for an associated flow where the plastic potential and the yield function are equal, one can obtain the following relation:

$$m_{pn} = \frac{2G}{K} m_{ql} \left(1 + O\left(\Delta\epsilon_p, \Delta\epsilon_q\right)\right) \tag{4.129}$$

The tangent matrix can therefore be approximated by its symmetric part. In order to confirm this statement, the comparison between the non-symmetric and symmetrized tangent moduli was carried out with two small strain increments: 5.10^{-4} and 10^{-4}. The relative errors between these two tangent moduli were calculated similarly as in Eq. 4.128 (Fig. 4.9b).

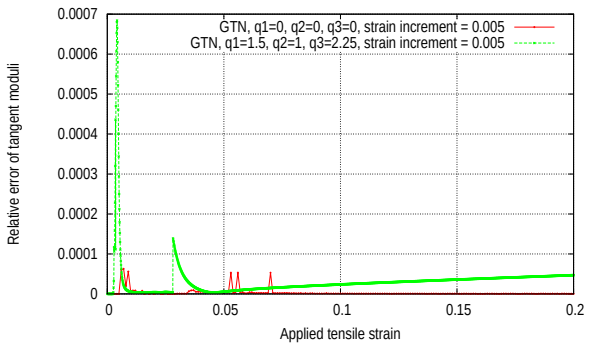

(a) *The relative error between the numerical and analytical tangent moduli during the simulation for the two cases: von Mises model (GTN with $q_1 = q_2 = q_3 = 0$) and GTN model.*

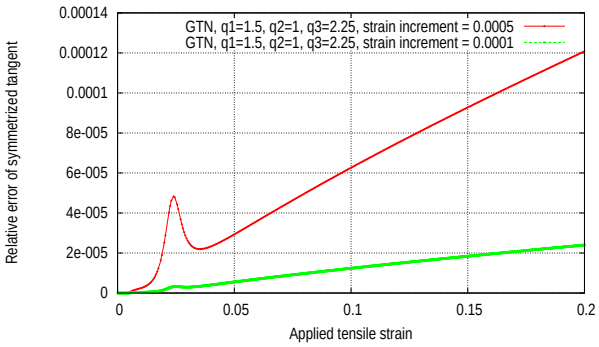

(b) *The relative error between the symmetrized tangent and the analytical tangent with GTN model for two different strain increments: 5.10^{-4} and 10^{-4}.*

Fig. 4.9: *Accuracy analysis of analytical tangent modulus.*

From this figure, one can see that except the irregular zone at the beginning, the relative error due to the symmetrization increases with the applied strain. This irregular zone ([0.018,0.03] of deformation - which

can also be observed in Fig. 4.9a) occurs just after the elastic-plastic transition. With the hardening law used, stress increases rapidly with strain in this zone, which leads to the perturbation in tangent moduli calculation. With a smaller strain increment (green curve), the discrepancy is strongly decreased.

Globally, the error is still small and the above-mentioned approximation is reasonable. Such approximation will only affect the convergence rate of the Newton-Raphson iterations, not the accuracy of its results ([Aravas, 1987]). A symmetric tangent modulus will thus be used in the following.

4.4 Validation of the implementation

In Forge2009®, the Prandtl-Reuss (P-R) module allows solving the local integration of behavior equations for an incompressible case with the P-R flow rule (von Mises plasticity: von Mises criterion + P-R flow rule). The Gurson module developed here does the same task for the compressible plasticity model (where the yield surface depends also on the hydrostatic pressure or the mean stress). Moreover, this module has to be validated for an incompressible case, i.e. without the presence of porosity. In this section, the validation for an incompressible case is obtained by the comparison between the Gurson module and Prandt-Reuss module in Forge2009®, while the validation for a compressible case is carried out by comparing with Abaqus. Throughout the validation simulations, the Ludwik hardening law is used (see Eq. 1.97), with the following parameters: $K = 116.46(MPa)$, $n = 0.184$, $a = 5.56$ (these parameters correspond to the hardening parameters of a high carbon steel grade in large deformation). The parameters of GTN model have been taken from the literature (see Table 4.1).

GTN model								
q_1	q_2	q_3	f_0	ϵ_N	S_N	f_N	f_c	f_f
1.5	1	2.25	0.003	0.3	0.1	0.006	0.026	0.15

Table 4.1: *Parameters used for simulations validation of the GTN model.*

4.4.1 Comparison with Prandtl-Reuss - Incompressible plasticity

In order to validate the new implementation, the comparison between the solver compiled with Gurson module and the solver compiled with Prandtl-Reuss module was carried out. This comparison was based on the simulation of a tensile test on a notched round bar, with the same time increment and mesh size (without remeshing). Only one fourth of the specimen was modeled (Fig. 4.10). The von Mises plasticity model was employed to test the solution of stress and strain fields without the presence of porosity. All the variables were extracted at the end of simulation.

A displacement of 2 mm was applied on the upper surface while the lower surface was fixed. Moreover, since only one fourth of specimen was modeled, symmetric conditions were also imposed on the lateral surfaces. The equivalent plastic strain (Fig. 4.11a) and stress fields (equivalent stress, hydrostatic pressure, and the first principal stress - Figs. 4.11b, 4.12a and 4.12b) are the same. Finally, the load-displacement curves were plotted together (Fig. 4.13). The results show the validity of the Gurson solver for an incompressible plasticity case.

4.4.2 Comparison with Abaqus - Compressible plasticity

In this section, comparisons with Abaqus are carried out to validate the developed module for a compressible plasticity case. Three tests have been chosen for these validations: hydrostatic tensile test (homogeneous deformation), tensile test on notched round bar (heterogeneous deformation, high stress triaxiality) and shear test on butterfly shaped specimen (heterogeneous deformation, low or zero stress triaxiality).

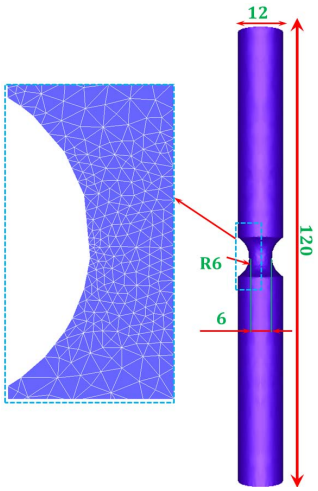

Fig. 4.10: *Uniaxial notched round specimen and the modeled part in the numerical simulations (all dimensions are in mm).*

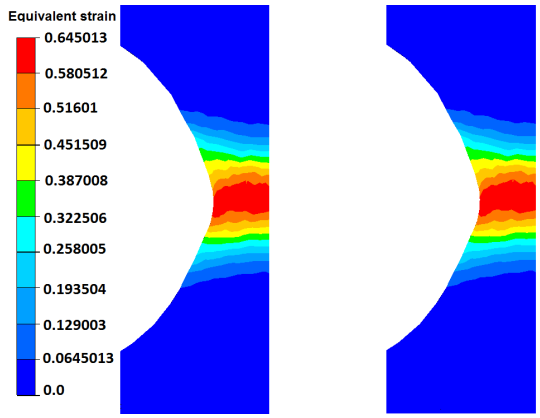

(a) *Equivalent plastic strain: Prandtl-Reuss (left) and Gurson (right).*

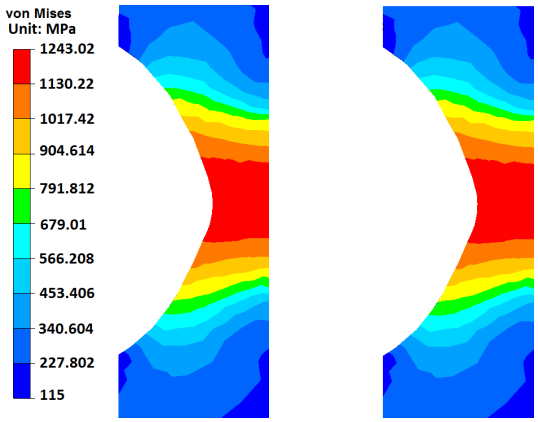

(b) *VM equivalent stress: Prandtl-Reuss (left) and Gurson (right).*

Fig. 4.11: *Comparison between the PR solver and Gurson solver.*

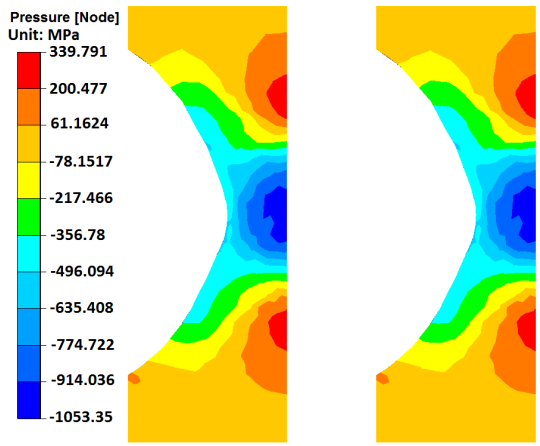

(a) *Hydrostatic pressure: Prandtl-Reuss (left) and Gurson (right).*

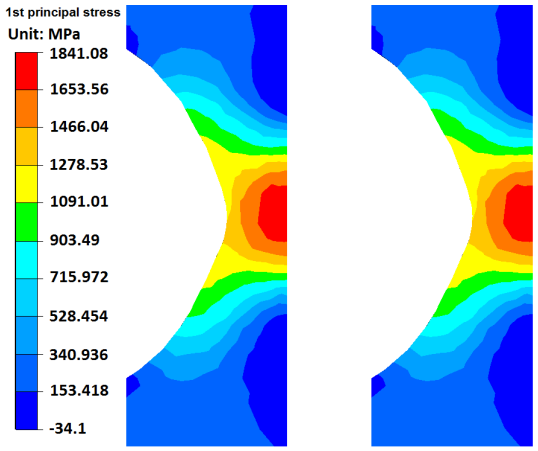

(b) *The first principal stress: Prandtl-Reuss (left) and Gurson (right).*

Fig. 4.12: *Comparison of hydrostatic stress and the first principal stress between the PR solver and Gurson solver.*

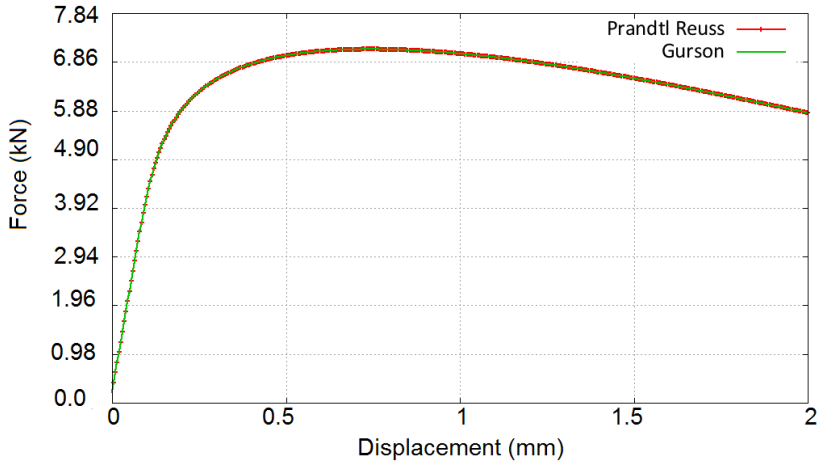

Fig. 4.13: *The force-displacement curves obtained from tensile test simulations with Gurson and P-R modules. Only a quarter of specimen is modeled.*

4.4.2.1 Homogeneous deformation: hydrostatic tension

In Forge2009®, the velocity-pressure FE formulation is employed, the pressure is calculated at nodes by solving the equilibrium equations. The default solution of pressure independent elastoplastic equations provides the plastic increment and the deviatoric part of the stress tensor at integration points. However, in a pressure dependent elastoplastic case, the solution of local integration provides not only the deviatoric part of the stress tensor but also the hydrostatic pressure calculated at integration points. The problem is to know if these two pressures (one calculated at integration points by solving the elastoplastic equation, the other obtained by solving the equilibrium equations at nodes) are equivalent. In order to answer this question, a hydrostatic tensile test is defined to validate the solution of pressure in the developed module. The Abaqus software is used here for validation purposes. Abaqus is a validated FE code widely used in industrial and academic environment ([ABAQUS-6.9, 2009]). It is based on a standard displacement FE formulation and the GTN model is available both in Standard and Explicit versions. Note that the coalescence and final failure of the elements are only possible in Abaqus Dynamics Explicit (Explicit solver - solves for the true dynamic equilibrium) with the POROUS FAILURE CRITERIA option ([ABAQUS-6.9, 2009]). Theoretically, the explicit solver, without the iterative solution and the calculation of global tangent modulus, is less expensive in calculation time. However, to obtain accurate results, the time increment for time integration must be chosen smaller than the stability limit, which is defined as:

$$\Delta t_{stable} = \frac{L_c}{c_d} \tag{4.130}$$

where L_c (mm) is the smallest characteristic element length and c_d $(mm.s^{-1})$ is the dilatational wave speed of the material. This wave speed depends on the Young's modulus (E) and material density (ρ) through ([ABAQUS/Explicit, 2005]):

$$c_d = \sqrt{\frac{E}{\rho}} \tag{4.131}$$

The application of explicit dynamics to model the quasi-static process in its natural time period requires millions of time increments, the calculation time is sometimes significantly higher than the implicit one. To overcome this drawback, some techniques have been employed to reduce the CPU time:

- Increasing the load rate: we artificially reduce the time scale of the process by increasing the load rate. The strain-rate is therefore higher than the natural strain-rate of the real process. This technique is not applicable for rate sensitive materials.
- Mass scaling: this technique consists in increasing the material density by a factor X^2. From Eqs. 4.130 and 4.131, the stable time step is reduced by a factor of X.

The goal of these techniques is to model the process with as few time increments as possible (either decreasing the process time or increasing the mass) for inertia forces to remain insignificant. In our simulation, the mass scaling technique was employed with $X = 4$ and the inertial force was checked to be negligible.

Without coalescence A comparison between the present development and Abaqus is carried out on a cube of 1 mm^3 (Fig. 4.14). A displacement of 0.2 mm was applied on the three adjacent surfaces (surfaces 1, 2 and 3 in Fig. 4.14) resulting in a uniform volumetric expansion (at constant displacement speed of 10 mm/s). Symmetry conditions were applied on 3 other free-surfaces.

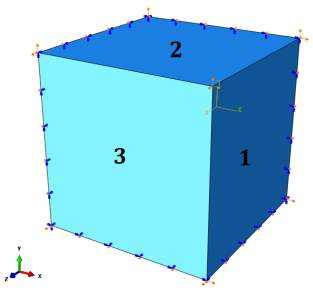

Fig. 4.14: *Hydrostatic tension on a cube.*

Since Forge2009® uses tetrahedron elements, C3D4 elements were employed in Abaqus to model this cube with 6 elements. Note that there is neither coalescence nor failure criteria introduced in this first comparison, which aims at validating the growth and nucleation stages as well as the solution of pressure fields.

The results obtained for stress and strain fields are homogeneous (error of 10^{-2}). A sensor has been set up to follow the evolution of the mean stress (-hydrostatic pressure) and the void volume fraction during the test. The results are presented in Fig. 4.15, which shows a good agreement between Abaqus and the present development (with Forge2009®). The analytical solution for this problem is also presented as a reference solution, using the formulations presented in section 5.2 of [Aravas, 1987]. These equations are integrated using the forward Euler method with a strain increment about 1/1000 the yield strain as recommended by Aravas. Both results obtained with the present development and Abaqus are consistent with the reference solution. Moreover, for Forge2009® results, the pressure calculated at integration points (solving elastoplastic equation) and the pressure calculated at nodes (equilibrium equations) are identical, which also validates the numerical implementation.

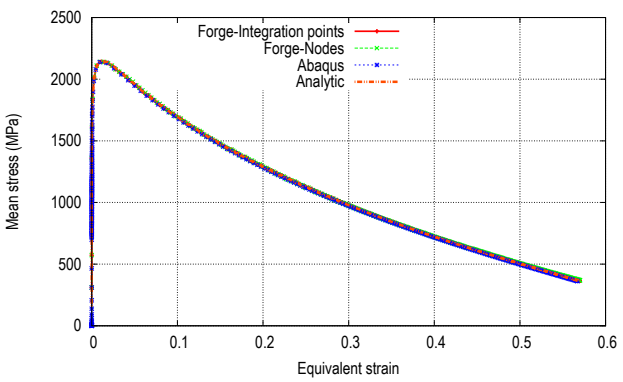

(a) *Evolution of the mean stress.*

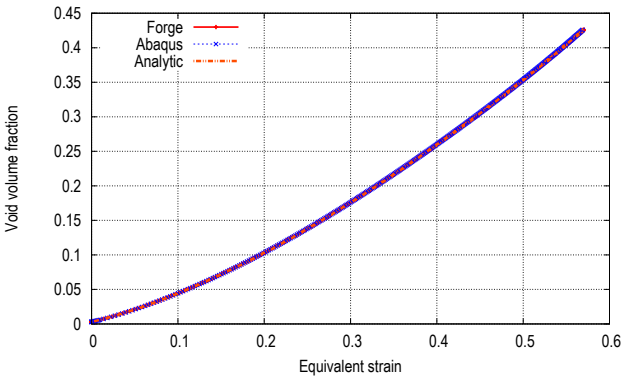

(b) *Evolution of the void volume fraction.*

Fig. 4.15: *Comparison between the present development (with Forge2009®) and Abaqus for the hydrostatic tensile test on a cube without coalescence.*

With coalescence In order to validate the coalescence stage, the same test was carried out with this cube. A displacement up to fracture ($f = f_f = 0.15$) was applied on 3 surfaces (surfaces 1, 2 and 3 in Fig. 4.14) and symmetry conditions on the other 3 surfaces. The results of the evolution of the pressure and the void volume fraction are represented in Fig. 4.16. Again, the same tendencies can be observed. Moreover, for the simulation with the present development, the two pressures are consistent.

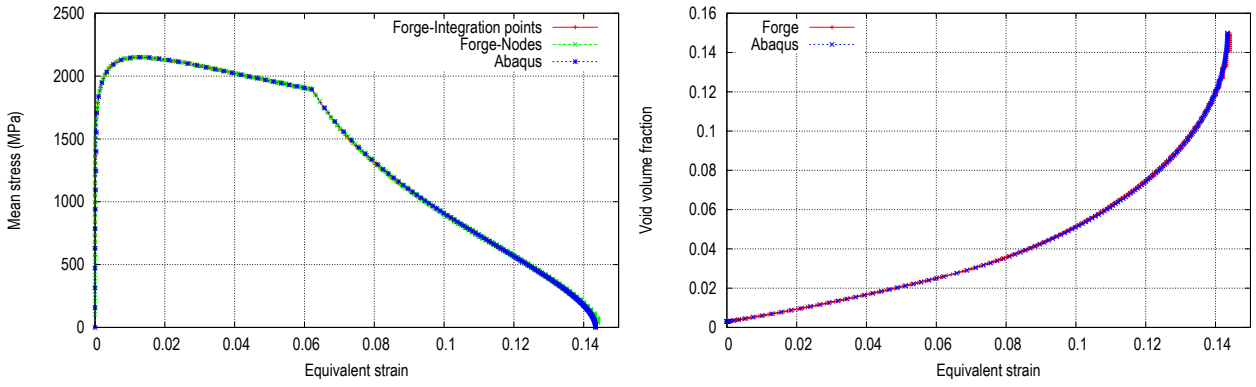

(a) *Evolution of pressure.* **(b)** *Evolution of void volume fraction.*

Fig. 4.16: *Comparison between the present development (with Forge2009®) and Abaqus for the hydrostatic tensile test on a cube with coalescence. The Abaqus Explicit version is used to model failure.*

4.4.2.2 Heterogeneous deformation: tensile test on notched round bar

The specimen geometry is shown in Fig. 4.10. A displacement of 1.8 mm in the vertical direction is imposed on the upper boundary with a constant velocity equal to 1 mm/s. For the simulation with Abaqus, after some tests, C3D10 elements (10 node quadratic tetrahedra) were selected as giving the best results (smooth fields). The Abaqus/Standard version was used for the simulation without coalescence. The failure simulation (i.e. with coalescence) was also carried out with the Explicit version, on a 3D model, with an equivalent mesh size, which employed C3D10M elements (modified 10 node quadratic tetrahedra). In the following, the comparison of contour plots are presented for the non-coalescence case only. The comparison with coalescence is presented briefly through the evolution of porosity of a material point located in the notch area.

Stress state The comparison of stress state at the end of simulations is shown in Fig. 4.17 where the von Mises equivalent stress and the hydrostatic pressure are plotted. In the notch center, the material is under high tension, which leads to a strong increase of porosity in this region (see Fig. 4.19). Generally, the stress fields are the same in the two cases.

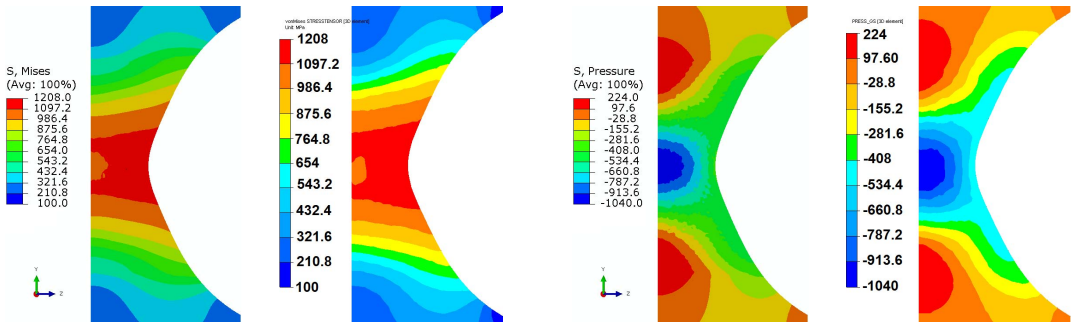

(a) *The von Mises equivalent stress (left: Abaqus, right: the present development.* **(b)** *The hydrostatic pressure (left: Abaqus, right: the present development.*

Fig. 4.17: *The von Mises equivalent stress and the hydrostatic pressure (without coalescence).*

Deformation state The comparison of the equivalent strain contour plots is presented in Figs. 4.18a and 4.18b. Deformed meshes are also displayed (note that in this case, there was no remeshing during the simulations). Although slight difference can be observed, generally, Abaqus and Forge2009® with our development are in good agreement.

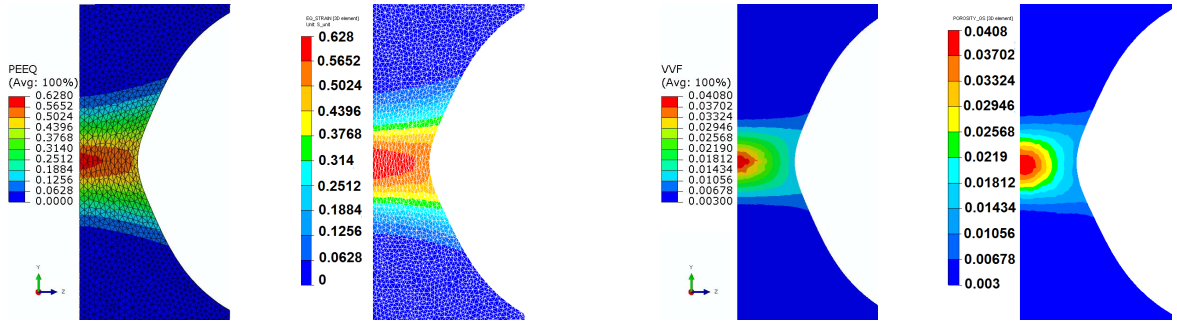

(a) *Abaqus.* **(b)** *The present development.* **(c)** *Abaqus.* **(d)** *The present development.*

Fig. 4.18: *Comparison between Abaqus and the present development in a non-coalescence case: Equivalent strain (a), (b); void volume fraction (c), (d).*

Damage state The contour plots of the void volume fraction are presented in Figs. 4.18c and 4.18d. The void volume fraction is higher in the center, and the fracture initiation is predicted to occur in this zone. This localization of damage is consistent with experimental observations, where the fracture initiates in the center zone, then propagates outward. The results obtained with the two FE codes are in good agreement.

The evolution of void volume fraction as the function of plastic strain of a material point, located at notch center, is also plotted in Fig. 4.19. In the first comparison, which does not account for void coalescence, the increase of voids is due to the void growth and nucleation; the results are in good agreement (red and green curves). For the comparison accounting for coalescence (and a failure criteria), the Abaqus simulation was carried out with the Explicit solver. The result is slightly different between the present development and Abaqus in this case (blue and purple curves in Fig. 4.19), which is most likely due to the meshes used. With the local coupled damage model, the softening behavior due to damage depends strongly on mesh size as stated in many previous studies (e.g. [Jirásek, 1998]): a finer mesh leads to a faster damage accumulation. In order to overcome this limitation, a non-local formulation should be employed, which is out of the scope of this study.

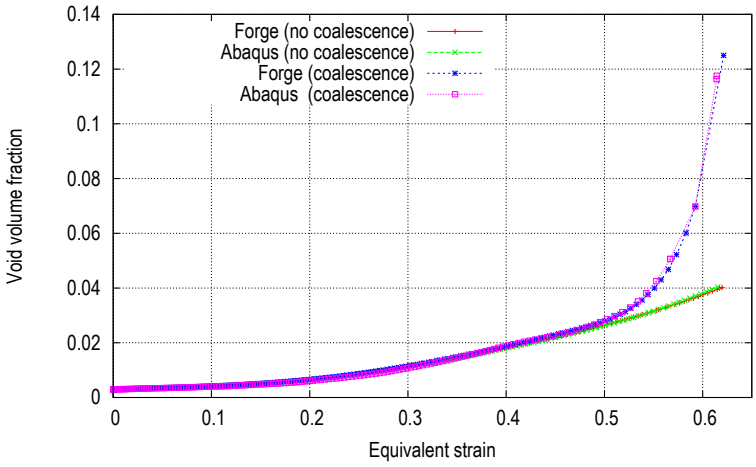

Fig. 4.19: *Comparison the void volume fraction-equivalent plastic strain curves, with or without coalescence.*

The consistency between the two pressure fields in the mixed velocity-pressure formulation As stated above, for a mixed velocity-pressure FE formulation, ensuring the consistency between the two resulting pressure fields is a major point of the implementation work. A sensor was set up at a material point (node) in the notch area (where damage is significant) to track the evolution of pressure with the equivalent plastic strain. The comparisons are presented in Fig. 4.20. Without coalescence (red and green curves), the pressures at nodes and at integration points (interpolated at nodes for post-processing purpose) are in good agreement. With coalescence, where strong localization of damage occurs, the difference between the two pressures is noticeable, but the same tendency can be observed (blue and purple curves). This difference is mainly due to the instability when material loses strength dramatically; the second reason may be the interpolation error from integration points to nodes. Globally, the two pressures are consistent.

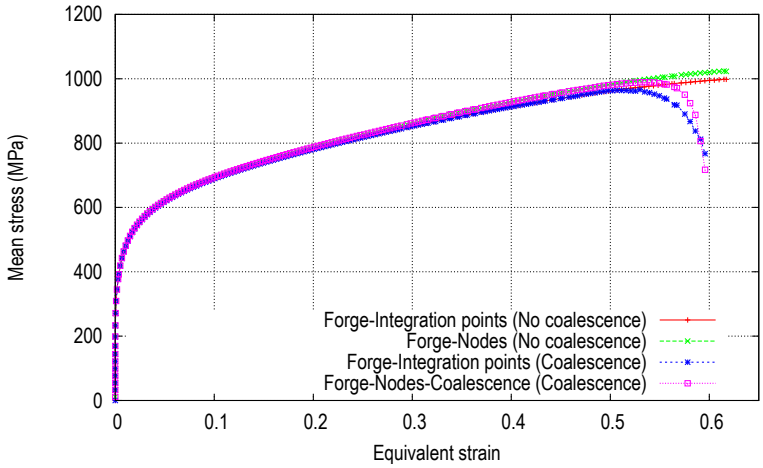

Fig. 4.20: *Comparison of the two pressures for the simulation with the present development (in Forge2009®) at a critical point in notch area. The results were obtained from the simulations with/without coalescence.*

4.4.2.3 Heterogeneous deformation: shear test on butterfly specimen

The simulations of shear test were carried out on the butterfly-shaped specimen (Fig. 4.21).

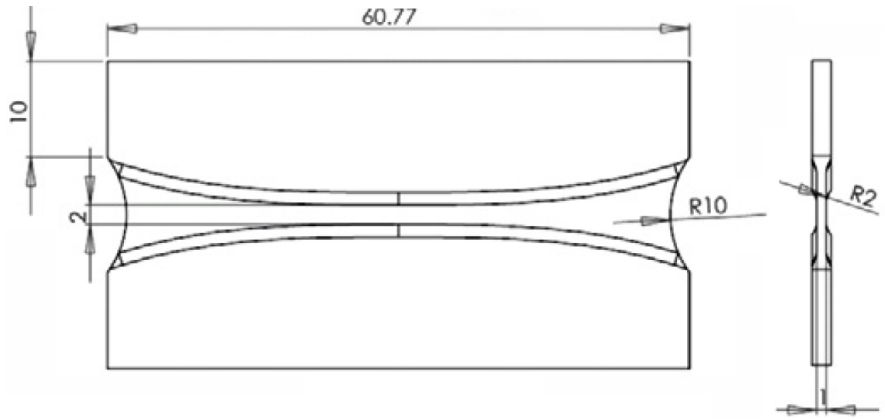

Fig. 4.21: *Butterfly specimen geometry ([Dunand and Mohr, 2011],[Luo et al., 2012]). All dimensions are in mm.*

This specimen was used by [Luo et al., 2012] and the geometry as well as the mesh file of this specimen was provided by Meng Luo. It was designed to have fracture initiation near the center under shear-dominated loading ([Dunand and Mohr, 2011]). For numerical simulations, only a half (in thickness) of the gauge section was modeled (Figs. 4.22a and 4.22b show the initial FE meshes used in Abaqus and Forge2009® respectively).

A displacement of 5 mm in the horizontal direction (x direction) was imposed to the upper boundary with

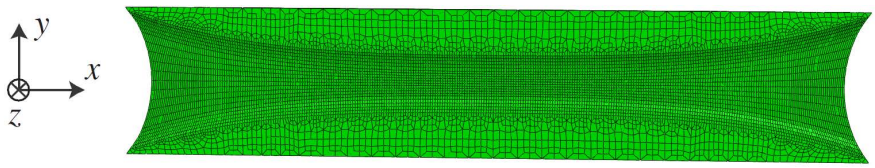

(a) *Abaqus FE mesh.*

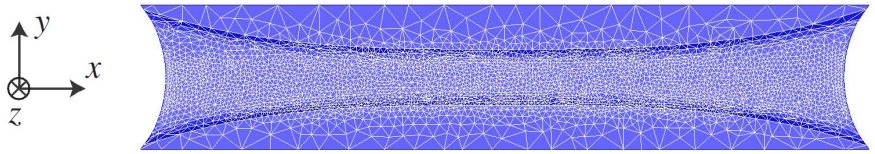

(b) *Forge2009® FE mesh.*

Fig. 4.22: *Initial meshes.*

a constant velocity (0.01 mm/s), while the displacement was kept zero along the y direction. This imposed displacement does not allow a pure shear state but rather a shear-dominated loading state. For the simulation with Abaqus, the C3D8R element was used (an 8-node linear brick element, with reduced integration and hourglass control [ABAQUS-6.9, 2009]). The deformed meshes are shown in Figs. 4.23a and 4.23b.

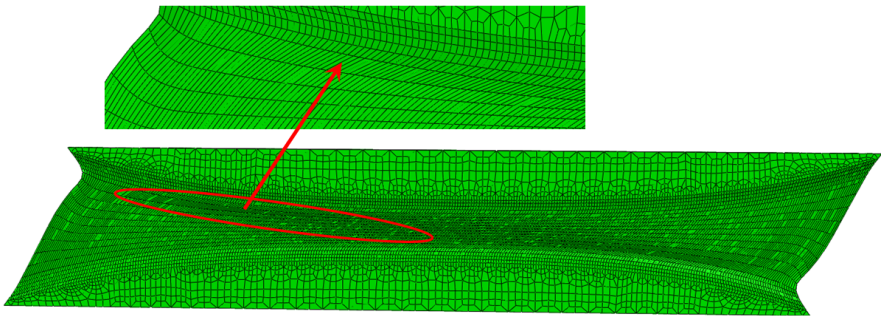

(a) *Abaqus FE deformed mesh.*

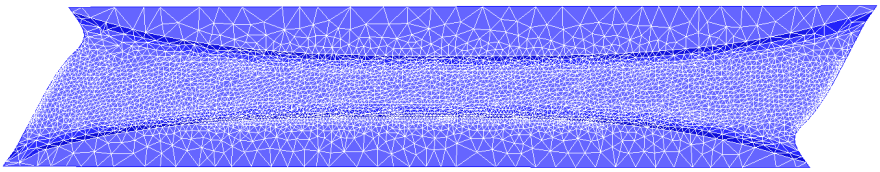

(b) *Forge2009® FE deformed mesh.*

Fig. 4.23: *Deformed meshes at the end of simulations.*

From these figures, one can observe that the deformed mesh of Abaqus was strongly distorted because there was no remeshing during the simulation, especially in the zoomed area (in comparison with the regular deformed mesh of Forge2009®, where remeshing was employed).

Deformation state Fig. 4.24a and 4.24b represent the contour plots of the equivalent plastic strain at the end of the simulations obtained with Abaqus and Forge2009® respectively[11]. The results are similar, except the maximum in the concentration zones where mesh is distorted (Abaqus simulation). The concentration of deformation in this zone is principally due to the strongly distorted mesh in the Abaqus simulation.

Stress state The contour plots of the von Mises equivalent stress as well as the first principal stress and the hydrostatic pressure are represented in Figs. 4.25, 4.26 and 4.27. Globally, the stress states are identical in these two simulations, except some differences always in the strongly distorted zone. Moreover, from Fig.

[11] Attention to different color scales used by the two programs.

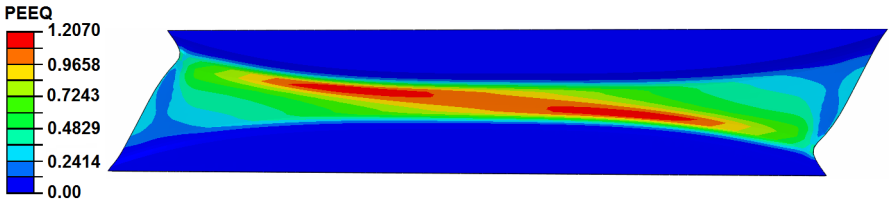

(a) *Abaqus.*

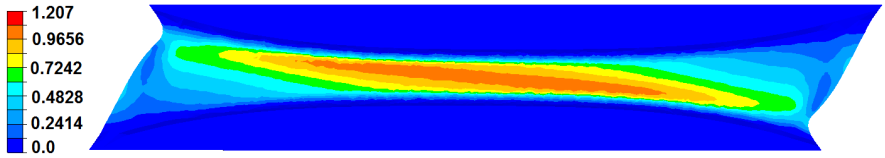

(b) *Forge.*

Fig. 4.24: *Equivalent plastic strain.*

4.27, highly compressive zones can be observed (orange and red zones). We can see afterward that in these zones, the void volume fraction will decrease due to the void closure in compression if there are no nucleation and coalescence.

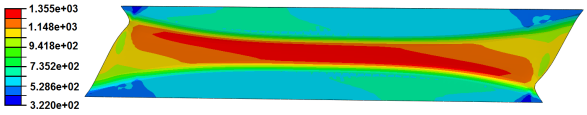

(a) *Abaqus.*

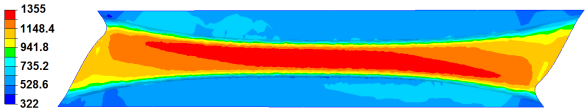

(b) *The present development with Forge2009®.*

Fig. 4.25: *Von Mises equivalent stress.*

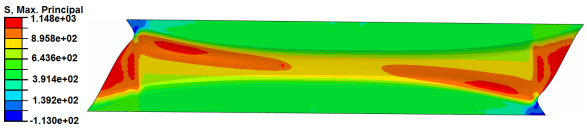

(a) *Abaqus.*

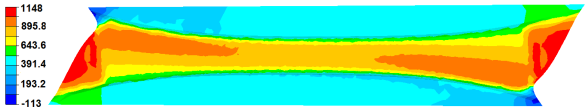

(b) *The present development with Forge2009®.*

Fig. 4.26: *The first principal stress.*

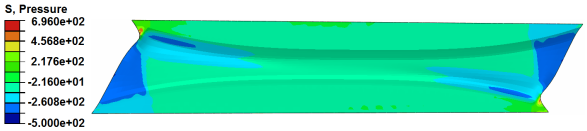

(a) *Abaqus.*

(b) *The present development with Forge2009®.*

Fig. 4.27: *Hydrostatic pressure.*

Damage state (void volume fraction) Fig. 4.28 represents the plot of void volume fraction at the end of simulation without void nucleation and coalescence.

In this case (shear-dominated loading), the void growth is thus disabled in the "shear regions" (the center zone of the butterfly-shaped specimen). As one can observe, in this center zone, void does not grow and f keeps the initial value (3.10^{-3}); while in the blue zone, the void volume fraction decreases due to void closure under "compressive" loading[12]. We observe some difference at borders but globally, the contour plots show similar results between the two programs.

[12]Note that in this case we activated the void closure by allowing a decrease of void volume fraction in compression (as in Abaqus)

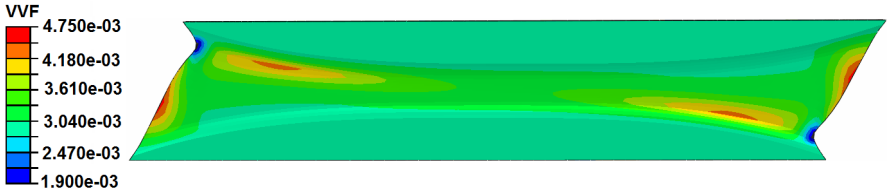

(a) *Abaqus.*

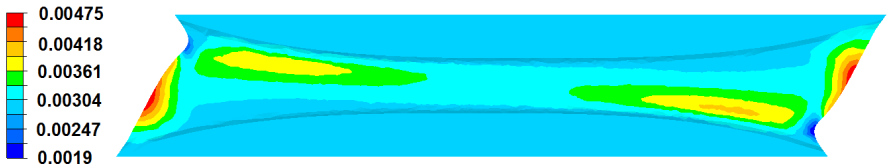

(b) *The present development with Forge2009®.*

Fig. 4.28: *The void volume fraction without nucleation and coalescence.*

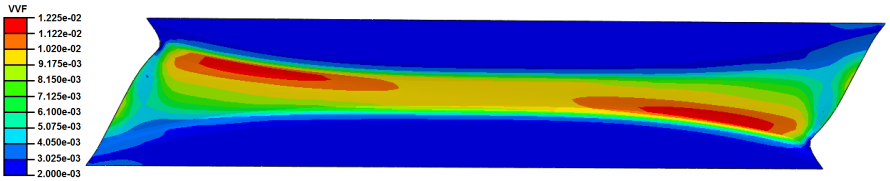

(a) *Abaqus.*

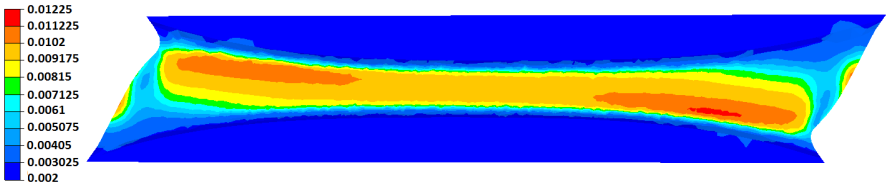

(b) *The present development with Forge2009®.*

Fig. 4.29: *The void volume fraction with nucleation and coalescence.*

In order to compare the void evolution with nucleation and coalescence activated, the contour plots of void volume fraction are represented in Fig. 4.29. Note that at the end of simulation, there was still no coalescence ($f = 0.00475 < f_c = 0.026$). Therefore, the increase of void volume fraction with respect to the above case (Fig. 4.28) is totally due to the void nucleation in the high deformation zone. The result of Abaqus showed a higher nucleation in the high distortion zone, where the deformation is significant. Except this zone, the results of Abaqus and our development are in agreement. Moreover, the value of the void volume fraction at the end of simulation is quite small in comparison with the failure value ($f_f = 0.15$). From the results obtained of void volume fraction, the original GTN model totally failed to capture the damage under the studied shear dominated loading.

Load-displacement curve The load-displacement curves are plotted together (Fig. 4.30) and show the same result. Note that in this case, the coalescence as well as the nucleation was activated. The void volume fraction seemed has minor effect on the macroscopic load-displacement curves since its value is quite small.

Qualitative damage localization with two modified GTN models In this paragraph, qualitative results concerning damage localization obtained with two modified GTN models (by Xue and by Nahshon & Hutchinson) are presented. The aim is to illustrate the ability of these two modified models in predicting damage localization for shear-dominated stress state. The parameter k_ω was chosen equal to 3 for N&H modified

only for validation purpose. Except this simulation, throughout the present dissertation, the void closure was not accounted in the GTN model.

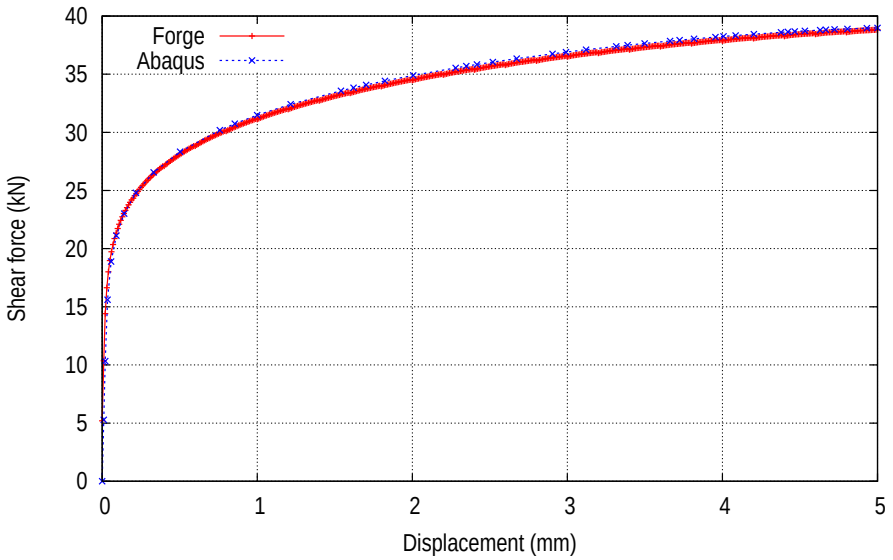

Fig. 4.30: *The comparison of load-displacement curves. Only a half of the specimen is modeled.*

model, while $q_3^* = 3.72$ and $q_4 = 1/3$ as proposed by Xue. Fig. 4.31 shows the damage localization obtained with these two models.

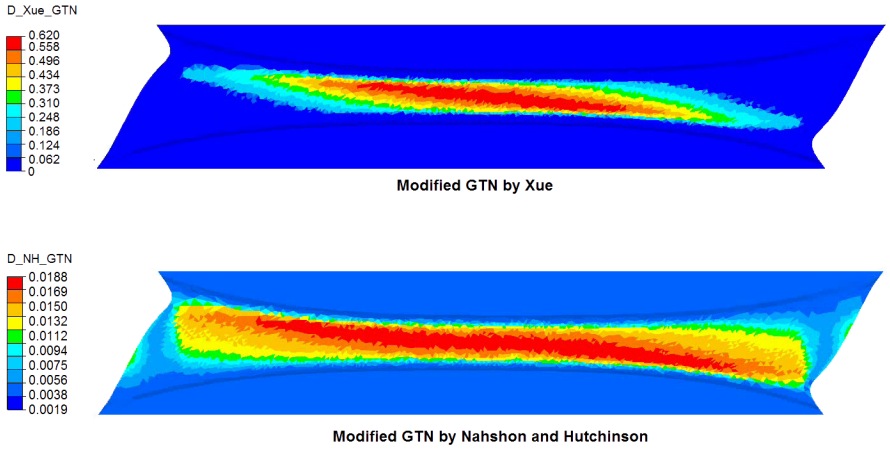

Fig. 4.31: *Damage localization obtained with two models: modified GTN by Xue (above) and modified GTN by Nahson & Hutchinson.*

With both models, damage is higher on the shear band, which is consistent with experimental result of [Luo et al., 2012] (see Fig. 3 of [Luo et al., 2012]) and which cannot be captured using the original GTN model (see Fig. 4.29).

4.5 Summary of Chapter 4

This chapter detailed the implementation of the GTN model into the mixed velocity-pressure FE software Forge2009®. The return mapping algorithm and Euler backward method were used for the local integration of constitutive equations. Formulations for tangent modulus of Aravas and of Zhang were revisited and compared. Validation of the developed module was carried out for a von Mises case (incompressible) by comparing with the existing module in Forge2009® (Prandtl-Reuss module). For compressible cases, Abaqus was used for validation purpose, for both homogeneous and heterogeneous deformation. All the results obtained validate and prove the accuracy of the present development.

4.6 Résumé en français

Ce chapitre a présenté en détail l'implémentation du modèle de Gurson-Tvergaard-Needleman (GTN) dans le contexte de la formulation éléments finis mixte en vitesse-pression. Ce modèle est à la fois un modèle de plasticité compressible (avec la présence de la pression dans le critère de plasticité) et un modèle d'endommagement (en utilisant le variable interne f pour décrire la fraction volumique de vide).

Dans la première partie, le modèle GTN ainsi que ses modifications ont été présentés.

Ensuite, dans la deuxième partie, l'intégration locale de la loi constitutive a été abordée en détail. La méthode proposée par [Aravas, 1987] a été utilisée, où l'incrément de déformation plastique a été décomposé en deux composantes : la déformation volumique $\Delta\epsilon_p$ et la déformation déviatorique $\Delta\epsilon_q$. Afin de calculer le module tangent, deux formulations proposées par Zhang ([Zhang, 1995b]) et par Aravas ([Aravas, 1987, Govindarajan and Aravas, 1995]) ont été souvent utilisées dans la littérature pour les critères de plasticité qui dépendent de la pression. Ces deux formulations ont été montrées équivalentes. En outre, comme le logiciel Forge2009® est basé sur une formulation mixte en vitesse-pression, le champ de pression est obtenu aux nœuds en résolvant le système global des équations d'équilibre, tandis que la partie déviatorique du tenseur de contrainte est obtenue aux points d'intégration en résolvant l'intégration locale des équations constitutives. Pour un critère de plasticité qui prend en compte la pression, on obtient également la pression aux points d'intégration. Nous avons modifié l'équation de conservation de la masse dans Forge® afin de prendre en compte la compressibilité plastique. Avec cette modification, le champ de pression obtenu aux nœuds est compatible avec le champ de pression obtenu aux points d'intégration.

La troisième partie a été consacrée à étudier la précision du module tangent analytique. Des calculs de comparaison ont été menés afin de comparer le module tangent analytique et le module tangent numérique (obtenu par la technique de perturbation). Le résultat a montré que la formule analytique était exacte. En outre, afin de pourvoir utiliser le solveur symétrique, le module tangent a été symétrisé et comparé avec le module non-symétrisé pour étudier l'erreur due à cette symétrisation. Le résultat a montré que la symétrisation n'influençait pas la précision.

Dans la quatrième partie, des calculs de validation ont étés présentés. Dans un premier temps, notre développement a été validé sur un cas incompressible, par une comparaison avec le module Prandtl-Reuss. Ce module, qui existait dans Forge2009®, résout des équations constitutives du modèle de plasticité incompressible. Le résultat a validé notre module dans le cas incompressible. Ensuite, des validations sur des cas compressibles ont été réalisées en comparant avec Abaqus. Les résultats ont montré la cohérence entre notre développement et Abaqus pour différents types de chargement : traction hydrostatique (déformation homogène) ; traction sur éprouvette entaillée ; cisaillement sur éprouvette "butterfly" (déformation hétérogène).

Chapter 5

Identification of GTN model based on micro-macro tests for high carbon steel

Contents

Introduction

In this chapter, the identification of the GTN and modified GTN models for the studied high carbon steel is detailed. The calibration process is based on both in situ tensile test (conducted at ESRF by the laboratory MATEIS of INSA Lyon) and the mechanical tests performed by the present author. First, a literature review on the identification of the GTN model is given, followed by a short presentation of the in situ X-ray micro-tomography technique. Then the experimental results from in situ X-ray tomography observation is exploited and modeled to characterize different mechanisms of ductile damage (e.g. void growth and nucleation). The identification of the GTN model is then given, in which a formulation for nucleation strain is proposed to better reproduce our experimental results. Finally, the modified GTN models by Xue and by Nahshon and Hutchinson are identified based on the torsion test presented in section 2.2.

5.1 Literature review and experimental tests used

5.1.1 Literature review

The parameters of the original GTN model can be classified into three groups:

1. Flow stress of material matrix, which is supposed to be isotropic. The number of parameters depends on the hardening laws used. In our study, the Ludwik hardening law is adopted to describe the strain hardening of material matrix for the in situ tensile test; there are thus three parameters that need to be identified.

2. The parameters q_1, q_2 ($q_3 = q_1^2$) in the yield function.

3. The parameters related to the mechanisms of damage: initial void volume fraction (f_0), nucleation (f_N, ϵ_N, S_N), coalescence and failure (f_c, f_f).

Many authors in the literature carried out the identification of the GTN model parameters on different materials. The identification of the original GTN model is often based on the tensile test on notched round bar or compact tension (CT) specimen, where the deformation is localized in the notch area and the stress triaxiality is relatively high. An inverse analysis methodology is often used to identify this set of parameters (e.g. [Abbasi et al., 2011]), based on the stress-strain curves (or load-displacement curves). However, in these identifications, the 3 parameters q_1, q_2, q_3 are often taken from the study of [Needleman and Tvergaard, 1984], in which: $q_1 = 1.5$, $q_2 = 1$ and $q_3 = (q_1)^2$. Note that a high value of q_1 or q_2 leads to a high "retraction" of the yield surface (see Fig. 5.1 and [Hor, 2011]). The nucleation parameters (f_N, ϵ_N, S_N) are also often fixed since the measurement of these parameters is not straightforward. In [Hor, 2011], the author summarized the values of these three variables in the literature, which is reported in Table 5.4 of [Hor, 2011].

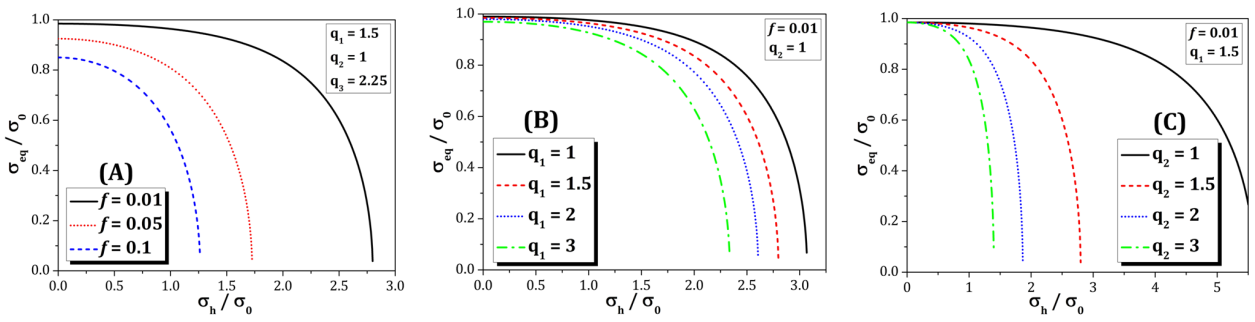

(a) *Porosity.* **(b)** q_1. **(c)** q_2.

Fig. 5.1: *The sensitivity of the yield surface with the porosity and the GTN parameters q_1 and q_2 ([Hor, 2011]).*

Recently, new and advanced experimental techniques allow identifying more accurately the values of the GTN model parameters. He and coworkers ([He et al., 2011]) among others, used the in situ tensile test with scanning electron microscope (SEM) to determine these parameters. This identification was based on the counting of void volume fraction at three damage states. This method gave them relatively exact values of the initial void volume fraction as well as at 3 instants of measurement. However, this method could not give a continuous increase of void volume fraction with the plastic strain and could not distinguish the two different damage mechanisms: void nucleation and growth. Moreover, the 3 values of q_1, q_2, q_3 were also fixed as in [Needleman and Tvergaard, 1984].

The characterization of each stage of ductile damage requires the continuous monitoring of damage during the deformation, which can be done by X-ray tomography measurements ([Weck et al., 2008, Maire et al., 2008, Landron et al., 2011]). Bettaieb and co-workers [Bettaieb et al., 2011] used this technique to identify the parameters of the extended GTN model with kinematic hardening for DP steel. More recently, [Thuillier et al., 2012] identified the GTN model parameters for aluminum alloy, based on a hybrid study of micro-tomography observations and numerical modeling. However, in their numerical simulation with Abaqus Explicit, the coalescence was not taken into account and no fracture criterion was defined.

In the present study, the parameters of the GTN models are identified based on in situ X-ray tomography tensile tests as well as macro-mechanical tensile tests on round bar (RB) and notched round bars (NRB) with different notch radii. Tomography observations were carried out by Le Moal and Cassone from MATEIS-INSA Lyon ([Le Moal and Cassone, 2012]) in the framework of the METAL project. We exploited and analyzed these observations to identify the damage mechanisms and the GTN model (combining with the mechanical presented in section 2.2). The parameter of the extension for shear loading was determined from the torsion test.

5.1.2 Material and experimental tests

5.1.2.1 Material

The material used in the present study is a high carbon steel grade, which has experienced patenting to obtain a fine pearlite structure. All the specimens used in the mechanical tests were extracted from the longitudinal direction of steel rods of maximum diameter of 17 mm. The mechanical properties of this steel grade have been shown to be isotropic in the patented state.

5.1.2.2 Tomography observations

X-ray micro-tomography was used to quantify damage during in situ tensile tests on notched round bar. In this experiment, the characterized object rotates around a single axis while a series of 2D X-ray absorption images is recorded. This series of images is reconstructed to produce a 3D digital image where each voxel (volume element or 3D pixel) represents the X-ray absorption at that point (see Fig. 5.2a). The experimental setup is shown in Fig. 5.2b, on ID15 and ID19 beam lines at the European Synchrotron Radiation Facility (ESRF) in Grenoble, France. The ID15 beam line has a resolution of 1.1 μm voxel size and each scan lasts 5 seconds, while the ID19 one has a resolution of 0.7 μm voxel size but more time is needed to acquire each scan. The ID15 was used principally in the present study and the results with ID19 confirmed ID15 observations ([Le Moal and Cassone, 2012]). For the present study, interrupted in situ test was used on ID19 beam line while continuous testing was used on ID15.

For the interrupted method, during imaging, the deformation is stopped but maintained constant; while for the continuous characterization, imaging is carried out continuously during the deformation without interruption. The latter procedure is obviously better to characterize the evolution of the sample during the tensile test, but the drawback is that the scan time has to be small compared to the deformation speed to avoid blurring of the images ([Landron, 2011]). For this reason, this method is more suitable for ID15 beam line, in which the scan time is shorter than the ID19. It was demonstrated that the results obtained with the two methods (interrupted or continuous) are similar (see [Maire et al., 2007, Suéry et al., 2010] for

more details).

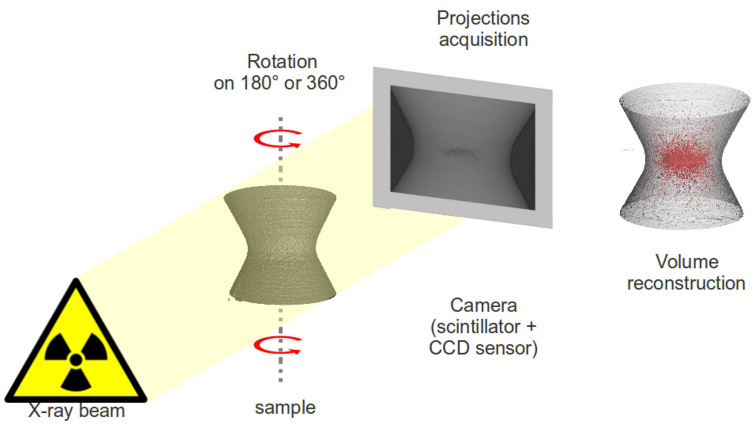

(a) *X-ray tomography principle: the object to characterize rotates around a single axis while a series of 2D X-ray absorption images is recorded, which are then reconstructed to produce a 3D digital image.*

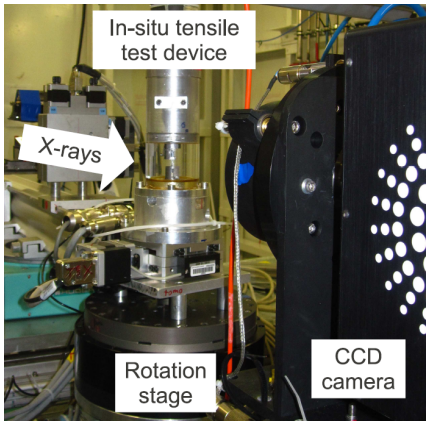

(b) *Tensile machine is mounted on the rotation stage of tomograph to achieve the in situ tensile test.*

Fig. 5.2: *X-ray tomography principle (a) and in situ experimental setup at the ID15 beam line - ESRF (b) (figure adapted from ([Landron, 2011])).*

The geometry of the tensile specimen is presented in Fig. 5.3 (as in [Landron, 2011]), which gives a value of the initial stress triaxality of 0.43 according to Bridgman's formula:

$$\eta = \frac{1}{3} + ln(1 + \frac{a}{2R}) \tag{5.1}$$

where η is the stress triaxiality, a is the minimum radius of cross section, R is the notch radius.

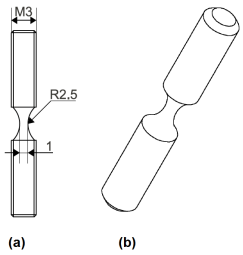

Fig. 5.3: *Tensile sample: 2.5 mm radius notched specimen (a), 3D view (b). All dimensions are in mm (figure adapted from [Landron et al., 2011]).*

Due to the strong localization of deformation and high triaxiality in the central area of notch, this area is assumed to have the highest level of damage. Therefore, only a central cubic volume of $(385\mu m)^3$ was chosen for the quantification of damage. During the in situ tensile test[1], the area of minimal cross section S was measured to calculate the average true strain as well as the true stress in the minimal cross section of the specimen:

$$\epsilon_{loc} = ln(\frac{S_0}{S}), \quad \sigma_{true} = \frac{F}{S} \tag{5.2}$$

where S_0 is the initial minimum cross section (mm^2); F is the measured force (kN). By measuring the curvature radius of notch (R) and the radius of the minimal cross section $(a = \sqrt{S/\pi})$, the stress triaxiality ratio can be calculated via Eq. 5.1, which was validated by numerical simulations.

[1]Throughout the present study, the term "in situ" refers to "in situ X-ray tomography", unless otherwise indicated.

5.2 Tomography result analyses

5.2.1 Quantification of ductile damage processes

In order to quantify damage in the studied steel, the same procedure as in [Maire et al., 2008, Landron et al., 2011] was used in the present study. The image processing was performed ([Le Moal and Cassone, 2012]) with the ImageJ freeware ([Abramoff et al., 2004]). Damage can be quantitatively observed in 3D as shown in Fig. 5.4 for different strain levels.

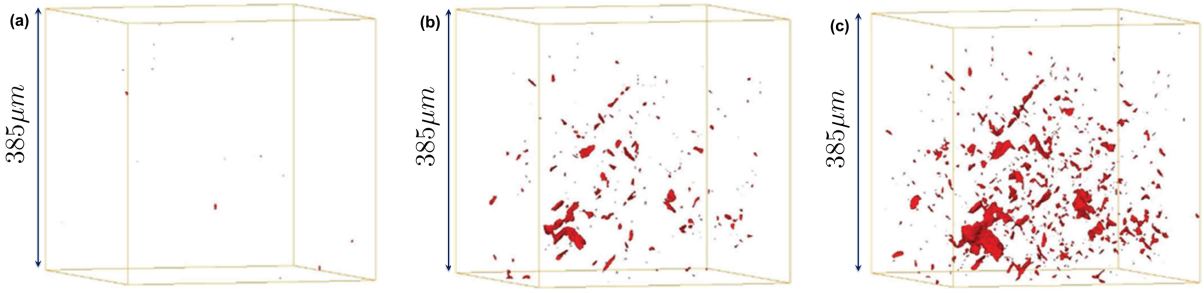

Fig. 5.4: *3D view of damage in the controlled volume at the specimen center at different strain levels: (a) $\epsilon_{loc} = 0.02$, (b) $\epsilon_{loc} = 0.25$, and (c) $\epsilon_{loc} = 0.32$ (see Eq. 5.2). Zoomed pictures show largest voids observed. The loading was applied in the vertical direction.*

"Local" void coalescence can be observed in Fig. 5.4b where voids start to link together. Fig. 5.4c corresponds to the last scan just before fracture, where coalescence can be observed: voids linked together to form series of voids about 45° with respect to loading direction. However, it will be shown in the following section that the coalescence is made of *"local"* events since no clear influence of coalescence on the nucleation and growth was observed (see Figs. 5.6a and 5.6b in the following section). This level of strain (0.32) is assumed to be the strain at fracture.

The results from the ID19 beamline, with higher resolution, help to complement the observations from the ID15 beamline. Fig. 5.5a shows the observed inclusion and porosity at a deformation of 0.25. Only one inclusion was detected for this resolution, at which the matrix-particle decohesion was not noticeable. Nevertheless, several long cavities were observed, which formed an angle with tensile direction, which also confirmed the void orientation in Fig. 5.4c. An in situ SEM interrupted tensile test was also carried out to examine the microstructure evolution. At the strain level of 0.2, cavities can also be observed inside the slip bands (without inclusion), which are about 45° with respect to loading direction (horizontal direction in Fig. 5.5b).

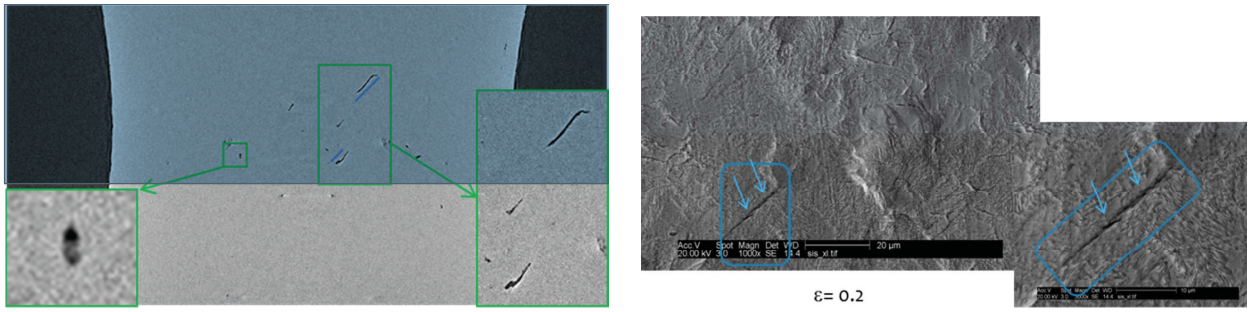

(a) *Inclusion and elongated cavities obtained with the ID19 beamline observation at 0.25 strain level. Load was applied in vertical direction.*

(b) *SEM observation at strain level of 0.2, showing cavity development inside slip bands. Load was applied in horizontal direction.*

Fig. 5.5: *Observation of voids orientation with (a) ID19 beamline and (b) SEM observation.*

The quantification of void nucleation process was carried out by counting the variation of the number of

voids in the controlled volume (Fig. 5.6a) while the void growth process was characterized by the variation of the average diameter of the 20 largest voids of the population (Fig. 5.6b). Simple models can be used to simulate separately these processes. For void growth prediction, the Rice and Tracey (R&T) criterion (Eq. 5.3 - [Rice and Tracey, 1969]) or Huang's formulation (Eq. 5.4 - [Huang, 1991]) can be used as in several publications in the literature, e.g. [Maire et al., 2008, Landron et al., 2011, Thuillier et al., 2012]:

$$\frac{dR}{R} = \alpha_{RT} exp\left(\frac{3}{2}\eta\right) d\overline{\epsilon}_p \tag{5.3}$$

$$\frac{dR}{R} = \begin{cases} \alpha_{Huang}\eta^{0.25} exp\left(\frac{3}{2}\eta\right) d\overline{\epsilon}_p & if \quad \eta \leq 1 \\ \alpha_{Huang} exp\left(\frac{3}{2}\eta\right) d\overline{\epsilon}_p & if \quad \eta > 1 \end{cases} \tag{5.4}$$

where $\alpha_{RT} = 0.283$ and $\alpha_{Huang} = 0.427$ as proposed initially by Rice and Tracey ([Rice and Tracey, 1969])[2] and Huang ([Huang, 1991]); R is the radius of an isolated void in perfectly plastic matrix ([Rice and Tracey, 1969]), which can be approximated by the average radius of the 20 largest voids ([Landron, 2011]). Void nucleation can be phenomenologically simulated by different types of functions of equivalent plastic strain: polynomial function [Bouaziz et al., 2008], exponential function [Maire et al., 2008], or based on Argon criterion of decohesion [Landron et al., 2012]. These procedures were successfully applied for several recent studies, e.g. [Maire et al., 2008, Landron et al., 2011, Landron, 2011]. However, the 3 stages of ductile damage may occur simultaneously and affect each other, care must be taken when applying the separate forms to simulate each process.

In order to account for the influence of void nucleation on void growth, [Bouaziz et al., 2008, Maire et al., 2008] modified the R&T formulation (Eq. 5.3) as:

$$\frac{dR}{d\overline{\epsilon}_p} = \alpha_{RTm} exp\left(\frac{3}{2}\eta\right) R - \frac{1}{N}\frac{dN}{d\overline{\epsilon}_p}(R - R_0) \tag{5.5}$$

where dN and N are the nucleation rate and the void density respectively; R_0 is the radius of cavities just after their nucleation. This equation is referred to as *"the modified R&T formulation"* hereinafter. The evolution of the number of cavities per volume unity (or the void density) can be modeled by a product of linear and exponential functions of the equivalent plastic strain:

$$N = A\frac{\overline{\epsilon}_p}{\epsilon_N} exp\left(\frac{\overline{\epsilon}_p}{\epsilon_N}\right) \tag{5.6}$$

where A is a material constant (mm^{-3}); ϵ_N is the critical strain, at which the nucleation starts to occur, which is assumed as a function of the stress triaxiality (η):

$$\epsilon_N = \epsilon_{N_0} exp(-\eta) \tag{5.7}$$

In order to isolate the void growth process, the evolution of the average diameter of the 20 largest voids was modeled, using Eq. 5.3, while the void nucleation process was modeled separately using Eq. 5.6. The equivalent diameter was calculated from the total volume of cavity, which was measured by counting the number of voxels attributed to each cavity. The absolute error of this measurement of diameter is thus constant (of the order of several voxels) and the relative error depends on the diameter itself. It is rather important for small cavities ([Maire et al., 2008]).

The comparisons between the experimental results and the numerical results are presented in Fig. 5.6a and Fig. 5.6b for void nucleation and void growth processes respectively.

As one can observe in Fig. 5.6b, the evolution of the average diameter of the 20 largest voids can be predicted by the R&T formulation but it is not the case for the average diameter of all voids, which varies slightly with the plastic strain. As mentioned above, this tendency can be explained by the competition between the void growth and the void nucleation processes: the nucleation of new voids (small size) reduces

[2]The original formulation of R&T is: $\frac{dR}{R} = C(v_L) exp\left(\frac{3}{2}\eta\right) d\overline{\epsilon}_p$, where v_L is the *"Lode variable"*, which is defined by the three principal components of remote strain field: $v_L = -\frac{3\dot{\epsilon}_2}{\dot{\epsilon}_1 - \dot{\epsilon}_3}$, where $\dot{\epsilon}_1 \geq \dot{\epsilon}_2 \geq \dot{\epsilon}_3$. $C(v_L)$ can be approximated as: $C(v_L) \approx 0.279 + 0.004 v_L$. In uniaxial tensile state, $v_L = 1$, $C(v_L)$ is thus reduced to α_{RT}, which equals 0.283.

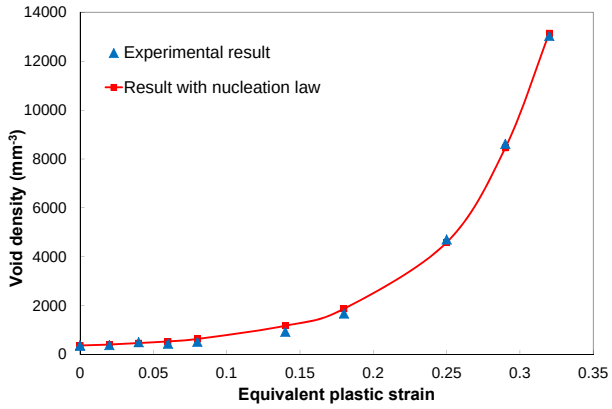

(a) *Evolution of the void density, which characterizes the void nucleation process.*

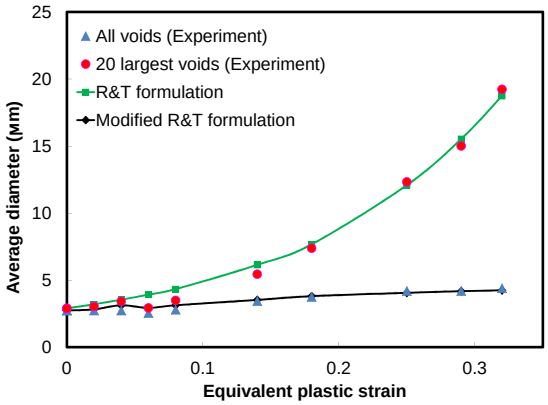

(b) *Evolution of average diameter of the 20 largest voids and average diameter of all voids.*

Fig. 5.6: *Tomography X results of voids evolution.*

the average diameter while the growth of voids increases the average diameter of all voids. Using the modified R&T formulation (Eq. 5.5) allows reproducing numerically the evolution of the average diameter of all voids (black curve in Fig. 5.6b). The identified parameters are reported in Table 5.1.

R&T	Nucleation law		Modified R&T formulation	
α_{RT}	A	ϵ_{N_0}	α_{RTm}	$R_0(\mu m)$
2.657	202.1	0.176	2.078	2.43

Table 5.1: *Identified parameters for voids nucleation and growth.*

Note that the modified R&T formulation was used to simulate the evolution of the average diameter of all voids but this measurement was not the key parameter. In reality, large voids are often the origin of final fracture. The average diameter of the 20 largest voids is thus more important to be followed and simulated.

In addition, continuous increase of the void density can be observed (also the rate of void nucleation), which suggests that void nucleation dominates void coalescence (when voids are linked, the total number of voids decreases). In fact, coalescence took place as shown in Fig. 5.4c but its influence on the void evolution was not noticeable (Figs. 5.6a and 5.6b). If the coalescence phase becomes important, it will slow down the increasing rate of void density and the average diameter of 20 largest voids could increase rapidly (as in Fig. 5.7a and Fig. 5.7b from [Landron, 2011]).

5.2.2 Discussion

- Influence of resolution: apparently, with the X-ray tomography technique, the void nucleation result is strongly influenced by the resolution since very small voids can only be detected under high resolution. In [Landron et al., 2012], the authors observed no significant influence of the resolution on the void growth process for a dual-phase steel. In the present study, two resolutions (with ID15 and ID19 beamlines) were also compared in terms of the overall evolution of the void volume fraction with the plastic strain. No difference was noticed ([Le Moal and Cassone, 2012]).

- Non-spherical cavities: as revealed in Figs. 5.5a and 5.5b, the cavities observed are elongated and make an angle about 45° to loading direction. This orientation of voids is most likely linked with the orientation of the slip planes created during the deformation. The Rice and Tracey formulation for void growth as well as the formulation proposed by Maire and co-workers for voids nucleation ([Maire et al., 2008]) were based on spherical void assumption. In our particular case, void is far from

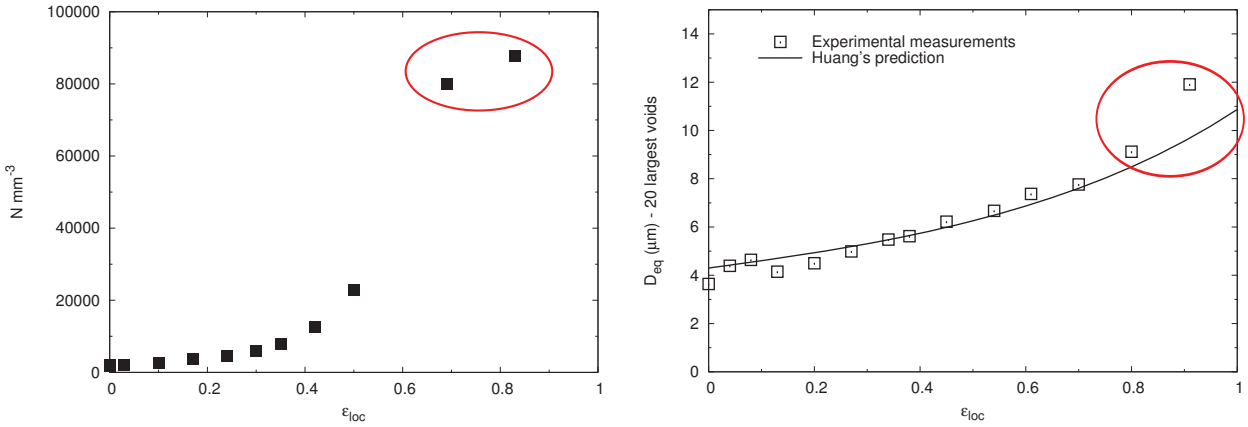

(a) *Evolution of void density (number of voids/mm^3), showing the strong influence of coalescence when the equivalent plastic strain is about 0.7.*

(b) *The void growth with the prediction by Huang model, showing a strong increase of the average diameter of the 20 largest voids when coalescence occurs.*

Fig. 5.7: *Result of [Landron, 2011] showing the strong influence of the coalescence phase on void nucleation and growth.*

being spherical. The use of these formulations must therefore be taken with caution. More complex void growth and nucleation formulations accounting for particular void shape are necessary in a future study (e.g. [Madou and Leblond, 2012]).

- Modified GTN model identification: in the above section, the void growth and void nucleation processes have been successfully modeled (both separately and simultaneously). The question is to see how to integrate the identified porosity evolution into the GTN model. Similar work was carried out by [Bettaieb et al., 2011, Fansi et al., 2013] where the authors considered that the modeled material contained one isolated spherical void, which was equivalent in volume as all the voids in real material. The real voids of material were replaced by N identical voids with the same radius R, which were then approximated by one single void with the equivalent radius equal to: $R_{eq} = \sqrt[3]{N}R$. There is no particular difficulty in implementing these equations into the GTN model, but the parameters identification needs the real evolution of voids density as well as voids size during the calibration tests. In the present study, the parameters calibration for the modified GTN model is carried out using the in situ X-ray tomography tensile test on notched round bar as well as other mechanical tests (tensile test on RB and NRB, torsion test). Apart from in situ tensile tests, the measurement of the evolution of cavities during other tests was not performed. For this reason, the classical GTN model is used in the present study (see section 4.1.2). The identification of this model is based on the real evolution of porosity from in situ X-ray tomography tensile test as well as the load-displacement curves from other classical tensile tests on RB and NRB. The identification of the parameter for the shear extension of GTN model (e.g. the parameter k_ω for N&H's modification) is achieved through the calibration from torsion test on cylinder specimens.

5.3 Models identifications

5.3.1 Hardening identification

The matrix material is considered to be isotropic and the plastic deformation is isochoric, obeying the J_2 plasticity theory. The hardening identification of the studied steel grade was detailed in [Cao et al., 2013b]. It was based on the cylinder compression test and tensile tests. The hardening law used was a modified form of Voce law ([Voce, 1955]), in which the flow stress is defined as:

$$\sigma_0 = \sigma_{p0} + \left(\sigma_{ps} - \sigma_{p0} + K_2\bar{\epsilon}^p\right)\left(1 - exp(-n\bar{\epsilon}^p)\right) \tag{5.8}$$

where: σ_0 is the flow stress of material matrix, n and K_2 are material parameters; $\sigma_{p0} = \sigma_0(\bar{\epsilon}^p = 0)$; $\sigma_{ps} = \sigma_0\,(\bar{\epsilon}^p \to \infty)$ if $K_2 = 0$. The unit of K_2, σ_{p0} and σ_{ps} is MPa. The identified hardening law was validated for different mechanical tests: compression, torsion and tensile tests. The identified parameters are reported in Table 5.2. From the in situ tensile test carried out by the MATEIS laboratory [Le Moal and Cassone, 2012], the value of equivalent stress and equivalent strain can be extracted from each scan via Eq. 5.2. These data are then used to identify a hardening law suitable for this test (Table 5.2). The Ludwik law ([Ludwik, 1996]) was employed to approximate the experimental stress-strain curve, in which the flow stress of material matrix is defined as:

$$\sigma_0 = \sqrt{3}K(1 + a\bar{\epsilon}^{pn}). \tag{5.9}$$

where $K(MPa)$, a and n are three material parameters to be identified. Fig. 5.8 shows the comparison between the experimental stress-strain curve and the numerical curves with identified Ludwik and modified Voce laws.

Modified Voce ([Cao et al., 2013b])				**Ludwik (In situ tensile test)**		
$\sigma_{p0}(MPa)$	$\sigma_{ps}(MPa)$	n	$K_2(MPa)$	$K(MPa)$	a	n
601.146	1113.194	37	100	350	1.105	0.1349

Table 5.2: *Identified hardening parameters for the high carbon steel.*

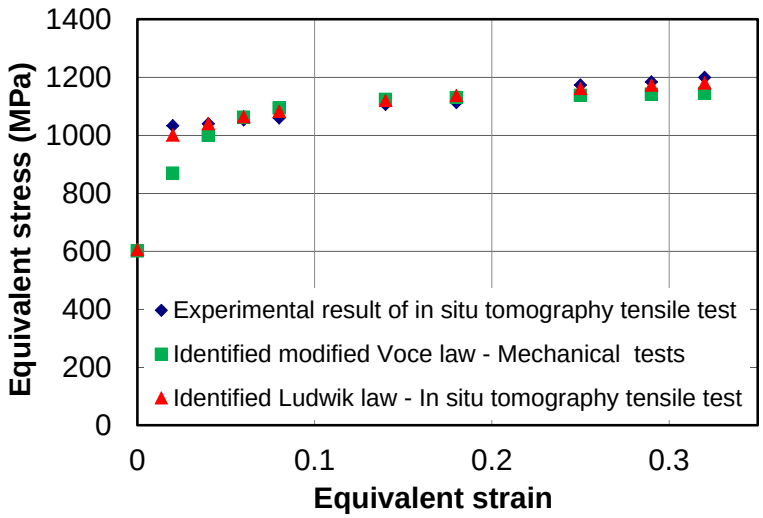

Fig. 5.8: *Comparison between the experimental result and numerical simulations with identified Ludwik and modified Voce laws.*

One can observe that the identified Ludwik law gives a better result for this test. The result obtained with the identified modified Voce law is also quite accurate. As stated above, this law was identified from different loading paths (tension, compression), which has been showed to be important for complex loading case applications. The comparison in Fig. 5.8 confirms the validity of our identified modified Voce law for different stress state.

Remark Note that the modified Voce law was identified based on different mechanical tests and was validated up to relatively large strain (in compression test). This law gave the overall best result for the tests used for identification. However, if one uses only one mechanical test to identify the hardening law (e.g. tensile test on RB), one can have a better curve fitting with another law (see Fig. 2.15b in Chapter 2). The point is, for complex loading applications, the use of a hardening law suitable for different stress states is necessary, but for a given test, better damage parameters can be obtained by using a law more appropriate for this test. Here, the Ludwik hardening law for the material matrix was only used for this in situ tensile test to have best

result for damage parameter identifications. The present author also emphasizes that the use of the modified Voce law is also valid, but the identified damage model parameters are *slightly* less accurate since this law is not as good as Ludwik's law in this tensile test. However, if the identified Ludwik law is used for compression test, the result is not precise.

5.3.2 GTN and shear extended GTN models identification

The GTN model was identified by using both the in situ tensile test and "macro" tensile tests[3]. We first used the in situ tensile test and observations to identify several measurable parameters (f_0, f_f, f_N) and also "phenomenological parameters" (q_1). "Macro" tensile tests were then used to verify identified parameters.

5.3.2.1 In situ tensile test

The evolution of the void volume fraction with the equivalent plastic strain is presented by the blue diamond symbol in Fig. 5.9a, in which each point represents the value at each scan.

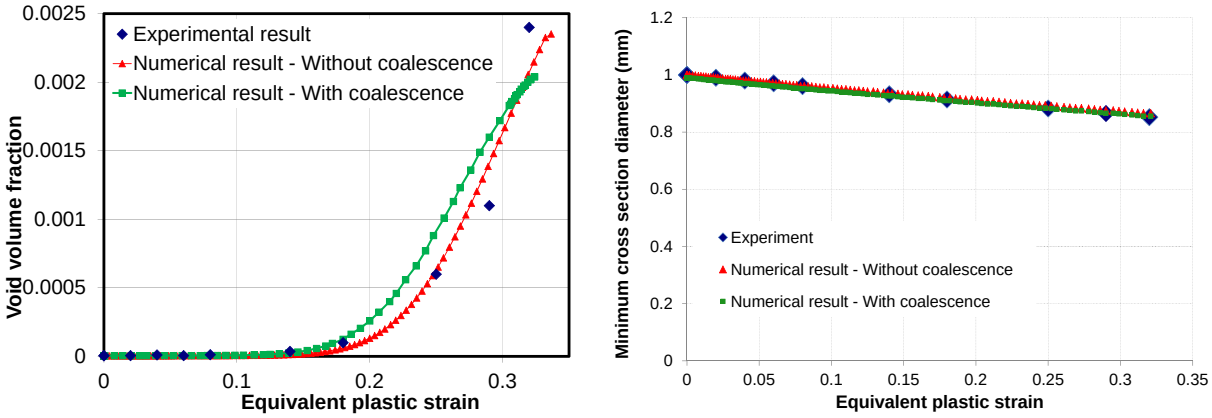

(a) *Evolution of the void volume fraction with the local equivalent plastic strain.*

(b) *Variation of the radius of minimum cross section during the in situ tomography tensile test.*

Fig. 5.9: *Comparison between the experimental result and the numerical result obtained with identified GTN parameter using Forge2009®.*

As mentioned above, in the present in situ tensile test, the nucleation mechanism seems dominant due to the fact that no clear influence of coalescence was found on void evolution (numbers of void, average size of voids - see Fig. 5.6). However, "local" coalescence was observed and we did not have any information concerning the real void evolution in "macro" tensile tests. For this reason, two different identifications were carried out for the GTN model: one without coalescence criterion (which is, in our opinion, more suitable for this particular material) and the other with coalescence (using parameter f_c).

Moreover, the last scan before fracture showed a void volume fraction of 0.0024. This value can be considered as *the void volume fraction at fracture* for the present in situ tensile test[4]. In addition, the initial porosity f_0 can be measured thanks to the X-ray tomography observation. For the constitutive parameters q_1 and q_2, they have the same influence on the yield surface as shown in Fig. 5.1: the increase of these parameters leads to the retraction of the yield surface. In addition, the q_1 parameter affects the post coalescence behavior (if coalescence is activated $f_u^* = 1/q_1$) and the q_2 parameter appears in the exponential term; it is often kept equal to 1 in the literature. With the latter choice, the exponential term in $cosh$ function in Eq. 4.27 reduces to $3/2\eta$, which is consistent with the equation proposed by Rice and Tracey (Eq. 5.3). It is probably the reason why q_2 is kept equal to 1 in the literature. Therefore, q_2 is assumed to equal unity while q_1 is a parameter to be identified. Finally, 4 parameters q_1, f_N, ϵ_N, S_N need to be calibrated from the result of in situ tomography

[3]The term "macro" or "micro" in this context must be understood as the size of specimens used.
[4]In reality, this value would be higher at the instant of fracture.

tensile test. The evolutions of the porosity and the minimum cross section radius as functions of the equivalent plastic strain are used for the identification process by inverse analysis[5]. The identified parameters are reported in Table D.3 while the comparisons between the experimental and numerical results are shown in Fig. 5.9.

The result obtained shows a good agreement between the experiment and the numerical simulation.

- A better result is obtained for a model without coalescence (Fig. 5.9a). Moreover, the identified value $f_c = 0.002$ for the coalescence case is near the final value at fracture. It means, if coalescence takes place, post-coalescence leading to fracture is quite fast. Since the case without coalescence gives a better result and is in agreement with the identification for damage mechanisms in section 5.2.1 (where no clear influence of coalescence was observed), this model will be used hereafter.
- The identified parameter q_1 is consistent with the value of 1.5 proposed by Tvergaard and Needleman.
- As mentioned above, in the present in situ tomography tensile test, the nucleation phase is dominant The value of ϵ_N is found equal to 0.29, which is in relatively good agreement with Fig. 5.6a, where the void nucleation increases rapidly around 0.26 to 0.3 of equivalent plastic strain. Note that the increase of void volume fraction was due to the combination of void growth and nucleation where the void growth itself was non-linear.
- The values of f_0 and f_f identified from in situ observations are quite small, which is probably due to the resolution used in the observations and this particular material. Moreover, the present author emphasizes that the value $f_f = 0.0024$ corresponds to the *last scan before fracture* in the in situ test (but in the present author opinion, the true value at fracture is of the same order of magnitude). The value of f_N is high because dominant nucleation is *assumed*.

5.3.2.2 Mechanical tensile tests

This identified set of parameters was then used for the tensile tests on RB and NRB as well as the torsion test. The transferability of these parameters from one test to another is questionable since some parameters might depend on the stress state (e.g. ϵ_N or f_f). In the present study, we suggested that the parameter ϵ_N depends on the stress triaxiality through an exponential function (similar to Eq. 5.7)[6]:

$$\epsilon_N = \epsilon_{N_0} exp(-B\eta) \tag{5.10}$$

where η is the stress triaxiality, which can be taken as the initial stress triaxiality if the loading is nearly proportional; B and ϵ_{N_0} are two parameters to be identified. The comparison between numerical and experimental load-displacement curves for tensile tests are presented in Fig. 5.10a and Fig. 5.10b. The parameters were calibrated to have the same *displacements to fracture* for the numerical simulations as for the experimental results (i.e. at the imposed displacement equal to the experimental displacement to fracture, the values of f_f in numerical simulations reaches 0.0024, which was identified from the in situ tensile test).

Let us discuss first the ductility of this material, represented by the local strain to fracture at different stress triaxiality levels. As shown in Fig. 5.11, the strains to fracture for different "monotonic" tests were plotted as a function of the *initial stress triaxiality*: the blue symbols represent the tensile test on axisymmetric specimens ($\bar{\theta} = 1$); the green symbols represent the plane strain tensile test ($\bar{\theta} = 0$) and torsion test ($\bar{\theta} = 0$, $\eta = 0$).

One can observe that the red point, from in situ X-ray tomography tensile test on notched round bar, lies below the extrapolated curve of strain to fracture at this stress state (i.e. the approximate curve for the blue diamond symbols in Fig. 5.11). This result shows that the studied material is *less ductile* in the in situ tensile test, meaning that at small scale, **the influence of the increase of porosity on material ductility seems more important than at large scale**. Since the nucleation is dominant in the present in situ test, the early

[5]The evolution of the minimum cross section diameter was used principally for verification purpose since at this small value of porosity, this diameter mostly depended on the hardening law used.

[6]As experimentally observed by Kao and co-workers ([Kao et al., 1990] - see Fig. 1.30b, Chapter 1), the nucleation strain may increase with the applied hydrostatic pressure (i.e. when the stress triaxiality decreases).

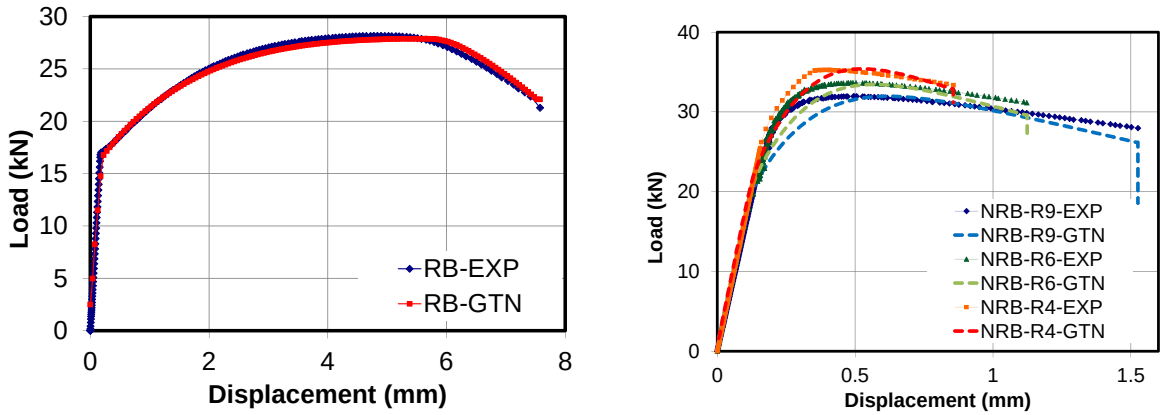

(a) *RB specimen.* **(b)** *NRB specimens.*

Fig. 5.10: *Experimental and numerical load-displacement curves of tensile tests with the identified GTN model.*

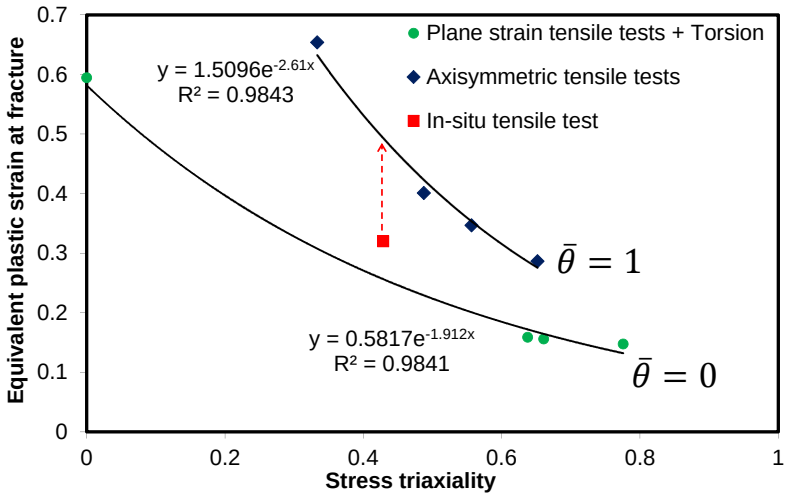

Fig. 5.11: *The experimental local strain at fracture is plotted against the initial stress triaxiality for different tests: tensile test on axisymmetric specimens ($\bar{\theta} = 1$), plane strain tensile test ($\bar{\theta} = 0$), torsion test ($\bar{\theta} = 0$, $\eta = 0$) as well as the in situ tensile test. The approximate exponential functions are presented with their corresponding coefficients of determination R^2. Note that the x variable represents the stress triaxiality while the y variable stands for the local fracture strain.*

fracture in the in situ test can be assumed governing by the "early" maximum nucleation. It is defined through the value of plastic strain at which the nucleation rate is maximum (i.e. ϵ_N).

Remark The observation mentioned above is strongly qualitative, just based on **two** in situ tensile tests with two different resolutions. About the size effect, since the *size of pore* is significantly smaller than that of "micro" specimen (1 mm diameter), there is no clear reason for earlier fracture of small specimens. This fact also raises a question on the link between the measurement of the physical quantity representing damage (i.e. void) and its real effect on mechanical properties (e.g. strength and rigidity). If we consider another microstructure size, for example, the *grain size*. This size is still significantly smaller than that of specimen and the same remark as above can be drawn. However, several authors showed the influence of the ratio of the number of grains on surface to the grains in volume (e.g. [Ran et al., 2013]). For a small specimen, this ratio is higher than that of large specimen and thus can have different effects on fracture behavior. However, in the present author point of view, this effect can be noticeable *if ductile crack initiates on specimen surface*. In the in situ tensile test as well as mechanical tensile tests, cracks initiated at the specimen center and thus the explanation of the difference in ductility between "micro" and "macro" specimens based on the above-mentioned ratio is not convincing. The size effect on ductility is still an open question.

Fig. 5.12 represents the identified parameter for the function in Eq. 5.10 where the value of ϵ_N for each test is plotted against its initial stress triaxiality. As one can observe, the values obtained with mechanical tensile tests can be approximated by Eq. 5.10 with $\epsilon_{N_0} = 1.412$ and $B = 2.712$, and the representation of the in situ tensile test lies under this curve. Since this value is relatively small in the in situ tensile test, the nucleation process is assumed to increase rapidly at this strain level.

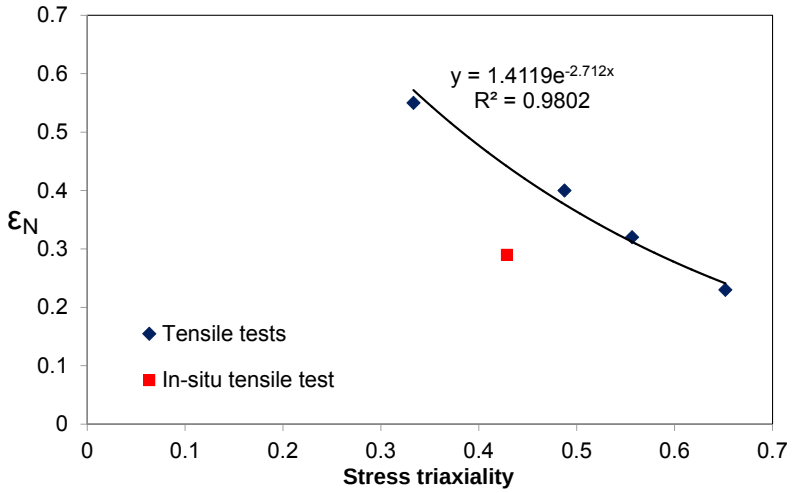

Fig. 5.12: *The "nucleation strain" ϵ_N is plotted against the initial stress triaxiality for different monotonic tensile tests on axisymmetric specimens. The x variable represents the stress triaxiality while the y variable stands for ϵ_N in the approximate exponential function.*

5.3.2.3 Discussion

As discussed above, micro specimens in the present study were *less ductile* than macro specimens. Nucleation takes place earlier when stress triaxiality increases (Eq. 5.10). Observation showed a dominant nucleation process in the present in situ test, and the above observation could be explained through a low value of *nucleation strain* (ϵ_N). The present author did not find any publication in the literature, which shows a totally consistent result between in situ X-ray tomography observation and mechanical tests for the GTN model identification. We also emphasize that for in situ test, only two tests were carried out to validate the reproducibility and result depended on resolution (using two beamlines ID15 and ID19 [Le Moal and Cassone, 2012]). Moreover, small specimens are strongly sensitive to experimental setup (alignment) and material microstructure (e.g. second phase particles - again, its size is significantly smaller than that of specimen in our study), size effect is still an open question. Extensive in situ tests in the future could help to better understand the difference between micro and macro tests.

5.3.3 Identification of the extended GTN models

The extensions of Nahshon & Hutchinson (with the modification of Nielsen and Tvergaard) and Xue for the GTN model were presented in section 4.1.4.1 and 4.1.4.2. In this section, the implementation of these two models in Forge2009® is first introduced, then their identifications are presented.

5.3.3.1 Implementation of GTN model extensions for shear loading

Xue's extension The implementation of the GTN model was presented in the previous chapter. For the shear extension by Xue, we adopted the "damage counter approach", which means the damage parameter does not influence elastoplasticity (the yield surface is still the GTN surface, with the presence of the void volume fraction as an internal variable). For such an approach, the damage parameter is calculated through a user-subroutine at the end of time increment once all state variables are updated.

N&H's extension As presented in section 4.1.4.1, an additional term was added in the evolution of the porosity. The implementation of N&H's modification was carried out with the "weak coupling" between the two internal state variables ($\overline{\epsilon}$ and f in the GTN model): in the local integration, at each time increment, the porosity was assumed constant during the increment and was updated at the end of increment using updated equivalent plastic strain (internal variable) and updated stress. The weak coupling helped to simplify the resolution. However, in order to obtain accurate results, time step must be chosen small enough. A comparison was carried out between strong coupling and weak coupling for a tensile test on notched round bar (see Appendix C.2), which showed a good agreement between the two approaches.

5.3.3.2 Xue's extension

For this extension, the parameter q_4 is derived from analytical calculation: $q_4 = 1/3$ for 3D case. The phenomenological parameter f_c^* must be identified since in the present study, we assumed that the increase of voids is due principally to nucleation and growth. By re-analyzing Xue's analytical developments, the parameter $q_4 = 1/3$ seems correct and the parameter q_3^* was adjusted to fit our experimental results.

The two parameters f_c^* and q_3^* were identified by inverse analysis to have $D = D_c = 0.98$ [7] at the end of simulation[8] (i.e. fracture at the end of test was predicted), which gave $f_c^* = 0.0019$ and $q_3^* = 0.85$. The result of damage variable at the end of simulation is shown in Figs. 5.13a (GTN model) and 5.13b (modified GTN by Xue).

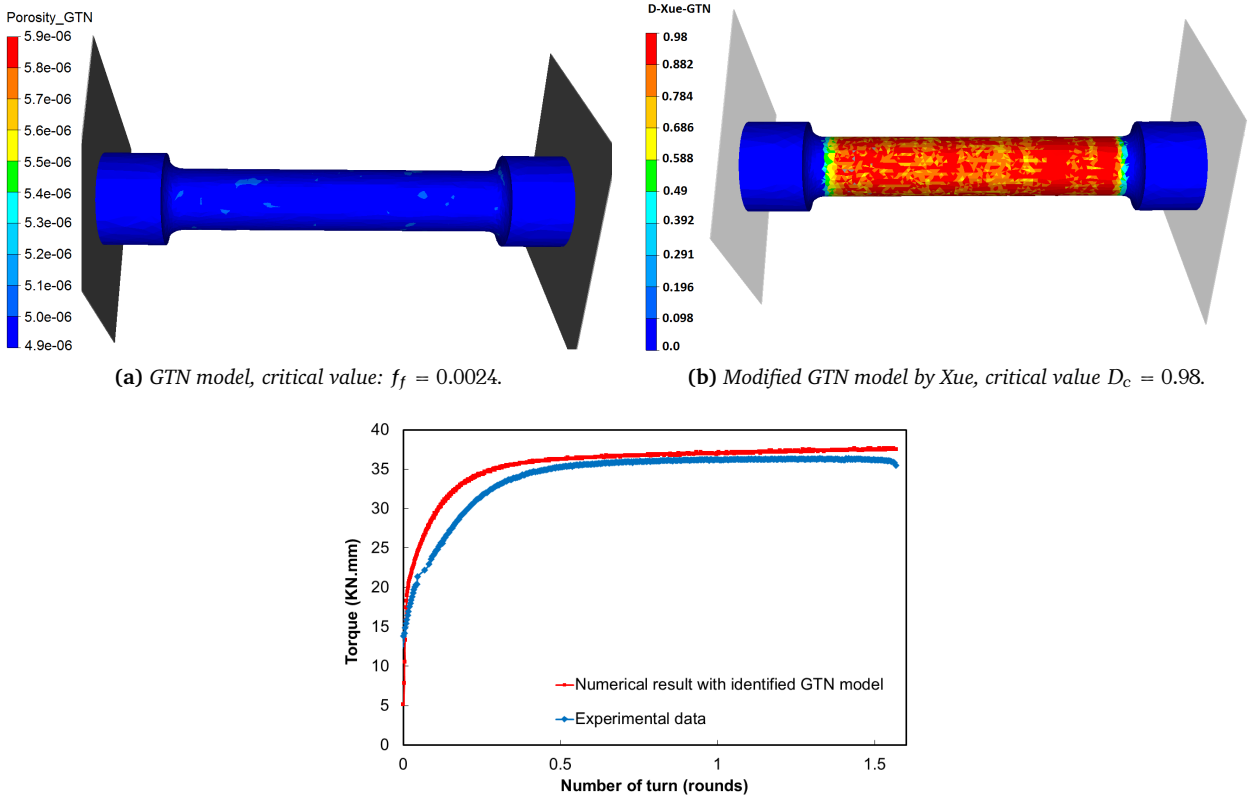

(a) *GTN model, critical value:* $f_f = 0.0024$.

(b) *Modified GTN model by Xue, critical value* $D_c = 0.98$.

(c) *Torque-number of turn curve.*

Fig. 5.13: *Damage variable of GTN model (a) and Xue's modification for GTN model (b) at the end of torsion test simulation with identified parameters. The torque-number or rotations curves for the two cases are the same since the damage counter approach was used (c).*

As expected, the GTN model failed to predict damage in torsion test (maximum value of porosity at the end

[7] The critical value is unity. However, to avoid numerical instability when $D = D_c$ (in case of coupling, the GTN yield surface reduces to the origin), we fixed the maximum value of damage equal to 0.98 instead of 1.

[8] The torque-number of rotations curve was also used but since the damage counter approach was employed, only f influenced the yield surface, and in a negligible way. The torque-number of rotations curve was therefore less sensitive to D.

of test is less than 5.9 10^{-6}, to be compared with the critical value $f_f = 0.0024$). For the extended GTN model by Xue, note that because of the difficulty in torsion simulation[9], variable field is not really homogenous. The torque-number of rotations curve is also represented in Fig. 5.13c, where the numerical result with the GTN model is compared with the experimental result (since the damage counter approach was used, the curves obtained with GTN model and modified GTN model by Xue are similar. A negligible influence of this modification on the result of tensile tests was also verified (moderate to high stress triaxiality).

5.3.3.3 N&H's extension

For the N&H modification, one single parameter needs to be identified (k_ω). The parameters of Nielsen and Tvergaard's modification were fixed as proposed by these authors: $T_1 = 0, T_2 = 0.5$. The torsion test was used to calibrate the parameter k_ω. This value was identified as $k_\omega = 8$, higher than the range $1 < k_\omega < 3$ proposed by Nahshon and Hutchinson ([Nahshon and Hutchinson, 2008]). Note that in [Nahshon and Hutchinson, 2008], the minimum value of initial void volume fraction chosen by the authors for their numerical tests was $f_0 = 0.001$, which was significantly higher than the value measured for the studied steel ($f_0 = 4.92\ 10^{-6}$). For this reason, higher value of k_ω is needed to reach the critical value of porosity, which defines fracture. We believe that this is the main reason for which a higher value of k_ω was obtained. However, extensive shear-dominated mechanical tests should be employed to confirm the value identified. The N&H's extension is thus not used for industrial applications.

5.4 Summary of Chapter 5

This chapter presents the identification of the GTN model and its extensions for high carbon steel using both in situ and mechanical tests. Results are summarized as:

- The matrix hardening law parameters were identified based on an in situ tensile test, which showed a good agreement with the identified hardening law from mechanical tests (presented in Chapter 2).
- From in situ tomography observations, void nucleation and growth can be modeled separately using Rice & Tracey equation for void growth (20 largest voids) and a formulation proposed by [Maire et al., 2008] for void nucleation (based on the number of voids). Moreover, to model the variation of average size of all voids, these two mechanisms have to be combined using a formulation proposed by [Bouaziz et al., 2008, Maire et al., 2008]. Identification of the corresponding parameters was carried out in post-processing and the results are in good agreement with experimental measurement.
- Identification of GTN model was carried out first on in situ tensile test using models both without and with coalescence as proposed by [Tvergaard and Needleman, 1984]. Results of the above damage mechanisms modeling (void nucleation and growth) showed that void coalescence is less influent on overall void evolution. Identification of GTN model confirmed the latter remark, which showed that better results are obtained with the model without coalescence.
- Macro-mechanical tests were then used to verify the identified parameters from in situ tensile test. A formulation for nucleation strain was proposed to better describe our experimental results. This formulation is based on the assumption that void can nucleate earlier at higher stress triaxiality (which was experimentally observed by Kao and co-workers [Kao et al., 1990] - Fig. 1.30b). Parameters of this formulation were also identified, along with parameters identified from in situ test (Table D.3 and D.4). They allowed reproducing our experimental results, both for micro (porosity-local strain curve)

[9] It is worth emphasizing a difficulty in torsion simulation: with a few rounds of rotation, if remeshing is not used during the simulation, the mesh at the end of the simulation is strongly distorted, unrealistic results are obtained. However, if remeshing is used, the number of remeshings must be high (since about 1.6 rotations are simulated), errors of variables transfer are high. For this reason, a method was proposed by Transvalor - Forge® software company, which can be considered as a modification of the Arbitrary Lagrangian-Eulerian (ALE) method. The results are more consistent (both local strain and stress state values), but some errors still exist: strain and damage field at the end of simulation is not really homogenous, as shown in Fig. 5.13b.

and macro tests (load-displacement curves). However, a mismatch in ductility between the microscopic and macroscopic tensile tests still exists, which need further elaboration in the future.

- Finally, we carried out the identification of modified GTN models (by Xue and by Hutchinson) based on torsion test. These models will be used to study the damage in forming processes in the next chapter.

5.5 Résumé en français

Dans ce chapitre, les travaux d'identification du modèle de GTN et ses modifications pour les chargements de type cisaillement ont été présentés. Ces identifications sont basées à la fois sur un essai de traction in situ à l'aide de la micro-tomographie aux rayons X et d'essais mécaniques "macroscopiques". Ce chapitre a été divisé en plusieurs parties. Dans la première partie, une revue bibliographique sur l'identification du modèle GTN et le principe de la tomographie aux rayons X ont été présentés. La méthode pour traiter des résultats de la traction in situ sous tomographie X a été aussi abordée.

Ensuite, les résultats de la traction in situ ont été analysés. Des observations in situ ont donné des résultats sur l'évolution continue de la fraction volumique du vide au cours de l'essai ainsi que sur les mécanismes de l'endommagement ductile : la germination et la croissance. Dans notre essai, nous avons remarqué que l'influence de la coalescence n'était pas remarquable. L'information sur la germination a été déduite en comptant le nombre de pores dans le volume de contrôle, tandis que la croissance a été caractérisée par l'augmentation du diamètre moyen des vingt plus gros pores. Le fait d'utiliser les vingt plus gros pores nous aide à isoler la phase de croissance. Afin de modéliser ces deux mécanismes, nous avons utilisé les équations proposées par Rice et Tracey [Rice and Tracey, 1969] (pour la croissance) et par [Maire et al., 2008] (pour la germination). Cependant, l'évolution de l'ensemble des pores a montré une compétition des deux mécanismes si l'on regarde l'évolution du diamètre moyen de tous les pores : le diamètre moyen est resté quasiment constant au cours de l'essai; et la croissance de la porosité existante fait le augmenter, tandis que la germination des nouveaux pores (petits) diminue le diamètre moyen de toute la population. Pour pouvoir modéliser cette évolution, la formule développée dans [Bouaziz et al., 2008, Maire et al., 2008] a été utilisée. Les paramètres de ces lois ont été identifiés en post-traitement, ce qui nous a permis de modéliser les mécanismes d'endommagement ductile.

Dans la troisième partie, l'identification des paramètres d'écrouissage ainsi que du modèle GTN a été présentée pour l'acier haut carbone (C62). Tout d'abord, nous avons identifié une loi d'écrouissage de type linéaire puissance (loi de Ludwik) à partir de la courbe contrainte-déformation issue de l'essai de traction in situ. En plus, l'identification de la loi d'écrouissage de ce matériau a été présentée dans la section 2.2.3.4 du chapitre 2 grâce aux essais mécaniques (traction et compression). Ces deux lois d'écrouissage identifiées ont été montrées cohérentes. Ensuite, l'identification du modèle GTN a été présentée avec les deux cas : avec ou sans la coalescence. Le résultat de l'identification sur l'essai in situ a montré que le modèle sans coalescence donne un meilleur résultat sur la courbe porosité-déformation, ce qui a confirmé notre remarque en première partie que la coalescence n'était pas essentielle dans notre essai. Ce jeu de paramètres identifiés à partir de l'essai in situ a été validé sur des essais de traction réalisés sur des éprouvettes plus grandes. L'objectif était de vérifier que ce jeu de paramètres permettait de prédire la rupture dans ces essais (i.e. $f = f_f$ à la fin des simulations), et de vérifier les courbes force-déplacement. La déformation pour laquelle le taux de germination est maximal (ϵ_N) a été prise comme une fonction exponentielle décroissante de la triaxialité. Cela signifie que la germination va avoir lieu plus tôt si la triaxialité est plus forte. Avec cette loi identifiée et le jeu des paramètres issus de l'essai in situ, l'ensemble de nos essais a été reproduit correctement. Finalement, l'identification du modèle GTN modifié par Xue et par Nahshon & Hutchinson (N&H) a été réalisée, basée sur l'essai de torsion. A noter que le modèle modifié par Xue a été implémenté grâce à une routine utilisateur, alors que l'extension de N&H a été implémentée sous forme d'un couplage faible : dans l'intégration locale des équations constitutives, à chaque incrément de temps, la porosité est fixée au cours de l'incrément. Cette variable est mise à jour à la fin de l'incrément en utilisant la déformation plastique et la contrainte mises à jour. Cette approximation est jugée acceptable du fait des petites déformations à chaque incrément.

Part III

Process applications and discussions

Chapter 6

Applications to cold forming processes

Contents

Introduction

Now that we have both elastoplastic and damage parameters, this chapter aims at applying the identified damage models to real forming processes for three materials. In the present PhD thesis, 3 forming processes are studied: wire drawing, rolling (Ugitech, ArcelorMittal) and cold pilgering (AREVA/CEZUS). All the experiments on processes were carried out by the industrial partners. The technological input data (die geometry, die kinematic) of processes simulations were also supplied by them. We will apply our developed and identified hardening and damage models on these processes. In the following section, for each process on a material, mechanical analyses of that process will be given first, then the comparison between different damage models will be presented (see Table 6.1 for the damage models used for each material).

Damage model	High carbon steel	Zirconium alloy	Stainless steel
Lemaitre	•	•	•
Xue phenomenological	•	-	-
B&W	•	•	•
MMC	-	•	-
GTN	•	-	-
Modified GTN - Xue	•	-	-

Table 6.1: *List of damage models used for each type of material: • indicates that the corresponding model was used. The choice was based on the ability to identify the model as well as on industrial needs.*

6.1 Processes for high carbon steel (C62)

The validation on high carbon steel was divided into two types: qualitative and quantitative validations. Two processes were studied: wire drawing (both qualitative and quantitative validations) and wire flat rolling (qualitative validation). Damage models used were B&W, Lemaitre, Xue and GTN, which were identified in sections 3.2 and 5.3.2.

6.1.1 Mechanical analysis of multi-pass wire drawing process

6.1.1.1 Process descriptions

The studied wire drawing process consists of 4 passes with the characteristics described in Table 6.2[1]. The inlet velocity of pass 1 was 333 mm/s and it increases from pass 2 to pass 4 due to "material flux" conservation (continuous drawing). The results of pass 1 and pass 4 will be presented to study the influence of section reduction on mechanical properties.

Pass	Radius (mm)	Section reduction (%)	Semi die angle (°)	Shape factor (Δ)
Initial	10.5			
1	**9.5**	**18.14**	**6**	**2.09**
2	8.6	18.04	6	2.1
3	7.86	16.47	6	2.32
4	**7**	**20.69**	**6**	**1.86**

Table 6.2: *Characteristics of the 4 studied drawing passes.*

[1]The studied 4 drawing passes are the first four passes of the "ultimate drawing" laboratory test presented in section 6.1.2.

We recall the definition of the shape factor Δ for wire drawing (see section 1.1.3):

$$\Delta = \frac{D_i + D_f}{D_i - D_f} sin(\alpha) = \frac{\left(1 + \sqrt{1 - r}\right)^2}{r} sin(\alpha) \tag{6.1}$$

where D_i, D_f are initial and final diameters of wire, r is the reduction ratio, α is the semi die angle. From this equation, Δ **increases with** α **and increases as** r **decreases**.

The friction between wire and die was modeled by the Tresca law (see Eq. 1.25), with $\overline{m} = 0.02$. The hardening law used for our simulations was the point-per-point type, valid for a large strain range (plastic strain up to 3). This curve could be approximated by a linear power law as shown in Fig. 6.1.

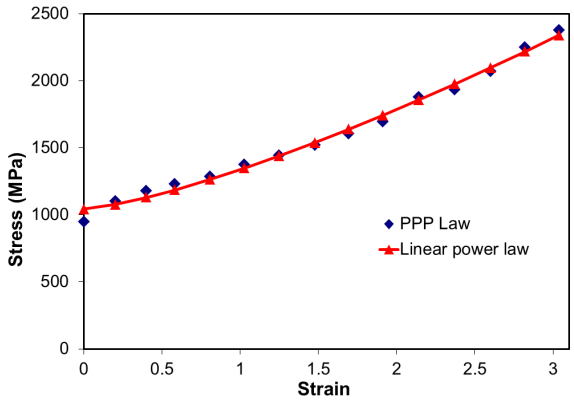

Fig. 6.1: *Hardening law used.*

6.1.1.2 Equivalent plastic strain and strain rate

Fig. 6.2 represents the strain rate field at steady state for two cases: pass 1 and pass 4. The strain-rate is higher at inlet and outlet contact points and also in the wire core, and is equal to zero outside the working zone. Note that the strain-rate is one of the most important factors, which influences the damage accumulation process. **The damage accumulation process occurs only in this working zone** (with a non-zero strain-rate). This important remark will be repeated hereafter. For the comparison between the two passes, one can observe that the first pass has smaller values of strain-rate (Figs. 6.3a and 6.3b) [2].

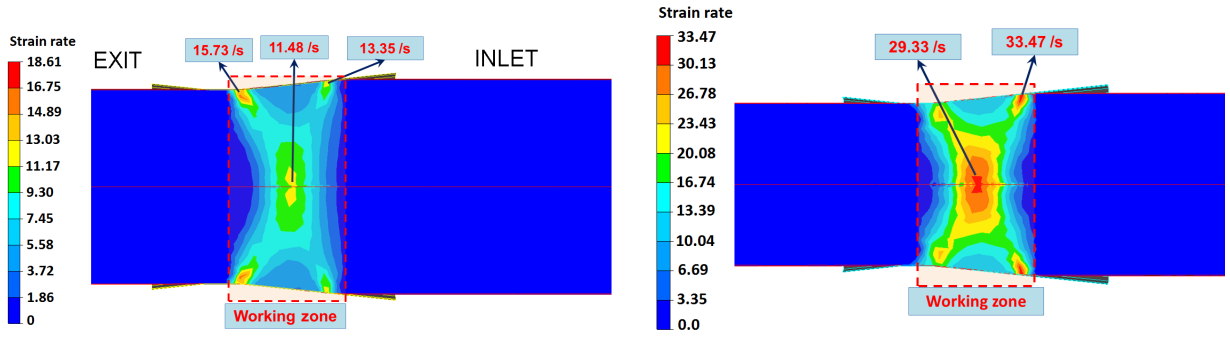

(a) *Pass 1* **(b)** *Pass 4*

Fig. 6.2: *Strain-rate distribution at steady state.*

From Fig. 6.2, we can observe that the strain-rate map is strongly heterogeneous both in radial and axial directions. Shear bands can also be observed. The equivalent strain is larger on the wire surface than in the wire core due to a stronger shear effect on the wire surface (see Fig. 6.3), and the difference of these values can be approximated as: $\Delta\epsilon = tan(\alpha/2)$, where α is the inlet semi-angle.

[2] There are two factors that lead to the difference of strain-rates between these two passes: (1) the reduction ratio of the first pass is smaller than that of the fourth pass, and (2) the drawing speed of the first pass is also smaller than that of the fourth pass - 666 mm/s.

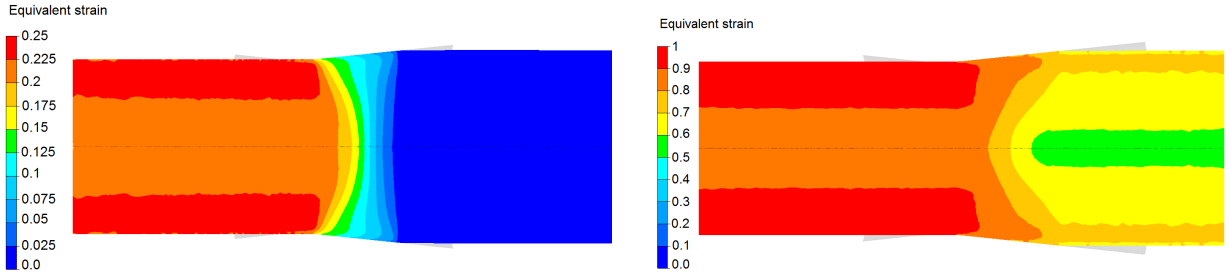

(a) *Pass 1* **(b)** *Pass 4*

Fig. 6.3: *Equivalent plastic train distribution at steady state.*

6.1.1.3 The 1^{st} principal stress

In the wire drawing process, the drawn wire is pulled by an axial tension to pass through the dies. The axial stress is therefore expected to be the dominant stress and can also be approximated by the first principal stress (or the largest principal stress). Fig. 6.4 shows the distribution of the first principal stress at steady states for the 1^{st} pass and the 4^{th} pass.

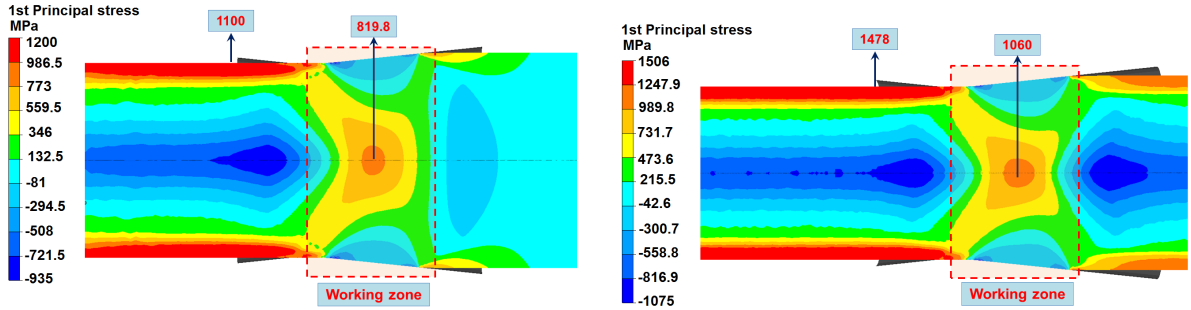

(a) *Pass 1* **(b)** *Pass 4*

Fig. 6.4: *The first principal stress at steady state.*

Inside the working zone where the damage accumulation occurs, the first principal stress is highest in the core (819.8 MPa in 1^{st} pass and 1060 MPa in 4^{th} pass) and is negative in the contact zone. For this reason, all the damage models based on the first principal stress (e.g. Latham-Cockcroft model) tend to predict higher damage in the wire core (see section 6.1.1.6).

Moreover, comparing pass 1 and pass 4 (Δ decreases), the principal stress (which can be approximated by the axial stress) increases. This can be explained by the increased hardening at the 4^{th} pass. Moreover, the increase on surface can also be explained by the increase of friction effects (because of the increase of contact length: $L_D = \frac{D_i - D_f}{2sin(\alpha)}$) when the reduction ratio increases.

6.1.1.4 The stress triaxiality ratio

The stress triaxiality maps are shown in Figs. 6.5a and 6.5b. These figures represent only the values that are greater than $-1/3$ (the cut-off value of stress triaxiality).

Similar distribution of stress triaxiality between the two cases can be observed, except a slight difference at die inlet (marked zone in Fig. 6.5b). This difference may be due to the difference in contact length. Nevertheless, the value of the stress triaxiality in this zone is small (between -0.33 and -0.231) and thus does not disturb the result.

The representation of the stress triaxiality helps to capture the potential position for damage nucleation and growth. In the working zone, the triaxiality is greater in the wire core and has positive values at these positions. Since the strain-rate is also greater in the wire core, damage models based on triaxiality (e.g. Oyane, Lemaitre) often predict damage at this position (see section 6.1.1.6 and section 6.1.2.2 for more details).

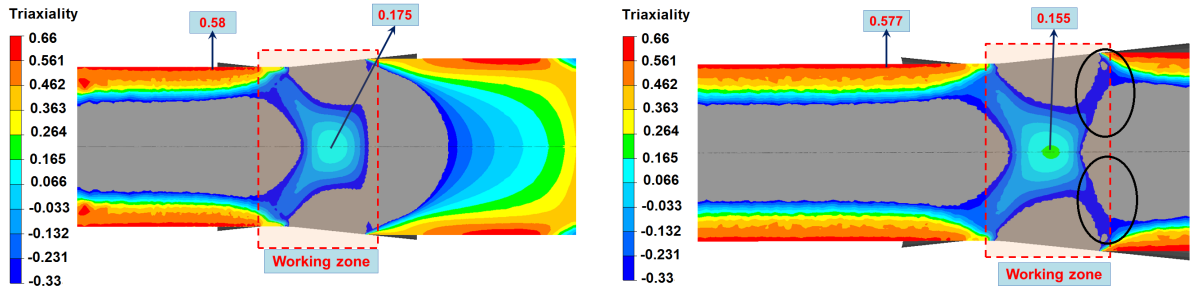

(a) *Pass 1* **(b)** *Pass 4*

Fig. 6.5: *The triaxiality at steady state.*

6.1.1.5 The Lode angle parameter

In this section, we use the following definition of the Lode parameter: $\mu = \frac{2\sigma_2 - \sigma_1 - \sigma_3}{\sigma_1 - \sigma_3}$. Note that $\mu \approx -\overline{\theta}$ ($\mu = -\overline{\theta}$ for some conventional stress state, e.g. uniaxial tension, torsion - see section 1.4.2.1).

Figs. 6.6a and 6.6b represent the distributions of Lode angle parameter.

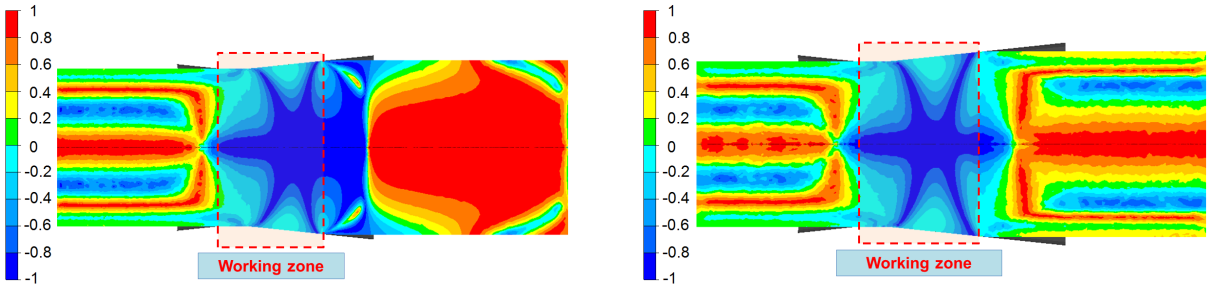

(a) *Pass 1* **(b)** *Pass 4*

Fig. 6.6: *The Lode angle parameter μ at steady state.*

Through these figures, no clear difference is found between these two cases. The difference before inlet is due to residual stress; for the first pass, there is no residual stress while for the fourth pass, the residual stress of previous drawing pass is accounted for. The Lode parameter is equal to -1 in the wire core in the working zone, which means the wire core is under a stress state equivalent to pure tension (to a spherical stress state). Before and after entering the working zone, the Lode parameter is equal to 1 in the wire core, which means the wire core is under a stress state equivalent to uniaxial compression. Therefore, one can observe a tendency of "compression-tension-compression" of material in the wire core during this process. To confirm this statement, numerical sensors were placed at the wire core to study the evolution of mechanical fields of a material point at this position.

Fig. 6.7 shows the evolutions of hydrostatic pressure and axial stress of a material point in the wire core.

The sign shifts "positive-negative-positive" of hydrostatic pressure and "negative-positive-negative" of axial stress confirm the above statement. These figures also reveal the complexity of the loading path that a material point undergoes through the process: one material point passes from compression to tension states as wire passes through dies[3].

6.1.1.6 Damage criteria: qualitative investigation

In this section, 2 damage criteria - Latham-Cockcroft (LC), Oyane - are considered. These criteria are predefined in Forge®2009 and do not require any parameter identification.

[3]Nevertheless, since the deformation only takes place in the working zone, the damage accumulation only occurs in this zone.

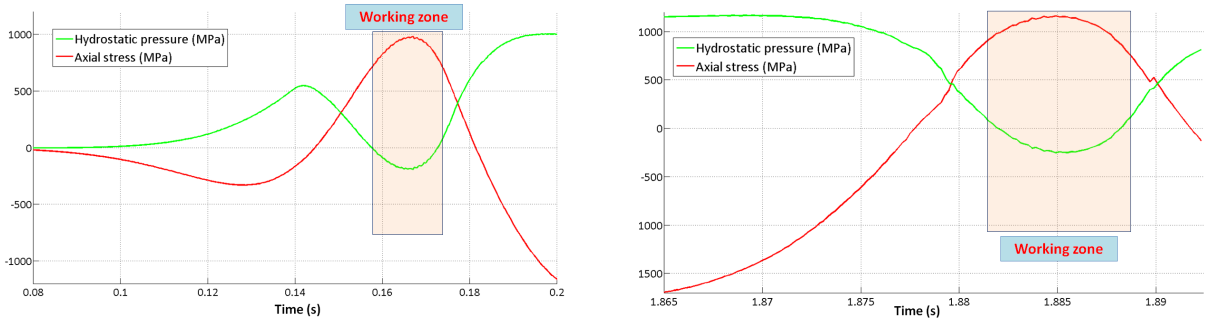

(a) *Pass 1* **(b)** *Pass 4*

Fig. 6.7: *Evolution of hydrostatic pressure and axial stress at a material point in the wire core, during the wire drawing process for the first and the fourth passes.*

Latham-Cockcroft (LC) criterion: $D_{LC} = \int_0^{\overline{\epsilon}_p} max(\sigma_1,0)d\overline{\epsilon}_p$, where D_{LC} is the LC damage indicator, $\overline{\epsilon}_f$ is the equivalent fracture strain. The locations where the damage accumulation occurs correspond to non-zero equivalent strain rate and positive first principal stress.

Oyane criterion: $D_{OY} = \int_0^{\overline{\epsilon}_p} max(1 + \frac{3\sigma_h}{\sigma_{eq}},0)d\overline{\epsilon}_p$, where D_{OY} is the Oyane damage indicator. The locations where the damage accumulation occurs correspond to non-zero equivalent strain rate and positive triaxiality.

Figs. 6.8a and 6.8b represent the damage variables for two criteria: LC and Oyane respectively. As stated before, in this process, the models that are based on the first principal stress or the stress triaxiality tend to predict damage mainly in the wire core.

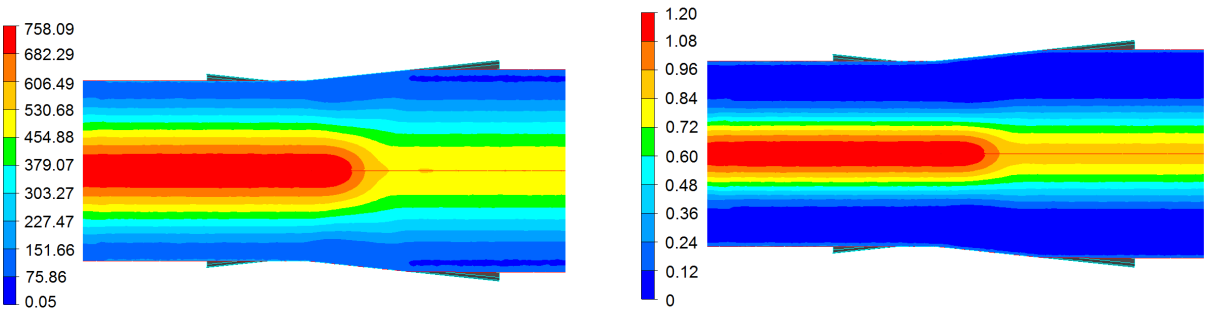

(a) *LC model* **(b)** *Oyane model*

Fig. 6.8: *The damage variable at 4^{th} drawing pass (without damage coupling with the material behavior, i.e. without weakening effect).*

6.1.2 "Ultimate wire drawing"

The first application is the "ultimate wire drawing" process, in which the wire is drawn until fracture. For a detailed analysis of microstructure evolution and damage growth during ultimate drawing for C72 steel, see [Massé, 2010]. In this reference, the author presented the observations using Scanning Electron Microscope (SEM). In the present study, we concentrate on the comparisons between our identified and developed damage models for fracture prediction, both quantitatively and qualitatively (i.e. localization position[4] and instant of fracture).

[4]In the present context, the term *"damage localization"* must be interpreted as *the maximum damage locations*.

6.1.2.1 Process description

The ultimate wire drawing on C62 steel grade was done at ArcelorMittal Research center. It consisted of 14 passes whose characteristics are presented in Fig. D.1a and D.1b. The initial diameter was 21 mm and the final diameter was 4.6 mm.

6.1.2.2 Damage prediction analyses

As expected, for such a process, damage is higher in the wire core than in the wire skin. Fig. 6.9 shows damage distributions (on the longitudinal and transverse cross sections) at second drawing pass with three different models: Bai & Wierzbicki, Xue and Lemaitre, which confirm high localization of damage in the wire core. Moreover, between the two coupled models, we can observe a strong localization in the wire center with the Lemaitre model can be observed, while for the Xue model, damage changes gradually from the wire core to the wire surface.

The reason is that for the models based on the Lode parameter and the stress triaxiality, shear influence is accounted for, which is maximum on the wire surface. In the working zone, since the stress triaxiality in the wire skin is *close to* its cut-off value (-1/3), damage accumulation predicted by the Lemaitre model is not noticeable.

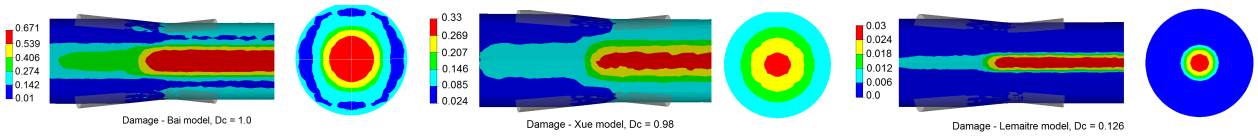

(a) **(b)** **(c)**

Fig. 6.9: *Damage at steady state of second drawing pass for different models: (a) Bai & Wierzbicki, (b) Xue and (c) Lemaitre. The values are represented on the longitudinal and transverse cross sections.*

Since damage was higher in the wire core, numerical sensors were set at this position to follow damage evolution as well as to determine the instant of fracture (i.e. when damage variables reach their critical values). Fig. 6.10 represents the increase of damage variables with the accumulated equivalent plastic strain during multi-pass wire drawing. Note that since remeshing took place after each drawing pass (to avoid mesh distortion), the values may slightly change due to the error of field transfer from old mesh to new mesh. For this reason, in Fig. 6.10, a small jump after each pass may be observed.

As can be seen in Fig. 6.10a, for the Bai & Wierzbicki uncoupled model, damage increases proportionally with the cumulative plastic strain. Fracture is predicted at the 4^{th} pass with this model when the damage variable reaches its critical value (unity). The Xue model and the Lemaitre model predict fracture at 5^{th} pass (see Figs. 6.10b and 6.10c). With these two models, we can also observe that damage is only activated from a certain level of plastic strain due to the presence of plastic strain threshold for damage initiation.

In Fig. 6.10d, for the identified GTN model (see section 5.3.2 in Chapter 5), from the first to the fourth drawing passes, porosity increases with the plastic strain but the value is still small (since the initial porosity was small, $f_0 = 4.92\ 10^{-6}$). The porosity then increases sharply with the equivalent plastic strain (pass 5 and pass 6) because nucleation is maximum at this strain level (the "nucleation strain" ϵ_N is obtained thanks to Eq. 5.10 and the stress triaxiality level at the wire center is around 0.15 - Fig. 6.5). After this strong nucleation period, the porosity increases slightly with the equivalent plastic strain and reaches its critical value at the 13^{th} pass. From this result, it seems that the choice of a Gaussian distribution to represent the strain-driven nucleation process in the GTN model is questionable, since one assumes that nucleation is nearly deactivated when the plastic deformation is greater than $\epsilon_N + 3S_N$.

Fig. 6.11 represents the contour plot of the void volume fraction at different drawing passes, showing also the strong localization of damage in the wire center for the GTN model.

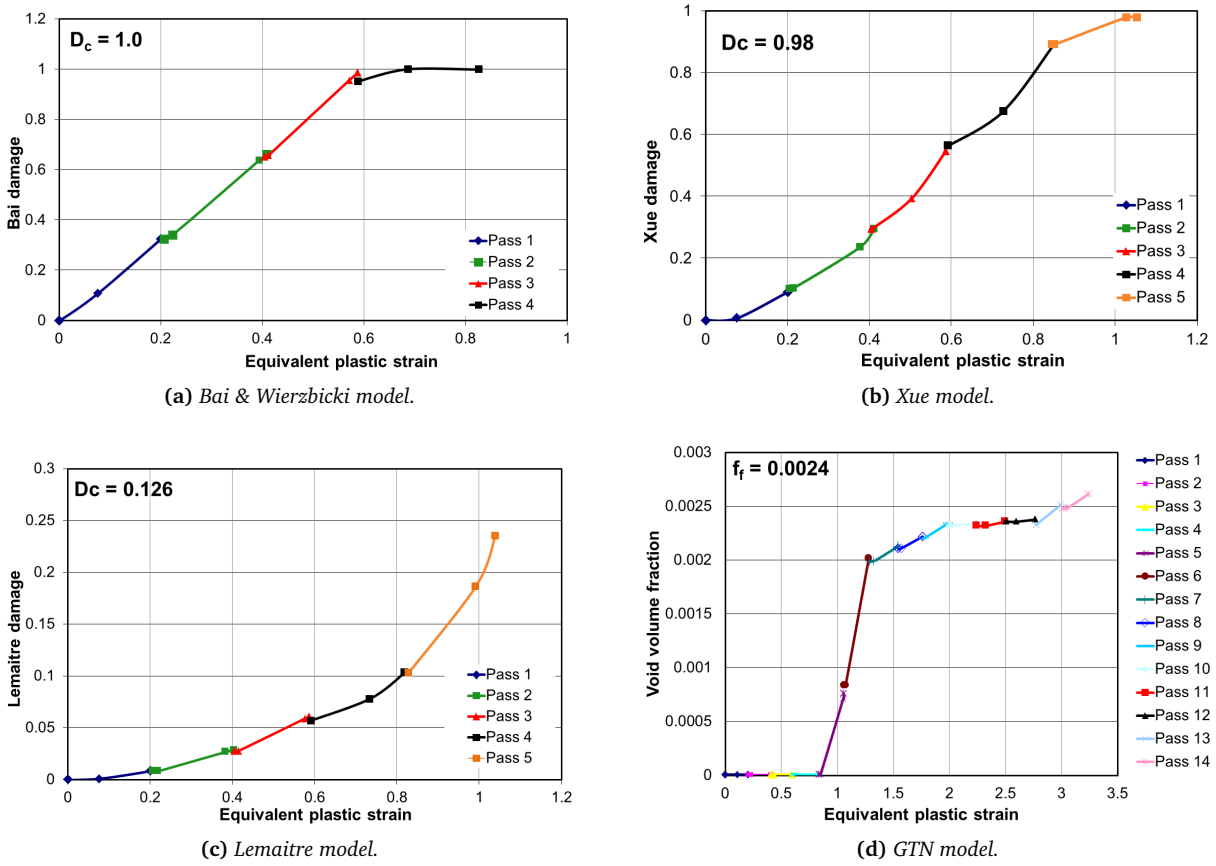

(a) *Bai & Wierzbicki model.*

(b) *Xue model.*

(c) *Lemaitre model.*

(d) *GTN model.*

Fig. 6.10: *Evolution of damage variables of a material point located at the wire center for different models (a) Bai & Wierzbicki, (b) Xue, (c) Lemaitre and (d) GTN.*

6.1.2.3 Conclusions

The above comparisons between our four identified models lead to the following conclusions concerning qualitative (localization) and quantitative results (instant of fracture):

1. All four identified damage models show a good agreement with experimental observation in terms of damage localization (in the wire core).

2. The three studied phenomenological models (Bai & Wierzbicki, Xue and Lemaitre) cannot predict accurately the instant of fracture initiation. These models predicted fracture at the 4^{th} or the 5^{th} pass, which was far from experimental result (the 14^{th} pass). For the GTN model, this model predicted damage at the 13^{th}pass, which is comparable with the experimental result. However, this result must be taken with caution since in the present author opinion, the use of Gaussian distribution to describe the nucleation for this material is not the most suitable.

6.1.3 Application to rolling process - Qualitative validation

In this section, all the above-mentioned damage models are compared qualitatively based on the prediction of damage localization in rolling processes.

6.1.3.1 Mechanical analyses

In the real process, after 4 passes of drawing (see section 6.1.1), the wire is subjected to 3 rolling passes. Details of mechanical aspects were given in section 1.1.2 of Chapter 1. In this section, we just focus on the first rolling pass for qualitative results.

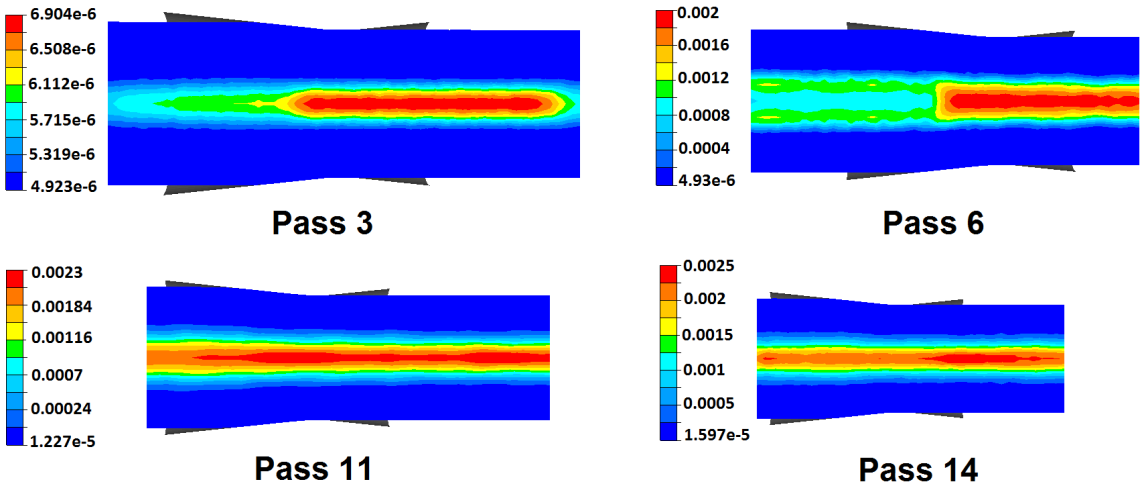

Fig. 6.11: *Contour plot of the void volume fraction at different drawing passes, showing damage localization at the wire center (GTN model).*

The schematic of the studied wire flat rolling process was presented in Fig. 1.1 (Chapter 1). The studied process is one stage cold rolling of wire, with the height reduction (ΔH) of 3mm and the roll rotation speed is 20 rpm ($\approx$ 2.09 rad/s - [Cao et al., 2013b]). For the mechanical analyses, the stress and strain history from the 4 previous drawing passes was accounted for.

Fig. 6.12a shows the strain-rate distribution on the longitudinal cross section when wire passes through the rotating rolls. Strain rate is higher at the entrance contact point and in the "wire" center. Fig. 6.12b shows its distribution on the cross section (A-A) perpendicular to the rolling section, where strain rate is higher on the blacksmith cross.

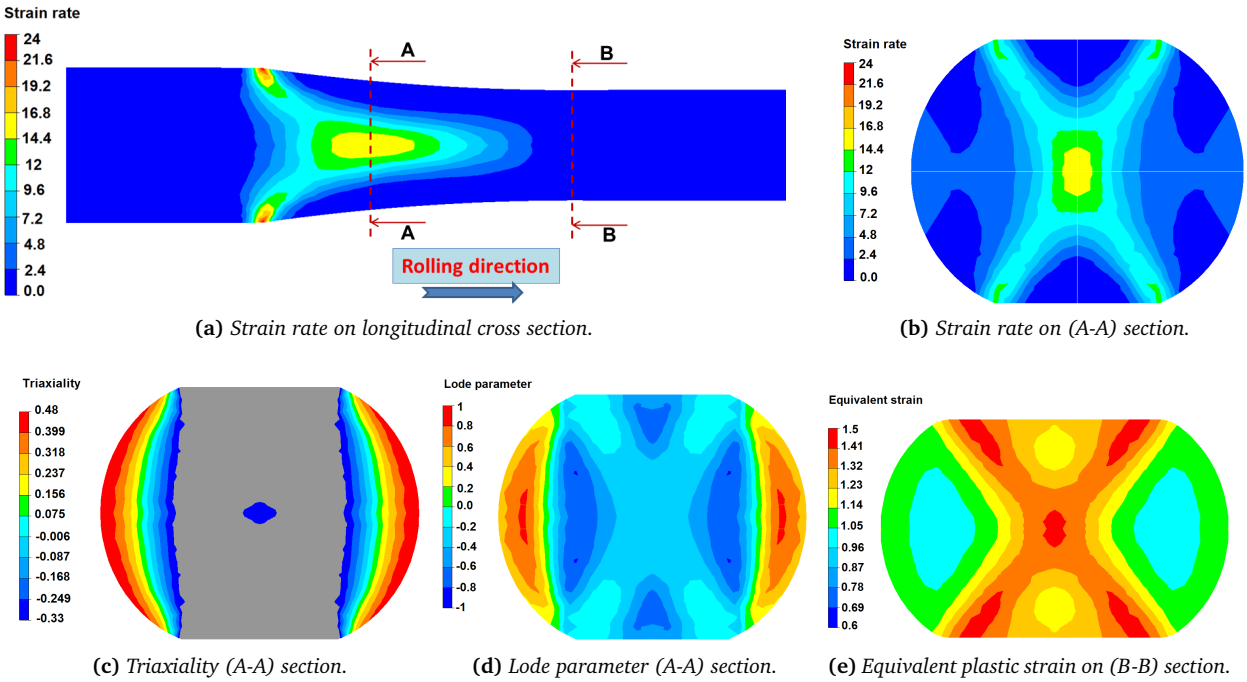

(a) *Strain rate on longitudinal cross section.*

(b) *Strain rate on (A-A) section.*

(c) *Triaxiality (A-A) section.*

(d) *Lode parameter (A-A) section.*

(e) *Equivalent plastic strain on (B-B) section.*

Fig. 6.12: *Mechanical fields in rolling process: (a) Strain-rate on longitudinal cross section; (b) strain rate, (c) stress triaxiality and (d) Lode parameter on cross section (A-A), (e) equivalent plastic strain on cross section (B-B).*

Figs. 6.12c and 6.12d represent the contour plots of the stress triaxiality and the Lode parameter on the cross section (A-A), the position where wire was in contact with rolls. For the stress triaxiality, only values

greater than $-1/3$ are presented; the triaxiality is greater in the barreling zone (lateral free surface). For this reason, as it will be shown in the following (section 6.1.3.2), damage models based only on the stress triaxiality tend to predict maximum damage in this zone.

Regarding the Lode parameter, a cross band ("shear" band) where $\overline{\theta} \approx 0$ can be observed in Fig. 6.12d. As mentioned before, $\overline{\theta} = 1$ represents a stress state equivalent to uniaxial tension; and when $\overline{\theta} = 0$, the stress state is equivalent to pure shear.

Fig. 6.12e shows the strain map on the cross section (B-B) at bite exit. For such a process, strain concentrates on the blacksmith cross and in the flattened wire center, although strain was higher on the wire surface at the end of the 4^{th} drawing pass (i.e. before rolling - see Fig. 6.3).

6.1.3.2 Comparison between studied damage models

Two validation cases were considered:

1. Rolling without influence of previous drawing.
2. Rolling with stress and strain history of previous 4 drawing passes.

Without influence of previous drawing process Fig. 6.13 represents damage distribution for different models on a cross section perpendicular to the rolling direction at the end of rolling.

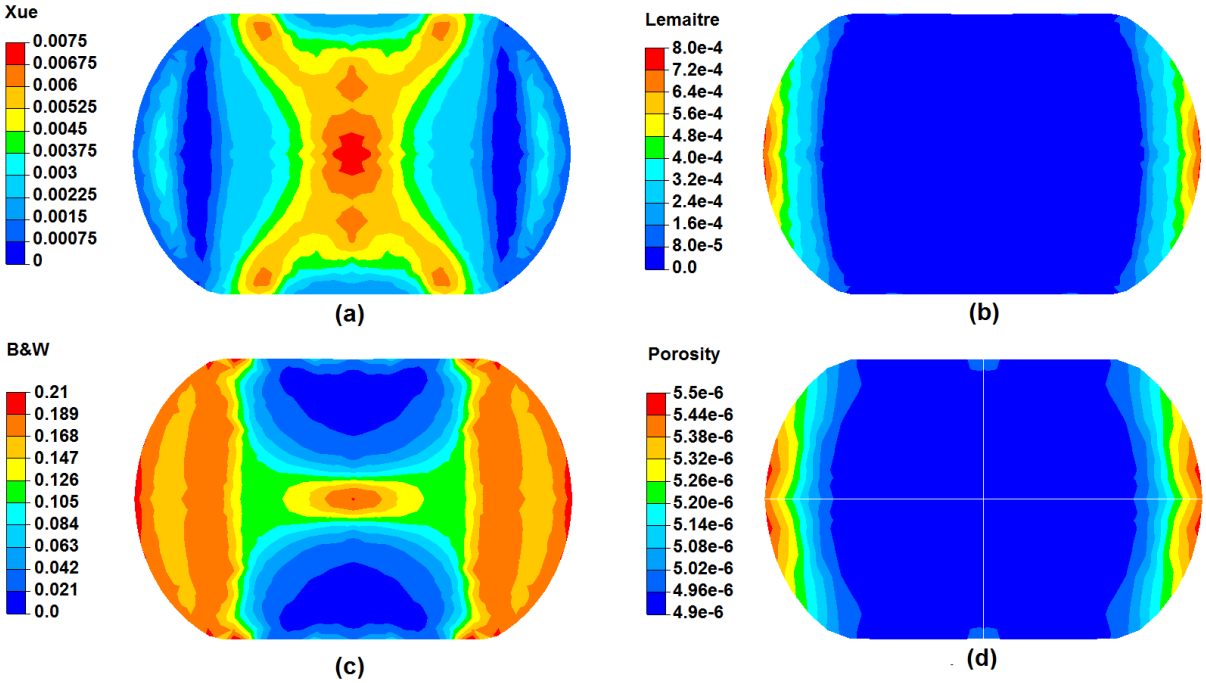

Fig. 6.13: *Damage on a cross section perpendicular to the rolling direction with different models: (a) Xue, (b) Lemaitre, (c) B&W and (d) GTN. The mechanical history of 4 previous drawing passes is not accounted for.*

First, the Xue model predicts higher damage in the wire core and on the black-smith cross (Fig. 6.13a), where strain localization takes place (see Fig. 6.12e). With this model, damage and strain localize at the same position. This cross was also the position where the Lode parameter was zero and the stress triaxiality was negative during the deformation process (i.e. when wire passed through rolls - see Figs. 6.12c and 6.12d). We also observe a "secondary maximum" of damage in the lateral zone.

Stress triaxiality- (or pressure-) based damage models (i.e. Lemaitre and GTN), as expected, predict maximum damage in the barreling zone (Figs. 6.13b and 6.13d), where the stress triaxiality is positive when deformation takes place (Fig. 6.12c). Note that porosity growth is extremely small with the GTN model.

For the B&W model, damage is higher at the barreling zone and also in the center (6.13d)). Secondary maximum is also observed near the barreling zone.

Accounting for stress and strain history from 4 previous drawing passes Fig. 6.14 represents damage distribution for different models when the deformation and stress history from 4 previous drawing passes was taken into account.

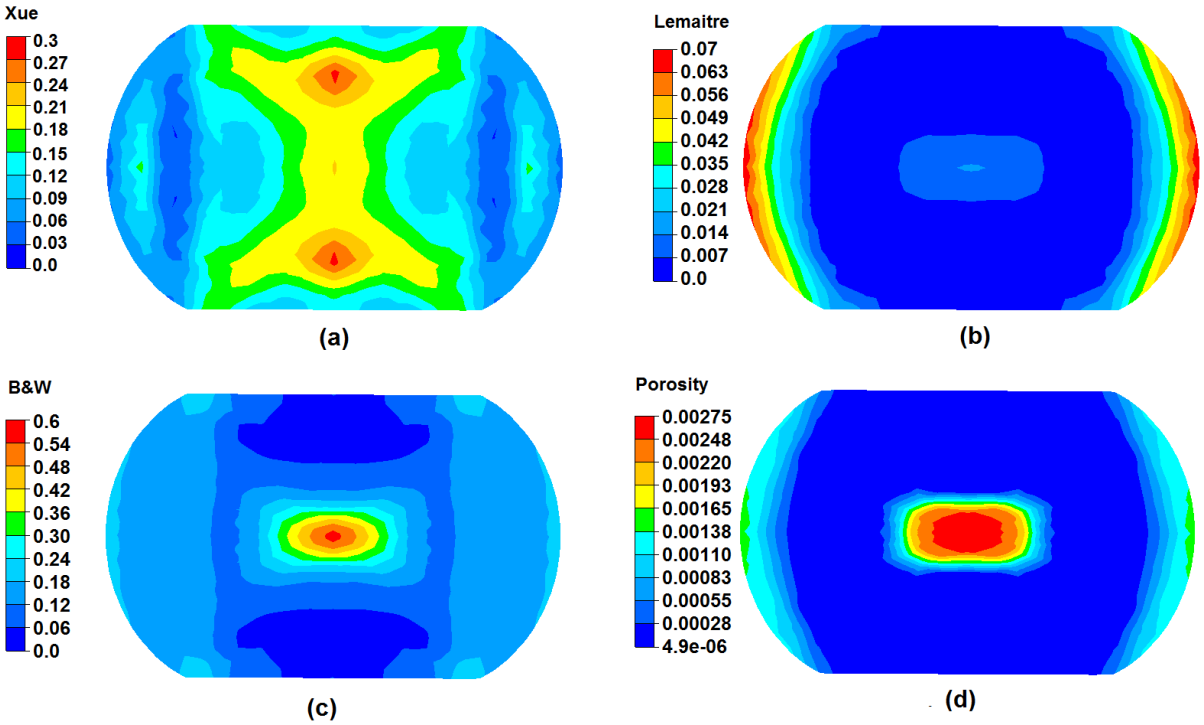

Fig. 6.14: *Damage on a cross section with different models: (a) Xue, (b) Lemaitre, (c) B&W and (d) GTN. The mechanical history of 4 previous drawing passes is accounted for.*

From Fig. 6.14, the difference with respect to Fig. 6.13 is clear. For the two coupled phenomenological models, damage is still higher in the cross band with Xue's model and in the barreling zone with Lemaitre model. Note that for the latter model, a slight increase of damage in the flat wire center can be observed, where the equivalent plastic strain is high (higher than the strain threshold ϵ_D - Fig. 6.12e) and the stress triaxiality is higher than its cut off value of $-1/3$ (see Fig. 6.12c). Again, secondary maximum of damage is also observed in the barreling zone with the Xue model.

Both B&W and GTN models predict higher damage in the wire center (see Figs. 6.14c and d). Note that for the GTN model, at this level of strain, nucleation has taken place and the porosity is significantly higher in the wire center. The porosity in the barreling zone is smaller, although this zone has high stress triaxiality, but the strain-rate is small when the wire enters the working zone (so nucleation rate is small).

Experimental result As presented in section 1.6.1 of Chapter 1, the experimental result of Massé showed a higher density of voids in the wire core and on the blacksmith cross as well as several voids at lateral surface (see Fig. 1.41 or Fig. 6.15).

In [Massé, 2010], the results showed that the strain path change modified voids expansion mode. In the wire drawing process, the growth of voids followed the axial direction (as the axial direction was the dominant direction), while in the rolling process, the void growth followed the transverse direction (since the material was compressed vertically between 2 rolls). Back to Fig. 6.15, one can observe that the extension of decohesions in the wire core and in the blacksmith cross follows the transverse direction while in the free edge zone, there was no significant expansion in the transverse direction. Moreover, the inclusions located in the branches of the blacksmith cross seem to have a preferential orientation due to rotation associated with shear strain in this area. The author mentioned a higher void density as well as a higher flattening of cavities in the wire core than at the free edge zone. The decohesion in the free edge zones follows principally the axial direction due to the 4 previous drawing passes [Massé, 2010]. This means there was no significant

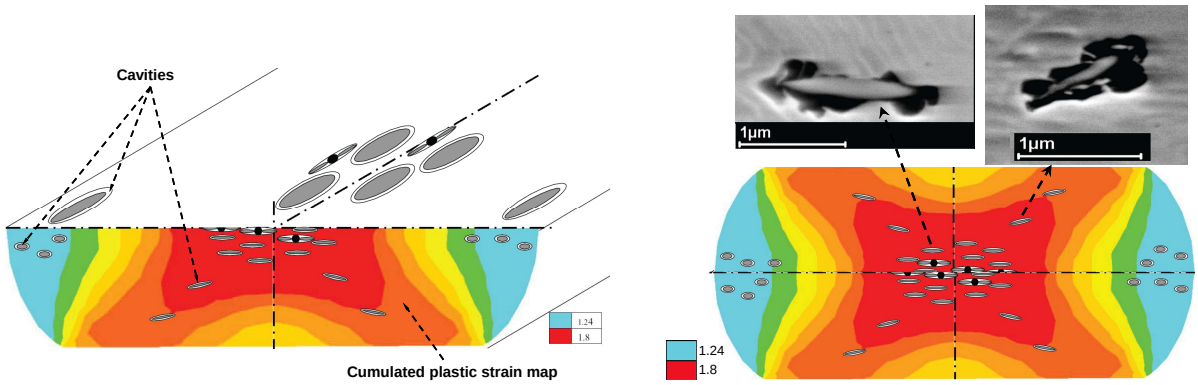

(a) *The sketch shows the decohesion in axial direction due to the wire drawing process and in axial direction due to the rolling process. Moreover, void rotation can be observed in the blacksmith cross.*

(b) *The zoomed pictures show flattened deformable inclusions in the wire core and in the blacksmith cross (SEM pictures).*

Fig. 6.15: *3D-sketch of the damage state at the end of rolling superimposed to strain map obtained by FEM analysis (color) (figure adapted from [Massé, 2010]).*

extension of decohesion due to rolling in this zone. Therefore, although the experimental observation proved the existence of voids around inclusions in the free edge zones, these voids were probably created during drawing and extended slightly during rolling. For this reason, final fracture will initiate principally in the wire core and in the blacksmith cross. The ability of a damage model to predict precisely these locations is indeed essential.

Among the above-studied models, the Xue model gives relatively good results concerning damage localization during rolling. With this model, damage is localized on the blacksmith cross, and less significant but also noticeable damage in the barreling zone can also be observed (Figs. 6.13a and 6.14a), where in the reality, voids expanded slightly.

The models based on the pressure or the stress triaxiality (Lemaitre, GTN) cannot provide the localization of damage in the shear zone (Figs. 6.13b and d, Figs. 6.14b and d). For the B&W model (Figs. 6.13c and 6.14c), it can be considered as an intermediate case, where damage is significantly higher in the core and nearly equivalent at other positions except the position under contact surface with rolls.

GTN model modified by Xue Since the GTN model gives relatively correct result both qualitatively and quantitatively for the wire drawing process (see section 6.1.2) and the error in damage localization for rolling process is expected because its formulation is based on volumetric part of stress tensor, we will investigate the result with its modification accounting for the influence of the third deviatoric stress invariant in the formulation (GTN model modified by Xue). Fig. 6.16 represents the damage localization obtained (identified in section 5.3.3), with or without deformation history of 4 previous drawing passes.

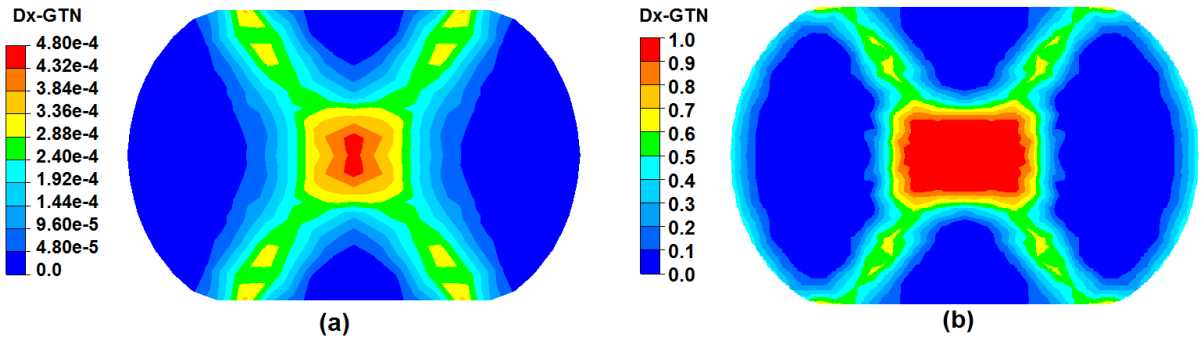

Fig. 6.16: *Damage localization in rolling with modified GTN model: (a) without deformation history from drawing; (b) with deformation history.*

As observed in Fig. 6.16a, damage is strongly localized in the blacksmith cross and in the wire center (without the deformation history from wire drawing). This localization is in good agreement with experimental results concerning the influence of rolling process on damage. With the influence of the deformation history from 4 previous drawing passes, the localization is high in the blacksmith cross and also in the barreling zone, which is consistent with damage observation during chained wire drawing - rolling process. However, this is only a qualitative conclusion since the parameter of Xue's modification was identified only from the torsion test. Moreover, the experimental results of damage in the rolling process for the C62 steel grade is not available. The microstructure observations from [Massé, 2010] were carried out on a C72 steel grade. Nevertheless, it is reasonable to assume that damage localization would be the same.

6.2 Application to stainless steel processes

6.2.1 Process description

The objective of the experimental test is to compare two different processes in terms of limit reduction. Starting from the same initial wire (D_i = 5.56 mm), two processes (wire drawing and rolling) were used to reduce the wire section until final fracture. This experimental comparison helps choosing the most relevant process and also validating the ability of numerical simulation with our developed damage models to predict failure.

6.2.1.1 Wire drawing process

The studied wire drawing process consists of 8 passes, with the corresponding normalized section reduction ratios[5] presented in Fig. 6.17. The final wire diameter after 8 drawing passes is 2.7 mm. The drawing speed was about 1 ms^{-1}.

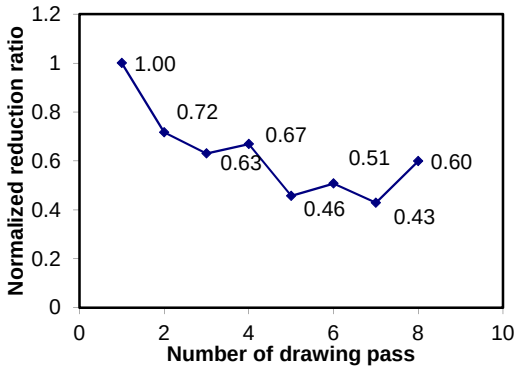

Fig. 6.17: *Normalized section reduction ratio of each drawing pass.*

6.2.1.2 Wire rolling process

The studied process consists of 5 passes, each pass involves 2 stands (3+3 rolls or 2+2 rolls). The first pass used the 3+3 technology, where 2 stands of 3 rolls were set next to each other (see Fig. 6.18a). For each stand, one roll made an angle of 120° with another. For the other four rolling passes, the 2+2 rolls were used, which consisted of one horizontal stand and one vertical stand of 2 rolls (see Fig. 6.18b). The normalized section reduction ratios for each pass are shown in Fig. 6.19. The final wire diameter at the exit of the 5^{th} pass is 3.1 mm.

[5]The section reduction ratio is normalized by the maximum reduction (the first drawing pass).

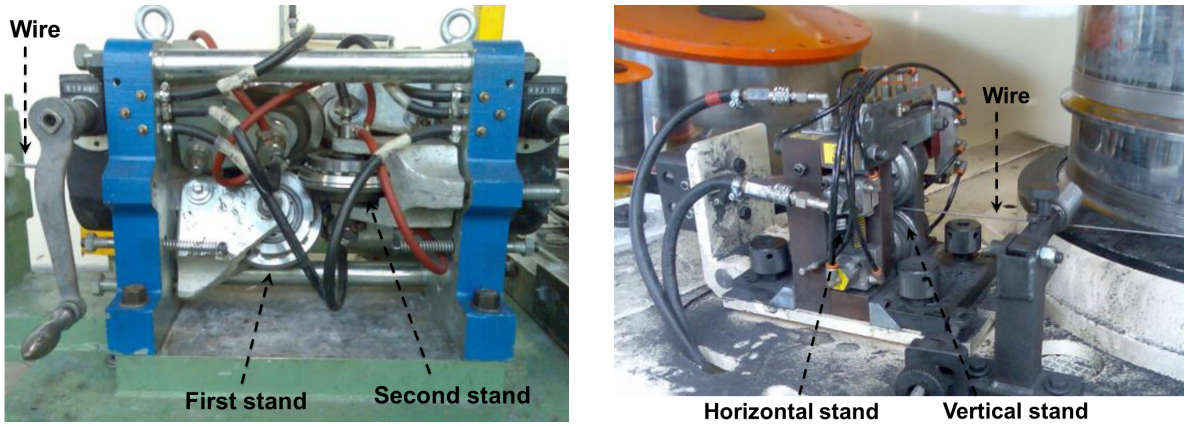

(a) *3+3 technology.* **(b)** *2+2 technology.*

Fig. 6.18: *The rolling mills used in the experimental study [Vachey, 2011].*

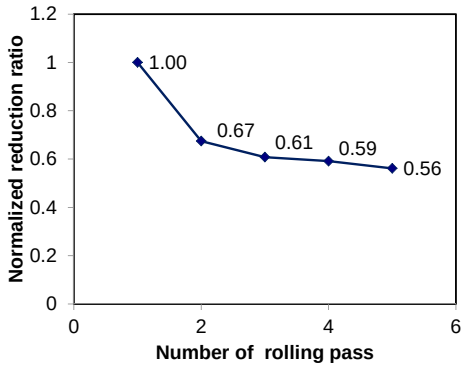

Fig. 6.19: *The 5 passes wire rolling process studied: normalized section reduction ratio of each pass.*

6.2.2 Process simulation

For the process simulations, the identified Hansel Spittel law from section 2.4 (or Hollomon's law due to the simplification) was used. The damage models used were B&W (identified in section 3.4) and Lemaitre (identified in Appendix C.1.1). Only the results obtained with B&W model are presented. The results with Lemaitre model are presented in Appendix C.1.2.

6.2.2.1 Wire drawing process

For the simulation of wire drawing, we used different values of Coulomb's friction coefficient μ (see Table 6.3) and the limiting friction parameter was set to $\overline{m} = 0.07$ (Eq. 6.2):

$$\tau = min(\overline{m}\frac{\overline{\sigma}}{\sqrt{3}}, \mu\sigma_n). \tag{6.2}$$

These friction parameters were measured by fitting experimental drawing forces.

Pass	1	2	3	4	5	6	7	8
μ	0.01	0.04	0.03	0.025	0.025	0.015	0.015	0.005

Table 6.3: *Identified Coulomb's friction coefficient for all the drawing passes.*

Die angles were also measured from experiment, which gave $\alpha/2 = 5 - 10^o$ (Fig. 6.20).

Mechanical analyses of the wire drawing process are detailed in section 1.1.3. We focus on the results concerning strain and damage fields.

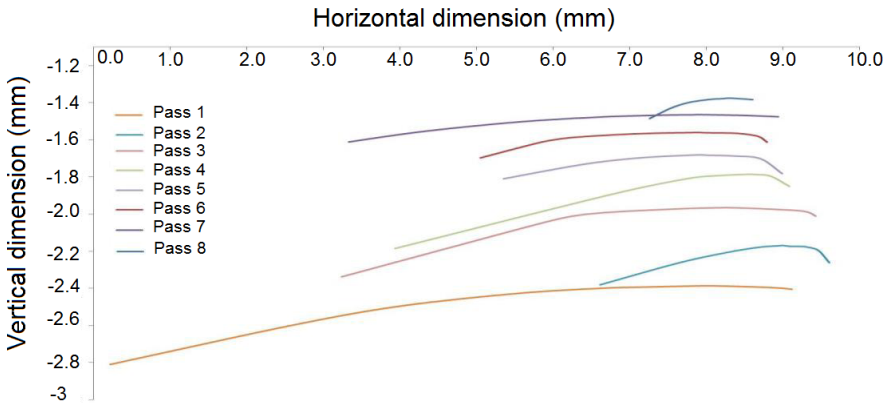

Fig. 6.20: *Geometry of 8 dies used for wire drawing process on stainless steel (figure adapted from [Vachey, 2011a]).*

Equivalent plastic strain The accumulated plastic strain maps of the eight drawing passes are presented in Fig. 6.21. The results are represented on the longitudinal cross section of wire. As can be observed, for this process, the strain on the surface is significantly higher than in the wire core. At the end of the 8^{th} pass, the equivalent plastic strain on the surface reaches 1.85.

Damage Numerical results of damage are presented in Fig. 6.22 for all eight passes. The identified B&W model predicts damage higher in the wire core, except for the first pass. This model also predicts the presence of damage on the wire surface, although its value is smaller than in the wire core. Moreover, after eight drawing passes, the damage parameter reaches 0.9 in the wire core, which is not far from the critical value ($D_c = 1$).

A numerical sensor was set up at wire center to follow the evolution of stress and damage during the eight drawing passes. With the hardening law used, the material hardens continuously during drawing (Fig. 6.23a). The increase of damage is nearly proportional to the equivalent plastic strain, except for pass 1 and pass 7: the contact length of the dies for these two passes is significantly higher than those of other drawing passes (or the die angles of these two passes are lower than those of other passes), which leads to a higher compression in the wire core (see e.g. Figs 6.22 and 6.20 for dies geometry). The damage in the wire core therefore increases moderately in these two passes. In addition, high contact lengths in these two passes (1 and 7) lead to strong increase of damage on the surface.

Moreover, one can observe from Fig. 6.23b, for the first drawing pass, strain increases without too much increase of damage. In order to explain this observation, the evolution of stress triaxiality and damage were plotted together only when the studied material point entered the die (or the deformation zone, i.e. positive strain rate - Figs. 6.24a and 6.24b). In Fig. 6.24b, we can see that damage accumulation occurs only if the stress triaxiality is greater than the cut-off value of $-1/3$. This fact can explain the evolution of damage for pass 1 in Fig. 6.23b: at first, damage increases proportionally with equivalent plastic strain; then the increase of plastic strain does not induce the increase of damage; and finally damage increases moderately with plastic strain. This analysis confirms the above statement about the influence of die angle (or contact length) on damage accumulation in the wire core.

Comparison with experimental results Experimental evidence also revealed systematic fracture at the end of the 8^{th} pass. Different drawing tests were carried out and frequent cracks at 8^{th} pass at die exit were observed. At this stage, wire diameter was reduced to 2.70 mm (i.e. reduction of 76% from 5.56 mm initial diameter wire). It can be considered as the “drawability limit”.

Fig. 6.25a shows small size chevron cracks on the wire surface. These chevron cracks may be due to the presence of pre-existing defects on the wire. The tracks of a chevron crack can also be observed on the SEM image (Fig. 6.25b). This image shows dimpled fracture at wire center, the result of ductile damage. However,

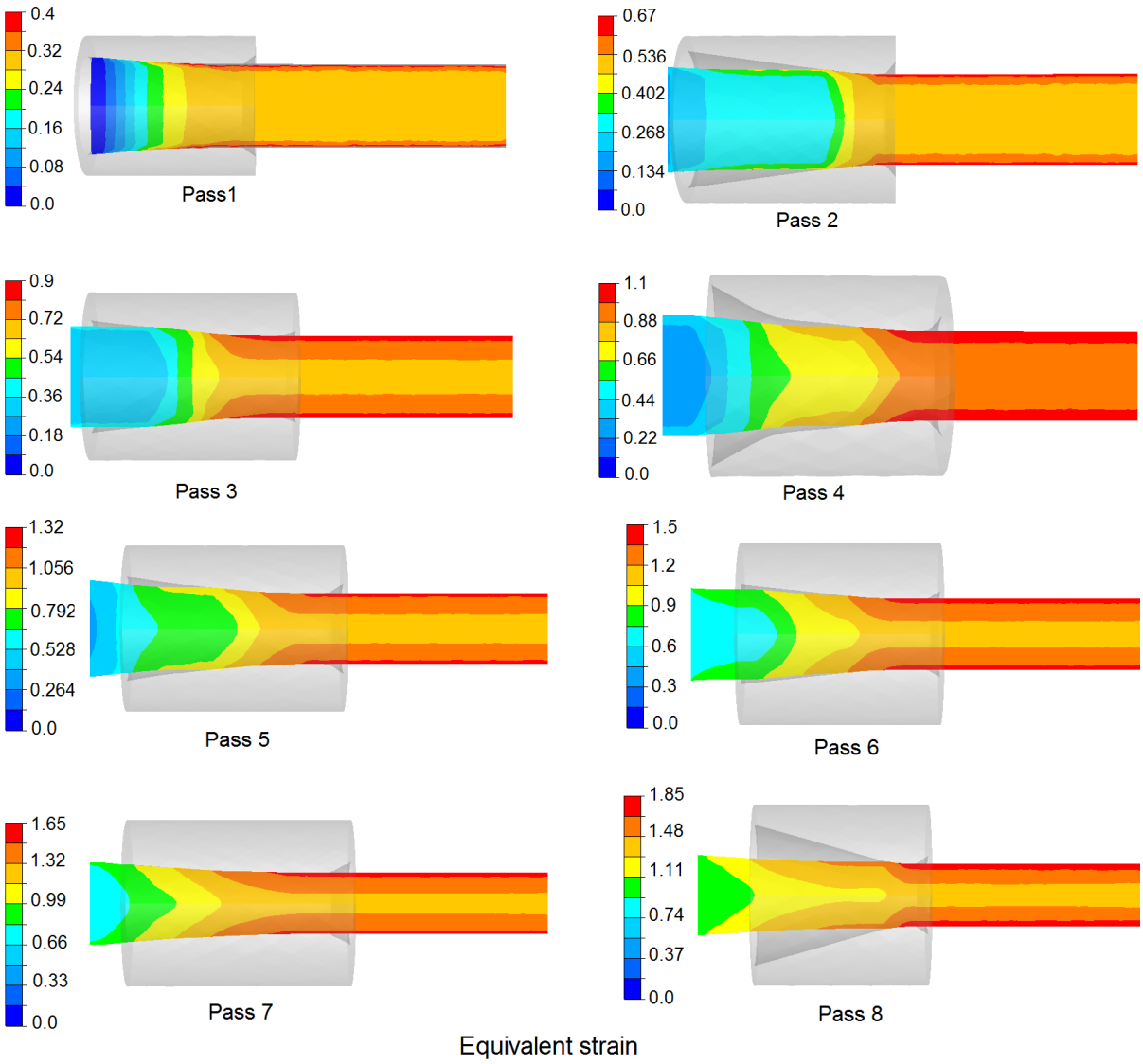

Fig. 6.21: *Accumulated equivalent plastic strain for the 8 passes of wire drawing.*

track of chevron crack near wire surface shows a rather "brittle crack", where crack was initiated at a small surface defect, then propagated due to the presence of pores, to form the final macro-crack.

As in the old saying: "A chain is only as strong as its weakest link"[6], or, in the present application, the drawn wire is only as strong as its weakest "point", i.e. the location containing defects. In our case, assuming that the wire surface had initial defects, they then developed during the deformation process and became a stress concentrator, where crack could easily initiate. Fig. 6.26a shows the defects observed on the wire surface upstream using SEM.

From these observations, it can be concluded that ductile damage (i.e. development of voids) occurs in the wire center (due to the presence of dimples on fracture surface), which can be captured by the identified B&W model. Nevertheless, cracks seem to initiate first at defects on the wire surface, which cannot be captured by numerical models without accounting for initial defects.

In order to test wire damage behavior with the presence of initial defects, artificial defects (geometrical defects) were introduced on the wire surface (Fig. 6.26b). The result of damage obtained with B&W model for the first two passes are shown in Figs. 6.26c and 6.26d.

As expected, the initial defects act as damage concentrators. However, the defects introduced were quali-

[6]As in [Lund and Byrne, 2001], the authors reassessed the experimental results of the tensile strength test of Leonardo Da Vinci and gave an explanation for these results based on material heterogeneity.

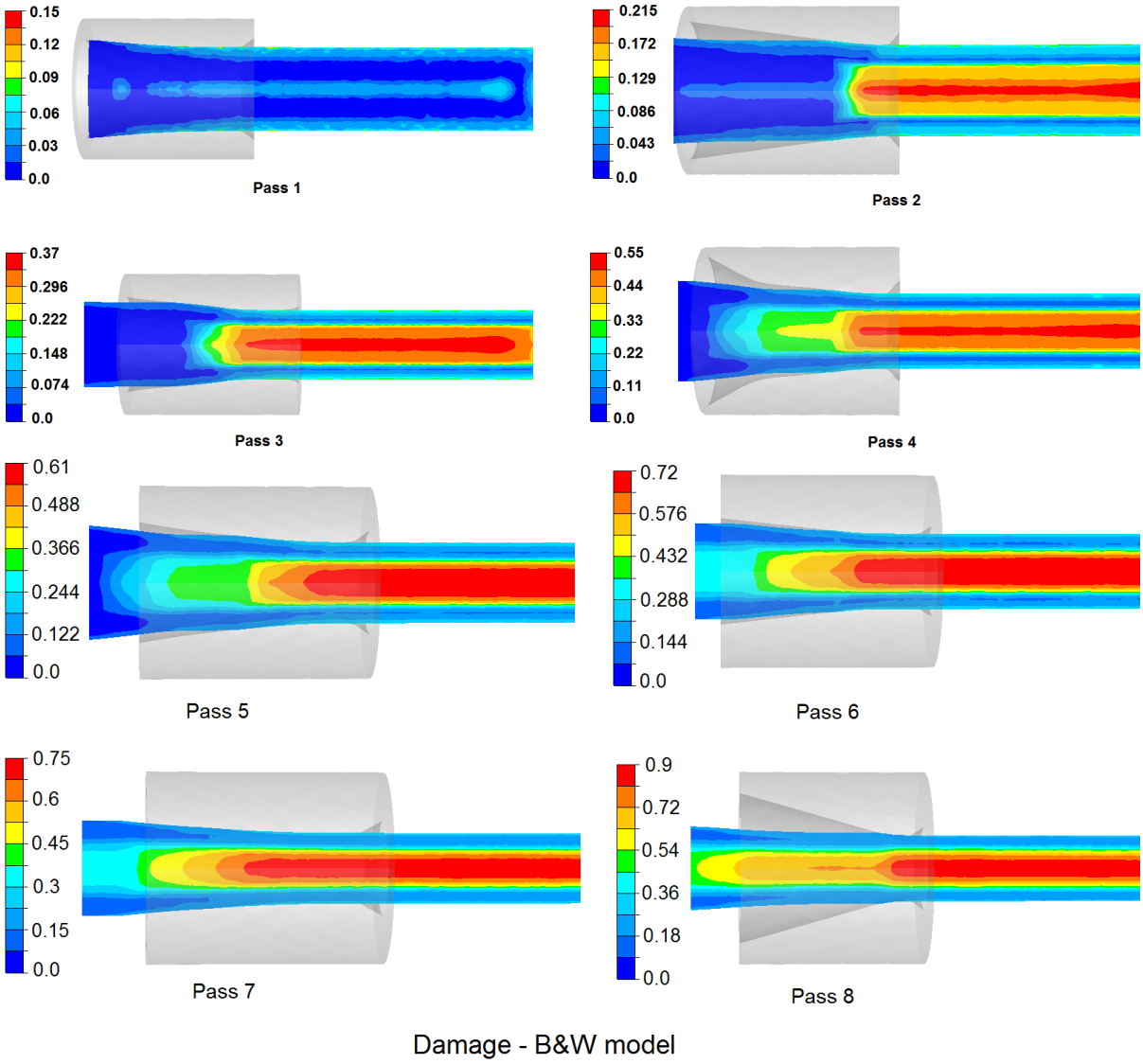

Fig. 6.22: *B&W damage parameter for the 8 passes of wire drawing*

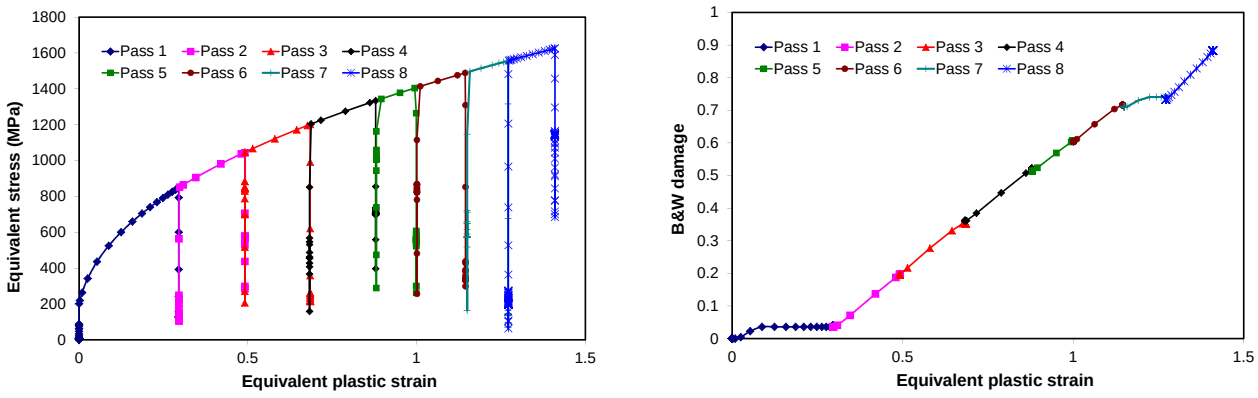

(a) *Evolution of von Mises equivalent stress.*

(b) *Evolution of B&W damage parameter.*

Fig. 6.23: *Evolution of equivalent stress (a) and damage (b) of a material point located at wire center during the eight drawing passes.*

tative and did not correspond to real defects (shape, size)[7].

[7]The size of this defect is equivalent to the real defect (depth) but its form does not correspond to the real one.

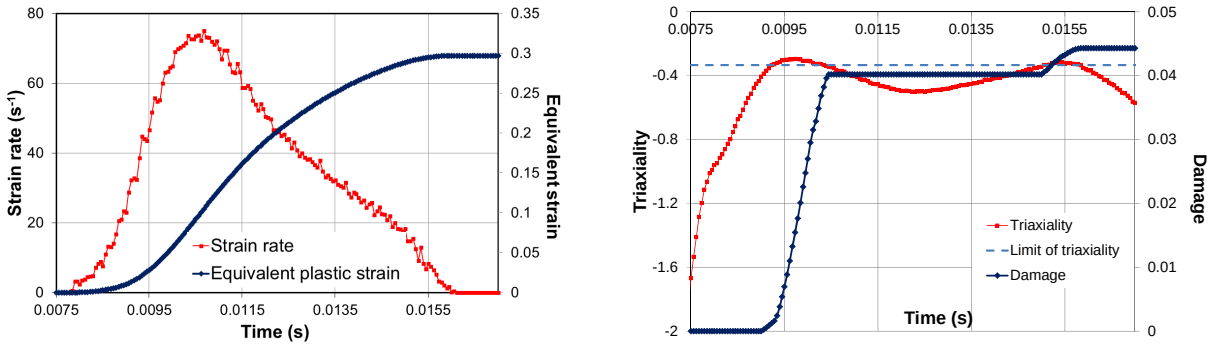

(a) (b)

Fig. 6.24: *The evolution of strain rate and equivalent plastic strain (a), damage and triaxiality (b) when the studied material point at wire center enters the working zone.*

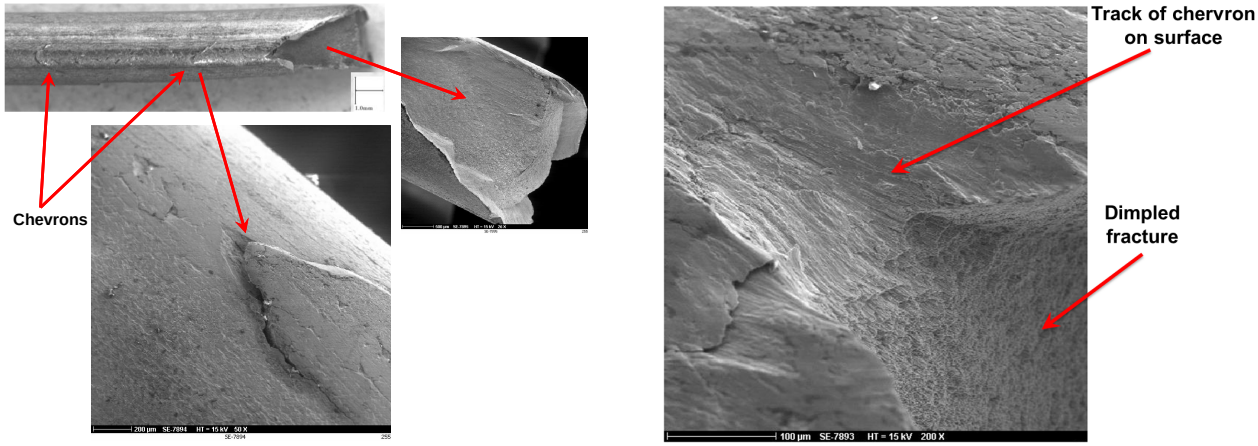

(a) (b)

Fig. 6.25: *SEM images of cracks observed at the end of 8 passes wire drawing: (a) chevrons on the wire surface; (b) dimpled fracture in the wire center and track of chevron on the wire surface.*

6.2.2.2 Wire rolling process

Figs. 6.27a and 6.27b represent numerical models for 3+3 and 2+2 technologies respectively (see Figs. 6.18a and 6.18b for real rolls). We modeled only a part of wire about 15 cm long to reduce CPU time. The mesh of the wire is also presented in Fig. 6.27c.

Regarding the friction, $\overline{m} = 1$ and $\mu = 0.05$ for the first stand; $\overline{m} = 1$ and $\mu = 0.06$ for the second stand. Only the results of strain and damage fields for first and last passes are analyzed here.

Fig. 6.28 represents contour plots of strain and damage fields at the exit of first (Figs. 6.28a and 6.28b) and second stands (Figs. 6.28c and 6.28d) of the first pass (3+3 technology).

From Figs. 6.28c and 6.28d, at the exit of the second stand of the first pass, both strain and damage are higher on the surface than in the wire core. Higher strain and damage at *"flashes"* [8] can be observed, which may be due to the gap between dies. However, as shown in the following, these positions are neither the final critical position of damage nor the plastic strain one. Fig. 6.29a shows the distribution of the accumulated equivalent plastic strain on a longitudinal cross section surface for the first four passes, while Fig. 6.29b shows the strain map at the end of rolling, which reveals that the wire core reaches a value around 1.8 in the center.

From Fig. 6.29a, for the first pass, longitudinal cross section shows higher strain at the bottom position, which confirms the distribution observed in Fig. 6.28c at die exit: higher strain at 3 ***flash positions***, the strain distribution is thus non-symmetric on the longitudinal cross-section. However, after four rolling stages,

[8] The term "flash" refers to the excess material due to the gap between the dies.

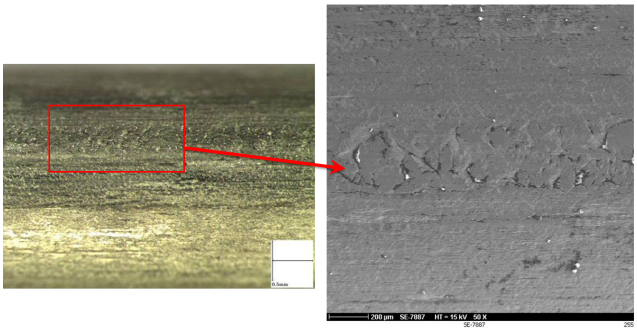

(a) *Defects on wire surface observed with SEM.*

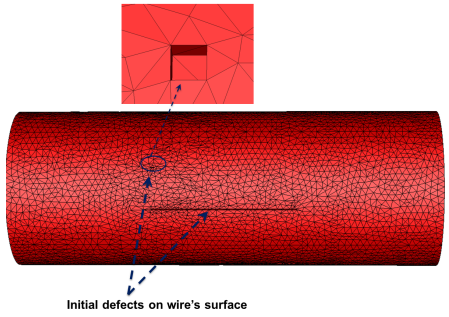

(b) *Numerical initial defects on wire's surface.*

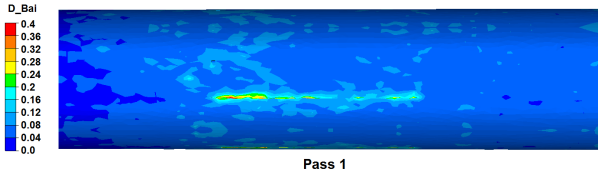

(c) *Damage on surface after 1 pass.*

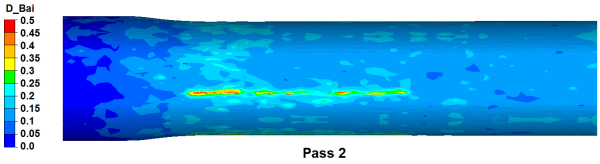

(d) *Damage on surface after 2 pass.*

Fig. 6.26: *Drawing of wire containing initial surface's defects.*

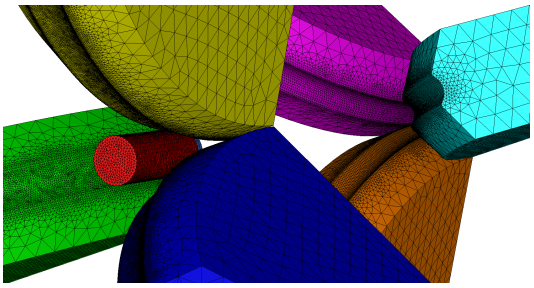

(a) *3+3 technology.*

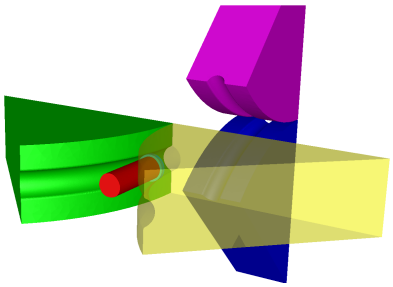

(b) *2+2 technology.*

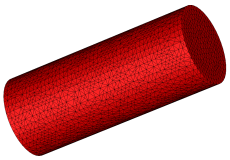

(c) *Mesh used.*

Fig. 6.27: *The studied rolling mills and mesh used.*

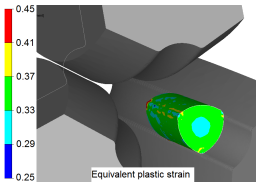

(a) *Equivalent plastic strain - stand 1.*

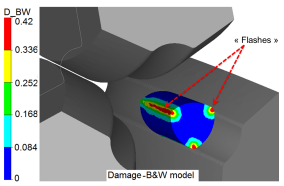

(b) *Damage - stand 1.*

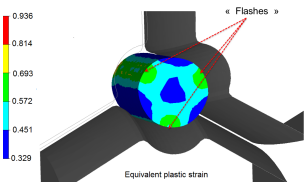

(c) *Equivalent plastic strain - stand 2.*

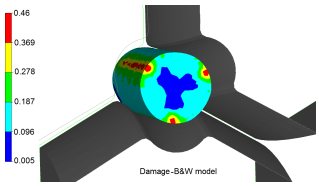

(d) *Damage - stand 2.*

Fig. 6.28: *Strain and damage fields at exits of first stand (a,b) and second stand (c,d).*

at the end of the last past (i.e. 5^{th} pass), strain is higher in the wire core than on the wire surface and the distribution is more symmetric on the cross section (Fig. 6.29b). Note that this non-symmetric distribution is due to the mesh used and principally the tools setup.

Comparison with experimental result of damage Fig. 6.30a shows damage contour at the end of rolling. Damage is higher on the surface, where critical value $D_c = 1$ is reached, which means that fracture occurs and crack initiates on the surface. Two maximum damage positions can be observed, one coincides with the bottom flash, and the other is at the opposite side.

Experimental results also showed cracks at this stage of rolling. Theses cracks were also initiated on the

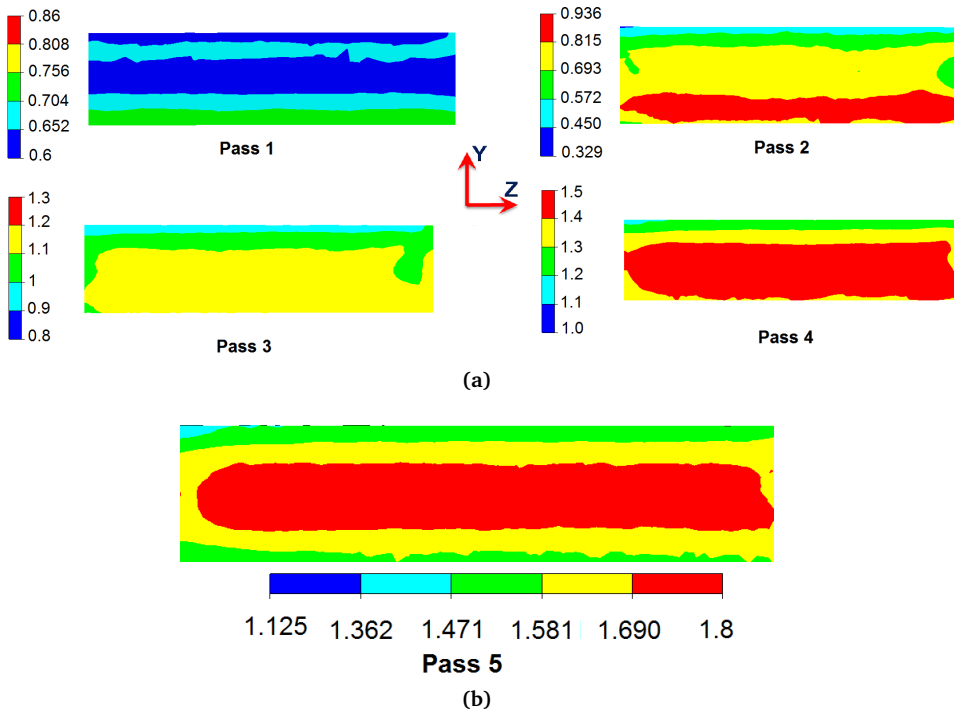

Fig. 6.29: *Evolution of accumulated plastic strain on the longitudinal cross section (z is the rolling direction): (a) from pass 1 to pass 4; (b) at the end of* 5^{th} *pass.*

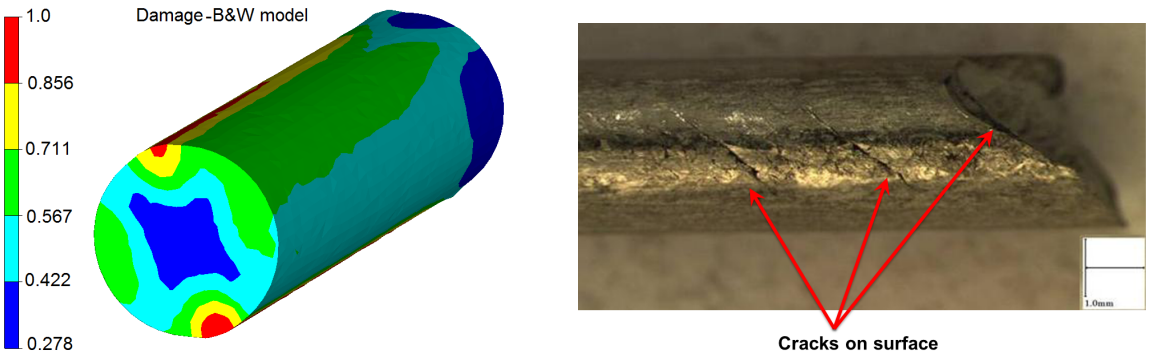

(a) *Contour plot of damage parameter.*

(b) *Experimental observation of cracked wire, showing crack on wire surface.*

Fig. 6.30: *Numerical and experimental results at the end of* 5^{th} *pass of rolling.*

wire surface (see Fig. 6.30b). In Fig. 6.30b, cracks can be observed along the wire surface, with a macro-crack that led to wire failure. From this observation, we can conclude that the numerical simulation gives correct results both in terms of location of fracture as well as instant of fracture (at the end of the 5^{th} rolling pass).

6.2.2.3 Comparison between the two processes

Starting from the same wire with the initial diameter $D_i = 5.56$ mm, two processes, drawing and rolling, led to two different maximum reductions. For the rolling process, fractures always occur at the 5^{th} pass, where wire diameter at exit was about 3.1 mm. For wire drawing process, we can go further by reducing the wire diameter to 2.7 mm (8^{th} pass of drawing). We can conclude that wire was more *"ductile"* when formed by drawing. The reason may be due to the differences in processes themselves and the forming schedule as well (i.e. reduction at each pass).

Moreover, the last pass of rolling (output diameter was 3.1 mm) could be compared with the 6^{th} pass of drawing (output diameter was 3.12 mm). At this stage, wire was more hardened on surface with wire drawing and in the wire core with rolling (see Figs. 6.21 and 6.29b). For the wire drawing, strain is higher

on the wire surface and damage is higher in the wire core, while for the wire rolling, strain is higher in the wire core and damage is higher on the wire surface.

6.2.3 Conclusions

Based on the results on wire drawing and rolling for the studied stainless steel, the following conclusions can be drawn:

1. For the wire drawing process, both B&W and Lemaitre models (Appendix C.1.2) give relatively correct results in terms of the instant of fracture. At 8^{th} pass, the Lemaitre variable reaches its critical value while maximum value of B&W damage is 0.9, in comparison with its critical value of 1. Experimental evidence also revealed noticeable track of *ductile damage* in the wire core (dimpled fracture surface). Such a localization of ductile damage in the wire core can be predicted by the identified damage models. However, in experimental results, it seemed that *cracks initiated at defects* on the wire surface, which could not be captured by a numerical model without initial defect at the wire surface. Artificial defects were introduced and the results qualitatively showed that with the presence of initial defects, ductile damage can be high both in the wire core and at the defects.

2. For the rolling process, both models predicted relatively accurately localization of damage (on the wire surface) and the instant of fracture (at 5^{th} rolling pass).

Remark It should be noted that in the present study on the stainless steel, the influences of strain rate and temperature are not accounted for neither in plasticity nor in damage constitutive equations. It has been shown in the literature (e.g. [Teng, 2005]) that the strain rate and the increase of temperature could influence material ductility. Moreover, it seems the studied stainless steel might sensitive to strain rate. Further detailed studies of these influences are perspectives of the present study.

6.3 Application to zirconium alloy process

In this section, the application to cold pilgering of zirconium alloy $M5^{TM}$ is given (see section 1.1.4 of Chapter 1 for a review of this process). The material parameters as well as damage models were identified and presented in sections 2.3.3 and 3.3.

6.3.1 Process analyses

6.3.1.1 Process description

For the analyses of the cold pilgering process, one forward-backward stroke simulation is studied. The same process simulation as in [Lodej et al., 2006] was used. As indicated in [Lodej et al., 2006, Montmitonnet, 2007], it takes 80-100 cycles for a material point to move from the preform side to the finished tube side and computing all these strokes is unrealistic. Since this process is pseudo-periodic in machine frame (see section 1.1.4), all necessary information can be obtained by studying one cycle. However, this simulation requires the initiation of stress and strain fields as well as the tube geometry. The same initiation as in [Lodej et al., 2006, Montmitonnet, 2007] was employed: stress field was initialized to zero and the equivalent strain: $\overline{\epsilon} = ln\left(\frac{S(z=0)}{S(z)}\right)$, where $S(z)$ represents the area of the cross section at the position z (see Fig. 6.31a). The dimension of preform tube was the same as in [Lodej et al., 2006]. The formed tube was 9.52 mm in external diameter and 0.6 mm in thickness. If deformation was homogeneous during the process, this would correspond to an elongation ratio of 5.36 (see [Lodej et al., 2006]).

The tools are assumed rigid, which is a strong hypothesis for this process. All contacts are unilateral, with two friction coefficients $\mu = 0.05$, $\overline{m} = 1$ for both internal and external surfaces. The rotation speed of die is 49 rad. s^{-1}, corresponding to a translation velocity of $5m.s^{-1}$.

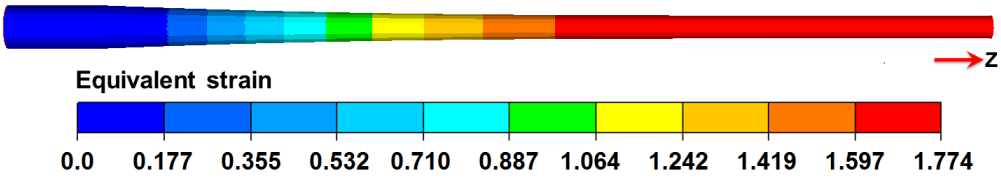

(a) *Strain initiation.*

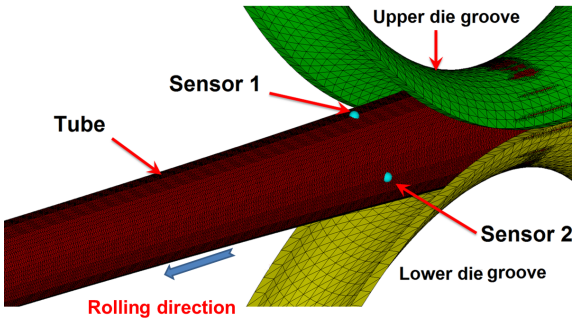

(b) *Mesh used and numerical sensors.*

Fig. 6.31: *Characteristics of the pilgering process numerical simulation.*

A very fine mesh is used, with about 1680000 elements and 326000 nodes (Fig. 6.31b). The time step is chosen fixed $\Delta t = 5\,10^{-5} s$ and the CPU time is about 806 hours ($\approx$ 1 month) on a cluster of 12 processors, for one forward-return stroke. Two numerical sensors are set up (Fig. 6.31b) to follow the mechanical history of two material points: one located at upper surface (full contact with groove bottom - sensor 1) and the other located at the side relief area (no or less contact with die during the process).

6.3.1.2 Mechanical analyses

Strain state The evolutions of plastic strain and strain rate for two sensors are presented in Fig. 6.32.

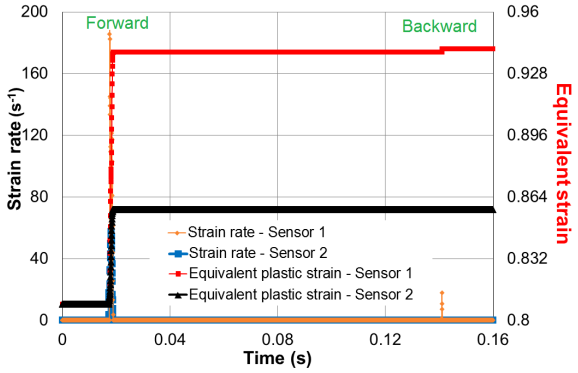

Fig. 6.32: *Evolution of equivalent plastic strain and strain rate of two material points during the process.*

Regarding sensor 1, two instants for which the plastic strain increases, corresponding to forward and backward contacts with dies, can be observed. However, for sensor 2, the backward stroke does not cause plastic strain. Although the increase of plastic strain for backward stroke is small, the return stroke cannot be considered as elastic. Moreover, since the position of the sensor 1 is in full contact with the die, the strain rate is higher than that of sensor 2. In the following, we will only consider the forward contact instant (time between 0.017s and 0.019s), when the deformation and damage accumulation takes place.

Stress state Fig. 6.33a represents the evolution of the stress triaxiality and the Lode parameter. Fig. 6.33b represents the evolution of two damage variables (B&W and MMC models) when the two studied material

points enter in contact with dies[9].

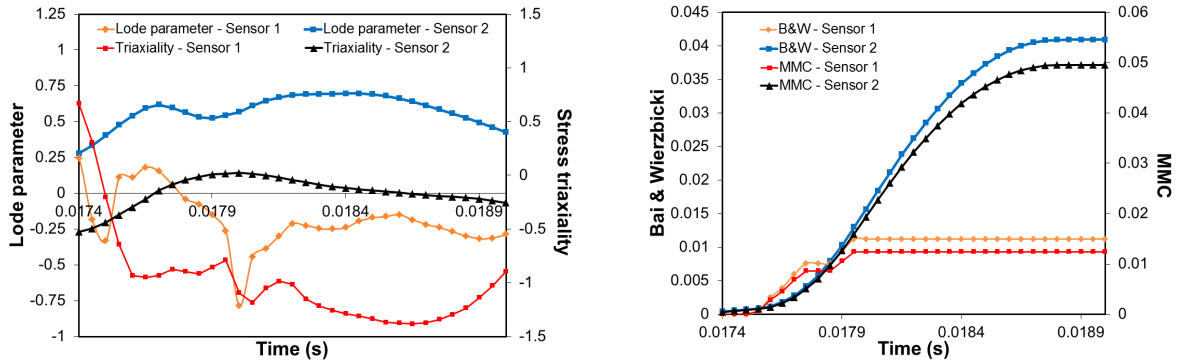

(a) *Lode parameter and stress triaxiality in the working zone.*

(b) *Evolution of damage with B&W and MMC models.*

Fig. 6.33: *Evolution of mechanical properties during the deformation process (i.e. non-zero strain rate) of forward stroke.*

The values of the stress triaxiality and the Lode parameter are negative for the sensor 1, which means this position is under high compression. Damage development at this position is therefore less significant as confirmed by Fig. 6.33b. For the sensor 2, positive Lode parameter and near zero and slightly positive stress triaxiality lead to higher increase of damage than the sensor 1, but these values are still small.

Remarks In this section, Lagrangian sensors were used to follow the evolution of mechanical properties of two material points at different positions on the *outer surface* to reveal the *complexity* of loading paths. Since a material point changes position after each stroke because the tube rotates 51° then advances 2 mm, its position may change from the side relief (sensor 2) to the groove bottom (sensor 1). The strain path thus changes accordingly (Figs. 6.32 and 6.33a). However, simulation of only one stroke cannot capture the whole mechanical history as this process is periodical in machine frame, not material frame. A method was proposed in [Lodej et al., 2006] to deduce the whole history of a material point by using Eulerian sensors instead of Lagrangian ones. The trajectory of a material point initially located at preform position was determined after multiple advances and rotations of tube. Eulerian numerical sensors were then placed at these successive positions at the beginning of each cycle. Scanning all the time steps of the computation, the history of the studied material point could be obtained at each position. By combining all the sensors at successive positions corresponding to the whole trajectory (56 cycles [10]), full mechanical history could be obtained.

6.3.1.3 Damage localization

One forward-return stroke For this process, three damage models are considered: B&W, MMC and Lemaitre, identified in section 3.3. Note that with a single forward-return stroke, the result obtained concerning the damage localization is qualitative. Fig. 6.34 shows an example of damage on the outer (a) and on the inner (b) surfaces obtained with the MMC model. It shows higher damage on the inner surface and damage is maximum on a "critical cross section" shown in Fig. 6.34b.

Fig. 6.35 shows the damage localization on the critical cross section (i.e. maximum damaged section) obtained with the three models: MMC, B&W and Lemaitre.

These three models predict maximum damage localization at the same position: on inner surface under die groove. This position thus has more risk of crack initiation, contrary to real cracks observed during the process (see Fig. 1.44), which are frequently on the outer surface. However, secondary maxima can also be

[9] Since the coupled damage model modifies strain field due to the coupling (because of a softened behavior when damage grows), for the analysis of process, only uncoupled damage models are used.

[10] It was shown in [Lodej et al., 2006] that it took 56 cycles for the material point to move from preform to the end of the deformation zone.

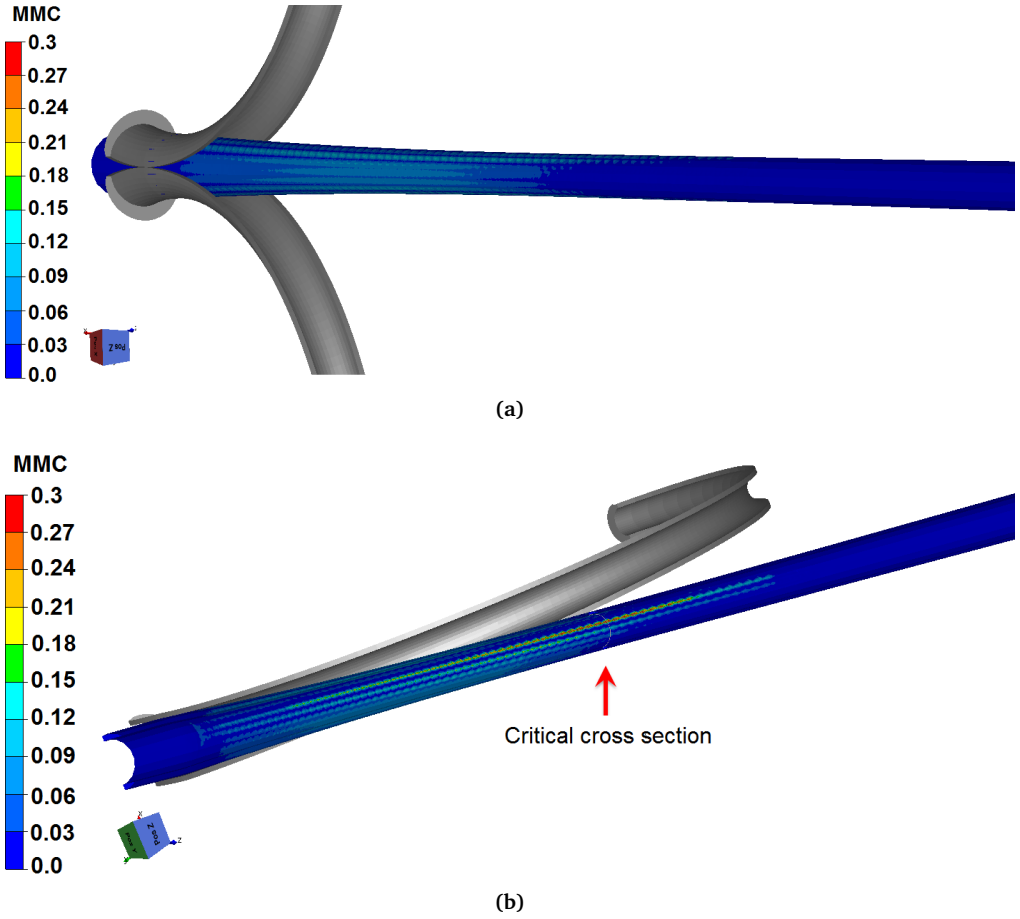

Fig. 6.34: *Damage on the outer (a) and inner (b) surfaces obtained with the MMC model.*

observed on the external surface: they are less intense, but more numerous. Nothing precludes the possibility that damage at these positions can accumulate when the whole process is simulated.

Moreover, in order to capture the gradient of strain in the thickness, the number of elements in the thickness must be high enough (at least 4 element "layers" in radial direction - see Fig. 6.36a). Two meshes were used in the present study: coarse mesh (4 "layers" for the simulation of 4 strokes - Fig. 6.36a) and fine mesh (8 "layers" for the simulation of 1 stroke - Fig. 6.36b). Moreover, care must be taken to keep a same element aspect ratio between the two meshes, to avoid the influence of this ratio: the cross section of the coarse mesh has 32 "slices" compare to 64 "slices" of the fine mesh. Nevertheless, the cross section of the mesh used is not perfectly circular, where *corners* can be observed. This may also lead to some numerical "noise" at these positions where damage is higher than at other positions of cross section. Moreover, the use of a fine mesh enables a more regular distribution of mechanical fields on the cross section.

Four forward-return strokes In order to investigate the influence of the number of strokes on damage localization, the simulation of 4 forward-return strokes was performed. Because this process is time consuming, we carried out the simulation with only 4 strokes and with a coarser mesh (about 210000 elements, 47400 nodes, and CPU time of 571 hours on a 6 processors computer).

Fig. 6.37 shows damage localization on critical cross section obtained with the two uncoupled damage models (B&W, MMC). Two critical cross sections are distinguished: section 1 with higher damage on the internal surface, and section 2 with higher damage on the external surface. With the Lemaitre coupled model, due to the strong localization of damage (coupling with elastoplasticity), the critical position remains the same as the one obtained from the first case (with one forward-return).

From this figure, one can observe that at the end of 4 forward-return strokes, damage can be critical both on internal and external surfaces. Again, the present author emphasizes that these results are qualitative and

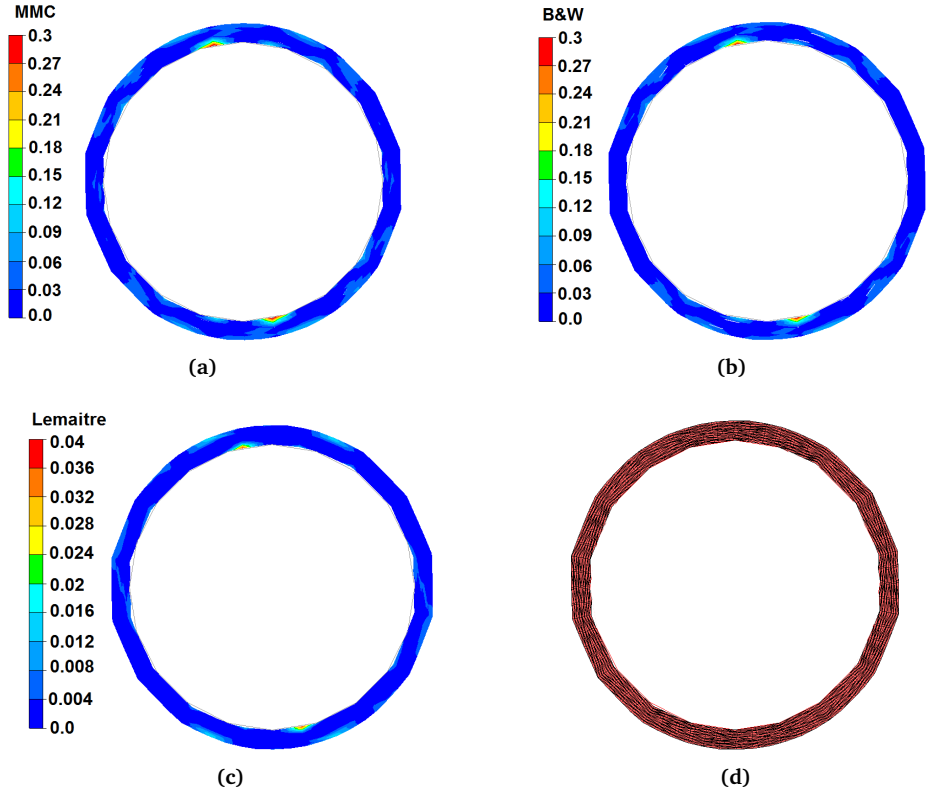

Fig. 6.35: *Damage localization on the critical cross section with the three models: (a) MMC, (b) B&W and (c) Lemaitre; (d) mesh of the critical cross section.*

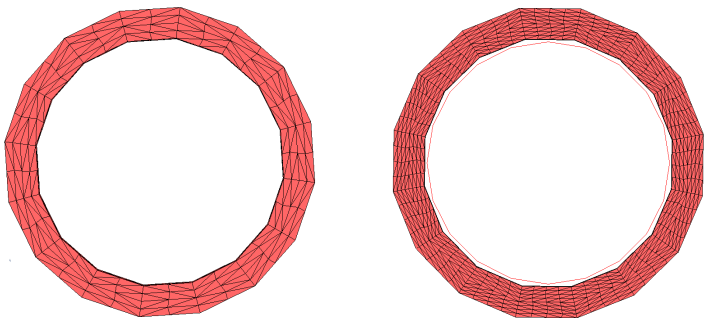

(a) *Coarse mesh.* **(b)** *Fine mesh.*

Fig. 6.36: *Meshes used for the simulation of 1 stroke (a) and 4 strokes (b), view from preform position, showing the number of element over thickness.*

the present author cannot have a *strict* conclusion since a complete simulation of the whole process cannot be carried out due to the huge CPU time. For this reason, parallel to the present PhD thesis, the CEMEF launched another PhD project ([Kpodzo, 2013]), in collaboration with AREVA / CEZUS, which aimed at accelerating the simulation of this process and increasing the accuracy of the results. The present author believes that a whole process simulation will be possible in the future and will thus improve the accuracy of damage computation.

6.3.2 Conclusions

The following conclusions can be drawn:

1. Numerical analyses of process showed that both forward and return strokes deform the tube. Moreover,

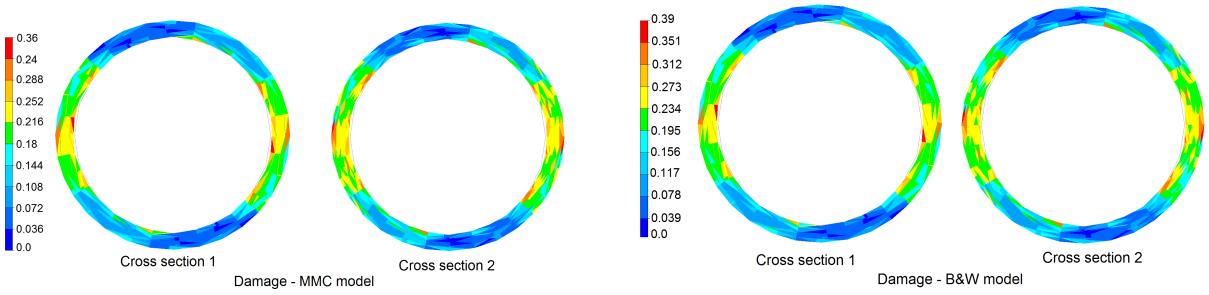

Fig. 6.37: *Damage distribution on the two critical cross sections: (a) MMC model, (b) B&W model.*

since damage can also develop during the return stroke, the return stroke cannot be considered as purely elastic and must be accounted for in damage investigation.

2. Qualitative study concerning damage localization with 3 different models (MMC, B&W and Lemaitre) showed that for one forward-return stroke, damage was higher on the inner surface. However, for 4 forward-return strokes, damage can be higher on the inner or the outer surfaces. This result showed that study of one stroke could not give correct result in terms of damage localization. Further work needs to be carried out on the simulation of the process and/or using the method proposed by [Lodej et al., 2006] to improve damage analyses.

6.4 Summary of Chapter 6

This chapter presents the application of the identified damage models to 3 materials and different forming processes. The list of models used for each material is given in Table 6.1. The principal results are summarized here:

- For the high carbon steel studied, application to ultimate wire drawing processes showed damage localization in the wire core for all the 4 studied damage models: B&W, Lemaitre, Xue, and GTN. However, among these models, only the GTN model gave satisfactory results for the prediction of the instant of fracture. The latter model predicted fracture at the 13^{th} pass, in agreement with the experimental result, which showed fracture at the 14^{th} pass. This also revealed the importance of model identification: for a better result of damage prediction, model parameters should be calibrated both from "macro" and "micro" data. Such an identification is sometimes delicate and some results are incompatible as in the present study. Qualitative simulation on the wire flat rolling showed that accounting for mechanical history of preceding forming process (i.e. wire drawing in our case) could modify the damage localization. Among the studied models, only the Xue model and the GTN model modified by Xue give correct results in terms of damage localization for wire flat rolling.

- For the stainless steel studied, two alternative processes were investigated: wire drawing and rolling. Both damage models (B&W and Lemaitre) gave correct results for both localization and instant of fracture for the rolling process. Concerning the wire drawing process, these models also predicted ductile damage higher in the wire core, as observed in experiment. However, crack initiation position could not be captured since in the experiments, crack was very likely initiated at defects on the wire surface. By introducing an artificial defect on surface, such localization on surface was explained.

- Regarding the studied zirconium alloy $M5^{TM}$, the pilgering process was used for the validation. The qualitative study concerning damage localization with 3 different models (MMC, B&W and Lemaitre) showed that for one forward-return stroke, damage was higher on the inner surface. However, for 4 forward-return strokes, damage can be higher on the inner or the outer surfaces. This result shows that

study of one stroke could not give correct results in terms of damage localization. Nevertheless, due to the huge CPU time, the simulation of the whole process is not possible. For this reason, parallel to the present PhD thesis, the CEMEF launched another PhD project ([Kpodzo, 2013]), in collaboration with AREVA / CEZUS, which aimed at accelerating the simulation of this process and increasing the accuracy of the results. We believe that a whole process simulation will be possible in the future. Moreover, applying the method proposed in [Lodej et al., 2006] would be interesting.

6.5 Résumé en français

Ce chapitre présente des applications à la simulation des procédés industriels, en utilisant les modèles d'endommagement identifiés dans les chapitres précédents. Une liste des modèles utilisés pour chaque matériau a été présentée dans le Tableau 6.1. Pour chaque procédé, une analyse mécanique a tout d'abord été donnée, suivie par des résultats concernant l'endommagement.

Dans la première partie, des applications sur l'acier haut carbone ont été présentées. Il s'agit des procédés de tréfilage suivi de laminage de fil. Quatre modèles ont été comparés pour cet acier : B&W, Xue, Lemaitre et GTN. Des validations à la fois qualitatives et quantitatives ont été montrées. Pour le procédé de tréfilage ultime, qui consiste en 14 passes de tréfilage, tous ces modèles ont donné une bonne localisation de l'endommagement au cœur du fil. Pourtant, seul le modèle GTN a pu prédire précisément l'instant de la rupture, défini numériquement par les valeurs critiques des variables d'endommagement. Ce modèle a prédit la rupture à la treizième passe, alors que les autres modèles (i.e. B&W, Xue, Lemaitre) ont prédit la rupture aux quatrième ou cinquième passes. Les résultats expérimentaux d'ArcelorMittal ont montré une rupture à la quatorzième passe. Ce résultat montre que, pour certains matériaux, l'identification des modèles d'endommagement devrait être basée à la fois sur des essais macroscopiques et sur des propriétés microscostructurales (e.g. le taux de porosité), qui caractérisent le phénomène physique (i.e. l'endommagement). La deuxième validation, plutôt qualitative, a été réalisée sur le procédé de laminage. Pour cette validation, deux cas ont été testés: un avec l'histoire de contrainte et de déformation du tréfilage précédent, l'autre sans prendre en compte le tréfilage précédent. Pour les modèles basés sur la triaxialité ou la pression (Lemaitre, GTN), l'endommagement est plus grand dans les zones de grande triaxialité : les rives. Cependant, quand l'histoire de la déformation et de la contrainte a été prise en compte, la localisation de l'endommagement a changé : l'endommagement au centre du fil est important pour le modèle GTN à cause de la germination, maximale à ce niveau de déformation. Le modèle d'endommagement de Xue a prédit une localisation de l'endommagement maximal au niveau de la croix du forgeron. Le modèle B&W a prédit un endommagement maximal au centre. Le résultat expérimental de Massé ([Massé, 2010]) a été retenu pour validation qualitative de la localisation de l'endommagement. Cet auteur a mené des observations sous Microscopie Électronique à Balayage (MEB) de l'état d'endommagement du fil qui passait 4 passes de tréfilage et 3 passes de laminage. L'auteur a constaté une densité des pores plus importante au centre du fil et aussi sur la croix du forgeron (voir Fig. 6.15). De plus, les porosités autour des inclusions situées sur la croix du forgeron ont subi une rotation à cause du cisaillement dans cette zone. Le résultat a aussi montré une faible extension latérale des pores situés dans la partie bombée. Sur la base de ce résultat expérimental, seuls les modèles de Xue identifiés (Xue phénoménologique modifié et GTN modifié par Xue) ont pu prédire une telle localisation de l'endommagement. Cependant, cette conclusion reste qualitative car nous n'avons pas pu effectuer d'observations sur le matériau étudié ici.

Dans la deuxième partie, les résultats d'application au tréfilage et au laminage d'un acier inoxydable ont été présentés. Deux modèles d'endommagement ont été comparés : B&W et Lemaitre, qui ont été identifiés dans le chapitre précédent. Seul le résultat avec le modèle B&W a été présenté dans ce chapitre (voir l'Annexe C.1 pour le résultat avec le modèle de Lemaitre). Le tréfilage consistait en 8 passes, où les casses ont été observées expérimentalement à la fin de la huitième passe. Pour la simulation numérique, à la fin de la huitième passe, la valeur maximale d'endommagement du modèle de B&W était de 0.9, à comparer avec la valeur critique de 1. Ce modèle a prédit la localisation de l'endommagement au cœur du fil, qui était

cohérent avec le résultat expérimental, où on a observé des cupules au cœur du fil cassé. Cependant, les sites d'amorçage des fissures dans les expériences étaient sur des défauts surfaciques. Une simulation de deux passes de tréfilage avec des défauts surfaciques artificiels a été menée et a montré une concentration importante de l'endommagement sur ces positions. Etant donné que la taille et la forme des défauts artificiels utilisés ne correspondent pas aux vrais défauts, ce résultat n'est que qualitatif. Concernant le laminage, il s'agissait d'un procédé de 5 passes, dont la technologie utilisée a été représentée à la Fig. 6.18. Au contraire du tréfilage, le laminage a montré une déformation plus importante à cœur et un endommagement plus important sur la surface. Le résultat expérimental d'Ugitech a aussi montré une rupture systématique sur la surface à la fin du laminage. Le modèle de B&W ainsi que le modèle de Lemaitre (Annexe C.1) ont montré une bonne localisation de l'endommagement et prédit correctement l'instant de la rupture : à la fin de cinquième passe. De plus, à partir du fil initial de même diamètre ($D_i \approx 5.56$ mm), le tréfilage a permis d'aller plus loin sur la réduction ($D_f = 2.7$ mm pour le tréfilage et $D_f = 3.1$ mm pour le laminage). La raison était peut-être liée aux procédés eux-mêmes ainsi qu'à la "stratégie"' de mise en forme (i.e. la descente de réduction).

Dans la troisième partie, l'application à l'alliage de zirconium a été présentée, avec le laminage à pas de pèlerin. Du fait du temps de calcul énorme de la simulation de ce procédé, seulement deux simulations avec 1 coup de cage (un aller-retour) et 4 coups de cage ont été réalisées. Une analyse mécanique a été présentée, qui a montré le caractère complexe du chargement au cours de ce procédé. Trois modèles d'endommagement ont été envisagés (B&W, MMC, et Lemaitre), qui ont été identifiés dans la section 3.3. Pour le cas d'un coup de cage, ces trois modèles ont prédit la même localisation de l'endommagement sur la surface interne du tube. Par contre, pour 4 coups de cage et avec les modèles découplés (B&W, MMC), la position où l'endommagement est maximum pouvait être sur la surface interne ou externe du tube. Pour le modèle de Lemaitre, dû au couplage avec l'élastoplasticité et la forte localisation de l'endommagement (le caractère local de la variable d'endommagement couplé), les résultats sur la localisation de l'endommagement d'un ou de quatre coups de cage n'étaient pas différents. Ces résultats ont montré que l'étude d'un seul coup de cage n'a pas pu donner un résultat représentatif de la localisation de l'endommagement. De plus, le résultat expérimental montrait des défauts plutôt sur la surface externe (Fig. 1.44). Ceci pourrait impliquer que pour pouvoir connaître précisément le site d'amorçage des fissures, la simulation complète du procédé (environ 80-100 coups de cage) est nécessaire. En parallèle à ce travail, le CEMEF a lancé une thèse en collaboration avec AREVA / CEZUS ([Kpodzo, 2013]), qui vise à accélérer le temps de calcul et augmenter la précision pour la simulation de ce procédé. Nous croyons qu'une simulation complète du procédé sera possible dans un avenir proche, ce qui permettra de tester les critères de rupture et modèles d'endommagement sur l'ensemble du procédé. De plus, la méthode proposée dans [Lodej et al., 2006] est intéressante pour avoir l'histoire mécanique complète de chaque point matériel, et sera appliquée dans un avenir proche.

Chapter 7

Discussions, conclusions and perspectives

7.1 Summary of thesis

The present thesis aims at improving the damage and fracture prediction for different cold forming processes and different materials. In the context of metal forming simulations involving large plastic strain in multiple forming stages as well as multiaxial and non-proportional loadings, the prediction of ductile fracture needs "robust" models which satisfy three conditions: (1) physical mechanisms of the onset of damage and fracture must be captured; (2) the models have to be suitable for numerical implementation and applicable for real size structure simulations; and (3) models parameters should be convenient for identification. Regarding different damage approaches proposed in the literature, disagreement still exists on the ability of these approaches in fracture prediction for non-proportional and multiaxial loading cases. The principal objective of the present study is to supply critical analyses of the advantages and drawbacks of these approaches for industrial applications (on three different materials and 3 different processes)[1]. Due to the high number of materials and processes involved, it was impossible to identify and apply all the implemented models to all the materials and processes.

To reach the goals of the project, three main tasks were accomplished:

1. A mechanical tests campaign was carried out with different loading configurations on three different materials: high carbon steel, zirconium alloy and stainless steel. Different isotropic hardening laws were used, enhanced (depending on material) and identified for these three materials.

2. Different damage models were enhanced and implemented in the FE software Forge2009®: coupled phenomenological models (enhanced Xue, enhanced Lemaitre); phenomenological uncoupled formulations (B&W, MMC); micro-mechanical models (GTN, modified GTN by Xue and by Nahshon and Hutchinson). All these models constitute a rich database for damage study. These models were identified and compared: high carbon steel (B&W, Xue, Lemaitre, GTN and GTN modified by Xue); zirconium alloy (MMC, B&W, Lemaitre, and enhanced Lemaitre); stainless steel (B&W, Lemaitre).

3. Detailed mechanical analyses of different forming processes were carried out (wire drawing, wire-rolling and pilgering). These analyses help explaining the application results using the above-mentioned damage models and materials.

In the following, each task is detailed.

[1] In a more rigorous consideration, there are four processes that have been studied in the present PhD thesis: wire drawing, wire flat rolling, wire rolling and pilgering. The second and the third processes can be classified as rolling.

7.1.1 Mechanical tests and plastic behavior identification

In the present study, series of uniaxial mechanical test has been used to identify damage and hardening models. Several specimens' geometry was studied to vary stress configurations in terms of triaxiality and Lode parameter. A detailed method to obtain isotropic hardening parameters was presented, involving the identification of a non-linear friction law parameters in compression test based on geometry variation. The inverse analysis based on multi-objectives optimization was used throughout the present study to obtain hardening and damage parameters based on the data from different loading configurations. It is worth noting that, when instability involves (e.g. after necking in tensile tests), the softening of material (characterized from the global load-displacement curve) is the result of two phenomena: necking and damage induced softening. If the identification is based only on the tensile test, local measurement (e.g. continuous geometry following) is required to obtain accurate results. In the present study, except for the in situ tensile test on high carbon steel, only global quantities (load- displacement curves) were used, but different mechanical tests (with different stress configurations) were used to enrich the objective functions required for the identification procedure, and thus have more accurate results.

7.1.2 Three approaches of ductile damage

In the present study, the author implemented different damage models, from phenomenological models to micromechanical model. First, recently developed uncoupled formulations proposed by MIT team (MMC and B&W models) were analyzed and implemented. These models were first based on an assumption of proportional loading to define the fracture strain for a given loading as a function of the stress triaxiality and the Lode parameter. The latter parameter was recently taken into account in damage models to better describe the shear damage mechanism occurring under low stress triaxiality. These models suffer from several limitations, among which the two principals are: the applicability to non-proportional loadings and their purely phenomenological nature (i.e. no physical parameters involved). In the present author point of view, the first limitation can be "overcame", if we reconsider the signification of the $\overline{\epsilon}_f$ function: it is a weighting function used to calculate the damage variable D along the strain path and *"coincides"* with the strain to fracture in proportional loadings (see the discussion in section 3.5). In order to overcome the second limitation, the use of physically inspired uncoupled approaches can be considered, which is discussed in section 7.2.2.2.

The coupled phenomenological damage models (Lemaitre, Xue) allow accounting for the influence of damage on material strength. The Xue model was enhanced in the present study to account for the coupling between damage and elasticity as well as the damage threshold defined by a critical value of the equivalent plastic strain. The latter modification is necessary for the studied material (high carbon steel) since for this material, damage (voids) is not noticeable below a certain threshold of the equivalent plastic strain (see Fig. 5.9a in Chapter 5). The Lemaitre model was also enhanced to account for the third deviatoric stress invariant and was successfully applied to a torsion test on zirconium alloy. Further studies will be carried out in the future to validate the proposed enhanced model.

Regarding the micromechanical approach, the GTN model was implemented in a mixed velocity-pressure FE formulation. Note that the implementation of the above-mentioned models (even the coupled damage models) is not an issue since there is no "direct" influence of damage on plasticity criterion and J_2 plasticity is adopted. For the GTN yield function, the presence of the damage variable, the void volume fraction, makes the yield surface sensitive to pressure and the implementation of this model requires special attention. The modified models of the GTN model to account for shear damage ([Nahshon and Hutchinson, 2008] and [Xue, 2008]) were also implemented. Moreover, it must be underlined that the extensions of the GTN model by Nahshon and Hutchinson and by Xue were introduced in a somehow phenomenological way.

All these models' parameters were identified principally based on mechanical tests in different loading configurations. The method for models calibration was also detailed both for uncoupled and coupled models. The GTN model was identified using both mechanical test and an in situ X ray micro-tomography tensile test (conducted by the laboratory MATEIS). A formulation for nucleation strain was proposed, which was based

on the idea that nucleation rate is higher at higher stress triaxiality. With this proposition, the fracture in mechanical tensile tests was accurately captured.

7.1.3 Processes analyses and applications

Final applications to forming processes were carried out for 3 materials.

For the applications on the high carbon steel grade (wire drawing, wire flat rolling), the identified GTN model gives correct results both quantitatively and qualitatively in terms of damage prediction for the ultimate wire drawing process. Other models (enhanced Xue, Lemaitre and B&W) give correct results in terms of damage localization but they failed to predict the instant of fracture. With this observation, it may suggest that only the model that was physical inspired and was identified both from microstructural observation (void) and macroscopic event (load-displacement curve) can give correct results in terms of the instant of fracture[2]. However, for other applications on stainless steel, the identified B&W and Lemaitre model gave relatively correct result both quantitatively and qualitatively on the ductile fracture prediction. These results suggest that it may depend on material that the use of phenomenological approach is legitimate. Apparently, for the studied high carbon steel, we are in the case of a particular material (strong evolution of microstructure during multi-stages forming process, voids are strongly elongated, etc.). In any case, an important result of damage prediction for industrial forming processes - the ductile damage localization - was well captured with the identified phenomenological models.

Regarding more complex applications, for the pilgering process on zirconium alloy, maximum damage localization can be on the outer or inner surfaces at the end of 4 strokes. Porosities are observed mainly near the inner and outer surfaces of the tube, which can be captured by using the developed models. Moreover, cracks are often observed on external surface, which may be predicted by using the MMC and B&W models.

For the wire-flat rolling process on high carbon steel, among phenomenological models, only the modified Xue model gave correct results in terms of damage localization. The GTN model was thus modified by adopting the Xue's extension and this modified model gave correct localization of damage for wire flat rolling. This fact shows that, regarding the physical origin of model, a given damage model can be modified by adding a suitable *"ingredient"* (e.g. a Lode dependent term). If this "ingredient" is well-established, different models may converge to a same prediction in terms of damage localization (e.g. adding the Lode dependent term proposed by Xue to the GTN model helps obtaining a good localization of damage in wire flat rolling).

7.2 Conclusions, suggestions and future studies

7.2.1 Conclusions

Thanks to the present study, a rich database of failure criteria and ductile damage models was built for cold forming processes simulations. The whole procedure was detailed in this work, from models constructions (analyses, modifications and implementations) to models' parameters identification. Successful applications in real industrial processes show the correctness of the underlying assumptions (e.g. the shear effect was accounted for by using a Lode dependent term in damage models). Moreover, the present study also contributes to answer the question about the applicability of different ductile damage approaches to non-proportional, multiaxial loadings. It suggests that one can use a phenomenological model for certain applications if the formulations are well defined. Moreover, one can also construct a good "modular" model by combining different "ingredients" if these "ingredients" are well established. It is worth noting that, there are limited studies in literature that validates damage models for both mechanical tests and industrial applications with multi-stages processes, even by the original authors of the model.

[2]Evidently, the good localization prediction is implied here.

7.2.2 Suggestion: use of more physical based damage models

Apart from the fact that more detailed studies must be carried out on each material and each process, in the present author point of view, results that are more reliable could be obtained from the damage models that are constructed in a physically based manner to account for microstructural event. The present author suggests two following research orientations to construct a more "powerful" fracture predictive tool from both scientific and industrial points of view.

7.2.2.1 Scientific viewpoint

As we know, a good physically based model involves a tradeoff between simplicity and the predictions quality. For the simplicity, the physics must be simplified as much as possible and only the key dominant factor remains. If the predictions are good, it means that not only a reliable predictive tool is obtained, but also that the underlying physical assumptions are correct and that the physics phenomenon was well captured. Sometimes the physics is too complicated and no physical model is available. A phenomenological model is then fully justified, even though it will not deliver much insight on the physics. Microscopically, damage is linked with the growth of voids. Regarding the coupled damage models (Xue, Lemaitre), from a strict physical viewpoint, the evolution of damage variable does not link with a microstructure change (e.g. the variation of voids in material). Because, if voids grow, the total volume of material must change (maybe very small) since the matrix is incompressible, this cannot be captured by the use of these phenomenological models. GTN model is of great interest, although it still suffers some limitations: the nucleation and coalescence laws are purely phenomenological, which cannot be used for all materials. The GTN model has an advantage that it allows volume change by void *growth*. This type of yield function can be retained, and anisotropic plasticity can also be accounted for (see e.g. [Benzerga and Besson, 2001]). However, the nucleation and coalescence laws should be replaced by more physical inspired formulations, such as the nucleation law proposed by Bouaziz and Maire and their coworkers ([Bouaziz et al., 2008, Maire et al., 2008]); Thomason or Brown and Emburry criteria for coalescence ([Brown and Emburry, 1973]), etc. In addition, void growth is also influenced both by material's microstructure (particles, elongated grains with heterogeneous phases, etc.) and forming processes itself (e.g. elongated voids are observed in drawing direction). Some extensions of the GTN model were proposed to account for ellipsoidal void (e.g. [Gologanu et al., 1993, Madou and Leblond, 2012]) should be used[3].

One can imagine such a physically based damage model, coupled with a regularization technique to obtain mesh-independent solutions (e.g. non-local formulation), using a physical based hardening model with the parameters identified from both microstructural measurements and different loading configurations using both uniaxial and multiaxial mechanical tests . *This type of model can be constructed in a future study and its application is extremely promising from a scientific point of view*. However, such a complex *"configuration"* is difficult to apply to industrial applications[4].

7.2.2.2 Industrial viewpoint

For industrial applications, the use of a simple model, easy to identify and implement, is usually preferred. The main reason may be linked with the common need of engineering application: simulation must supply in a *short time* a *reliable* prediction. In addition, it can be due to a particular need of industry: for some applications (e.g. tube pilgering for nuclear application), only the early nucleation stage of voids is of interest because once voids nucleate, it is too late to ensure a sufficiently quality product. For this reason, the use of uncoupled models might be accurate enough (since at this stage, the influence of damage on material strength is not noticeable). The use of uncoupled models, as developed in the present study, should be

[3]However, as far as we know, these models were not applied to complex applications such as multi-stages forming processes. In addition, the description of voids which is done in all these GTN family models remains idealized in the sense that it does not account for particles fragmentation and real forms of voids. In that sense, these models have clearly more physical bases than the phenomenological approaches, but they still based on an idealized representation of voids and different underlying assumptions that have not been clarified.

[4]Moreover, such a physical based approach would however require a deeper analysis of the material microstructure and of its evolution during the multi-stages forming process, which was not possible in the present study.

legitimate if they can supply a reliable prediction (based on their ability in fracture prediction for different loading configurations). The physical origin of models, in this case, is secondary. Another track to constitute a damage model can be based on the combination of different physically based criteria: a nucleation law (e.g. Gaussian function [Chu and Needleman, 1980], exponential function [Bouaziz et al., 2008]) combined with a void growth criterion (e.g. [Rice and Tracey, 1969] or [Huang, 1991]) and a void coalescence criterion (e.g. [Thomason, 1968] or [Tvergaard and Needleman, 1984]). This approach is indeed interesting from a microstructural point of view, and has few parameters to be identified. Moreover, since no coupling is involved, the mesh size influence may be neglected. However, since it is *physically* based, the identification of some of the parameters should be based on microstructure measurements. Furthermore, from a strict physical viewpoint, this type of model is not really physics, because no volume change due to void growth is accounted for as mentioned above. *To summarize, for industrial applications, if one wants to use physically inspired models, the above-proposed type of model combining different formulations may be employed; and the identification should be based on microstructure measurements.*

7.2.3 Future studies

Although comprehensive studies have been performed in the present thesis on the ductile damage in forming processes, many topics are of prime interest for future studies apart from the suggestion on damage model in the above section:

1. *Experimental work.* It is necessary to perform multi-axial mechanical tests to better calibrate the implemented damage models for a better precision in non-proportional loading. Moreover, micro specimen can be used to perform mechanical tests to clarify size effects (the difference in ductility between micro and macro specimens). The use of in situ X ray tomography experiments would be useful in such a study.

2. *Physically inspired hardening model.* In the present study, the hardening models used are purely phenomenological. More physical hardening models may be used in future studies (e.g. accounting for the austenite-martensite kinetic transformation for stainless steel[5]) to better describe the hardening or softening of the material.

3. *Rate and temperature sensitivity.* The influences of strain rate and temperature are accounted neither on the yield stress, nor on damage evolution. Depending on the material, such influences can be important. Identifying their influences and accounting for them will be the subject of future studies, especially for rate sensitive material.

4. *Anisotropic plasticity and damage* In the present study, isotropic plasticity is assumed and damage is represented as a scalar. Both plasticity and damage models should be extended for anisotropic material in future studies.

5. *Non-local formulation.* As mentioned in section 3.2.1 and throughout the dissertation, the use of a regularization technique (e.g. non-local formulation) is necessary to obtain a mesh-independent solution for coupled damage models. It may be expensive (in terms of CPU time) for industrial applications due to the use of an extremely fine mesh. However, it helps obtaining reliable results when softening is involved.

[5]The model proposed by [Beese and Mohr, 2011] was implemented in Forge2009® by the present author but the identification needs physical measurements, which could not be performed in the present study.

Bibliography

[ABAQUS-6.9, 2009] ABAQUS-6.9. *ABAQUS/Standard Version 6.9, Users manual*. Dassault Systems, Simulia Corp, Providence, RI, USA., 2009. *Cited on pages 155 and 160.*

[ABAQUS/Explicit, 2005] ABAQUS/Explicit. *ABAQUS/Explicit: Advanced topics - Lecture 5: Quasi-static analyses.* Dassault Systems, Simulia Corp, Providence, RI, USA., 2005. *Cited on page 155.*

[Abbasi et al., 2011] M. Abbasi, M. Ketabchi, H. Izadkhah, D. H. Fatmehsaria, and A. N. Aghbash. Identification of GTN model parameters by application of response surface methodology. *Procedia Engineering*, 10(0):415 – 420, 2011. *Cited on page 166.*

[Abe, 2010] H. Abe. Method of Evaluating Workability in Cold Pilgering of Zirconium Alloy Tube. *Materials Transactions*, 51(7):1200–1205, 2010. *Cited on page 75.*

[Abramoff et al., 2004] M. D. Abramoff, P. J. Magelhaes, and S. J. Ram. Image processing with ImageJ. *Biophotonics Int*, 11(7):36–42, 2004. *Cited on page 169.*

[Acharya and Bassani, 2000] A. Acharya and J. L. Bassani. Lattice incompatibility and a gradient theory of crystal plasticity. *Journal of the Mechanics and Physics of Solids*, 48(8):1565–1595, 2000. *Cited on page 62.*

[Achouri et al., 2013] M. Achouri, G. Germain, P. Dal Santo, and D. Saidane. Experimental characterization and numerical modeling of micromechanical damage under different stress states. *Materials & Design* , 50(0):207 – 222, 2013. *Cited on pages 11, 59, 60, 76, 78, and 136.*

[Aliaga, 2000] C. Aliaga. *Simulation numérique par éléments finis en 3D du comportement thermomécanique au cours du traitement thermique d'aciers : application à la trempe de pièces forgées ou coulées*. PhD thesis, École Nationale Supérieure des Mines de Paris, April 2000. In French. *Cited on pages 18, 43, 44, 45, and 49.*

[Aravas, 1987] N. Aravas. On the numerical integration of a class of pressure-dependent plasticity models. *International Journal for Numerical Methods in Engineering*, 24(7):1395–1416, 1987. *Cited on pages 134, 142, 147, 149, 152, 153, 156, 164, and 250.*

[Argon and Im, 1975] A.S. Argon and J. Im. Separation of second phase particles in spheroidized 1045 steel, Cu-0.6pct Cr alloy, and maraging steel in plastic straining. *Metallurgical Transactions A*, 6:839–851, 1975. *Cited on pages 54 and 56.*

[Argon et al., 1975] A. S. Argon, J. Im, and R. Safoglu. Cavity formation from inclusions in ductile fracture. *Metallurgical Transactions A*, 6:825–837, 1975. *Cited on pages 54 and 56.*

[Arnold et al., 1984] D. Arnold, F. Brezzi, and M. Fortin. A stable finite element for the stokes equations. *Calcolo*, 21:337–344, 1984. *Cited on pages 37, 42, and 43.*

[Avitzur, 1968] B. Avitzur. *Metal forming: Processes and analysis*. McGraw-Hill, Kierger, Huntington, N.Y., 2nd edition, 1968. ISBN 978-0070025103. *Cited on pages 32 and 74.*

[Avitzur, 1980] B. Avitzur. *Metal Forming: The Application of Limit Analysis*. Marcel Dekker, New York, 1980. ISBN 978-0824768478. *Cited on pages 11 and 74.*

[Bai, 2008] Y. Bai. *Effect of loading history on necking and fracture*. PhD thesis, Massachusetts Institute of Technology (MIT), 02 2008. *Cited on pages 109, 110, and 115.*

[Bai and Wierzbicki, 2008] Y. Bai and T. Wierzbicki. A new model of metal plasticity and fracture with pressure and Lode dependence. *International Journal of Plasticity*, 24(6):1071 – 1096, 2008. *Cited on pages 10, 11, 17, 18, 19, 52, 68, 69, 72, 77, 78, 81, 107, 110, 127, 261, 262, 263, 264, and 265.*

[Bai and Wierzbicki, 2010] Y. Bai and T. Wierzbicki. Application of extended Mohr-Coulomb criterion to ductile fracture. *International Journal of Fracture*, 161(1):1–20, 2010. *Cited on pages 69, 107, 111, 112, 120, 125, 126, and 129.*

[Banabic, 2010] D. Banabic. *Sheet Metal Forming Processes*. Springer Berlin Heidelberg, 2010. ISBN 978-3-540-88112-4. *Cited on pages 72 and 240.*

[Banerjee, 2001] S. Banerjee. Nuclear Applications: Zirconium Alloys. In *Encyclopedia of Materials: Science and Technology (Second Edition)*, pages 6287 – 6299. Elsevier, Oxford, 2 edition, 2001. ISBN 978-0-08-043152-9. *Cited on page 92.*

[Bao, 2003] Y. Bao. *Prediction of ductile cracked formation in uncracked bodies*. PhD thesis, Massachusetts Institute of Technology (MIT), 09 2003. *Cited on pages 85 and 86.*

[Bao, 2005] Y. Bao. Dependence of ductile crack formation in tensile tests on stress triaxiality, stress and strain ratios. *Engineering Fracture Mechanics*, 72(4):505–522, 2005. *Cited on pages 64 and 66.*

[Bao and Wierzbicki, 2004] Y. Bao and T. Wierzbicki. On fracture locus in the equivalent strain and stress triaxiality space. *International Journal of Mechanical Sciences*, 46(1):81–98, 2004. *Cited on pages 11, 18, 59, 64, 66, 67, 69, 72, 76, and 78.*

[Bao and Wierzbicki, 2004a] Y. Bao and T. Wierzbicki. A Comparative Study on Various Ductile Crack Formation Criteria. *Journal of Engineering Materials and Technology*, 126(3):314–324, 2004a. *Cited on pages 11, 61, 65, 66, and 69.*

[Bao and Wierzbicki, 2005] Y. Bao and T. Wierzbicki. On the cut-off value of negative triaxiality for fracture. *Engineering Fracture Mechanics*, 72(7):1049–1069, 2005. *Cited on pages 64, 69, 83, 94, 108, 125, and 126.*

[Barlat et al., 2007] F. Barlat, J. W. Yoon, and O. Cazacu. On linear transformations of stress tensors for the description of plastic anisotropy. *International Journal of Plasticity*, 23(5):876 – 896, 2007. *Cited on page 240.*

[Barsoum and Faleskog, 2007] I. Barsoum and J. Faleskog. Rupture mechanisms in combined tension and shear–Micromechanics. *International Journal of Solids and Structures*, 44(17):5481 – 5498, 2007. *Cited on page 69.*

[Barsoum and Faleskog, 2007a] I. Barsoum and J. Faleskog. Rupture mechanisms in combined tension and shear–Experiments. *International Journal of Solids and Structures*, 44(6):1768 – 1786, 2007a. *Cited on pages 11, 53, 68, 69, 70, 77, and 78.*

[Barsoum and Faleskog, 2011] I. Barsoum and J. Faleskog. Micromechanical analysis on the influence of the Lode parameter on void growth and coalescence. *International Journal of Solids and Structures*, 48 (6):925 – 938, 2011. *Cited on pages 13, 124, and 125.*

[Beese and Mohr, 2011] A. M. Beese and D. Mohr. Effect of stress triaxiality and Lode angle on the kinetics of strain-induced austenite-to-martensite transformation. *Acta Materialia*, 59(7):2589 – 2600, 2011. *Cited on pages 103 and 214.*

[Beese and Mohr, 2012] A. M. Beese and D. Mohr. Anisotropic plasticity model coupled with Lode angle dependent strain-induced transformation kinetics law. *Journal of the Mechanics and Physics of Solids*, 60(11):1922 – 1940, 2012. *Cited on pages 51 and 103.*

[Beese et al., 2010] A. M. Beese, M. Luo, Y. Li, Y. Bai, and T. Wierzbicki. Partially coupled anisotropic fracture model for aluminum sheets. *Engineering Fracture Mechanics*, 77(7):1128 – 1152, 2010. *Cited on pages 11, 67, 69, 77, and 78.*

[Benzerga, 2000] A. A. Benzerga. *Rupture ductile des tôles anisotropes*. PhD thesis, Ecole nationale supérieure des Mines de Paris, 03 2000. In French. *Cited on pages 10, 11, 55, 56, and 58.*

[Benzerga and Besson, 2001] A. A. Benzerga and J. Besson. Plastic potentials for anisotropic porous solids. *European Journal of Mechanics - A/Solids*, 20(3):397 – 434, 2001. *Cited on pages 52, 135, and 213.*

[Benzerga and Leblond, 2010] A. A. Benzerga and J.-B. Leblond. Ductile Fracture by Void Growth to Coalescence. In *Advances in Applied Mechanics*, volume 44, pages 169 – 305. Elsevier, 2010. *Cited on pages 11, 54, 56, and 58.*

[Benzerga et al., 2004] A. A. Benzerga, J. Besson, and A. Pineau. Anisotropic ductile fracture: Part II: theory. *Acta Materialia*, 52(15):4639 – 4650, 2004. *Cited on pages 52 and 135.*

[Benzerga et al., 2012] A. A. Benzerga, D. Surovik, and S. M. Keralavarma. On the path-dependence of the fracture locus in ductile materials – Analysis. *International Journal of Plasticity*, 37(0):157 – 170, 2012. *Cited on pages 110 and 129.*

[Beremin, 1981] F. M. Beremin. Cavity formation from inclusions in ductile fracture of A508 steel. *Metallurgical Transactions A*, 12:723–731, 1981. *Cited on pages 55 and 56.*

[Berveiller and Zaoui, 1978] M. Berveiller and A. Zaoui. An extension of the self-consistent scheme to plastically-flowing polycrystals. *Journal of the Mechanics and Physics of Solids*, 26(5–6):325 – 344, 1978. *Cited on page 55.*

[Besson, 2010] J. Besson. Continuum Models of Ductile Fracture: A Review. *International Journal of Damage Mechanics*, 19(1):3 – 52, 2010. *Cited on pages 18, 59, and 136.*

[Besson, 2013] J. Besson. A two length scale non-local model to describe ductile rupture at low stress triaxiality. In *Conference Proceedings - CFRAC 2013*, number 1, page 101, Repro Fetterle, Prague, Czech Republic, 2013. *Cited on page 113.*

[Besson et al., 2001] J. Besson, D. Steglich, and W. Brocks. Modeling of crack growth in round bars and plane strain specimens. *International Journal of Solids and Structures*, 38(46–47):8259 – 8284, 2001. *Cited on page 268.*

[Besson et al., 2003] J. Besson, D. Steglich, and W. Brocks. Modeling of plane strain ductile rupture. *International Journal of Plasticity*, 19(10):1517 – 1541, 2003. *Cited on page 268.*

[Besson et al., 2010] J. Besson, G. Cailletaud, J.-L. Chaboche, S. Forest, and M. Blétry. *Non-linear mechanics of materials*. Springer, College Station, Texas, 1st edition, 2010. ISBN 978-90-481-3355-0. *Cited on page 63.*

[Bettaieb et al., 2011] M. B. Bettaieb, X. Lemoine, O. Bouaziz, A. M. Habraken, and L. Duchêne. Numerical modeling of damage evolution of DP steels on the basis of X-ray tomography measurements. *Mechanics of Materials*, 43(3):139 – 156, 2011. *Cited on pages 167 and 172.*

[Beyer, 2001] H. G. Beyer. *The theory of evolution strategies*. Number 2. Springer, 2001. *Cited on page 89.*

[Bonfoh et al., 2004] N. Bonfoh, P. Lipinski, A. Carmasol, and S. Tiem. Micromechanical modeling of ductile damage of polycrystalline materials with heterogeneous particles. *International Journal of Plasticity*, 20(1):85–106, 2004. *Cited on page 62.*

[Bonora et al., 2005] N. Bonora, D. Gentile, A. Pirondi, and G. Newaz. Ductile damage evolution under triaxial state of stress: theory and experiments. *International journal of plasticity*, pages 981–1007, 2005. *Cited on page 60.*

[Bouaziz et al., 2008] O. Bouaziz, E. Maire, M. Giton, J. Lamarre, Y. Salingue, and M. Dimichiele. A model for initiation and growth of damage in dualphase steels identified by x-ray micro-tomography. *Revue de Métallurgie*, 105:102–107, 2008. *Cited on pages 26, 170, 179, 180, 213, and 214.*

[Bouchard et al., 2008] P.-O. Bouchard, L. Bourgeon, H. Lachapèle, E. Maire, C. Verdu, R. Forestier, and R. E. Logé. On the influence of particle distribution and reverse loading on damage mechanisms of ductile steels. *Materials Science and Engineering: A*, 496(1–2):223 – 233, 2008. *Cited on page 57.*

[Bouchard et al., 2011] P.-O. Bouchard, J.-M. Gachet, and E. Roux. Ductile damage parameters identification for cold metal forming applications. In Gary Menary, editor, *AIP Conference Proceedings - ESAFORM 2011*, volume 1353, pages 47–52, Belfast, Royaume-Uni, 2011. *Cited on page 95.*

[Bouchard et al., 2011] P.-O. Bouchard, L. Bourgeon, S. Fayolle, and K. Mocellin. An enhanced Lemaitre model formulation for materials processing damage computation. *International Journal of Material Forming*, 4:299–315, 2011. *Cited on pages 62, 107, 108, 109, and 125.*

[Brezzi and Fortin, 1991] F. Brezzi and M. Fortin. *Mixed and hybrid finite element methods*. Springer-Verlag New York, Inc., NY, USA, 1991. ISBN 0-387-97582-9. *Cited on page 43.*

[Bridgman, 1952] P. W. Bridgman. *Studies in large plastic flow and fracture*. Harvard University Press, Cambridge, Massachusetts, 1952. *Cited on pages 11, 63, 64, 83, 88, 108, and 125.*

[Brown and Emburry, 1973] L. M. Brown and J. D. Emburry. A Model of Ductile Fracture in Two Phase Materials. *Proceeding of 3rd International conference on the Strength of Metals and Alloys, Cambridge*, 1973. *Cited on pages 59 and 213.*

[Budiansky et al., 1982] B. Budiansky, J. W. Hutchinson, and S. Slutsky. Void growth and collapse in viscous solid. *The Rodney Hill 60th anniversary volume*, pages 13–34, 1982. *Cited on page 61.*

[Burden and Faires, 2000] R. L. Burden and D. J. Faires. *Numerical Analysis*. Brooks Cole, 7 edition, December 2000. ISBN 0534382169. *Cited on page 152.*

[Cailliez, 2012] A. Cailliez. Caractérisation au MEB de l'état d'endommagement de fils tréfilés de nuance C62. *R&D report - ArcelorMittal Long Carbon R&D Grandrange*, 2012. *Cited on pages 11 and 82.*

[Cao, 2011] T.-S. Cao. *Mechanical analyses of the wire-drawing process - Xue damage model development - First year progress report*. PhD thesis, Ecole nationale supérieure des Mines de Paris, 06 2011. *Cited on pages 13, 109, and 110.*

[Cao et al., 2012] T.-S. Cao, C. Bobadilla, P. Montmitonnet, and P.-O. Bouchard. Comparative study of phenomenological coupled damage models – Application to industrial forming processes, Proceedings of SF2M annual meeting. volume 100, pages 27–28, Paris, France, 2012. *Cited on page 114.*

[Cao et al., 2013a] T.-S. Cao, A. Gaillac, P. Montmitonnet, and P.-O. Bouchard. Identification methodology and comparison of phenomenological ductile damage models via hybrid numerical-experimental analysis of fracture experiments conducted on a zirconium alloy. *International Journal of Solids and Structures*, 50(24):3984 – 3999, 2013a. *Cited on pages 13 and 119.*

[Cao et al., 2013b] T.-S. Cao, C. Bobadilla, P. Montmitonnet, and P.-O. Bouchard. On the development and identification of phenomenological damage models - Application to industrial wire drawing and rolling processes. *Key Engineering Materials*, 554 - 557:213–226, 2013b. *Cited on pages 172, 173, and 190.*

[Cao et al., 2013c] T.-S. Cao, P. Montmitonnet, and P.-O. Bouchard. A detailed description of the Gurson–Tvergaard–Needleman model within a mixed velocity–pressure finite element formulation. *International Journal for Numerical Methods in Engineering*, 96(9):561–583, 2013c. *Cited on page 134.*

[Capus and Cockcroft, 1962] J. M. Capus and M. G. Cockcroft. Relative slip and deformation during cold rolling. *Journal of the Institute of Metals*, 90:289 – 297, 1962. *Cited on page 31.*

[Chaboche, 1984] J.-L. Chaboche. Anisotropic creep damage in the framework of continuum damage mechanics. *Nuclear Engineering and Design*, 79(3):309–319, 1984. *Cited on page 61.*

[Chandrakanth and Pandey, 1993] S. Chandrakanth and P. C. Pandey. A new ductile damage evolution model. *International Journal of Fracture*, 60:R73–R76, 1993. *Cited on page 62.*

[Chen and Mizuno, 1990] W.-F. Chen and E. Mizuno. *Nonlinear analysis in soil mechanics: theory and implementation / W.F. Chen and E. Mizuno* . Elsevier, Amsterdam, 1990. ISBN 0444430431. *Cited on pages 16 and 238.*

[Chu and Needleman, 1980] C. C. Chu and A. Needleman. Void Nucleation Effects in Biaxially Stretched Sheets. *Journal of Engineering Materials and Technology*, 102(3):249–256, 1980. *Cited on pages 51, 57, 135, 136, and 214.*

[Coulomb, 1776] C. A. Coulomb. *Essai sur une application des règles de maximis & minimis à quelques problèmes de statique, relatifs à l'architecture.* Paris, De l'Imprimerie Royale, 1776. *Cited on pages 111 and 236.*

[Coupez, 1995] T. Coupez. Stable stabilized finite element for 3d forming calculation. *Internal report - CEMEF*, 1995. *Cited on page 44.*

[Coupez et al., 2000] T. Coupez, H. Digonnet, and R. Ducloux. Parallel meshing and remeshing. *Applied Mathematical Modelling*, 25(2):153 – 175, 2000. *Cited on page 37.*

[Cox and Low, 1974] T. B. Cox and J. R. Low. An investigation of the plastic fracture of AISI 4340 and 18 Nickel-200 grade maraging steels. *Metallurgical Transactions*, 5:1457–1470, 1974. *Cited on page 56.*

[Croix, 2002] P. Croix. *Endommagement et rupture des métaux anisotropes pour la dynamique et les crash des véhicules*. PhD thesis, Université de Valenciennes et du Hainaut-Cambrésis, 2002. In French. *Cited on page 136.*

[Croix et al., 2003] P. Croix, F. Lauro, J. Oudin, and J. Christlein. Improvement of damage prediction by anisotropy of microvoids. *Journal of Materials Processing Technology*, 143-144:202 – 208, 2003. *Cited on page 138.*

[de Souza Neto et al., 2008] E. A. de Souza Neto, D. Perić, and D. R. J. Owen. *Computational Methods for Plasticity: Theory and Applications*. John Wiley & Sons, Ltd, 2008. ISBN 9780470694626. *Cited on pages 16, 231, 237, 238, 239, and 240.*

[DeMania, 1995] D. A. DeMania. *The influence of martensitic transformation on the formability of 304L stainless steel sheet*. PhD thesis, Massachusetts Institute of Technology (MIT), 06 1995. *Cited on page 103.*

[Dennis and Schnabel, 1996] J. E. Dennis and R. B. Schnabel. *Numerical Methods for Unconstrained Optimization and Nonlinear Equations (Classics in Applied Mathematics, 16)*. Society for Industrial and Applied Mathematics, 1996. ISBN 0898713641. *Cited on page 152.*

[Dhar et al., 1996] S. Dhar, R. Sethuraman, and P. M. Dixit. A continuum damage mechanics model for void growth and micro crack initiation. *Engineering Fracture Mechanics*, 53(6):917 – 928, 1996. *Cited on page 74.*

[Dieter, 1976] George E. Dieter. *Mechanical metallurgy*. McGraw-Hill, New York, 2d ed. edition, 1976. ISBN 0070168911. *Cited on pages 28, 29, 31, 72, and 74.*

[Dixit and Dixit, 1995] U. S. Dixit and P. M. Dixit. An analysis of the steady-state wire drawing of strain-hardening materials. *Journal of Materials Processing Technology*, 47(3-4):201 – 229, 1995. *Cited on page 33.*

[Dodd and Boddington, 1980] B. Dodd and P. Boddington. The causes of edge cracking in cold rolling. *Journal of Mechanical Working Technology*, 3(3–4):239 – 252, 1980. *Cited on page 72.*

[Drucker, 1949] D. C. Drucker. Relations of experiments to mathematical theories of plasticity. *Journal of Applied Mechanics*, 16:349–357, 1949. *Cited on page 238.*

[Drucker and Prager, 1952] D. C. Drucker and W. Prager. Soil Mechanics and Plasticity Analysis of Limit Design. *Quarterly Journal of Applied Mathematics*, 10:157–162, 1952. *Cited on page 237.*

[Dunand and Mohr, 2010] M. Dunand and D. Mohr. Hybrid experimental–numerical analysis of basic ductile fracture experiments for sheet metals. *International Journal of Solids and Structures*, 47(9):1130 – 1143, 2010. *Cited on pages 98, 99, and 120.*

[Dunand and Mohr, 2011] M. Dunand and D. Mohr. Optimized butterfly specimen for the fracture testing of sheet materials under combined normal and shear loading. *Engineering Fracture Mechanics*, 78(17): 2919 – 2934, 2011. *Cited on pages 14, 68, and 159.*

[Dunand and Mohr, 2011] M. Dunand and D. Mohr. On the predictive capabilities of the shear modified Gurson and the modified Mohr–Coulomb fracture models over a wide range of stress triaxialities and Lode angles. *Journal of the Mechanics and Physics of Solids*, 59(7):1374 – 1394, 2011. *Cited on pages 68 and 111.*

[El Khaoulani and Bouchard, 2012] R. El Khaoulani and P.-O. Bouchard. An anisotropic mesh adaptation strategy for damage and failure in ductile materials. *Finite Elements in Analysis and Design*, 59(0):1 – 10, 2012. *Cited on page 268.*

[Engelen et al., 2003] Roy A.B. Engelen, Marc G.D. Geers, and Frank P.T. Baaijens. Nonlocal implicit gradient-enhanced elasto-plasticity for the modelling of softening behaviour. *International Journal of Plasticity*, 19(4):403 – 433, 2003. *Cited on pages 62 and 113.*

[Eshelby, 1957] J. D. Eshelby. The Determination of the Elastic Field of an Ellipsoidal Inclusion, and Related Problems. *Proceedings of the Royal Society of London. Series A, Mathematical and Physical Sciences*, 241 (1226):376–396, 1957. *Cited on page 55.*

[Fansi et al., 2013] J. Fansi, T. Balan, X. Lemoine, E. Maire, C. Landron, O. Bouaziz, M. B. Bettaieb, and A. M. Habraken. Numerical investigation and experimental validation of physically based advanced GTN model for DP steels . *Materials Science and Engineering: A*, 569(0):1 – 12, 2013. *Cited on page 172.*

[Farrugia, 2006] D. C. J. Farrugia. Prediction and avoidance of high temperature damage in long product hot rolling. *Journal of Materials Processing Technology*, 177(1-3):486 – 492, 2006. *Cited on pages 11, 71, and 72.*

[Farrugia et al., 2009] D. Farrugia, Z. Husain, V. Santisteban, J. Bianchi J. Llanos, P. Vescovo, J. Pera, J. Rodriguez-Ibabe, C. Revilla, J. Fredriksson, J. Demurger, R. Forestier, and B. Kieber. *PACROLP: the*

prediction and avoidance of cracking in long product hot rolling. EUROPEAN COMMISSION, Directorate-General for Research, Research Fund for Coal and Steel Unit, 2009. ISBN 978-92-79-11983-5. *Cited on page 72.*

[Fayolle, 2008] S. Fayolle. *Modélisation numérique de la mise en forme et de la tenue mécanique des assemblages par déformation plastique : application au rivetage auto-poinçonneur*. PhD thesis, Ecole nationale supérieure des Mines de Paris, 11 2008. In French. *Cited on pages 10, 45, 49, 62, and 113.*

[Feld-Payet, 2010] S. Feld-Payet. *Amorçage et propagation de fissures dans les milieux ductiles non locaux*. PhD thesis, Ecole nationale supérieure des Mines de Paris, 11 2010. *Cited on page 268.*

[Fields and Backofen, 1957] D. F. Fields and W. A. Backofen. Determination of strain-hardening characteristics by torsion testing. *Proceedings of the 60th Annual Meeting of the American Society for Testing and Materials*, 57:1259–1272, 1957. *Cited on pages 51, 85, and 247.*

[Filipovic et al., 2006] M. Filipovic, C. Ericsson, and H. Överstam. Behaviour of surface defects in wire rod rolling. *Steel Research International*, 77(6):439–444, 2006. *Cited on page 72.*

[Forge2009®, 2009] Forge2009®. *FORGE/Documentation - Partie 6 - Solveur*. Transvalor S. A, Sophia Antipolis, France., 2009. *Cited on pages 10, 40, and 41.*

[Fortin, 1981] M. Fortin. Old and new finite elements for incompressible flows. *International Journal for Numerical Methods in Fluids*, 1(4):347–364, 1981. *Cited on page 44.*

[Fourment et al., 1999] L. Fourment, J. L. Chenot, and K. Mocellin. Numerical formulations and algorithms for solving contact problems in metal forming simulation. *International Journal for Numerical Methods in Engineering*, 46(9):1435–1462, 1999. *Cited on page 41.*

[Gachet, 2013] J. M. Gachet. *Conception integrée de flasques de sièges automobiles - Etude de l'endommagement ductile*. PhD thesis, Ecole nationale supérieure des Mines de Paris, 09 2013. In French. *Cited on pages 69, 77, and 78.*

[Gaillac, 2007] A. Gaillac. *Endommagement d'alliages de zirconium, impact sur la laminabilité*. PhD thesis, Institut national polytechnique de Grenoble, 10 2007. In French. *Cited on pages 11, 18, 24, 76, 77, 78, 93, and 99.*

[Gaillac and Barberis, 2007] A. Gaillac and P. Barberis. Endommagement d'alliages de zirconium: traction et fatigue. 2007. In French. *Cited on page 93.*

[Gologanu et al., 1993] M. Gologanu, J. B. Leblond, and J. Devaux. Approximate models for ductile metals containing non-spherical voids–Case of axisymmetric prolate ellipsoidal cavities. *Journal of the Mechanics and Physics of Solids*, 41(11):1723 – 1754, 1993. *Cited on pages 13, 51, 135, 137, and 213.*

[Goods and Brown, 1979] S. H. Goods and L. M. Brown. Overview No. 1: The nucleation of cavities by plastic deformation. *Acta Metallurgica*, 27(1):1 – 15, 1979. *Cited on page 54.*

[Gotoh, 1977] M. Gotoh. A theory of plastic anisotropy based on yield function of fourth order (plane stress state)—II. *International Journal of Mechanical Sciences*, 19(9):513 – 520, 1977. *Cited on page 240.*

[Govindarajan and Aravas, 1995] R. M. Govindarajan and N. Aravas. Pressure-dependent plasticity models: Loading-unloading criteria and the consistent linearization of an integration algorithm. *Communications in Numerical Methods in Engineering*, 11(4):339–345, 1995. *Cited on pages 134, 142, 147, 148, and 164.*

[Gronostajski, 2000] Z. Gronostajski. The constitutive equations for FEM analysis. *Journal of Materials Processing Technology*, 106(1–3):40 – 44, 2000. *Cited on pages 50 and 51.*

[Gurland and Plateau, 1963] J. Gurland and J. Plateau. The mechanism of ductile rupture of metals containing inclusions. *Trans. ASM*, 56:442–454, 1963. *Cited on page 54.*

[Gurson, 1977] A. L. Gurson. Continuum Theory of Ductile Rupture by Void Nucleation and Growth: Part I-Yield Criteria and Flow Rules for Porous Ductile Media. *Journal of Engineering Materials and Technology*, 99(1):2–15, 1977. *Cited on pages 51, 57, 62, 107, 134, and 142.*

[Haltom et al., 2013] S. S. Haltom, S. Kyriakides, and K. Ravi-Chandar. Ductile failure under combined shear and tension. *International Journal of Solids and Structures*, 50(10):1507 – 1522, 2013. *Cited on pages 11, 67, 77, and 78.*

[Hansel and Spittel, 1979] A. Hansel and T. Spittel. Kraft- und Arbeitsbedarf Bildsamer Formgebungsverfahren. *VEB Deutscher Verlag fur Grundstoffindustrie, Leipzig*, 1979. in German. *Cited on pages 51 and 100.*

[He et al., 2011] M. He, F. Li, and Z. Wang. Forming Limit Stress Diagram Prediction of Aluminum Alloy 5052 Based on GTN Model Parameters Determined by In Situ Tensile Test. *Chinese Journal of Aeronautics*, 24(3):378 – 386, 2011. *Cited on page 167.*

[Hencky, 1924] H. Hencky. Zur Theorie plastischer Deformationen und der hierdurch im Material hervorgerufenen Nebenspannungen. *Proceedings of the First International Congress on Applied Mechanics, Delft*, 1924. *Cited on page 236.*

[Hill, 1948] R. Hill. A Theory of the Yielding and Plastic Flow of Anisotropic Metals. *Proceedings of the Royal Society of London. Series A. Mathematical and Physical Sciences*, 193(1033):281–297, 1948. *Cited on page 240.*

[Hollomon, 1944] J. H. Hollomon. The effect of heat treatment and carbon content on the work hardening characteristics of several steels. *Transactions of American Society for Metals*, 106(32):123, 1944. *Cited on page 50.*

[Hor, 2011] A. Hor. *Simulation physique des conditions thermomécaniques de forgeage et d'usinage : caractérisation et modélisation de la rhéologie et de l'endommagement*. PhD thesis, Arts et Métiers ParisTech, 01 2011. In French. *Cited on pages 14, 63, and 166.*

[Hu, 2007] W. Hu. Constitutive modeling of orthotropic sheet metals by presenting hardening-induced anisotropy. *International Journal of Plasticity*, 23(4):620 – 639, 2007. *Cited on page 240.*

[Huang, 1991] Y. Huang. Accurate Dilatation Rates for Spherical Voids in Triaxial Stress Fields. *Journal of Applied Mechanics*, 58(4):1084–1086, 1991. *Cited on pages 57, 170, and 214.*

[Itskov, 2000] M. Itskov. On the theory of fourth-order tensors and their applications in computational mechanics. *Computer Methods in Applied Mechanics and Engineering*, 189(2):419 – 438, 2000. *Cited on pages 149 and 231.*

[Jirásek, 1998] M. Jirásek. Nonlocal models for damage and fracture: Comparison of approaches. *International Journal of Solids and Structures*, 35(31–32):4133 – 4145, 1998. *Cited on pages 113 and 158.*

[Johnson and Mellor, 1962] W. Johnson and P. B. Mellor. *Plasticity for mechanical engineers*. D. Van Nostrand Company LTD, London, 1962. *Cited on page 86.*

[Kachanov, 1958] L. M. Kachanov. On creep rupture time. *Proc. Acad. Sci. USSR Div. Eng. Sci.*, 8:26–31, 1958. *Cited on page 61.*

[Kanetake et al., 1995] N. Kanetake, M. Nomura, and T. Choh. Continuous observation of microstructural degradation during tensile loading of particle reinforced aluminium matrix composites. *Materials Science and Technology*, 11(12), 1995. *Cited on page 54.*

[Kao et al., 1990] A. S. Kao, H. A. Kuhn, O. Richmond, and W. A. Spitzig. Tensile fracture and fractographic analysis of 1045 spheroidized steel under hydrostatic pressure. *Journal of Materials Research*, 5(1): 83–91, 1990. *Cited on pages 11, 65, 66, 175, and 179.*

[Komori, 2008] K. Komori. Evolution of void volume fraction for simulating inner fracture defects related to in drawing of high-carbon steel wire rods. *Theoretical and Applied Fracture Mechanics*, 50(2):157 – 166, 2008. *Cited on pages 11 and 74.*

[Kpodzo, 2013] K. W. Kpodzo. *Une méthode multi maillages multi physiques: application à la mise en forme à froid*. PhD thesis, Ecole nationale supérieure des Mines de Paris, 2013. In French. *Cited on pages 206, 208, and 209.*

[Krauer and Hora, 2012] J. Krauer and P. Hora. Enhanced material models for the process design of the temperature dependent forming behavior of metastable steels. *International Journal of Material Forming*, 5:361–370, 2012. *Cited on pages 51 and 103.*

[Kweon, 2012] S. Kweon. Damage at negative triaxiality. *European Journal of Mechanics - A/Solids*, 31(1): 203 – 212, 2012. *Cited on pages 59 and 78.*

[Kweon et al., 2010] S. S. Kweon, A. J. Beaudoin, and R. J. McDonald. Experimental Characterization of Damage Processes in Aluminum AA2024-O. *Journal of Engineering Materials and Technology*, 132(3), 2010. *Cited on pages 59 and 78.*

[Landron, 2011] C. Landron. *Ductile damage characterization in Dual-Phase steels using X-ray tomography*. PhD thesis, L'Institut National des Sciences Appliquées de Lyon, 12 2011. *Cited on pages 10, 11, 14, 15, 54, 58, 59, 63, 167, 168, 170, 171, and 172.*

[Landron et al., 2011] C. Landron, E. Maire, O. Bouaziz, J. Adrien, L. Lecarme, and A. Bareggi. Validation of void growth models using X-ray microtomography characterization of damage in dual phase steels. *Acta Materialia*, 59(20):7564 – 7573, 2011. *Cited on page 170.*

[Landron et al., 2011] C. Landron, E. Maire, J. Adrien, and O. Bouaziz. Damage characterization in Dual-Phase steels using X-ray tomography. In *Optical Measurements, Modeling, and Metrology*, volume 5 of *Conference Proceedings of the Society for Experimental Mechanics Series*, pages 11–18. Springer New York, 2011. ISBN 978-1-4614-0227-5. *Cited on pages 14, 167, 168, 169, and 170.*

[Landron et al., 2012] C. Landron, E. Maire, J. Adrien, O. Bouaziz, M. Di Michiel, P. Cloetens, and H. Suhonen. Resolution effect on the study of ductile damage using synchrotron X-ray tomography. *Nuclear Instruments and Methods in Physics Research Section B: Beam Interactions with Materials and Atoms*, 284 (0):15 – 18, 2012. *Cited on pages 170 and 171.*

[Lapovok and Hodgson, 2009] R. Lapovok and D. Hodgson. A damage accumulation model for complex strain paths: Prediction of ductile failure in metals. *Journal of the Mechanics and Physics of Solids*, 57 (11):1851 – 1864, 2009. *Cited on page 75.*

[Le Moal and Cassone, 2012] C. Le Moal and Y. Cassone. Damage of cold drawn pearlitic steels. *Internship report - INSA Lyon*, 2012. *Cited on pages 167, 169, 171, 173, and 177.*

[Leblond et al., 1995] J. B. Leblond, G. Perrin, and J. Devaux. An improved Gurson-type model for hardenable ductile metals. *European journal of mechanics and Solids*, 14(4):499 – 527, 1995. *Cited on pages 51, 135, and 137.*

[Lee and Mear, 1999] B. J. Lee and M. E. Mear. Stress concentration induced by an elastic spheroidal particle in a plastically deforming solid. *Journal of the Mechanics and Physics of Solids*, 47(6):1301 – 1336, 1999. *Cited on pages 55 and 56.*

[Lee and Mear, 1999a] B. J. Lee and M. E. Mear. Evolution of elliptical voids in power-law viscous solids. *Mechanics of Materials*, 31(1):9 – 28, 1999a. *Cited on page 55.*

[Lemaitre, 1986] J. Lemaitre. Local approach of fracture. *Engineering Fracture Mechanics*, 25(5-6):523–537, 1986. *Cited on pages 61 and 107.*

[Lemaitre and Desmorat, 2005] J. Lemaitre and R. Desmorat. *Engineering Damage Mechanics: Ductile, Creep, Fatigue and Brittle Failures*. Springer, Berlin, 2005. ISBN 978-3-540-21503-5. *Cited on pages 19, 62, 63, 107, 108, 109, 240, and 241.*

[Li and Wierzbicki, 2010] Y. Li and T. Wierzbicki. Prediction of plane strain fracture of AHSS sheets with post-initiation softening. *International Journal of Solids and Structures*, 47(17):2316 – 2327, 2010. *Cited on page 69.*

[Lin et al., 2008] H. S. Lin, Y. C. Hsu, and C. C. Keh. Inhomogeneous deformation and residual stress in skin-pass axisymmetric drawing. *Journal of Materials Processing Technology*, 201(1-3):128 – 132, 2008. *Cited on page 33.*

[Lode, 1925] W. Lode. Versuche über den einflußder mittleren hauptspannung auf die fließßgrenze. *Zeitschrift für angewandte mathematik und mechanik*, 5:142–144, 1925. *Cited on page 108.*

[Lodej et al., 2006] B. Lodej, K. Niang, P. Montmitonnet, and J.-L. Aubin. Accelerated 3D FEM computation of the mechanical history of the metal deformation in cold pilgering of tubes. *Journal of Materials Processing Technology*, 177(1–3):188 – 191, 2006. *Cited on pages 24, 34, 202, 204, 207, 208, and 209.*

[Ludwik, 1996] P. Ludwik. *Elemente Der Technologischen Mechanik*. Berlin: J. Springer, 1996. ISBN 0898713641. *Cited on pages 50, 91, and 173.*

[Lund and Byrne, 2001] J. R. Lund and J. P. Byrne. Leonardo da Vinci's tensile strength tests : Implications for the discovery of engineering mechanics. *Civil engineering and environmental systems*, 18:243–250, 2001. *Cited on page 197.*

[Lund and Schuh, 2004] A. C. Lund and C. A. Schuh. The Mohr–Coulomb criterion from unit shear processes in metallic glass. *Intermetallics*, 12(10–11):1159 – 1165, 2004. *Cited on pages 111 and 237.*

[Luo et al., 2012] M. Luo, M. Dunand, and D. Mohr. Experiments and modeling of anisotropic aluminum extrusions under multi-axial loading – Part II: Ductile fracture. *International Journal of Plasticity*, 32–33 (0):36 – 58, 2012. *Cited on pages 14, 69, 111, 120, 159, and 163.*

[Madou and Leblond, 2012] K. Madou and J.-B. Leblond. A Gurson-type criterion for porous ductile solids containing arbitrary ellipsoidal voids—I: Limit-analysis of some representative cell. *Journal of the Mechanics and Physics of Solids*, 60(5):1020 – 1036, 2012. *Cited on pages 172 and 213.*

[Mae et al., 2007] H. Mae, X. Teng, Y. Bai, and T. Wierzbicki. Calibration of ductile fracture properties of a cast aluminum alloy. *Materials Science and Engineering: A*, 459(1-2):156–166, 2007. *Cited on pages 68 and 69.*

[Maire et al., 2007] E. Maire, V. Carmona, J. Courbon, and W. Ludwig. Fast X-ray tomography and acoustic emission study of damage in metals during continuous tensile tests. *Acta Materialia*, 55(20):6806–6815, 2007. *Cited on page 167.*

[Maire et al., 2008] E. Maire, O. Bouaziz, M. Di Michiel, and C. Verdu. Initiation and growth of damage in a dual-phase steel observed by X-ray microtomography. *Acta Materialia*, 56(18):4954 – 4964, 2008. *Cited on pages 26, 63, 167, 169, 170, 171, 179, 180, and 213.*

[Malcher et al., 2012] L. Malcher, F. M. Andrade Pires, and J. M. A. César de Sá. An assessment of isotropic constitutive models for ductile fracture under high and low stress triaxiality . *International Journal of Plasticity*, 30–31(0):81 – 115, 2012. *Cited on pages 263 and 264.*

[Marsden and Hughes, 1983] J. E. Marsden and T. J. R. Hughes. *Mathematical Foundations of Elasticity*, volume 51. Dover, 1983. *Cited on page 147.*

[Mashayekhi et al., 2011] M. Mashayekhi, N. Torabian, and M. Poursina. Continuum damage mechanics analysis of strip tearing in a tandem cold rolling process. *Simulation Modelling Practice and Theory*, 19 (2):612–625, 2011. *Cited on page 63.*

[Massé, 2010] T. Massé. *Study and optimization of high carbon steel flat wires*. PhD thesis, Ecole nationale supérieure des Mines de Paris, 01 2010. *Cited on pages 10, 11, 16, 18, 24, 33, 35, 61, 73, 77, 78, 82, 187, 192, 193, 194, and 208.*

[McAllen and Phelan, 2007] P. J. McAllen and P. Phelan. Numerical analysis of axisymmetric wire drawing by means of a coupled damage model. *Journal of Materials Processing Technology*, 183(2-3):210 – 218, 2007. *Cited on page 75.*

[McClintock, 1968] F. A. McClintock. A criterion of ductile fracture by the growth of holes. *ASME J. Appl. Mech*, 35:363–371, 1968. *Cited on pages 59 and 61.*

[McClintock et al., 1966] F. A. McClintock, S. M. Kaplan, and C. A. Berg. Ductile fracture by hole growth in shear bands. *International Journal of Fracture*, 2:614–627, 1966. *Cited on pages 51 and 110.*

[Mediavilla et al., 2006] J. Mediavilla, R. H. J. Peerlings, and M. G. D. Geers. Discrete crack modelling of ductile fracture driven by nonlocal softening plasticity. *International Journal For Numerical Methods In Engineering*, 66(4):661–688, 2006. *Cited on page 268.*

[Mediavilla et al., 2006a] J. Mediavilla, R. H. J. Peerlings, and M. G. D. Geers. A robust and consistent remeshing-transfer operator for ductile fracture simulations. *Computers and Structures*, 84(8-9):604–623, 2006a. *Cited on page 268.*

[Mescall et al., 1983] J. Mescall, R. Papirno, and J. McClaughlin. Stress and Deformation States Associated with Upset Tests in Metals. *Compression testing of homogeneous Materials and composites - ASTM STP 808*, pages 7 – 48, 1983. *Cited on page 110.*

[Mohr and Beyer, 1928] C. O. Mohr and K. Beyer. *Abhandlungen Aus Dem Gebiete Der Technischen Mechanik 3. erweiterte Aufl. zur Jahrhundertfeier der Technischen Hochschule Dresden*. Berlin: W. Ernst & Sohn, 1928. *Cited on pages 111 and 236.*

[Mohr and Henn, 2007] D. Mohr and S. Henn. Calibration of Stress-triaxiality Dependent Crack Formation Criteria: A New Hybrid Experimental-Numerical Method. *Experimental Mechanics*, 47:805–820, 2007. *Cited on page 110.*

[Monchiet and Bonnet, 2013] V. Monchiet and G. Bonnet. A Gurson-type model accounting for void size effects. *International Journal of Solids and Structures*, 50(2):320 – 327, 2013. *Cited on pages 51 and 135.*

[Montmitonnet, 2007] P. Montmitonnet. From Steady-State To Cyclic Metal Forming Processes. *AIP Conference Proceedings*, 908(1):209–214, 2007. *Cited on pages 36 and 202.*

[Montmitonnet, 2011] P. Montmitonnet. Scientific backgrounds of metal forming processes. *Scientific course - Center for material forming*, 2011. *Cited on pages 10, 31, and 32.*

[Montmitonnet et al., 2002] P. Montmitonnet, R. Logé, M. Hamery, Y. Chastel, J.-L. Doudoux, and J.-L. Aubin. 3D elastic–plastic finite element simulation of cold pilgering of zircaloy tubes. *Journal of Materials Processing Technology*, 125–126(0):814 – 820, 2002. *Cited on pages 34 and 36.*

[Muhlich and Brocks, 2003] U. Muhlich and W. Brocks. On the numerical integration of a class of pressure-dependent plasticity models including kinematic hardening. *Computational Mechanics*, 31:479–488, 2003. *Cited on pages 52, 135, and 142.*

[Nadai, 1950] A. Nadai. *Theory of flow and fracture of solids*, volume 1. McGraw-Hill, New York, 2nd edition, 1950. *Cited on page 236.*

[Nagtegaal, 1982] J. C. Nagtegaal. On the implementation of inelastic constitutive equations with special reference to large deformation problems. *Computer Methods in Applied Mechanics and Engineering*, 33 (1-3):469 – 484, 1982. *Cited on page 146.*

[Nahshon and Hutchinson, 2008] K. Nahshon and J. W. Hutchinson. Modification of the Gurson Model for shear failure. *European Journal of Mechanics - A/Solids*, 27(1):1 – 17, 2008. *Cited on pages 52, 107, 135, 138, 139, 179, and 211.*

[Needleman and Rice, 1978] A. Needleman and J. C. Rice. Limit to ductility set by plastic flow localization. *Mechanics of sheet metal forming*, pages 237–267, 1978. *Cited on pages 56 and 57.*

[Needleman and Tvergaard, 1984] A. Needleman and V. Tvergaard. An analysis of ductile rupture in notched bars. *Journal of the Mechanics and Physics of Solids*, 32(6):461–490, 1984. *Cited on pages 51, 58, 62, 135, 142, 166, and 167.*

[Nerino et al., 2011] A. Nerino, M. Deaver, C. Nagele, and J. Reinhart. HPTR's past, present, and future. *The Tube and Pipe Journal*, pages 20 – 24, 2011. *Cited on pages 35 and 36.*

[Nielsen and Tvergaard, 2009] K. L. Nielsen and V. Tvergaard. Effect of a shear modified Gurson model on damage development in a FSW tensile specimen. *International Journal of Solids and Structures*, 46 (3-4):587 – 601, 2009. *Cited on pages 14, 139, and 141.*

[Nielsen and Tvergaard, 2010] K. L. Nielsen and V. Tvergaard. Ductile shear failure or plug failure of spot welds modelled by modified Gurson model. *Engineering Fracture Mechanics*, 77(7):1031 – 1047, 2010. *Cited on page 139.*

[Olson and Cohen, 1975] G.B. Olson and M. Cohen. Kinetics of strain-induced martensitic nucleation. *Metallurgical Transactions A*, 6(4):791–795, 1975. *Cited on page 103.*

[Ortiz and Popov, 1985] M. Ortiz and E. P. Popov. Accuracy and stability of integration algorithms for elastoplastic constitutive relations. *International Journal for Numerical Methods in Engineering*, 21(9): 1561–1576, 1985. *Cited on page 142.*

[Palchik, 2006] V. Palchik. Application of Mohr–Coulomb failure theory to very porous sandy shales. *International Journal of Rock Mechanics and Mining Sciences*, 43(7):1153 – 1162, 2006. *Cited on pages 111 and 237.*

[Pardoen and Hutchinson, 2000] T. Pardoen and J. W. Hutchinson. An extended model for void growth and coalescence. *Journal of the Mechanics and Physics of Solids*, 48(12):2467 – 2512, 2000. *Cited on pages 51, 59, and 135.*

[Pardoen et al., 1998] T. Pardoen, I. Doghri, and F. Delannay. Experimental and numerical comparison of void growth models and void coalescence criteria for the prediction of ductile fracture in copper bars. *Acta Materialia*, 46(2):541 – 552, 1998. *Cited on page 57.*

[Pardoen et al., 2010] T. Pardoen, F. Scheyvaerts, A. Simar, C. Tekoglu, and P. R. Onck. Multiscale modeling of ductile failure in metallic alloys. *Comptes Rendus Physique*, 11(3-4):326 – 345, 2010. *Cited on pages 58 and 59.*

[Peerlings et al., 1996] R. H. J. Peerlings, R. De Borst, W. A. M. Brekelmans, and J. H. P. De Vree. Gradient enhanced damage for quasi-brittle materials. *International Journal for Numerical Methods in Engineering*, 39:3391–3403, 1996. *Cited on pages 62, 112, and 113.*

[Peerlings et al., 2001] R. H. J. Peerlings, M. G. D. Geers, R. de Borst, and W. A. M. Brekelmans. A critical comparison of nonlocal and gradient-enhanced softening continua. *International Journal of Solids and Structures*, 38(44-45):7723–7746, 2001. *Cited on pages 62 and 113.*

[Peng et al., 2009] J. Peng, P. D. Wu, Y. Huang, X. X. Chen, D. J. Lloyd, J. D. Embury, and K. W. Neale. Effects of superimposed hydrostatic pressure on fracture in round bars under tension. *International Journal of Solids and Structures*, 46(20):3741 – 3749, 2009. *Cited on page 66.*

[Perchat, 2000] E. Perchat. *MINI-élément et factorisation incomplètes pour la parallelisation d'un solveur de Stokes 2D : application au forgeage*. PhD thesis, École Nationale Supérieure des Mines de Paris, 2000. In French. *Cited on page 44.*

[Ran et al., 2013] J. Q. Ran, M. W. Fu, and W. L. Chan. The influence of size effect on the ductile fracture in micro-scaled plastic deformation. *International Journal of Plasticity*, 41(0):65 – 81, 2013. *Cited on page 176.*

[Renon, 2002] N. Renon. *Simulation numérique par éléments finis de des grandes déformations des sols. Application à la scarification*. PhD thesis, Ecole nationale supérieure des Mines de Paris, 01 2002. In French. *Cited on page 239.*

[Rice and Tracey, 1969] J. R. Rice and D. A. Tracey. On the ductile enlargement of voids in triaxial stress fields. *Journal of the Mechanics and Physics of Solids*, 17:201–217, 1969. *Cited on pages 51, 57, 60, 61, 110, 134, 170, 180, and 214.*

[Santacreu et al., 2006] P. O. Santacreu, J. C. Glez, G. Chinouilh, and T. Frölich. Behaviour model of austenitic stainless steels for automotive structural parts. *Steel Research International*, 77(9-10):686–691, 2006. *Cited on page 103.*

[Schacht et al., 2003] T. Schacht, N. Untermann, and E. Steck. The influence of crystallographic orientation on the deformation behaviour of single crystals containing microvoids. *International Journal of Plasticity*, 19(10):1605–1626, 2003. *Cited on page 62.*

[Schwefel, 1993] H. P. Schwefel. *Evolution and Optimum Seeking: The Sixth Generation*. John Wiley & Sons, Inc., NY, USA, 1993. ISBN 0471571482. *Cited on page 89.*

[Seabra et al., 2013] M. R. R. Seabra, P. Sustaric, J. M. A. Cesar de Sa, and T. Rodic. Damage driven crack initiation and propagation in ductile metals using XFEM. *Computational Mechanics*, 52(1):161–179, 2013. *Cited on page 268.*

[Shrivastava et al., 1982] S. C. Shrivastava, J. J. Jonas, and G. Canova. Equivalent strain in large deformation torsion testing : Theoretical and practical considerations. *Journal of the Mechanics and Physics of Solids*, 30(1-2):75 – 90, 1982. *Cited on page 84.*

[Simo and Hughes, 1998] J. C. Simo and T. J. R. Hughes. *Computational Inelasticity*. Springer-Verlag, New-York, 1998. *Cited on page 239.*

[Simo and Taylor, 1985] J. C. Simo and R. L. Taylor. Consistent tangent operators for rate-independent elastoplasticity. *Computer Methods in Applied Mechanics and Engineering*, 48(1):101–118, 1985. *Cited on pages 143, 146, and 240.*

[Simo and Taylor, 1986] J. C. Simo and R. L. Taylor. A return mapping algorithm for plane stress elastoplasticity. *International Journal for Numerical Methods in Engineering*, 22(3):649–670, 1986. *Cited on pages 143 and 240.*

[Siruguet and Leblond, 2004] K. Siruguet and J. B. Leblond. Effect of void locking by inclusions upon the plastic behavior of porous ductile solids–I: theoretical modeling and numerical study of void growth. *International Journal of Plasticity*, 20(2):225 – 254, 2004. *Cited on pages 51, 135, and 138.*

[Son et al., 2008] I. H. Son, J. D. Lee, S. Choi, D. L. Lee, and Y. T. Im. Deformation behavior of the surface defects of low carbon steel in wire rod rolling. *Journal of Materials Processing Technology*, 201(1–3):91 – 96, 2008. *Cited on page 72.*

[Son et al., 2011] S. B. Son, Y. K. Lee, S. H. Kang, H. S. Chung, J. S. Cho, J. T. Moon, and K. H. Oh. A numerical approach on the inclusion effects in ultrafine gold wire drawing process. *Engineering Failure Analysis*, In Press, Corrected Proof, 2011. *Cited on page 75.*

[Starck, 1992] B. Starck. *Approche expérimentale et modélisation de l'essai de traction torsion sur des matériaux élastoplastiques: applications à l'étude de l'anisotropie et de l'endommagement*. PhD thesis, Ecole nationale supérieure des Mines de Paris, 09 1992. In French. *Cited on pages 71, 77, and 78.*

[Strehlau, 2006] O. Strehlau. Introducing cold pilger mill technology. *The Tube and Pipe Journal*, pages 20 – 24, 2006. *Cited on pages 10, 35, 36, and 37.*

[Stringfellow et al., 1992] R. G. Stringfellow, D. M. Parks, and G. B. Olson. A constitutive model for transformation plasticity accompanying strain-induced martensitic transformations in metastable austenitic steels. *Acta Metallurgica et Materialia*, 40(7):1703 – 1716, 1992. *Cited on page 103.*

[Suéry et al., 2010] M. Suéry, J. Adrien, C. Landron, S. Terzi, E. Maire, L. Salvo, and J.-J. Blandin. Fast in-situ X-ray micro tomography characterisation of microstructural evolution and strain-induced damage in alloys at various temperatures. *International Journal of Materials Research*, 101(9):1080–1088, 2010. *Cited on page 167.*

[Swift, 1952] H. W. Swift. Plastic instability under plane stress. *Journal of the Mechanics and Physics of Solids*, 1(1):1 – 18, 1952. *Cited on pages 50, 91, 95, and 100.*

[Tai, 1990] W. H. Tai. Plastic damage and ductile fracture in mild steels. *Engineering Fracture Mechanics*, 37 (4):853–880, 1990. *Cited on page 62.*

[Tai and Yang, 1986] W. H. Tai and B. X. Yang. A new microvoid-damage model for ductile fracture. *Engineering Fracture Mechanics*, 25(3):377–384, 1986. *Cited on page 62.*

[Tang and Lee, 1995] C. Y. Tang and W. B. Lee. Effects of damage on the shear modulus of aluminum alloy 2024T3. *Scripta Metallurgica et Materialia*, 32(12):1993 – 1999, 1995. *Cited on pages 11, 70, 77, and 78.*

[Tang et al., 2003] C. Y. Tang, T. C. Lee, and B. Rao. An experimental study of shear damage and failure of aluminium alloy 2024T3. *Journal of Materials Processing Technology*, 139(1-3):208 – 211, 2003. *Cited on pages 11, 70, 77, and 78.*

[Tang et al., 2011] K. K. Tang, Z. X. Li, and J. Wang. Numerical simulation of damage evolution in multi-pass wire drawing process and its applications. *Materials and Design*, 32(6):3299 – 3311, 2011. *Cited on page 75.*

[Tardif and Kyriakides, 2012] N. Tardif and S. Kyriakides. Determination of anisotropy and material hardening for aluminum sheet metal. *International Journal of Solids and Structures*, 49(25):3496 – 3506, 2012. *Cited on page 99.*

[Teng, 2005] X. Teng. *High velocity impact fracture*. PhD thesis, Massachusetts Institute of Technology (MIT), 02 2005. *Cited on pages 125 and 202.*

[Thomason, 1968] P. F. Thomason. A theory for ductile fracture by internal necking of cavities. *Journal: Institute of metals*, (96):360 – 365, 1968. *Cited on pages 59, 74, and 214.*

[Thomason, 1990] P. F. Thomason. *Ductile Fracture of Metals*. Pergamon Press, Oxford, United Kingdom, 1990. ISBN 978-0080401782. *Cited on pages 57, 58, and 74.*

[Thuillier et al., 2012] S. Thuillier, E. Maire, and M. Brunet. Ductile damage in aluminium alloy thin sheets: Correlation between micro-tomography observations and mechanical modeling. *Materials Science and Engineering: A*, 558(0):217 – 225, 2012. *Cited on pages 167 and 170.*

[Timoshenko, 1953] S. Timoshenko. *History of strength of materials: with a brief account of the history of theory of elasticity and theory of structures*. McGraw-Hill, New York, 1953. *Cited on pages 235 and 236.*

[Tvergaard, 1981] V. Tvergaard. Influence of voids on shear band instabilities under plane strain conditions. *International Journal of Fracture*, 17:389–407, 1981. *Cited on pages 51 and 135.*

[Tvergaard, 1989] V. Tvergaard. Material failure by void growth to coalescence. volume 27 of *Advances in Applied Mechanics*, pages 83 – 151. Elsevier, 1989. *Cited on pages 52 and 135.*

[Tvergaard, 1998] V. Tvergaard. Interaction of very small voids with larger voids. *International Journal of Solids and Structures*, 35(30):3989 – 4000, 1998. *Cited on page 57.*

[Tvergaard and Needleman, 1984] V. Tvergaard and A. Needleman. Analysis of the cup-cone fracture in a round tensile bar. *Acta Metallurgica*, 32(1):157 – 169, 1984. *Cited on pages 51, 58, 59, 62, 107, 135, 136, 179, and 214.*

[Tvergaard and Niordson, 2004] V. Tvergaard and C. Niordson. Nonlocal plasticity effects on interaction of different size voids. *International Journal of Plasticity*, 20(1):107–120, 2004. *Cited on page 62.*

[Vachey, 2011] C. Vachey. Etude de la transformation à froid de la nuance X pour des données de la thèse "Modélisation de l'endommagement à froid pour des trajets de chargement complexes". *Technical note*, 2011. *Cited on pages 10, 16, 25, 100, and 195.*

[Vachey, 2011a] C. Vachey. Etude de la transformation à froid de la nuance X. 2011a. In French (confidential document). *Cited on pages 16 and 196.*

[Vanegas Marquez, 2011] E. Vanegas Marquez. *Numerical modeling of ODS steel tubes pilgering*. PhD thesis, Ecole nationale supérieure des Mines de Paris, 12 2011. *Cited on pages 35, 36, and 70.*

[Vega et al., 2009] G. Vega, A. Haddi, and A. Imad. Investigation of process parameters effect on the copper-wire drawing. *Materials and Design*, 30(8):3308 – 3312, 2009. *Cited on page 33.*

[Vegter and van den Boogaard, 2006] H. Vegter and A. H. van den Boogaard. A plane stress yield function for anisotropic sheet material by interpolation of biaxial stress states. *International Journal of Plasticity*, 22(3):557 – 580, 2006. *Cited on page 240.*

[Venkata Reddy et al., 1996] N. Venkata Reddy, P. M. Dixit, and G. K. Lal. Central Bursting and Optimal Die Profile for Axisymmetric Extrusion. *Journal of Manufacturing Science and Engineering*, 118(4): 579–584, 1996. *Cited on page 75.*

[Venkata Reddy et al., 2000] N. Venkata Reddy, P. M. Dixit, and G. K. Lal. Ductile fracture criteria and its prediction in axisymmetric drawing. *International Journal of Machine Tools and Manufacture*, 40(1):95 – 111, 2000. *Cited on pages 74 and 75.*

[Voce, 1955] E. Voce. A practical strain-hardening function. *Metallurgica*, 51:219–226, 1955. *Cited on pages 50, 91, and 172.*

[von Mises, 1913] R. von Mises. Mechanik der festen Körper im plastisch deformablen Zustand. *Göttin. Nachr. Math. Phys.*, 1:582–592, 1913. *Cited on page 236.*

[Weck, 2007] A. Weck. *The role of coalescence on ductile fracture*. PhD thesis, McMaster University, 3 2007. *Cited on pages 18, 58, and 59.*

[Weck and Wilkinson, 2008] A. Weck and D. S. Wilkinson. Experimental investigation of void coalescence in metallic sheets containing laser drilled holes. *Acta Materialia*, 56(8):1774 – 1784, 2008. *Cited on pages 11 and 58.*

[Weck et al., 2008] A. Weck, D. S. Wilkinson, E. Maire, and H. Toda. Visualization by X-ray tomography of void growth and coalescence leading to fracture in model materials. *Acta Materialia*, 56(12):2919 – 2928, 2008. *Cited on page 167.*

[Wen et al., 2005] J. Wen, Y. Huang, K. C. Hwang, C. Liu, and M. Li. The modified Gurson model accounting for the void size effect. *International Journal of Plasticity*, 21(2):381 – 395, 2005. *Cited on pages 51 and 135.*

[Wilkins et al., 1980] M. L Wilkins, R. D. Streit, and J. E. Reaugh. Cumulative-strain-damage model of ductile fracture: simulation and prediction of engineering fracture tests. *Technical report UCRL-53058, Lawrence Livermore National Laboratory*, 1980. *Cited on page 107.*

[Wistreich, 1955] J. G. Wistreich. Investigation of the Mechanics of Wire Drawing. *Proceedings of the Institution of Mechanical Engineers 1847-1996*, 169:654 – 678, 1955. *Cited on pages 10, 33, and 34.*

[Xie et al., 2011] H. B. Xie, Z. Y. Jiang, and W. Y. D. Yuen. Analysis of friction and surface roughness effects on edge crack evolution of thin strip during cold rolling. *Tribology International*, 44(9):971 – 979, 2011. *Cited on page 72.*

[Xue, 2007] L. Xue. Damage accumulation and fracture initiation in uncracked ductile solids subject to triaxial loading. *International Journal of Solids and Structures*, 44(16):5163 – 5181, 2007. *Cited on pages 108, 109, and 126.*

[Xue, 2007a] L. Xue. *Ductile fracture modeling - Theory, experimental investigation and numerical verification*. PhD thesis, Massachusetts Institute of Technology (MIT), 06 2007a. *Cited on pages 107 and 264.*

[Xue, 2008] L. Xue. Constitutive modeling of void shearing effect in ductile fracture of porous materials. *Engineering Fracture Mechanics*, 75(11):3343 – 3366, 2008. *Cited on pages 14, 52, 107, 135, 140, 141, and 211.*

[Xue and Wierzbicki, 2009] L. Xue and T. Wierzbicki. Numerical simulation of fracture mode transition in ductile plates. *International Journal of Solids and Structures*, 46(6):1423 – 1435, 2009. *Cited on page 53.*

[Xue et al., 2010] Z. Xue, M. G. Pontin, F. W. Zok, and J. W. Hutchinson. Calibration procedures for a computational model of ductile fracture. *Engineering Fracture Mechanics*, 77(3):492 – 509, 2010. *Cited on pages 98 and 99.*

[Yoshida et al., 2011] F. Yoshida, S. Tamura, T. Uemori, and H. Hamasaki. A User-friendly 3D Yield Function for Steel Sheets and Its Application. *AIP Conference Proceedings*, 1383(1):807–814, 2011. *Cited on page 240.*

[Yu, 2002] M.-H. Yu. Advances in strength theories for materials under complex stress state in the 20th Century. *Applied Mechanics Reviews*, 55(3):169–218, 2002. *Cited on pages 235 and 236.*

[Zhang, 1995b] Z. L. Zhang. Explicit consistent tangent moduli with a return mapping algorithm for pressure-dependent elastoplasticity models. *Computer Methods in Applied Mechanics and Engineering*, 121(1-4):29 – 44, 1995b. *Cited on pages 134, 142, 147, 149, and 164.*

[Zhang et al., 2000] Z. L. Zhang, C. Thaulow, and J. Ødegård. A complete Gurson model approach for ductile fracture. *Engineering Fracture Mechanics*, 67(2):155 – 168, 2000. *Cited on pages 57, 58, 60, and 135.*

[Zhou and Shiflet, 1992] D. S. Zhou and G. J. Shiflet. Ferrite: Cementite crystallography in pearlite. *Metallurgical Transactions A*, 23(4):1259–1269, 1992. *Cited on page 82.*

Appendix A

Some additional elements of material mechanics

A.1 Some notions of tensor analysis

In this section, some notations and fundamentals of vector and tensor calculus are introduced, which are extensively employed throughout this manuscript. For further information on tensor calculations, see [Itskov, 2000] or chapter 2 of [de Souza Neto et al., 2008].

Let $\mathcal{E}$ an n-dimensional Euclidean space and $\mathcal{U}$ its associative space of n-dimensional vectors. In the following definitions, $\underline{\boldsymbol{u}}$ and $\underline{\boldsymbol{v}}$ are two vectors in $\mathcal{U}$.

A.1.1 Second order tensor

A.1.1.1 Some definitions

- The second order tensors $\boldsymbol{T}$ maps each vector $\underline{\boldsymbol{u}}$ into another vector $\underline{\boldsymbol{v}}$: $\underline{\boldsymbol{v}} = \boldsymbol{T}\underline{\boldsymbol{u}}$.
- $\boldsymbol{T}$ is said to be symmetric when: $\boldsymbol{T}=\boldsymbol{T}^T$, where $\boldsymbol{T}^T$ is the transpose of $\boldsymbol{T}$.
- The symmetric part of tensor $\boldsymbol{T}$ is defined as: $sym(\boldsymbol{T}) = 1/2\left(\boldsymbol{T} + \boldsymbol{T}^T\right)$, whereas: $skew(\boldsymbol{T}) = 1/2\left(\boldsymbol{T} - \boldsymbol{T}^T\right)$ is its skew part, which satisfy: $\boldsymbol{T} = sym(\boldsymbol{T}) + skew(\boldsymbol{T})$.

A.1.1.2 Matrix representations in Cartesian coordinate frames

- The second-order tensor can be represented as:

$$\boldsymbol{T} = T_{ij}\underline{\boldsymbol{e_i}} \otimes \underline{\boldsymbol{e_j}} \tag{A.1}$$

  where $T_{ij} = \underline{\boldsymbol{e_i}}\boldsymbol{T}\underline{\boldsymbol{e_j}}$ and $[\underline{\boldsymbol{e}}] = \left[\underline{\boldsymbol{e_1}}, \underline{\boldsymbol{e_2}}, ..., \underline{\boldsymbol{e_n}}\right]$ is a set of n mutually *orthogonal vectors* (where $\underline{\boldsymbol{e_i}}.\underline{\boldsymbol{e_j}} = \delta_{ij}$), which defines an *orthonormal basis* of $\mathcal{U}$.

- The trace of a tensor is the sum of the diagonal terms of its Cartesian matrix representation:

$$tr(\boldsymbol{T}) = T_{ij}\delta_{ij} = T_{ii} \tag{A.2}$$

- The norm (or the Euclidean norm) of a tensor is defined as:

$$\|\boldsymbol{T}\| = \sqrt{\boldsymbol{T} : \boldsymbol{T}} \tag{A.3}$$

- A tensor $\boldsymbol{T}$ is said to be *orthogonal* when: $\boldsymbol{T}^T = \boldsymbol{T}^{-1}$, where $\boldsymbol{T}^{-1}$ is the inverse of $\boldsymbol{T}$. If the determinant of the orthogonal tensor $\boldsymbol{T}$ equals 1, it is called **a rotation**.

- **The characteristic equation**: the *eigenvalues* T_i of a tensor $\boldsymbol{T}$ are the solutions of the characteristic equation:

$$det(\boldsymbol{T} - \lambda \boldsymbol{I}) = -\lambda^3 + \lambda^2 I_1 - \lambda I_2 + I_3 = 0 \tag{A.4}$$

where I_1, I_2 and I_3 are the principal invariants of $\boldsymbol{T}$, which are defined as:

$$I_1(\boldsymbol{T}) = tr(\boldsymbol{T}) = T_{ii} \tag{A.5}$$

$$I_2(\boldsymbol{T}) = 1/2\left[tr(\boldsymbol{T})^2 - tr(\boldsymbol{T}^2)\right] \tag{A.6}$$

$$I_3(\boldsymbol{T}) = det(\boldsymbol{T}) \tag{A.7}$$

The spectral theorem . *Let $\boldsymbol{T}$ is a symmetric tensor, then $\boldsymbol{T}$ has the following representation called the spectral decomposition:*

$$\boldsymbol{T} = \sum_i^n T_i \underline{\boldsymbol{e_i}} \otimes \underline{\boldsymbol{e_i}} \tag{A.8}$$

where T_i is the eigenvalue or principal value, corresponding to the eigenvector e_i, which is the principal axis of $\boldsymbol{T}$. In the principal frame, $\boldsymbol{T}$ can be presented under the form of a diagonal matrix:

$$\mathbf{T} = \begin{pmatrix} T_1 & 0 & . & . & . & 0 \\ 0 & T_2 & . & . & . & 0 \\ . & . & . & . & . & . \\ . & . & . & . & . & . \\ . & . & . & . & . & . \\ 0 & 0 & . & . & . & T_n \end{pmatrix}$$

In this case ($\boldsymbol{T}$ is symmetric), the principal invariants can be expressed as:

$$I_1(\boldsymbol{T}) = T_1 + T_2 + T_3 \tag{A.9}$$

$$I_2(\boldsymbol{T}) = T_1T_2 + T_2T_3 + T_1T_3 \tag{A.10}$$

$$I_3(\boldsymbol{T}) = T_1T_2T_3 \tag{A.11}$$

Polar decomposition theorem . *Let $\boldsymbol{F}$ be a **positive definite tensors**[1]. There exist symmetric positive definite tensors $\boldsymbol{U}$, $\boldsymbol{V}$, and a rotation $\boldsymbol{R}$ that satisfy:*

$$\boldsymbol{F} = \boldsymbol{RU} = \boldsymbol{VR} \tag{A.12}$$

*The compositions $\boldsymbol{RU}$ and $\boldsymbol{VR}$ are unique, which are the **right and left polar decompositions** respectively. The two tensors $\boldsymbol{U}$ and $\boldsymbol{V}$ can be obtained through:*

$$\boldsymbol{U} = \sqrt{\boldsymbol{F}^T\boldsymbol{F}}, \text{ and } \quad \boldsymbol{V} = \sqrt{\boldsymbol{F}\boldsymbol{F}^T} \tag{A.13}$$

A.1.2 Fourth order tensor

Generally, a fourth oder tensor maps second-order tensors into second order tensors[2]: $\boldsymbol{u} = \underset{\sim}{\underset{\sim}{\boldsymbol{T}}}\boldsymbol{v}$, where $\boldsymbol{u}$ and $\boldsymbol{v}$ are two second-order tensors, $\underset{\sim}{\underset{\sim}{\boldsymbol{T}}}$ is a fourth-order tensor:

$$\underset{\sim}{\underset{\sim}{\boldsymbol{T}}} = T_{ijkl}\underline{\boldsymbol{e_i}} \otimes \underline{\boldsymbol{e_j}} \otimes \underline{\boldsymbol{e_k}} \otimes \underline{\boldsymbol{e_l}} \tag{A.14}$$

A.1.3 Isotropic tensors

An isotropic tensor is a tensor the components of which are independent of the basis (i.e. a second-order isotropic tensor satisfies: $\boldsymbol{T} = \boldsymbol{RTR}^T$, where $\boldsymbol{R}$ is a **rotation**).

[1] A tensor $\boldsymbol{F}$ is said to be positive definite when: $\underline{\boldsymbol{Z}}\boldsymbol{F}\underline{\boldsymbol{Z}}^T > 0$, with $\underline{\boldsymbol{Z}} \in \mathfrak{U}$.

[2] The fourth order tensor can also map a vector into third-order tensor or a third-order tensor into a vector, which is out of the scope of the present study.

A.2 The strain and stress measures

A.2.1 The gradient of deformation

Let $\mathcal{A}$ be a time-dependent field. If $\mathcal{A}$ is expressed as a function of material point $\underline{\boldsymbol{p}}$, $\mathcal{A}$ is said to be a *material field*. If $\mathcal{A}$ is expressed as a function of $\underline{\boldsymbol{x}} = \vec{x}(t) = \varphi(\underline{\boldsymbol{p}},t)$, then $\mathcal{A}$ is a said to be a *spatial field*.

The deformation gradient of the motion φ is a second-order positive definite tensor $\boldsymbol{F}$:

$$\boldsymbol{F}(\underline{\boldsymbol{p}},t) = \nabla_p \varphi(\underline{\boldsymbol{p}},t) = \frac{\partial \underline{\boldsymbol{x}}}{\partial \underline{\boldsymbol{p}}} = \boldsymbol{I} + \nabla_p \underline{\boldsymbol{u}} \tag{A.15}$$

where ∇_p stands for the material gradient, $\boldsymbol{I}$ is the identity second-order tensor. The deformation gradient is a linear operator, which relates the material fiber $d\underline{\boldsymbol{p}}$ in the reference configuration with their counterpart $d\underline{\boldsymbol{x}}$ in deformed configuration. A deformation of the deformable object $\mathcal{B}$ (see section 1.2.1) with uniform deformation gradient is called a *homogeneous deformation*. Moreover, since $\boldsymbol{F}$ is positive definite, it can have the polar decomposition as in Eq. A.12:

$$\boldsymbol{F} = \boldsymbol{R}\boldsymbol{U} = \boldsymbol{V}\boldsymbol{R} \tag{A.16}$$

where $\boldsymbol{U}$ and $\boldsymbol{V}$ are the right and left *stretch tensors* respectively. The polar decomposition theorem states that the deformation of a material element can be decomposed into a *pure stretch* and a *pure rotation*. Note that $det(\boldsymbol{F}) = det(\boldsymbol{U}) = det(\boldsymbol{V}) = J$. The stretch tensors can be calculated from the *right and left Cauchy-Green strain tensors* $\boldsymbol{C}$ and $\boldsymbol{B}$:

$$\boldsymbol{C} = \boldsymbol{U}^2 = \boldsymbol{F}^T\boldsymbol{F}, \text{ and } \quad \boldsymbol{B} = \boldsymbol{V}^2 = \boldsymbol{F}\boldsymbol{F}^T \tag{A.17}$$

A stretch: a deformation such that there **exist** 3 material vectors, which will change in length, but not in orientation. The deformation gradient is thus symmetric and positive definite. Since the deformation gradient in this case is symmetric, the stretch is diagonal in its principal basis, with the 3 principal stretches that equal to the ratio of deformed and undeformed lengths of the three non-rotating material fibers.

A rotation A deformation that material vectors are permitted to change the orientation but do not change their length. The associated deformation gradient is orthogonal.

A.2.2 The strain measures

The deformation gradient, which contains the information of both material rotation (unstrained) and material stretching (strained), is the best measure of *deformation*. However, to quantify the *straining* (change of the distance between material particles), the strain measure need to be defined.

A.2.2.1 The Lagrangian strain measure

The family of Lagrangian strain (reference strain) tensors, which are the strain measures in the Lagrangian frame, is defined as:

$$\boldsymbol{E}^{(m)} = \begin{cases} 1/m(\boldsymbol{U}^m - \boldsymbol{I}) & ,if \quad m \neq 0 \\ ln(\boldsymbol{U}) & ,if \quad m = 0 \end{cases} \tag{A.18}$$

The Green-Lagrange strain tensor $\boldsymbol{L} = \boldsymbol{E}^{(2)}$ is a member of this family:

$$\boldsymbol{L} = \boldsymbol{E}^{(2)} = 1/2(\boldsymbol{U}^2 - \boldsymbol{I}) = 1/2(\boldsymbol{C} - \boldsymbol{I}) = 1/2(\boldsymbol{F}^T\boldsymbol{F} - \boldsymbol{I}) = 1/2\left[\nabla_p \underline{\boldsymbol{u}} + (\nabla_p \underline{\boldsymbol{u}})^T + (\nabla_p \underline{\boldsymbol{u}})^T \nabla_p \underline{\boldsymbol{u}}\right] \tag{A.19}$$

The Green-Lagrange strain is a strain that results from the pure reference (right) stretch prior to the rotation part of the deformation. If we superimpose even more rotation (material rotation), the Green-Lagrange strain remains unchanged. This measure is an objective measure, which satisfies the principle of material frame indifference.

A.2.2.2 The Eulerian strain measure

The Eulerian counterpart of the Lagrangian family (spatial strain) is defined as:

$$\boldsymbol{\epsilon}^{(m)} = \begin{cases} 1/m(\boldsymbol{V}^m - \boldsymbol{I}) & ,if \quad m \neq 0 \\ ln(\boldsymbol{V}) & ,if \quad m = 0 \end{cases} \tag{A.20}$$

where $\boldsymbol{V}$ is the left stretch tensor. With $m = 2$, the formula for the Eulerian counterpart of Green-Lagrange tensor (the **Signorini strain**) can be obtained:

$$\boldsymbol{\epsilon}^{(2)} = 1/2(\boldsymbol{V}^2 - \boldsymbol{I}) = 1/2(\boldsymbol{B} - \boldsymbol{I}) = 1/2(\boldsymbol{F}\boldsymbol{F}^T - \boldsymbol{I}) = 1/2\left[\nabla_p \underline{\boldsymbol{u}} + (\nabla_p \underline{\boldsymbol{u}})^T + \nabla_p \underline{\boldsymbol{u}}(\nabla_p \underline{\boldsymbol{u}})^T\right] \tag{A.21}$$

The Lagrangian strain tensor and its Eulerian counterpart are related through:

$$\boldsymbol{\epsilon}^{(m)} = \boldsymbol{R}\boldsymbol{E}^{(m)}\boldsymbol{R}^T \tag{A.22}$$

A.2.2.3 The infinitesimal strain tensor

If the gradient of displacement is small, the second-order term $\nabla_p \underline{\boldsymbol{u}}(\nabla_p \underline{\boldsymbol{u}})^T$ can be neglected. The Lagrangian tensors (Eq. A.18) and its Eulerian counterpart (Eq. A.20) are equal. Therefore, the Green-Lagrange tensor and its counterpart are defined as:

$$\boldsymbol{E}^{(2)} \approx \boldsymbol{\epsilon}^{(2)} \approx 1/2\left[\nabla_p \underline{\boldsymbol{u}} + (\nabla_p \underline{\boldsymbol{u}})^T\right] = \boldsymbol{\epsilon} \tag{A.23}$$

where $\boldsymbol{\epsilon}$ designates the infinitesimal strain tensor, also called *Cauchy's strain tensor*, which is employed to measure strains under small deformations. Moreover, for any m, the following expression has been proved:

$$\boldsymbol{E}^{(m)} \approx \boldsymbol{\epsilon}^{(m)} \approx \boldsymbol{\epsilon} \tag{A.24}$$

Throughout the present manuscript, the term strain tensor refers to the Cauchy strain tensor, unless otherwise indicated.

A.2.3 The stress measures

The concept of *stress* is used to describe mathematically the surface forces. The surface forces might be the boundary forces (with exterior) or the internal interaction forces (between different parts of a body). Before reviewing the different measures of stress, let us recall Cauchy's axiom.

A.2.3.1 The Cauchy stress tensor

Cauchy's Axiom. *Let $\mathcal{S}$ be an oriented surface of a body $\mathcal{B}$ with a normal vector $\underline{\boldsymbol{n}}$ at point x. The surface force at x depends on $\mathcal{S}$ only through its normal $\underline{\boldsymbol{n}}$.*

This axiom means that the forces transmitted across any surfaces with normal $\underline{\boldsymbol{n}}$ at x [3] are all identical. This surface force is called the *Cauchy stress vector* and is denoted as: $\underline{\boldsymbol{t}}(\boldsymbol{n})$ [4]. Furthermore, the dependence of $\underline{\boldsymbol{t}}(\boldsymbol{n})$ upon $\underline{\boldsymbol{n}}$ is linear (which is the consequence of the linear and angular momentum balances). Thus, there exists a second-order tensor $\boldsymbol{\sigma}(\boldsymbol{x})$, that maps $\underline{\boldsymbol{n}}$ to $\underline{\boldsymbol{t}(\boldsymbol{n})}$ (see Appendix A.1.1):

$$\underline{\boldsymbol{t}}(\boldsymbol{n},\boldsymbol{x}) = \boldsymbol{\sigma}(\boldsymbol{x})\underline{\boldsymbol{n}} \tag{A.25}$$

where $\boldsymbol{\sigma}(\boldsymbol{x})$ is the *Cauchy stress tensor* (or simply *stress tensor*). Moreover, from the angular momentum balance, $\boldsymbol{\sigma}(\boldsymbol{x})$ is demonstrated to be symmetric (which allows the application of spectral theorem - Eq. A.8 and the calculus of principal invariants are defined as in Eqs. A.9, A.10, A.11). **Throughout this manuscript, the term stress tensor refers to the Cauchy stress tensor, unless otherwise indicated.**

[3] The point x has the position vector $\underline{\boldsymbol{x}}$.
[4] $\underline{\boldsymbol{t}}(\boldsymbol{n})$ depends on $\underline{\boldsymbol{n}}$, x, and time (t).

A.2.3.2 The first and second Piolar-Kirchoff stress tensors

In Eq. A.25, $\underline{\boldsymbol{t}}(\boldsymbol{n},\boldsymbol{x})$ represents the force per unit *deformed* area (i.e. in the deformed configuration). We now define $\underline{\boldsymbol{t}}'$ as the counterpart of $\underline{\boldsymbol{t}}(\boldsymbol{n},\boldsymbol{x})$, which is the force per unit *reference* area:

$$\underline{\boldsymbol{t}}' = \frac{ds}{ds_0}\underline{\boldsymbol{t}}(\boldsymbol{n},\boldsymbol{x}) = \frac{ds}{ds_0}\boldsymbol{\sigma}(\boldsymbol{x})\underline{\boldsymbol{n}} \tag{A.26}$$

where ds is the infinitesimal element of a surface normal to $\underline{\boldsymbol{n}}$ in the deformed configuration and ds_0 is its reference counterpart. Let $\underline{\boldsymbol{m}}$ be the unit normal to the surface with infinitesimal element ds_0 in the reference configuration. The *first Piola-Kirchoff stress tensor* $\boldsymbol{P}$ relates $\underline{\boldsymbol{t}}'$ and m by:

$$\underline{\boldsymbol{t}}' = \boldsymbol{P}\underline{\boldsymbol{m}} \tag{A.27}$$

By some mathematical developments, the relation between $\boldsymbol{\sigma}$ and $\boldsymbol{P}$ can be obtained:

$$\boldsymbol{P} = J\boldsymbol{\sigma}\boldsymbol{F}^{-T} \tag{A.28}$$

where $\boldsymbol{F}^{-T}$ is the inverse of the transpose of deformation gradient ($\boldsymbol{F}$), $J = det(\boldsymbol{F})$ (when $J = 1$, the deformation is isochoric or volume-preserving). Note that $\boldsymbol{P}$ is generally not symmetric. As the Cauchy stress tensor is symmetric, its counterpart in Lagrangian approach is also expected to be symmetric. If one wants to use a symmetric tensor, the following definition may be useful:

$$\boldsymbol{S} = J\boldsymbol{F}^{-1}\boldsymbol{\sigma}\boldsymbol{F}^{-T} \tag{A.29}$$

where $\boldsymbol{S}$ is the *second Piolar-Kirchoff stress tensor*, which is a symmetric tensor.

A.2.3.3 Other stress measures

- The *Kirchoff stress tensor* $\boldsymbol{\tau}$, which is defined by: $\boldsymbol{\tau} = J\boldsymbol{\sigma}$.
- The *Biot stress* (or *Jaumann stress*) is a symmetric tensor (the symmetric part of $\boldsymbol{P}^T\boldsymbol{R}$, $\boldsymbol{R}$ is the rotation tensor) and does not have any physical interpretation (but it is the energy conjugate to the right stretch tensor $\boldsymbol{U}$).

A.3 Yield criterion under a complex stress state

The yield criteria as well as the failure criteria[5] are in the same framework of *strength theory*, which deals with the yield and failure of materials under a complex stress state ([Timoshenko, 1953, Yu, 2002]). In the present study, we concentrate on the yield and failure criteria for ductile metals. For other types of materials, interested readers can refer to [Yu, 2002] for a review. In this section, several usual *isotropic* yield criteria, which have been widely used in engineering applications, are revisited. Then the representations of these criteria in the stress space as well as some discussions on their implementations are given.

A.3.1 Criteria without hydrostatic pressure influence (incompressible plasticity)

The Tresca criterion - The maximum shear stress criterion The Tresca yield criterion assumes that yielding occurs when the maximum shear stress reaches a critical value. The maximum shear stress can be expressed through the principal stresses ($\sigma_1 \geq \sigma_2 \geq \sigma_3$) as:

$$\tau_{max} = \frac{1}{2}(\sigma_1 - \sigma_3) \tag{A.30}$$

The yield function can be written as:

$$\phi(\boldsymbol{\sigma}, \alpha) = \frac{1}{2}(\sigma_1 - \sigma_3) - \tau_y(\alpha) \tag{A.31}$$

[5] Multiaxial fatigue criteria, multiaxial creep conditions are not considered in the present study.

where τ_y is the *shear* yield stress, which is assumed to depend on a hardening variable. With a similar procedure for a *pure shear* stress state, the yield criterion for the *uniaxial* stress state can be written as:

$$\phi(\boldsymbol{\sigma}, \alpha) = (\sigma_1 - \sigma_3) - \sigma_y(\alpha) \tag{A.32}$$

where σ_y is the *uniaxial* yield stress ($\sigma_y = 2\tau_y$ according to Tresca's criterion). This criterion can also be written in terms of stress invariants

$$\phi(\boldsymbol{\sigma}, \alpha) = 2\sqrt{J_2}cos(\theta_L) - \sigma_y \tag{A.33}$$

where J_2 is the second invariant of the deviatoric stress tensor; θ_L is the Lode angle; σ_y is the uniaxial yield stress.

The von Mises criterion - The maximum distorsion energy criterion The von Mises criterion ([von Mises, 1913]) states that yielding occurs when the second invariant of deviatoric stress tensor J_2 reaches a critical value.

$$J_2 = R(\alpha) \tag{A.34}$$

Where $R(\alpha)$ represents a function of hardening internal variable α. Von Mises initially proposed this model because of its simplicity. Hencky ([Hencky, 1924]) showed that the condition in Eq. A.34 is equivalent to the condition of maximum distorsion energy[6], i.e. the yielding occurs when the distorsion energy reaches a critical value. This result gave a physical meaning to the von Mises criterion. Another physical interpretation of this criterion might be understood as the maximum octahedral shear stress criterion ([Nadai, 1950]). This is the shear stress on the octahedral plane[7], the plane that makes equal angles with the principal axes: $\tau_{oct} = \sqrt{2/3J_2}$. For a uniaxial stress state (e.g. $\sigma_{xx} = \sigma$, other components are zero), the J_2 invariant can be written as:

$$J_2 = \frac{1}{3}\sigma^2 \tag{A.35}$$

The von Mises yield function can therefore be written as:

$$\phi(\boldsymbol{\sigma}, \alpha) = q(\boldsymbol{\sigma}) - \sigma_y(\alpha) \tag{A.36}$$

where σ_y is the uniaxial yield stress, which can account for hardening of material; $q(\boldsymbol{\sigma}) = \sqrt{3J_2(\boldsymbol{\sigma})}$ is the so-called von Mises equivalent stress. With the same procedure, for a pure shear stress state, the von Mises criterion writes:

$$\phi(\boldsymbol{\sigma}, \alpha) = \sqrt{J_2(\boldsymbol{\sigma})} - \tau_y(\alpha) \tag{A.37}$$

where $\tau_y(\alpha)$ is the shear yield stress, which can be related with the uniaxial yield stress $\sigma_y(\alpha)$:

$$\sigma_y(\alpha) = \sqrt{3}\tau_y(\alpha) \tag{A.38}$$

A.3.2 Criteria involving hydrostatic pressure influence (compressible plasticity)

Mohr-Coulomb criterion The Mohr-Coulomb (M-C) *yield* criterion and the M-C *failure* criterion are also known as the M-C strength theory (Coulomb (1736-1806), Mohr (1835-1918)), which is one of the early works on strength theory after Leonardo da Vinci (1452-1519) and Galileo Galilei (1564-1642) in the 16-20^{th} ([Timoshenko, 1953]). Coulomb [Coulomb, 1776] stated that fracture is due to sliding along a given plane, when the shear force on this plane is larger than the cohesive resistance in shear of this plane. After this first result, Coulomb enhanced this early model to get a better agreement with experimental results, by accounting for the friction caused by the normal stress on this plane. This can be considered as the first version of the M-C *failure* criterion ([Yu, 2002]).

Mohr ([Mohr and Beyer, 1928]) then made a more complete study on material strength, in which the author considered failure in broad senses: it can be yielding or fracture of material. Using the famous

[6] Distorsion energy: $\frac{1}{2G}\,\boldsymbol{s} : \boldsymbol{s}$.

[7] The octahedral plane is the plane with the normal vector $\vec{n}_{oct} = \{1,1,1\}$ in the principal stress space. The stress acting on this plane can be resolved into a normal octahedral stress $\sigma_{oct} = -p$ and a shear octahedral stress $\tau_{oct} = \sqrt{2}\sigma_{eq}/3$.

Mohr's circle (the principal circles), the author proposed a criterion, which used the maximum and minimum principal stresses (an extension of Tresca criterion). Mohr's criterion can be tracked back to the work of Coulomb, and therefore this criterion is referred to as the M-C strength theory. In this part, the M-C theory of yielding is presented. The failure criterion is discussed in 3.1.2.2.

The M-C yield criterion states that the yielding occurs when the combination of shear stress τ and normal stress σ_n in a plane reaches a critical value:

$$(\tau + tan(\varphi)\sigma_n)_y = c_2 \tag{A.39}$$

where φ is the angle of internal friction (or frictional angle); c_2 is the "shear resistance" or cohesion; the subscript y denotes yielding. Geometrical signification of this criterion is presented in Fig. A.1 with the use of Mohr's circles. Yielding occurs when the largest Mohr's circle (i.e. the circle corresponding to the maximum and minimum principal stresses) is tangent with the critical line define by function A.39 in the space (σ_n, τ).

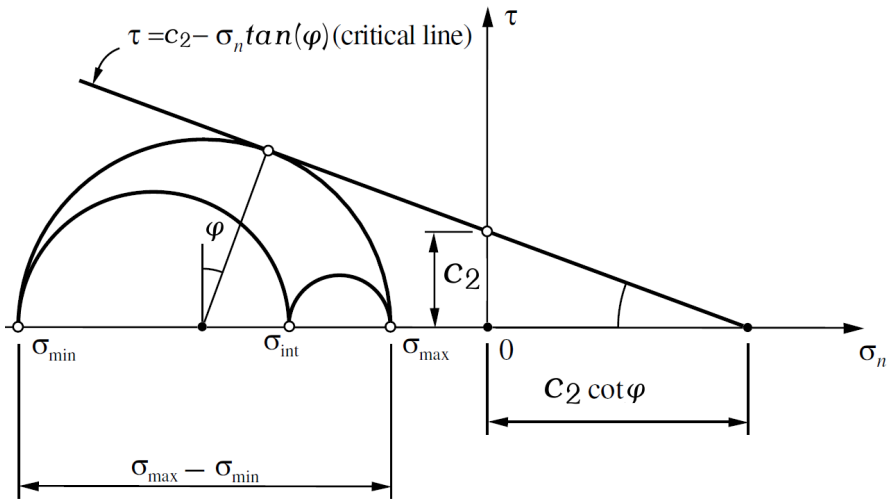

Fig. A.1: *Representation of the M-C yield criterion in Mohr's plane. The elastic domain contains all the stress states for which all three Mohr's circles are below the critical line, defined by function A.39 (figure adapted from [de Souza Neto et al., 2008]).*

From Fig. A.1 and after some straightforward analytical manipulations, the yield function of M-C criterion can be written in terms of the principal stresses:

$$\phi(\boldsymbol{\sigma}, c_2) = (\sigma_{max} - \sigma_{min}) + (\sigma_{max} + \sigma_{min})sin(\varphi) - 2c_2cos(\varphi) \tag{A.40}$$

where σ_{max} and σ_{min} are the maximum and minimum principal stresses respectively ($\sigma_{max} = \sigma_1$, $\sigma_{min} = \sigma_3$, if $\sigma_1 \geq \sigma_2 \geq \sigma_3$). In terms of stress invariants, this criterion can be written as:

$$(cos\theta_L - \frac{1}{\sqrt{3}}sin\theta_L sin\varphi)\sqrt{J_2} - I_1 sin\varphi - c_2 cos\varphi \tag{A.41}$$

where θ_L is the Lode angle; J_2 is the second invariant of deviatoric stress tensor; I_1 is the first invariant of Cauchy stress tensor. The Mohr-Coulomb yield surface is a non-smooth surface, for which, numerical implementation is not straightforward. This model has been widely used in rock and soil mechanics (e.g. [Palchik, 2006]) as well as in the brittle materials community (e.g. [Lund and Schuh, 2004]).

Drucker-Prager criterion The Drucker-Prager criterion ([Drucker and Prager, 1952]) may be considered as a modification of von Mises criterion by introducing pressure-sensitivity, or a smooth approximation of the M-C criterion. The condition of onset of plastic yielding following the D-P criterion writes:

$$\sqrt{J_2} + p\alpha_{DP} = c_{DP} \tag{A.42}$$

where α_{DP} and c_{DP} are two material parameters. If $\alpha_{DP} = 0$, this criterion becomes the von Mises criterion. In order to define a smooth approximation of M-C yield surface (the reason of the necessity of such an approximation is discussed in A.3.3), the yield function of the D-P criterion can be written from Eq. A.42:

$$\phi(\boldsymbol{\sigma}, c_2) = \sqrt{J_2} + p\alpha_{DP} - \xi c_2 \tag{A.43}$$

where c_2 is the cohesion defined in the M-C criterion; α_{DP} and ξ are two adjustable parameters, which depend on the stress state of the expected approximation of M-C criterion. For example, if one wants to approximate the M-C non-smooth yield surface by the D-P smooth surface for the uniaxial tensile stress state and the biaxial compression stress state, the choice of α_{DP} and ξ are the following:

$$\alpha_{DP} = \frac{6sin\varphi}{\sqrt{3}(3 + sin\varphi)}, \quad \xi = \frac{6cos\varphi}{\sqrt{3}(3 + sin\varphi)} \tag{A.44}$$

A.3.3 Discussions

Representation of yield functions in principal stress space The representation of the V-M and the Tresca yield surfaces is given in Fig. A.2, which shows that the two criteria can coincide in uniaxial tensile test state (Fig. A.2a) or in pure shear stress state (Fig. A.2b - see Eq. A.32 and Eq. A.36)[8]. Moreover, one can observe that the V-M yield surface is smooth whereas the Tresca yield surface has 6 corners, at which the normal direction to the surface is not unique.

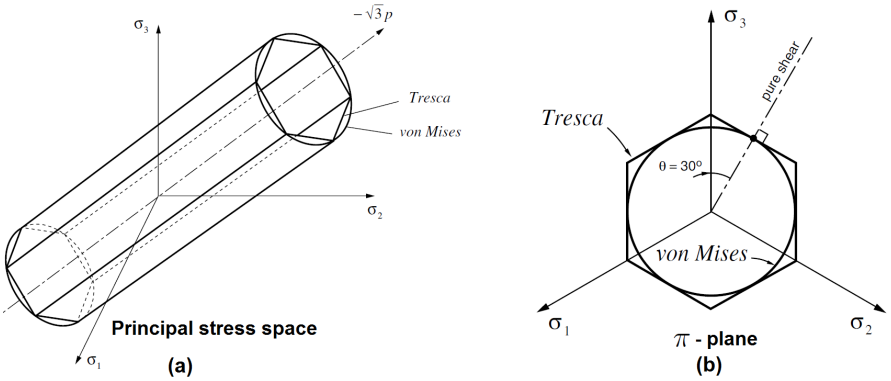

Fig. A.2: *Representation of von Mises and Tresca yield surfaces in the principal stress space (a) and on the π-plane (b) (figure adapted from [de Souza Neto et al., 2008, Chen and Mizuno, 1990]).*

For the pressure-dependent yield criteria (M-C and D-P), their yield surfaces are presented in Fig. A.3a (principal stress space) and Fig. A.3b (π plane).

As one can observe in Fig. A.3a, the M-C surface is non-smooth whereas the D-P surface is smooth. The latter can be considered as a smooth approximation of the former. For example, for the uniaxial tension and the biaxial compression stress states, the D-P surface coincides with the M-C surface by choosing appropriate values of the two parameters α_{DP} and ξ as in Eq. A.44. The D-P surface in this case is the *inner-edges* in Fig. A.3b. Similarly, for the stress states corresponding to the uniaxial compression and biaxial tension, the conditions for which the D-P yield surface coincides with the M-C's are the following:

$$\alpha_{DP} = \frac{6sin\varphi}{\sqrt{3}(3 - sin\varphi)}, \quad \xi = \frac{6cos\varphi}{\sqrt{3}(3 - sin\varphi)} \tag{A.45}$$

The D-P yield surface in this case is presented in Fig. A.3b by the outer edges. Moreover, from Fig. A.3a, there are two points A and A', which correspond to the resistance limits of the material to the hydrostatic tension

[8]Drucker [Drucker, 1949] proposed an intermediate yield surface between von Mises's and Tresca's, which involved the second and third deviatoric stress invariants.

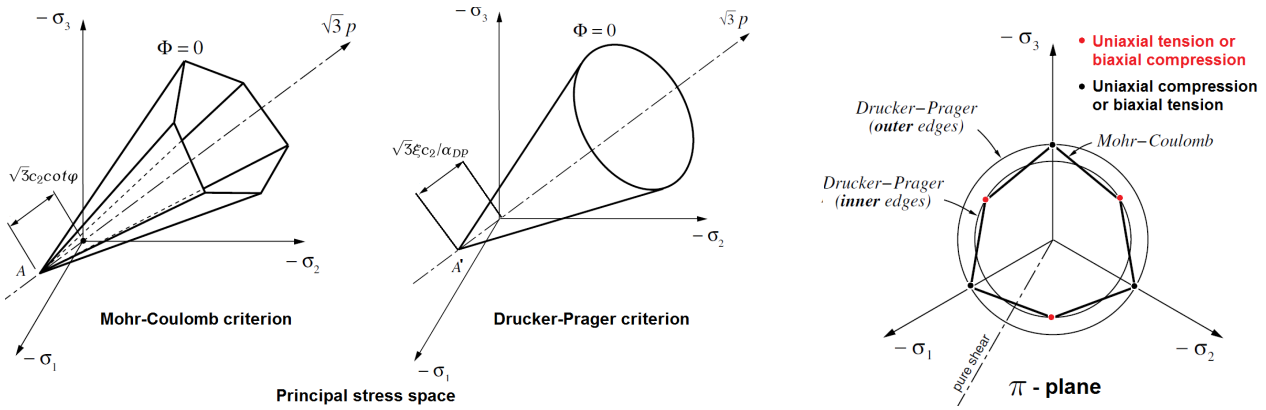

(a) *The M-C and D-P yield surfaces in the principal stress space, showing the apex of the pyramid (point A on the M-C yield surface and the apex of the cone (point A' on the D-P yield surface). These two point represent the resistance limits of the material to the tensile pressures for the two criteria respectively.*

(b) *The M-C yield surface in the π-plane and the two particular cases of the D-P yield surfaces, in which the D-P yield surface coincide with that of M-C.*

Fig. A.3: *Representation of the M-C and the D-P yield surfaces in the principal stress space (a) and on the π-plane (b) (figure adapted from [de Souza Neto et al., 2008]).*

for the two criteria M-C and D-P respectively. The stress state of these two points is the pure hydrostatic tension, with the pressures defined as:

$$p(A) = c_2 cot\varphi \text{ (M-C criterion)}; \qquad p(A') = c_{DP}/\alpha_{DP} = \xi c_2/\alpha_{DP} \text{ (D-P criterion)} \tag{A.46}$$

Limited strength under hydrostatic tension is a typical characteristics of concrete, rock ans soils, to which the M-C and D-P criteria have been widely used (see [de Souza Neto et al., 2008] for more details).

Use of associative or non-associative plasticity - Normality principle As stated above, if the yield function is chosen as the plastic flow potential, then the plasticity model is called *associative* plasticity. In the associative plasticity model, since the plastic strain rate is obtained from the plastic flow potential (Eq. 1.91), the plastic flow direction is thus normal to the yield surface. This is the so-called *normality principle*. Several references in the literature (e.g. [Simo and Hughes, 1998, de Souza Neto et al., 2008]) showed that the associative law and normality rule are the consequence of the maximum plastic dissipation principle, which states: "Among all admissible pairs of stress state $\boldsymbol{\sigma}$ and hardening force $\underline{\boldsymbol{A}}$, the actual state maximizes the plastic dissipation function: $\boldsymbol{\sigma} : \dot{\boldsymbol{\epsilon}}^p - \underline{\boldsymbol{A}} * \underline{\boldsymbol{\alpha}}$ for a given strain rate and rate of hardening internal variables"[9]. This principle has been shown to hold in crystal plasticity and particularly for metals. For other materials (such as granular material or rocks and soils), its validity is questionable and the use of a non-associative law may be essential. Throughout the present dissertation, only associative laws are considered. Interested readers can refer to [Renon, 2002] for a study of soils mechanics with Forge®, the FEM software used in the present study.

Prandtl-Reuss flow rule If one uses the von Mises yield function as the plastic flow potential, then the so-called Prandtl-Reuss (P-R) flow rule is obtained. The normal vector of yield surface at the current stress state, which is also the plastic flow direction, is defined as (note that this vector is not a unit vector in this context):

$$\boldsymbol{N}_{PR} = \frac{\partial \phi_{VM}}{\partial \boldsymbol{\sigma}} = \frac{\partial \sqrt{3J_2}}{\partial \boldsymbol{\sigma}} = \sqrt{\frac{3}{2}} \frac{\boldsymbol{s}}{\|\boldsymbol{s}\|} \tag{A.47}$$

where ϕ_{VM} denotes the von Mises yield function; $\boldsymbol{s}$ is the deviatoric stress tensor. The flow rule is defined as:

$$d\boldsymbol{\epsilon}^{\boldsymbol{p}} = d\lambda \boldsymbol{N}_{PR} = d\lambda \sqrt{\frac{3}{2}} \frac{\boldsymbol{s}}{\|\boldsymbol{s}\|} \tag{A.48}$$

The *P-R flow rule* is often used with the *von Mises* yield criterion to define the *von Mises associative plasticity model* or shortly, the von Mises plasticity model. The FE software Forge2009®, which is used throughout the present study, uses the P-R flow rule to solve the local integration of isotropic incompressible plasticity model.

[9] the $*$ symbol denotes the appropriate product of $\underline{\boldsymbol{A}}$ and $\underline{\boldsymbol{\alpha}}$.

Numerical implementation aspect The integration algorithm for elastoplastic constitutive equations can be done with the return mapping algorithm, or the elastic prediction - plastic correction algorithm ([Simo and Taylor, 1985, Simo and Taylor, 1986]). Details about this method are given in section 4.2.2, where this process is used for the local integration of the GTN model. For the von Mises smooth yield surface and pressure-insensitive yield criteria, the procedure is quite simple. However, for the Tresca and M-C yield criteria, the integration is not straightforward due to the presence of 6 corners (at which the yield functions are non-differentiable if the associative law is used). For the Tresca criterion, the multisurface representation can be used (i.e. using 6 functions to represent 6 surfaces of the Tresca's yield surface). On each surface, the normal direction is unique and so does the plastic flow direction. The plastic flow for each surface is defined by a couple of plastic multiplier and normal direction $(d\lambda_i, \boldsymbol{N}_i)$, for $i = 1...6$. The difficulty lies on the normal direction at corners, which is not unique. To overcome this problem, at each corner, the plastic flow is defined by a linear combination of the plastic flows of the two adjacent surfaces (e.g. $d\boldsymbol{\epsilon^p}_{12} = d\lambda_1 \boldsymbol{N}_1 + d\lambda_2 \boldsymbol{N}_2$, where $d\boldsymbol{\epsilon^p}_{12}$ is the plastic flow at the corner, which is the intersection of the two surfaces 1 and 2). For the integration of the pressure-sensitive yield criteria (M-C, D-P), care must be taken when treating the apex (the two point A and A' in Fig. A.3a). Associative flow rules can be employed similarly to the von Mises criterion (for D-P criterion) and Tresca (for M-C criterion). However, in [de Souza Neto et al., 2008], the authors showed that using the associative rule for these two criteria (M-C and D-P) might overestimate the dilatancy (or the volumetric strain rate, since these models account for the influence of the hydrostatic pressure). Using the non-associative law can avoid this problem ([de Souza Neto et al., 2008]) but can lead to a non-symmetric tangent matrix. The computation cost is then higher. Furthermore, as shown in Eq. A.33 and Eq. A.41, the Tresca and the M-C yield functions can be written as functions of invariants. Using these forms of yield function for the integration procedure must be limited due to the high degree of non-linearity induced by the trigonometric function involved in the definition of Lode angle θ_L. The multi-surface representation is less complex in terms of numerical implementation.

A.3.4 Anisotropic yield functions

In the present study, isotropic plasticity is used. All the above-mentioned yielding criteria can be written as functions of the principal stresses, which are thus the isotropic yield functions. The anisotropic yield functions employ all the component of stress tensor to construct the formulation, which cannot be reduced to principal stresses representations. One of the most popular anisotropic plasticity models is the Hill48 quadratic model ([Hill, 1948]). This model is nowadays still popular in industrial application due to rather easy parameter identification and the yield function being a convex function. The identification is often based on either the Landford coefficients (R-value) in different orientations or different directional yield stresses since this model is too simple to be capable to adjust in the same time these two measures. For this fact, 2 sets of parameters can be obtained and the validity of the identified parameters from each approach for the other approach is not guaranteed. Later developments are based on the use of different forms for the yield function: polynomial functions (as in [Gotoh, 1977] for 2D version, [Hu, 2007] for 3D version), linear transformation of stress tensor ([Barlat et al., 2007]), Bezier interpolation ([Vegter and van den Boogaard, 2006]). Recently, [Yoshida et al., 2011] proposed a user-friendly yield function, which has been shown to be valid to describe the yielding for various types of steel sheets. For a detailed review of plastic anisotropy, interested readers can refer to [Banabic, 2010].

A.4 Continuum Damage Mechanics

In this section, some important points of Continuum Damage Mechanics are reviewed. Most of the content of this part is summarized from chapter 1 of the book: "Engineering Damage Mechanics" ([Lemaitre and Desmorat, 2005]). First of all, some basic definitions are reminded below.

Concept of continuous media In reality, the *continuum* fields associated with the body are *discrete* (e.g. in real life, forces, the continuum mathematical representation of which is the stress tensor, are transferred by the interactions between atoms, which are discrete quantities). The mechanics of continuous media give birth to the Representative Volume Element (RVE)[10], which is the smallest volume of material for which the continuum representation makes sense. On this RVE, all properties are represented by *homogenized* variables (such as stress and strain measures). The continuum mechanics studies the physics of continuous materials.

Strain equivalence principle The strain associated with a damage state under the applied stress is equivalent to the strain associated with the undamaged state under the effective stress.

Effective stress : describes the impact of damage on the macro-behavior of material. The effective stress tensor is the one that should be applied to an undamaged material, in order to get the same strain tensor as the one obtained from the damaged material under the actual stress tensor.

A.4.1 Thermodynamic framework of damage

The thermodynamics of irreversible processes allows modeling materials behavior throughout 3 steps:

1. State variables definitions: observable or internal variables, which define the present state of the corresponding physical mechanism (deformation, degradation of materials).
2. State potential and associated variable (e.g. the variables which are associated with the internal state variables) definitions: from this potential, one can derive the state laws.
3. Dissipation potential definition: one can derive from this potential, the evolution laws of state variables (which are associated with the dissipative mechanisms).

i) State variables Table A.1 represents the state and associated variables.

Mechanisms	Type	State variables		Associated variables
		Observable	Internal	
Thermoelasticity	Tensor	ϵ_{ij}		σ_{ij}
Entropy	Scalar	T		s
Plasticity	Tensor		$\epsilon^{\mathrm{p}}_{ij}$	$-\sigma_{ij}$
Isotropic hardening	Scalar		r	R
Kinematic hardening	Tensor		α_{ij}	X_{ij}
Damage	Scalar (isotropic)		D	$-Y$
	Tensor (anisotropic)		D_{ij}	$-Y_{ij}$

Table A.1: *State and associated variables [Lemaitre and Desmorat, 2005].*

ii) State potential and state laws The Helmholtz specific energy is taken as the state potential of material but it is more convenient to consider the potential as the Gibbs specific free enthalpy (ψ^*) deduced from Helmholtz free energy by a partial Legendre transformation ([Lemaitre and Desmorat, 2005]):

$$\psi^* = \psi^*_e + \frac{1}{\rho}\sigma_{ij}\epsilon^p_{ij} - \psi_p - \psi_T \tag{A.49}$$

where:

- ψ^*_e: the elastic contribution which is affected by damage to model the coupling between elasticity and damage through the effective stress concept $\tilde{\sigma}$.

[10] A finer resolution than the RVE size is the statistical volume element (SVE), the element of statistical mechanics, which is out of scope of the present study.

- $\psi_P = \frac{1}{\rho}\left(\int_0^r R dr + \frac{1}{3}C\alpha_{ij}\alpha_{ij}\right)$: plastic hardening contribution with parameter C accounts for the linear part of the kinematic hardening.
- ψ_T: the temperature contribution which defines the heat capacity of materials.

From the state potential, one can obtain the state laws which are the thermoelasticity laws:

$$\epsilon_{ij} = \rho\frac{\partial\psi^*}{\partial\sigma_{ij}} = \rho\frac{\partial\psi_e^*}{\partial\sigma_{ij}} + \epsilon_{ij}^p \tag{A.50}$$

The expression of ϵ_{ij}^e can derive from Eq. A.50:

$$\epsilon_{ij}^e = \rho\frac{\partial\psi_e^*}{\partial\sigma_{ij}} \qquad s = \frac{\partial\psi^*}{\partial T} \tag{A.51}$$

The associated variables are defined as follows:

$$R = -\rho\frac{\partial\psi^*}{\partial r} \qquad X_{ij} = -\rho\frac{\partial\psi^*}{\partial\alpha_{ij}} \tag{A.52}$$

$$-Y = -\rho\frac{\partial\psi^*}{\partial D} \quad \text{or} \quad -Y_{ij} = -\rho\frac{\partial\psi^*}{\partial D_{ij}} \tag{A.53}$$

The Clausius-Duhem inequality, which represents the second principle of thermodynamics, is satisfied when the damage rate is positive:

$$\sigma_{ij}\dot{\epsilon}_{ij}^p - \dot{\omega}_s + Y_{ij}\dot{D}_{ij} - \frac{q_i T_{,i}}{T} \geq 0 \tag{A.54}$$

The physical signification of this formula is: the total dissipation is the sum of the dissipation due to plastic power ($\sigma_{ij}\dot{\epsilon}_{ij}^p$), minus the stored energy density rate ($\dot{\omega}_s = R\dot{r} + X_{ij}\alpha_{ij}$), plus the dissipation due to damage ($Y_{ij}\dot{D}_{ij}$) and plus the thermal energy ($\vec{q}$ is the thermal flux) is positive. This dissipation is transformed into heat.

iii) Dissipation potential and evolution laws The dissipation potential is a convex function of associated variables: $F = F(\sigma, R, X_{ij}, Y(or\, Y_{ij}), D(or\, D_{ij}), T)$. This function can be represented as: $F = f + F_X + F_D$; where f, F_X, F_D are the plastic potential function (the yield function for associative plasticity), the nonlinear kinematic hardening dissipative potential, and the damage dissipative potential. The evolution laws derived from this function can be expressed as:

$$\dot{\epsilon}_{ij}^p = -\dot{\lambda}\frac{\partial F}{\partial(-\sigma_{ij})} = \dot{\lambda}\frac{\partial F}{\partial(\sigma_{ij})} \tag{A.55}$$

$$\dot{r} = -\dot{\lambda}\frac{\partial F}{\partial R} \tag{A.56}$$

$$\dot{\alpha}_{ij} = -\dot{\lambda}\frac{\partial F}{\partial X_{ij}} \tag{A.57}$$

$$\dot{D} = -\dot{\lambda}\frac{\partial F}{\partial(-Y)} = \dot{\lambda}\frac{\partial F}{\partial Y} \quad \text{scalar damage} \tag{A.58}$$

$$\dot{D}_{ij} = -\dot{\lambda}\frac{\partial F}{\partial(-Y_{ij})} = \dot{\lambda}\frac{\partial F}{\partial Y_{ij}} \quad \text{tensor damage} \tag{A.59}$$

Remark Throughout the present dissertation, the influence of temperature on the damage process will be neglected.

A.4.2 Microdefects closure effect

During compression, the microdefects (microcracks) of materials may close, that might increase the load carrying area and material stiffness may then partly or fully recover. This phenomenon is called: "microdefects closure effect". Consider $\tilde{E}^+$ and $\tilde{E}^-$, the effective elasticity moduli in tension and compression. For uniaxial state of stress, the effective stress, which accounts for the microdefects closure effect, can be defined as:

- $\frac{\sigma}{1-D}$ in tension, with D is the relative reduction of load carrying area in tension ($D = 1 - \frac{\tilde{E}^+}{E}$),
- $\frac{\sigma}{1-hD}$ in compression, with hD is the relative reduction of load carrying area in compression ($hD = 1 - \frac{\tilde{E}^-}{E}$), or $h = \frac{E-\tilde{E}^-}{E-\tilde{E}^+}$.

The parameter h is called the "microdefects closure parameter" which is material dependent. For most materials, by measuring the ratio $\frac{E-\tilde{E}^-}{E-\tilde{E}^+}$, Lemaitre showed that $h \approx 0.2$.

For 3D stress states, the distinction between tension and compression is not straightforward. One method was proposed to define the positive and negative parts of a tensor, which was based on the three principal values of that tensor. The positive part ($\langle \mathbf{s} \rangle^+$ or $\langle \mathbf{s} \rangle^+_{ij}$) of a symmetric tensor $\mathbf{s}$ is defined from its positive eigenvalue s_K and the corresponding normalized eigenvectors $\vec{q}$:

$$\langle \mathbf{s} \rangle^+_{ij} = \sum_{K=1}^{3} \langle s_K \rangle q_i^K q_j^K \tag{A.60}$$

$$\langle \mathbf{s} \rangle^-_{ij} = s_{ij} - \langle \mathbf{s} \rangle^+_{ij} \tag{A.61}$$

where $< . >$ represents the positive part of a scalar and is defined as $< x >= \begin{cases} x & \text{, if x} \geq 0 \\ 0 & \text{, if x} < 0 \end{cases}$

A.4.3 Damage evolution

From the thermodynamic framework (section A.4.1), the damage evolution law can be derived from the dissipation potential:

$$\dot{D} = \dot{\lambda} \frac{\partial F_D}{\partial (Y)} \quad \text{or} \quad \dot{D}_{ij} = \dot{\lambda} \frac{\partial F_D}{\partial Y_{ij}} \tag{A.62}$$

A.4.3.1 Damage threshold

Damage threshold is a limit of a physical parameter (e.g. accumulated plastic strain p_D, stored energy ω_D) from which damage begins to occur. The stored energy for a case of elasto-(visco)-plasticity with isotropic and kinematic hardening, is defined as:

$$\omega_s = \int_0^t (R\dot{r} + X_{ij}\dot{\alpha}_{ij}) dt \tag{A.63}$$

These values (p_D and ω_D) depend on material and type of loading.

A.4.3.2 Critical value of damage variable

At the other end of the damage evolution, when $max(D(\vec{n})) = D_c$ a mesocrack is initiated. The damage critical value D_c is a material parameter. For many materials, this value is about 0.2 to 0.5 (the value of critical damage for anisotropic damage has the same order of magnitude).

A.4.4 Isotropic damage

A.4.4.1 State potential

The strain potential for linear isotropic elasticity and isotropic damage (using scalar D) can be written as:

$$\rho \psi_e^* = \frac{1+\nu}{2E} \frac{\sigma_{ij}\sigma_{ij}}{1-D} - \frac{\nu}{2E} \frac{\sigma_{kk}^2}{1-D} \tag{A.64}$$

where E is Young's modulus, ν the Poisson ratio. The elasticity law derived from this potential with the introduction of effective stress $\tilde{\sigma}_{ij} = \frac{\sigma_{ij}}{1-D}$, is defined as:

$$\epsilon_{ij}^e = \rho \frac{\partial \psi_e^*}{\partial \sigma_{ij}} = \frac{1+\nu}{E} \tilde{\sigma}_{ij} - \frac{\nu}{E} \tilde{\sigma}_{kk} \delta_{ij} \tag{A.65}$$

The variable associated with the damage variable, named energy density release rate, is derived from the state potential:

$$Y = \rho \frac{\partial \psi_e^*}{\partial D} = \frac{\overline{\sigma}^2}{2E(1-D)^2}\left[\frac{2}{3}(1+\nu) + 3(1-2\nu)\left(\frac{-p}{\overline{\sigma}}\right)^2\right] = \frac{\overline{\sigma}^2}{2E(1-D)^2} R_v \tag{A.66}$$

where $R_v = \frac{2}{3}(1+\nu) + 3(1-2\nu)\left(\frac{-p}{\overline{\sigma}}\right)^2$ is the triaxiality function.

A.4.4.2 Microdefects closure effect for isotropic damage

The isothermal state potential is given in Eq. A.67.

$$\rho\psi_e^* = \frac{1+\nu}{2E}\left[\frac{\langle\boldsymbol{\sigma}\rangle_{ij}^+\langle\boldsymbol{\sigma}\rangle_{ij}^+}{1-D} + \frac{\langle\boldsymbol{\sigma}\rangle_{ij}^-\langle\boldsymbol{\sigma}\rangle_{ij}^-}{1-hD}\right] - \frac{\nu}{2E}\left[\frac{\langle\sigma_{kk}\rangle^2}{1-D} + \frac{\langle-\sigma_{kk}\rangle^2}{1-hD}\right] \tag{A.67}$$

From this equation, one can obtain the elastic strain and the energy density release rate $Y = \rho\frac{\partial\psi^*}{\partial D}$:

$$\epsilon_{ij}^e = \frac{1+\nu}{E}\left[\frac{\langle\boldsymbol{\sigma}\rangle_{ij}^+}{1-D} + \frac{\langle\boldsymbol{\sigma}\rangle_{ij}^-}{1-hD}\right] - \frac{\nu}{E}\left[\frac{\langle\sigma_{kk}\rangle}{1-D} + \frac{\langle-\sigma_{kk}\rangle}{1-hD}\right]\delta_{ij} \tag{A.68}$$

$$Y = \frac{1+\nu}{2E}\left[\frac{\langle\boldsymbol{\sigma}\rangle_{ij}^+\langle\boldsymbol{\sigma}\rangle_{ij}^+}{(1-D)^2} + \frac{h\langle\boldsymbol{\sigma}\rangle_{ij}^-\langle\boldsymbol{\sigma}\rangle_{ij}^-}{(1-hD)^2}\right] - \frac{\nu}{2E}\left[\frac{\langle\sigma_{kk}\rangle^2}{(1-D)^2} + \frac{h\langle-\sigma_{kk}\rangle^2}{(1-hD)^2}\right] \tag{A.69}$$

The effective stress is defined as:

$$\tilde{\sigma}_{ij} = \frac{\langle\boldsymbol{\sigma}\rangle_{ij}^+}{1-D} + \frac{\langle\boldsymbol{\sigma}\rangle_{ij}^-}{1-hD} + \frac{\nu}{1-2\nu}\left[\frac{\delta_{kl}\langle\sigma\rangle_{kl}^+ - \langle\sigma\rangle_{kk}}{1-D} + \frac{\delta_{kl}\langle\sigma\rangle_{kl}^- + \langle-\sigma\rangle_{kk}}{1-hD}\right]\delta_{ij} \tag{A.70}$$

A.4.4.3 Evolution laws

Observations and experiments showed that damage is also governed by the plastic strain through the plastic multuplier $\dot{\lambda}$:

$$\dot{D} = \dot{\lambda}\frac{\partial F_D}{\partial Y} \quad \text{if} \quad p > p_D \quad \text{or} \quad \omega_s > \omega_D \tag{A.71}$$

where p_D and ω_D were defined in section A.4.3. The dissipative potential function is defined as:

$$F = f + F_X + F_D \tag{A.72}$$

$$f = \left(\frac{\boldsymbol{\sigma}}{1-D} - \mathbf{X}\right)_{eq} - R - \sigma_y = \sigma_v \tag{A.73}$$

$$F_D = \frac{S}{(s+1)(1-D)}\left(\frac{Y}{S}\right)^{s+1} \tag{A.74}$$

where

- $\left(\frac{\boldsymbol{\sigma}}{1-D} - \mathbf{X}\right)_{eq} = \sqrt{\frac{3}{2}\left(\frac{\sigma_{ij}^D}{1-D} - X_{ij}\right)\left(\frac{\sigma_{ij}^D}{1-D} - X_{ij}\right)}$
- σ_v: viscous stress (for plasticity: σ_v=0), S and s are two material parameters (which might depend on temperature).

The normality rule:

$$\dot{\epsilon}_{ij}^p = \dot{\lambda}\frac{\partial F}{\partial\sigma_{ij}} = \dot{\lambda}\frac{\partial f}{\partial\sigma_{ij}} = \frac{\frac{\sigma_{ij}^D}{1-D} - X_{ij}}{\left(\frac{\boldsymbol{\sigma}}{1-D} - \mathbf{X}\right)_{eq}}\frac{\dot{\lambda}}{1-D} \tag{A.75}$$

$$\dot{r} = -\dot{\lambda}\frac{\partial F}{\partial R} = -\dot{\lambda}\frac{\partial f}{\partial R} = \dot{\lambda} \tag{A.76}$$

The accumulated plastic strain rate $\dot{p}$ derived from Eq. A.75:

$$\dot{p} = \sqrt{\frac{2}{3}\dot{\epsilon}_{ij}^p\dot{\epsilon}_{ij}^p} = \frac{\dot{\lambda}}{1-D} \tag{A.77}$$

The damage evolution rule writes:

$$\dot{D} = \dot{\lambda}\frac{\partial F_D}{\partial Y} = \frac{\dot{\lambda}}{1-D}\left(\frac{Y}{S}\right)^s = \dot{p}\left(\frac{Y}{S}\right)^s \tag{A.78}$$

Finally, the complete isotropic damage constitutive equations can be summarized as:

Isotropic damage constitutive equations

$$\dot{D} = \begin{cases} \dot{p}\left(\frac{Y}{S}\right)^s & ,if \quad p > p_D \quad (\omega_s > \omega_D) \\ 0 & ,if\ not \end{cases} \tag{A.79}$$

When $D = D_c$: mesocracks initiation occurs. The variables Y is defined in Eqs. A.66, and A.69.

Remarks The effective stresses are defined in section A.4.2 and Eq. A.70. However, in the case which accounts for the microdefects closure effects, this effect does not interfere in the expression of von Mises criterion (f), in which $\frac{\sigma}{1-D}$ is used. According to Lemaitre, the reason is that the plasticity mechanism is controlled by slips and produced by shear stress, which affect in the same manner regardless their signs.

A.4.5 Anisotropic damage

A.4.5.1 State potential

The state potential $\rho\psi_e^*$ for anisotropic damage, represented by the tensor $\mathbf{D}$ is:

$$\rho\psi_e^* = \frac{1+\nu}{2E}H_{ij}\sigma_{jk}^D H_{kl}\sigma_{li}^D + \frac{3(1-\nu)}{2E}\frac{\sigma_h^2}{1-\eta D_H} \tag{A.80}$$

$$H_{ij} = (\mathbf{I}-\mathbf{D})_{ij}^{-1/2} \tag{A.81}$$

where $\boldsymbol{\sigma}^D$ is the deviatoric part of the stress tensor $\boldsymbol{\sigma}$, $D_H = \frac{1}{3}D_{kk}$. The associated variable with the damage tensor $\mathbf{D}$ is the energy density release rate tensor, $\boldsymbol{\Upsilon}$, which is derived from the Gibbs energy: $\frac{\partial\psi^*}{\partial D_{ij}}$. However, the damage evolution law is not a function of $\boldsymbol{\Upsilon}$ but the effective elastic energy density: $\overline{Y} = \int \tilde{\sigma}_{ij}d\epsilon_{ij}^e$. The expressions of this variable and the symmetric effective stress tensor are given in Eqs. A.82 and A.83 below:

$$\overline{Y} = \frac{1}{2}\tilde{\sigma}_{ij}\epsilon_{ij}^e \tag{A.82}$$

$$\tilde{\sigma}_{ij} = \left(H_{ik}\sigma_{kl}^D H_{lj}\right)^D + \frac{\sigma_h}{1-\eta D_H} \tag{A.83}$$

where:

$$\tilde{R}_v = \frac{2}{3}(1+\nu) + 3(1-2\nu)\left(\frac{\tilde{\sigma}_h}{\tilde{\sigma}_{eq}}\right)^2 \tag{A.84}$$

$$\tilde{\sigma}_{eq} = \left(\mathbf{H}\boldsymbol{\sigma}^D\mathbf{H}\right)_{eq} = \left[\frac{3}{2}\left(\mathbf{H}\boldsymbol{\sigma}^D\mathbf{H}\right)_{ij}^D\left(\mathbf{H}\boldsymbol{\sigma}^D\mathbf{H}\right)_{ij}^D\right]^{1/2} \tag{A.85}$$

$$\tilde{\sigma}_h = \frac{\sigma_h}{1-\eta D_H} \tag{A.86}$$

A.4.5.2 Microdefects closure effect for anisotropic damage

Let us define:

$$H_{ij}^p = (\mathbf{I}-\mathbf{D})_{ij}^{-1/2} \qquad H_{ij}^n = (\mathbf{I}-h_a\mathbf{D})_{ij}^{-1/2} \tag{A.87}$$

where p and n stand for *positive* and *negative* respectively, and the parameter h_a has the same signification as h in the isotropic damage. For most materials, Lemaitre showed that $h_a = 0$ ($h = 0.2$ for the isotropic damage). The positive part of deviatoric stress tensor is defined as:

$$\sigma_{+ij}^D = \sum_{K=1}^{3}\langle\lambda_K\rangle\left[(\mathbf{H}^p)_{ik}^{-1}T_k^K\right]\left[(\mathbf{H}^p)_{jl}^{-1}T_l^K\right] \tag{A.88}$$

where λ_K and $\vec{T}^K$ are the eigenvalues and eigenvectors of the non-symmetric matrix $(\mathbf{H}^p\boldsymbol{\sigma}^D)$. With the same approach, one can obtain the negative part corresponding to the matrix $(\mathbf{H}^n\boldsymbol{\sigma}^D)$. The state potential and elasticity law derived from it (with $\mathbf{h_a} = \mathbf{0}$) are given in Eqs. A.89 and A.90:

$$\rho\psi_e^* = \frac{1+\nu}{2E}\left[H^p_{ij}\sigma^D_{+jk}H^p_{kl}\sigma^D_{+li} + H^n_{ij}\sigma^D_{+jk}H^n_{kl}\sigma^D_{+li}\right] + \frac{3(1-2\nu)}{2E}\left[\frac{\langle\sigma_h\rangle^2}{1-\eta D_H} + \langle-\sigma_h\rangle^2\right] \tag{A.89}$$

$$\epsilon^e_{ij} = \frac{1+\nu}{E}\left[\left(H^p_{ik}\sigma^D_{+kl}H^p_{lj}\right)^D + \left(\left\langle\boldsymbol{\sigma}^D\right\rangle^-\right)^D_{ij}\right] + \frac{(1-2\nu)}{E}\left[\frac{\langle\sigma_h\rangle}{1-\eta D_H} - \langle-\sigma_h\rangle\right]\delta_{ij} \tag{A.90}$$

The effective stress tensor:

$$\tilde{\sigma}_{ij} = \left(H^p_{ik}\sigma^D_{+kl}H^p_{lj}\right)^D + \left(H^n_{ik}\sigma^D_{-kl}H^n_{lj}\right)^D + \left[\frac{\langle\sigma_h\rangle}{1-\eta D_H} - \langle-\sigma_h\rangle\right]\delta_{ij} \tag{A.91}$$

Finally, the effective energy density for the case $\mathbf{h_a} = \mathbf{0}$ is defined as:

$$\overline{Y} = \frac{1+\nu}{2E}tr\left(\mathbf{H}^p\boldsymbol{\sigma}^D_+\mathbf{H}^p\right)^2 + \frac{3(1-2\nu)}{2E}\frac{\langle\sigma_h\rangle^2}{(1-\eta D_H)^2} \tag{A.92}$$

A.4.5.3 Evolution laws

The damage dissipation potential is now modified as:

$$F_D = \left(\frac{\overline{Y}(\boldsymbol{\epsilon}^e)}{S}\right)^s Y_{ij}\left|\frac{d\boldsymbol{\epsilon}^p}{dr}\right|_{ij} \tag{A.93}$$

where $\dot{r} = \dot{\lambda}$. The operator $|.|$, which applied to a tensor means the absolute value of that tensor in terms of principal components. These following equations define the effective elastic energy density and the effective stress triaxiality function:

$$\overline{Y} = \frac{\tilde{\sigma}^2_{eq}\tilde{R}_v}{2E} \tag{A.94}$$

$$\tilde{R}_v = \frac{2}{3}(1+\nu) + 3(1-2\nu)\left(\frac{\tilde{\sigma}_h}{\tilde{\sigma}_{eq}}\right)^2 \tag{A.95}$$

where $\tilde{\sigma}_{eq}$ and $\tilde{\sigma}_h$ are defined in Eqs. A.85 and A.86. The complete constitutive equations for anisotropic damage can be summarized as:

Anisotropic damage constitutive equations

$$\dot{D}_{ij} = \begin{cases} \dot{p}\left(\frac{\overline{Y}}{S}\right)^s\left|\dot{\boldsymbol{\epsilon}^p}\right|_{ij} & ,if \quad p > p_D \quad (\omega_s > \omega_D) \\ 0 & ,if \quad not \end{cases} \tag{A.96}$$

This equation shows that the principal directions of damage rate tensor coincide with those of the plastic strain rate. When the largest principal value of damage tensor reaches the critical damage value: $max(D_I) = D_c$, the mesocracks initiation occurs.

A.5 Fields-Backofen method

The Fields-Backofen method (F-B) is often used to obtain the *stress-strain* curve from the *torque-number of turns* curve in the plastic region. Using this method requires following assumptions:

1. Homogeneous and isotropic behavior of material.
2. No flow localization.
3. Transverse sections remain straight (no displacement along the z-axis, i.e. the specimen is deformed by pure shear).
4. The gauge section of a tubular specimen is represented as a solid cylinder of radius R, twisted by torque Γ applied to one end of the specimen, while the other end is fixed (Fig. A.4).

A.5.1 Stress and strain analyses

The strain-rate tensor and stress-tensor correspond to a material point at position r ($r \leq R$ - see Fig. A.4 for the notation):

$$\dot{\boldsymbol{\epsilon}} = \begin{pmatrix} 0 & 0 & 0 \\ 0 & 0 & \frac{\pi r \dot{N}}{L} \\ 0 & \frac{\pi r \dot{N}}{L} & 0 \end{pmatrix} \quad , \quad \boldsymbol{\sigma} = \begin{pmatrix} 0 & 0 & 0 \\ 0 & 0 & \tau(r) \\ 0 & \tau(r) & 0 \end{pmatrix} \tag{A.97}$$

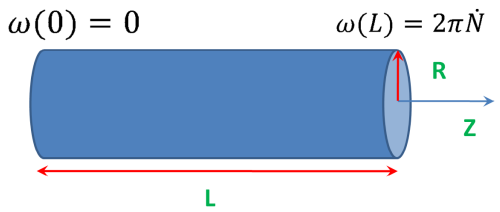

Fig. A.4: *Torsion specimens.*

The generalized or effective strain rate is defined as:

$$\dot{\overline{\epsilon}} = \sqrt{\frac{2}{3}(\dot{\boldsymbol{\epsilon}} : \dot{\boldsymbol{\epsilon}})} = \frac{2\pi r \dot{N}}{\sqrt{3}L} \tag{A.98}$$

Finally, the accumulated equivalent strain can be obtained by integrating the following equation:

$$\overline{\epsilon} = \int_0^t \frac{2\pi r \dot{N}}{\sqrt{3}L} = \frac{2\pi r N}{\sqrt{3}L} \tag{A.99}$$

The generalized or the equivalent stress is defined as: $\overline{\sigma} = \sqrt{3}\tau(r)$.

Let us consider an annular element of radius r and width dr having an area of $2\pi r dr$. The contribution of this element to the total torque is the product of the shear force on it ($\tau(r)2\pi r dr$) and the level arm r: $d\Gamma = \tau(r)2\pi r dr.r$. The total torque can be calculated as:

$$\Gamma = \int_0^R 2\pi r^2 \tau(r) dr \tag{A.100}$$

A.5.2 The Fields-Backofen method

Starting from the Fields-Backofen constitutive equation [Fields and Backofen, 1957]:

$$\sigma_0 = A\overline{\epsilon}^n \dot{\overline{\epsilon}}^m \tag{A.101}$$

where σ_0 is the flow stress of material; A is a function of temperature; n is the strain hardening coefficient; m is the strain-rate sensitivity (m and n can also depend on temperature). Eq. A.100 can be written as:

$$\Gamma = \int_0^R \frac{\overline{\sigma}}{\sqrt{3}} 2\pi r^2 dr = \int_0^R \frac{A\overline{\epsilon}^n \dot{\overline{\epsilon}}^m}{\sqrt{3}} 2\pi r^2 dr \tag{A.102}$$

With $\dot{\overline{\epsilon}}$ and $\overline{\epsilon}$ defined in Eq. A.98 and Eq. A.99, the following relationship can be deduced:

$$\Gamma = \frac{\overline{\sigma}(R)}{\sqrt{3}} \frac{2\pi R^3}{m+n+3} = \tau(R) \frac{2\pi R^3}{m+n+3} \tag{A.103}$$

From this equation, the formula for shear stress can be obtained:

$$\tau(R) = \frac{\Gamma(m+n+3)}{2\pi R^3} \tag{A.104}$$

The two parameters m and n are calculated as follows:

$$n = \left(\frac{\partial ln(\Gamma)}{\partial ln(N)} \right)_{\dot{N},T} \tag{A.105}$$

$$m = \left(\frac{\partial ln(\Gamma)}{\partial ln(\dot{N})} \right)_{N,T} \tag{A.106}$$

Two torsions tests were carried out at the same rotation speed and do not account for the influence of strain-rate. The coefficient m is therefore chosen equal to 0. The strain hardening parameter can be calculated graphically by measuring the slope of the *ln(Γ)-ln(N)* curve in the plastic region. The results are shown in Fig. A.5.

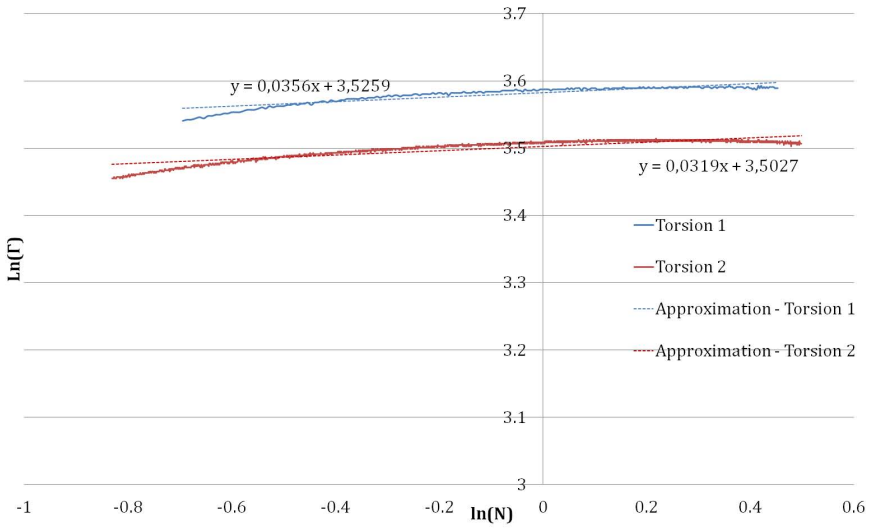

Fig. A.5: *The curves of logarithm of torque and number of turn to identify the parameter of F-B.*

In this figure, the dot-line curves represent the approximative slopes of the *ln(Γ)-ln(N)* curves. From this figure, the value of n is around 0.036 (torsion 1). The equivalent stress-equivalent strain curve is finally obtained by the following equations:

$$\begin{cases} \overline{\sigma} = \sqrt{3} \frac{\Gamma(m+n+3)}{2\pi R^3} \\ \overline{\epsilon} = \frac{2\pi r N}{\sqrt{3} L} \end{cases} \tag{A.107}$$

with $m = 0$ and $n = 0.036$.

For a general case when the yield stress is defined as an arbitrary function of the equivalent plastic strain and strain rate, it can be demonstrated that the same result can be obtained:

$$\begin{cases} \overline{\sigma} = \sqrt{3}\frac{\Gamma(\widetilde{m}+\widetilde{n}+3)}{2\pi R^3} \\ \\ \overline{\epsilon} = \frac{2\pi r N}{\sqrt{3}L} \end{cases} \tag{A.108}$$

where $\widetilde{n} = \left(\frac{\partial ln(\Gamma)}{\partial ln(N)}\right)_{\dot{N},T}$ and $\widetilde{m} = \left(\frac{\partial ln(\Gamma)}{\partial ln(\dot{N})}\right)_{N,T}$. In this case, they are two material parameters, not the hardening coefficient and the strain-rate sensitivity.

Appendix B

GTN model equations

B.1 Stiffness matrix coefficients for Newton-Raphson method in GTN model local integration

This section presents the calculations of the constants J_{ij} that involved in equations 4.68. These constants correspond to the constants in Appendix 1 of [Aravas, 1987]. Only the calculation of J_{11} is demonstrated here, the other coefficients could be obtained by the same procedure.

$$J_{11} = \frac{\partial \phi_1}{\partial \Delta\epsilon_p} = \frac{\partial g}{\partial q} + \Delta\epsilon_p \frac{\partial \left(\frac{\partial g}{\partial q}\right)}{\partial \Delta\epsilon_p} + \Delta\epsilon_q \frac{\partial \left(\frac{\partial g}{\partial p}\right)}{\partial \Delta\epsilon_p} \tag{B.1}$$

From the fact that the two terms $\frac{\partial g}{\partial q}$ and $\frac{\partial g}{\partial p}$ could be the functions of p, q, and $\boldsymbol{H^\alpha}$, the above equation could be written as:

$$J_{11} = \frac{\partial g}{\partial q} + \Delta\epsilon_p \left(\frac{\partial^2 g}{\partial q \partial p} \frac{\partial p}{\partial \Delta\epsilon_p} + \sum_{\alpha=1}^{n} \frac{\partial^2 g}{\partial q \partial H^\alpha} \frac{\partial H^\alpha}{\partial \Delta\epsilon_p} \right) + \Delta\epsilon_q \left(\frac{\partial^2 g}{\partial p^2} \frac{\partial p}{\partial \Delta\epsilon_p} + \sum_{\alpha=1}^{n} \frac{\partial^2 g}{\partial p \partial H^\alpha} \frac{\partial H^\alpha}{\partial \Delta\epsilon_p} \right) \tag{B.2}$$

where $\frac{\partial p}{\partial \Delta\epsilon_q} = \frac{\partial q}{\partial \Delta\epsilon_p} = 0$. Accounting for $\frac{\partial p}{\partial \Delta\epsilon_p} = K$, we can obtain:

$$J_{11} = \frac{\partial g}{\partial q} + \Delta\epsilon_p \left(K \frac{\partial^2 g}{\partial q \partial p} + \sum_{\alpha=1}^{n} \frac{\partial^2 g}{\partial q \partial H^\alpha} \frac{\partial H^\alpha}{\partial \Delta\epsilon_p} \right) + \Delta\epsilon_q \left(K \frac{\partial^2 g}{\partial p^2} + \sum_{\alpha=1}^{n} \frac{\partial^2 g}{\partial p \partial H^\alpha} \frac{\partial H^\alpha}{\partial \Delta\epsilon_p} \right) \tag{B.3}$$

The same procedure was employed to obtain other constants, which are listed below:

$$J_{12} = \frac{\partial g}{\partial p} + \Delta\epsilon_p \left(-3G \frac{\partial^2 g}{\partial q^2} + \sum_{\alpha=1}^{n} \frac{\partial^2 g}{\partial q \partial H^\alpha} \frac{\partial H^\alpha}{\partial \Delta\epsilon_q} \right) + \Delta\epsilon_q \left(-3G \frac{\partial^2 g}{\partial p \partial q} + \sum_{\alpha=1}^{n} \frac{\partial^2 g}{\partial p \partial H^\alpha} \frac{\partial H^\alpha}{\partial \Delta\epsilon_q} \right) \tag{B.4}$$

$$J_{21} = K \frac{\partial \phi}{\partial p} + \sum_{\alpha=1}^{n} \frac{\partial \phi}{\partial H^\alpha} \frac{\partial H^\alpha}{\partial \Delta\epsilon_p} \tag{B.5}$$

$$J_{22} = -3G \frac{\partial \phi}{\partial q} + \sum_{\alpha=1}^{n} \frac{\partial \phi}{\partial H^\alpha} \frac{\partial H^\alpha}{\partial \Delta\epsilon_q} \tag{B.6}$$

Finally, the derivations of internal state variables $\underline{\boldsymbol{H}}^{\boldsymbol{\alpha}}$ with respect to $\Delta\epsilon_p$ and $\Delta\epsilon_q$ can be obtained from Eq. B.14.

B.2 Variational form of internal state variables in GTN model

In this part, the variational form of the internal state variables $\underline{\boldsymbol{H}}^{\boldsymbol{\alpha}}$ will be developed

$$\Delta\underline{\boldsymbol{H}}^{\boldsymbol{\alpha}} = \underline{\boldsymbol{h}}^{\alpha}\left(\Delta\boldsymbol{\epsilon}^{\boldsymbol{p}},p,q,\underline{\boldsymbol{H}}^{\boldsymbol{\beta}}\right) = \underline{\boldsymbol{h}}^{\alpha}\left(\Delta\epsilon_p,\Delta\epsilon_q,p,q,\underline{\boldsymbol{H}}^{\boldsymbol{\beta}}\right) \tag{B.7}$$

The variation of internal state variables $\underline{\boldsymbol{H}}^{\boldsymbol{\alpha}}$ is the function of the set of internal state variables $\underline{\boldsymbol{H}}^{\boldsymbol{\beta}}$ and the current stress and strain variables ($\Delta\epsilon_p$,$\Delta\epsilon_q$,p,q - to simplify the notation, these variables are noted as x_i, with $i = 1..4$). The differentiation of internal state variables:

$$\partial\underline{\boldsymbol{H}}^{\boldsymbol{\alpha}} = \sum_{\beta=1}^{n}\frac{\partial\underline{\boldsymbol{h}}^{\boldsymbol{\alpha}}}{\partial H^{\beta}}\partial H^{\beta} + \sum_{i=1}^{4}\frac{\partial\underline{\boldsymbol{h}}^{\boldsymbol{\alpha}}}{\partial x_i}\partial x_i \tag{B.8}$$

or:

$$\partial\underline{\boldsymbol{H}}^{\boldsymbol{\alpha}} - \sum_{\beta=1}^{n}\frac{\partial\underline{\boldsymbol{h}}^{\boldsymbol{\alpha}}}{\partial H^{\beta}}\partial H^{\beta} = \sum_{i=1}^{4}\frac{\partial\underline{\boldsymbol{h}}^{\boldsymbol{\alpha}}}{\partial x_i}\partial x_i \tag{B.9}$$

Eq. B.9 is presented under vectorial form, which can be written for each component H^{α} ($1 \leq \alpha \leq n$) as:

$$\partial H^{\alpha} - \sum_{\beta=1}^{n}\frac{\partial h^{\alpha}}{\partial H^{\beta}}\partial H^{\beta} = \sum_{i=1}^{4}\frac{\partial h^{\alpha}}{\partial x_i}\partial x_i \tag{B.10}$$

$$\sum_{\beta=1}^{n}\left(\delta_{\alpha\beta} - \frac{\partial h^{\alpha}}{\partial H^{\beta}}\right)\partial H^{\beta} = \sum_{i=1}^{4}\frac{\partial h^{\alpha}}{\partial x_i}\partial x_i \tag{B.11}$$

where $\delta_{\alpha\beta}$ is the Kronecker notation. Let $\boldsymbol{\Delta}$ is the matrix with the component $\Delta_{ij} = \delta_{ij} - \frac{\partial h^i}{\partial H^j}$ and $\underline{\boldsymbol{b}}$ is the vector with the component $b_i = \sum_{k=1}^{4}\frac{\partial h^i}{\partial x_k}\partial x_k$ ($1 \leq i,j \leq n$), we get:

$$\boldsymbol{\Delta} \bullet \partial\underline{\boldsymbol{H}}^{\boldsymbol{\alpha}} = \underline{\boldsymbol{b}} \tag{B.12}$$

By inverting $\boldsymbol{\Delta}$:

$$\partial\underline{\boldsymbol{H}}^{\boldsymbol{\alpha}} = \boldsymbol{\Delta}^{-1} \bullet \underline{\boldsymbol{b}} = \boldsymbol{c} \bullet \underline{\boldsymbol{b}} \tag{B.13}$$

where $\boldsymbol{c}$ is the inversion matrix of $\boldsymbol{\Delta}$, with the component $c_{\alpha\beta} = \left(\delta_{\alpha\beta} - \frac{\partial h^{\alpha}}{\partial H^{\beta}}\right)^{-1}$ (in this context, this expression must be understood as: the matrix $\boldsymbol{c}$ is the inversion of the matrix $\boldsymbol{\Delta}$, where $\Delta_{\alpha\beta} = \left(\delta_{\alpha\beta} - \frac{\partial h^{\alpha}}{\partial H^{\beta}}\right)$). Finally, for each component H^{α}:

$$\partial H^{\alpha} = \sum_{\beta=1}^{n} c_{\alpha\beta}\left[\frac{\partial h^{\beta}}{\partial\Delta\epsilon_p}\partial\Delta\epsilon_p + \frac{\partial h^{\beta}}{\partial\Delta\epsilon_q}\partial\Delta\epsilon_q + \frac{\partial h^{\beta}}{\partial p}\partial p + \frac{\partial h^{\beta}}{\partial q}\partial q\right] \tag{B.14}$$

B.3 Coefficients in Aravas's approach

The coefficients A_{ij} and B_{ij} ($1 \leq i,j \leq 2$) appearing in Eqs. 4.86 and 4.87 are listed below:

$$A_{11} = K\frac{\partial\phi}{\partial p} + \sum_{\alpha=1}^{n}\sum_{\beta=1}^{n}\frac{\partial\phi}{\partial H^{\alpha}}c_{\alpha\beta}\left(\frac{\partial h^{\beta}}{\partial\Delta\epsilon_p} + K\frac{\partial h^{\beta}}{\partial p}\right) \tag{B.15}$$

$$A_{12} = -3G\frac{\partial\phi}{\partial q} + \sum_{\alpha=1}^{n}\sum_{\beta=1}^{n}\frac{\partial\phi}{\partial H^{\alpha}}c_{\alpha\beta}\left(\frac{\partial h^{\beta}}{\partial\Delta\epsilon_q} - 3G\frac{\partial h^{\beta}}{\partial q}\right) \tag{B.16}$$

$$B_{11} = K\left(\frac{\partial\phi}{\partial p} + \sum_{\alpha=1}^{n}\sum_{\beta=1}^{n}\frac{\partial\phi}{\partial H^{\alpha}}c_{\alpha\beta}\frac{\partial h^{\beta}}{\partial p}\right) \tag{B.17}$$

$$B_{12} = -2G\left(\frac{\partial\phi}{\partial q} + \sum_{\alpha=1}^{n}\sum_{\beta=1}^{n}\frac{\partial\phi}{\partial H^{\alpha}}c_{\alpha\beta}\frac{\partial h^{\beta}}{\partial q}\right) \tag{B.18}$$

$$A_{21} = \frac{\partial \phi}{\partial q} + K\left(\Delta\epsilon_p \frac{\partial^2 g}{\partial p \partial q} + \Delta\epsilon_q \frac{\partial^2 g}{\partial p^2}\right) + \sum_{\alpha=1}^{n}\sum_{\beta=1}^{n}\left(\Delta\epsilon_p \frac{\partial^2 \phi}{\partial q \partial H^\alpha} + \Delta\epsilon_q \frac{\partial^2 \phi}{\partial p \partial H^\alpha}\right) c_{\alpha\beta}\left(\frac{\partial h^\beta}{\partial \Delta\epsilon_p} + K\frac{\partial h^\beta}{\partial p}\right) \tag{B.19}$$

$$A_{22} = \frac{\partial \phi}{\partial p} - 3G\left(\Delta\epsilon_p \frac{\partial^2 g}{\partial q^2} + \Delta\epsilon_q \frac{\partial^2 g}{\partial p \partial q}\right) + \sum_{\alpha=1}^{n}\sum_{\beta=1}^{n}\left(\Delta\epsilon_p \frac{\partial^2 \phi}{\partial q \partial H^\alpha} + \Delta\epsilon_q \frac{\partial^2 \phi}{\partial p \partial H^\alpha}\right) c_{\alpha\beta}\left(\frac{\partial h^\beta}{\partial \Delta\epsilon_q} - 3G\frac{\partial h^\beta}{\partial q}\right) \tag{B.20}$$

$$B_{21} = K\left(\Delta\epsilon_p \frac{\partial^2 g}{\partial p \partial q} + \Delta\epsilon_q \frac{\partial^2 g}{\partial p^2}\right) + K\sum_{\alpha=1}^{n}\sum_{\beta=1}^{n}\left(\Delta\epsilon_p \frac{\partial^2 \phi}{\partial q \partial H^\alpha} + \Delta\epsilon_q \frac{\partial^2 \phi}{\partial p \partial H^\alpha}\right) c_{\alpha\beta}\frac{\partial h^\beta}{\partial p} \tag{B.21}$$

$$B_{22} = -2G\left(\Delta\epsilon_p \frac{\partial^2 g}{\partial q^2} + \Delta\epsilon_q \frac{\partial^2 g}{\partial p \partial q}\right) - 2G\sum_{\alpha=1}^{n}\sum_{\beta=1}^{n}\left(\Delta\epsilon_p \frac{\partial^2 \phi}{\partial q \partial H^\alpha} + \Delta\epsilon_q \frac{\partial^2 \phi}{\partial p \partial H^\alpha}\right) c_{\alpha\beta}\frac{\partial h^\beta}{\partial q} \tag{B.22}$$

B.4 Coefficients in Zhang's approach

The coefficients A'_{ij} and B'_{ij} $(1 \le i,j \le 2)$ appearing in section 4.2.3.2 are listed below:

$$A'_{11} = \frac{\partial g}{\partial q} + \sum_{\alpha=1}^{n}\sum_{\beta=1}^{n}\left(\Delta\epsilon_p \frac{\partial^2 g}{\partial q \partial H^\alpha} + \Delta\epsilon_q \frac{\partial^2 g}{\partial p \partial H^\alpha}\right) c_{\alpha\beta}\frac{\partial h^\beta}{\partial \Delta\epsilon_p} + \sum_{\alpha=1}^{n}\sum_{\beta=1}^{n}\left(\Delta\epsilon_p \frac{\partial^2 g}{\partial q \partial H^\alpha} + \Delta\epsilon_q \frac{\partial^2 g}{\partial p \partial H^\alpha}\right) c_{\alpha\beta}\frac{\partial h^\beta}{\partial \Delta\epsilon_p} \tag{B.23}$$

$$A'_{12} = \frac{\partial g}{\partial p} + \sum_{\alpha=1}^{n}\sum_{\beta=1}^{n}\left(\Delta\epsilon_p \frac{\partial^2 g}{\partial q \partial H^\alpha} + \Delta\epsilon_q \frac{\partial^2 g}{\partial p \partial H^\alpha}\right) c_{\alpha\beta}\frac{\partial h^\beta}{\partial \Delta\epsilon_q} + \sum_{\alpha=1}^{n}\sum_{\beta=1}^{n}\left(\Delta\epsilon_p \frac{\partial^2 g}{\partial q \partial H^\alpha} + \Delta\epsilon_q \frac{\partial^2 g}{\partial p \partial H^\alpha}\right) c_{\alpha\beta}\frac{\partial h^\beta}{\partial \Delta\epsilon_q} \tag{B.24}$$

$$B'_{11} = \frac{1}{3}\Delta\epsilon_p\left(\frac{\partial^2 g}{\partial p \partial q} + \sum_{\alpha=1}^{n}\sum_{\beta=1}^{n}\frac{\partial^2 \phi}{\partial q \partial H^\alpha} c_{\alpha\beta}\frac{\partial h^\beta}{\partial p}\right) + \frac{1}{3}\Delta\epsilon_q\left(\frac{\partial^2 g}{\partial p^2} + \sum_{\alpha=1}^{n}\sum_{\beta=1}^{n}\frac{\partial^2 \phi}{\partial p \partial H^\alpha} c_{\alpha\beta}\frac{\partial h^\beta}{\partial p}\right) \tag{B.25}$$

$$B'_{12} = -\Delta\epsilon_p\left(\frac{\partial^2 g}{\partial q^2} + \sum_{\alpha=1}^{n}\sum_{\beta=1}^{n}\frac{\partial^2 \phi}{\partial q \partial H^\alpha} c_{\alpha\beta}\frac{\partial h^\beta}{\partial q}\right) - \Delta\epsilon_q\left(\frac{\partial^2 g}{\partial p \partial q} + \sum_{\alpha=1}^{n}\sum_{\beta=1}^{n}\frac{\partial^2 \phi}{\partial p \partial H^\alpha} c_{\alpha\beta}\frac{\partial h^\beta}{\partial q}\right) \tag{B.26}$$

$$A'_{21} = \sum_{\alpha=1}^{n}\sum_{\beta=1}^{n}\frac{\partial \phi}{\partial H^\alpha} c_{\alpha\beta}\frac{\partial h^\beta}{\partial \Delta\epsilon_p} \quad \text{and} \quad A'_{22} = \sum_{\alpha=1}^{n}\sum_{\beta=1}^{n}\frac{\partial \phi}{\partial H^\alpha} c_{\alpha\beta}\frac{\partial h^\beta}{\partial \Delta\epsilon_q} \tag{B.27}$$

$$B'_{21} = -\left[\frac{\partial \phi}{\partial q} + \sum_{\alpha=1}^{n}\sum_{\beta=1}^{n}\frac{\partial \phi}{\partial H^\alpha} c_{\alpha\beta}\frac{\partial h^\beta}{\partial q}\right] \tag{B.28}$$

$$B'_{22} = \frac{1}{3}\left[\frac{\partial \phi}{\partial p} + \sum_{\alpha=1}^{n}\sum_{\beta=1}^{n}\frac{\partial \phi}{\partial H^\alpha} c_{\alpha\beta}\frac{\partial h^\beta}{\partial p}\right] \tag{B.29}$$

B.5 List of derivations for GTN model

In this section, in order to simplify the notation, $sinh$ and $cosh$ are refereed to $sinh(-\frac{3q_2}{2}\frac{p}{\sigma_0})$ and $cosh(-\frac{3q_2}{2}\frac{p}{\sigma_0})$.

- Yield surface: associative plasticity: $g = \phi = \phi(p,q,\underline{\boldsymbol{H}}^{\alpha}) = \left(\frac{q}{\sigma_0}\right)^2 + 2q_1 f^* cosh(-\frac{3q_2}{2}\frac{p}{\sigma_0}) - 1 - q_3 f^{*2}$.
- Internal state variables:

$$\Delta\overline{\epsilon}^p = \Delta H^1 = h^1 = \frac{-p\Delta\epsilon_p + q\Delta\epsilon_q}{(1-f)\sigma_0} \tag{B.30}$$

$$\Delta f = \Delta H^2 = h^2 = (1-f)\Delta\epsilon_p + A(\overline{\epsilon}^p)\Delta\overline{\epsilon}^p \tag{B.31}$$

  where $A(\overline{\epsilon}^p)$ was defined in Eq. 4.62.

- Derivations appear in Eq. B.3:

$$\frac{\partial\phi}{\partial p} = -\frac{3q_1q_2f^*sinh}{\sigma_0} \quad , \quad \frac{\partial^2\phi}{\partial p^2} = \frac{9}{2}\frac{q_1q_2^2f^*}{\sigma_0^2}cosh \quad , \quad \frac{\partial\phi}{\partial q} = \frac{2q}{\sigma_0^2} \quad , \quad \frac{\partial^2\phi}{\partial q\partial p} = 0 \tag{B.32}$$

$$\frac{\partial^2\phi}{\partial q\partial H^1} = \frac{\partial^2\phi}{\partial q\partial\overline{\epsilon}^p} = -\frac{4qH}{\sigma_0^3} \tag{B.33}$$

$$\frac{\partial^2\phi}{\partial q\partial H^2} = \frac{\partial^2\phi}{\partial q\partial f} = 0 \tag{B.34}$$

$$\frac{\partial^2\phi}{\partial p\partial H^1} = \frac{\partial^2\phi}{\partial p\partial\overline{\epsilon}^p} = \left(-\frac{3q_1q_2sinh}{\sigma_0}\right)\frac{df^*}{df} \tag{B.35}$$

$$\frac{\partial^2\phi}{\partial p\partial H^2} = \frac{\partial^2\phi}{\partial p\partial f} = \left(\frac{3q_1q_2f^*H}{\sigma_0^2}sinh - \frac{9}{2}\frac{q_1q_2^2pHf^*}{\sigma_0^3}cosh\right)\frac{df^*}{df} \tag{B.36}$$

- The derivation of $\frac{\partial H^\alpha}{\partial\Delta\epsilon_p}$ and $\frac{\partial H^\alpha}{\partial\Delta\epsilon_q}$ with $\alpha = 1,2$ can be obtained from Eq. B.14, which requires the following partial derivations of h_1 and h_2:

$$\frac{\partial h_1}{\partial\Delta\epsilon_p} = \frac{-p - K\Delta\epsilon_p}{(1-f)\sigma_0} \quad , \quad \frac{\partial h_1}{\partial\Delta\epsilon_q} = \frac{q - 3G\Delta\epsilon_q}{(1-f)\sigma_0} \tag{B.37}$$

$$\frac{\partial h_2}{\partial\Delta\epsilon_p} = (1-f) - A\frac{p + K\Delta\epsilon_p}{(1-f)\sigma_0} \quad , \quad \frac{\partial h_2}{\partial\Delta\epsilon_q} = A\frac{q - 3G\Delta\epsilon_q}{(1-f)\sigma_0} \tag{B.38}$$

$$\frac{\partial h_1}{\partial p} = \frac{-\Delta\epsilon_p}{(1-f)\sigma_0} \quad , \quad \frac{\partial h_1}{\partial q} = \frac{\Delta\epsilon_q}{(1-f)\sigma_0} \tag{B.39}$$

$$\frac{\partial h_2}{\partial p} = -A\frac{\Delta\epsilon_p}{(1-f)\sigma_0} \quad , \quad \frac{\partial h_2}{\partial q} = A\frac{\Delta\epsilon_q}{(1-f)\sigma_0} \tag{B.40}$$

$$\frac{\partial h_1}{\partial H^1} = -H\frac{-p\Delta\epsilon_p + q\Delta\epsilon_q}{(1-f)\sigma_0^2} \quad , \quad \frac{\partial h_1}{\partial H^2} = \frac{-p\Delta\epsilon_p + q\Delta\epsilon_q}{(1-f)^2\sigma_0} \tag{B.41}$$

$$\frac{\partial h_2}{\partial H^1} = \frac{dA}{d\overline{\epsilon}^p}\Delta H^1 - AH\frac{-p\Delta\epsilon_p + q\Delta\epsilon_q}{(1-f)\sigma_0^2} \quad , \quad \frac{\partial h_2}{\partial H^2} = -\Delta\epsilon_p + A\frac{-p\Delta\epsilon_p + q\Delta\epsilon_q}{(1-f)^2\sigma_0} \tag{B.42}$$

- Derivations of the yield surface with respect to the internal state variables:

$$\frac{\partial\phi}{\partial H^1} = -\frac{2q^2H}{\sigma_0^3} + \frac{3q_1q_2f^*pH}{\sigma_0^2}sinh \tag{B.43}$$

$$\frac{\partial\phi}{\partial H^2} = (2q_1cosh - 2f^*q_3)\frac{df^*}{df} \tag{B.44}$$

$H = \frac{\partial\sigma_0}{\partial\overline{\epsilon}^p}$

- Additional derivations for B.3 and B.4:

$$\frac{\partial^2\phi}{\partial p\partial H^1} = \frac{3q_1q_2f^*H}{\sigma_0^2}sinh - \frac{9}{2}\frac{q_1q_2^2pHf^*}{\sigma_0^3}cosh \tag{B.45}$$

$$\frac{\partial^2\phi}{\partial p\partial H^2} = -\frac{3q_1q_2}{\sigma_0}sinh\frac{df^*}{df} \tag{B.46}$$

$$\frac{\partial^2\phi}{\partial q\partial H^1} = \frac{-4qH}{\sigma_0^3} \tag{B.47}$$

$$\frac{\partial^2\phi}{\partial q\partial H^2} = 0 \tag{B.48}$$

B.6 Hessian contribution for global assembly

This section details the calculation of $\frac{\partial \mathbf{R}_e^{p'}}{\partial \vec{\mathbf{v}}^I}$ and $\frac{\partial \mathbf{R}_e^{p'}}{\partial p_h}$ appeared in Eq. 4.122 and Eq. 4.123. The latter derivation is straightforward. The calculation of the first derivation leads to the calculation of the following terms: (1): $\frac{\partial\dot{\lambda}}{\partial\dot{\boldsymbol{\epsilon}}(\vec{\mathbf{v}}^I)}$ and (2): $\frac{\partial}{\partial\dot{\boldsymbol{\epsilon}}(\vec{\mathbf{v}}^I)}\left(\frac{\partial g}{\partial p}\right)$.

(1) Starting from: $\Delta\lambda = \Delta\epsilon_q\left(\frac{\partial g}{\partial q}\right)^{-1}$ (Eq. 4.40), one can obtain:

$$\frac{\partial\dot{\lambda}}{\partial\dot{\boldsymbol{\epsilon}}(\vec{\mathbf{v}}^I)} = \frac{\partial\Delta\lambda}{\partial\boldsymbol{\epsilon}(\vec{\mathbf{v}}^I)} = \frac{\partial\Delta\epsilon_q}{\partial\boldsymbol{\epsilon}}\left(\frac{\partial g}{\partial q}\right)^{-1} + \Delta\epsilon_q\frac{\partial}{\partial\boldsymbol{\epsilon}}\left(\frac{\partial g}{\partial q}\right) \tag{B.49}$$

By accounting for $\Delta\epsilon_q = \frac{q^T-q}{3G}$, the above equation can be rearranged as:

$$\frac{\partial\Delta\lambda}{\partial\boldsymbol{\epsilon}} = \frac{\left(\frac{\partial q^T}{\partial\boldsymbol{\epsilon}} - \frac{\partial q}{\partial\boldsymbol{\epsilon}} - \Delta\epsilon_q\frac{\partial}{\partial\boldsymbol{\epsilon}}\left(\frac{\partial g}{\partial q}\right)3G\left(\frac{\partial g}{\partial q}\right)^{-1}\right)}{3G\left(\frac{\partial g}{\partial q}\right)} \tag{B.50}$$

The right hand side of Eq. B.50 can be obtained by introducing the following derivations:

$$\frac{\partial q^T}{\partial\boldsymbol{\epsilon}} = \frac{3G}{q^T}\underset{\sim}{\boldsymbol{J}}.\boldsymbol{s}^T \tag{B.51}$$

$$\frac{\partial q}{\partial\boldsymbol{\epsilon}} = \frac{3}{2q}\frac{\partial\boldsymbol{s}}{\partial\boldsymbol{\epsilon}}.\boldsymbol{s} \tag{B.52}$$

$$\frac{\partial}{\partial\boldsymbol{\epsilon}}\left(\frac{\partial g}{\partial q}\right) = \frac{2}{\sigma_0^2}\frac{\partial q}{\partial\boldsymbol{\epsilon}} - \frac{4}{\sigma_0^3}H\frac{\partial\overline{\epsilon}^p}{\partial\boldsymbol{\epsilon}} \tag{B.53}$$

(2) From Eq. B.32, $\frac{\partial g}{\partial p}$ is the function of f, p and σ_0. Therefore, its derivation with respect to $\boldsymbol{\epsilon}$ can be written as:

$$\frac{\partial}{\partial\dot{\boldsymbol{\epsilon}}}\left(\frac{\partial g}{\partial p}\right) = \frac{\partial}{\partial\boldsymbol{\epsilon}}\left(\frac{\partial g}{\partial p}\right).dt = \left[\frac{\partial}{\partial f}\left(\frac{\partial g}{\partial p}\right)\frac{\partial f}{\partial\boldsymbol{\epsilon}} + \frac{\partial}{\partial\sigma_0}\left(\frac{\partial g}{\partial p}\right)\frac{\partial\sigma_0}{\partial\boldsymbol{\epsilon}} + \frac{\partial}{\partial p}\left(\frac{\partial g}{\partial p}\right)\frac{\partial p}{\partial\boldsymbol{\epsilon}}\right].dt \tag{B.54}$$

Note that for a pure hydrostatic loading case (e.g. hydrostatic tension case in section 4.4.2.1), since $q = 0$, the calculation of $\frac{\partial\Delta\lambda}{\partial\boldsymbol{\epsilon}}$ is based on $\Delta\lambda = -\Delta\epsilon_p\left(\frac{\partial g}{\partial p}\right)^{-1}$ (Eq. 4.39) with a same procedure.

Appendix C

Supplementary results

C.1 Lemaitre model identification for a stainless steel - Applications to forming processes.

C.1.1 Identification of Lemaitre model

In this section, the Lemaitre model identification result for the studied stainless steel is presented. The identification was carried out by inverse analysis using the load-displacement curve of tensile test on RB, which was based on softening effect of damage (see section 3.4 for the identification of B&W model). Fig. C.1 represents the comparison between experimental and numerical curves with or without damage coupling.

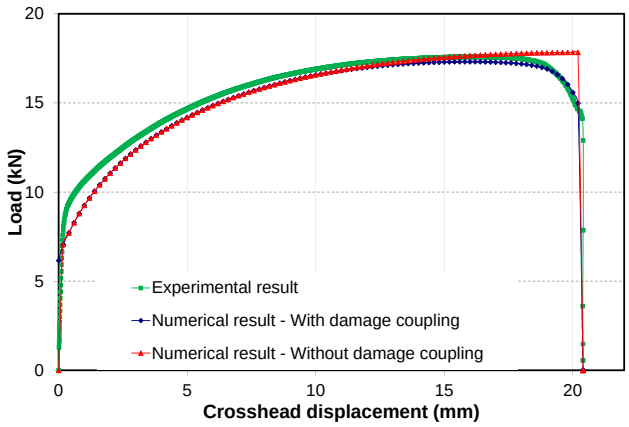

Fig. C.1: *Comparison between experimental and numerical load-displacement curves of tensile test on RB. The curve with damage coupling takes into account the softening of damage, using the Lemaitre model.*

As can be observed in Fig. C.1, damage coupling allows modeling accurately the softening of material during tensile test. Note that the curve without coupling was obtained with the hardening law identified in section 2.4.3.2. The identified parameters are presented in Table C.1. The critical value of damage where fracture occurs is $D_c = 0.321$.

Lemaitre			
$S(MPa)$	s	ϵ_D	D_c
4.5	2	0.202	0.321

Table C.1: *Identified Lemaitre damage model parameters for the stainless steel.*

C.1.2 Application to forming processes

This section presents the application of the identified Lemaitre model to two forming processes: wire drawing and rolling. Descriptions of these processes are given in section 6.2.1.

C.1.2.1 Wire drawing process

Fig. C.2 represents the contour plot of damage in 8 passes of drawing.

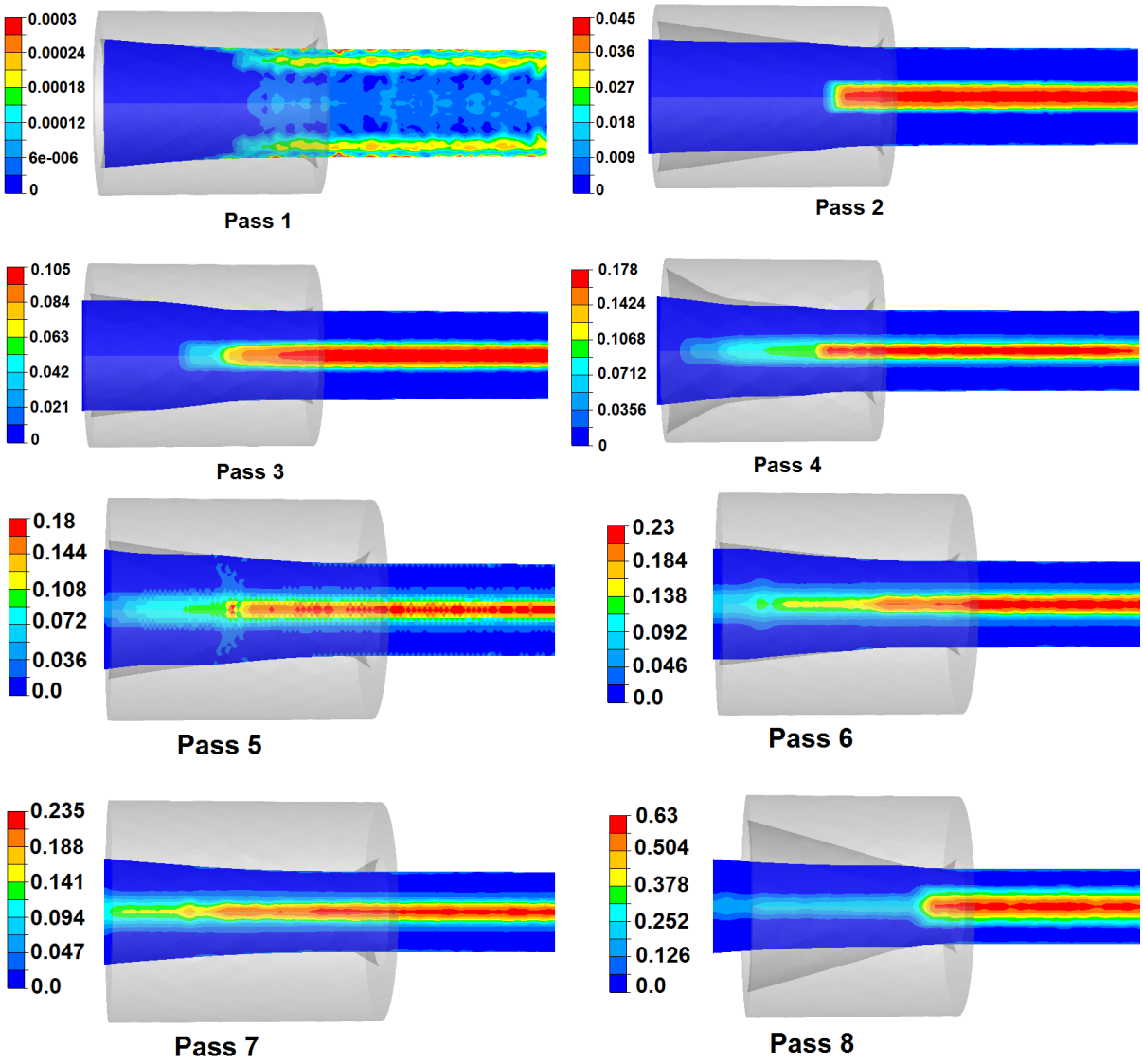

Fig. C.2: *Lemaitre damage parameter along the 8 passes of wire drawing*

Except for the first pass, damage is higher in the wire core (similar to B&W model - section 6.2.2.1) because the semi angle is small and the contact length is high, shear effect on the surface is important. However, the Lemaitre damage variable is strongly localized in the wire core, while for the B&W model, damage changes gradually from the wire core to the wire surface. Moreover, damage increment after the first pass is significantly small because of the presence of the strain threshold ϵ_D in the Lemaitre model.

As we identified above (Table C.1), the critical value of this model is $D_c = 0.321$. At the exit of 7^{th} pass, the maximum damage value in wire core was still below this critical value ($D_{max} \approx 0.235$ at exit). However, at the exit of 8^{th} pass, the maximum value of damage in the wire core reached 0.63 ($> D_c$), which means fracture occurred. In order to better understand the evolution of damage in the last pass, numerical sensor was set up at the wire center, where damage was highest.

Fig. C.3a represents the evolution of the equivalent strain and the strain rate while Fig. C.3b represents the evolution of the triaxiality and the damage variable.

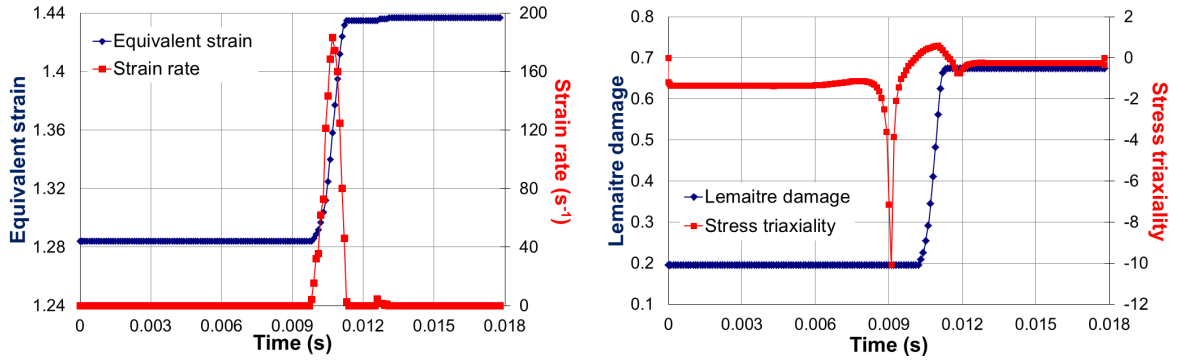

(a) (b)

Fig. C.3: *Evolution of strain rate and equivalent plastic strain (a); triaxiality and damage (b) during the* 8^{th} *drawing pass.*

In Fig. C.3a, the strain-rate becomes positive when the numerical sensor enters working zone (time $\in [0{,}01 : 0.11]s$). As shown in section 6.1.1, damage accumulation only takes place in this working zone and we observe a sharp increase of cumulative plastic strain (blue curve in Fig. C.3a) and damage (blue curve in Fig. C.3b). Moreover, the positive stress triaxiality favors the increase of damage, which explains the sharp increase of damage after 8^{th} pass[1].

C.1.2.2 Rolling process

Fig. C.4 represents the contour plot of Lemaitre damage variable at the end of rolling process (5^{th} pass).

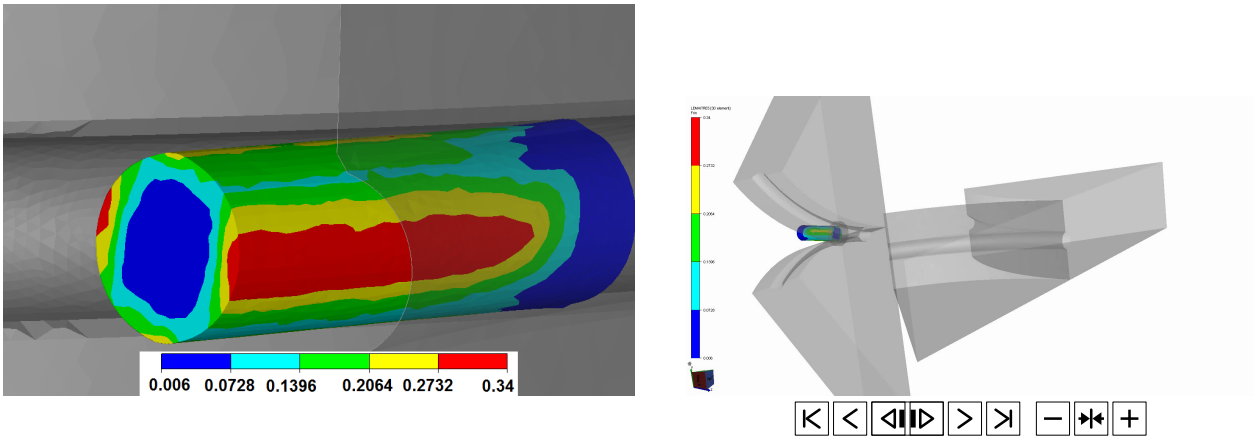

Fig. C.4: *Damage at the end of* 5^{th} *rolling pass. An illustration of the last pass of the studied process shown on the right (it is a video, which can be watched in the electronic version of the thesis).*

Damage is higher on the lateral surface, in which the maximum value ($D_{max} \approx 0.34$) is higher than the critical value, which means failure. As explained in section 6.2.2.2 and Fig. 6.18b, except the first pass, all other rolling passes used 2+2 technology (i.e. wire passed successively a vertical stand then a horizontal stand). In order to know exactly the instant of fracture (i.e. the instant when damage variable attained its critical value), numerical sensor was set up at the lateral surface, where damage was highest. The evolutions of different variables are presented in Figs. C.5a and C.5b.

In Fig. C.5a, when strain rate was positive, that was the instant that the studied material point on rolled wire surface entered the rolls. Since the first stand was a horizontal stand and the studied material point was

[1]The sharp increase of damage is also due to the non-linear evolution of Lemaitre damage variable.

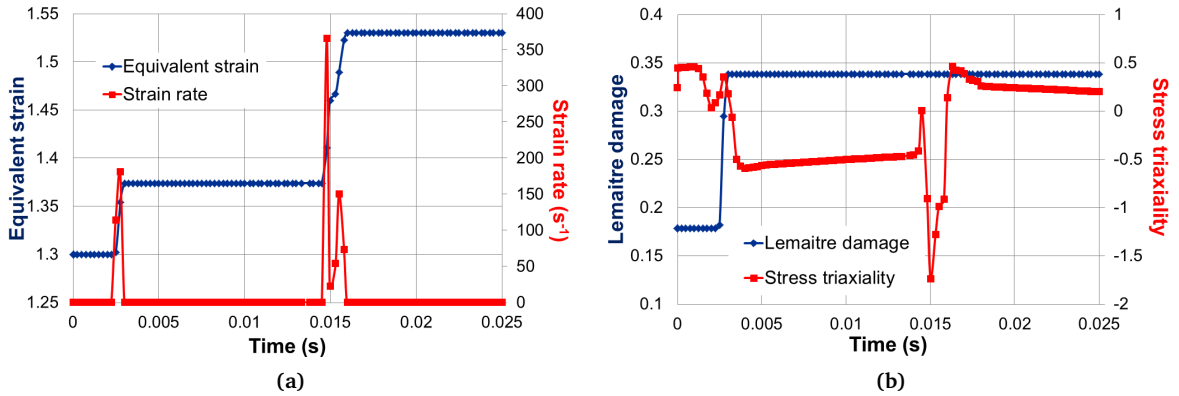

Fig. C.5: *Evolution of strain rate and equivalent plastic strain (a); triaxiality and damage (b) during the* 5^{th} *rolling pass (sharp peak observed is due to the storage time).*

on the lateral horizontal surface, it did not enter in contact with rolls. At this point, material underwent a lateral extension due to vertical force (similar to barreling zone in compression test), the stress triaxiality was then positive, which was confirmed by the red curve in Fig. C.5b. Therefore, when the studied material point entered the first stand, strain rate and triaxiality were positive, which led to a sharp increase of damage, as in Fig. C.5b - blue curve. Moreover, before entering this first stand, the value of damage was lower than the critical value. Fracture was predicted numerically to occur at this stage.

When this material point entered the second stand (horizontal rolls), it entered in contact with rolls, which led to a high strain rate, a sharp increase of cumulative plastic strain (Fig. C.5a), but the damage variable did not change because the stress triaxiality was highly negative (Fig. C.5b).

C.1.2.3 Conclusion of processes application with the identified Lemaitre model

The identified Lemaitre model can predict quite accurately both the localization of ductile damage (in the wire core for the wire drawing process and on the wire surface for the rolling process) and the instant of fracture. The numerical result is in good agreement with experimental result in terms of ductile fracture prediction (see section 6.2.2).

C.2 Comparison between weak and strong couplings in GTN model

This section presents the comparison between weak and strong couplings for local integration of GTN model. Weak coupling means in the local integration, at each time increment, the porosity is assumed constant during the increment and is updated at the end of increment using updated equivalent plastic strain (internal variable) and updated stress. A tensile test on notched round bar was used for validation purpose, in which specimen geometry was presented in Fig. 4.10 and loading was described as in section 4.4.1. A displacement of 1.5 mm was applied on the upper end of specimen ($v = 1mm/s$), while the other end was fixed.

The result of mechanical fields at the end of simulations are presented in Fig. C.6. We observe a good agreement between these two approaches. The time step was chosen fixed (0.01 s) and the CPU time for the two cases are equivalent.

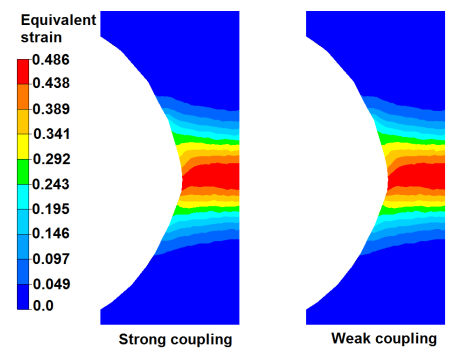

(a) *Equivalent plastic strain*

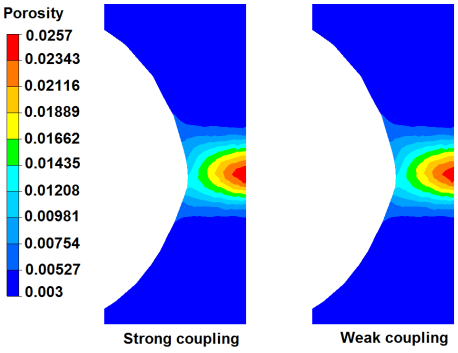

(b) *Porosity.*

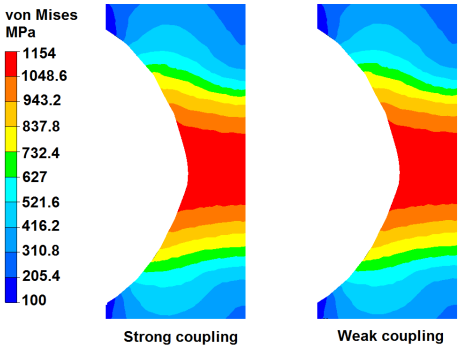

(c) *von Mises equivalent stress.*

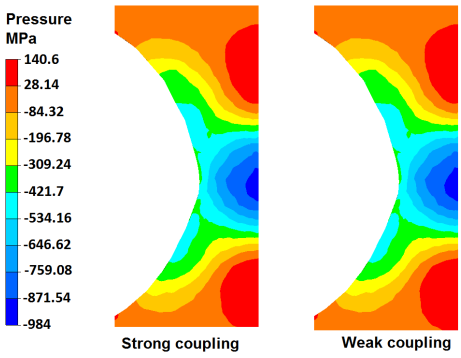

(d) *Hydrostatic pressure.*

Fig. C.6: *Comparison between the results of weak and strong couplings.*

Numerical sensors were then set up at notch center. The evolution of porosity as well as von Mises stress and mean stress are presented in Fig. C.7. A good agreement is obtained.

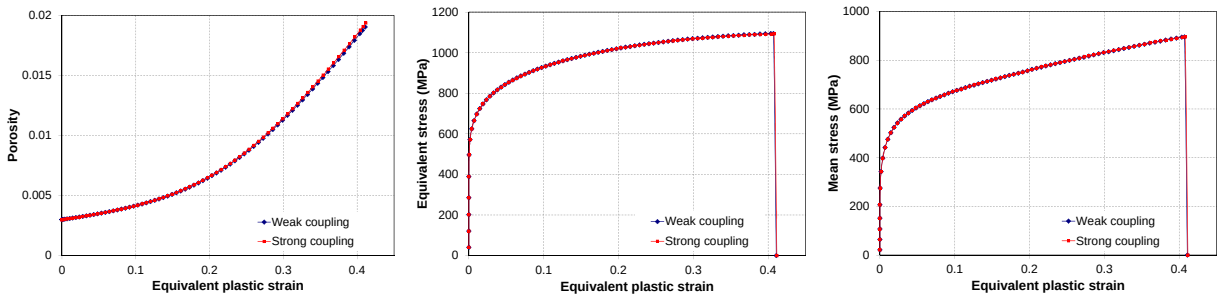

(a) *Porosity.* **(b)** *von Mises equivalent stress.* **(c)** *Mean stress.*

Fig. C.7: *Results obtained from numerical sensors at specimen notch center with two coupling methods.*

C.3 Third deviatoric stress invariant dependent plasticity - Implementation and identification

In section 2.2.3.4, the identification of the hardening law for the high carbon steel was carried out, based on axisymmetric compression and axisymmetric tension tests, using the modified Voce hardening law. A series of fracture tests on flat grooved (FG) specimens was carried out to supply more data for the identification of the B&W fracture criterion (see section 3.2.2). However, the use of the identified modified Voce hardening law for these tests shows an important difference between the experimental load-displacement curves and the numerical ones (see Figs. C.11e, C.11f, C.11g, the green and blue curves). These results raise a question on the validity of hardening model (or the J_2 plasticity criterion used) for these experiments (or for this material)[2]. Moreover, anisotropy is not the governing factor for two reasons: firstly, the specimens were machined from a same location and direction of a steel wire; secondly, the anisotropy of this material has been shown to be negligible. The difference between the two series of tensile tests (axisymmetric specimens and flat grooved specimens) is the stress state that the specimens are subjected to: axisymmetric stress state with axisymmetric specimens ($\bar{\theta} = 1$, $\eta > 1/3$) and plane strain state with flat specimens $\bar{\theta}$, $\eta > 1/\sqrt{3}$[3].

This section deals with the development and implementation of a plasticity criterion accounting for the influence of the third deviatoric stress invariant (through the Lode parameter).

C.3.1 Model analysis

C.3.1.1 Phenomenological Lode dependent functions

The following forms of yield criterion are proposed:

$$\frac{\sqrt{3J_2}}{g\left(\bar{\theta}\right)} - \sigma_0 = 0 \tag{C.1}$$

where $g\left(\bar{\theta}\right)$ is a function of the Lode parameter (or a function of J_2 and J_3); σ_0 is the flow stress of material; $\sqrt{3J_2}$ is the von Mises equivalent stress. For an axisymmetric tensile stress state, at which the modified Voce hardening model was identified:

$$\frac{\sqrt{3J_2}}{g\left(\bar{\theta} = 1\right)} - \sigma_0 = 0 \tag{C.2}$$

The von Mises condition is obtained if $g\left(\bar{\theta} = 1\right) = 1$, which means that in this case, the identified hardening parameters from the uniaxial axisymmetric tensile test with J_2 plasticity can be used. The function $g\left(\bar{\theta}\right)$ is defined to satisfy the condition: $g\left(\bar{\theta} = 1\right) = 1$. With this choice, the calibration of the flow stress function is simpler. Two types of functions for $g\left(\bar{\theta}\right)$ are investigated: polynomial and trigonometric functions.

Polynomial function The following form of polynomial function is proposed:

$$g\left(\bar{\theta}\right) = C_s + (C_{ax} - C_s)\bar{\theta}^2 \tag{C.3}$$

where $C_t = g\left(\bar{\theta} = 1\right)$ (= 1 in the present case); $C_c = g\left(\bar{\theta} = -1\right)$; $C_s = g\left(\bar{\theta} = 0\right)$, $C_{ax} = \begin{cases} C_t & ,if \quad \bar{\theta} \geq 0 \\ C_c & ,if \quad \bar{\theta} < 0 \end{cases}$

[2]Normally, these tests are rarely used to calibrate the plasticity parameters since strain field is heterogeneous. Homogeneous strain mechanical tests are preferred for plasticity calibration (e.g. uniaxial compression on cylinder when barreling is small or uniaxial tension on smooth specimen before necking).

[3]As shown in section 3.2.2, Fig. 3.7b, the plane strain state is not obtained with these specimens but the Lode parameter values are small and tend to zero when the deformation increases.

Trigonometric function Bai and Wierzbicki [Bai and Wierzbicki, 2008] proposed a Lode dependent function, which takes a trigonometric form:

$$g\left(\bar{\theta}\right) = C_s + \left(C_{ax} - C_s\right)\left(\gamma_{\bar{\theta}} - \frac{\gamma_{\bar{\theta}}^{m+1}}{m+1}\right) \tag{C.4}$$

where $\gamma_{\bar{\theta}} = \frac{\sqrt{3}}{2-\sqrt{3}}\left[\frac{1}{\cos(\bar{\theta}\pi/6)} - 1\right]$, which respects the conditions: $\gamma_{\bar{\theta}}(\bar{\theta}=1) = 1$, $\gamma_{\bar{\theta}}(\bar{\theta}=0) = 0$ and $\gamma_{\bar{\theta}}(\bar{\theta}=-1) = 1$. The high order power term $\frac{\gamma_{\bar{\theta}}^{m+1}}{m+1}$ was introduced to make the yield surface smooth and differentiable with respect to Lode angle θ around $\gamma_{\bar{\theta}} = 1$.

C.3.1.2 Discussion about the proposed polynomial function

Here, a short comparison between the proposed Lode dependence function (polynomial form) and that proposed by Bai & Wierzbicki is presented by investigating the yield loci in plane stress state. Similar to B&W function, a high order term is added to the proposed polynomial function to obtain a smooth yield surface around $\bar{\theta} = \pm 1$:

$$g\left(\bar{\theta}\right) = C_s + \left(C_{ax} - C_s\right)\left(\bar{\theta}^2 - \frac{\bar{\theta}^{2k}}{2k}\right) \tag{C.5}$$

The yield surfaces are compared in Fig. C.8.

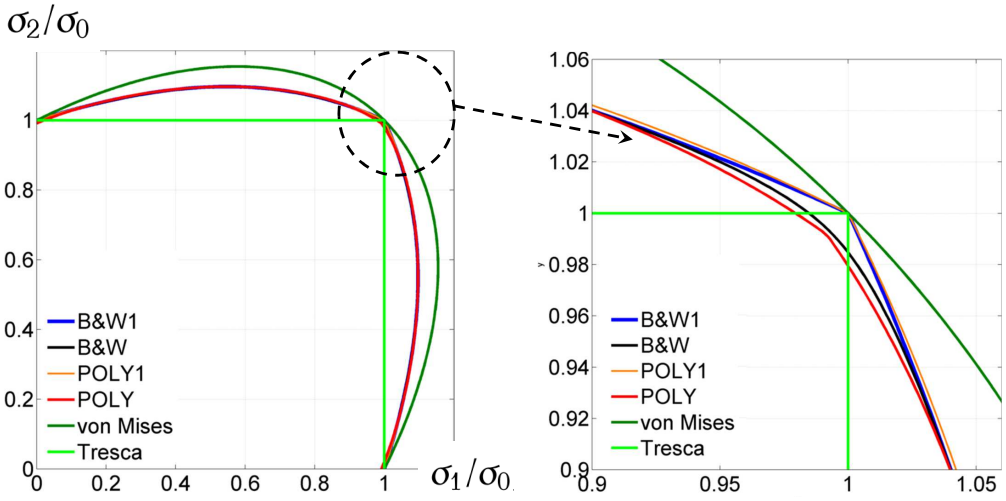

Fig. C.8: *Comparison of von Mises (vM), Bai & Wierzbicki (B&W), and the proposed yield surfaces with polynomial function in plane stress condition (POLY). The B&W1 surface is the function without the high order term* $\frac{\gamma_{\bar{\theta}}^{m+1}}{m+1}$ *and the B&W yield surface obtained with* $C_c = C_t = 1$, $C_s = 0.95$ *and* $m = 6$. *The POLY1 is the yield surface using polynomial function without the high order term (Eq. C.3); the POLY surface is the yield surface using polynomial function with the high order term (*$k = 3$ *- Eq. C.5).*

From Fig. C.8, the yield surfaces obtained with the two above-mentioned formulations are nearly coincident, except at the "corners" (where $\bar{\theta} = \pm 1$). Introduction of the high order terms in each case help obtaining smooth surfaces around these points.

From this observation, both above-mentioned phenomenological functions could be used. In the present study, the function proposed by Bai and Wierzbicki is employed (because the results in literature are available for the validation) and it is referred to as B&W function.

C.3.2 Model implementation

C.3.2.1 Implementation

The yield criterion (Eq. C.1) can be written as:

$$\sqrt{3J_2} - \sigma_0 g\left(\bar{\theta}\right) = \sqrt{3J_2} - \sigma_0 \left[C_s + \left(C_{ax} - C_s\right)\left(\gamma_{\bar{\theta}} - \frac{\gamma_{\bar{\theta}}^{m+1}}{m+1}\right)\right] = 0 \tag{C.6}$$

Fig. C.9 shows the comparison of the von Mises, Tresca and Bai & Wierzbicki yield surfaces. The zoomed area around $\theta = 1$ reveals the sharp angle of the surface B&W1 (without the high order term $\frac{\gamma_{\bar{\theta}}^{m+1}}{m+1}$), while the B&W is smooth with the presence of this term.

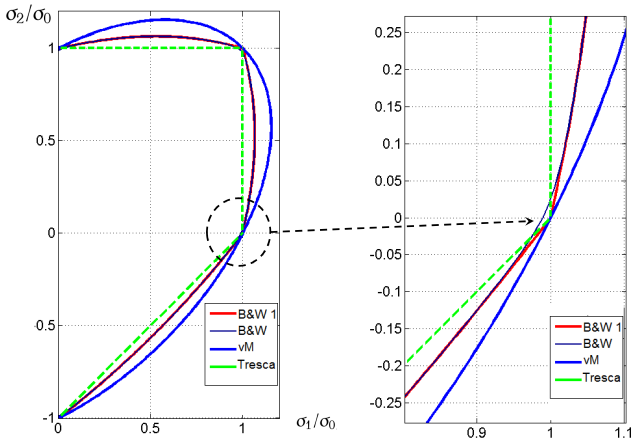

Fig. C.9: *Comparison of von Mises (vM), Tresca and Bai & Wierzbicki (B&W) yield surfaces in plane stress condition. The B&W1 surface is the function without the high order term* $\frac{\gamma_{\bar{\theta}}^{m+1}}{m+1}$ *and the B&W yield surface obtained with* $C_c = C_t = 1$, $C_s = 0.95$ *and* $m = 6$.

The implementation was simplified by using a "weak coupling": the variable of Lode parameter at time step n was used to solve the plastic constitutive equation at integration point at time step $n+1$ and was assumed constant during this time increment. This parameter was updated at the end of time step using the updated stress tensor. This weak coupling may lead to some slight error in the solution (as shown in the following section) but with less CPU time.

C.3.2.2 Validation

In order to validate the implementation, a comparison between the present development in Forge® and the simulation carried out by Bai and Wierzbicki ([Bai and Wierzbicki, 2008]) was performed. Note that in [Bai and Wierzbicki, 2008], the authors also added a pressure dependent term in the plasticity criterion:

$$\sqrt{3J_2} - \sigma_0 g\left(\bar{\theta}\right) = \sqrt{3J_2} - \sigma_0 \left(C_s + \left(C_{ax} - C_s\right)\left(\gamma_{\bar{\theta}} - \frac{\gamma_{\bar{\theta}}^{m+1}}{m+1}\right)\left[1 - c_\eta(\eta - \eta_0)\right]\right) = 0 \tag{C.7}$$

where η is the stress triaxiality; c_η and η_0 are two material parameters to be identified. In the present study, this term is not used, the yield criterion is insensitive to pressure. However, for validation purpose, this term is used only for the comparative simulations (with the choice $c_\eta = 0$, Eq. C.6 could be obtained). The tensile test on the aluminum 2024-T351 with the NRB-R4 was chosen. The diameter of the minimal cross section is 8 mm; the diameter of the specimen shoulder is 15 mm; the gauge length is 25.5 mm; the notch radius is 4 mm. The material parameters used are presented in Table C.2.

The load-displacement curves obtained with the present simulation and the simulation of Bai & Wierzbicki are compared in Fig. C.10a. Note that in this figure, the curve obtained with the present development in Forge2009® (blue curve with diamond symbols) is compared to the violet curve with star symbols since both corrections for yield criterion (pressure, Lode parameter) are accounted for[4]. A difference around 2% of load is observed in the plastic zone.

[4]The superposition of the two graphs was done using Adobe Photoshop Cs5.

Young's modulus	Poisson's ratio	Stress-strain curve	η_0	c_η	C_s	C_t	C_c	m
72400 (MPa)	0.3	$\sigma_0 = 908(0.0058 + \overline{\epsilon_p})^{0.1742}$	1/3	0.09	0.855	1.0	0.9	6

Table C.2: *Material properties of aluminum 2024-T351 used for validation simulations. Data are taken from [Bai and Wierzbicki, 2008].*

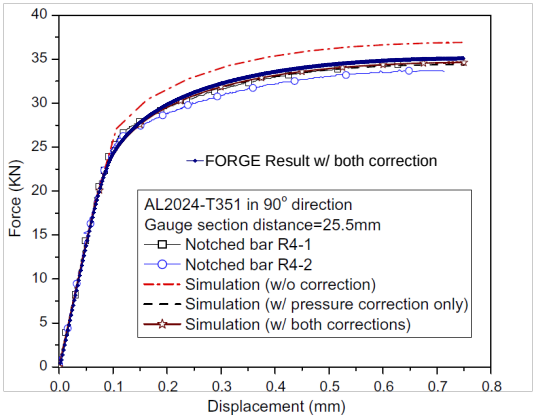

(a) *Load-displacement curves, compared with the result of [Bai and Wierzbicki, 2008]. The applied displacement is 0.75 mm.*

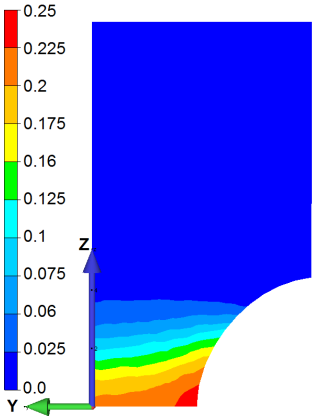

(b) *Equivalent plastic strain obtained with the present development (at 0.94 mm of displacement).*

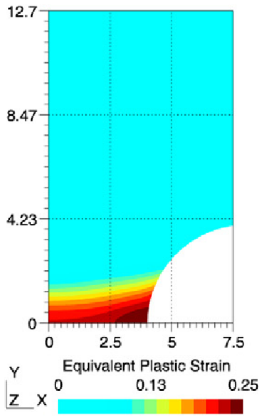

(c) *Equivalent plastic strain - result of [Malcher et al., 2012] (at 0.94 mm of displacement).*

Fig. C.10: *Results of comparative simulations obtained with the B&W yield criterion.*

In terms of local field, the comparison of the equivalent plastic strains at 0.94 mm of displacement was carried out between the present simulation and that of [Malcher et al., 2012] (see Figs. C.10b and C.10c)[5]. Note that the color scales in these figures are different: [Malcher et al., 2012] used non-uniform scale while a uniform scale is used in our result. Slight difference is also observed but negligible. Globally, the two results are in good agreement.

C.3.3 Model identification for the studied high carbon steel

The inverse analysis process was used to identify the parameters of the Lode dependent function in the yield function (Eq. C.6) based on the tensile tests on flat grooved specimens ($C_s = 0.8$) and the compression test ($C_c = 0.95$). The high order term is fixed to $m = 6$. The hardening used is the modified Voce law, identified in section 2.2.3.4 of Chapter 2 (Table 2.4), with $\sigma_{ps} = 1153.94$.

The results for tensile tests on NRB and flat-grooved specimens as well as the compression test are shown in Fig. C.11, compared with the experimental curves and the result with the modified Voce hardening law (without using the Lode dependent term).

For the axisymmetric tensile tests, the modification does not have a strong influence (Figs. C.11a, C.11b, C.11c). With the presence of the C_c term, non-symmetric plastic behavior (in tension and in compression) can be described using only an isotropic hardening law. With the identified value $C_c = 0.95 < 1$, the load-displacement curve obtained with the present development better approximates the experimental curves. Regarding the tensile tests on FG specimens, the present development helps to better capture the experimental results, although some differences still exist.

[5]Since there are no results of stress and strain fields presented in [Bai and Wierzbicki, 2008], the result of [Malcher et al., 2012] is taken. Note that in [Malcher et al., 2012], the authors presented the numerical simulations of Bai & Wierzbicki's tests with Bai & Wierzbicki's model, using their implementation in an "in house" FEM code.

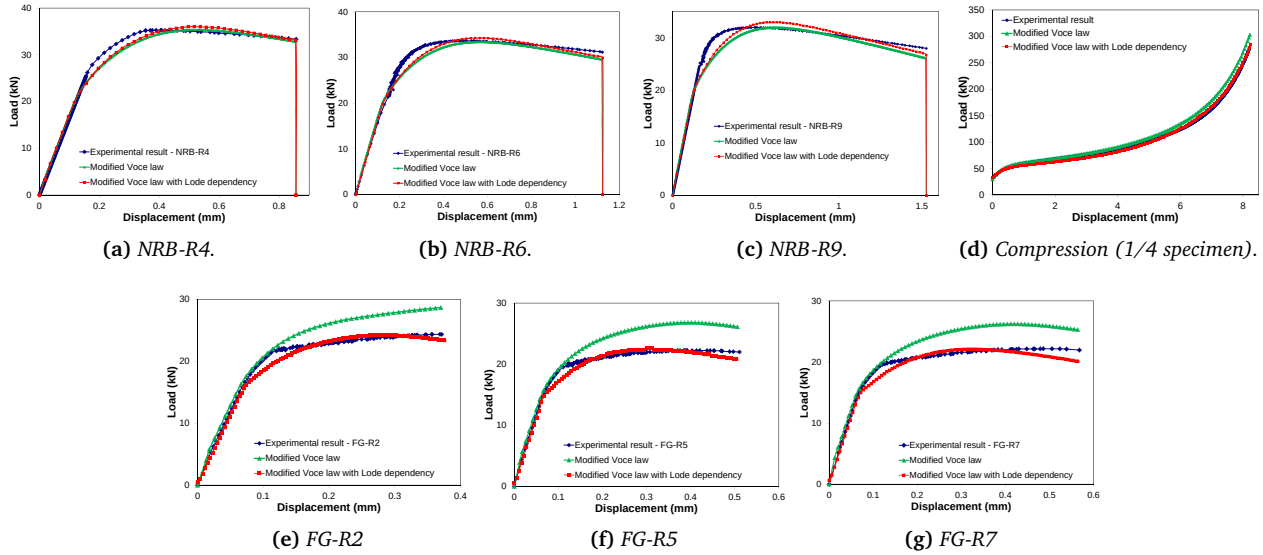

(a) *NRB-R4.* **(b)** *NRB-R6.* **(c)** *NRB-R9.* **(d)** *Compression (1/4 specimen).*

(e) *FG-R2* **(f)** *FG-R5* **(g)** *FG-R7*

Fig. C.11: *Comparison of load-displacement curves of mechanical tests using the implemented plasticity criterion and its identified parameters.*

C.3.4 Closure remarks

In this section, the Lode dependent function proposed by [Bai and Wierzbicki, 2008] has been introduced in the yield criterion to account for the influence of the third stress invariant on yielding. This modification was implemented in Forge2009® in a simplified manner. The implementation was validated by comparing with the results of [Bai and Wierzbicki, 2008] and [Malcher et al., 2012]. Finally, identification of models parameters was carried out for the studied high carbon steel and the experimental curves of tensile tests on FG specimens can be reproduced with a good agreement. However, for future applications, a full implementation is needed to have a better accuracy. Moreover, the proposed polynomial form function could be investigated in future studies.

C.4 Several simulations of damage to fracture transition

In this section, several examples of fracture modeling are presented, using the enhanced coupled Xue model, combined with remeshing technique and element removal. This method has some advantages and limitations as following:

- There is no need to define the crack path because it is based on elements removal (kill elements). Elements are removed if their damage values reach a critical value. Moreover, this method is continuous, which means one can control the whole process, from the damage growth and crack initiation, to the crack propagation.
- This approach depends on the mesh size used for both damage (because non local formulation is missing here) and crack growth (crack initiation takes the size of element). In addition, the fracture energy cannot be well controlled with this method.

C.4.1 Diagonal fracture pattern in uniaxial compression

The simulation of fracture pattern in compression test was carried out on the aluminum 2024-T351 using the material parameters presented in Table C.2 and the experimental result of [Bai and Wierzbicki, 2008]. For this compression test, the parameter of Xue model was taken from [Xue, 2007a]. The strain threshold for

damage initiation is $\epsilon_D = 0.06$ and the critical value of damage at fracture is $D_c = 0.9$. The simulation used full model of cylinder to avoid unrealistic high energy dissipation when cracks form due to symmetry. The initial diameter of the cylinder is 8 mm and the height is 11.25 mm.

The comparison between our numerical simulation of crack growth and the experimental result of [Bai and Wierzbicki, 2008] is presented in Fig. C.12. The mesh at the end of simulation is also shown in this figure.

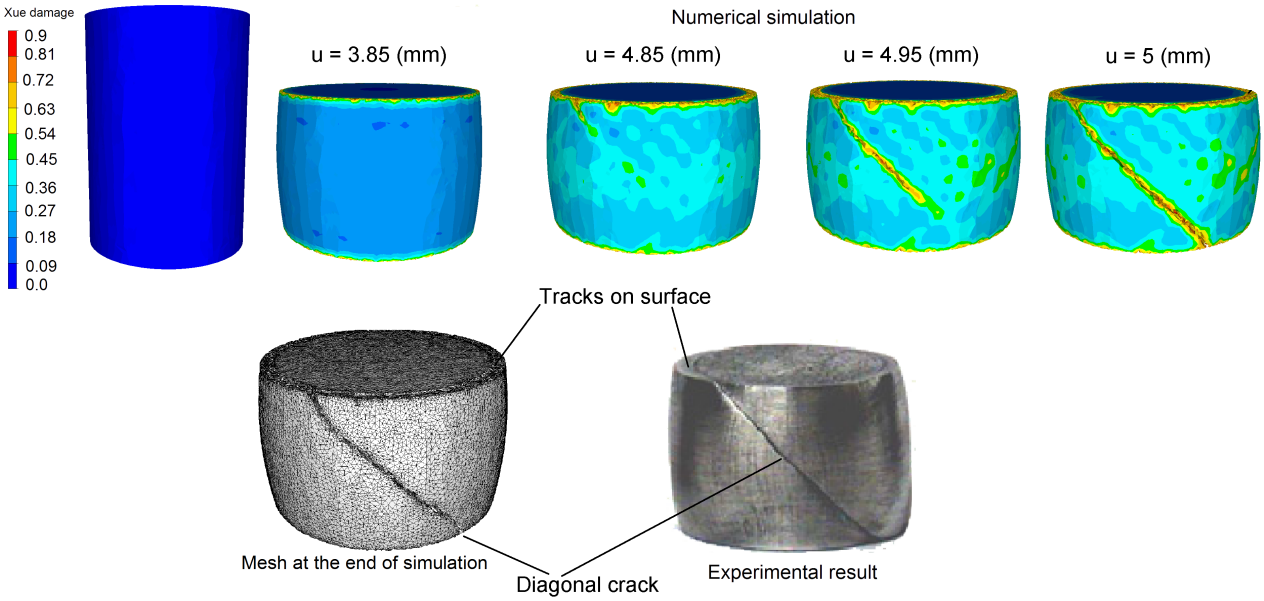

Fig. C.12: *Comparison between the simulation of crack formation in compression test and the experimental result of Bai & Wierzbicki ([Bai and Wierzbicki, 2008]).*

The numerical result is in good agreement with the experimental result regarding the fracture pattern[6].

C.4.2 Slant fracture in tensile test on FG specimen

The tensile test on FG-R7 is investigated, using our experimental result on the high carbon steel (presented in section 3.2.2). The used parameters of the enhanced Xue model are: $\epsilon_{f0} = 0.6, p_L = 1735, q = 0.236, k = 1, m = 2, \beta = 2, \gamma = 1.1, \epsilon_{DX} = 0.054, D_c = 0.6$. The experimental result of cracked specimen is represented in Fig. C.13a, showing a slant surface, while the numerical is represented in Fig. C.13b.

Fig. C.13b also reveals a lateral necking through width direction, which shows that the plane strain condition is not fulfilled. In order to better understand the crack initiation and growth, the sequence of crack formation is represented in Fig. C.14. The meshes at different instants are also shown in Fig. C.15.

As observed in Fig. C.14, crack initiates at the specimen center, then propagates through thickness following a direction about 45^o to the loading direction. Then, the crack propagates outward (through width) to totally separate the specimen. The numerical result of fracture surface is in good agreement with the experimental one.

C.4.3 Cup-cone fracture in NRB tensile test

The fracture observed in the tensile tests on round bars or NRB is often the cup-cone fracture, where crack initiates at the specimen center then propagates outward in the first stage (flat mode). A shear lip forms at the circumferential edge of the outer surface (slant mode) and a cup-cone fracture is obtained. The tensile test on NRB-R6 is investigated, using our experimental result on the high carbon steel (presented in section

[6]It must be emphasized that the use of a suitable damage model is important to capture such a fracture pattern. The Lemaitre coupled damage model was also tested but it could not produce this fracture.

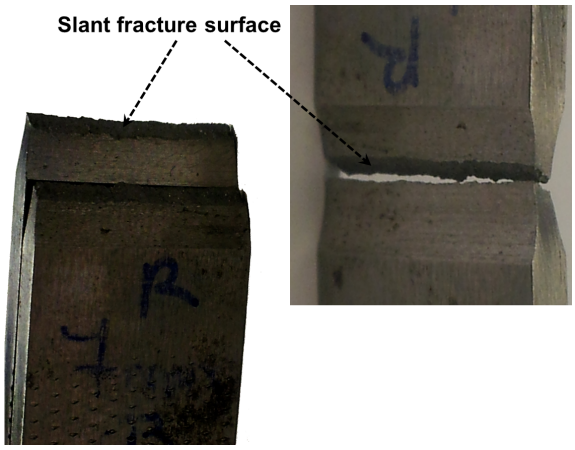

(a) *Slant fracture surface and lateral necking observed.*

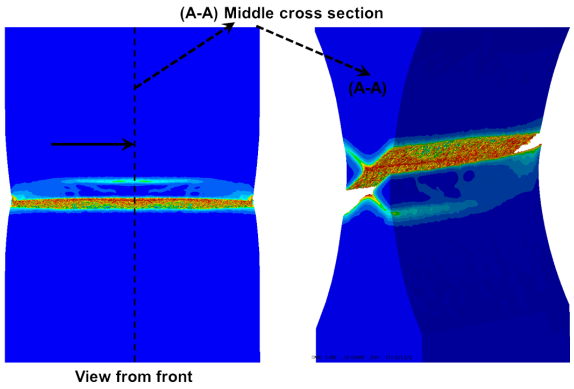

(b) *Left figure shows the lateral "necking" and the right figure shows the view from the middle cross section.*

Fig. C.13: *Comparison between the experimental (a) and numerical (b) fracture surfaces of FG-R7 specimen.*

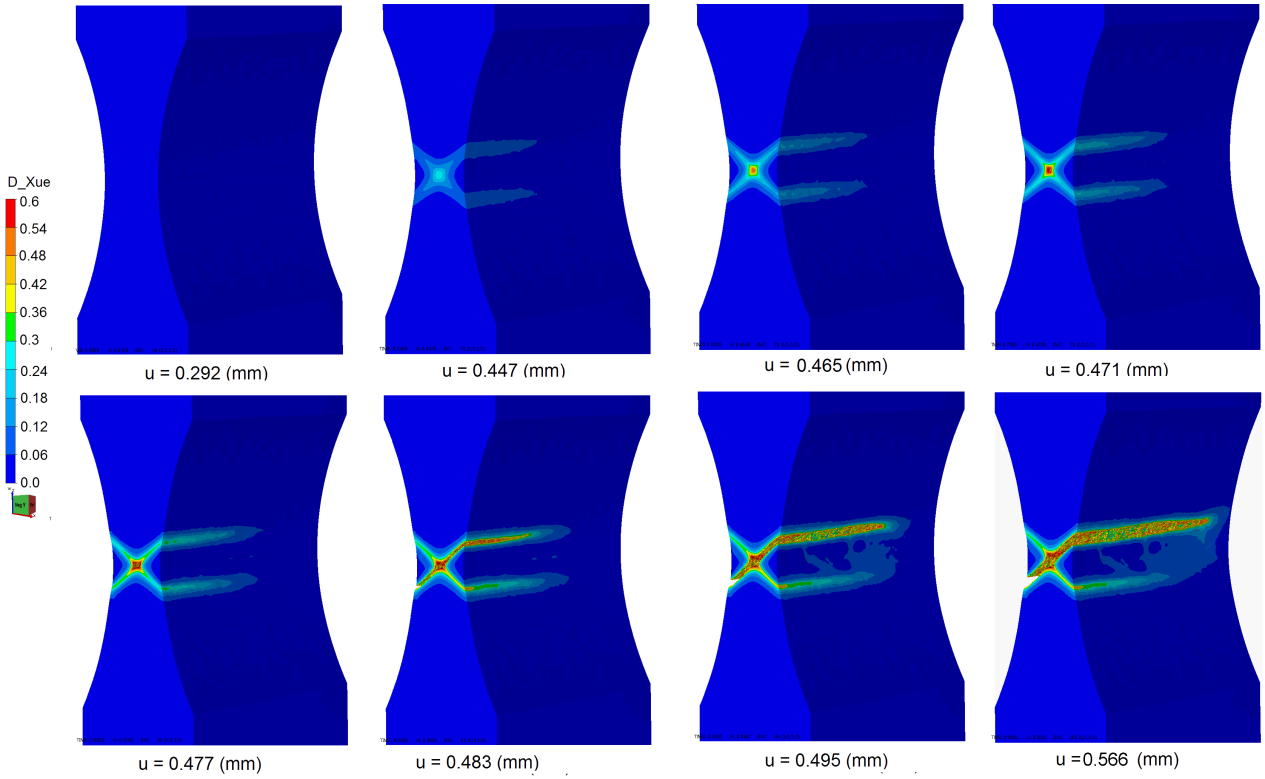

Fig. C.14: *Sequence of crack initiation and growth in tensile test on FG specimen represented on a half of the specimen.*

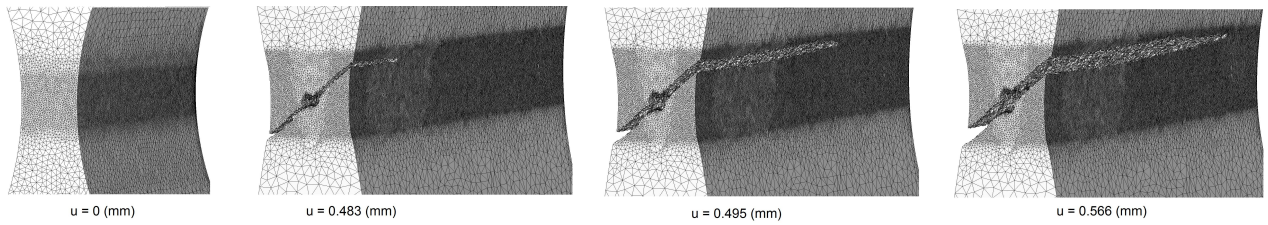

Fig. C.15: *Meshes at different instants.*

3.2.2). The same set of parameters as in section C.4.2 is used. The comparison between the experimental and numerical fracture surfaces is shown in Fig. C.16.

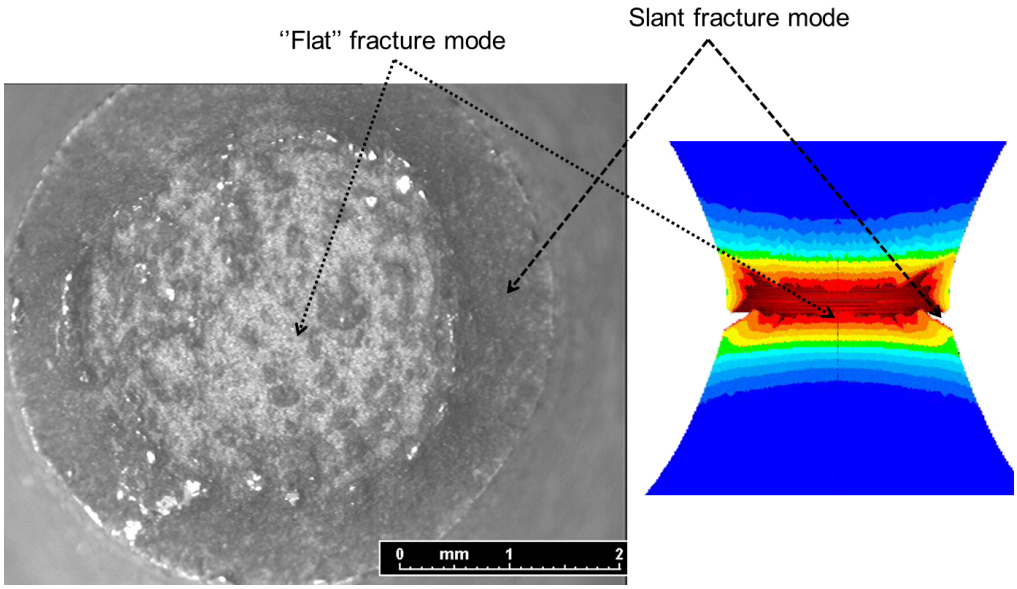

Fig. C.16: *Comparison between the experimental (left) and the numerical (right) fracture surfaces of NRB-R6 tensile specimen (view from middle vertical cross section).*

Fig. C.16 shows that the numerical simulation with the enhanced Xue model and identified parameters gives relatively correct result in terms of crack propagation prediction. The sequence of crack formation is represented in Fig. C.17. The meshes at different instants are also shown in Fig. C.18.

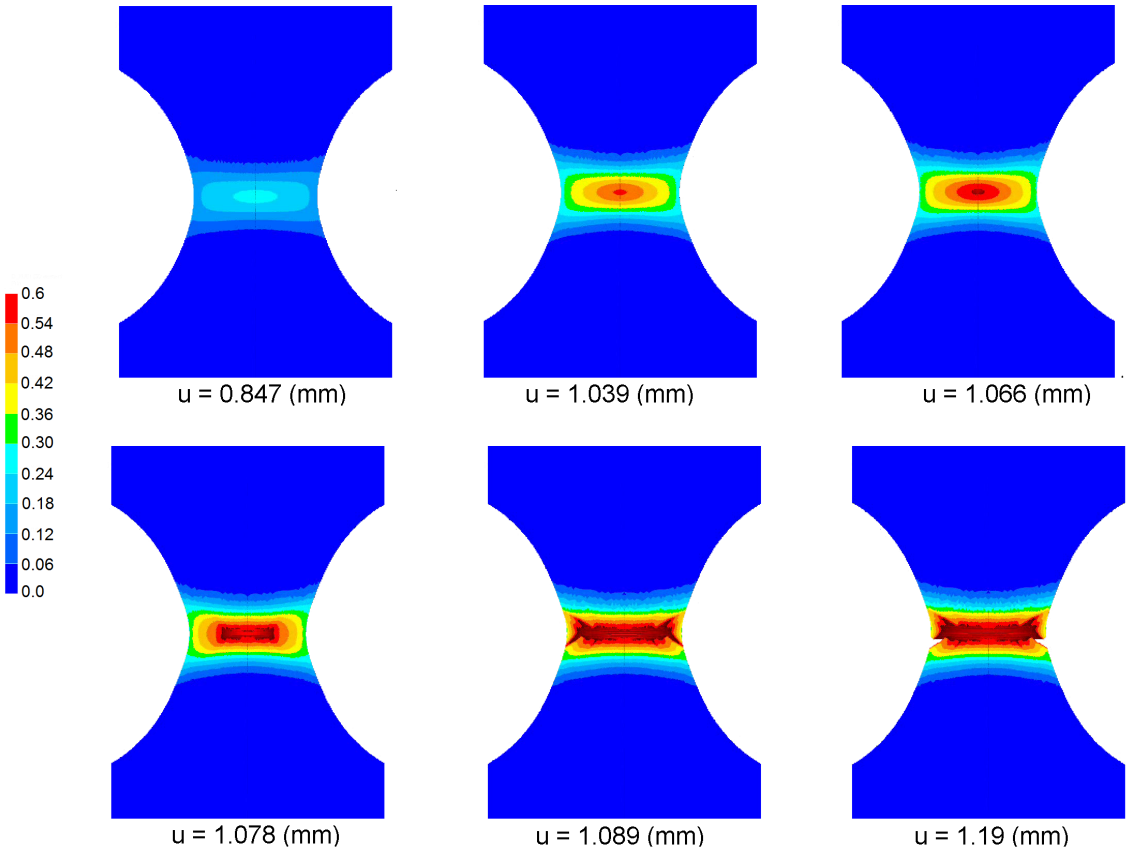

Fig. C.17: *Sequence of crack initiation and growth in tensile test on NRB-R6 specimen represented on a half of the specimen.*

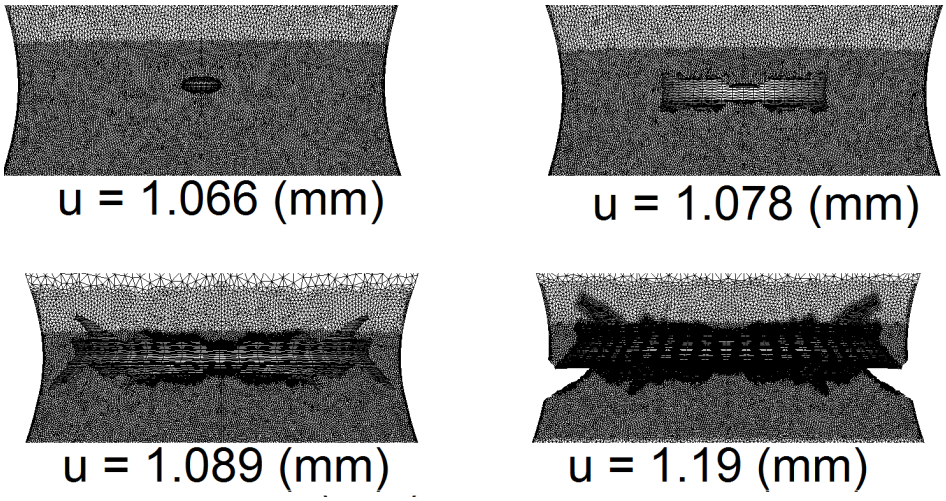

Fig. C.18: *Meshes at different instants.*

C.4.4 Closure remarks

Damage to fracture transition has become a popular topic in the ductile fracture scientific community. Indeed, the transition from a damage continuous approach to a discontinuous fracture is not straightforward both from mechanical and numerical points of view. Besson and co-workers ([Besson et al., 2001, Besson et al., 2003]) used Gurson and Rousselier models combined with a localization indicator for results analyses (based on bifurcation analysis) to model plane strain and cup-cone fractures formation. Mediavilla and coworkers ([Mediavilla et al., 2006a, Mediavilla et al., 2006]) used both coupled and uncoupled approaches and remeshing technique to propagate a crack. More recently, Feld-Payet ([Feld-Payet, 2010]) also employed this technique with a non-local formulation in a framework of three fields FE formulation to model crack propagation. El Khaoulani and Bouchard ([El Khaoulani and Bouchard, 2012]) used anisotropic mesh adaptation combined with error estimation based on the Lemaitre damage variable and its gradient to obtain a cup-cone fracture in axisymmetric tensile test. Successful applications were achieved by these authors to model principally 2D (or 2D axisymmetric) crack propagation. Seabra and coworkers [Seabra et al., 2013] proposed an approach using the XFEM technique to model crack propagation without remeshing. Once again, only 2D applications were carried out.

Despite its drawbacks, the element removal technique is a convenient way to model the damage to fracture transition for 3D configurations. Mesh dependency may deteriorate the stress field computation at the crack tip, which would be particularly problematic for brittle fracture when the crack path is computed based on stress intensity factor. For ductile fracture, the crack path is less sensitive to the local stress field at the crack tip. Fracture can be driven by ductile damage values and the use of the element erosion with a sufficiently fine mesh conducts to good crack path prediction as shown in above applications.

The enhanced coupled Xue model combined with element erosion and remeshing technique allows reproducing accurately the crack initiation and growth for different mechanical tests. Except for the compression test where the experimental result is taken from the result of Bai and Wierzbicki, the two other types of test (tension on axisymmetric and flat specimens) are compared with our experimental results on a high carbon steel, using real material parameters identified. The proposed method predicts relatively accurately different fracture modes in different loading configurations: diagonal crack in compression, slant mode in tensile test on FG specimen, cup-cone mode in tensile test on NRB specimen. It must also be emphasized that the use of a suitable damage model (as in the present study) is important to capture accurately first the localization of damage (then when damage reaches its critical value, the damage to fracture transition takes place). However, the fracture energy cannot be accurately controlled and the solution depends on mesh size. These problems will be the subject of our future study. Nevertheless, these short validations show the ability of such a continuous approach to model crack growth without the need of introducing an artificial instability.

Appendix D

Confidential information

This section regroups the confidential information concerning the high carbon steel. In the first part, all the damage models parameters identified for this material are presented. In the second part, the parameters concerning the industrial processes are given. The present appendix will be deleted from the public version of the present dissertation.

D.1 Confidential parameters - High carbon steel

Lemaitre				**Xue**								
$S(MPa)$	s	ϵ_D	D_c	ϵ_{f0}	$p_L(MPa)$	q	k	m	β	γ	D_c	ϵ_{DX}

Table D.1: *Identified damage models' parameters.*

Bai and Wierzbicki					
D_1	D_2	D_3	D_4	D_5	D_6

Table D.2: *Identified damage model parameters.*

q_1	q_2	q_3	f_0	f_f	f_N	ϵ_N	S_N

Table D.3: *Identified GTN model parameters (without coalescence).*

q_1	q_2	q_3	f_0	f_c	f_f	f_N	ϵ_N	S_N

Table D.4: *Identified GTN model parameters (with coalescence).*

D.2 Confidential processes parameters

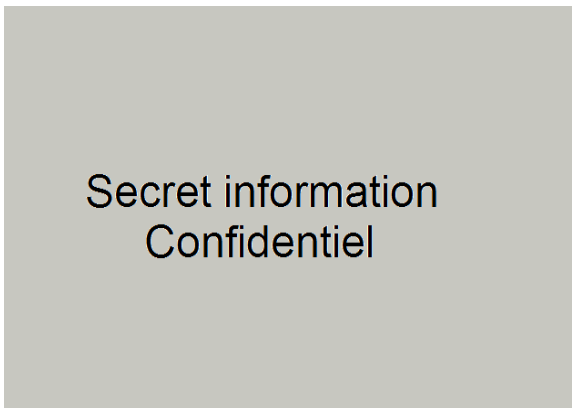

(a) *Velocity.*

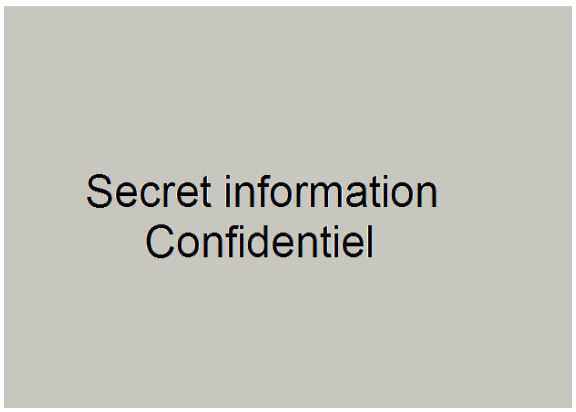

(b) *Reduction per pass.*

Fig. D.1: *Characteristics of the ultimate wire drawing studied (14 passes).*

This page is intentionally left blank.

Modélisation de l'endommagement ductile sous trajets de chargement complexes

RESUME : Ce travail de thèse vise à une meilleure compréhension et prise en compte des mécanismes d'endommagement ductile au cours des procédés de mise en forme à froid. Le tréfilage, le laminage de fils et le laminage à pas de pèlerin sont pris comme exemples d'application. Une grande attention est portée également à la méthodologie d'identification des paramètres des modèles d'endommagement implémentés. Trois approches de l'endommagement ductile ont été étudiées : des critères de rupture phénoménologique, des modèles phénoménologiques couplés et des modèles micromécaniques. Ces modèles ont été implémentés dans Forge®, et les algorithmes ont dû être adaptés à sa formulation mixte vitesse-pression et à son élément fini (P1+/P1). Parallèlement aux développements numériques, différents essais mécaniques ont été effectués sur trois matériaux différents (acier haut carbone, acier inoxydable et alliage de zirconium) pour identifier les paramètres des modèles d'écrouissage et d'endommagement. Des essais de traction in situ sous micro-tomographie aux rayons X ont été exploités pour l'identification des mécanismes d'endommagement ductile (germination, croissance et coalescence), ainsi que l'identification du modèle micromécanique. Enfin, la dernière partie de ce travail a consisté à réaliser des études comparatives de ces différents modèles d'endommagement pour les différents procédés de mise en forme et différents matériaux. Concernant le tréfilage et le laminage de l'acier inoxydable, un bon accord entre les simulations numériques et les résultats expérimentaux a été obtenu. Pour l'acier à haute teneur en carbone (perlitique), le modèle micro-mécanique GTN a donné le meilleur résultat à la fois qualitativement et quantitativement pour le tréfilage ultime. Par ailleurs, la comparaison entre les différents modèles sur différents procédés (laminage du fil avec l'acier haut carbone, laminage à pas de pèlerin avec l'alliage de zirconium) a aidé d'une part à mettre en évidence le rôle important du troisième invariant de la contrainte déviatorique sur la localisation de l'endommagement dans les procédés de mise en forme où le cisaillement est dominant. D'autre part, elle montre que le processus d'identification lui-même devrait se fonder sur la mesure de la microstructure afin de garantir un résultat précis lors de l'application aux procédés.

Mots clés : endommagement ductile, mise en forme, chargement complexe, éléments finis mixtes.

Modeling ductile damage for complex loading paths

ABSTRACT : The present PhD thesis aims at a better understanding and modeling of ductile damage mechanisms during cold forming processes, with wire drawing, rolling and cold pilgering as examples. In addition, special attention is paid to implemented damage models parameters identification methodology. All three approaches of ductile damage were investigated: uncoupled phenomenological fracture criteria; coupled phenomenological models; micromechanical model. These models have been implemented in Forge®, which required adaptation of algorithms to its mixed velocity-pressure formulation and to its finite element (P1+/P1). Parallel to the numerical work, various mechanical tests on three different materials (high carbon steel, stainless steel and zirconium alloy) were carried out for work hardening, and damage models parameters identification. In situ X-ray micro-tomography tensile tests have also been exploited for the identification of ductile damage mechanisms (nucleation, growth and coalescence) as well as the identification of micromechanical model. Finally, we carried out comparative studies of these models on our three abovementioned forming processes and materials. Regarding wire drawing and rolling of stainless steel, good agreement between numerical simulations and experimental results was found. For high carbon perlitic steel ultimate wire drawing, the GTN micro-mechanical model has given the best result, both qualitatively and quantitatively. Moreover, the comparison of the different models on different processes (wire rolling on high carbon steel, cold pilgering on zirconium alloy) highlights on the one hand the important role of the third deviatoric stress invariant in damage localization for shear-dominated forming processes. It shows on the other hand that the identification process itself should be based on microstructure measurements to provide accurate results in forming application.

Keywords: ductile damage, forming process, complex loading paths, mixed FEM

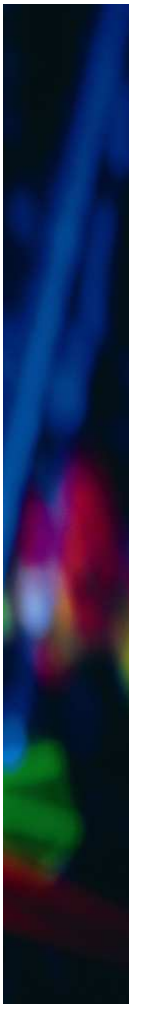

MINES ParisTech

ParisTech
INSTITUT DES SCIENCES ET TECHNOLOGIES
PARIS INSTITUTE OF TECHNOLOGY